Paolo Francesco Scaramuzzino

Flight Simulator Transfer of Training Effectiveness in Helicopter Maneuvering Flight

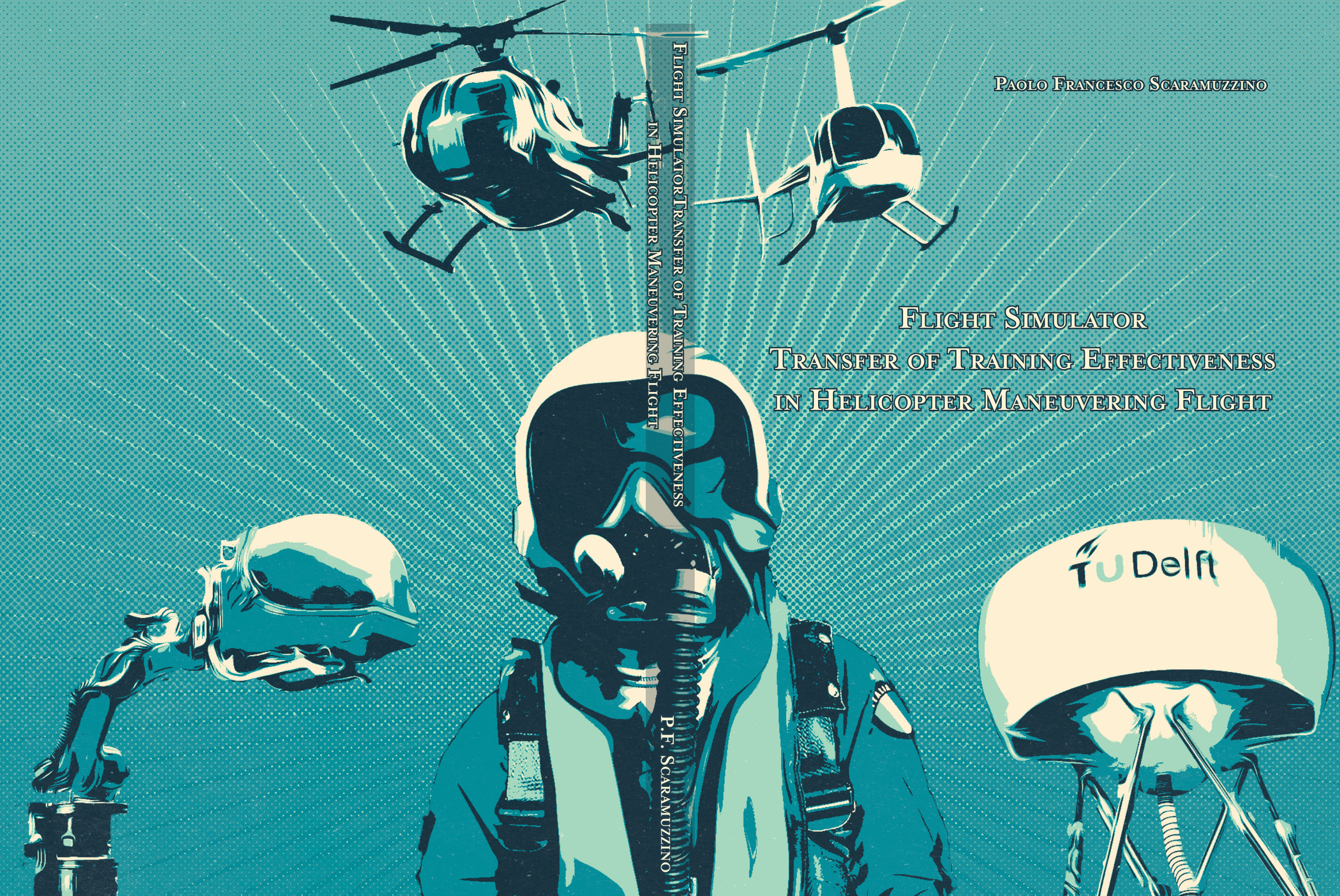

Flight Simulator Transfer of Training Effectiveness in Helicopter Maneuvering Flight

P.F. Scaramuzzino

FLIGHT SIMULATOR TRANSFER OF TRAINING EFFECTIVENESS IN HELICOPTER MANEUVERING FLIGHT

FLIGHT SIMULATOR
TRANSFER OF TRAINING EFFECTIVENESS
IN HELICOPTER MANEUVERING FLIGHT

Dissertation

for the purpose of obtaining the degree of doctor
at Delft University of Technology
by the authority of the Rector Magnificus prof. dr. ir. T.H.J.J. van der Hagen,
chair of the Board for Doctorates
to be defended publicly on Thursday 24, November 2022 at 12:30

by

Paolo Francesco SCARAMUZZINO

Master of Science in Aerospace Engineering,
Politecnico di Milano, Milano, Italy,
Born in Melito di Porto Salvo, Italy.

This dissertation has been approved by the

promotor: Dr. M. D. Pavel
promotor: Prof. dr. G. Quaranta
copromotor: Dr. ir. D. M. Pool

Composition of the doctoral committee:

Rector Magnificus,	chairperson
Dr. M. D. Pavel,	Technische Universiteit Delft, promotor
Prof. dr. G. Quaranta,	Politecnico di Milano, promotor
Dr. ir. D. M. Pool,	Technische Universiteit Delft, copromotor
Independent members:	
Prof. dr. J. Dankelman,	Technische Universiteit Delft
Prof. dr. E. L. Groen,	Cranfield University/TNO
Prof. dr. F. Topputo,	Politecnico di Milano
Prof. dr. M. White,	University of Liverpool
Prof. dr. D. Casalino,	Technische Universiteit Delft, reserve member

Prof. dr. ir. M. Mulder and Ir. O. Stroosma have contributed greatly to the preparation of this dissertation.
The doctoral research has been carried out in the context of an agreement on joint doctoral supervision between Politecnico di Milano, Italy and Delft University of Technology, the Netherlands.


The doctoral research has been carried out in the context of the European Joint Doctorate NITROS (Network for Innovative Training on Rotorcraft Safety) project. This project has received fundings from the European Union's Horizon 2020 research and innovation programme under the Marie Skłodowska-Curie grant agreement N° 721920.

Keywords: helicopter dynamics, flight simulation, transfer of training, training effectiveness, hover, autorotation

Printed by: Ipskamp Printing, Enschede, The Netherlands

Front & Back: P.F. Scaramuzzino.

Copyright © 2022 by P.F. Scaramuzzino

ISBN 978-94-6366-626-8

An electronic version of this dissertation is available at
`http://repository.tudelft.nl/`.

If you want to find the secrets of the universe,
think in terms of energy, frequency and vibration.

Nikola Tesla

Considerate la vostra semenza:
fatti non foste a viver come bruti,
ma per seguir virtute e canoscenza.

Consider your origins:
you were not made to live as brutes,
but to follow virtue and knowledge.

Dante Alighieri, Inferno

To my family

CONTENTS

SUMMARY

This research aims to advance the state-of-the-art requirements for helicopter pilot training in flight simulators contributing to the rotorcraft safety enhancement framework. It has been conducted as part of the Marie Skłodowska-Curie European Joint Doctorate NITROS (Network for Innovative Training on Rotorcraft Safety).

Training has always been the traditional answer to help pilots deal with flying vehicles and scenarios that, without adequate preparation, would otherwise be unforgiving. Due to the risks and costs involved in training for such critical circumstances, the exclusive use of in-flight training is untenable, especially for helicopters. A combination of *simulator* and *in-flight* training is the solution adopted to reduce accident rates and human fatalities in a safe and efficient manner and to fulfill the ever-harsher mandate for flawless performance required by the military domain. Inevitably, the use of simulation to support pilot training brings forward the issue of *skills and performance transfer* from the simulator to the actual aircraft, which is addressed in this thesis in relation to helicopters.

The primary focus of flight simulation *transfer-of-training* research is to assess how learning a task in a flight simulator affects the trainee's performance capabilities in the same task in the actual aircraft. To explicitly measure the transfer of behavior learned in a certain setting (e.g., a simulator) to the evaluation setting of interest (e.g., a real aircraft), transfer-of-training experiments are one of the few available methods for direct evaluation of the *training effectiveness*. To measure pilot transfer of skills at least two groups of participants are required. The speed of learning in the actual aircraft by one (or more) "experimental" group(s), previously trained in the simulator, need to be compared with the learning performance of a "control" group having received no special previous training. While this design enables to directly assess the effectiveness of a simulator, it requires strictly balanced groups according to participants' relevant prior training and experience to deliver meaningful results.

Several variations of this basic transfer model, named a *true-transfer* design, have also been proposed. The most popular is the *simulator-to-simulator* transfer model, also known as *quasi-transfer* design. In quasi-transfer experiments, participants are not transferred to the real-world setting, but to a different, often more realistic or enhanced, simulation environment. The quasi-transfer paradigm relies on the assumption that the more realistic simulator acts as a valid replacement for the actual aircraft. Although this is a strong assumption, its effectiveness for evaluating skill transfer is corroborated by experimental evidence. Furthermore, a quasi-transfer design avoids the costs, hazards, and scheduling hindrances (e.g., interruptions due to bad weather) of a true-transfer experiment and offers the possibility of safely investigating dangerous situations such as engine failures. Another issue arising from true-transfer studies (and from flight tests in general) is the reliability of the performance measurements in the real-world setting. Moreover, there are inevitable psychological differences in a pilot's mindset between

training in a simulator or in the actual aircraft. This is not necessarily a disadvantage from a training perspective, because relieving the trainee of the stress and the workload deriving from auxiliary duties (e.g., safety and flight regulation aspects, communication, periodic systems monitoring, etc.) enables devoting more mental resources to learning.

For this thesis, three quasi-transfer-of-training experiments were conducted to test the effectiveness of flight simulator training for two different helicopter tasks: *hover* and *autorotation*. The ability to hover, i.e., to remain in a nearly stationary flight condition, is the main capability that differentiates helicopters from fixed-wing aircraft. The ability to autorotate, i.e., to keep the rotor spinning by means of the airflow passing through it, is an essential emergency maneuver that enables helicopter pilots to often safely reach the closest suitable landing site in the event of an engine failure.

These two maneuvers were not randomly chosen. The choice was based on the fact that hover and autorotation pertain to different phases of the helicopter pilot training syllabus. While both maneuvers need to be mastered by helicopter pilots, hover is generally the very first maneuver that student pilots learn to perform, whereas autorotation is practiced only when the trainee demonstrates a sufficient level of proficiency in maintaining/controlling the airspeed and the rotorspeed. Therefore, hover and autorotation can be characterized as a "basic" and an "advanced" maneuver, respectively. Furthermore, hover is performed in normal operating conditions, whereas an autorotation represents an abnormal mode of operation for helicopters and is thus performed only in emergency circumstances. On the other hand, hover is performed by helicopter pilots on a daily basis (or at least every time they fly). Fortunately, nowadays engine reliability is high and they seldomly fail, meaning that real power-out autorotations are not performed often. However, to be prepared for a potential occurrence, simulated engine-failures (generally with a power-recovery, i.e., terminating in a hover) are practiced during recurrent training and proficiency checks. It is therefore evident that issues in simulator training of the hover maneuver need to be assessed especially in relation to novices (*ab-initio* training), while those in simulator training of the autorotation maneuver require a focus on experienced pilots (*recurrent* training).

The type of maneuver (e.g., basic or advanced), the operating condition (e.g., normal or abnormal mode of operation), and the trainees' characteristics (e.g., novice or experienced pilots) are all factors that play a role in the level of simulator *fidelity* needed for effective training. In contrast to the unquestioning and unceasing pursuit of high fidelity, which is typical of the simulation industry and is also supported by current regulations for flight simulator training devices, there is increasing evidence that adding more fidelity beyond a certain point results in a diminished degree of transfer of skills, especially for *nonexpert* pilots. Indeed, high fidelity also means high complexity, which generally requires more cognitive effort, thus increasing the trainee's workload, which may, in turn, impede simulator learning.

With the goal to seek more clarity with respect to the relation between fidelity and training effectiveness, a first quasi-transfer-of-training experiment was conducted, in which the simulator's objective fidelity (i.e., the quality of the cueing systems) was the independent variable. Two groups of task-naïve learners (a total of twenty-four participants) underwent a hover part-task training program, formulated according to *Cognitive Load Theory*, an instructional design theory that reflects the way humans process

information. The experimental group first trained in a low-fidelity simulator (a Computer Based Trainer at the Max Planck Institute for Byological Cybernetics) and then transferred to a high-fidelity setting (the CyberMotion Simulator at the Max Planck Institute for Byological Cybernetics), while the control group received all its training in the high-fidelity simulator. The two groups were balanced according to participants' manual control skills, which were evaluated through a pre-experimental aptitude test (a two-axes compensatory tracking task). During the evaluation phase, which both groups performed in the high-fidelity simulator, no statistically significant differences were found between the two groups in all the dependent measures. Of course, this does not directly imply that the two simulators are equally effective, as the hover part-task training program likely had a mitigating effect, supporting the idea that the lack of simulator objective fidelity can be compensated by the use of instructional design (i.e., a proper training program tailored to the trainees' needs). This can be verified in future experiments using a third group of task-naïve learners, trained with a different hover training program in the low-fidelity simulator who are then transferred to the high-fidelity setting to prove this hypothesis.

This thesis also describes two quasi-transfer-of-training experiments that focused on autorotation and had the same setup (the SIMONA Research Simulator at Delft University of Technology), but used two different helicopter flight mechanics models, characterized by a different level of fidelity. The lower-fidelity model was chosen to gain a simple understanding of the flight dynamics in autorotation, that could then be more easily extended to a higher-fidelity model. These experiments, in which the helicopter dynamics were chosen as the independent variable, were motivated by an example of in-flight-to-in-flight negative transfer of training reported in several helicopter accidents. Indeed, many engine failure accidents result from an apparent loss in rotor performance (different helicopter dynamics), which is unexpected for pilots who only practiced autorotations with a power recovery (i.e., terminating in a hover). For helicopters with free-turbine engines, even in a ground-idle setting, the engine still transmits some power to the rotor. This is a clear example of in-flight-to-in-flight negative transfer of training: practicing power-recovery autorotations (task A) interferes with learning or performing real power-out autorotations (task B) for helicopters with free-turbine engines, due to the fact that there is a crucial mismatch between the helicopter dynamics characteristics in the two task situations. Here, a pilot's mental model of the helicopter is not representative of the actual helicopter, which requires a different control strategy than learned during training.

Experienced helicopter pilots participated in the two quasi-transfer-of-training experiments on autorotation. They were divided in two groups, which were balanced according to participants' background (license type) and experience (flight hours), and performed a straight-in autorotation maneuver with two different helicopter dynamics presented in a different sequence. The two dynamics used in the experiments were selected to require a different level of pilot control compensation. To this end, a sensitivity analysis on the helicopter eigenmodes was performed to understand which design parameters control the autorotative flare index, a metric to evaluate autorotative performance in terms of available energy over required energy and thus influence helicopter dynamics in autorotation. This was achieved through the structural evaluation

and comparison of the helicopter natural modes of motion in steady-descent autorotation. Thirty-two configurations were compared by individually varying the main rotor blade chord, the main rotor radius, the main rotorspeed and the helicopter weight from the baseline value (Bo-105 helicopter) to get eight different values of the autorotation index, spanning from 5 to 40 ft^3/lb. This range was chosen after comparing the autorotative flare indices for various existing helicopters. Among these configurations, the two requiring the most and the least pilot control compensation were selected.

In the first experiment on autorotation, fourteen pilots performed the straight-in autorotation maneuver controlling a 3-degrees-of-freedom (DOF) longitudinal dynamics + rotor speed DOF model. Ten pilots performed the same task with a 6-DOF rigid-body dynamics + rotor speed DOF model in the second experiment. In both experiments clear positive transfer was found from the most to the least demanding helicopter dynamics, but not the opposite. This is observed especially for the rate of descent at touch-down, which is considered the key indicator of a smooth landing. The outcome of these two experiments suggests the need to update the current simulator training syllabus for autorotation to include a wide range of helicopter configurations with different handling characteristics. Such configurations can be obtained for example considering different models of the same helicopter family, to give to the trainee the opportunity to familiarize with helicopters with different sizes, dynamics and "feel". This can help inexperienced pilots to better understand that an autorotation is not a "by-the-numbers" procedure and that adaptability and judgement of the pilot should always cover a prominent role in the accomplishment of the task.

To strenghten the experiments on autorotation, a thourough analysis was conducted to investigate the effects of the rotorspeed degree-of-freedom in autorotation on the classical rigid-body modes. Although the developed 3-DOF and 6-DOF models are characterized by a different level of fidelity, good agreement in terms of stability characteristics of the longitudinal modes of motion was found between the two models. Especially the phugoid and the heave-subsidence modes are strongly affected by the additional rotorspeed degree of freedom, meaning that autorotation requires a different stabilization strategy by the pilot with respect to straight level flight. On the contrary, the pitch subsidence in both models and the lateral-directional modes in the 6-DOF rigid-body helicopter model do not change significantly in steady-descent in autorotation with respect to straight level flight.

In conclusion, this thesis provides enhanced insight into helicopter pilot training in flight simulators by addressing two critical training tasks, hover (Part I of this thesis) and autorotation (Part II of this thesis), that represent two of a helicopter's most unique capabilities. With these new insights, this thesis lays the foundations for an enhanced understanding of the future requirements for helicopter pilots training in flight simulators, which will become even more important considering the current trends towards Urban Air Mobility. Indeed, the transition from helicopters as a niche sector in the aerospace industry to the widespread future use of personal aerial vehicles (PAVs) based on rotorcraft concepts needs to be accompanied by a disruptive change in aviation regulations, encompassing every aspect of safety, including training. Even though these future PAVs will be characterized by a high level of automation, the human operators will keep playing an important role in the safe operation of the flight, hence raising the need to develop training requirements for PAV pilots.

NOMENCLATURE

$\alpha_{(\cdot)}$	Angle of incidence	(rad)
β_i	i-th blade flapping angle $i = 1 : N_b$	(rad)
$\beta_{(\cdot)}$	Angle of sideslip	(rad)
χ	Wake skew angle	(rad)
$\delta W_{(\cdot)}$	Virtual work	(J)
δ	Blade profile drag coefficient	(-)
δ_0	Collective lever input	(% of the available stroke)
δ_0	Zero order blade profile drag coefficient	(-)
δ_2	Second order blade profile drag coefficient	(-)
δ_t	Throttle	(% of the total stroke)
δ_{1s}	Longitudinal cyclic stick input	(% of the available stroke)
η	Engine efficiency	(-)
Γ	Circulation	(m^2/s)
γ	Flight path angle	(rad)
$\hat{\psi}_{(\cdot)}$	Gear rotation (torsional rotation at the end of a shaft) in reduced coordinates	(rad)
λ	Total inflow	(-)
λ_i	i-th eigenvalue	(rad/s)
λ_i	Induced inflow	(-)
μ	Advance ratio	(-)
μ_L	Gain of the open-loop transfer function of the rotorspeed governor	(-)
μ_z	Normalized vertical speed	(-)
ν_ξ	Non-dimensiona lead-lag frequency	(-)
ω_b	Third order break-frequency of the washout filter	(rad/s)
ω_n	Eigenvalue's pulsation	(rad/s)
ω_n	Natural break-frequency of the washout filter	(rad/s)
ω_ξ	Lead-lag frequency	(rad/s)
ω_{bw}	Notch filter bandwidth	(rad/s)
ω_f	Fuel mass rate	(kg/s)

Ω_{mr}	Main rotor speed at idle	(deg/s or % of the value at idle)
ω_{nf}	Notch filter frequency	(rad/s)
ϕ	Roll angle	(°)
ϕ_c	Critical phase	(rad)
ϕ_m	Phase margin	(rad)
ψ	Yaw angle	(°)
ψ_i	i-th blade azimuth angle $i = 1 : N_b$	(rad)
$\psi_{(\cdot)}$	Gear rotation (torsional rotation at the end of a shaft)	(rad)
ρ_b	Main rotor blade mass density	(kg/m^3)
ρ_{air}	Air density	(kg/m^3)
σ	Solidity	(-)
θ	Pitch angle	(°)
θ_0	Main-rotor collective pitch angle	(rad)
$\theta_{0_{tr}}$	Tail-rotor collective pitch angle	(rad)
θ_{tw}	Main-rotor blade twist angle	(rad)
$\vec{\omega}$	Angular velocity vector of the helicopter	(rad/s)
$\vec{\psi}$	Vector containing gear rotations	(rad)
ξ_0	Collective lead-lag	(rad)
ξ_i	i-th blade lead-lag angle $i = 1 : N_b$	(rad)
ζ	Damping ratio of the washout filter	(-)
ζ	Eigenvalue's damping ratio	(-)
$\delta\vec{u}$	Perturbation of the input vector	
$\delta\vec{x}$	Perturbation of the state vector	
$\delta\vec{x}_0$	Perturbation of the initial condition	
$\delta\vec{x}_{ZIR}$	Natural (or Zero Input) Response (ZIR)	
$\delta\vec{x}_{ZSR}$	Forced (or Zero State) Response (ZSR)	
$\hat{I}_{(\cdot)}$	Reduced inertia	(kgm^2)
$\hat{K}_{(\cdot)}$	Reduced stiffness	(Nm/rad)
$\hat{Q}_{(\cdot)}$	Reduced torque	(N m)
$\hat{\mathbf{K}}_{(\cdot)}$	Reduced stiffness matrix of the drivetrain torsional dynamics	
$\hat{\mathbf{M}}_{(\cdot)}$	Reduced inertia matrix of the drivetrain torsional dynamics	
$\mathbf{A}$	State matrix of the helicopter model	
$\mathbf{A}$	State matrix	

$\mathbf{B}$	Control matrix
$\mathbf{B}$	Input matrix of the helicopter model
$\mathbf{C_e}$	Engine damping matrix of the drivetrain torsional dynamics
$\mathbf{C_S}$	Structural damping matrix of the drivetrain torsional dynamics
$\mathbf{C}$	Output matrix
$\mathbf{D}_{tpp}$	Damping matrix of the tip-path plane dynamics
$\mathbf{J}_P$	Inertia tensor of the helicopter ..... (kgm^2)
$\mathbf{K_i}$	Gain matrix of the control system ($i = 0:4$)
$\mathbf{K}_{(\cdot)}$	Stiffness matrix of the drivetrain torsional dynamics
$\mathbf{K}_{tpp}$	Stiffness matrix of the tip-path plane dynamics
$\mathbf{M}_{(\cdot)}$	Inertia matrix of the drivetrain torsional dynamics
$\mathbf{S}_P$	Tensor of static moments with respect to point P ..... (kgm)
$\mathbf{S}^B_{321}$	Transformation matrix from body to North-East-Down reference frame
$\mathbf{T}$	Transformation matrix from lagrangian to reduced coordinates
$\mathbf{W}$	Right eigenvectors matrix
RMS	Combined pitch and roll root mean square ..... (°)
$\text{RMS}_{\Delta\psi}$	Root mean squared heading error ..... (°)
$\text{RMS}_{\Delta P}$	Root mean squared position error with respect to the target hover position ..... (m)
$\text{RMS}_{\Delta x}$	Root mean squared longitudinal position error with respect to the target hover position (m)
$\text{RMS}_{\Delta y}$	Root mean squared lateral position error with respect to the target hover position .. (m)
$\text{RMS}_{\Delta z}$	Root mean squared vertical position error with respect to the target hover position . (m)
RMS_{ϕ}	Root mean squared roll error ..... (°)
RMS_{θ}	Root mean squared pitch error ..... (°)
RMS_{V}	Root mean square of the linear velocity ..... (m/s)
$\mathrm{d}\vec{l}$	Length of a tip vortex element ..... (m)
$\vec{a}$	Linear acceleration vector ..... (m/s^2)
$\vec{a}_{tpp}$	Vector containing tip-path plane angles ..... (rad)
$\vec{b}_l$	Versors of the body reference frame ($l = 1:3$)
$\vec{e}_{321}$	Vector containing Euler angles
$\vec{F}$	Vector of the total force ..... (N)
$\vec{f}_{tpp_{precone}}$	Known term in the tip-path plane dynamics due to rotor precone ..... (s^{-2})
$\vec{f}_{tpp}$	Known term in the tip-path plane dynamics ..... (rad)

$\vec{g}_l$	Versors of the inertial reference frame ($l = 1:3$)	
$\vec{h}_l$	Versors of the hub-body reference frame ($l = 1:3$)	
$\vec{j}_l$	Versors of the first intermediate reference frame ($l = 1:3$)	
$\vec{k}_{i,j}$	Gain vector ($i, j = 1:4$)	
$\vec{k}_l$	Versors of the second intermediate reference frame ($l = 1:3$)	
$\vec{M}_P$	Vector of the total moment with respect to a generic point P	(N m)
$\vec{Q}$	Vector containing required and available torques	(N m)
$\vec{Q}$	Vector of the linear momentum	(kgm/s)
$\vec{r}$	Distance between a generic point P and a tip vortex element	(m)
$\vec{u}$	Input vector of the helicopter model	
$\vec{u}_c$	Control system input vector	
$\vec{u}_p$	Pilot input vector	
$\vec{V}$	Linear velocity vector of the helicopter	(m/s)
$\vec{v}_i^{\mathrm{H}}$	i-th left eigenvector	
$\vec{w}_i$	i-th right eigenvector	
$\vec{x}_I$	State vector of the helicopter model in the inertial frame	
$\vec{x}$	State vector of the helicopter model	
A_1	Lateral cyclic pitch angle	(rad)
a_{0_p}	Precone angle	(rad)
a_0	Coning angle	(rad)
a_1	Longitudinal flapping angle	(rad)
a_{kj}	Elements of the state-matrix	
AI	Autorotative flare index	(ft^3/lb)
B_1	Longitudinal cyclic pitch angle	(rad)
b_1	lateral flapping angle	(rad)
c	Main rotor blade chord	(m)
C_ξ	Main-rotor blade lead-lag hinge damping	(Nms/rad)
C_H	Horizontal force coefficient	(-)
C_Q	Torque coefficient	(-)
C_T	Thrust coefficient	(-)
DL	Disk loading	(lb/ft^2)
e_ξ	Lead-lag hinge offset	(m)

F	F-statistic in the Analysis of Variance
F_x	x-component of the total force vector in the body reference frame ..... (N)
F_y	y-component of the total force vector in the body reference frame ..... (N)
F_z	z-component of the total force vector in the body reference frame ..... (N)
G	Transfer function of the engine-drivetrain+lead-lag dynamics
g_{tr}	Tail-rotor gearing ..... (-)
H	Closed-loop transfer function of the rotorspeed governor
H	Horizontal force ..... (N)
h	Altitude ..... (ft)
h_R	Hub height with respect to the helicopter center of gravity ..... (m)
H_{ce}	Controlled element transfer function
i_s	Main-rotor shaft tilt angle ..... (rad)
I_β	Main rotor blade flap moment of inertia ..... (kgm^2)
$I_{()}$	Components of the inertia tensor of the helicopter ..... (kgm^2)
I_ξ	Main-rotor blade lead-lag moment of inertia ..... (kgm^2)
K	Scaling gain of the washout filter ..... (-)
k	k^{th} time sample ..... (-)
k_I	Integral constant in the PID rotorspeed governor
k_p	Proportional constant in the PID rotorspeed governor
K_β	Flapping hinge restraint ..... (Nm/rad)
K_ξ	Main-rotor blade lead-lag hinge stiffness ..... (Nm/rad)
K_{ce}	Controlled element gain
L	x-component of the external moment vector in the body reference frame ..... (Nm)
L	Open-loop transfer function of the rotorspeed governor
M	y-component of the external moment vector in the body reference frame ..... (Nm)
m	Helicopter mass ..... (kg)
m_b	Main rotor blade mass ..... (kg)
m_{ID}	Maneuver identifier ..... (-)
M_q	Pitch-damping stability derivative ..... (Nms/rad)
M_u	Speed stability derivative ..... (Ns)
N	z-component of the external moment vector in the body reference frame ..... (Nm)
N_b	Number of blades on main rotor ..... (-)
N_s	Number of time samples ..... (-)

n_u	Input vector size	(-)
N_v	Number of elements in which each tip vortex is discretized	(-)
n_x	State vector size	(-)
N_{ad}	Number of landings at least within adequate performance	(- or % of the total number)
N_{des}	Number of landings within desired performance	(- or % of the total number)
NF	Notch filter transfer function	(-)
P	Position magnitude	(m)
p	Roll rate	(deg/s)
$P_{(\cdot)}$	Power	(W)
p_{ki}	Mode Participation Factor of the i-th mode on the k-th state	
q	Pitch rate	(deg/s)
$Q_{(\cdot)}$	Torque	(N m)
$q_{(\cdot)}$	Dynamic pressure	(Pa)
R	Transfer function of the rotorspeed governor	
r	Yaw rate	(deg/s)
$r_{(\cdot)}$	Reciprocal of the gear ratio	(-)
s	Laplace variable	(1/s)
S_ξ	Main-rotor blade lead-lag static moment	(kg m)
T	Thrust	(N)
t	Time	(s)
t_0	Initial time	(s)
t_h	Blade airfoil mean thickness	(m)
U	U-statistic in the Mann-Whitney U test	
u	x-component of the linear velocity vector of the helicopter in the body reference frame	(m/s)
u_{col}	Collective input	(°)
u_{lat}	Lateral cyclic input	(°)
u_{lon}	Longitudinal cyclic input	(°)
u_{ped}	Pedal input	(°)
V	Linear velocity magnitude	(m/s)
v	y-component of the linear velocity vector of the helicopter in the body reference frame	(m/s)
V_f	Helicopter flight speed	(m/s)

V_x	x-component of the helicopter velocity in the North-East-Down reference frame . (m/s)
V_y	y-component of the helicopter velocity in the North-East-Down reference frame . (m/s)
V_{hor}	Horizontal speed ..... (kn)
V_z	Rate of descent ..... (ft/min)
W	Helicopter weight ..... (kg_f or N)
w	z-component of the linear velocity vector of the helicopter in the body reference frame . (m/s)
w_i	Induced velocity ..... (m/s)
X	x-component of the external force vector in the body reference frame ..... (N)
x	x-axis component of the position vector ..... (m)
x_R	Hub longitudinal position with respect to the helicopter center of gravity ..... (m)
X_u	Surge-damping stability derivative ..... (N s/m)
Y	y-component of the external force vector in the body reference frame ..... (N)
y	y-axis component of the position vector ..... (m)
Z	Z-statistic in the Wilcoxon signed-rank test
Z	z-component of the external force vector in the body reference frame ..... (N)
z	z-axis component of the position vector ..... (m)
Z_w	Heave-damping stability derivative ..... (N s/m)
df	Number of degrees of freedom used in a statistical test
p	p-value (Significance)
t	t-statistic in the t-test

Subscripts

$cush$	Cushion
des	Desired/reference
eng	Engine
f	Failure
fl	Flare
fn	Vertical fin
fus	Fuselage
$grav$	Gravity
h	Hub
igb	Intermediate gearbox
IGE	In ground effect

le	Left engine
mgb	Main gearbox
mr	Main-rotor
OGE	Out of ground effect
re	Right engine
$reac$	Reaction
rec	Recovery
rot	Rotation
s_1	Long drive shaft (connecting main gearbox and intermediate gearbox)
s_2	Intermediate shaft (connecting intermediate gearbox and tail-rotor gearbox)
td	Touchdown
tgb	Tail-rotor gearbox
tp	Horizontal tailplane
tpp	Tip-path plane
tr	Tail-rotor

Notation

$\angle(\cdot)$	Transfer function phase
$\dot{()}$	Time derivative
$\frac{\mathrm{d}(\cdot)}{\mathrm{d}(\cdot)}$	Derivative
$(Q-P)$	Position vector of the point Q with respect to the point P
$\lvert(\cdot)\rvert$	Transfer function amplitude
$\vec{V}_{P/I}$	Velocity vector of the point P with respect to the reference frame I

ACRONYMS

AATD Advanced Aviation Training Device
AC Aerodynamic Center
ADS Aeronautical Design Standard
AG Action Group
AGARD Advisory Group for Aerospace Research and Development
AI Autorotation Index
ATD Aviation Training Device
AVT Applied Vehichle Technology

BATD Basic Aviation Training Device
BITD Basic Instrument Training Device

CAST Commercial Aviation Safety Team
CBT Computer Based Trainer
CBTs Computer Based Trainers
CG Center of Gravity
CLT Cognitive Load Theory
CMS CyberMotion Simulator
CWA Classical Washout Algorithm

DLP Digital Light Processing
DOF Degree of Freedom
DOF Degree of Freedom
DT Desktop Trainer
DTM Direct Transient Method
DUECA Delft University Environment for Communication and Activation

E Easy dynamics
EASA European Union Aviation Safety Agency
EHE Group starting the experiment with the easy dynamics
EHSAT European Helicopter Safety Analysis Team
EJD European Joint Doctorate
ESR Early Stage Researcher

FAA Federal Aviation Administration
FFS Full Flight Simulator
FNPT Flight and Navigation Procedure Trainer
FOV Field of View
FSTD Flight Simulator Training Device
FSTDs Flight Simulator Training Devices
FTD Flight Training Device

GARTEUR Group for Aeronautic Research and Technology in Europe

H Hard dynamics
HC Helicopter
HEH Group starting the experiment with the hard dynamics
HPX Horsepower Extraction

ICAO International Civil Aviation Organization
ID Increasing Difficulty
IHST International Helicopter Safety Team
IMU Inertia Measurement Unit
IP instructor pilot
IR Intervention Recommendations

JHSAT Joint Helicopter Safety Analysis Team

LOFT Line-Oriented Flight Training

MAF Moving Average Filter
MCA Motion Cueing Algorithm
MPF Mode Participation Factor
MPI Max Planck Institute
MTE Mission Task Element

NATO North Atlantic Treaty Organization
NHST Null Hypothesis Significance Testing
NITROS Network for Innovative Training on Rotorcraft Safety
NoE Nap-of-the-Earth
NRC National Research Council

OCM Optimal Control Model
OTW Out-the Window

PCATD Personal Computer-Based Aviation Traineing Device

qToT quasi-Transfer-of-Training

RMS Root Mean Square
RMSE Root Mean Squared Error
RPM Revolutions per minute

SIMONA Simulation Motion Navigation
SPM Structural Pilot Model
SPS Standard Problem Statement
SRS SIMONA Research Simulator

ToT Transfer-of-Training

1

INTRODUCTION

1.1. HELICOPTER SAFETY: A COMPLEX CHALLENGE

Over time, helicopters have become an essential means of transportation and have provided invaluable help in both civil and military contexts, such as air ambulances and search and rescue. The source of this widespread application lies in helicopters' remarkable versatility that outweighs their outward clumsiness and lack of clean and elegant lines, which may result in the aspect of a "flying brick" to the layman's eye.

Although the first studies on helicopters date back to Leonardo da Vinci's "airscrew" in 1493 (Fig. 1.1a), well in advance of the first fixed-wing airplanes, the first successful helicopter design, the Sikorsky VS-300 (Fig. 1.1b), upon which current conventional helicopters are based, was conceived by Sikorsky in 1939, more than 30 years later than the Wright Flyer [Apostolo, 1984].

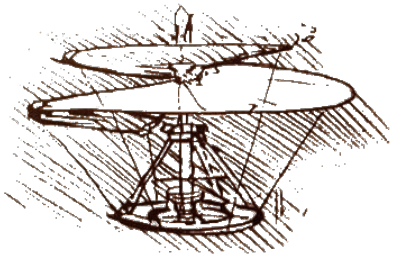

(a) Drawing of Leonardo da Vinci's "airscrew". (Source: Wikipedia)

(b) The first helicopter designed and built by Igor Sikorsky, the VS-300. (Source: Wikipedia)

Figure 1.1: Two examples of pioneering helicopter designs: Leonardo da Vinci's *"airscrew"* (a) and Igor Sikorsky's *VS-300* (b).

The negative public perception of helicopter flight safety is related to the higher accident rates for rotary-wing aircraft compared to airplanes. This negative historical trend

depends upon several factors, such as more than 30 years delay with respect to fixed-wing aircraft development, the need to understand the problems posed by helicopters in terms of aerodynamics, engineering, stability and vibrational control, and the hostile operational environment in which they are usually operated.

To revert this negative trend, many rotorcraft safety initiatives were launched since 2005, starting from the International Helicopter Safety Team (IHST) with the ambitious goal of reducing the helicopter accident rate by 80% in 10 years. The IHST was based on the Commercial Aviation Safety Team (CAST) model [International Helicopter Safety Team, 2012], which revealed itself to be very successful in reducing the number of accidents occurring in commercial aviation. However, that was a comparatively easy task, because all the operators involved in commercial aviation are well-organized companies with safety management systems already in place. The IHST is facing a different situation, because it is dealing with all types of helicopter operations (e.g., commercial air transport, specialised operations and non-commercial operations). Therefore, there is a need to communicate not only with commercial operators (e.g., passengers carrier, offshore, aerial work, etc.), but also with non-commercial operators, such as pilot training schools and private pilots.

A safety enhancement is possible only through a partnership between the authorities and the rotorcraft community and industry. Thus, not only the rule-makers and the manufacturers, but also the operators, the private pilots, the research institutes, and the universities should be kept in the loop.

Although still far away from the zero (fatal) accidents target as Harris [2007] discussed in his Nikolsky Lecture, all rotorcraft safety initiatives contribute to the development of a proactive approach to anticipate helicopter accident causes with an early solution. In this respect, the Marie Skłodowska-Curie European Joint Doctorate NITROS (Network for Innovative Training on Rotorcraft Safety) project (Fig. 1.2) focused on improving rotorcraft safety by training Early Stage Researchers (ESRs) to develop a mindset based on design for safety and use it to tackle critical aspects of rotorcraft design. As part of the NITROS project, the research presented in this thesis has been conducted by ESR 12 and concerns simulator training for helicopter pilots, which was identified by safety reports as one of the most crucial interventions to reduce helicopter accident rates [European Helicopter Safety Analysis Team, 2010, 2015; U.S. Joint Helicopter Safety Analysis Team, 2011a,b].

1.2. THE ROLE OF TRAINING IN ROTORCRAFT SAFETY

Hundreds of accident investigation reports have been analyzed by different helicopter safety teams [European Helicopter Safety Analysis Team, 2010, 2015; U.S. Joint Helicopter Safety Analysis Team, 2011a,b] with the purpose of identifying safety issues and suggestions for safety enhancement. To achieve this goal, they adapted the process used successfully by the CAST to make it consistent with characteristics and potential limitations present in helicopter data [International Helicopter Safety Team, 2012]. This is a rigorous and structured method that allows a detailed analysis of helicopter accidents from available public data (e.g., safety reports) and utilizes a data-driven approach to characterize and develop safety interventions that mitigate risks. It consists in the analysis of the event sequence for each accident allowing the identification of the problem

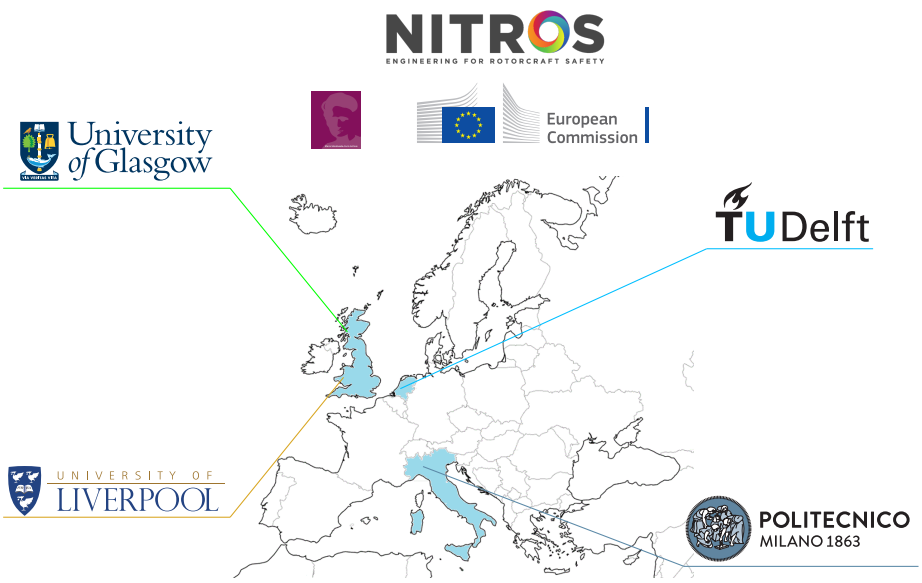

Figure 1.2: NITROS (Network for Innovative Training on Rotorcraft Safety) universities network.

statements (*what went wrong*) and any contributing factors (*why a problem occurred*) for the appropriate event. These factors are then coded using standardized taxonomies, which enable accident aggregation and statistical analysis. The Standard Problem Statements (SPS) taxonomy was used, whose structure consists of three levels: the first level identifies the main area of the SPS. The second and third levels provide more detail about the factors that played a role in the accident. To develop strategies that can prevent or mitigate a given problem or contributing factor, the Intervention Recommendations (IR) taxonomy was adopted, which is characterized by a three-level structure as the SPS.

The analyses conducted by the U.S. Joint Helicopter Safety Analysis Team [2011a,b] and the European Helicopter Safety Analysis Team [2010, 2015] with this method both highlight the same issues of concern and the same improvement actions. Most of the accidents in the data set were classified as the result of pilot-related factors, such as pilot judgement and actions, ground duties and pilot situational awareness (Fig. 1.3a). For this reason, recommendations to prevent accidents are predominantly related to the *"Training/Instruction"* and *"Safety Management interventions"* (Fig. 1.3b).

An examination of Intervention Recommendations at Level 3 details more specific recommendations for a specific Level 1 group. This is shown in Fig. 1.3c for the Training/Instructional category, which shows the top 10 Level 3 Intervention Recommendations for this category according to the analysis conducted by the U.S. Joint Helicopter Safety Analysis Team [2011a,b]. It is worth mentioning that the top 10 Level 3 Training/Instructional Intervention Recommendations are also enumerated among the top 20 overall Intervention Recommendations. Fig. 1.3c highlights which training aspects currently still need to be consolidated. In particular, the development of a standardized training program for autorotation and emergency aircraft handling, as well as the improvement of simulator training for basic and advanced maneuvers, are essential for enhancing helicopter safety.

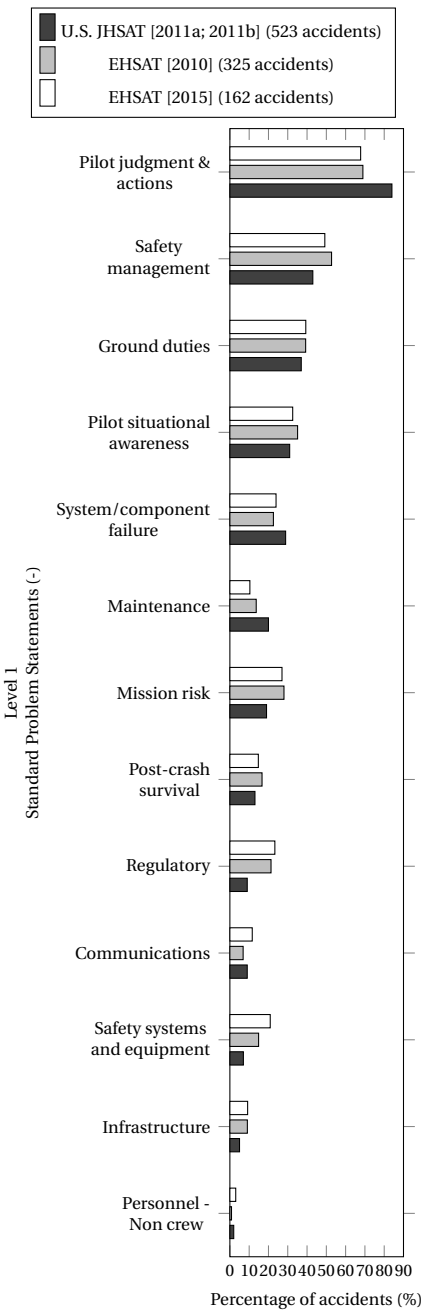

(a) Percentage of analyzed accidents where Level 1 Standard Problem Statements was assigned at least once [European Helicopter Safety Analysis Team, 2010, 2015; U.S. Joint Helicopter Safety Analysis Team, 2011a,b].

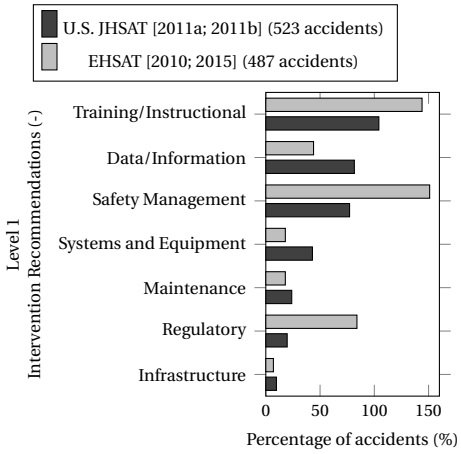

(b) Percentage of analyzed accidents where Level 1 Intervention Recommendations was assigned at least once [European Helicopter Safety Analysis Team, 2010, 2015; U.S. Joint Helicopter Safety Analysis Team, 2011a,b].

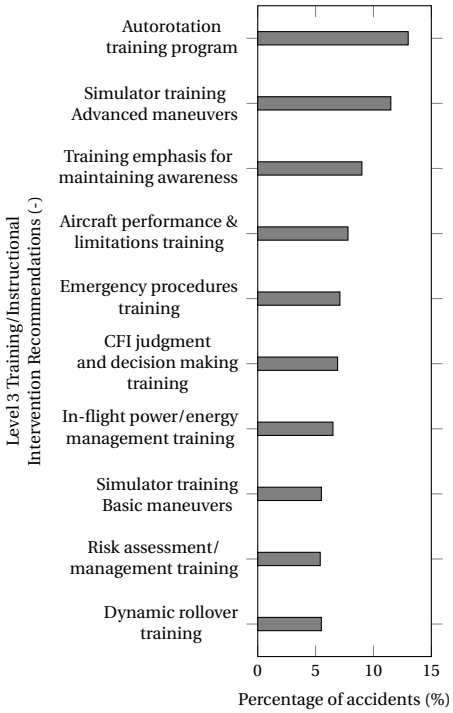

(c) Top 10 Level 3 Training/Instructional Intervention Recommendations [U.S. Joint Helicopter Safety Analysis Team, 2011a,b] (523 accidents).

Figure 1.3: Helicopter safety teams accident analysis [European Helicopter Safety Analysis Team, 2010, 2015; U.S. Joint Helicopter Safety Analysis Team, 2011a,b]

These two areas of improvement are interrelated. Pilots can acquire robust and flexible flying skills only through extensive practice. In this way, they will be able to react promptly and avoid many possible errors when unpredictable emergency situations are encountered during flight. However, extensive in-flight training is expensive and dangerous [Thompson et al., 2008]. Therefore, a combination of simulator and in-flight training is desirable, especially during the training of hazardous scenarios. Nonetheless, to replace or complement in-flight training with simulator training without incurring unrealistic training and negative transfer of skills, there is a clear need to bridge the gap between simulator training and real helicopter operations [Hays et al., 1989].

1.3. THE ROLE OF SIMULATION IN AVIATION TRAINING

The value of flight simulation in pilot training is unquestionable. The development of flight training devices enables trainees to conduct a significant part of flight training on the ground, with consequent benefits in terms of safety and costs. This was enabled by the advent of analogue computing and the subsequent onset of digital computers, which led to a significant improvement in the fidelity of flight models that can be run in real-time [Allerton, 2009]. Advances in simulator motion and visual systems were also possible as a result of the growth in computational power and the decrease in electronic component size [Allerton, 2009].

The simulation industry has always been driven by striving for improved realism. Indeed, the use of sophisticated and advanced technologies makes a flight simulator more attractive to be procured [Farmer et al., 1999]. However, this approach is leading to flight simulators that are almost as complex and expensive as the aircraft they mimic. Furthermore, flight simulators that are mainly based on a technology-push process are not always fit for the intended training purpose [Farmer et al., 1999].

Therefore, when developing a training program, the needs of the specific training task should always cover a prominent role with respect to simulator complexity [Caro, 1973]. The training developer needs to understand what characteristics of the task must be emphasized in order to train someone to perform that specific task [Farmer et al., 1999; Hays et al., 1989], for instance by tailoring the training program to the trainees experience (e.g., ab-initio versus recurrent training). This is often achieved through interviews with subject matter experts (persons familiar with the type of tasks to be trained) to determine how the training system and associated training media should be configured to meet the requirements [Hays et al., 1989].

The specification of training media characteristics is often referred to as the "*fidelity question*" [Hays et al., 1989]. Essentially, the fidelity question asks how similar to the actual task situation a training situation must be to provide efficient and effective training. Different definitions of fidelity as the metric for evaluating the quality of simulator devices exist. For example, *objective fidelity* pertains to the quality of the cueing systems and is quantified in relation to those cues that can be objectively measured [AGARD, 1980]. The pilot/trainee's perception plays a role in those cues that are subjectively experienced [AGARD, 1980], which led to the notion of *perceptual fidelity*, defined as the accuracy of the perceived cues Hays [1980]. *Behavioral fidelity* refers to the accuracy of pilot response to perceived cues Hays [1980], *model fidelity* is associated with the accuracy of the aircraft model response to pilot input [Pavel, 2001; Pavel et al., 2013], and *error*

fidelity refers to the accuracy in pilot's performance [Ashkenas, 1986]. These definitions are summarized graphically in Fig. 1.4, where they are represented as fidelity gaps between a flight simulator and an actual aircraft. A conceptual bridge is necessary to link the actual task requirements to the fidelity of the training system, which will never replicate the actual aircraft exactly. Fig. 1.4 depicts both systems as a control loop closed by the pilot/trainee, whose behavior/action depends on the available (objective and perceived) cues and affects the aircraft/aircraft model response, which in turn influences the available cues.

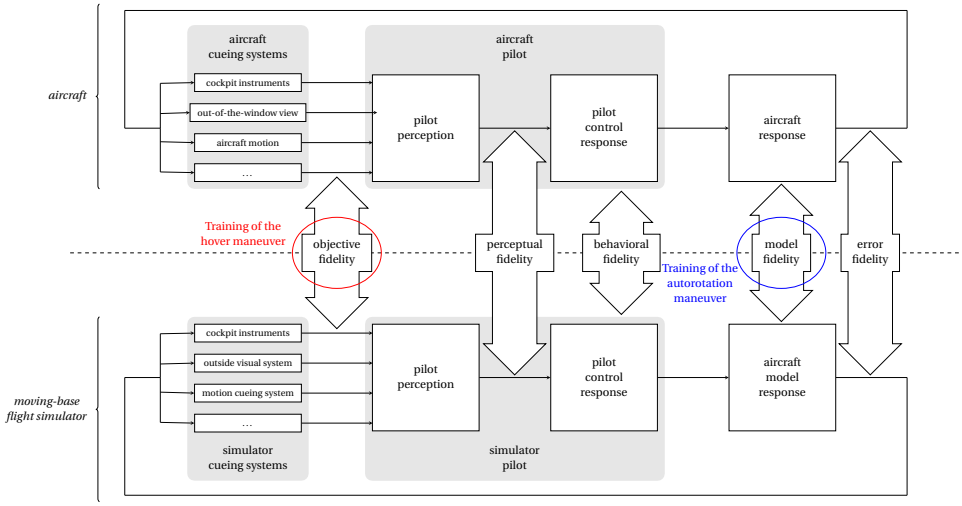

Figure 1.4: Schematic representation of the different facets of simulator fidelity (Pool [2012]).

Objective fidelity comprises three simulator components that have maximum cost and technology impact on current flight simulators, i.e., the visual and motion systems characteristics and the vehicle mathematical model [AGARD, 1980]. Together, these components are responsibe for the *environmental cues*, i.e., the cues due to flight. *Equipment cues* instead are related to perceptual fidelity, because they provide a duplication of the appearance and feel of the operational equipment (e.g., cockpit layout, instruments, controls, etc.). Since only those cues that are a necessary condition for the fulfillment of a specific training objective are essential, the definition of cueing requirements is usually achieved through a tradeoff between equipment and environmental cue fidelity (Fig. 1.5). According to the misconception that the higher the level of fidelity, the higher degree of transfer of training will occur, training simulators are generally characterized by a high level of equipment and environmental cue fidelity. However, simulator fidelity gives only an indication of a device's realism and not necessarily of its training capability. As a result, simulator realism, intended especially as objective fidelity, is not the most appropriate criterion to state training simulator design requirements [AGARD, 1980].

Besides the practical impossibility of a one-to-one correspondence between simulator systems and the actual aircraft [Ashkenas, 1986], another key challenge is represented by the inevitable differences in psychological factors that come with training

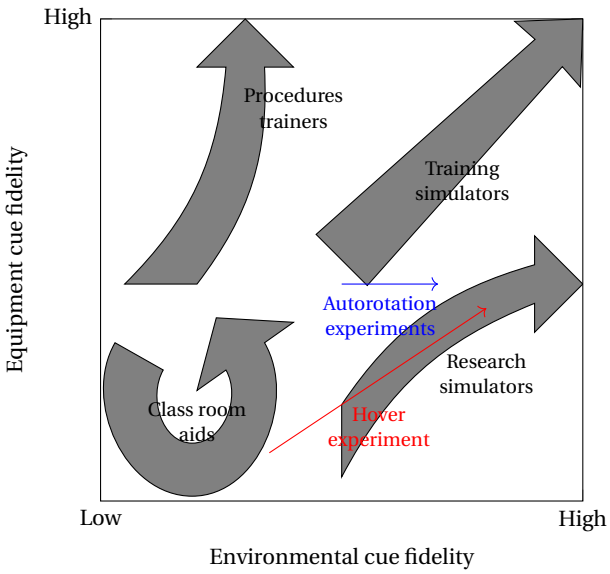

Figure 1.5: Tradeoff between equipment and environmental cue fidelity (AGARD [1980]).

in an intrinsically safe environment for situations that could be lethal in the real operation. Nonetheless, recent research [Landman, 2019] has demonstrated the possibility to induce startle and surprise within simulator scenarios and elicit the performance issues arising from pilots' need to reframe under pressure. For example, to evaluate pilot/crew performance in operational decision making, line-oriented flight training (LOFT) is adopted [Lofaro et al., 2008], in which the crew has to deal with abnormal situations, which are *not pre-briefed*, occurring during representative line operations.

The occurrence of flight simulator negative transfer of training can thus be tackled from at least two different perspectives: 1) task requirements vs fidelity and 2) pilots' mindset in flight simulators. While both deserve further attention, especially with respect to helicopter pilots training, this thesis focuses on the former perspective, by analyzing the training task requirements for two critical maneuvers in helicopter pilot training: hover from an objective fidelity standpoint and autorotation from a model fidelity perspective, see the red and blue highlights in Fig. 1.4 and 1.5.

1.4. RESEARCH GOAL & QUESTIONS

Pilot training and flight simulators play a crucial role in rotorcraft safety. However, to spread the use of flight simulators in helicopter pilot training, it is necessary to minimize the chances of insufficiently realistic training settings and negative transfer of skills. This thesis contributes to this key point by providing indications for the development of helicopter training simulator criteria. Therefore, this thesis has the following ambitious goal:

Goal of this thesis

Contribute to an enhanced understanding of the future requirements for helicopter pilot training in flight simulators.

To this end, this research considers two representative helicopter tasks, hover and autorotation, and analyzes them in detail to understand the relation between transfer of training and simulator fidelity, especially as related to the quality of the cueing system and the mathematical model. Therefore, this thesis answers the following main research questions:

(1) **How does simulator objective fidelity, due to variations in the quality of the cueing systems, affect the initial training of the hover maneuver?**

(2) **How do variations in the controlled helicopter dynamics affect the recurrent training of the autorotation maneuver?**

The hover and autorotation maneuvers are most relevant in different phases of the training syllabus (either ab-initio or recurrent training), allowing to identify differences in terms of requirements for basic and advanced simulator training, as well as for task-naïve learners and experienced pilots.

1.5. APPROACH

This thesis aims to contribute to an enhanced understanding of the future requirements for helicopter pilots training in flight simulators, providing indications for the development of guidelines for such novel training when the helicopter is flown in two of its most characteristic modes of operation: hover and autorotation. To achieve this goal, the thesis first challenges the common misconception, based on a misinterpretation of the "identical elements" theory by [Thorndike, 1903], that high simulator fidelity necessarily results in higher training effectiveness. A first quasi-transfer-of-training experiment with task-naïve learners trained for the hover maneuver demonstrates that desktop trainers may be a valid alternative to high-fidelity simulators if supported by a suitable training program.

This thesis then challenges the risk mitigation approach, according to which emergency situations must be first practiced with easier aircraft [Coyle, 2008]. Such an approach is essential during in-flight training, but can be set aside during simulator training, due to the inherently safe nature of flight simulators. Two quasi-transfer-of-training experiments with experienced helicopter pilots trained for an autorotation maneuver demonstrate that positive transfer of skills occurs from a relatively hard to a relatively easy helicopter dynamics, but not the opposite, suggesting that starting the training with more difficult to control helicopter dynamics fosters the development of skills that can be easily adpted to easier conditions.

1.5.1. ANALYSIS OF THE TRAINING TASKS

BASIC MANEUVER: HOVER INITIAL TRAINING

The ability to hover is the main capability that differentiates helicopters from fixed-wing aircraft. It is a basic flight maneuver and, as such, it is essential for helicopter pilots to master it. Therefore, hover is the first maneuver that student pilots learn to perform. Instructor pilots usually teach this task by dividing it in sub-tasks and taking advantage of the dual flight controls. The foundations of this "*part-task*" teaching method lie in cognitive psychology. In particular, Sweller developed an instructional design theory, called Cognitive Load Theory (CLT), that reflects the way humans process information [Sweller, 1994; Sweller et al., 1998].

Cognitive Load Theory provides a basis for predicting that training strategies reducing the intrinsic load of a task during training enable more resources to be devoted to learning [Wickens et al., 2013]. Two closely related strategies that accomplish this goal, either by simplifying tasks in early training trials or by dividing tasks in parts, are increasing difficulty (ID) and part-task training (PTT), respectively.

Task-naïve learners benefit more from load-reducing strategies during the training process than experienced learners do. For this reason, a part-task training program for initial hover training in flight simulators was developed at the Max Planck Institute for Biological Cybernetics [Fabbroni et al., 2017a], after consultation with an instructor pilot. This part-task training proved to be effective in a number of quasi- and true-transfer-of-training experiments [Fabbroni et al., 2018, 2017b]. It consists of a sequence of five tasks characterized by an increasing level of difficulty and is intended to teach the role of each flight control with a step-by-step approach. To achieve this goal, an autopilot based on optimal control theory was designed [Baron et al., 1970; Kleinman et al., 1970]. This autopilot mimics the behavior of an instructor pilot sitting next to their student and acting on the dual controls to help him. Such training program was adopted to demonstrate the importance of instructional design over simulator objective fidelity. According to Alessi [1988], CLT also applies to the relation between simulator objective fidelity and training effectiveness. In contrast to the common belief that higher simulator fidelity will likely result in higher degrees of transfer-of-training [Klauer, 1997], based on a misinterpretation of the "identical elements" theory by [Thorndike, 1903], Alessi stated that high fidelity also means high complexity, which will require more cognitive skills, thus increasing the trainee's workload, which will, in turn, impede learning [Liu et al., 2008]. Alessi [1988] also hypothesized a non-linear relation between learning and fidelity which depends on many factors, such as the trainee's experience (i.e., novice vs. expert pilots).

In agreement with the "Alessi Hypothesis", Noble [2002] suggests the existence of an optimal point beyond which adding more fidelity (intended as total-fidelity) results in a diminished degree of transfer of skills of *nonexpert* pilots. Lintern [1995], appealing to the "identical elements" theory [Thorndike, 1903], asserts that skill transfer effects observed in simulator training may be explained through invariant perceptual properties of the task environment and provides a different interpretation of the theory with respect to that proposed by Klauer [1997]: transfer will occur between the first task (simulation) and the second task (real world) if the first task contains specific component activities that are held by the second task. Klauer [1997, p. 13] affirms that *"The closer a flight simulator corresponds to the actual flight environment (i.e., high physical fidelity),*

the more skills will transfer to the aircraft", while Lintern assumes that only a relatively low-dimensional set of properties supports training transfer and claims that *"It is those properties that need not be represented accurately, or even at all"* [Lintern, 1995, p. i].

With the goal to seek more clarity with respect to the relation between fidelity and training effectiveness, a quasi-transfer-of-training experiment was conducted in this thesis, in which simulator objective fidelity was chosen as the independent variable. Two groups of task-naïve learners underwent the hover part-task training program formulated by Fabbroni et al. [2017a], with the experimental group first trained in a low-fidelity simulator and then transferred to a high fidelity setting and the control group who received all its training in the high fidelity simulator.

ADVANCED MANEUVER: AUTOROTATION RECURRENT TRAINING

Another critical training scenario is represented by autorotation, which is a technique used by helicopter pilots to reach the closest suitable landing site in the event of partial or total power failure. Autorotation is accomplished through a combination of rule-based and skill-based control behaviors [Rasmussen, 1983]. The training effectiveness of currently available flight simulators on rule-based and knowledge-based pilot behavior is widely recognized and accepted [Caro, 1973; Durlach et al., 2000; Pool, 2012]. For skill-based control behavior, however, for which training involves pilots' intimate familiarization with the inherent dynamics and handling qualities of the aircraft they are dealing with, many efforts still need to be devoted to fill the fidelity gap between simulator and in-flight training [Hosman, 1999; Pool, 2012; Schroeder et al., 2001]. Although also hover requires a combination of rule-based and skill-based control behaviors, the need for high-accuracy models and high-fidelity simulation is especially felt for flight conditions that are the result of abnormal modes of operation, such as autorotation, and for experienced learners [Alessi, 1988; Hays et al., 1989]. A schematic representation of such skill-based manual control tasks is depicted in Fig. 1.4, in the form of two closed-loop pilot-vehicle systems representative of how these kind of tasks are performed in real flight and in a flight simulator, respectively.

Given the importance of the relationship between pilot control behavior and the controlled aircraft dynamics for skill-based manual control tasks, the analysis of the behavioral fidelity gap (see Fig. 1.4) is paramount to enhance flight simulator training [Miletović, 2020]. Also for autorotation, pilots' control strategies are directly related to the helicopter dynamics they have to fly. This is proven by the fact that many engine failure accidents are the result of an apparent loss in rotor performance (different helicopter dynamics), which is unexpected by pilots that practiced only autorotations with a power recovery (i.e., terminating in a hover). Such an unexpected behavior may arise in helicopters with free-turbine engines, in which the engine is still transmitting some power to the rotor even in ground idle setting [Prouty, 2009]. The accident reported by Prouty [2009, p. 161] is an example of in-flight-to-in-flight negative transfer of training: practicing power-recovery autorotations (task A) interferes with learning or performing power-out autorotations (task B) for helicopters with free-turbine engines, due to the fact that there is a strong mismatch between the helicopter dynamics characteristics in the two task situations, meaning that the pilot's mental model of the helicopter is not representative of the actual helicopter, which requires a different control strategy than the one learnt during training to accomplish the task.

As is often the case, the investigation of accident causes provides the grounds to conduct research into unexplored areas to hinder new occurrences ascribable to the same circumstances. For this reason, a significant part of this thesis is devoted to the investigation of the effects of helicopter dynamics on autorotation training transfer. This was achieved through the execution of two quasi-transfer-of-training experiments with experienced helicopter pilots. Participants were divided in two groups and performed the autorotation maneuver controlling two different helicopter dynamics in a different sequence.

The simulator experiments were preceded by a sensitivity analysis on the helicopter eigenmodes to understand what design parameters mostly influence the helicopter dynamics in autorotation, and consequently pilot's control strategy, to wisely select the two dynamics to be used in the experiments. To this end, the classical approach adopted to study the stability and control of both fixed- and rotary-wing aircraft, consisting in the linearization of the equations of motion around an equilibrium point and in the evaluation of the natural modes of motion of the equivalent linear system [Padfield, 2007], is applied to the steady-descent phase of the autorotation maneuver.

Both the theoretical insight into the flight mechanics in autorotation and the experimental findings are presented for two helicopter flight mechanics models with increasing order (3-DOF longitudinal dynamics and 6-DOF rigid-body dynamics).

1.5.2. PILOT-IN-THE-LOOP EXPERIMENTS

Transfer-of-Training (ToT) experiments are one of the few available techniques that can be used to explicitly measure simulator training effectiveness [AGARD, 1980]. Quasi-transfer studies, also known as Simulator-to-Simulator Transfer experiments, employ tasks where participants alternate between different simulators or where some change in task or configuration is performed in the same simulated environment. In contrast, real-flight transfer studies investigate whether certain skills can be acquired in a simulator and successfully transferred to actual flight. The quasi-transfer paradigm relies on the assumption that simulators act as a valid replacement for the actual aircraft. Although this is a strong assumption, it is corroborated by experimental evidence [Taylor et al., 1993]. Furthermore, a quasi-transfer design avoids the costs, hazards, and scheduling hindrances (e.g., interruptions due to bad weather) of a true transfer and offers the possibility of safely investigating dangerous situations such as engine failures. Another issue arising from true-transfer studies (and from flight test data in general) is the reliability of the performance measurements in the real-world setting [Boldovici, 1987]. Moreover, although the pilot appears to be the only constant element in the two control systems, i.e., pilot-vehicle and pilot-simulator (Fig. 1.4), there may be inevitable psychological differences in a pilot's mindset between the two settings [Mulder et al., 2013; Pool, 2012; Schroeder et al., 2010]. This is not necessarily a disadvantage from a training perspective, because relieving the trainee of the stress and the workload deriving from auxiliary duties (e.g., safety and flight regulation aspects, communication, periodic systems monitoring, etc.) enables him to devote more resources to learning [Sweller, 1994; Sweller et al., 1998].

For this thesis, a series of quasi-transfer-of-training experiments was conducted to test the effectiveness of the training programs formulated according to the analysis of

the training tasks. The simulators used in this thesis are the Max Planck Institute CyberMotion Simulator (CMS) and Computer Based Trainer (CBT) and the Delft University of Technology SIMONA Research Simulator (SRS), which are shown in Fig. 1.6. One of the core elements of a flight simulator is the flight mechanics model, which replicates the response of the actual aircraft to pilot's control inputs. Different flight mechanics models have been used in this thesis, ranging from an identified model of the Robinson R-44 helicopter [Geluardi, 2016; Geluardi et al., 2018], suitable for hover and low-speed simulation, to a physics-based model with six rigid-body degrees-of-freedom (DOF), quasi-steady flapping dynamics, and uniform inflow [Talbot et al., 1982]. The physics-based model developed in this thesis for a conventional helicopter (one main rotor and one tail rotor) is generic (Appendix A). Therefore, it can be used to represent different helicopters by simply changing the input parameters of the model (e.g., rotor radius, helicopter weight, etc.). The physics-based model was validated against available trim flight test data for the Messerschmitt-Bölkow-Blohm Bo-105 helicopter in straight level flight [Padfield, 2007] (Appendix B) and tested in the simulator with experienced and qualified helicopter pilots. Although the model exhibits a good match with flight test data for most of the trim variables, the use of a uniform inflow model causes an underestimation (in absolute value) of the lateral cyclic pitch. Trim in steady autorotation and stability derivatives in level flight and steady autorotation of the developed model were verified against those of other models of the same helicopter (Appendices B and C) due to the lack of available flight test and identification data.

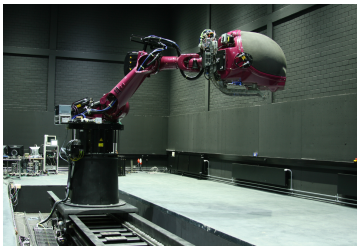

(a) The Max Planck Institute CyberMotion Simulator [Nieuwenhuizen et al., 2013].

(b) The Max Planck Institute Computer Based Trainer [Scaramuzzino et al., 2018].

(c) Delft University of Technology SIMONA Research Simulator [Stroosma et al., 2003].

Figure 1.6: Flight simulators used in this thesis: the CyberMotion Simulator (a), the Computer Based Trainer (b), and the SIMONA Research Simulator (c).

1.6. ASSUMPTIONS & LIMITATIONS

The following assumptions and limitations apply to the present work:

- Due to practical (risks and scheduling hindrances) and financial limitations, it was not possible to perform true-transfer experiments. Indeed, the experimental results obtained in this thesis (Chapters 3, 5 and 6) are all based on the quasi-transfer paradigm, which relies on the assumption that the more realistic simulator, i.e., the transfer setting, act as a valid replacement of the actual aircraft.
- A relatively low number of participants took part in the experiments conducted in this thesis (24 in the experiment presented in Chapter 3, 14 in that presented in Chapter 5 and 10 in the one presented in Chapter 6), which affects the reliability of the experimental outcomes due to lacking statistical power. This was mainly related to simulator availability for the experiment on initial hover training (Chapter 3), which included participants with no prior flight experience neither in actual helicopters nor in simulators. The experiments on autorotation training (Chapters 5 and 6) were addressed to experienced helicopter pilots instead, who represent only a small population in the Netherlands. This situation was further exacerbated by the Covid-19 pandemic, that made people more reluctant to travel for non-work related reasons and required the adoption of more stringent simulator protocols.
- It is assumed that the absence of differences between two groups of participants in a quasi-transfer-of-training experiment does not mean that the two simulators are equally effective.
- The main limitation of the methodology proposed in Chapter 4 for the analysis of the helicopter dynamics in autorotation consists in the fact that it is applicable only to the steady descent part of the autorotation maneuver, that can be considered as a trim condition. However, the steady descent in autorotation is not as demanding as the entry in autorotation for a pilot, which requires a prompt identification of the power failure and a proper sequence of actions to keep the rotorspeed in a safe range preventing loss of control. Indeed, according to Prouty [2009, (p. 163)]: *"A bad ending of an autorotation is usually survivable, but a bad beginning of an autorotation is usually not"*.
- The helicopter models used in the analysis of the helicopter dynamics in autorotation presented in Chapter 4 and in the experiments on autorotation transfer-of-training conducted in this thesis (Chapters 5 and 6) is characterized by uniform inflow and quasi-steady tip-path-plane dynamics (i.e., blade flapping angles are assumed to instantaneously adopt new equilibria as a result of changing flow conditions and pilot control inputs). Especially the assumption of uniform distribution of the induced velocity on the rotor disc is strong for autorotative flight in forward translation. Furthermore, the helicopter model used in the experiment presented in Chapter 5 was characterized only by the longitudinal dynamics (3-DOF symmetrical + main rotor RPM), which was considered acceptable since the final part of the autorotation is mainly a longitudinal maneuver, as confirmed also by the analysis conducted in Chapter 4.

1

1.7. THESIS OUTLINE

Fig. 1.7 shows a graphical representation of the structure of this thesis. First, a comprehensive literature review on simulator training is provided in Chapter 2. Then, Part I of this thesis, consisting of Chapter 3, describes the quasi-transfer-of-training experiment conducted to assess the effects of simulator objective fidelity on transfer of skills for a basic helicopter maneuver, i.e., hover.

Next, Part II, consisting of Chapters 4 to 6, is devoted to an advanced helicopter maneuver, i.e., autorotation. Furthermore, a distinction is made in Fig. 1.7 between chapter 4, that provides a theoretical insight into the flight mechanics in autorotation (chapter at left) and chapters 5 and 6, that present findings from flight simulator experiments (chapters at right), conducted to evaluate the effects of helicopter dynamics on autorotation transfer-of-training. Both the theoretical insight and the experimental findings are obtained for two helicopter flight mechanics models with increasing order (3-DOF longitudinal dynamics and 6-DOF rigid-body dynamics).

Finally, the main conclusions, recommendations and crucial directions for future research are presented in Chapter 7.

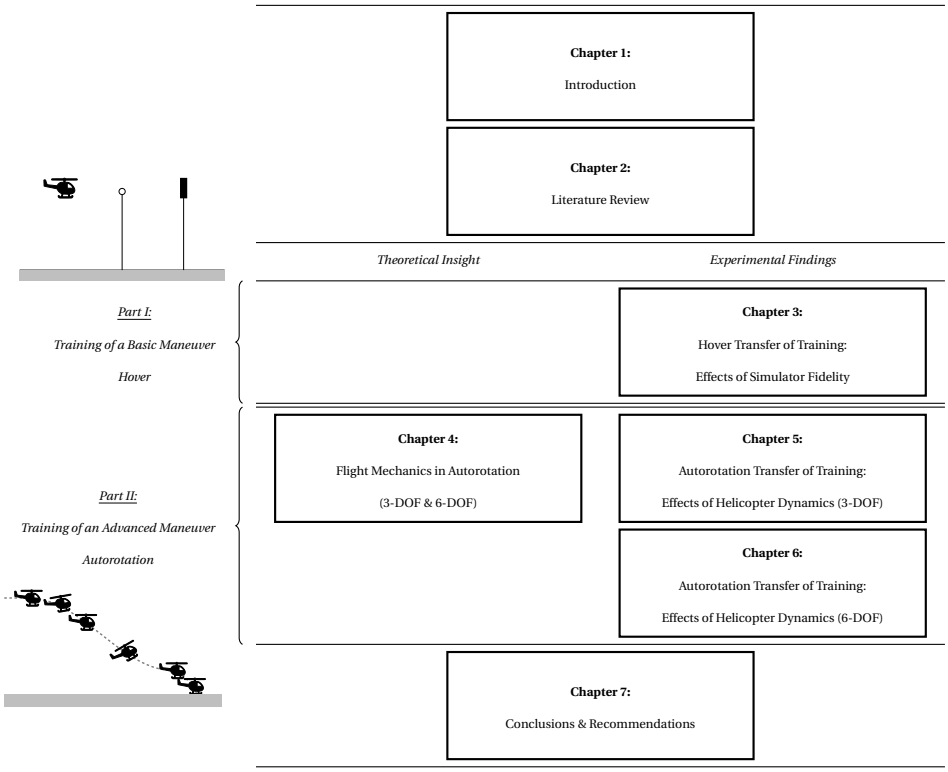

Figure 1.7: Graphical representation of the structure of this thesis.

2

LITERATURE REVIEW: TRAINING, MODELLING, AND SIMULATION

The main objective of this thesis is to understand what are the factors affecting simulator training effectiveness that can be used to minimize the chances of unrealistic training and negative transfer of skills. This requires expertise in three different areas: aviation training, helicopter dynamics modelling, and real-time flight simulation. Therefore, a literature review is conducted on the state-of-the-art in these three disciplines to reach an understanding of human behavior and learning process, and to develop effective training programs supported by an in-depth analysis of the training task, of which aircraft dynamics modelling is a key component.

The chapter is structured as follows. First, Section 2.1 presents the literature review about aviation training and flight simulation. The literature study on helicopter dynamics modelling is included in Section 2.2.

2.1. AVIATION TRAINING

This section is devoted to aviation training, but most of the topics covered apply, with the necessary adjustments, also to other fields in which individuals are asked to work with ever more complex and potentially dangerous technologies [National Research Council, 1985; Thompson et al., 2008], such as spacecraft, marine transportation (ships and submarines) [Zhao Lin et al., 1998], energy industry (nuclear power and mining) [Park et al., 2004], ground or surface transportation (cars, trucks, and trains) [Barendswaard, 2021], command and control (military, space, civil air traffic, and industrial) [Fothergill et al., 2009], tactical surface warfare (direct fire, tanks, artillery, missiles, electronics, and battle) [Boldovici, 1987], tactical strategic air warfare (ranges and air combat exercises) [Proctor et al., 2007, 2004], and health and medical care (surgical procedures) [Edmond et al., 1997; Lin et al., 2014; Rudman et al., 1998].

The variety of conditions that pilots may face during emergencies requires experience and judgment in order to react promptly and avoid the many possible errors. They cannot be expected to perform such tasks effectively the first time they are exposed to them. Extensive practice is thus necessary to handle situations that require flawless response and to act under excess of stress or cognitive workload. So, training has always been the traditional answer to help pilots deal with scenarios that, without the correct preparation, would otherwise be unforgiving [Vincenzi et al., 2009].

Due to the risks and costs involved in training for such critical circumstances, the exclusive use of in-flight training is untenable [Vincenzi et al., 2009]. A combination of simulator and in-flight training is the solution adopted to reduce accident rates and human fatalities in a safe and efficient manner and to fulfill the ever-harsher mandate for flawless performance required by the military domain [Vincenzi et al., 2009]. Inevitably, the use of simulation to support pilot training unearths the issue of skills and performance transfer from the simulator to the actual aircraft, which is addressed in this thesis in relation to helicopters.

This section focuses on the use of flight simulation for training purposes, providing an overview of the literature devoted to the assessment of the validity and functionality of simulators as training devices.

2.1.1. FLIGHT SIMULATORS

Flight simulators have been used in a wide range of aircraft types and applications. They create the illusion of flight by simulating equipment, tasks and environments, avoiding the use of the actual aircraft. A classic report by the National Research Council [1985] identified four fundamental purposes of simulation: (i) training; (ii) systems and equipment design, development, test, and evaluation; (iii) research on human performance; (iv) licensing and certification. The boundaries of this division are often blurry and applications may thus include more than one purpose. This is the case, for example, for the design of new systems (e.g., displays, flight control systems), which should always consider the effects on human control behavior and performance, as well as on the pilot's decision-making process and situational awareness, which in turn are related to training. Indeed, the use of increased automation may induce a sense of security in the pilot, who however should be trained to keep a high level of alertness and respond rapidly and correctly in the event of an unanticipated emergency or failure/malfunction of the

system.

While all the possible applications of flight simulators deserve consideration and further research is needed to make simulation the gold standard in each of its four fundamental purposes, the attention of this section will be pointed towards the use of flight simulators for pilot training.

ADVANTAGES AND LIMITATIONS OF FLIGHT SIMULATION

Flight simulators have been used for over a century to aid trainees in the acquisition, development, and maintenance of flying skills without leaving the ground. The increasing importance and pervasiveness of flight simulators for training purposes is rooted in the various capabilities and specific benefits they bring. Indeed, their use enables trainees to carry out operations which in the actual aircraft would be dangerous to life (of both trainer and trainee) and machine and may lead to considerable savings in terms of flying time, fuel consumption and aircraft life [Moroney et al., 2008]. Furthermore, aircraft not required for in-flight training can be used in revenue-producing flights [Moroney et al., 2008].

Along with safety and cost effectiveness, flight simulators bring advantages also in terms of impact on the environment, as simulated aircraft do not pollute nor consume fuel, thus being an environmentally sound solution for pilot training, and training flexibility. Indeed, they are available 24/7 and can be employed to simulate different scenarios in terms of location, weather conditions and emergency circumstances (e.g., engine failure), giving to the instructor the possibility to fully focus on teaching rather than taking care also of safety and flight regulation aspects.

Moreover, flight simulators enable the repeatability of the training task, which indeed can be reiterated with identical boundary conditions (e.g., wind) until the student attains the required criteria. Another benefit deriving from flight simulators' preset and reset capability is the opportunity to avoid flight hindrances (e.g., interruptions due to bad weather, conflicting traffic, time and fuel to reach/return to the altitude to start a new task or repeat the same), thus providing more training opportunities than an actual aircraft in the same amount of time.

Although aircraft may be equipped with different avionics systems, such as the inertial measurement unit (IMU), to measure the aircraft's states (e.g., specific forces, angular rates and orientation), in-flight data collection for training purposes is impractical or even infeasible, unlike simulator data collection, which provides the opportunity to evaluate student's performance and learning [Moroney et al., 2008].

All these considerations lead to the conclusion that flight simulation training is more efficient than in-flight training. However, efficiency needs to be accompanied by effectiveness. For this reason, many studies addressed the issue of flight simulators' training effectiveness to prevent the occurrence of unrealistic training and ensure positive transfer of skills to the actual aircraft (i..e., skills acquired during simulator training facilitate learning the actual task) [de Winter et al., 2012; Hays et al., 1992; Vaden et al., 2005]. Efforts were also devoted to the development of measures of transfer, learning and performance [Buckhout, 1962; Gawron, 2019b; Lane, 1986; Mixon et al., 1982; Roscoe, 1980].

The issue of negative transfer of training (i..e., skills acquired during simulator training hinder learning the actual task) is followed by several challenges that need to be

tackled to significantly improve the training effectiveness of flight simulators, such as the inevitable differences in psychological factors that come with training in an intrinsically safe environment for situations that could be lethal in the real operation and user acceptance. For instance, McCauley [2006] conducted a literature review examining helicopter transfer-of-training experiments where motion was an independent variable. He concluded that motion, noise, and vibration contribute to the realism, and therefore the pilot acceptance, of a simulator. However, there is virtually no scientific evidence to support the importance of motion platforms for effective skill transfer during simulator training, even if motion cues may be beneficial under certain conditions, such as tasks involving disturbance-rejection motion.

Overall, the advantages of flight simulator training prevail over its limitations (mainly the risks related to negative transfer of skills) as proved by the growing investment of resources in this area that led to the development by regulatory agencies of qualification procedures to certificate a flight simulator as a training device.

QUALIFICATION OF FLIGHT SIMULATOR TRAINING DEVICES

The ability of a flight simulator to replace or complement in-flight training hours is not left to chance, but is regulated by a well-structured qualification procedure within each aviation regulatory body's jurisdiction (e.g., FAA in the US, EASA in the EU, etc.).

The Federal Aviation Administration [1991, 1992, 1994, 2016] defines two qualification levels of Flight Simulator Training Devices (FSTD) with increasing level of complexity:

(a) Flight Training Devices (FTD), originally with seven sub-levels (1 to 7) only and exclusively for airplanes [Federal Aviation Administration, 1992]. Regulations that are currently in place [Federal Aviation Administration, 2016] comprise only four sub-levels (4 to 7), that were extended to helicopter simulators as well. Although existing devices retain their approval if shown to function as originally designed [Federal Aviation Administration, 2011, 61.4 (b)], level 1 to 3 simulators are no longer qualified by FAA.

(b) Full Flight Simulators (FFS) with four sub-levels (A, B, C, D) for airplanes and three sub-levels (B, C, D) for helicopters [Federal Aviation Administration, 2016]. Level A for helicopters is reserved for potential future use.

A device other than a full flight simulator or flight training device may be approved by the FAA for specific purposes [Federal Aviation Administration, 2011, 61.4 (c)]. This is the case for Aviation Training Devices (ATD) [Federal Aviation Administration, 2018], which are divided in Basic ATD (BATD) and Advanced ATD (AATD) and can be used for pilot training and aeronautical experience (including instrument currency), but not for practical tests, aircraft type specific training, or for an aircraft type rating.

The European Aviation Safety Agency [2012, 2018] instead distinguishes between four qualification levels of Flight Simulator Training Devices (FSTD) with increasing levels of complexity:

(a) Basic Instrument Training Devices (BITD), only for airplanes;

(b) Flight and Navigation Procedure Trainers (FNPT), with two sub-levels (I, II) for airplanes and three sub-levels (I, II, III) for helicopters;

(c) Flight Training Devices (FTD), with two sub-levels (1, 2) for airplanes and three sub-levels (1, 2, 3) for helicopters;

(d) Full Flight Simulators (FFS) with four sub-levels (A, B, C, D) for both airplanes and helicopters.

Both FAA and EASA qualification requirements are very strict and concern both hardware (e.g., visual, motion, and control loading systems, etc.) and software (e.g., flight mechanics model of the helicopter, motion cueing algorithms, etc.) components. These requirements need to be supported with a statement of compliance and, in some designated cases, an objective test, i.e., a quantitative assessment based on comparison with data, and/or a subjective test, i.e., qualitative assessments based on established standards as interpreted by a suitably qualified person (e.g., a pilot). This process leads to highly sophisticated, complex and expensive devices, whose training effectiveness should be accepted as an axiom, as stated by EASA [2018, (p. 44), 2012, (p. 34)]: *"Fidelity of modern FSTDs is sufficient to permit pilot assessment with the assurance that the observed behaviour will transfer to the aircraft."*. No emphasis is given on the training program, which must be adapted to the FSTD used in order to ensure positive transfer-of-training. Efforts in this direction were made by the International Civil Aviation Organization (ICAO) 2012; 2015.

Other types of flight simulators do exist, however, they are not considered in regulatory standards, because their training effectiveness is not proven. They can nevertheless be very useful, in particular for initial training or for the familiarization with the helicopter cockpit layout and instrumentation. There are different designations for this category of simulators. The most common example, because of its affordability and versatility, is the desktop trainer, also known as computer-based trainer (CBT) or personal computer-based aviation training devices (PCATD).

FIDELITY

Simulation fidelity is a controversial topic [National Research Council, 1985] and its application as a criterion to assess the effectiveness of training simulators raised more questions than it has answered [Cormier et al., 1987]. Also the definition of the notion of fidelity is a debated theme [Roza, 2005]. While a single definition encompassing all aspects of fidelity would reduce the confusion around the usage of this term, it would never be sufficiently precise or operational to be useful in the drawing up of guidelines for the development of a new training simulator.

The notion of fidelity was first introduced by Miller [1954] with the term *"degree of simulation"*, which has slowly disappeared from the jargon of training developers and researchers [Hays et al., 1989]. As a matter of fact, flight simulators will never be able to replicate the actual aircraft exactly, but provide varying *degrees* of physical reproduction, which depend upon many variables, such as the characteristics of the simulator itself, the task to be taught and the trainee's level of experience. Miller differentiated between *engineering* and *psychological* simulation, with the first being the degree of replication

of the physical and functional characteristics of operational equipment within very tight tolerance specifications, and the second being the extent to which responses learned during training transfer into appropriate action during operations. According to Miller [1954, p. 20] *"the development of training devices should rest on psychological simulation rather than engineering simulation"*.

However, current regulations for the qualification of FSTD [European Aviation Safety Agency, 2012, 2018; Federal Aviation Administration, 1991, 1992, 1994, 2016] focus only on engineering fidelity, assuming that increased simulation realism will bring benefits also in terms of training value. This might be true, but only up to a certain level, above which the gains in training effectiveness will become uneconomical [Cormier et al., 1987; Hays, 1980; Miller, 1954; National Research Council, 1985], leading to the partial or total loss of one of the main advantages of flight simulation, i.e., efficiency, due to the costs involved in building and maintaining a simulator that is as complex as the aircraft it should replace.

Furthermore, there are situations in which there is the desire to potentially deploy flight simulators into forward operating areas for mission rehearsal purposes [Proctor et al., 2004]. Of course, the size and complexity of a simulator (e.g., large screen and motion platform) will inevitably impact its deployment.

In agreement with Miller, the National Research Council [1985] proposed simulator training validity as a more productive concept than fidelity as a criterion for evaluating simulator requirements and highlighted the need to improve our understanding of behavioral processes relevant to simulation, by directing more research efforts towards the analysis of cognitive processes and development and use of human performance models. It is indeed easier to formulate simulator design criteria in terms of physical rather than behavioral requirements and the technological advancements in simulation are pushing towards this direction [National Research Council, 1985].

Although the dual interpretation of fidelity proposed by Miller provides a better understanding of the concept of fidelity, emphasizing the shortcomings of current regulations for FSTDs, it does not cover all the aspects of the concept, being still too general to develop user-oriented guidance in the design, acquisition, and deployment of training simulators. Hays [1980] conducted a literature review on simulator fidelity in order to determine how the term fidelity has been used, realizing that *"at the very least, a set of consistently used operational definitions of fidelity is required"* [Hays, 1980, p. 1]. Indeed, he found many different terms and definitions of fidelity in literature and often different "types" of fidelity are used to label the same concept. Such discrepancies characterize both academia (training researchers) and industry (simulator developers). Through this review, Hays identified four facets intrinsic to the concept of fidelity:

1. the degree to which the simulator duplicates the appearance and "feel" of the operational equipment, referred to as *physical* or *equipment fidelity*.

2. the degree to which the simulator duplicates the sensory stimulation which is received from the task situation, referred to as *functional* or *environmental fidelity*.

3. the degree to which the simulator is perceived by the trainee as being a duplicate of the operational equipment and the task situation, referred to as *psychological* or *perceptual fidelity*.

4. the correspondence between tasks performed on the actual equipment and tasks performed on the training simulator, referred to as *task* or *behavioral fidelity*.

It is evident that simulator representativeness of reality can be evaluated at different levels. For each of these levels, one or more definitions of fidelity has been proposed. In an effort at seeking clarity in the formalization of the fidelity concept, Pool [2012] summarized graphically the different definitions found in literature (Fig. 1.4). Perceptual and behavioral fidelity match, both in terms of naming and meaning, with the definitions presented by Hays [1980]. In other cases, the same fidelity concepts have been described with different labels than those identified by Hays or they, at least, overlap (e.g., *objective fidelity* comprises both physical (or equipment) and functional (or environmental) fidelity). Pool presented two facets of fidelity that were not identified by Hays in his literature review: *model* and *error fidelity*, which are described as the accuracy of the aircraft model response to pilot input [Pavel, 2001; Pavel et al., 2013], and as the accuracy in pilot's performance [Ashkenas, 1986], respectively.

Current regulations for FSTDs focus on objective and model fidelity [Miletović, 2020, p. 10, Tab. 1.2], even though behavioral fidelity should be paramount from a training effectiveness perspective. However, also the specifications in terms of validation of flight model (model fidelity) and cueing fidelity (which is part of objective fidelity) exhibit many deficiencies, especially in relation to rotorcraft. For example, Pavel et al. [2013] performed a comprehensive review of the criteria to validate models for helicopter FSTD qualification, underlining the limitations of the regulatory requirements to analyze the helicopter's off-axis response, which may lead to models that do not comply with the original vehicle's handling qualities. This means that pilots might still attribute deficiencies to the simulator flight model even when the specifications are met. To solve these discrepancies, a tuning process need to be undertaken requiring both physical and artificial adjustments to the structure and parameters of the model (*model tuning*). While physical tuning is justified because it is based on improved knowledge of fundamental principles or on physical insight deriving from flight tests performed in the actual aircraft, artificial tuning is simply the result of expert judgment [Pavel et al., 2013].

Weaknesses are found also in terms of criteria for evaluating simulator motion cueing fidelity for rotorcraft, which specify only robotic constraints and required response times of the motion cueing system [Miletović, 2020]. Furthermore, the procedure for motion system tuning is mainly qualitative and based on pilot subjective ratings. To address this issue, Miletović [2020] proposed a quantitative procedure to tune simulator motion systems based on modal analysis. This is achieved by coupling the linearized vehicle and motion cueing algorithm dynamics and by analyzing the modal distortion of human-perceived quantities (specific forces and angular rates) induced by the motion cueing algorithm. Quantitative tuning can therefore be conducted in a way that minimizes the distortion of the mode with higher participation in the specific task that is to be simulated.

As part of the Garteur HC/AG-21 (Rotorcraft Simulation Fidelity Assessment Predicted and Perceived Measures of Fidelity) and NATO AVT 296, attempts have been made also to rationalize the subjective evaluation process and ratings scales used to provide consistency across experiments [Pavel et al., 2021]. To this end the Simulator Fidelity Rating scale [Perfect et al., 2014] was developed to complement and augment current

FSTD regulations on those requirements that are poorly defined, and open to interpretation by the operator and qualifying body, and ADS-33E [US Army AMCOM, 2000] predicted handling qualities ratings were proposed as starting point metrics for the exposure of fidelity deficiencies.

2.1.2. TRANSFER-OF-TRAINING

Transfer-of-training (ToT), also known as transfer-of-learning, takes place whenever our *existing* knowledge, abilities, and skills affect the learning or performance of new tasks [Cormier et al., 1987]. Positive transfer occurs when later acquisition or performance is facilitated, while negative transfer may occur if training impedes performance in the real-world task. Simulation is used to stimulate and enhance our existing skills or to maintain proficiency in the performance of a certain task [Vincenzi et al., 2009]. Thus, simulation and transfer-of-training go hand in hand and are pervasive in our every-day life, accompanying us from childhood to adulthood [Cormier et al., 1987; Vincenzi et al., 2009].

It is important to emphasize that ToT is not just a matter of transferring what was learned in training to the actual real-world setting. The transfer phenomena are much more complex, because they might be influenced by all the prior-learned knowledge and skills [Cormier et al., 1987].

The primary focus of flight simulation transfer-of-training is to assess how learning one task in a flight simulator affects the trainee's performance capability of the same task in the actual aircraft [AGARD, 1980]. Transfer-of-training experiments are one of the few available methods for direct evaluation of the training effectiveness of flight simulators, in which the transfer of behavior learned in a certain setting (e.g., a simulator) to the evaluation setting of interest (e.g., a real aircraft) is explicitly measured, usually in terms of training time saved with respect to full in-flight training [Roscoe, 1980].

To measure transfer, at least two experimental groups of participants are required. Speed of learning in the actual aircraft by an experimental group, previously trained in the simulator, is compared with the learning performances of a control group having no special previous training or previously trained in the actual aircraft [AGARD, 1980]. Alternatively, the experimental group may be trained in a newly developed simulator and the control group in an existing one. This design then enables a comparison between the two simulators in terms of training effectiveness. The groups must be carefully matched, of course, in terms of relevant prior training and experience.

Variations of the basic transfer model have also been proposed [AGARD, 1980]:

1. Self-control transfer model: this model is useful in a situation in which operational training is interrupted for a period of training in a simulator. In such a situation, the students could serve as their own control group, and performance data obtained in the operational aircraft immediately following simulator training could be compared with similar data obtained in the aircraft immediately prior to engaging in simulator training. The difference in these two sets of performance data could be attributed to the intervening simulator training program. However, the outcomes of such a study might be influenced by the confounding effects of forgetting (or reminiscence), particularly if there was a significant time interval between initial and subsequent practice in the operational vehicle [AGARD, 1980].

2. Pre-existing control transfer model: this model is useful when data collected from previous populations of students entirely trained in the actual aircraft or with prior training in an existing simulator are available. In this circumstance, the performance of the new population of student can be compared with those of previous populations to determine the effectiveness of the new simulator over the existing one or with respect to in-flight training only. For such a comparison to be valid, the pre-existing data must have been gathered under conditions which would have been applicable to a control group trained concurrently with the experimental group.

3. Uncontrolled transfer model: this model is used when circumstances preclude the employment of a separate control group, dictated by political, administrative, or safety considerations. Positive transfer occurs when students can perform a particular task in the operational vehicle, following its learning in the simulator, without an opportunity to learn that task in the operational vehicle. However, it can be argued that performance in the real world setting cannot be attributed solely to simulator training [AGARD, 1980].

4. Simulator-to-simulator transfer model: because evaluating the learned behavior in the real-world setting is often impractical or impossible, most investigation in fact consider "quasi-transfer-of-training" experiments, in which participants are not transferred to the true real-world setting, but to a different, often more realistic or enhanced, simulation environment. A quasi-transfer design avoids the cost, hazard, and scheduling hindrances (e.g., interruptions due to bad weather) of true transfer and offers the possibility of practicing dangerous situations such as engine failures in a safe environment. This model is based on the assumption that the more realistic simulator act as a valid replacement of the real-world setting.

5. Backward transfer model: in a backward transfer study, an operator who already has demonstrated proficiency of relevant training objectives in the operational vehicle is "transferred" to the simulator, where he is required to perform tasks corresponding to those he has mastered operationally. If he can perform such tasks to criterion levels without practice in the simulator, backward transfer is said to have occurred. This model is underpinned by the assumption that transfer from the simulator to the vehicle, although of unknown quantity, will be positive if backward transfer occurrs.

6. Simulator performance improvement model: this model is used when circumstances preclude the employment of a transfer model to determine simulator training effectiveness and rely on the assumption that the improved performance in the simulator will result in improved operational performance. To be useful, it should be considered as a necessary condition: if no performance improvement occurs in the simulator, none should be expected during actual operations.

7. Simulator fidelity model: this model has been extensively discussed in Sec. 2.1.1 and is underpinned by the (controversial) assumption that a high-fidelity simulator will yield high transfer and a low-fidelity simulator will yield less – or even negative – transfer. Current regulations on FSTD are based on this model.

8. Simulator training program analysis model: this model is based on an analysis conducted *a posteriori* to assess whether the simulator is fit for the training purpose. This model used in combination with the simulator fidelity model can be used to identify possible factors limiting the effectiveness of the simulator. Actually, this type of analysis is conducted during the design and development of a training simulator. It can of course be very useful when there is the need to adapt, for research purposes, an existing simulator to a training task different from its original designation.

9. Opinion survey model: simulator effectiveness is evaluated according to subjective ratings provided by operators, instructors, training specialists, and even students. This model may easily lead to erroneous conclusions.

All the transfer models have their own advantages and limitations, with the basic transfer model being the most convincing method to estimate the training effectiveness of a flight simulator. Many studies addressed this theme by performing transfer and quasi-transfer studies and, in many cases, no statistically significant differences in proficiency between the experimental and the control group is found [Powers et al., 1975]. Such findings are then used to support suggestions that the training device and the operational system are equally effective as training media, which basically means that the null hypothesis has been accepted. However, findings of "no difference" can, of course, result from causes other than the true absence of differences [Boldovici, 1987].

Research using the Neyman-Pearson approach [Neyman et al., 1933] may indeed be consistently biased in favor of Type I errors, i.e., rejecting the null hypothesis when it is in fact true, or Type II error, i.e., overlooking an effective action, therefore the null hypothesis is accepted but is false (see Tab. 2.1). Even if no differences are found and this could confidently be ascribed to the true absence of differences, the inductive leap to declarations of equal effectiveness would remain considerable [Boldovici, 1987].

Table 2.1: Error types in frequentist inference.

Error Types Table		The null hypothesis H_0 is	
		True	False
The null hypothesis H_0 is	not rejected	Correct inference (true negative)	Type II error (false negative)
	rejected	Type I error (false positive)	Correct inference (true positive)

The Null Hypothesis Significance Testing (NHST) approach [Fisher, 1955] should therefore be used in transfer-of-training studies instead of the Neyman-Pearson approach. According to NHST, every experiment only exists in order to provide effective chance of disproving the null hypothesis, i.e., the hypothesis of no correlation/no effect. So we can talk about real effects only if the null hypothesis has been conclusively rejected. Furthermore, the NHST has only a *via negativa* approach: the null hypothesis can never be accepted. When the null hypothesis is not rejected (high p-values), we may just say that the evidence is insufficient to support a conclusion. NHST focuses on reducing the

probability of Type I errors, but may still be subject to Type II errors, especially when the sample size is small.

Also meta-analyses [de Winter et al., 2012; Hays et al., 1992; Vaden et al., 2005] and other weight-of-evidence approaches, i.e., statistical analysis that combines the results of multiple scientific studies, are only as good as the data used and may suffer from both Type I and Type II errors [Boldovici, 1987]. When designing a simulator training effectiveness experiment, efforts need to be devoted to limiting sources of error, such as: (i) small sample size; (ii) subjects in the compared groups are not matched or randomly assigned; (iii) control groups are treated differently with respect to experimental groups; (iv) amount of practice is insufficient to affect proficiency; (v) measurement of performance in the real-world setting is unreliable (only in true-transfer studies); (vi) inappropriate analyses are used to estimate transfer.

2.2. HELICOPTER DYNAMICS MODELLING

One of the core elements of a flight simulator is the flight mechanics model, which replicates the response of the actual aircraft to pilot's control inputs. Two different modelling methods are often used for helicopter dynamics simulation. One is the system identification method, which has been shown to lead to useful linear models [Remple et al., 2006]. The other method is analytical modelling, which, in general, results in models that are physically meaningful (models derived with this method are also known as physics-based models) and are more accurate than those from the system identification method when the simulation scope is large [Padfield, 2007], unless model stitching of a collection of discrete-point identified models is used for full flight-envelope simulation [Tischler et al., 2016]. However, the disadvantage of analytical modelling is that the resulting model is generally more complex. A vast and dedicated body of literature is available both on mathematical modelling of helicopter flight dynamics, e.g., [Bramwell et al., 2001; Padfield, 2007], and aircraft and rotorcraft system identification, e.g., [Klein et al., 2006; Remple et al., 2006]. A combination of these two approaches is usually adopted to validate flight mechanics models integrated within training devices [Gray, 1998; Lu et al., 2011].

Models derived both from system identification (Chapter 3) and analytical modelling (Chapters 4 to 6) methods were used in this thesis. However, the model of a Robinson R-44 helicopter, identified in hover and low-speed flight at the Max Planck Institute for Byological Cybernetics [Geluardi, 2016; Geluardi et al., 2018], was employed out of the box to assess the effectiveness of a desktop trainer during initial hover training (Chapter 3). Whereas, a physics-based model of a conventional helicopter (one main rotor and one tail rotor) was specifically developed in this thesis (Chapter 4) and used to evaluate the effects of helicopter dynamics on autorotation transfer-of-training (Chapters 5 and 6). Indeed, autorotation is a multitask maneuver comprising several phases and, as such, requires a model that is valid for a broad range of operating conditions, making analytical models more appropriate than identified models. Therefore, this section is not intended as a discussion of the details of these two modelling methods, but instead, to provide a brief overview of the most used techniques to derive phisics-based models.

2.2.1. ANALYTICAL MODELS

The helicopter model is divided in components (e.g., main rotor, tail rotor, empennage, fuselage, engine-drive train-dynamics-and-rpm governor, and control systems), whose contribution to the total force and moment is accounted for by non-linear or mathematical sub-models describing their physical behavior.

The main rotor is by far the most complex element from a modelling perspective. Analytical estimation of the forces and moments generated by the main rotor is generally achieved through the use of a blade element model [Chen, 1979], which is called "total force-and-moment" model when small-angle assumptions are adopted [Chen et al., 1988]. Alternatively, when wind-tunnel test data are available, usually as non-linear functions of incidence and Mach number, numerical integration of the blade airfoil forces and moments can be used to estimate the main rotor forces and moments, leading to a mixed analytical-numerical model [Padfield, 2007].

Similarly for the other helicopter components, both analytical and numerical methods for force and moment estimation can be used depending on whether experimental data are available. For example, forces and moments generated by the horizontal tailplane or by the vertical fin can be estimated analytically using thin airfoil theory.

An important goal of helicopter simulation and modelling is a realistic prediction of the dynamic response to control inputs in comparison with flight test data [Padfield, 2007]. To reach the desired tolerances on the deviation of the model from the actual response, it may be necessary to increase model's physical complexity. Intrinsic in the helicopter nature is a strong coupling between its different components and increasing one component's complexity usually requires a refinement also of other components' model, leading to extremely complex flight models [Pavel, 2001].

To avoid unnecessarily complicated models, it is important to be able to predict the necessary helicopter's degrees of freedom to be simulated, which will depend on the application (e.g., maneuver simulation, handling qualities assessment, flight control system design). To this end, Pavel [2001, 2008] introduced the *critical pole distance criterion* and compiled an overview of the most commonly used models according to the necessary application (see Tab. 2.2), concluding that *"It is not sufficient to blindly extend a simulation model; one has to identify the right modes to be included in the right situations in order to obtain a good prediction of helicopter behaviour"* [Pavel, 2001, p. 43].

To simulate autorotation, that is the topic of interest of Chapters 4 to 6, the simplest flight mechanics model (i.e., with a rigid transmission) requires, besides the fuselage motion, the main rotor RPM as an additional degree of freedom, which is included through the torque equation [Padfield, 2007; Talbot et al., 1982]. However, the torque equation is found in literature in different forms. For example, the torque equation used by Talbot et al. [1982] does not include the coupling with the airframe and the contribution of the transmission to the rotor polar inertia is obtained by increasing the inertia of the blades by 10%. The torque equation introduced by Padfield [2007] includes the coupling with the airframe, but does not explain how to account for the contribution of the transmission to the rotor polar inertia. Furthermore, even though the engine torque is not necessary for the simulation of autorotation, both Talbot et al. [1982] and Padfield [2007] do not explain that the engine torque in their torque equation must be multiplied by the ratio between the engine RPM and the main rotor RPM and that the body yaw equation

Table 2.2: Simulation model complexity for various helicopter applications [Yilmaz, 2018, adapted from [Pavel, 2001]].

Model Complexity		6 DoF	8 DoF	9 DoF	10 DoF	12 DoF	16 DoF
Basic Aircraft							
Low frequency maneuver	articulated	□					
	hingeless	△	△	△			
high frequency maneuver	articulated		△	△			
	hingeless		□	△	△		
Helicopter+SCAS System							
Fuselage feedback	articulated	△	△				
	hingeless	△	□	△			
Fuselage/Rotor feedback	articulated			△	△	△	△
	hingeless			△	△	△	△
Full HHQ Basic aircraft							
Within envelope		△			△		△
At the boundary					△		□
Specific HHQ		△			△		△

□: Model used in most of the cases
△: Model used for some cases
HHQ: Helicopter Handling Qualities

6 DoF: Fuselage + Quasi-static Rotor
8 DoF: Fuselage + First Order Disc-tilt Dynamics
9 DoF: Fuselage + Second Order Disc-tilt Dynamics
10 DoF: Fuselage + Rotor Flap + RPM
12 DoF: Fuselage + Rotor Flap + Rotor Lead/Lag
16 DoF: Fuselage + Rotor Flap + Rotor Lead/Lag + Pitch + RPM

must be updated to accommodate a coupling term with the torque equation. Seeking clarity in this respect, a general model of the engine-drive train dynamics has been formally derived in Appendix D, as well as for the specific case of rigid transmission, with the torque equation in its complete form accounting for the coupling with the airframe and the contribution of the transmission to the rotor polar inertia (Eq. (D.51) from Appendix D.2.2).

Partially unexplored, at least from an academic standpoint, is the influence of the engine-drive train-dynamics and rpm governor on the helicopter flight mechanics and handling qualities. A helicopter and its engine(s) are usually designed and manufactured by different companies. Incompatibilities may occur when the two systems are joined, which could affect flight safety and performance [Hamers et al., 1997; Jaw et al., 1990], because the coupling between the rotor lead-lag dynamics and the engine-drive train torsional dynamics may cause torque oscillations and rotor speed variations. For this reason, the next section provides an overview of engine-drive train and rpm governor system modelling and the design approach for its integration with the airframe dynamics.

2.2.2. SURVEY ON ENGINE-DRIVE TRAIN DYNAMICS

It has been common practice in analyzing dynamic stability of helicopters in powered flight, to neglect the effect of variation of rotor angular velocity [Padfield, 2007]. Indeed, the vast majority of helicopters by design keep a constant rotorspeed (rpm) during flight.

This is actively controlled by the governor, which measures and regulates the speed of the engine. However, there are situations in which this assumption is no longer justified, as in the case of autorotative flight where the governor is disengaged and the pilot takes over the task of controlling the rotor rpm directly [Nikolsky, 1952; Nikolsky et al., 1949a,b]. Furthermore, the inclusion of the rotor rotational speed degree of freedom can have a strong impact on the helicopter dynamics and handling qualities, as the incorporation of the engine/fuel control, transmission and governor dynamics will unearth coupling terms causing interaction with the rotor/airframe dynamics [Johnson, 1975; Kuczynski et al., 1980]. Another key aspect is represented by the fact that the rotor torque perturbations and engine vibrations can produce significant drive train loads. To correctly estimate these loads, there is the need to implement a model that accounts for the coupling of the two rotors through the flexible drive-train, and for the engine damping and inertia [Weiss et al., 2020].

ENGINE DYNAMICS

A detailed representation of engine torque requires a complicated nonlinear function of many variables such as operating power setting, ambient pressure and temperature, and fuel flow. Talbot et al. [1982] and Padfield [2007] both consider a rigid transmission and use a simplified steady-state model of the engine torque Q_e response to the fuel injection ω_f, which is represented as a first order lag:

$$\frac{Q_e}{\omega_f} = \frac{K_e}{1+\tau_e s}$$

and as a lead–lag element:

$$\frac{Q_e}{\omega_f} = K_e \frac{1+\tau_{e_1} s}{1+\tau_{e_2} s}$$

respectively. The time constants $\tau_{(\cdot)}$ and gains $K_{(\cdot)}$ are defined according to engine characteristics and operating point. Indeed, these parameters usually are not fixed constants, given the non-linearity of engines Padfield [2007]. The governor control loop for the steady-state engine model acts on the main rotor speed $\dot{\psi}_{mr}$, as shown in Fig. 2.1, with the coupled rotor/airframe dynamics given by:

$$I_{mr}\left(\ddot{\psi}_{mr} - \dot{r}\right) = Q_e - (Q_{mr} + r_{tr} Q_{tr})$$

derived in Appendix D.2.2.

Among the available engine dynamics models for real-time applications, the simplest solution is represented by experimentally determined partial derivatives of changes of output torque to changes in turbine speeds and fuel flow [Hamers et al., 1997].

In agreement with this approach, Johnson [1975, 1988] adopts a linear engine model, including inertia, damping and control torques, of the form:

$$I_e \ddot{\psi}_e = Q_e = -Q_{e_{\dot{\psi}_e}} \dot{\psi}_e + Q_{e_{\delta_t}} \delta_t \tag{2.1}$$

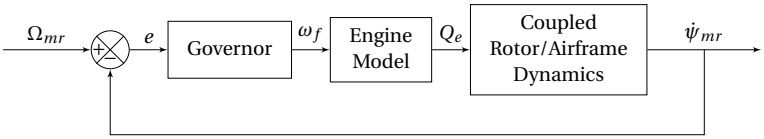

Figure 2.1: Block diagram for the controller of the governor with a steady-state engine model.

where δ_t is the throttle input, which is in a one to one relationship with the fuel mass rate ω_f, $Q_{e_{\dot{\psi}_e}} = \frac{\partial Q_e}{\partial \dot{\psi}_e}\Big|_{\delta_t=\text{const}}$ is the engine speed damping, and $Q_{e_{\delta_t}} = \frac{\partial Q_e}{\partial \delta_t}\Big|_{\dot{\psi}_e=\text{const}}$ is a control derivative. $Q_{e_{\dot{\psi}_e}}$ and $Q_{e_{\delta_t}}$ are both function of throttle position and engine speed.

According to Johnson [1975, 1988], the engine speed damping can be related to the engine trim operating conditions by:

$$Q_{e/\dot{\psi}_e} \approx (1-\eta)\frac{P_e^{trim}}{\Omega_e^2} \tag{2.2}$$

Q_{e/δ_t} is provided by the engine's manufacturer or can be approximated using a first order lag [Talbot et al., 1982] or a lead lag element [Padfield, 2007]. The governor control loop for the steady-state engine model acts on the engine speed, as shown in Fig. 2.2.

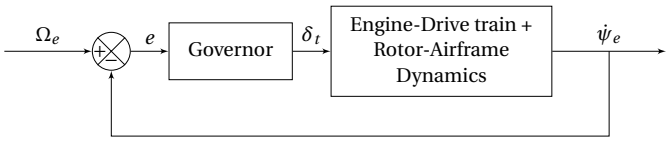

Figure 2.2: Block diagram for the controller of the governor with a linear engine model.

However, engine dynamics based on partial-derivative models may be unsatisfactory for certain applications [Ballin, 1988] due to their inaccuracy in matching experimental data [Kaplita, 1984]. Such models may indeed overlook important effects that could be accounted for only by modelling all the needed internal engine states and, just like all the linear models, tend to be valid only for a limited range of operating conditions. Therefore, their validity is always in question when used under conditions for which they are not designed.

An acceptable level of fidelity can be achieved by using an engine model comprising individual engine components (e.g., inlet, compressor, combustor, gas generator, power turbine, exhaust and spools), each of which is modeled based on thermodynamic laws governing the engine cycle. Such component-type simulations are used by engine manufacturers to study the steady-state and transient behavior of engines, but they are usually far too complex for use in real-time digital simulation. A component engine model which is simplified for real-time use is the most promising alternative to partial-derivative engine representations [Ballin, 1988], as demonstrated by the validation of the model of a UH-60 helicopter against flight test data [Ballin, 1987]. Such nonlinear engine models are available in analytical form [Liu et al., 1995a,b] or as look-up tables generated from the actual engine data or the transient engine simulation [Wong, 1993], known as the horsepower extraction engine model (HPX) and the direct transient method (DTM).

DRIVE TRAIN DYNAMICS

The drive train of a twin-engine conventional helicopter comprises two engine drive shafts, a main transmission with accessory drives, tail rotor drive shafts, an intermediate gearbox, and a tail rotor gearbox. Fig. 2.3 illustrates a schematic of the drive train architecture of a twin-engine conventional helicopter with all the main components involved and their connection.

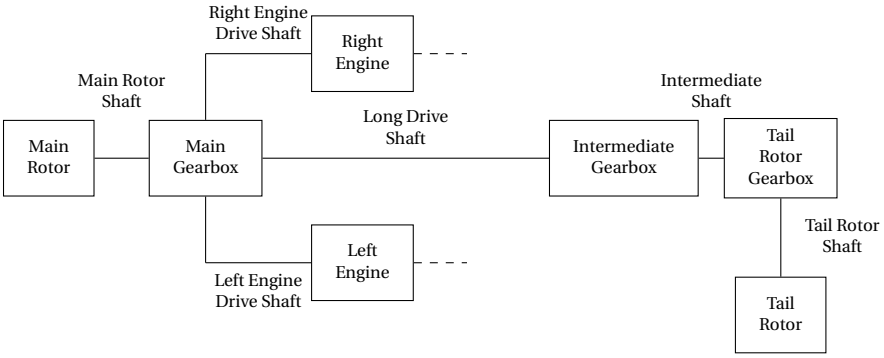

Figure 2.3: Schematic of a twin-engine conventional helicopter power train.

The drive train models generally used in real-time flight simulation consist of the torsional dynamics only [Johnson, 1975, 1988]. More realistic drive train models would require an extremely detailed level of 3D modeling (e.g., contact between neighboring gear wheels) [Weiss et al., 2020], which would make them unsuitable for real-time flight simulation applications. Furthermore, this level of complexity is not necessary for training and certification purposes. To derive the drive train torsional model, the following simplifications are often made [Weiss et al., 2020]:

1. Lumped inertia: each gear mesh will be modelled as a rigid disk, whose moment of inertia takes into account the inertia of the gear mesh and a portion of the inertia of the shaft connected to it. This contribution is determined according to the position of the center of flexibility of the shaft.

2. Lumped torsional stiffness: each shaft will be represented as a torsional spring, whose stiffness takes into account the torsional flexibility of the shaft (within the main torsional load path) and that of the gear meshes to which its ends are connected.

The differential equations of the engine-drive train torsional dynamics can be obtained from the equilibrium of the torques of the two rotors and the engine [Johnson, 1975, 1988].

COUPLING WITH THE ROTOR-AIRFRAME SYSTEM

Due to couplings in the rotor hub's rotational degree of freedom related to the in–plane inertial and centrifugal forces generated by the rotor blades, torsional drive train dynamics are likely to affect especially the lead–lag motion of the rotor blades [Muscarello et al.,

2017; Weiss et al., 2020]. To reveal such coupling terms, an analytical approach, based on rigid rotor blades and blade element dynamics, can be used [Chen, 1987], which drops the constant rotorspeed constraint in the derivation of the rotor torque equation and flap-lag dynamics. Yaw and heave degrees of freedom are the rigid-body dynamics that are affected the most by the engine-drive train dynamics, especially in hover [Chen, 1992; Hui, 1999]. For example, Chen [1992] demonstrated that by including rotor speed variations, the effective vertical damping decreases significantly with respect to that calculated with a constant speed assumption, thereby providing a better correlation with flight test data. Furthermore, he showed that collective flapping and flapping rate are the two most effective rotor states for feedback, much more effective than rotor speed, inflow and lead-lag.

However, this analytical approach does not follow the correct load path. Indeed, the engine torques are not applied directly to the hub, but are transmitted through the gear boxes, which are directly connected to the airframe [Muscarello et al., 2017]. Muscarello et al. [2017] propose a numerical approach to restore the correct torsional load path between the drive train and the airframe, by transferring the torsional loads to the structural nodes of a finite element model of the fuselage and by feeding back the torques generated by the fuselage deformation into the drive system. To unveil the influence of the drive train dynamics on the flexible rotor blade motion, a numerical approach based on multi-body dynamics can be used instead [Weiss et al., 2020].

GOVERNOR DESIGN

The governor measures and regulates the speed of the engine (engine rpm) using a feedback controller on the error in rpm (difference between the measured rpm and the reference value, which is 100%). The traditional hydromechanical power turbine governor is a proportional control [Liu et al., 1995b], but to achieve better performance proportional plus integral [Johnson, 1988], and in some cases rate feedback is usually adopted [Hui, 1999; Johnson, 1988; Talbot et al., 1982]. In addition, hydromechanical governor uses reset mode to set the power turbine time constant to attenuate the torsional peak of an engine-rotor drive train system [Wong, 1995]. This reset power turbine governor is a first order lag [Padfield, 2007]:

$$\frac{\omega_f}{\Omega_{mr} - \dot{\psi}_{mr}} = \frac{K_{p_{\omega_f}}}{1 + \tau_{\omega_f} s} \qquad \text{with proportional control,}$$

$$\frac{\omega_f}{\Omega_{mr} - \dot{\psi}_{mr}} = \frac{K_{P_{\omega_f}} + \frac{1}{s} K_{I_{\omega_f}}}{1 + \tau_{\omega_f} s} \qquad \text{with proportional plus integral control, and}$$

$$\frac{\omega_f}{\Omega_{mr} - \dot{\psi}_{mr}} = \frac{K_{P_{\omega_f}} + \frac{1}{s} K_{I_{\omega_f}} + s K_{D_{\omega_f}}}{1 + \tau_{\omega_f} s} \qquad \text{with PID control, and}$$

or a second order lag [Johnson, 1988]:

$$\frac{\omega_f}{\Omega_{mr}-\dot{\psi}_{mr}} = \frac{K_{p_{\omega_f}}}{1+\tau_{\omega_{f_1}}s+\tau_{\omega_{f_2}}s^2} \qquad \text{with proportional control,}$$

$$\frac{\omega_f}{\Omega_{mr}-\dot{\psi}_{mr}} = \frac{K_{P_{\omega_f}}+\frac{1}{s}K_{I_{\omega_f}}}{1+\tau_{\omega_{f_1}}s+\tau_{\omega_{f_2}}s^2} \qquad \text{with proportional plus integral control, and}$$

$$\frac{\omega_f}{\Omega_{mr}-\dot{\psi}_{mr}} = \frac{K_{P_{\omega_f}}+\frac{1}{s}K_{I_{\omega_f}}+sK_{D_{\omega_f}}}{1+\tau_{\omega_{f_1}}s+\tau_{\omega_{f_2}}s^2} \qquad \text{with PID control, and}$$

For tilt-rotors, the governor usually does not act on the fuel flow, but on the collective pitch of the blades of each rotor [Johnson, 1988]:

$$\frac{\theta_0-\theta_0^{TRIM}}{\Omega_{mr}-\dot{\psi}_{mr}} = \frac{K_{P_{\theta_0}}+\frac{1}{s}K_{I_{\theta_0}}}{1+\tau_{\omega_{\theta_{0_1}}}s+\tau_{\omega_{\theta_{0_2}}}s^2}$$

Such types of governors, typical of turboprops and known as blade-pitch or beta governors, are used in place of classical helicopter throttle governors, which otherwise would cause unsustainable torque transient in airplane mode [Muscarello et al., 2019] due to the much higher inflow experienced in this operating condition.

The disadvantage of the reset power turbine governor is that the control loop sacrifices response time for stability. This is because the reset control filters out the torsional peak at the torsional frequency and increases the phase angle at the same frequency, making more difficult the design of a high bandwidth governor. To minimize phase angle changes at the first torsional frequency, a notch filter is usually used in combination with or in place of the reset filter to attenuate this and higher frequencies torsional modes [Chen, 1992; Wong, 1995]. The transfer function of a standard notch filter is represented using Bode diagrams in Fig. 2.4:

$$NF(s) = \frac{s^2+\omega_{nf}^2}{s^2+\omega_{bw}s+\omega_{nf}^2}$$

The notch filter frequency ω_{nf}, which in the example of Fig. 2.4 is 10 rad/s, must be set equal to the torsional frequency that needs to be filtered.

The typical design goal for a robust controller is to require a gain margin of 6 dB at the torsional frequency [Kuczynski et al., 1980; Wong, 1995] and a phase margin of 45 deg [Kuczynski et al., 1980] or more. In general, when these margins are achieved by analysis, the actual flight characteristics of the helicopter are also satisfactory. Since the notch filter depends on the rotor-drive train system, different helicopter applications will require different notch filters [Wong, 1995].

A comparison between the governor controller based on the reset filter and that on the notch filter is conducted by Wong [1995] on an autorotation recovery simulation,

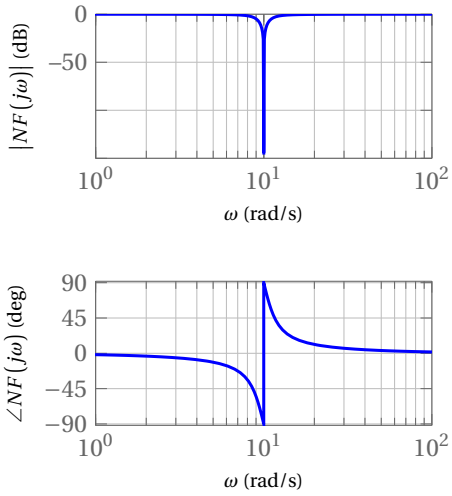

Figure 2.4: Bode plot of the notch filter transfer function.

which is considered especially challenging to the integration of engines in operational helicopters. A power recovery autorotation terminates in a hover as opposed to landing without power. This is always possible in a training situation, because the engine failure is not real, but simulated by disengaging the rotor shaft from the power shaft by means of a clutch with the engine in an idle state. Conversely from what one may think, there are many risks involved also in power recovery autorotations, especially when dealing with turbine engine helicopters due to the presence of the governor. Indeed, the feedback on the error in rpm is slow (frequency of the order of 1 Hz) and hence cannot anticipate power demands in a timely manner [Talbot et al., 1982]. This means that the outcome of the maneuver may be very sensitive to the choice of the power recovery time. Simulation results demonstrate that the notch filter design grants a faster recovery time with less rotor droops with respect to the reset filter [Wong, 1995].

To quickly accommodate large power changes, a synergistic approach between feedback on the error in rpm and feedforward on the collective input variation with respect to the trim value is usually adopted [Hui, 1999; Talbot et al., 1982], as shown in Fig. 2.5. A far more robust and reliable approach is proposed by Zheng et al. [2018], who used an engine nonlinear model predictive control, with an objective function that does not consider only the error in rpm, but also the deviation between the torque provided by the power turbine and that demanded by the helicopter.

For free turbine engines, in which the power turbine is not mechanically linked to the gas generator, the structure of the governor control system is more complex, comprising an inner control loop on the gas generator speed and an outer control loop on the power turbine speed [Hui, 1999; Wong, 1995], as shown in Fig. 2.6.

Deficiencies in the representation of the rotor speed dynamics and fuel control may lead to incorrect fuel flow and main rotor torque estimations, as well as inaccurate main-rotor-speed response to a collective input, incorrect blade-flap and lag response to rotor control inputs, adverse yaw response to collective inputs, and delayed vehicle response to all control inputs [Kaplita, 1984]. Ballin [1987] demonstrated the importance of mod-

elling the governor and the engine-drivetrain dynamics with a sufficient level of detail to avoid an unrealistic vehicle response to pilot control inputs.

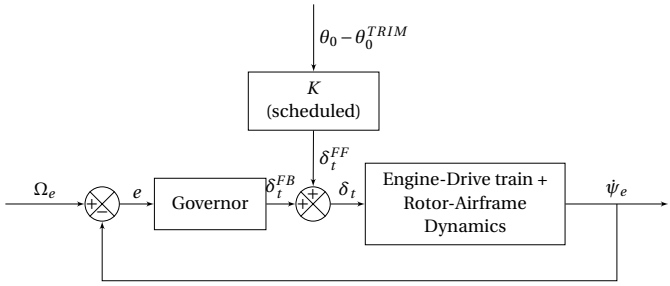

Figure 2.5: Block diagram for the controller of the governor with feedback on the engine speed and feedforward on the collective input.

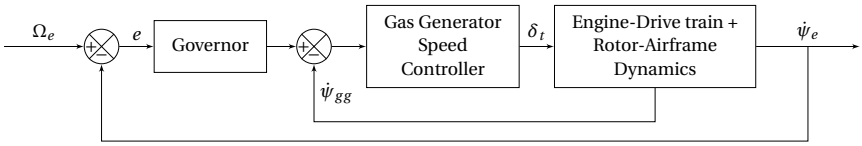

Figure 2.6: Block diagram for the controller of the governor with an inner control loop on the gas generator speed and an outer loop on the power turbine speed.

TRADITIONAL ENGINE/FUEL CONTROL DESIGN APPROACH

The traditional approach to the design of the engine and fuel control, from a helicopter system viewpoint, is to treat the low frequency dynamic stability and transient response of the isolated engine/drive system/rotor system [Kuczynski et al., 1980]. For example, the stiffness matrix of the isolated drive train system must be singular, because there is a rigid mode related to the rigid rotation of the engines, the drive shafts and the two rotors, and the drive train natural frequencies must be different than the integer multiples of the number of blades-per-revolution of the main rotor.

Furthermore, although the drive train bending dynamics can be neglected for preliminary certification purposes, there are some design aspects concerning bending that need to be considered, such as the so-called critical speed [Muscarello et al., 2017]. Indeed, bending produces an offset of the center of gravity of a shaft with respect to its rotation axis, thus acting as a periodic forcing function on the shaft with a frequency equal to the angular speed of the shaft. Therefore, it is paramount to check that the angular speed of a shaft differs from its bending frequencies. The check on the natural frequencies needs to be repeated also for the coupled engine-drive train and rotor system.

Once the torsional stability analysis is conducted during the design phase, the fuel control system can be designed from standard open loop Bode plots granting a gain margin of 6 dB at the torsional frequency [Kuczynski et al., 1980; Wong, 1995] and a phase margin of 45 deg [Kuczynski et al., 1980] or more (e.g., 60 deg). This process is described in detail in Appendix D.

Of course such a level of modelling detail may not be required for maneuver simulation (e.g., pilot training), but it is necessary for design and certification (e.g., dynamic stability analysis and flight control system design).

I

TRAINING OF BASIC FLYING SKILLS: HOVER

3

HOVER TRANSFER OF TRAINING: EFFECTS OF SIMULATOR FIDELITY

.

According to current regulations on Flight Simulator Training Devices [European Aviation Safety Agency, 2012], the ability of a flight simulator to replace or complement in-flight training is ascribed to a qualification procedure. The minimum standards for qualification that a flight simulator should comply with depend upon the type of training demanded (ab-initio and refresher training, type rating training with limited checking/testing capability or proficiency checks and skill tests) [European Helicopter Safety Team, 2015a,b]. The qualification requirements are very strict and concern both hardware (e.g., visual, motion, and control loading systems, etc.) and software (e.g., flight mechanics model of the helicopter, motion cueing algorithms, etc.) components. This process leads to highly sophisticated, complex and expensive devices. However, no emphasis is given on the training program (e.g., the structure and the focus should be adapted based on trainee's flight experience and on the difficulty of the task), which, on the contrary, should cover a prominent role with respect to simulator fidelity, especially during ab-initio training.

This chapter investigates the effectiveness of a low-fidelity flight simulator (in terms of equipment and visual and motion characteristics), which can be classified as a computer-based training device, on initial hover training using a part-task training program. The aim is to examine whether a low-fidelity simulator environment is equally capable as a higher fidelity simulator of teaching non-pilots to hover when a training program formulated according to instructional design theories is used. This has the potential to substantially reduce training costs and lead to a widespread use of flight simulators with a consequent reduction of risks. A positive outcome of this study may lay the foundations to investigate whether the hover part-task training program had a mitigating effect, compensating the lack of simulator fidelity. The chapter is structured as follows. First, an

The contents of this chapter have been published in: Scaramuzzino, P. F. et al. (2018). Effectiveness of a Computer-Based Helicopter Trainer for Initial Hover Training. In *44th European Rotorcraft Forum (ERF 2018)*, number 79, pages 1142–1156, Delft, September 18-20, 2018. NLR.

overview of the computer-based training devices is provided in Section 3.1 together with a literature review about their use in previous experiments. Then, the design of a quasi-transfer-of-training experiment performed on the CyberMotion Simulator (CMS) aimed at evaluating the effectiveness of the combination of a low-fidelity simulator with a part-task training program for initial hover training is presented in Section 3.2. The results from this experiment are documented and discussed in Sections 3.3 and 3.4, respectively. The chapter is concluded in Section 3.5.

3.1. LOW FIDELITY SIMULATORS: COMPUTER-BASED TRAINING DEVICES

Flight Simulator Training Devices (FSTDs) are crucial tools for pilot training. These devices are cost effective, flexible, and provide an inherently safe environment for training even hazardous scenarios [Allerton, 2010]. Simulators have been used for over a century to aid trainees in the acquisition, development, and maintenance of their flying skills without leaving the ground [Adorian et al., 1979; Allen, 1993; Page, 2000]. For rotorcraft it is highly desirable to be able to develop low-level flying skills in simulators, given the intrinsically difficult helicopter flight dynamics.

Since the computer software and hardware incorporated into a FSTD determine its developmental, operational, and maintenance costs, there is great academic and industrial interest in understanding simulation fidelity requirements needed to meet FSTDs users' needs [Rehmann et al., 1995]. One flexible and affordable training solution suitable for novice pilots currently considered is the low-fidelity "Desktop Trainer", also known as Computer Based Trainer (CBT).

Especially for training that makes use of low-fidelity CBT, it is critical to experimentally prove the effectiveness of the supplied training and the transfer of learned skills to the real world setting. Transfer-of-Training (ToT) experiments are one of the few available techniques that can be used to explicitly measure such training effectiveness. Numerous studies have been dedicated to verifying the effectiveness of training in CBT. Unfortunately, many investigations focus on instrument [Stewart II et al., 2001; Taylor et al., 1999] and situation awareness [Proctor et al., 2004] training only. Furthermore, in those studies that explicitly investigated the training of flying skills in CBT, the experimental evidence for training effectiveness has not always been consistent. For example, Ortiz [1994] trained sixty college students with no previous flight experience to perform a squared pattern maneuver. In this case even a true ToT experiment design was used: thirty of the subjects were trained in a CBT before flying the actual aircraft, while the remaining thirty received real-flight training only (Cessna 150 and 152). Statistical tests on the measured data showed that in the real aircraft the CBT-trained experimental group performed significantly better than the control group. In a separate study, Proctor et al. [2007] considered three different interface configurations (cabin with motion, cabin with no motion and CBT) and trained participants to perform a complex task of combat search and rescue, while controlling a model of the UH-60. Although not being a ToT experiment, their results showed that learning did not occur in the helicopter Computer Based Trainer, arguing that the provided time frame to master the task might not be acceptable to many possible users because of the monitor size. Recent investigations

by Fabbroni et al. [2017a,b], however, showed that hover skills acquired during fixed-base training in a CBT with a wide field-of-view display do transfer to a more realistic setting in a full-motion flight simulator.

The goal of this chapter is to explicitly evaluate the extent to which hover skills developed on a Computer Based Trainer are effectively transferred to a more realistic environment. To achieve this goal, a quasi-Transfer-of-Training (qToT) experiment [Taylor et al., 1993] with task-naïve participants was performed.

3.2. EXPERIMENT DESIGN

In the experiment, participants with no prior flight experience neither in actual helicopters nor in simulators, were trained to perform the hover maneuver controlling an identified model of a Robinson R44 civil light helicopter [Geluardi, 2016; Geluardi et al., 2018]. Two groups were considered. The first group (the "*experimental*" group) was trained on a CBT (Fig. 3.1a) and then transferred to the CyberMotion Simulator (CMS) (Fig. 3.1b). The second group (the "*control*" group) received the entire training in the CMS. A previously developed hover training program [Fabbroni et al., 2017a] was used to bring participants to a satisfactory level of performance. Previous works proved the effectiveness of the adopted training, which is designed as a realistic flight lesson divided into several phases.

(a) The Max Planck Institute Computer Based Trainer.

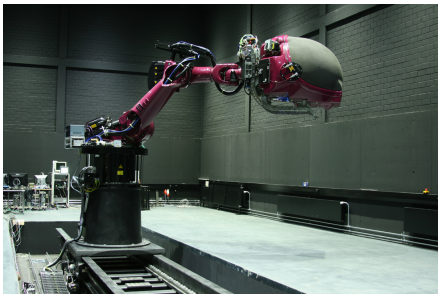

(b) The Max Planck Institute CyberMotion Simulator [Nieuwenhuizen et al., 2013].

Figure 3.1: Flight simulators used in the experiment: the Computer Based Trainer (a), and the CyberMotion Simulator (b).

3.2.1. PARTICIPANTS

A total of 24 task-naïve participants took part in the experiment, 15 male and 9 female. The participants had an average age of 26 years (σ = ±3.81 years). They were chosen based on a pre-experimental aptitude test intended to select for good manual control skills.

3.2.2. APTITUDE TEST

An effort was made to select the participants and to balance them equally over the two groups based on the performance they achieved in a two degrees-of-freedom (pitch and

roll) combined target-following and disturbance-rejection task. Indeed, to limit sources of error in transfer experiments, subjects should not be assigned randomly to one of the two groups [Boldovici, 1987] and pre-experimental tests to balance the two groups are often adopted, e.g., [Kaempf et al., 1990]. The task consisted of rejecting a disturbance signal acting on the controlled element, i.e., the dynamics that each subject had to control. The controlled element had dynamics that resemble the dynamics of an aircraft and for both the pitch and roll axes were described by the following transfer function:

$$H_{ce} = \frac{K_{ce}}{s(s+1)} = \frac{1}{s(s+1)} \tag{3.1}$$

The aptitude test was performed in the Control Loading Lab (Fig. 3.2a) at the Max Planck Institute for Biological Cybernetics. A side-stick was used to give inputs to the controlled element. Roll and pitch axis of the side-stick were both active during the experiment. Therefore, both rotation (Fig. 3.2c) and translation (Fig. 3.2d) of the horizon marker on the artificial horizon were presented on the display. No other cues were presented.

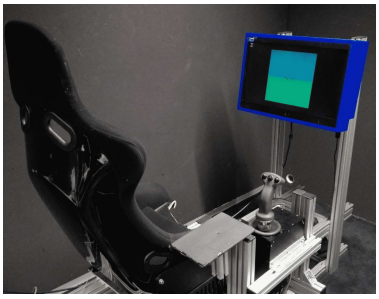

(a) Apparatus.

(b) Visual.

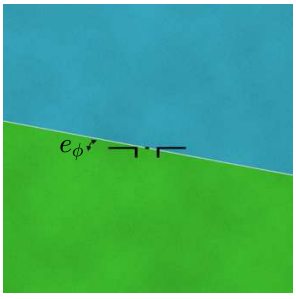

(c) Roll error.

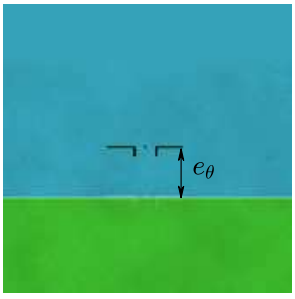

(d) Pitch error.

Figure 3.2: Experimental apparatus (a) and visual (b) (c) (d) used during the aptitude test.

The display used for the aptitude test is produced by VIEWPixx, VPixx Technologies Inc., Canada. The control device is an electrical control-loaded sidestick (Wittenstein Aerospace and Simulation GmbH, Germany). The sidestick was located on the right side of the chair where the participants were sitting. Thus, participants controlled the device using their right hand.

The aptitude test was composed of 10 trials. Each trial lasted 90 seconds. 33 participants were tested. Their performances in terms of Root Mean Squared (RMS) error are presented in Fig. 3.3 as box-whiskers plots. From this figure, it can be noticed that starting from the 7^{th} trial performances become stable as the median over the last 4 trials is almost constant and the between-subjects variability is smaller compared to the first trials. The outliers represent those participants who lost control in a particular trial.

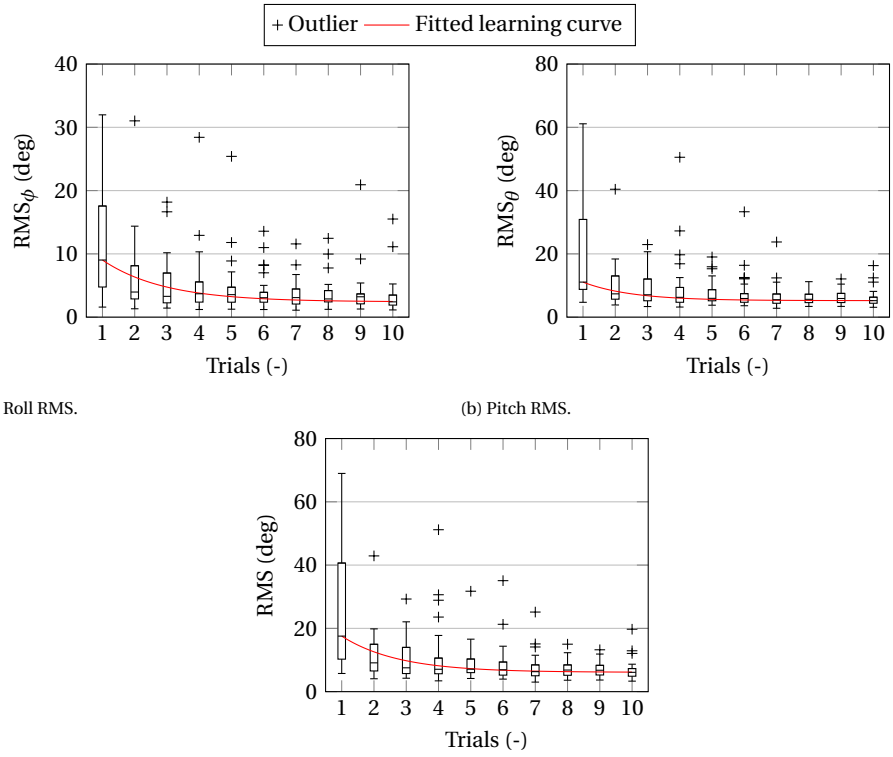

(a) Roll RMS.

(b) Pitch RMS.

(c) Combined pitch and roll RMS.

Figure 3.3: Performances of the participants in the aptitude test.

A criterion, able to describe both overall and final behavior of each participant, was established to select participants. If over the last 4 trials, a participant had a number of trials within the 3^{rd} quartile greater than 2, the participant was retained. If this number was lower than 2, the participant was excluded.

By applying this criterion, a total of five subjects were excluded. Two other participants were excluded because they did not comply with the safety requirements of the CyberMotion Simulator (CMS). Furthermore, two subjects left the study after the aptitude test due to personal reasons. The remaining twenty-four participants were ranked, based on their performance in the aptitude test, and methodically assigned to one of the two groups. From Fig. 3.4, it can be noticed that the two groups, on average, show equivalent performance for $\overline{\text{RMS}}$, $\overline{\text{RMS}_\phi}$ and $\overline{\text{RMS}_\theta}$. This is supported by independent-

samples T tests for all three metrics (Tab. 3.1), which indicate that there is no significant between-group difference.

Table 3.1: Independent-samples t-test between the two groups.

Metric	**t-test**		
	t	df	Sig. (2-tailed)
$\overline{\text{RMS}}$	−0.039	22	0.969
$\overline{\text{RMS}}_\phi$	−0.371	22	0.714
$\overline{\text{RMS}}_\theta$	0.154	22	0.879

Hence, the metrics show that the groups have been equally distributed in terms of manual control skills throughout the aptitude test. The independent-samples T test was applied only after checking that data were approximately normally distributed and with homogeneous variance.

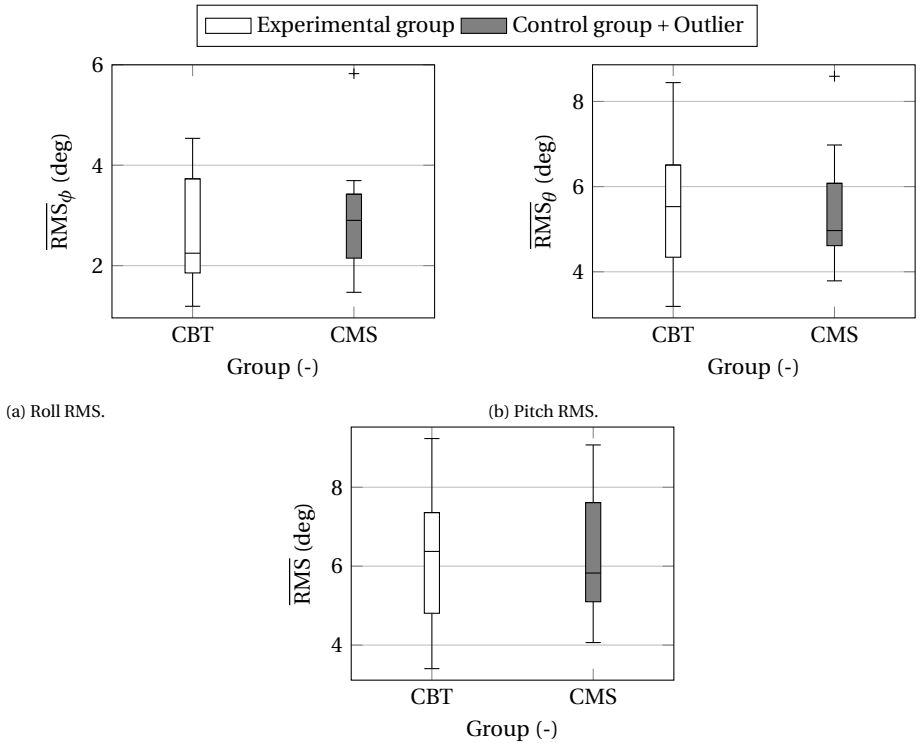

(a) Roll RMS.

(b) Pitch RMS.

(c) Combined pitch and roll RMS.

Figure 3.4: Groups balance - Comparison of the average performances in the aptitude test.

3.2.3. APPARATUS

This Section provides a description of the two considered helicopter simulators.

The CyberMotion Simulator (CMS) in Fig. 3.1b is an anthropomorphic robotic arm (KUKA Roboter, GmbH) mounted on a linear rail to provide a total of 8 degrees-of-freedom. Thanks to its high agility and motion envelope compared to Stewart platforms, the CMS is well suited for helicopter hover training [Nieuwenhuizen et al., 2013]. The end-effector consists of a custom-built helicopter cockpit with a 140° horizontal for 70° vertical field-of-view that allows for virtual environments to be projected. For the experiment described in this chapter, the cockpit was also equipped with a pilot seat and a commercial off-the-shelf helicopter control inceptor (Pro Flight Trainer PUMA) with no programmable control loading systems.

The motion of the CMS was generated by means of a classical Motion Cueing Algorithm (MCA) based on second-order high-pass washout filters [Reid et al., 1985, 1986]. The gains were manually tuned based on the evaluations of four expert Robinson R44 pilots, until a good matching between visual and motion cues was achieved [Geluardi et al., 2017].

The Computer Based Trainer (CBT) in Fig. 3.1a is equipped with a pilot seat, a 22.5 in display and the same control inceptor used in the CyberMotion Simulator (CMS). The display is produced by VIEWPixx, VPixx Technologies Inc., Canada.

As discussed at the beginning of the chapter, in this experiment, an identified model of a Robinson R44 civil light helicopter was used. This model was developed in previous research and experimentally validated [Geluardi et al., 2018].

The visual environment projected in the two simulators was developed in Unity® [Anonymous, 2016], see Fig. 3.5. It displays the inside of a Robinson R44 cockpit, while the out-of-the-window scenery consists of a heliport with a wide field in which the helicopter can move without encountering any obstacle. Markers, such as lines and dots, were drawn on the heliport ground to help the participants understand position and attitude of the helicopter. Moreover, hover boards were placed in the scenery and were used by the student pilots as reference points for accomplishing the experiment tasks. An artificial horizon, in the form of a head-up display, was also added to help the pilot estimate the attitude of the vehicle even for the experimental condition without motion cues (CBT).

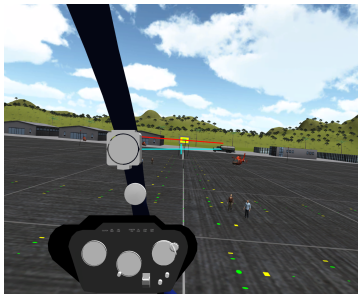

Figure 3.5: Hover scenario visual scene.

3.2.4. EXPERIMENT STRUCTURE

The main experiment was divided into three phases (Familiarization, Training and Evaluation) and was carried out on two different days, as shown in Tab. 3.2. In total, each participant was trained in the simulators for approximately 3 hours.

FAMILIARIZATION

All participants read a short briefing document before starting the experiment, explaining the basic setup of the experiment and the task to be performed. Besides the general information concerning the experiment setup, a detailed instruction was provided regarding the helicopter dynamics and flight controls, the presented visual environment and the program intended to teach the execution of the hover maneuver through a step-by-step training. This training program consisted of five tasks of increasing level of difficulty, summarized in Tab. 3.3. These tasks were selected based on consultations with a helicopter instructor pilot (IP) and based on the results of previous training experiments [Fabbroni et al., 2018, 2017a,b].

Specifically, they were defined as follows:

1. *Left/Right Hovering Turn* (Fig. 3.6a). In this task, participants control only the pedals. All the other axes are controlled by the autopilot described in Section 3.2.5. This maneuver starts in a stabilized hover at an altitude of 25 ft (≈ 7.5 m) in front of a hover board, placed 360 ft (≈ 110 m) in front of the starting position (see Fig. 3.5). The target is oriented 90° to the left and identified by an equally distant hover board. After reaching the target, the heading is to be maintained for 10 seconds. This maneuver is then repeated for a target oriented 90° to the right.
2. *Up/Down Vertical Repositioning* (Fig. 3.6b). In this task, participants control only the collective. All the other axes are controlled by the autopilot described in Section 3.2.5. This maneuver starts in a stabilized hover at an altitude of 25 ft (≈ 7.5 m) in front of a hover board, placed 300 ft (≈ 90 m) in front of the starting position. Additionally, a blue sphere is placed half-way between the starting position and the hover board to aid the participant in maintaining the correct vertical position. The target is placed 50 ft (≈ 15.25 m) above the starting position and identified by an equally distant hover board. After reaching the target, the altitude is to be maintained for 10 seconds. This maneuver is then repeated in the opposite direction, starting in a stabilized hover at an altitude of 75 ft (≈ 22.75 m).
3. *Up/Down Vertical Repositioning and Heading Hold* (Fig. 3.6b). This maneuver is analogous to the previous one, except for the fact that the participants also control the pedals and have to compensate for the couplings related to the use of the collective lever.
4. *Cyclic Control Hover* (Fig. 3.6c). In this task, participants control only the cyclic. All the other axes are controlled by the autopilot described in Section 3.2.5. This maneuver starts in a stabilized hover at an altitude of 25 ft (≈ 7.5 m) in front of a hover board, placed 360 ft (≈ 110 m) in front of the starting position. The participants objective is to maintain the helicopter in hover for 30 s minimizing position and heading error with respect to the initial position.
5. *Full Control Hover* (Fig. 3.6c). This maneuver is analogous to the previous one. However, in this case the participants also control the pedals and the collective.

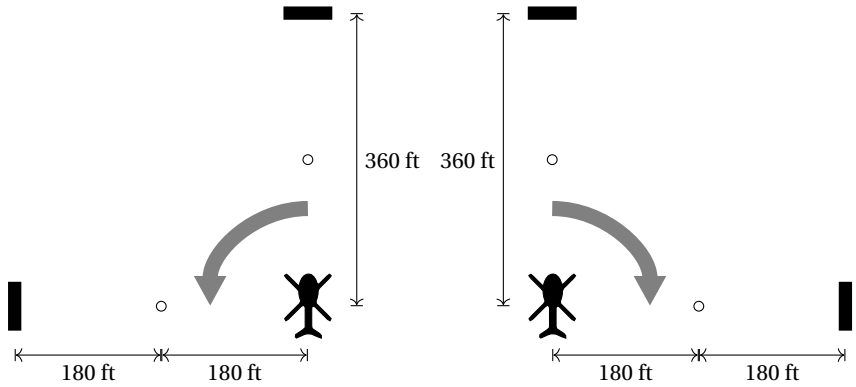

(a) Left/right hovering turn.

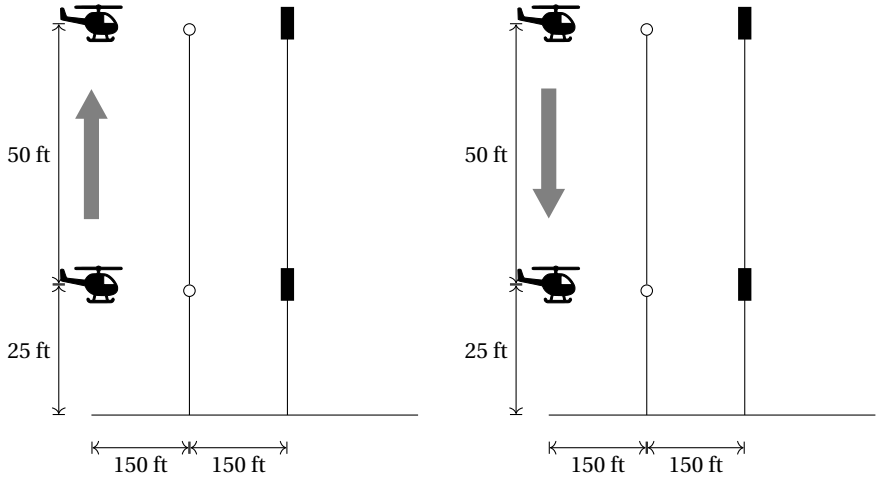

(b) Up/Down vertical repositioning (with and without automatic heading hold).

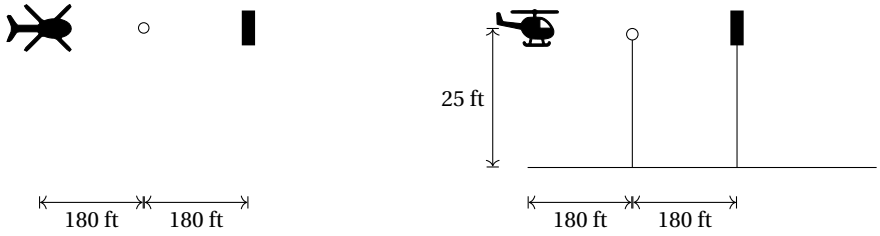

(c) Cyclic control and full control hover (top view on the left and side view on the right).

Figure 3.6: Hover part-task training program [Fabbroni et al., 2018, 2017a,b].

Geluardi et al. [2017] adopted the precision hover and lateral reposition mission task elements (MTEs) from ADS-33E [US Army AMCOM, 2000] (with minor modifications) to conduct a between subjects experiment with participants with no prior flying experience. Participants were divided in four groups and each group was assigned a model had to perform the MTEs with one of the four vehicle models used as independent variable in the experiment, i.e., an identified helicopter model, a H_∞ augmented system, a μ-synthesis augmented system, and a PAV model. Participants assigned to the identified helicopter model group were not able to accomplish the tasks, nor to keep the vehicle under control. For this reason, a simplified version of ADS-33E precision hover MTE was chosen, not requiring any low speed maneuver, but only small control adjustments to remain around the initial position. Definitions such as "desired" and "adequate" performance given in ADS-33E were not adopted here. These definitions are generally used to rate the ability of experienced helicopter pilots to perform an MTE. However, in this experiment participants were not requested to achieve the same performance level as highly trained helicopter pilots.

Table 3.2: Experiment phases.

Phase	**Experimental group**	**Control group**	**Duration**
Familiarization (Day 1)	Instructions session	Instructions session	15 minutes
	Part-task training in the CBT (Tab. 3.3)	Part-task training in the CMS (Tab. 3.3)	1 hour and 45 minutes
Training (Day 1)	Hover with all controls in the CBT	Hover with all controls in the CMS	30 trials of 30 seconds each
Evaluation/Transfer (Day 2)	Hover with all controls in the CMS	Hover with all controls in the CMS	30 trials of 30 seconds each

Table 3.3: Part-task training tasks.

m_{ID}	**Task**	**Controls used**	**Duration (min)**
1	Left/right Hovering Turn	Pedals	5
2	Up/down Vertical Repositioning	Collective	5
3	Up/down Vertical Repositioning, Heading Hold	Collective + Pedals	20
4	Hover A	Cyclic	30
0	Hover B	Cyclic + Collective + Pedals	30

TRAINING

During the experiment's Training phase (see Tab. 3.2), participants performed the Hover B maneuver for 30 trials of 30 seconds each in the simulator assigned to their group (CBT or CMS). During the first three trials of the Training phase, the CMS motion was disabled in order help participants of the CMS group get acquainted with the unaugmented helicopter. Hence, these trials were neglected.

EVALUATION/TRANSFER

After training, the experimental group (CBT) was transferred to the CyberMotion Simulator (CMS). Participants of both groups performed again the Hover B maneuver for 30 trials of 30 seconds each. During the first three trials of the Evaluation phase, participants of the CBT group were trained in the CMS without motion in order to get acquainted with the new simulation environment. Hence, these trials were neglected.

3.2.5. STUDENT HELPER

The part-task training was implemented in both simulators by using the software control system shown in Fig. 3.7. Here, the Helicopter Model to be controlled is a linear identified model of a Robinson R44 light-weight helicopter [Geluardi, 2016; Geluardi et al., 2018], described by the following state-space representation:

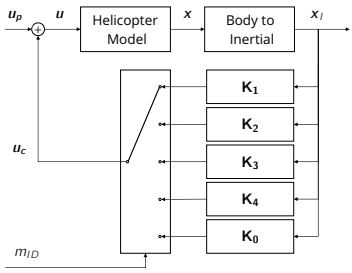

Figure 3.7: Logic of the controller used during the familiarization phase.

$$\dot{\vec{x}} = \mathbf{A}\vec{x} + \mathbf{B}\vec{u} \tag{3.2}$$

with $\vec{x} \in \mathbb{R}^{n_x=21}$, $\vec{u} = \begin{bmatrix} u_{lat} & u_{lon} & u_{ped} & u_{col} \end{bmatrix}^{\mathrm{T}} \in \mathbb{R}^{n_u=4}$.

The system of Eq. (3.2) is controlled by the combined action of student pilot $\vec{u}_p$ and software control system $\vec{u}_c$ as in Eq. (3.3).

$$\vec{u} = \vec{u}_p + \vec{u}_c = \vec{u}_p - \mathbf{K_i}\vec{x}_I \tag{3.3}$$

The gain matrix $\mathbf{K_i}$ is the result of an optimization problem, based on the Linear Quadratic Regulator design implemented by Fabbroni et al. [2017a]. For each maneuver m_{ID}, a specific gain matrix was calculated:

$$\mathbf{K_1} = \begin{bmatrix} \vec{k}_{1,1} \\ \vec{k}_{1,2} \\ \vec{0} \\ \vec{k}_{1,4} \end{bmatrix} \quad \mathbf{K_2} = \begin{bmatrix} \vec{k}_{2,1} \\ \vec{k}_{2,2} \\ \vec{k}_{2,3} \\ \vec{0} \end{bmatrix} \quad \mathbf{K_3} = \begin{bmatrix} \vec{k}_{3,1} \\ \vec{k}_{3,2} \\ \vec{0} \\ \vec{0} \end{bmatrix}$$
$$\mathbf{K_4} = \begin{bmatrix} \vec{0} \\ \vec{0} \\ \vec{k}_{4,3} \\ \vec{k}_{4,4} \end{bmatrix} \quad \mathbf{K_0} = \begin{bmatrix} \vec{0} \\ \vec{0} \\ \vec{0} \\ \vec{0} \end{bmatrix} \quad \in \mathbb{R}^{n_u \times n_x} \tag{3.4}$$

with $\vec{k_{i,j}} \in \mathbb{R}^{1 \times n_x} \quad \forall i, j$.

Specifically, $\mathbf{K_1}$ is the gain matrix associated with the Hovering Turn maneuver, $\mathbf{K_2}$ with the Vertical Repositioning maneuver, $\mathbf{K_3}$ with the Vertical Repositioning, Heading Hold maneuver and $\mathbf{K_4}$ with the Hover A maneuver. Instead, $\mathbf{K_0} = 0$ is associated with the Hover B maneuver, in which the student pilot is controlling the system with all control inputs.

In this setup the participants and the software control system never control the same channels at the same time.

3.2.6. HYPOTHESIS

The participants of the CBT group performed the Training phase relying solely on the visual cues produced by a 22.5 in desktop monitor. During this phase, their visual sensory system adapts to the small screen size. It is expected that training in simulation environments with poor cues will enhance perceptual learning. The improved perception skills of the participants of the CBT group can allow them to adjust their control strategy in order to adapt to the available cues in the new simulator. Thus, it is expected that the hover performance of the CBT group won't be worse than that achieved by the control group, once transferred to the CMS.

3.2.7. INDEPENDENT VARIABLES

The qToT experiment described in this chapter is influenced by three main distinct features of the two considered simulators:

- The presence of *motion cues*. This feature is crucial to evaluate the transfer of training from a fixed-base to a moving-base simulator;
- The *display type*. This feature influences the transfer from a desktop monitor to a large FOV cabin equipped with two projectors;
- The *immersiveness* of the simulation, determined by the difference between an office desk and the CMS cabin.

Because of the impossibility to isolate the individual contribution of each feature to the transfer of training, only one independent variable was in fact considered, i.e., the overall simulator's fidelity.

3.2.8. DEPENDENT VARIABLES

To investigate the effect of simulator's fidelity (independent variable) on hover performance, the following dependent measures were defined:

- *Number of completed trials.* The number of trials in which the control of the helicopter model was not lost for the full duration of the trial. This index can be used as an indication of the training effectiveness in maneuvers where the stability of the helicopter is not guaranteed by the controller, as in Hover A and Hover B (Table 3.3).

- *Position Scores.* The root mean squared (RMS) position error with respect to the target hover position was calculated at the end of each completed trial for longitudinal (x), lateral (y) and vertical (z) positioning and for the position magnitude ($P = \sqrt{x^2 + y^2 + z^2}$). Eq. (3.5) shows how these metrics are calculated, taking the longitudinal positioning as example.

$$\mathrm{RMS}_x = \sqrt{\frac{1}{N_s}\sum_{k=1}^{N}\left[x(k) - x(1)\right]^2} \tag{3.5}$$

  where N is the number of time samples considered in the trial.

  These indexes can be used to objectively evaluate the student pilots' performance while executing the maneuvers.

- *Heading Score.* The root mean squared (RMS) heading error was calculated at the end of each completed trial.

- *Velocity Score.* The root mean square (RMS) of the linear velocity was calculated at the end of each completed trial.

  This index can be used as an indication of hover stability.

- *Control activity.* To gain insights into the participants' control activity, the root mean squared (RMS) deviation with respect to the trim position for every helicopter control was computed at the end of each completed trial.

The part-task training during the Familiarization phase was time-based. Therefore, the total number of trials performed in each task is different for each participant. For this reason, results presented in this chapter focus on Training and Evaluation phases only.

3.2.9. DATA PROCESSING & ANALYSIS

Prior to performing the statistical tests, all the dependent measures defined in Section 3.2.8, except the number of completed trials, were averaged over the trials of each phase for every participant. Dependent-samples t-tests between the phases of the experiment for each group are conducted to investigate the within-subjects effect and independent-samples t-tests between the groups in each phase are adopted to examine the between-subjects effect.

3.3. EXPERIMENT RESULTS

The experimental results will be presented in the following figures as box-whiskers plots. On each box, the white circle represents the median over different data points. The box is delimited by the first and third quartiles, therefore it includes data points between the 25^{th} and the 75^{th} percentile. The difference between first and third quartiles defines the interquartile range. The two edges of the whiskers indicate the lowest and the highest data point within 1.5 of the interquartile range. All the data points not included in the whiskers are considered as outliers and they are represented by cross markers.

3.3.1. COMPLETED TRIALS

Fig. 3.8 shows the absolute and relative numbers of completed trials by participants of both groups in each phase. The data points on which each box plot is based are plotted next to it (filled circle markers), together with the mean value (diamond marker). It can be noticed that the experimental group (CBT) had a higher success rate than the control group (CMS) during the training phase, with an average number of completed trials that is almost twice as high (Tab. 3.4). This marked difference disappears in the evaluation phase, where performance of the CBT group remains almost unchanged. In the last session of the experiment, participants of both groups were able to stabilize the helicopter model in the CMS, on average, in the 60% of the runs, suggesting the effectiveness of the training program. Indeed, subjects without any prior flying experience, who participated in a previous study [Geluardi et al., 2017] and did not undergo a training phase, were not able to accomplish hover and low-speed tasks nor to stabilize the same helicopter model used in this experiment in any run.

The dramatically smaller number of completed runs for the CMS group during the training phase is, in hindsight, related to the stricter safety limits in the CMS. Furthermore, some of the participants in the CMS group may have been overwhelmed by the long stay in the CMS (two and a half hours), which is characterized by high vibrations level (due to its lower stiffness compared to Stewart platforms [Nieuwenhuizen et al., 2013]) and by a small cabin equipped with a large FOV projection screen.

Table 3.4: Group performance comparison in terms of average number of completed trials.

Phase	**Group**			
	CBT		CMS	
	Trials (/30)	Percentage (%)	Trials (/30)	Percentage (%)
Training	19	63	10	33
Evaluation	17	58	18	61

3.3.2. PERFORMANCE SCORES

The evolution of participants' performance is shown in Fig. 3.9 in terms of longitudinal position. This score was found to be the most illustrative of the performance score parameters considered in this experiment. The number that appears on the top (CMS group) or at the bottom (CBT group) of each boxplot represents the number of samples available, i.e., the number of participants that completed the corresponding trial. This

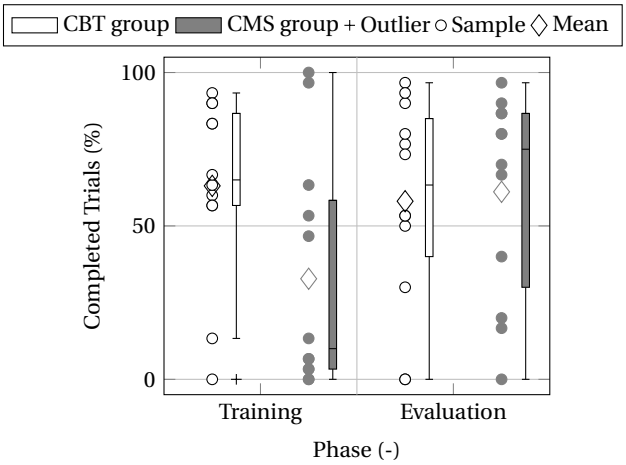

Figure 3.8: Distribution of the percent number of completed trials by participants of both groups in each phase.

additional information is provided in order to avoid a misleading interpretation of the results due to differences in the number of completed trials. At first glance, focusing on the training phase (Fig. 3.9a), the CMS group performs better than the CBT group, exhibiting also a lower within-group variability. However, for each trial the boxplot related to the CMS group is based on a number of samples that is, on average, half of the number of samples available for the CBT group (Fig. 3.8).

The CMS group shows a learning trend over the first half of the training phase, followed by a degradation in the performance registered in the last part of this phase. The CBT group displays fluctuating, but overall flat performance. The first session of the experiment culminated in the training phase and lasted approximately 2 hours and 30 minutes. Hence, the data in Fig. 3.9a suggest that participants may have been affected by fatigue towards the end of the session.

In the Evaluation phase (Fig. 3.9b), the comparison between the two groups becomes fairer with respect to the Training phase. Indeed, for each trial the boxplots of the two groups are based, on average, on the same number of samples (Fig. 3.8). Neglecting the first three trials of the Evaluation Phase (Section 3.2.4)[1] and trial 13[2], the CBT group almost immediately reaches performance comparable to that achieved by the CMS group, but even better in terms of within-group variability. For both groups, a learning trend appears in the second half of the evaluation phase. This trend is more pronounced for the CBT group.

[1] In the first three trials of the evaluation phase, the participants of the CBT group performed the task with the CMS motion disable for familiarization purposes.

[2] Trial 13 for the CMS group is not reliable because the boxplot is built only on 5 data points. This means that only 5 participants over 12 were able to complete that trial. By accident most participants lost control of the helicopter model and the trial was stopped before it was completed due to the strict safety limits of the CMS. The higher variability in one single trial could be expected for example after a break. However, all the trials in the evaluation phase were performed sequentially in one session of about 20 minutes. So this variability is ascribed to the randomness of human subject experiments.

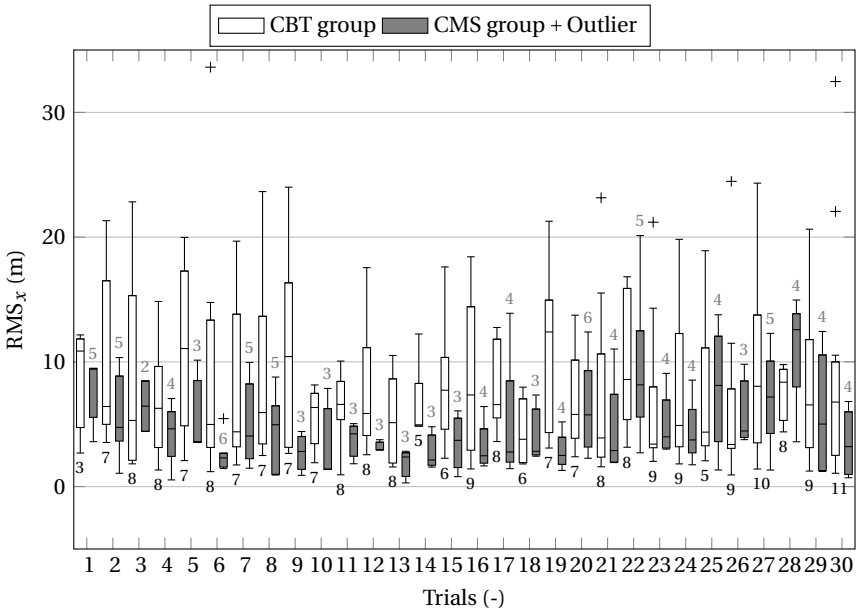

(a) Training phase.

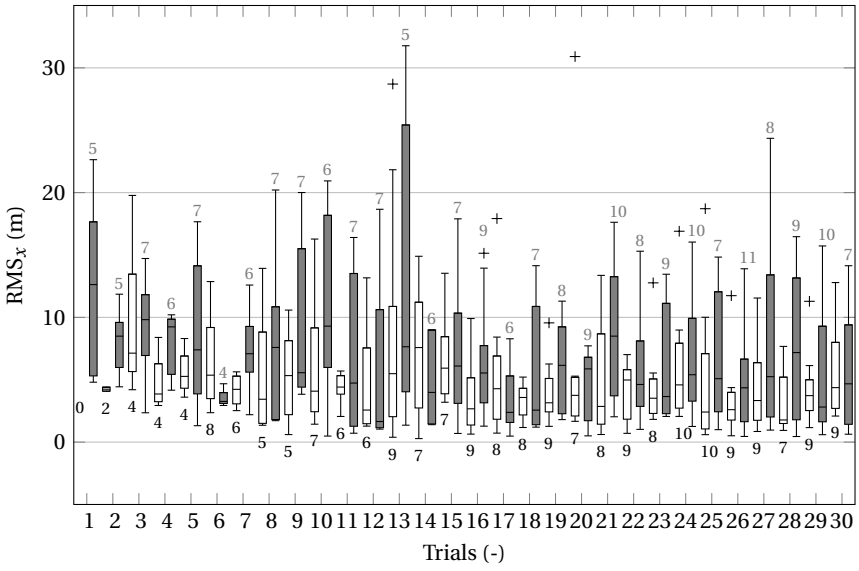

(b) Evaluation phase.

Figure 3.9: Evolution of the distribution of the longitudinal score for each group.

The effectiveness of the training was further investigated by averaging the scores defined in Section 3.2.8 over the completed trials by each participant. These metrics are shown in Fig. 3.10 as box-whiskers plots to compare the performance of the two groups in the Training and in the Evaluation phases. Boxplots are plotted together with the data points on which they are based. Each data point corresponds to one participant and the number that appears next to it represents the number of completed trials by that participant. As can be seen in Tab. 3.5, the CBT group significantly improved its performance from the training phase to the evaluation phase for every considered metric, except for the vertical score and the heading score.

For some metrics (longitudinal, heading, position and velocity scores), the enhancement of the performance is associated with a decrease of the within-group variability.

No significant difference was found between the two phases for the CMS group (Tab. 3.5). The participants of this group were not able to stabilize the helicopter in a large number of trials during the training phase. During the evaluation phase, they reach a level of performance close to that shown by the participants who were able to complete the task throughout the training phase. The increase in the number of completed trials in the evaluation phase (Tab. 3.4) leads to a growth in the within-group variability for almost every performance metric.

Table 3.5: Dependent-samples T test between training phase and evaluation phase.

Metric	**Group**	**t-test**		
		t	df	Sig. (2-tailed)
$\overline{\text{RMS}}_x$	CBT	4.570	9	0.001*
	CMS	−0.949	9	0.368
$\overline{\text{RMS}}_y$	CBT	3.075	9	0.013*
	CMS	−0.022	9	0.983
$\overline{\text{RMS}}_z$	CBT	−0.813	9	0.437
	CMS	−0.816	9	0.435
$\overline{\text{RMS}}_\psi$	CBT	0.787	9	0.451
	CMS			0.508[a]
$\overline{\text{RMS}}_P$	CBT	3.826	9	0.004*
	CMS	−0.556	9	0.592
$\overline{\text{RMS}}_V$	CBT	5.462	9	0.000*
	CMS	1.058	9	0.318

* Significant ($p < 0.05$) difference between compared samples.
[a] At least one sample not normally distributed. Related-samples Wilcoxon signed-rank test was applied instead of paired-samples T test.

Tab. 3.6 shows that the two groups achieved comparable performance. Indeed, the data of the two groups were not statistically different in any phase of the experiment. The largest difference was found for the longitudinal score during the training phase ($t(19) = 1.852,\ p = 0.08$) and is again related to the small number of trials completed by the CMS group.

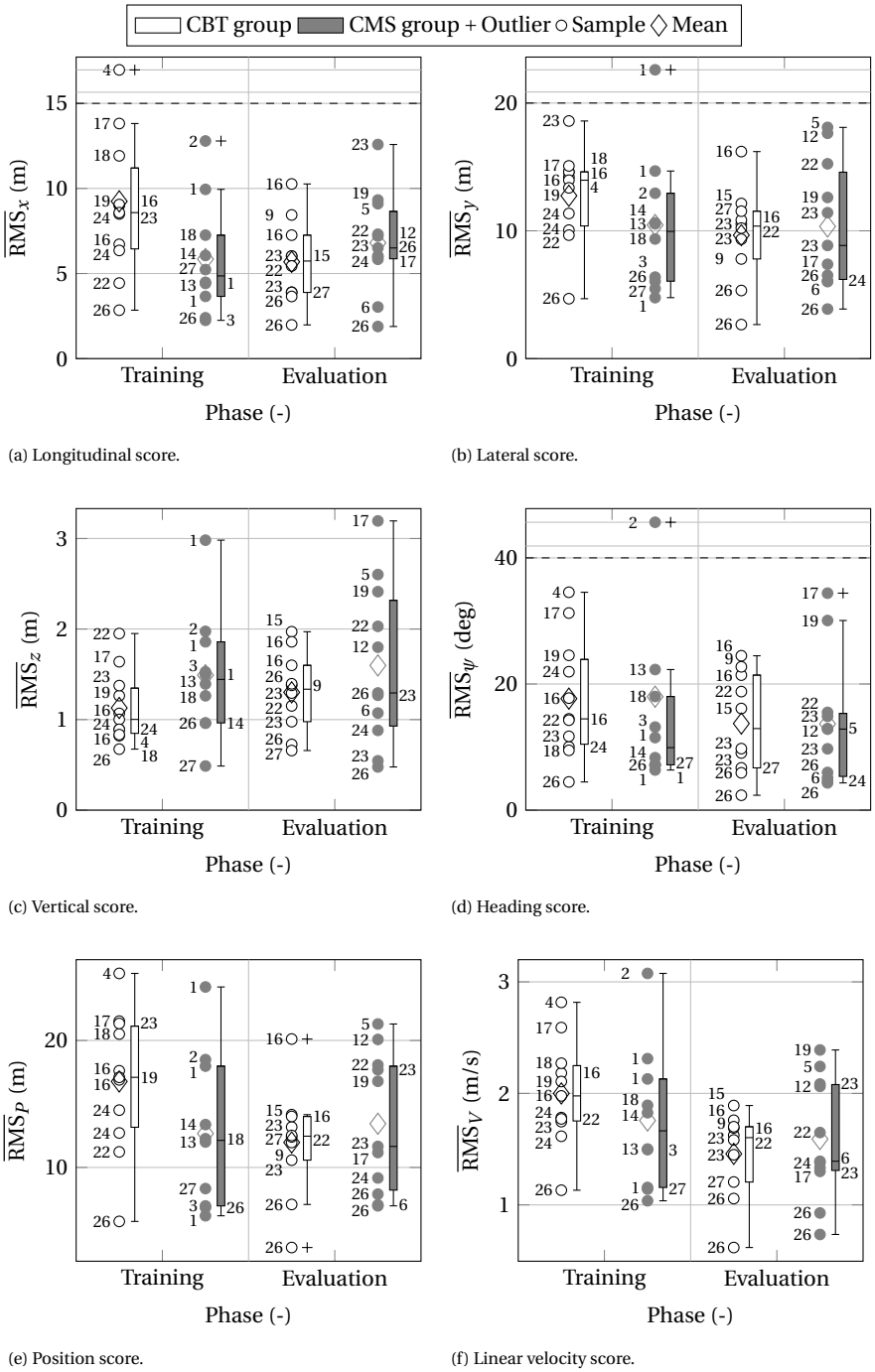

(a) Longitudinal score.

(b) Lateral score.

(c) Vertical score.

(d) Heading score.

(e) Position score.

(f) Linear velocity score.

Figure 3.10: Distribution of the average score for each group in each phase.

Table 3.6: Independent-samples T test between the two groups.

Metric	Phase	t-test		
		t	df	Sig. (2-tailed)
$\overline{\text{RMS}}_x$	T	1.852	19.000	0.080
	E	−0.930	19.000	0.364
$\overline{\text{RMS}}_y$	T	1.103	19.000	0.284
	E	−0.352	19.000	0.729
$\overline{\text{RMS}}_z$	T	−1.505	19.000	0.149
	E	−0.989	14.947	0.339
$\overline{\text{RMS}}_\psi$	T			0.251[a]
	E	0.015	19.000	0.988
$\overline{\text{RMS}}_P$	T	1.633	19.000	0.119
	E	−0.678	19.000	0.506
$\overline{\text{RMS}}_V$	T	1.004	19.000	0.328
	E	−0.638	19.000	0.531

[a] At least one sample not normally distributed. Independent-samples Mann-Whitney U test was applied instead of Independent-samples T test.

3.3.3. CONTROL EFFORT

To justify some of the results obtained in terms of performance, it is worth looking also at the participants' control activity. As shown in Fig. 3.10c and 3.10d, vertical and heading scores were the only two metrics in which no improvement was noticed from the training to the evaluation phase for the CBT group. This might be related to how participants were briefed. They were taught to first stabilize the helicopter, giving priority to the use of the cyclic stick. Thereafter, within the same run, they were required to hover, using the pedals and the collective lever to make adjustments of the helicopter's heading and altitude. This is also proven by the fact that both groups exhibit lower control activity for the pedals and the collective than for the longitudinal and the lateral cyclic (Fig. 3.11). Furthermore, for both groups there was no change in terms of control activity from the training to the evaluation phase for the longitudinal cyclic (Fig. 3.11a), the collective (Fig. 3.11c) and the pedals (Fig. 3.11d). Conversely, a decrease in the control activity from training to evaluation phase can be noticed for the lateral cyclic (Fig. 3.11b) for the CMS group, suggesting a reduction in the workload required from participants to stabilize the helicopter model. This can also be inferred from the increase in the number of trials completed by the CMS group in the evaluation phase.

3.4. DISCUSSION

The experiment presented in this chapter was designed to investigate how effective a CBT can be for hover training of novice pilots. The results of this quasi-Transfer-of-Training experiment confirm previous results in literature which showed how the effectiveness of a Flight Simulator Training Device (FSTD) depends more on the design of

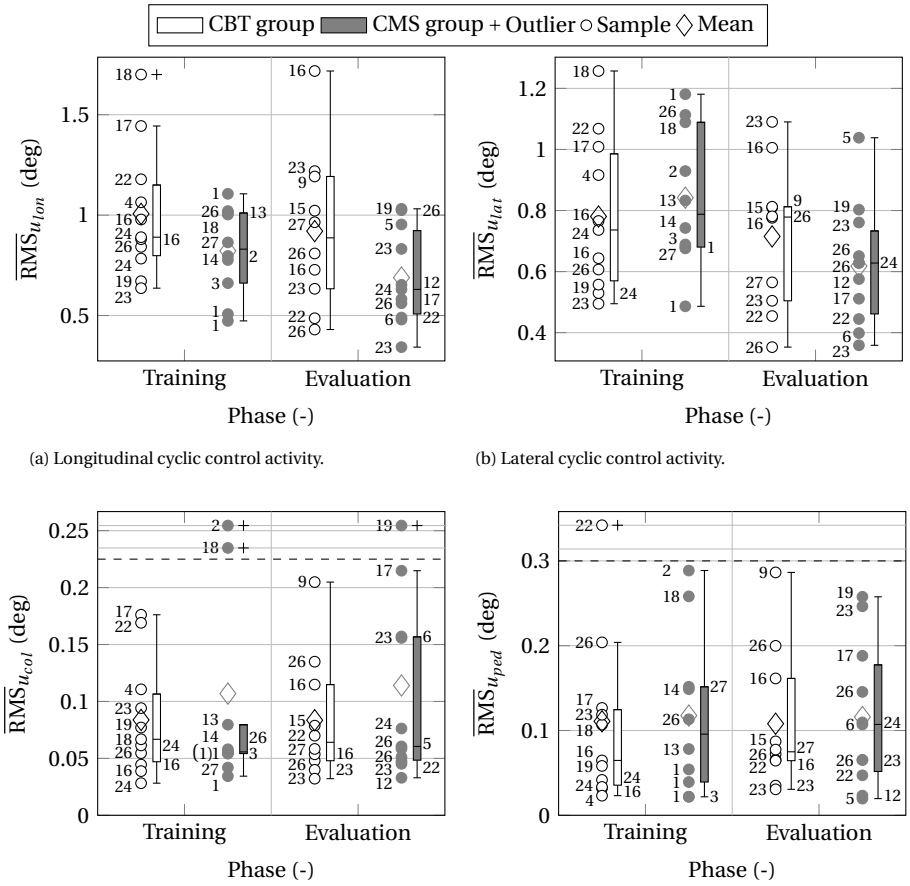

(a) Longitudinal cyclic control activity.

(b) Lateral cyclic control activity.

(c) Collective control activity.

(d) Pedals control activity.

Figure 3.11: Distribution of the average control activity for each group in each phase.

the training program than on the fidelity provided by the simulator itself [Caro, 1973]. Indeed, after approximately 2 hours and 30 minutes of practice in the respective simulators, the two groups of participants (CBT and CMS groups) showed almost identical proficiency levels in the evaluation phase.

Helicopters are unstable in hover, but the pilot acts as a feedback controller and uses the available (visual and motion) cues as source of information to close the loop and stabilize the system. Experienced pilots are taught to give priority to some of the available cues depending on the flight condition, but in general they are supposed to trust their instruments and ignore their vestibular sensory input. Despite this, simulator motion bases enable better in-simulator performance by experienced pilot and there is nearly unanimous preference to have this feature implemented in simulators [McCauley, 2006]. Novice pilots, instead, apparently gather information from the visual sensory system disregarding the presence of motion cues in hover and low-speed maneuvers [Fabbroni et al., 2018] (Tab. 3.6), at least for the current MCA set of parameters.

The quasi-Transfer-of-Training experiment showed that the part-task training was effective in teaching the basics of helicopter dynamics and control. Indeed, participants of both groups were able to consistently stabilize a Robinson R44 identified model at the end of the evaluation phase.

The biggest difference between the two groups occurred during the training phase and was related to the number of completed trials. In particular, the participants of the CBT group were able to complete, on average, 63% of the total number of trials for this phase, against only 33% of the CMS group. A possible reason for this result is that participants of the CMS group might have been overwhelmed by the impact with the CMS, which is characterized by high vibrations level and by a small cabin equipped with a large FOV projection screen. The duration of the first session of the experiment (2 hours and 30 minutes) might have increased the level of stress and fatigue, affecting the results of the training phase for the CMS group. As a future recommendation, it is advisable to split the experiment in three sessions in order to mitigate the influence of participants' fatigue on the results. Furthermore, biophysical measurements can be used in future studies to evaluate participants' workload and to determine if stress and fatigue were actually confounding factors.

The CBT group showed significant improvement in performance from the training phase to the evaluation phase for all the considered metrics, except for the vertical and the heading scores. As a consequence, it can be concluded that the pedals and the collective require additional attention during the part-task training, not only when they are used separately, but also in combination.

From the analysis carried out on the collected data, no differences between the CBT and CMS groups were found. Although the relatively low number of participants does not result in sufficient statistical power, the obtained results seem to confirm our hypothesis that CBTs may be a valid alternative to high-fidelity simulators in the training of task-naïve helicopter pilots, if supported by a suitable training program.

3.5. CONCLUSIONS

This chapter presented the results of a quasi-Transfer-of-Training experiment performed to compare the effectiveness of low- and high-fidelity flight simulators to train the hover maneuver to task-naïve helicopter pilots. Participants were divided into two groups: one trained in a Computer Based Trainer (low-fidelity) and one in the MPI CyberMotion Simulator (high-fidelity). The training session was followed by an evaluation session in which the group trained in the CBT was transferred to the CMS to evaluate the effects of the simulator fidelity on the Transfer-of-Training.

The results demonstrated the overall effectiveness of the training in both simulators, structured as a realistic flight lesson. Indeed, participants of both groups were able to stabilize the helicopter model, on average, in the 60% of the trials during the Evaluation phase. Moreover, no significant difference between CBT and CMS groups was found.

Although more experiments are needed to confirm the obtained results, the outcome of this experiment opens the possibility to replace or complement actual flight training hours with instruction hours on low-cost flight training devices. This can potentially reduce training costs and, eventually, pave the way towards a safety enhancement.

II

Training of Advanced Flying Skills: Autorotation

4

FLIGHT MECHANICS IN AUTOROTATION

Although improving current simulator training for basic maneuvers may have an impact on rotorcraft safety, as discussed in Chapter 3, the keystone for the zero accident goal is represented by the development of standardized training programs for autorotation and emergency aircraft handling and by the improvement of simulator training for advanced maneuvers [European Helicopter Safety Analysis Team, 2010, 2015; U.S. Joint Helicopter Safety Analysis Team, 2011a,b]. In particular, autorotation is one of the most critical training scenarios, because it is an emergency procedure performed by pilots to safely land the vehicle in the event of a power failure or tail-rotor failure. The loss of the engine strongly affects the helicopter dynamics, thus requiring the pilot to adapt their control technique to this variation.

This chapter investigates the changes in helicopter dynamics following total power failure, with the aim to gain insight into the required pilot control adaptation during autorotation. To this end, first a brief technical background regarding the autorotation maneuver is given in Section 4.1 and 4.2. Then, the analysis of the dynamic stability in autorotation (both for a 3-degrees-of-freedom (DOF) symmetrical helicopter model and for a 6-DOF rigid-body helicopter model) is performed in Section 4.3.1, together with a comparison with the dynamic stability in powered flight. Next, a sensitivity analysis is conducted in Section 4.3.2 to investigate the effect of autorotative flare index variations on the helicopter dynamics stability in autorotation. The results from these analyses are discussed in Section 4.4 and conclusions are drawn in Section 4.5.

The contents of this chapter have been published in:

Scaramuzzino, P. F. et al. (2019). Investigation of the Effects of Autorotative Flare Index Variation on Helicopter Flight Dynamics in Autorotation. In *45th European Rotorcraft Forum (ERF 2019)*, number 89, pages 893-906, Warsaw, September 17-19, 2019. PSAA.

Scaramuzzino, P. F. et al. (to be submitted). Investigation of the Effects of the Rotorspeed Degree of Freedom on Helicopter Flight Dynamics in Autorotation. *Journal of Guidance, Control, and Dynamics*.

4.1. INTRODUCTION

Autorotation is a flight condition in which the rotation of the rotor is sustained by the airflow, rather than by means of engine torque applied to the shaft. Helicopter pilots use autorotation following partial or total power failure, in order to reach the closest suitable landing site. In this condition, the energy stored in the rotor is preserved at the expense of the helicopter's potential energy (altitude). This means that the helicopter can sustain autorotation only by means of descending flight.

It has been common practice in analyzing dynamic stability of helicopters in powered flight to neglect the effects of variation of rotor angular velocity [Padfield, 2007]. Indeed, the vast majority of helicopters keep a constant rotorspeed (rpm) during flight. This function is fulfilled by the governor, which measures and regulates the speed of the engine. However, this assumption is no longer justified in case of autorotative flight where the governor is disengaged and the pilot takes over the task of controlling the rotor rpm directly. Power-off limits are usually between 85% and 110% of the nominal rpm [EASA, 2017], such that the rotor can still produce enough thrust without the risk of loss of control or structural damage. Therefore, the rotorspeed becomes an additional degree-of-freedom (DOF) in autorotation. There is little substantial literature about the analysis of the potential impact of this additional degree-of-freedom on helicopter flight dynamics in autorotation. Nikolsky and Seckel [Nikolsky, 1952; Nikolsky et al., 1949a,b] developed an analysis of the effects of autorotation on helicopter flight dynamics in both vertical and forward translation. This work dates back to the 1950s. More recent work was carried out by Houston [1996, 2000, 2002], who mainly focused on autogyros, for which autorotation is the normal mode of operation.

The present chapter aims at understanding how the rotorspeed degree-of-freedom impacts the classical rigid body modes, and therefore the handling qualities in autorotation. This is achieved by comparing the eigenmodes of a 3-DOF longitudinal helicopter model in straight level flight with those of a 4-DOF (3-DOF longitudinal + RPM) model in steady descent during autorotation, both representative of the Bo-105 helicopter. The same analysis was conducted on a higher fidelity helicopter model (6-DOF rigid-body helicopter model + RPM), i.e., the eigenvalues of the 6-DOF rigid-body model in straight level flight were compared with those of the 7-DOF (6-DOF + RPM) model in steady descent in autorotation.

Moreover, this chapter investigates the effects of *autorotative flare index* variations on helicopter stability in autorotation. There are many possible alternatives to express the autorotative characteristics of a helicopter [Fradenburgh, 1984; White et al., 1982; Wood, 1976]. The definition adopted in this thesis considers the autorotation index as the ratio between the available energy, stored in the rotor, and the energy required to arrest the rate of descent of the helicopter prior to ground contact which is proportional to weight and disk loading. This index has been chosen because it has shown to be a reasonably reliable indicator of the level of difficulty of making successful autorotative landings [Fradenburgh, 1984]. In a sensitivity study, every design parameter involved in the calculation of the autorotative flare index has here been varied in order to study the sensitivity of the helicopter's eigenmodes to changes in the autorotation index, and therefore understand whether any of these parameters has a strong impact on the stability of the system.

Pilots will need to adjust their control strategy based on the helicopter dynamics they control. As a consequence, different handling characteristics may put a different level of workload on the pilot to accomplish the task. This may also have implications for autorotation training from a safety perspective. For instance, during in-flight training of novice pilots it is desirable to adopt a progressive difficulty approach, starting in a low resource demanding configuration and then transitioning to a more challenging one [Coyle, 2008]. During simulator training instead, starting the training in the highest resource demanding setting may provide the pilot with more robust and flexible flying skills that can then be transferred to the actual helicopter [Nusseck et al., 2008]. The present study sets the basis for the experiments on autorotation training in flight simulators presented in Chapters 5 and 6, as it provides a methodology to estimate the level of difficulty of controlling a certain helicopter configuration during steady-descent in autorotation.

4.2. METHODOLOGY

The helicopter dynamics in autorotation are analyzed in terms of the stability characteristics of its modes of motion. In order to apply this approach to gain insight into the physics of the helicopter dynamic behavior in autorotation, it is worth to divide the autorotation maneuver in three phases: steady descent, cyclic flare and rotation and collective flare [Prouty, 2002] (points 2, 3 and 4 of Fig. 4.1, respectively). Since steady descent in autorotation is an equilibrium condition, it is possible to linearize the equations of motion around this condition and study the stability of the linearized system by analyzing the eigenvalues of the state matrix.

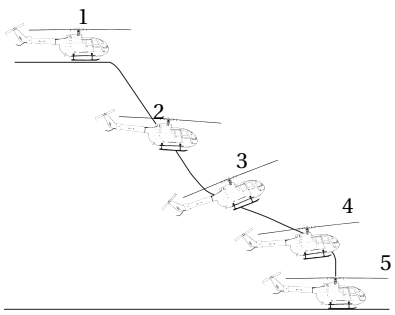

Figure 4.1: Autorotation phases (1: level flight, 2: steady descent, 3: cyclic flare, 4: rotation and collective flare, 5: touch-down).

Thirty-two different configurations have been considered (Tab. 4.1). These were obtained by individually varying some basic design parameters[1] of the baseline helicopter

[1]The term *design parameters* is generally used in preliminary helicopter sizing to designate tip speed, blade area/solidity, disk loading, and installed power [Talbot et al., 1986]. Such variables can be estimated using different methodologies such as sensitivity analysis of the performance equations [Hansen, 1984; Talbot et al., 1986], parametric design studies (e.g., Carpet Plots [Hansen, 1984]) or a combination of these methods [Davis

to get realistic values of the autorotative flare index, a metric that helps to size the rotor during preliminary design studies [Fradenburgh, 1984]. The baseline helicopter is the Bo-105 and its data were taken from Padfield [2007]. The procedure followed to select these configurations is explained in Sec. 4.2.2.

Table 4.1: Configuration test matrix.

Design parameter	Autorotative flare index AI (ft^3/lb)	Blade chord c (m)	Main rotor radius R (m)	Main rotor speed Ω_{mr} (rad/s)	Helicopter weight W (kg_f)
Blade chord	5	0.0578	4.91	44.4	2200
	10	0.1157			
	15	0.1735			
	20	0.2313			
	25	0.2892			
	30	0.3470			
	35	0.4049			
	40	0.4627			
Main rotor radius	5	0.2700	3.61	44.4	2200
	10		4.14		
	15		4.49		
	20		4.76		
	25		4.98		
	30		5.16		
	35		5.32		
	40		5.47		
Main rotor speed	5	0.2700	4.91	20.6	2200
	10			29.1	
	15			35.6	
	20			41.1	
	25			46.0	
	30			50.3	
	35			54.4	
	40			58.1	
Helicopter weight	5	0.2700	4.91	44.4	4753
	10				3361
	15				2744
	20				2377
	25				2126
	30				1941
	35				1797
	40				1681

The comparison of the dynamic behavior of the different configurations, in terms of eigenvalues, provides insight into which basic design parameters involved in the calculation of the autorotative index affect helicopter's stability in steady autorotative descent

et al., 1979; Hansen, 1984; Schoen et al., 1980] that can also account for design requirements (e.g., maximum speed, weight, fuselage drag, and design hover ceiling). As opposed to these relatively simple analyses which are typically used in the first preliminary design stages, helicopter sizing by Statistics using correlations and design trends in existing flying configurations represents a far more robust and reliable procedure, because it already considers many other practical engineering constraints that usually emerge only in later stages of the design process [Rand et al., 2004]. This method treats "classical" design parameters (e.g., tip speed, blade area, disk loading, and installed power) as derived variables from actual design parameters (e.g., the disk loading is calculated from the ratio between helicopter weight and disk area, which is a function of the rotor radius, one of the actual design parameters). In a similar fashion, the term design parameters is used in this thesis with the meaning of variables that are independent from each other, i.e., among which there is not a physical relationship.

the most, making it more difficult to control.

Some details regarding the flight dynamics model developed in this thesis and used in this Chapter (as well as in Chapters 5 and 6) are provided in Section 4.2.1. For a complete dissertation concerning the 3-DOF and the 6-DOF flight dynamics models the reader is referred to Appendix A. Details regarding the trim and the linearization procedures are covered in Appendices B and C, respectively.

4.2.1. FLIGHT MECHANICS MODEL

The aircraft equations of motion are derived from Newton-Euler dynamics equation in Appendix A [Padfield, 2007] and are repeated here for completeness.

$$\begin{aligned}
m\left(\dot{u}+qw-rv\right)+mg\sin\theta &= X\\
m\left(\dot{v}+ru-pw\right)-mg\cos\theta\sin\phi &= Y\\
m\left(\dot{w}+pv-qu\right)-mg\cos\theta\cos\phi &= Z\\
I_{xx}\dot{p}-I_{xz}\dot{r}+q\left(I_{zz}r-I_{xz}p\right)-rqI_{yy} &= L\\
I_{yy}\dot{q}+r\left(I_{xx}p-I_{xz}r\right)-p\left(I_{zz}r-I_{xz}p\right) &= M\\
I_{zz}\dot{r}-I_{xz}\dot{p}+q\left(-I_{xx}p+I_{xz}r\right)+pqI_{yy} &= N
\end{aligned} \tag{4.1}$$

The system of Eq. (4.1) represents the classical 6-DOF (degrees of freedom) rigid-body equations. To simulate autorotation, however, it is necessary to increase the order of the model, to include the main-rotor speed DOF. Assuming that the transmission is rigid, it is sufficient to add a single equation representing a torque balance [Padfield, 2007] and update the yaw dynamics equation to account for the coupling with the airframe:

$$\left(I_{zz}+I_R\right)\dot{r}-I_R\ddot{\psi}_m r-I_{xz}\dot{p}+q\left(-I_x p+I_{xz}r\right)+pqI_y = N \tag{4.2}$$

$$I_R\left(\ddot{\psi}_{mr}-\dot{r}\right) = \cancelto{0 \text{ in autorotation}}{Q_{eng}} - Q_{mr} - g_{tr}Q_{tr} \tag{4.3}$$

where I_R is the polar inertia of the rotor[2], $g_{tr}=\frac{\Omega_{tr}}{\Omega_{mr}}$. This equation is derived in Appendix D relaxing the constraint of rigid transmission, thus becoming a system of equations, known as engine-drivetrain dynamics.

The external forces and moments can be written as the sum of the contributions from the different aircraft components, which, for a conventional helicopter (one main rotor and one tail rotor), are: main rotor, tail rotor, fuselage, horizontal tailplane, and vertical fin.

CONTRIBUTION OF THE DIFFERENT HELICOPTER COMPONENTS TO EXTERNAL FORCES AND MOMENTS

Rotors The analytical expressions of forces and moments generated by the two rotors are taken from a report by Chen [1979, 1980], then implemented for piloted simulation

[2] The polar inertia of the rotor does not keep into account only the inertia of the blades, but also the inertia of the transmission.

by Talbot et al. [1982], which are derived according to the following simplifications and assumptions:

- The rotor blade was assumed to be rigid with linear twist.
- Uniform inflow was considered.
- Both flapping and inflow angles were assumed to be small.
- Simple strip theory was used.
- The reversed-flow region was ignored, and compressibility and stall effects were not considered.
- The tail rotor was modeled as a teetering rotor without cyclic pitch.

As an additional assumption, steady-state tip-path plane dynamics was considered for the model developed in this thesis. Furthermore, for the real-time simulation, quasi-steady dynamic inflow was used [Pavel, 2001].

Fuselage and Empennage Due to the availability of wind-tunnel data for the Bo-105 helicopter's fuselage and empennage [van der Wall, 2017], force and moment coefficients of these components are obtained from look-up tables as a function of incidence and sideslip. To model a generic helicopter for which wind-tunnel data are not available, the same approach used by Talbot et al. [1982] can be adopted, i.e., simple lifting-line theory assuming an elliptical lift distribution with uniform downwash and quadratic drag coefficient for the empennage, and two representation for small and large angles for the fuselage, linearly interpolated in the angle range not covered by those.

WAKE MODEL

To calculate the downwash at the different helicopter components (i.e., aerodynamic centers of the fuselage, horizontal tailplane and vertical fin, and tail-rotor hub), a wake model was implemented instead of using empirical models as Talbot et al. [1982]. Essentially, two different types of wake models exist: prescribed and free-wake models. Prescribed wake models are computationally more efficient than free-wake models, but also less accurate.

The wake model implemented in the flight mechanics model developed in this thesis is a prescribed wake model, known as Beddoes wake [Beddoes, 1985]. According to this wake model, each blade produces a tip vortex. Two different wake geometries can be adopted in this model: the undistorted wake, which assumes uniform inflow, and the distorted wake, which accounts for the departure from uniform inflow induced by the skewness of the wake. Among the several prescribed-wake models available, Beddoes wake was chose for its computational efficiency and predictive effectiveness [Leishman, 2006].

4.2.2. AUTOROTATION INDEX

The preliminary design phase of a new helicopter involves a trade-off procedure between performance in hover and in forward-flight [Johnson, 1994]. Different constraints should be taken into account in order to avoid infeasible solutions. Among all the design requirements, also performance in autorotation plays a crucial role [Fradenburgh, 1984]. Indeed, the ability of the pilot to land safely after total power failure does not depend only on their skills, but also on the physical characteristics of the helicopter. This consideration leads to the desire to quantify the autorotative characteristics of a given helicopter, tracing these back to its basic design parameters. Since the execution of the autorotation maneuver can be interpreted as an energy management task, a suitable index for measuring autorotative performance should account for the kinetic energy stored in the rotor.

Although several types of metrics can be defined [White et al., 1982; Wood, 1976], the *autorotation index (AI)* is basically a stored energy factor. The index used in this thesis (Eq. (4.4)), also known as *autorotative flare index*, was derived by Fradenburgh [1984] from simple momentum relations assuming that the helicopter is initially in a steady descent in autorotation, so that the problem becomes reducing the rate of descent prior to touch-down as much as possible.

$$AI = \frac{I_R \Omega_{mr}^2}{2WDL} \tag{4.4}$$

The autorotative flare index (Eq. (4.4)) can be interpreted as the ratio between the available energy (rotor kinetic energy $I_R\Omega_{mr}^2/2$, where I_R is the polar moment of inertia of the rotor system and Ω_{mr} is the rotor RPM) and the energy required to stop the rate of descent of the helicopter (proportional to the helicopter weight W and the disk loading DL). Thus, a high value of the index is desirable. In order to compare the values of this index for various helicopters, it is convenient to plot the parameter proportional to rotor kinetic energy per unit gross weight $I_R\Omega_{mr}^2/2/W$ versus disk loading DL. This graphical form is adopted in Fig. 4.2, where an overview of typical values of the autorotation index is given. Straight lines through the origin correspond to constant values of the index. Data for several well-known helicopters are shown and for all of them the autorotative index falls between 5 and 40 ft^3/lb.

Some of the parameters in Eq. (4.4) are closely related, hence it is not possible to isolate the contribution of each of them to the overall autorotative performance. For this reason, an approximate form of the autorotation index of Eq. (4.4) has been derived. For this approximation it is assumed that:

- the main rotor blade mass density ρ_b is uniform, so that its mass can be expressed as:

$$m_b \simeq \rho_b t_h R c \tag{4.5}$$

  where t_h is the blade airfoil mean thickness, c is the blade mean chord and R is the main rotor radius;

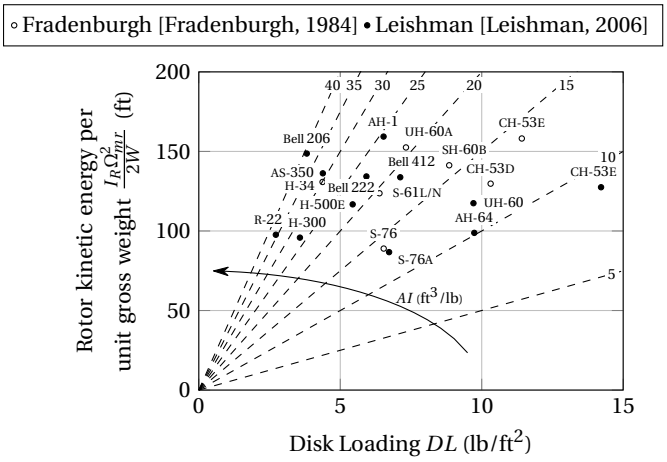

Figure 4.2: Autorotative indices for several helicopters at standard sea level conditions (revised from Fradenburgh [Fradenburgh, 1984] and Leishman [Leishman, 2006]).

- the main rotor blade flap moment of inertia I_β can be approximated with that of a thin rod:

$$I_\beta \simeq m_b \frac{R^2}{3} = \rho_b t_h \frac{cR^3}{3} \tag{4.6}$$

- the polar inertia of the rotor system I_R can be approximated as the product between the number of blades on main rotor N_b and the main rotor blade flap moment of inertia I_β:

$$I_R \simeq N_b I_\beta \simeq N_b \rho_b t_h \frac{cR^3}{3} \tag{4.7}$$

With these assumptions and using the definition of disk loading DL:

$$DL = \frac{W}{\pi R^2} \tag{4.8}$$

the autorotation index of Eq. (4.4) can be approximated as:

$$AI \simeq \frac{\pi}{6} N_b \rho_b t_h \frac{cR^5 \Omega_{mr}^2}{W^2} \tag{4.9}$$

Seven independent design parameters have been identified (N_b, ρ_b, t_h, c, R, Ω_{mr} and W). However, the number of blades on the main rotor N_b, blade mass density ρ_b,

and blade airfoil mean thickness t_h were fixed to the baseline value, reducing by three the number of independent design parameters. The rationale behind this choice is that such parameters are more related to blade dynamics and structural design than helicopter performance.

Each of the remaining four design parameters of Eq. (4.9) was varied individually to get eight different values of autorotation index, ranging from 5 to 40 ft^3/lb, for a total of 32 configurations that are summarized in Tab. 4.1 and shown graphically in Fig. 4.3. The reader should note that some of these configurations are not physically feasible. Indeed, these configurations do not correspond to existing helicopters, but they are hypothetical variants of the Bo-105 helicopter with different autorotation indexes.

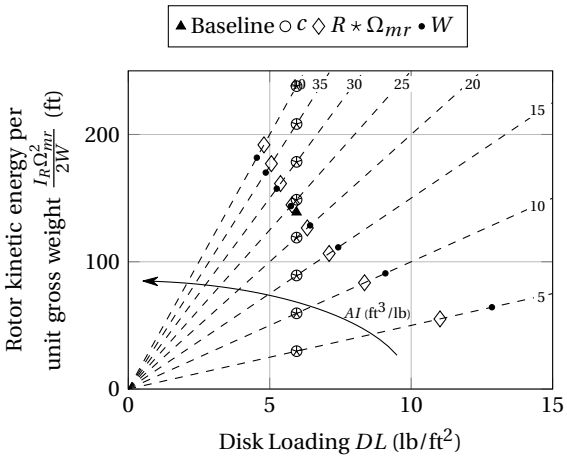

Figure 4.3: Autorotative indices for the helicopter's configurations listed in Tab. 4.1 at standard sea level conditions.

4.3. RESULTS

This section is split in two parts. The goal of the first part is to show the effects of the rotorspeed degree of freedom on classical rigid-body modes. This is achieved by comparing the eigenmodes of a 3-DOF longitudinal model in straight level flight with those of a 4-DOF (3-DOF longitudinal + RPM) model in steady descent during autorotation. Both models are representative of the Bo-105 helicopter. The same analysis was conducted on a higher fidelity helicopter model (6-DOF rigid-body helicopter model + RPM), i.e., the eigenmodes of the 6-DOF rigid-body model in straight level flight were compared with those of the 7-DOF (6-DOF + RPM) model in steady descent in autorotation.

The second part focuses on the effects of some of the basic design parameters involved in the calculation of the autorotative flare index on the helicopter's stability characteristics in autorotation.

4.3.1. EFFECT OF RPM ON RIGID-BODY MODES

ANALYSIS OF THE MODE PARTICIPATION FACTORS AT 60 KNOTS (3-DOF)

Modes in steady descent in autorotation cannot be easily matched with modes in level flight just by looking at the corresponding eigenvalues. Their identification in autorotation needs to be based on the analysis of the corresponding eigenvector by means of a comparison with the eigenvectors in level flight. Indeed, we expect a similar behavior in terms of states' participation for equivalent modes in the two flight conditions. However, using eigenvectors to estimate the participation of a mode on states with different dimensions (e.g., u [L/T] and q [1/T]) is not straightforward. For this reason, *Mode Participation Factors (MPF)*, calculated according to Eq. (C.58), are used in place of eigenvectors for mode identification purposes. Theoretical insight on MPF are provided in Appendix C.2.2. Bar plots have been used to compare the mode participation factors between level flight and steady autorotation at 60 kn horizontal speed (Fig. 4.4). The pitch subsidence mode exhibits a negligible participation along the rotorspeed DOF (Fig. 4.4c). In contrast, the phugoid (Fig. 4.4a) and the heave/rotorspeed (Fig. 4.4b) show a redistribution of the participation from the airframe states to the rotorspeed DOF in steady autorotation. In particular, there is a mild decrease in the participation along u and θ in favor of w and $\dot{\psi}_{mr}$ for the phugoid, while there is a strong decrease in the participation along w in favor of $\dot{\psi}_{mr}$ for the heave/rotorspeed.

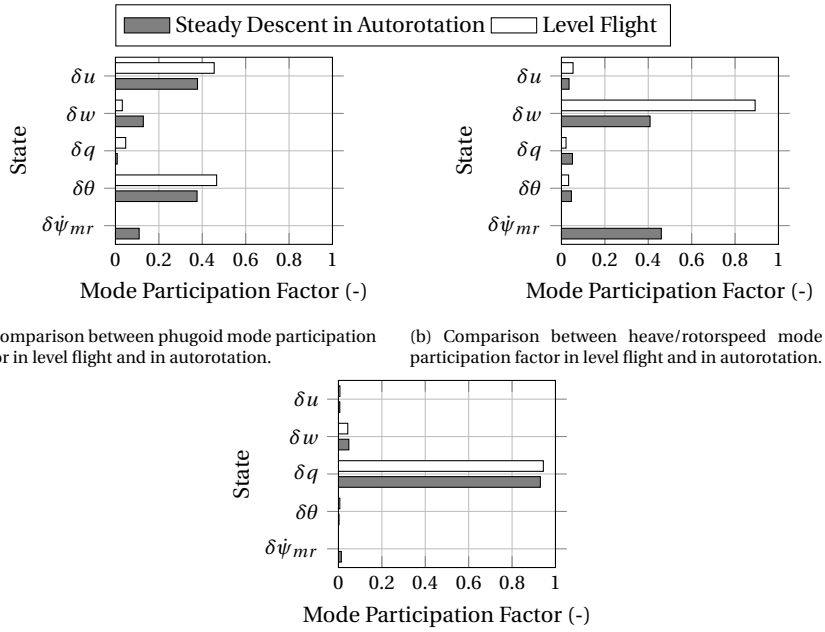

(a) Comparison between phugoid mode participation factor in level flight and in autorotation.

(b) Comparison between heave/rotorspeed mode participation factor in level flight and in autorotation.

(c) Comparison between pitch subsidence mode participation factor in level flight and in autorotation.

Figure 4.4: Comparison between mode participation factors in level flight and steady descent in autorotation for the baseline helicopter (Bo-105) according to the 3-DOF longitudinal + RPM model at 60 kn horizontal speed at standard sea level conditions.

EVOLUTION OF THE EIGENVALUES WITH HORIZONTAL SPEED (3-DOF)

Fig. 4.5 shows a comparison between the root locus in level flight (Fig. 4.5a, 4.5c and 4.5e) and steady descent in autorotation (Fig. 4.5b, 4.5d and 4.5f) for the baseline helicopter (Bo-105), according to the 3-DOF helicopter model. The root loci are parametrized with horizontal speed, showing the evolution of each mode from low-speed flight to 140 kn. Steady descent in autorotation is a condition in which the helicopter is descending at a constant rate of descent, whose value is such that the rotor torque is zero [Prouty, 2002]. This means that also the rate of descent changes with horizontal speed. These values are shown in Fig. 4.5d and 4.5f for three points (minimum speed, speed for minimum descent rate and maximum speed).

In steady descent in autorotation, the heave and the rotorspeed DOFs couple together giving rise to a set of complex conjugate poles (Fig. 4.5f). This heave-rotorspeed oscillation is the direct consequence of the coupling terms Q_w and $Z_{\dot{\psi}_{mr}}$ in the state-matrix of Eq. (C.41), as shown in Fig. 4.6. Here, a comparison is made between the fully coupled rotor-airframe system (non-zero rotor torque derivatives with respect to airframe states and airframe forces and moments derivatives with respect to rotorspeed in the state-matrix of Eq. (C.41)), the fully uncoupled rotor-airframe system (zero rotor torque derivatives with respect to airframe states and airframe forces and moments derivatives with respect to rotorspeed in the state-matrix of Eq. (C.41)) and two partially coupled rotor-airframe systems (one with non-zero Q_w and $Z_{\dot{\psi}_{mr}}$ and the other with non-zero Q_w, $Z_{\dot{\psi}_{mr}}$ and $M_{\dot{\psi}_{mr}}$ in the state-matrix of Eq. (C.41)) in the prediction of the heave/rotorspeed oscillation for the baseline helicopter at 60 kn horizontal speed. The fully uncoupled system features two stable real poles (Fig. 4.6a), among which the most damped exhibit participation primarily along the heave DOF (*heave subsidence*) as shown in Fig. 4.6b, whereas the other participates only along the rotorspeed DOF (*rotorspeed mode*). With the inclusion of the coupling terms Q_w and $Z_{\dot{\psi}_{mr}}$, the two real poles coalesce giving rise two a set of coumplex conjugate poles (Fig. 4.6a) with participation primarily along the heave and the rotorspeed DOFs (Fig. 4.6b). However, to achieve a better approximation of the heave/rotorspeed oscillation both in terms of frequency and damping, there is the need to include also $M_{\dot{\psi}_{mr}}$ (Fig. 4.6a).

In steady autorotation, the phugoid consists of two aperiodic poles at very low and very high speeds. At intermediate speeds, these two poles couple together, giving rise to a set of complex conjugate poles that is unstable only at low horizontal speeds (Fig. 4.5d). The pitch subsidence mode instead is almost identical in the two flight conditions.

Typical autorotative speeds range from 60 to 75 kn [Anonymous, 1979, 1995]. To gain more insight into the dynamic characteristics of the baseline helicopter in steady descent in autorotation, the vale of 60 kn horizontal speed was considered. Tab. 4.2 shows a comparison of eigenvalues, frequency and damping characteristics at 60 kn horizontal speed between level flight and steady descent in autorotation. The phugoid mode, which is unstable and lightly damped in level flight (time to double of approximately 33 s), becomes stable in steady autorotation (time to halve of approximately 48 s). The heave subsidence instead, which is stable and aperiodic in level flight (time to halve of approximately 1 s), couples with the rotorspeed degree of freedom, giving rise to a set of stable and highly damped periodic poles in steady autorotation (time to halve of approximately 2 s). The pitch subsidence slightly moves toward the left-hand side of the complex plane, but overall does not change significantly.

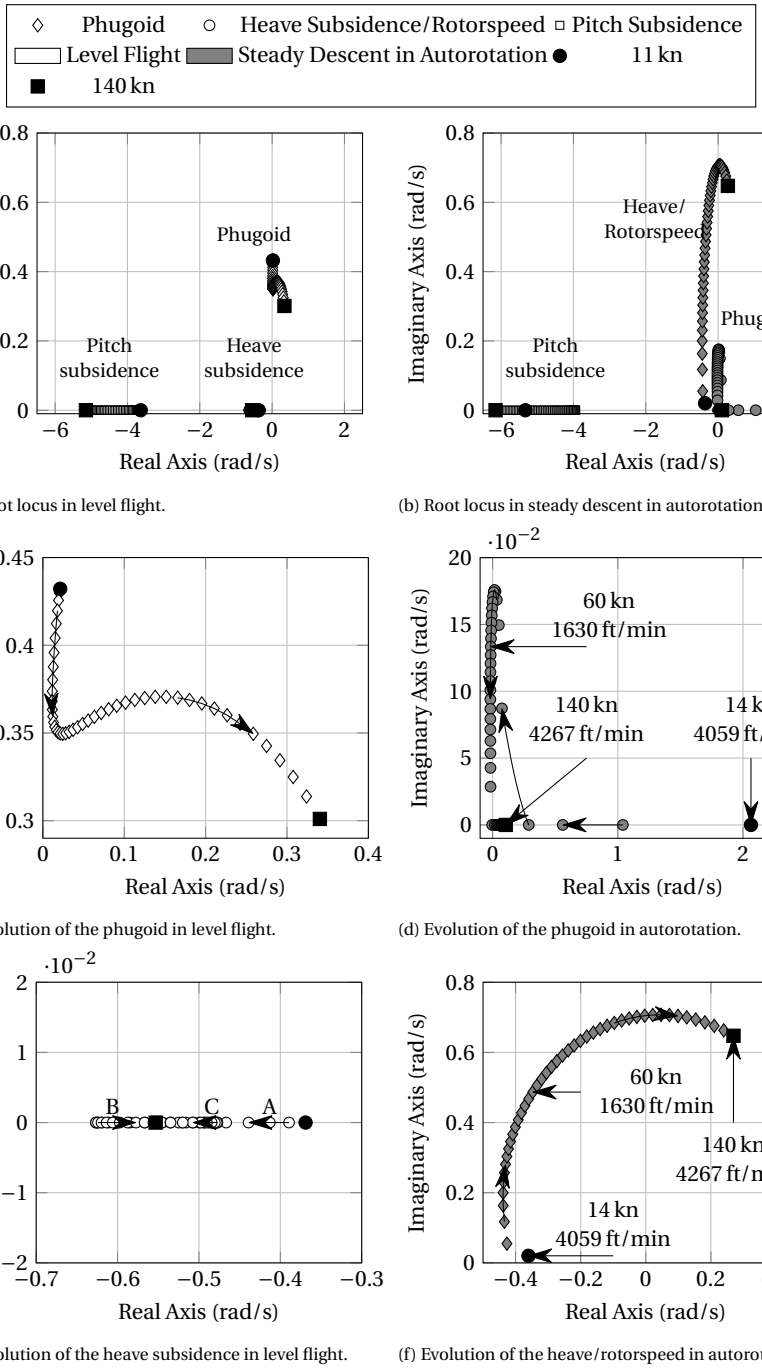

(a) Root locus in level flight.

(b) Root locus in steady descent in autorotation.

(c) Evolution of the phugoid in level flight.

(d) Evolution of the phugoid in autorotation.

(e) Evolution of the heave subsidence in level flight.

(f) Evolution of the heave/rotorspeed in autorotation.

Figure 4.5: Comparison between root loci in level flight and steady descent in autorotation for the baseline helicopter (Bo-105) according to the 3-DOF longitudinal + RPM model as a function of horizontal speed at standard sea level conditions.

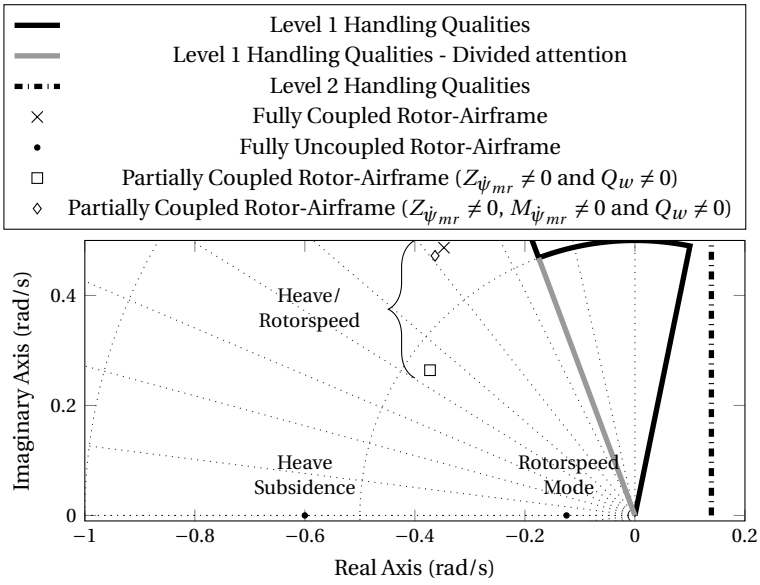

(a) Heave/rotorspeed eigenvalue.

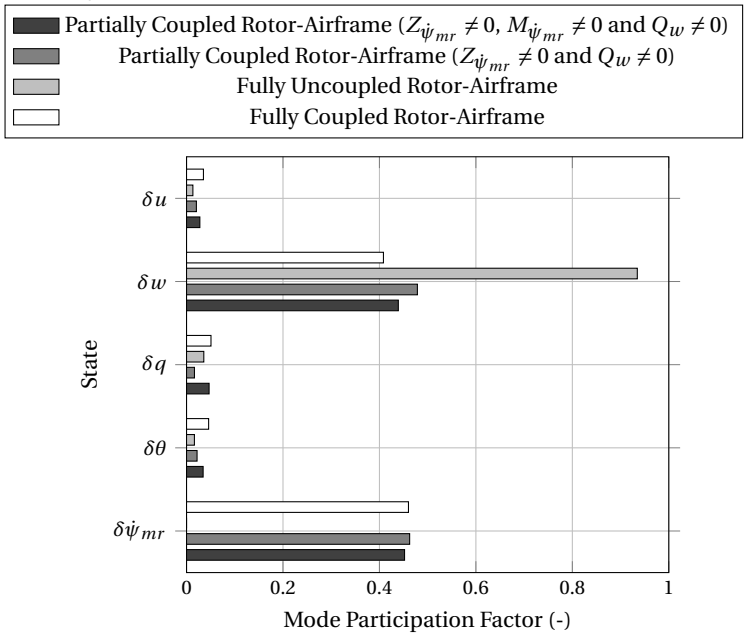

(b) Heave/rotorspeed Mode Participation Factor.

Figure 4.6: Comparison between the fully coupled rotor-airframe system, the fully uncoupled rotor-airframe system and two partially coupled rotor-airframe systems in the prediction of the heave/rotorspeed oscillation for the baseline helicopter at 60 kn horizontal speed at standard sea level conditions.

Table 4.2: Eigenvalues, frequency and damping characteristics at 60 kn for the baseline helicopter - Comparison between level flight and steady descent in autorotation according to the 3-DOF model.

Mode	Level flight				Steady descent in autorotation			
	λ (rad/s)		ω_n (rad/s)	ζ (-)	λ (rad/s)		ω_n (rad/s)	ζ (-)
	$\Re(\lambda)$	$\Im(\lambda)$			$\Re(\lambda)$	$\Im(\lambda)$		
Phugoid	0.0212	−0.3497	0.3503	−0.0605	−0.0146	−0.1334	0.1342	0.1087
	0.0212	0.3497	0.3503	−0.0605	−0.0146	0.1334	0.1342	0.1087
Heave/	−0.6197	0.0000	0.6197	1.0000	−0.3472	−0.4869	0.5980	0.5806
Rotorspeed					−0.3472	0.4869	0.5980	0.5806
Pitch sub.	−4.0783	0.0000	4.0783	1.0000	−4.2596	0.0000	4.2596	1.0000

ANALYSIS OF THE MODE PARTICIPATION FACTORS AT 60 KNOTS (6-DOF)

Sec. 4.3.1 showed that especially the phugoid and the heave/rotorspeed mode are strongly influenced by the inclusion of the rotorspeed DOF. In this section, mode participation fators are analyzed also for the 6-DOF + RPM model to confirm the results from the 3-DOF model and to investigate whether modes with participation primarily along lateral-directional states are also affected by the additional degree of freedom (rotorspeed DOF).

Fig. 4.7 shows a comparison of the mode participation factors between level flight and steady descent in autorotation at 60 kn horizontal speed according to the 6-DOF + RPM model. Unexpectedly, the coupling between the longitudinal and the lateral-directional planes seems weak, as longitudinal modes barely participates along lateral-directional states and the participation of lateral-directional modes along longitudinal states is nearly unnoticeable. Fig. 4.7a to 4.7c show that only the phugoid and the heave/rotorspeed exhibit a non-negligible participation along the rotorspeed state, confirming the results obtained with the 3-DOF + RPM model in Sec. 4.3.1. Fig. 4.7d to 4.7f show that lateral-directional modes of motion are not affected by the rotorspeed DOF, as they do not exhibit any participation along this DOF and their state participation is essentially the same in the two flight conditions. Such a result could be expected as the steady-descent in autorotation is mainly a longitudinal maneuver.

EVOLUTION OF THE EIGENVALUES WITH HORIZONTAL SPEED (6-DOF)

The same analysis conducted on the 3-DOF model in Sec. 4.3.1 is repeated in this section for the 6-DOF model to understand whether the 3-DOF model provides accurate results from the perspective of the dynamics stability of the longitudinal modes of motion.

Fig. 4.8 shows a comparison between the root locus in level flight (Fig. 4.8a) and steady descent in autorotation (Fig. 4.8b) for the baseline helicopter, according to the 6-DOF helicopter model. The root loci are parametrized with horizontal speed, showing the evolution of each mode from 10 kn to 120 kn. To examine the differences in terms of helicopter dynamic behavior in the two flight conditions, modes with participation primarily along longitudinal states (Fig. 4.10) and those with participation primarily along lateral-directional states (Fig. 4.9) are analyzed separately.

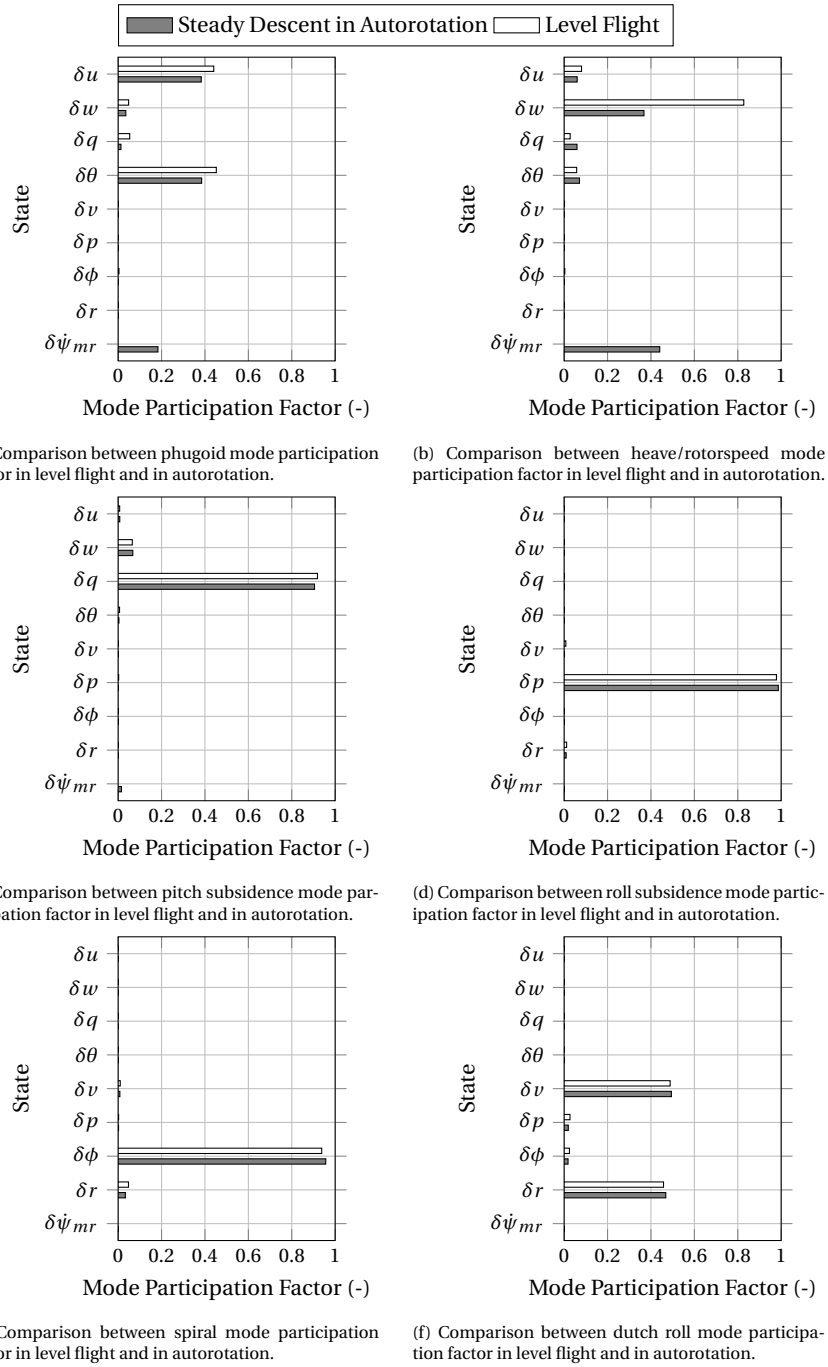

(a) Comparison between phugoid mode participation factor in level flight and in autorotation.

(b) Comparison between heave/rotorspeed mode participation factor in level flight and in autorotation.

(c) Comparison between pitch subsidence mode participation factor in level flight and in autorotation.

(d) Comparison between roll subsidence mode participation factor in level flight and in autorotation.

(e) Comparison between spiral mode participation factor in level flight and in autorotation.

(f) Comparison between dutch roll mode participation factor in level flight and in autorotation.

Figure 4.7: Comparison between mode participation factors in level flight and steady descent in autorotation for the baseline helicopter (Bo-105) according to the 6-DOF + RPM model at 60 kn horizontal speed at standard sea level conditions.

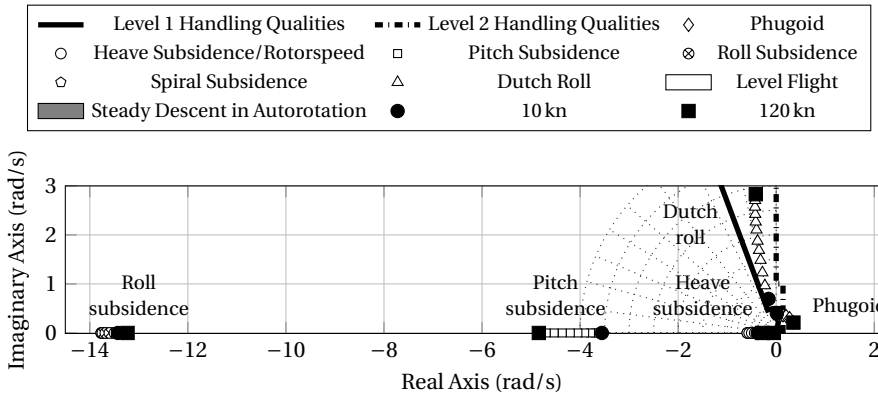

(a) Root locus in level flight.

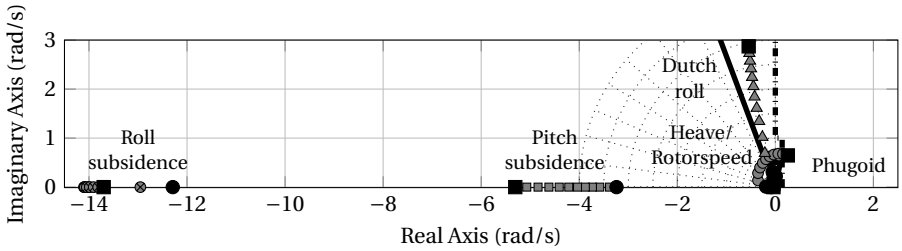

(b) Root locus in steady descent in autorotation.

Figure 4.8: Comparison between root loci in level flight and steady descent in autorotation for the baseline helicopter as a function of horizontal speed at standard sea level conditions.

Lateral-Directional Modes of Motion As expected from Sec. 4.3.1, lateral-directional modes of motion (roll subsidence, spiral subsidence and dutch roll) are almost unaffected by the incorporation of the rotorspeed degree of freedom (Fig. 4.9). These modes maintain the nature they have in straight level flight also in steady-descent in autorotation: the roll and the spiral subsidences are aperiodic modes and the dutch roll is a periodic mode in both flight conditions.

Longitudinal Modes of Motion The analysis conducted on the 3-DOF model (Sec. 4.3.1) demonstrated that the dynamic behavior of the helicopter in the two flight conditions is substantially different from the perspective of the stability of the longitudinal modes of motion (phugoid, heave subsidence and pitch subsidence).

This result is confirmed for the 6-DOF model, as shown in Fig. 4.10. In steady descent in autorotation, the rotorspeed degree of freedom couples with the heave subsidence, giving rise to a couple of complex conjugate poles (Fig. 4.10d) that is unstable only at low horizontal speeds. The phugoid is also affected by the rotorspeed degree of freedom: it becomes unstable only at high speeds (Fig. 4.10b). The pitch subsidence mode instead is almost unaffected by the addition of the rotorspeed state.

These results are in good agreement with those provided by the 3-DOF model (Fig. 4.5), especially at intermediate speeds, thus confirming that the rotorspeed degree of freedom has a strong influence only on the longitudinal rigid-body modes and that the 3-DOF model represent an acceptable compromise for the study of the stability in steady-descent in autorotation.

Tab. 4.3 shows a comparison of eigenvalues, frequency and damping characteristics at 60 kn airspeed between level flight and steady descent in autorotation, confirming for the longitudinal modes what had already been observed for the 3-DOF model in Tab. 4.2 and showing that lateral-directional modes overall do not change significantly.

Table 4.3: Eigenvalues, frequency and damping characteristics at 60 kn for the baseline helicopter - Comparison between level flight and steady descent in autorotation according to the 6-DOF model.

	Level flight				**Steady descent in autorotation**			
Mode	λ (rad/s)		ω_n (rad/s)	ζ (-)	λ (rad/s)		ω_n (rad/s)	ζ (-)
	$\Re(\lambda)$	$\Im(\lambda)$			$\Re(\lambda)$	$\Im(\lambda)$		
Phugoid	0.0324	−0.3553	0.3567	−0.0908	−0.0598	−0.1857	0.1951	0.3068
	0.0324	0.3553	0.3567	−0.0908	−0.0598	0.1857	0.1951	0.3068
Heave/	−0.5511	0.0000	0.5511	1.0000	−0.2563	−0.4927	0.5554	0.4615
Rotorspeed					−0.2563	0.4927	0.5554	0.4615
Pitch sub.	−3.9068	0.0000	3.9068	1.0000	−4.0351	0.0000	4.0351	1.0000
Roll sub.	−13.7649	0.0000	13.7649	1.0000	−14.1025	0.0000	14.1025	1.0000
Spiral sub.	−0.0471	0.0000	0.0471	1.0000	−0.0367	0.0000	0.0367	1.0000
Dutch roll	−0.3791	−1.8765	1.9145	0.1980	−0.4240	−1.8419	1.8900	0.2243
	−0.3791	1.8765	1.9145	0.1980	−0.4240	1.8419	1.8900	0.2243

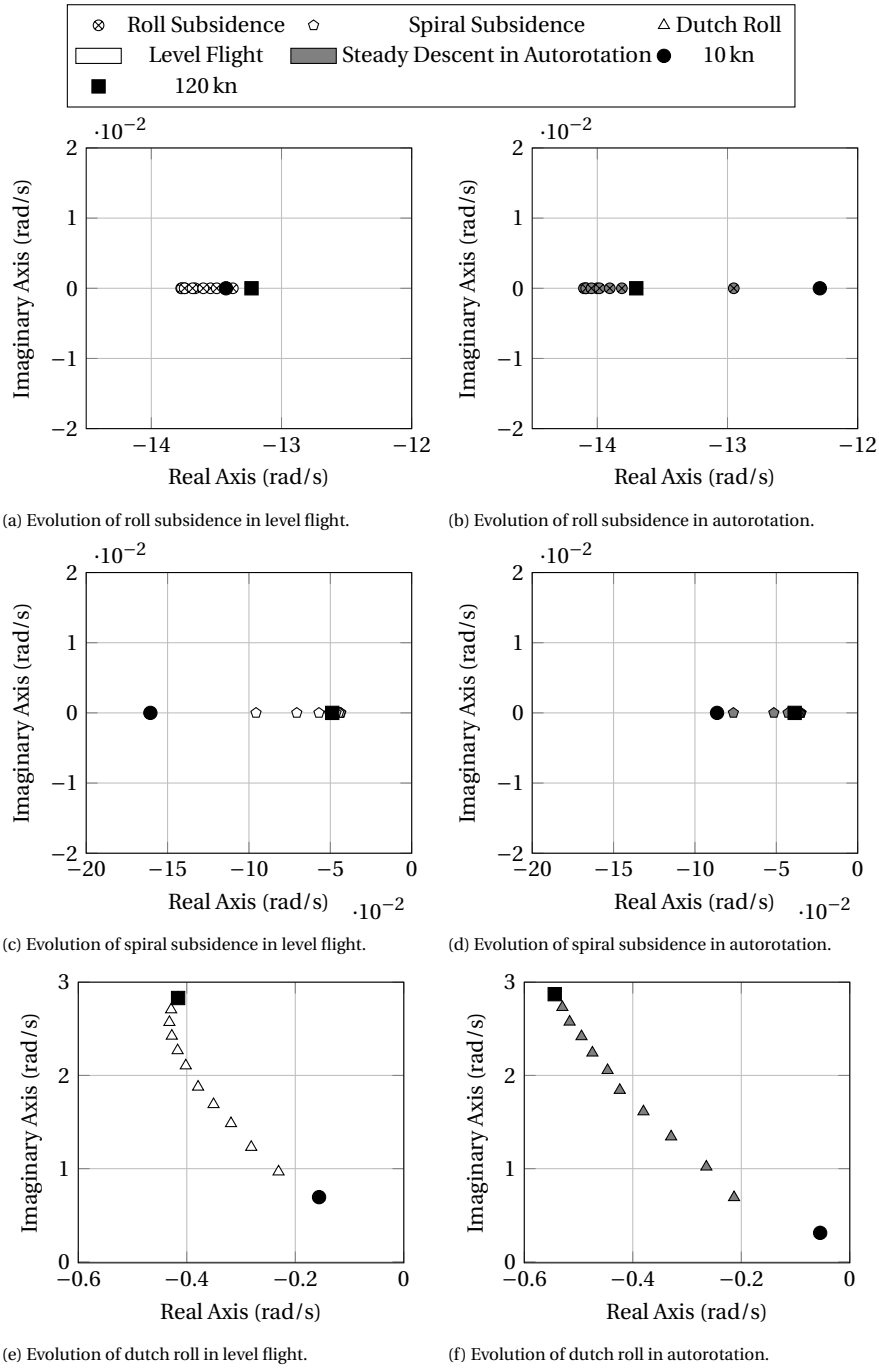

(a) Evolution of roll subsidence in level flight.

(b) Evolution of roll subsidence in autorotation.

(c) Evolution of spiral subsidence in level flight.

(d) Evolution of spiral subsidence in autorotation.

(e) Evolution of dutch roll in level flight.

(f) Evolution of dutch roll in autorotation.

Figure 4.9: Comparison between root loci in level flight and steady descent in autorotation for the baseline helicopter as a function of horizontal speed at standard sea level conditions for the lateral-directional modes of motion.

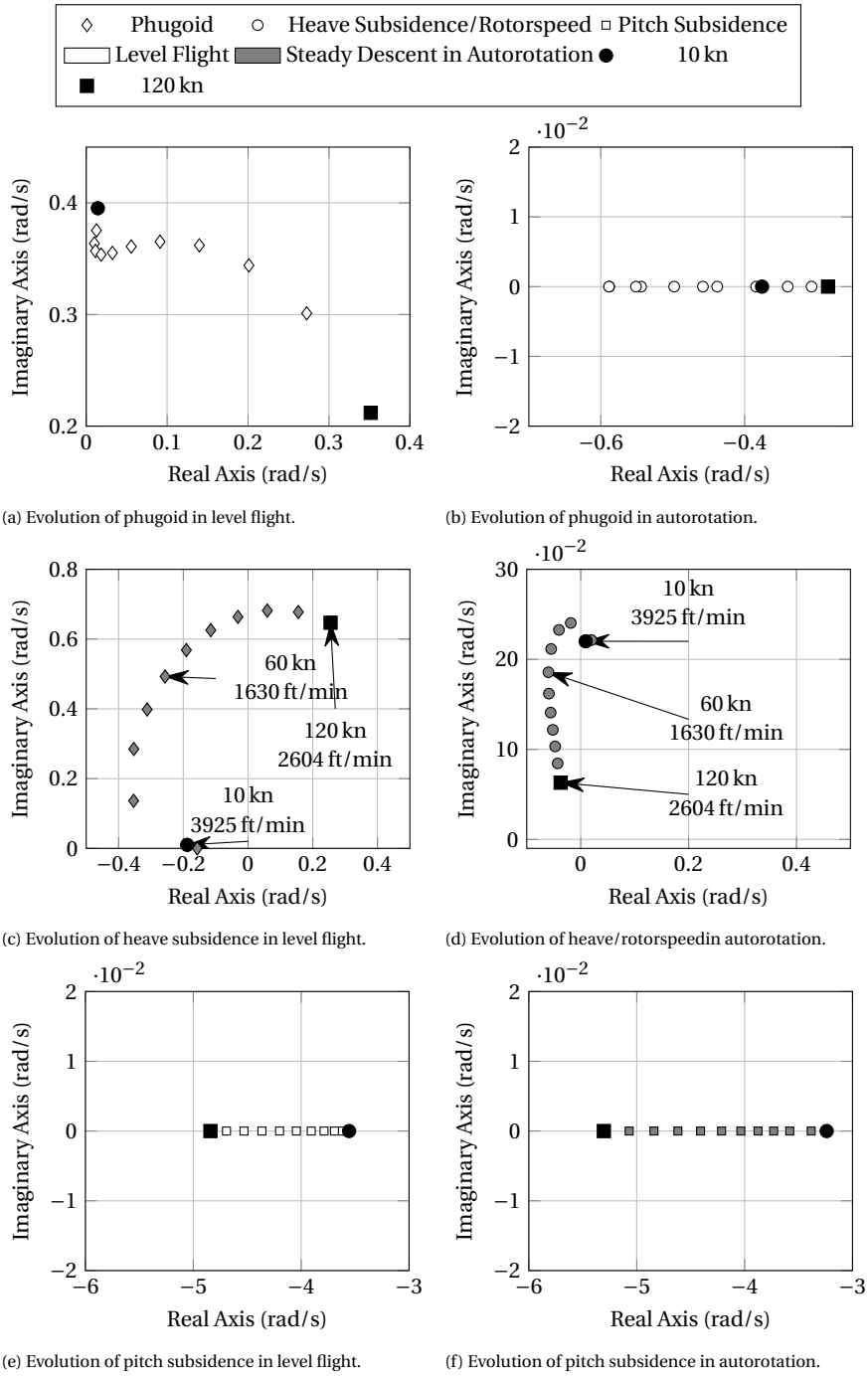

(a) Evolution of phugoid in level flight.

(b) Evolution of phugoid in autorotation.

(c) Evolution of heave subsidence in level flight.

(d) Evolution of heave/rotorspeedin autorotation.

(e) Evolution of pitch subsidence in level flight.

(f) Evolution of pitch subsidence in autorotation.

Figure 4.10: Comparison between root loci in level flight and steady descent in autorotation for the baseline helicopter as a function of horizontal speed at standard sea level conditions for the longitudinal modes of motion.

4.3.2. EFFECT OF AUTOROTATIVE INDEX DESIGN PARAMETERS ON HELICOPTER STABILITY CHARACTERISTICS IN AUTOROTATION

The stability characteristics of the set of helicopter configurations defined in Sec. 4.2.2 have been evaluated at 60 kn horizontal speed using the 3-DOF + RPM helicopter model and are shown in Fig. 4.11. This set of configurations has been divided into four subsets, each of which is related to a specific design parameter (see Tab. 4.1). Fig. 4.11a, 4.11b, 4.11c and 4.11d show the sensitivity of the modes to variations of the autorotative flare index due to changes in the main rotor blade chord c, main rotor radius R, main rotor RPM Ω and helicopter weight W, respectively.

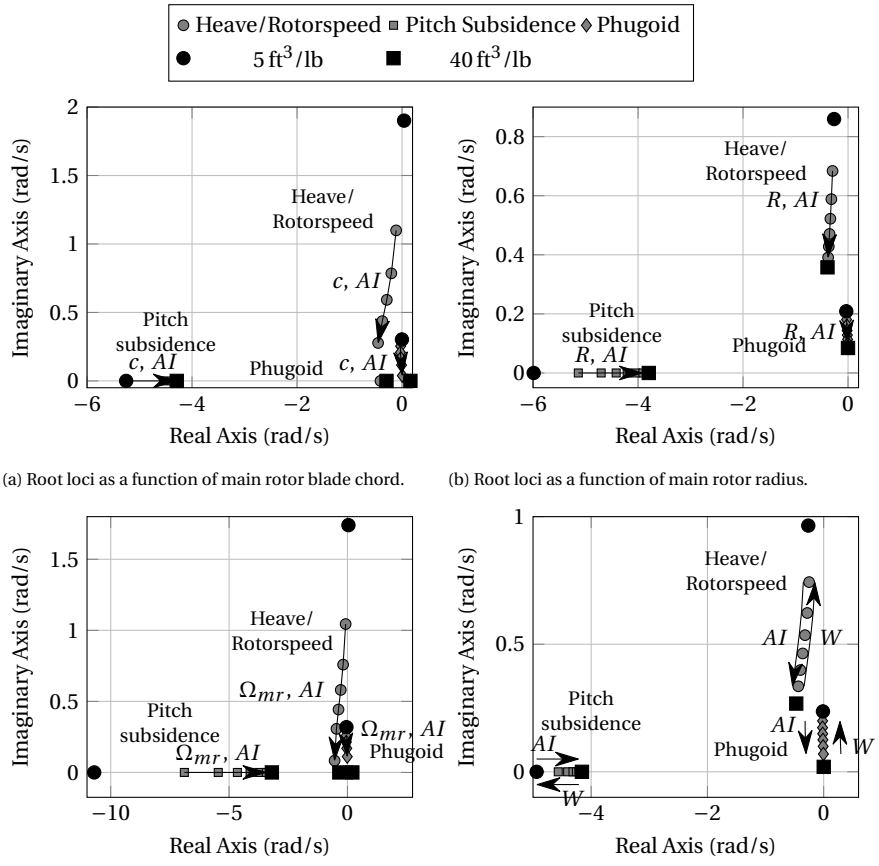

(a) Root loci as a function of main rotor blade chord.

(b) Root loci as a function of main rotor radius.

(c) Root loci as a function of main rotor RPM.

(d) Root loci as a function of helicopter weight.

Figure 4.11: Comparison between root loci in steady descent in autorotation at 60 kn horizontal speed for the different helicopter's configurations as a function of the autorotation index at standard sea level conditions according to the 3-DOF + RPM helicopter model.

For every subset of configurations, it can be noticed that increasing the autorotative flare index has:

- negative effects on the stability of the phugoid mode, which even becomes slightly unstable for high values of the index.
- positive effects on the stability of the heave/rotorspeed mode;
- negative effects on the stability of the pitch subsidence. However, the pitch subsidence remains stable;

To achieve greater insight into this trend, a sensitivity analysis of the eigenvalues to stability derivative perturbations was conducted. To this end, the elements of the state-matrix (Eq. (C.41)) of the baseline helicopter were varied individually in a range that was chosen according to the values assumed by that derivative for the helicopter configurations listed in Tab. 4.1. Fig. 4.12 shows the results of this analysis. Frequency (Fig. 4.12a and 4.12c) and damping ratio (Fig. 4.12b and 4.12d) were analyzed to evaluate the sensitivity of complex eigenvalues.

EFFECTS OF AUTOROTATIVE INDEX ON THE PHUGOID MODE

The sensitivity analysis of the phugoid frquency and damping ratio to stability derivative perturbations (Fig. 4.12a and 4.12b, respectively) demonstrates that the stability characteristics of the phugoid mode are mainly related to the speed stability derivative M_u. Increasing this derivative increases the stability of the phugoid (Fig. 4.13a). Fig. 4.14a shows that an increase in the autorotative flare index reduces M_u, thus making the phugoid mode less stable.

EFFECTS OF AUTOROTATIVE INDEX ON THE HEAVE/ROTORSPEED MODE

Fig. 4.6a showed that the stability derivative terms Q_w and $Z_{\dot{\psi}_{mr}}$ are responsible for the coupling between the heave and the rotorspeed modes. However, $M_{\dot{\psi}_{mr}}$ affects the heave/rotorspeed oscillation both in terms of frequency and damping. This is confirmed by Fig. 4.12c and 4.12d, according to which the stability characteristics of the heave/rotorspeed mode are mainly related to the stability derivative $M_{\dot{\psi}_{mr}}$, although all the derivatives of Z and M have a strong effect on the heave/rotorspeed damping (Fig. 4.12d). Increasing this derivative increases the stability of the heave/rotorspeed mode (Fig. 4.13b). Fig. 4.14b shows that an increase in the autorotative flare index increases $M_{\dot{\psi}_{mr}}$, thus making the heave/rotorspeed mode more stable.

EFFECTS OF AUTOROTATIVE INDEX ON THE PITCH SUBSIDENCE MODE

The sensitivity analysis of the pitch subsidence to stability derivative perturbations (Fig. 4.12e) demonstrates that the stability characteristics of the pitch subsidence mode are mainly related to the pitch-damping derivative M_q. Increasing this derivative decreases the stability of the phugoid (Fig. 4.13a). Fig. 4.14a shows that an increase in the autorotative flare index reduces M_q, thus making the pitch subsidence mode less stable.

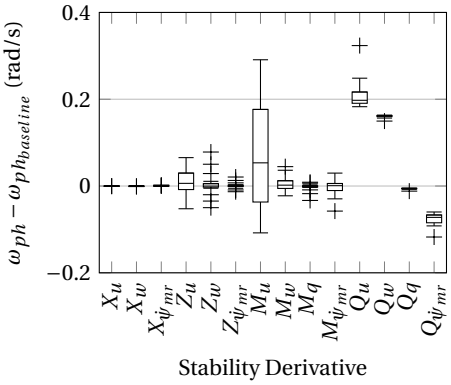

(a) Phugoid frequency sensitivity.

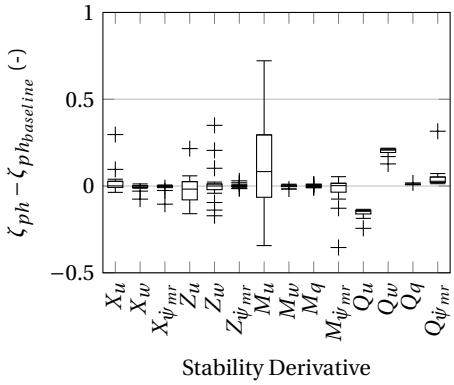

(b) Phugoid damping sensitivity.

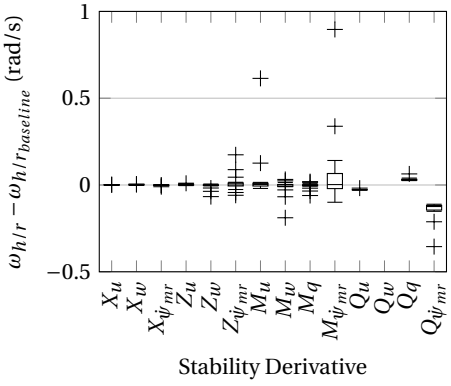

(c) Heave/Rotorspeed frequency sensitivity.

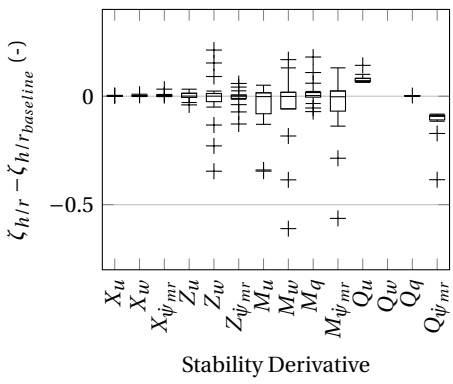

(d) Heave/Rotorspeed damping sensitivity.

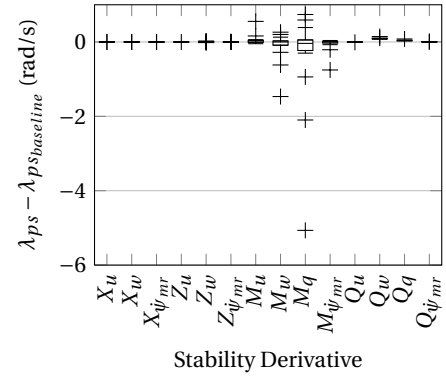

(e) Pitch subsidence sensitivity.

Figure 4.12: Eigenvalue Sensitivity to stability derivative perturbations.

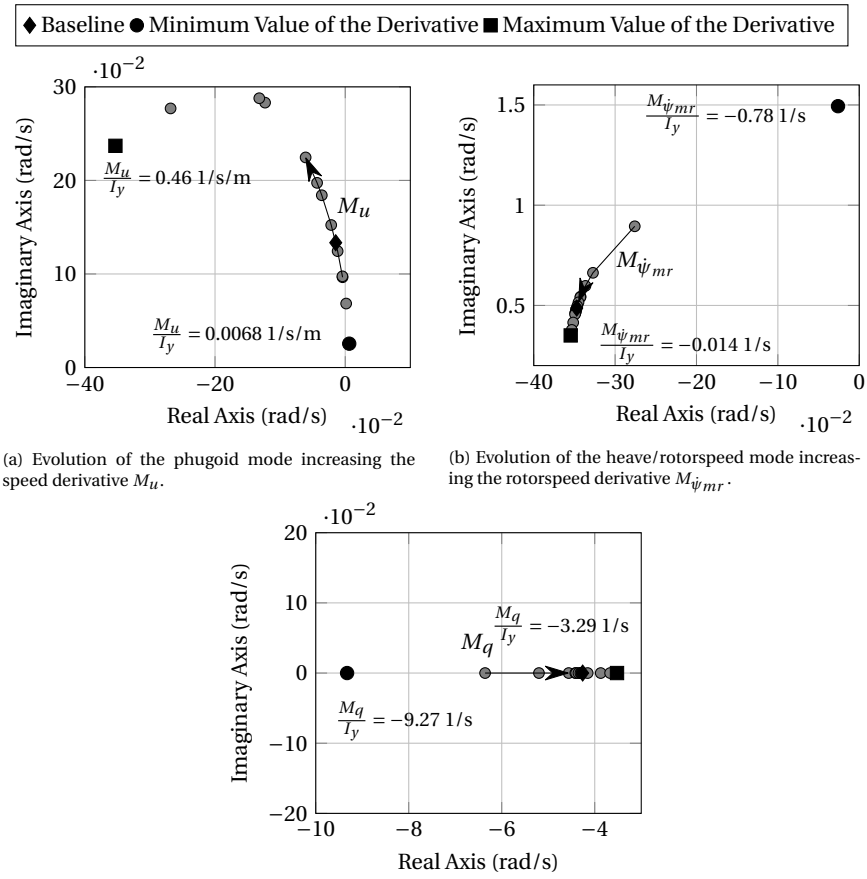

(a) Evolution of the phugoid mode increasing the speed derivative M_u.

(b) Evolution of the heave/rotorspeed mode increasing the rotorspeed derivative $M_{\dot{\psi}mr}$.

(c) Evolution of the pitch subsidence mode increasing the pitch-damping derivative M_q.

Figure 4.13: Root locus sensitivity.

4.4. DISCUSSION

The present chapter investigated the effects of the rotor RPM degree-of-freedom in autorotation on classical rigid-body modes for two helicopter models, characterized by a different level of fidelity (3-DOF longitudinal and 6-DOF rigid-body helicopter model). The proposed methodology relies on various classical assumptions (e.g., linearization and stability analysis), that make it applicable only to the steady descent part of the autorotation maneuver, which can be considered as an equilibrium condition.

According to the analysis carried out on both models, the helicopter dynamics change considerably in autorotation as the rotorspeed degree of freedom couples with the classical rigid body modes. Therefore, autorotation requires a different stabilization strategy by the pilot (this is shown through the "paper pilot" [Anderson, 1970; Dillow, 1971] developed in Appendix E) and should not be mistakenly considered only as an energy management task. Indeed, for both models the results show that there are two main differences between the modes in straight level flight and those in steady descent in au-

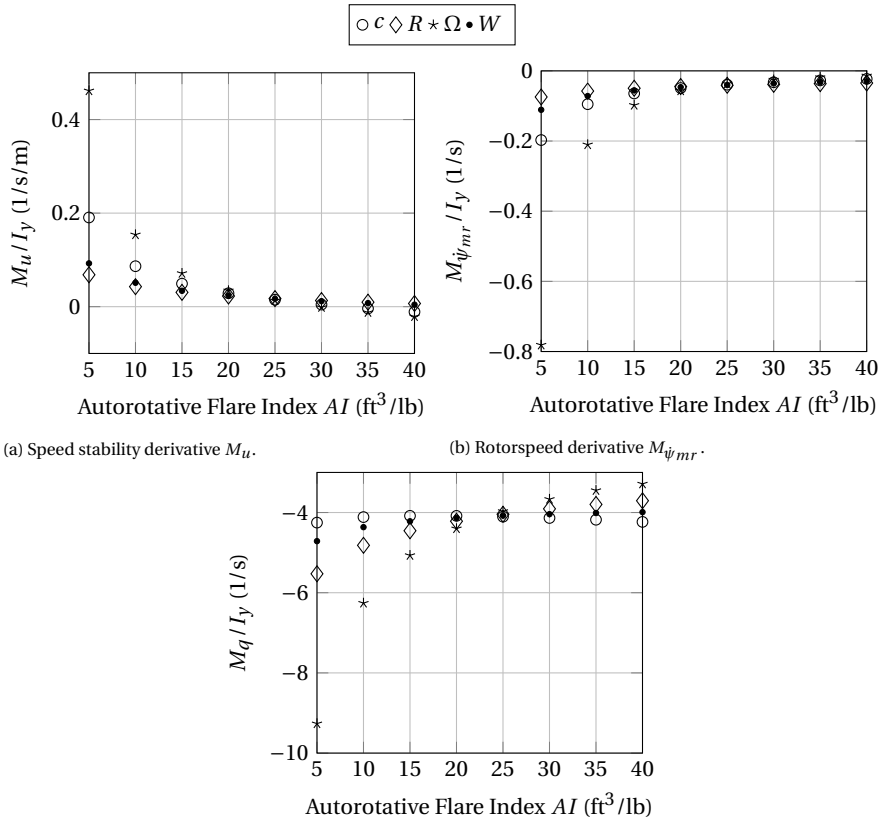

(a) Speed stability derivative M_u.

(b) Rotorspeed derivative $M_{\dot{\psi}_{mr}}$.

(c) Pitch-damping derivative M_q.

Figure 4.14: Stability derivatives as a function of autorotative flare index.

torotation for the baseline helicopter (Bo-105) considered in this study.

The first difference is that *the phugoid in autorotation is unstable only at very low or very high speeds*. The mode participation factor analysis at the typical autorotative speed shows that in steady descent in autorotation the phugoid is affected by the inclusion of the rotorspeed degree-of-freedom $\dot{\psi}_{mr}$ exhibiting a non-negligible participation along this state. This is achieved at the expenses of the participation along the surge speed u and the pitch angle θ that decreases with respect to straight level flight. This means that the speed derivative M_u and the pitch-damping derivative M_q, whose interaction is responsible for the instability of the phugoid in straight level flight, are not sufficiently coupled to induce the unstable phugoid oscillation.

The second difference is that *the heave subsidence mode couples with the rotorspeed degree of freedom, giving rise to a set of complex conjugate poles*. The mode participation factor analysis at the typical autorotative speed shows that in steady descent in autorotation this mode can be described as a heave/rotorspeed oscillation, as it exhibits participation primarily along these two states. There is a strong decrease in the participation along the heave speed w with respect to level flight in favor of the rotorspeed

degree-of-freedom $\dot{\psi}_{mr}$. It was demonstrated that the stability derivatives Q_w and $Z_{\dot{\psi}_{mr}}$ are responsible for the coupling between the heave and the rotorspeed modes. However, $M_{\dot{\psi}_{mr}}$ affects the heave/rotorspeed oscillation both in terms of frequency and damping.

A good agreement in terms of stability characteristics of the longitudinal modes of motion is found between the two models. Furthermore, the lateral-directional modes of the 6-DOF rigid-body helicopter model + RPM overall do not change significantly in steady-descent in autorotation with respect to straight level flight, as demonstrated by the "paper pilot" [Anderson, 1970; Dillow, 1971] developed in Appendix E, which is characterized by the same lateral-directional control loops and gains in the two flight conditions. These results have implications on the model fidelity requirements for autorotation training, as they suggests that a 3-DOF longitudinal helicopter model + RPM may be already a good starting point to learn the execution of the autorotation maneuver. Of course, considering the high-order (coupled fuselage/rotor dynamics) and highly coupled nature of the helicopter dynamics compared to a fixed-wing aircraft, higher order models may be desirable to provide the pilot with those cues that are important for the failure identification and prompt reaction (e.g., initial yaw after failure that cannot be modelled with a 3-DOF longitudinal model).

The present chapter has also investigated whether large variations of the autorotative flare index strongly affect helicopter dynamics in autorotation, because this may have consequences on pilot control strategy and workload. The autorotative flare index is used in any helicopter development program by Sikorsky Aircraft [Fradenburgh, 1984] as a metric for satisfactory autorotative characteristics and, within certain constraints, appears to be a reasonably reliable indicator of the relative ease of making successful autorotative landings. Four independent design parameters are involved in the calculation of the simplified version of this index: the main rotor blade chord, the main rotor radius, the rotor RPM and the helicopter weight. Each was varied individually from the baseline value to get eight different values of the autorotation index, spanning from 5 to 40 ft^3/lb. This range was chosen after comparing the index for various existing helicopters.

For each of the four sub-sets of configurations, the sensitivity of the eigenvalues to changes in the autorotation index shows the same results. When the autorotative flare index increases, the stability of the phugoid mode worsens, because the speed stability derivative M_u decreases. The same holds for the pitch subsidence (the pitch-damping stability derivative M_q increases), whereas the opposite happens for the heave/rotorspeed mode (the rotorspeed stability derivative $M_{\dot{\psi}_{mr}}$ increases). Thus, higher values of the autorotation index, representative of good autorotative performance in terms of available energy over required energy, do not necessarily mean better stability characteristics. Of course these considerations hold for synthetic variations of the baseline helicopter, the Bo-105. Future work is necessary to understand whether this behavior holds in general or depends on the underlying helicopter dynamics.

The main limitation of the proposed methodology consists in the fact that it is applicable only to the steady descent part of the autorotation maneuver, which is not the most demanding phase for the pilot [Prouty, 2009]. A procedure for the quantitative assessment of handling qualities in autorotation, accounting for all the phases of the maneuver, need to be implemented. To this end, the "paper pilot" [Anderson, 1970; Dillow, 1971] developed in Appendix E can be used by comparing pilot performance for

different helicopter configurations when the same gains are used or by comparing pilot gains when the same autorotation performance are achieved flying different configurations. As an alternative, pilot-in-the-loop experiments with test pilots awarding handling quality ratings to the different helicopter configurations can be performed. The latter approach was chosen in this thesis, because, due to the lack of flight test data in autorotation, pilot evaluation was used also as a validation step of the helicopter model.

In order to gain insight into how pilots adapt their control strategy to the variation of the helicopter dynamics in autorotation and to the changes in the autorotative flare index, as a next step, pilot-in-the-loop experiments will be conducted on the SIMONA Research Simulator at Delft University of Technology (see Chapters 5 and 6). Prior to the experiments, a test pilot will be invited to fly and evaluate the model in the simulator and to perform the autorotation maneuver with the different helicopter's configurations analyzed in the present chapter. Pilot ratings, pilot commentary and some objective performance metrics will be collected in order to isolate two flyable configurations characterized by different workloads required by the pilot. The selected configurations will be then used in two quasi-transfer-of-training experiments to test whether the group of participants that starts the training in the most challenging setting develops more robust and flexible flying skills than the group that starts the training in the least demanding setting, as previous experimental evidence has shown [Nusseck et al., 2008].

4.5. CONCLUSION

The present chapter applied linear dynamics system theory to assess helicopter stability characteristics in autorotation. In order to achieve this goal, the classical system of equations describing the helicopter flight dynamics, which comprises the rigid-body degrees of freedom of the fuselage, has been augmented by the rotor torque equation. Indeed, the main difference with respect to powered flight is that in autorotation the rotor RPM becomes a true degree of freedom, because the governor is disengaged and no longer fulfils the task of keeping the rotorspeed constant. The validity of this analysis is restricted to the steady descent phase of the autorotation maneuver, that can be considered as an equilibrium condition.

The results show that the helicopter dynamics change considerably in autorotation as a consequence of the fact that the rotorspeed degree of freedom couples with the classical rigid-body modes. Therefore, autorotation requires a different control strategy by the pilot and should not be considered only as an energy management task, as it is qualified by the autorotative flare index. Indeed, high values of the index may also lead to degraded stability characteristics and hence a possibly more difficult autorotation.

Future work is necessary to understand how strongly pilots are influenced across different autorotative flare index (AI) settings and whether problems in skill tranfer between high/low AI helicopters exist.

5

AUTOROTATION TRANSFER OF TRAINING: EFFECTS OF HELICOPTER DYNAMICS (3-DOF)

Chapter 4 presented a sensitivity analysis investigating the effect of autorotative flare index variations on the helicopter dynamics stability in autorotation. This analysis allows to determine which values of the index lead to degraded stability characteristics of the helicopter in autorotation, thus requiring high control compensation to the pilot. However, high pilot intervention does not necessarily hamper acquisition of skills and transfer of training, especially for experienced pilots [Wickens et al., 2013]. On the contrary, previous experimental evidence [Nusseck et al., 2008] demonstrates that positive transfer of skills occurs from high pilot control compensation dynamics to low control compensation dynamics, but not the opposite.

This chapter investigates the effects of two sets of helicopter dynamics (chosen among those studied in Chapter 4) on pilots learning process and transfer of learned skills during autorotation training, one requiring low and the other high pilot control compensation. The chapter is structured as follows. First, the design of a quasi-transfer-of-training experiment performed on the SIMONA Research Simulator (SRS) aimed at evaluating whether the helicopter dynamics affect the transfer of trained autorotation flying skills is presented in Section 5.2. The results from this experiment are documented and discussed in Sections 5.3 and 5.4, respectively. The chapter is concluded in Section 5.5.

The contents of this chapter have been published in: Scaramuzzino, P. F. et al. (2022). Effects of Helicopter Dynamics on Autorotation Transfer of Training. *Journal of Aircraft*, 59(1):73-88. https://doi.org/10.2514/1.C036217.

5.1. INTRODUCTION

Pilot training and flight simulators play a crucial role in rotorcraft safety. Accident analyses carried out by the U.S. U.S. Joint Helicopter Safety Analysis Team [2011a,b] and the European Helicopter Safety Analysis Team [2010, 2015] pointed out that the development of a standardized training program for autorotation and emergency aircraft handling, as well as the improvement of simulator training for basic and advanced maneuvers, are essential. A combination of simulator and in-flight training is desirable, especially during the training of hazardous scenarios. The variety of conditions that pilots may face during emergencies requires experience and judgment in order to react promptly and avoid the many possible errors. Extensive practice is necessary to acquire robust and flexible piloting skills, giving the pilots the ability to adapt to different aircraft configurations and types. Because in-flight training is expensive and potentially dangerous, simulator training is the only viable alternative. Especially for rotorcraft, simulator usage has the potential to substantially reduce costs and risks, as shown by Memon et al. [2019]. However, to avoid unrealistic training and negative transfer of skills when similar situations are encountered during actual flight, there is the need to bridge the gap between simulator scenarios and reality for edge-of-the-envelope flight.

Autorotation is considered to be a key critical training scenario [Coyle, 2013; Prouty, 2009; Rogers et al., 2000]. It is a flight condition where the rotation of the rotor is sustained by the airflow moving up through the rotor, rather than by means of engine torque applied to the shaft. Helicopter pilots use autorotation following partial or total engine power failure to reach the nearest suitable landing site. The energy stored in the rotor is preserved at the expense of the helicopter's potential energy, i.e., the altitude. Therefore, a helicopter can sustain autorotation only by means of descending flight.

One key challenge for obtaining representative simulation and effective pilot training in ground-based simulators is ensuring a sufficiently realistic flight model [White et al., 2019]. While this is true for flight simulation in general, the need for high-accuracy models is especially felt for flight conditions that are the result of abnormal modes of operation, such as autorotation. For example, the representation of the rotor wake plays an essential role in rotorcraft flight mechanics models. Houston et al. [2003] have investigated how vorticity transport models, as opposed to the simpler finite-state induced velocity models [Chen, 1990], affect modeling quality for autorotation. Furthermore, many studies [Houston, 1996, 2000, 2002, 2003; Nikolsky, 1952; Nikolsky et al., 1949a,b] have focused on the effects of the variable rotor angular speed in autorotation, which are usually neglected in powered-flight rotorcraft models. Finally, key efforts were also devoted to model development and validation against wind tunnel and/or flight test data in autorotation and in the vortex ring state region for non-conventional helicopters, such as rotary decelerators of falling objects (e.g., ejection seat equipped with a folded rotor) [Seter et al., 2014] and coaxial helicopters [Bauknecht et al., 2018; Feil et al., 2021].

Besides model fidelity, pilots' perception and their use of available cues is another aspect that should not be underestimated in flight simulation for training purposes [Jones, 2017; Mulder et al., 2013; Pool et al., 2016]. One of the most debated issues regarding simulator cueing is whether full-motion simulators are actually needed to achieve superior training quality. While this can be considered a general simulation question, there are peculiarities for each aircraft class, e.g. fixed-wing, helicopters, that require to perform

a specific assessment for each one of them. Decker et al. [1986] and Kaiser et al. [2001] investigated the effects of a range of visual and motion cues settings on pilots' ability to perform unpowered helicopter landings. Both works showed that helicopter touchdown performance, along with pilot opinion, improved with increased motion fidelity. However, in-simulator performance and simulator acceptance by the pilots are not metrics of training effectiveness when no transfer paradigm is adopted. To overcome the inconsistency among the results of the individual studies on the need of motion bases [McCauley, 2006], de Winter et al. [2012] conducted a meta-analysis on 24 transfer-of-training experiments with motion as an independent variable, using both fixed- and rotary-wing aircraft models, showing that there is no overall evidence that motion improves performance in real aircraft, even though positive effects in favor of motion are observed in quasi-transfer studies and for individuals without flight experience learning disturbance-rejection tasks or maneuvers of vehicles with low dynamic stability, such as helicopters. Since then, other transfer-of-training experiments were performed for both fixed-wing aircraft [Pool et al., 2016; Zaal et al., 2015] and helicopters [Fabbroni et al., 2018, 2017a,b]. Most of these experiments use a quasi-transfer paradigm, where trained skills are applied on a simulator with capabilities that are beyond those of a typical training simulator [AGARD, 1980], corroborating the assumption that such simulators act as a valid replacement for the actual aircraft. Similar results are obtained in all these studies: the need of simulators with a motion system cannot be claimed. On the contrary, subjects who trained in poorer cueing situations developed control strategies that positively transfer to higher fidelity simulators.

Despite these recent efforts devoted to achieving more accurate rotorcraft models and clarifying the relation between simulator cueing and training effectiveness, only a few studies have explicitly investigated the effects of rotorcraft model fidelity and dynamics variations on pilot behaviour and (transfer of) training, e.g., [Nusseck et al., 2008; Pavel et al., 2013; Timson et al., 2011]. Especially for a critical hands-on maneuver such as autorotation, pilots need to adjust their control strategy according to the helicopter dynamics they control [AGARD 1980; Hosman, 1999; Hettinger et al., 2003]. Helicopters with different handling characteristics may require very different skills from pilots to accomplish the task. Earlier experiments in training a lateral sidestep hover maneuver [Nusseck et al., 2008], showed that flight-naïve participants – i.e., without any previous real or simulated flight experience – are more likely to develop robust and flexible flying skills when they start the training in a helicopter with agile system dynamics. According to Nusseck et al. [2008], starting the training of a certain task with the most challenging configuration provides the pilot with the ability to accomplish the same task with every other configuration after a short adaptation phase.

This result is consistent with the principle of perceptual learning, which Gold et al. [2010, (p. R46)] define as *"experience-dependent enhancement of our ability to make sense of what we see, hear, feel, taste or smell. These changes are permanent or semi-permanent, as distinct from shorter-term mechanisms like sensory adaptation or habituation. Moreover, these changes are not merely incidental but rather adaptive and therefore confer benefits, like improved sensitivity to weak or ambiguous stimuli"*. Thus, training with the highest resource-demanding setting enhances perceptual learning, and the improved perception skills allow pilots trained in this setting to more easily adjust their control

strategy when transferred to another, easier condition.

This chapter investigates whether the acquisition of flying skills for autorotation, and their transfer, are affected by the helicopter dynamics. We hypothesized that certain dynamics may lead to the development of a more robust control behavior, one that can be easily adapted to a helicopter with different dynamics, yielding substantial benefits in terms of engine failure handling capabilities.

The results of a quasi-Transfer-of-Training (qToT) experiment with fourteen experienced helicopter pilots,divided in two groups, performed in TU Delft's SIMONA Research Simulator (SRS) are presented to corroborate this hypothesis. Several metrics have been used to compare the performance at touchdown. Additionally, a novel method, referred to as Control Event Detection (CED), is presented, to allow an in-depth analysis of pilot control actions involved in a successful autorotative landing.

5.2. METHODS

5.2.1. TASK

In rotorcraft handling quality research, experimental tasks are usually defined according to the specifications of the mission-oriented design standard, ADS-33E [US Army AMCOM, 2000]. Although conceived for military rotorcraft, ADS-33E is widely used to assess handling qualities characteristics of commercial rotorcraft as well, as there is no counterpart in the civil domain. However, the use of ADS-33E Mission Task Elements (MTEs) is not always relevant, especially in the design of training tasks. Furthermore, ADS-33E does not have a specific Autorotation Maneuver MTE. Since there are no specific handling quality metrics for autorotation, pilot-in-the-loop autorotation maneuvers are usually evaluated based on subjective pilot feedback and comments and on objective measurements of landing survivability metrics [Sunberg et al., 2015].

For this experiment, a MTE was defined for the straight-in autorotation maneuver; the proposed test course is shown in Fig. 5.1. The simulation starts with the helicopter trimmed in straight level flight at 60 knots air speed, at an altitude of 1,000 ft. The symmetry plane of the helicopter is aligned with the center line of a runway, whose starting point is located 3,281 ft ahead the helicopter initial position. The pilot has to keep constant speed and altitude until the power failure is triggered from the control room. As soon as the pilot recognizes the unannounced failure, he has to recover starting a steady descent in autorotation, maintaining 60 knots air speed and keeping the rotor RPM in the green arc of the tachometer. When close enough to the ground the pilot has to flare, to reduce both the rate of descent and the forward speed and finally level the skids with the ground, to avoid tail strike, and pull-up the collective to cushion the touchdown. The contact accelerations at touchdown were not modeled. Therefore, the simulation stopped automatically once the center of gravity of the helicopter reached two meters above the ground.

Performance standards for the straight-in autorotation maneuver are adapted from Sunberg et al. [2014, 2015] and are listed in Tab. 5.1. The values of the horizontal speed and of the rate of descent at touchdown refer to the AH-1G helicopter [Sunberg et al., 2015], which has a similar skid landing gear as the baseline helicopter (Bo-105) considered in this chapter. Therefore, these were not changed. Although characterized by a

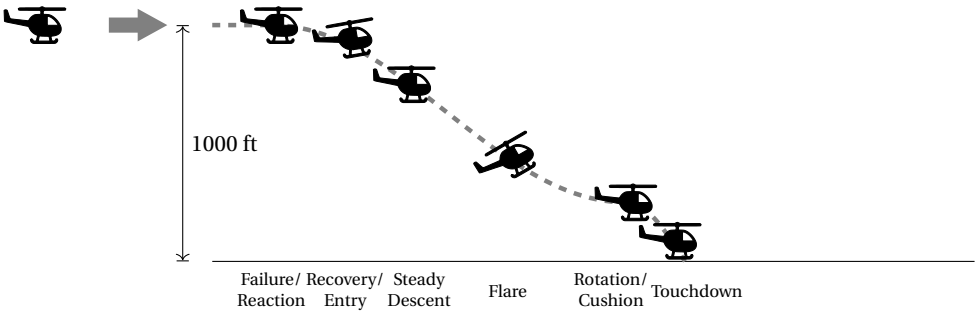

(a) Side view.

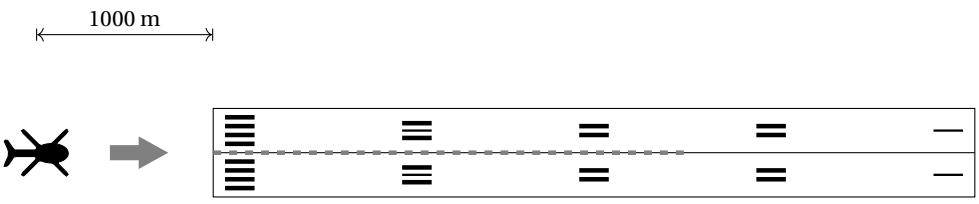

(b) Top view.

Figure 5.1: Suggested course for straight-in autorotation maneuver.

similar landing system, the AH-1G and the Bo-105 are different helicopters, with different performance and intended role. Indeed, the AH-1G is a two-blades rotor, single-engine attack helicopter, whereas the Bo-105 is a light, twin-engine, multi-purpose helicopter with a four-blades hingeless rotor. The maximum values of the pitch angle at touchdown, which are responsible of preventing tail strike, were slightly increased due to the different helicopter geometry. Indeed, due to its longer and lower tail boom, the AH-1G helicopter cannot afford to touch down with the same fuselage pitch as the Bo-105.

Desired performance translates into a successful landing, i.e., the helicopter's final state at ground contact is such that the aircraft and crew survivability are not threatened. Adequate performance translates into marginal landing conditions, that would likely result in damage to the aircraft, but be survivable to the occupants and the equipment. The values presented in Tab. 5.1 are defined according to landing survivability metrics that are based on specifications for military helicopters' structural design [Department of the Air Force and Navy Bureau of Aeronautics, 1954; Department of the Army, 1974] and on the accident analysis conducted by Crist et al. [1981].

The threshold values for desired and adequate performance must not only be adapted to the helicopter geometry and type of landing gear, but also according to the ground surface (e.g., paved, concrete, grass, etc.) on which the helicopter touches down. The values listed in Tab. 5.1 can be considered reasonable for landing on a paved or concrete surface. The landing gear on skid-equipped helicopters is designed to spread laterally under load, dissipating the residual amount of kinetic energy deriving from a non sufficiently effective flare and cushion. This is of course possible only on relatively hard surfaces. Touchdowns to soft surfaces, such as grass, are extremely dangerous, as the skid tubes

dig a small depression in the surface and are therefore prevented from moving sideways. This means that the landing gear does not operate in its design conditions and some of the loads that it should withstand are transferred to other parts of the structure. These may bent and eventually fail.

Another problem of touchdowns to soft surfaces is that the friction on a soft surface is greater than a paved hard surface. This is due to the larger contact area between the skids and the surface. The greater friction combined with the high center of gravity of a helicopter may easily lead to a nose over. In these conditions it is extremely important to reduce (in absolute value) the minimum pitch attitude to mitigate tip over occurrences. Furthermore, grass can always hide uneven ground.

The combination of requirements on lateral speed and horizontal speed translates into a requirement also on the sideslip/track angle, that together with the requirement on yaw rate should be responsible for preventing roll-over issues due to the difference between where the airframe nose is pointing and the direction it is travelling. Also in this case it is extremely important to adapt the desired and adequate performance threshold values according to the touchdown surface.

Table 5.1: Performance – Straight-in Autorotation Maneuver (adapted from Sunberg et al. [2015]).

Metric	**Performance**			
	Desired		**Adequate**	
	Minimum	Maximum	Minimum	Maximum
Pitch angle at touchdown θ_{td} (deg)	−5	12	−5	18
Horizontal speed at touchdown $V_{x_{td}}$ (kn)	0	30	0	40
Rate of descent at touchdown $V_{z_{td}}$ (ft/min)	0	480	0	900
Pitch rate at touchdown q_{td} (deg/s)	−30	20	−50	40

5.2.2. HELICOPTER DYNAMICS

Participants performed the straight-in autorotation task by controlling a four degrees-of-freedom (3-DOF longitudinal dynamics plus rotorspeed DOF), non-linear and generic helicopter model with steady flapping dynamics (see Section 4.2.1 and Appendix A). This generic model can be used in combination with different parameters sets to approximate the dynamic response of any conventional helicopter configuration. Since the final part of the autorotation is mainly a longitudinal maneuver, the use of a 3-DOF symmetrical helicopter model is acceptable.

In Section 4.3.2, the stability characteristics in autorotation of helicopters with a different autorotative flare index (AI) [Fradenburgh, 1984] were compared. The AI can be interpreted as the ratio between the available energy, i.e., rotor kinetic energy $I_R\Omega^2/2$, where I_R is the polar moment of inertia of the rotor system and Ω is the rotor RPM, and the energy required to stop the rate of descent of the helicopter, proportional to the helicopter weight W and the disk loading DL. Therefore, high values of the index are desirable. In order to compare the values of this index for various helicopters, it is convenient to plot the parameter proportional to rotor kinetic energy per unit gross weight $I_R\Omega^2/2/W$ versus disk loading DL. This graphical form is adopted in Fig. 5.2, where an

overview of typical values of the autorotation index is given. Straight lines through the origin correspond to constant values of the index. Several helicopters have been considered and all of them have an autorotative index between 5 and 40 ft^3/lb. However, it can be noted that values of the index above 30 ft^3/lb can only be achieved by single-engine helicopters, whereas values below 15 ft^3/lb are typical of large helicopters (maximum mass greater than 9072 kg).

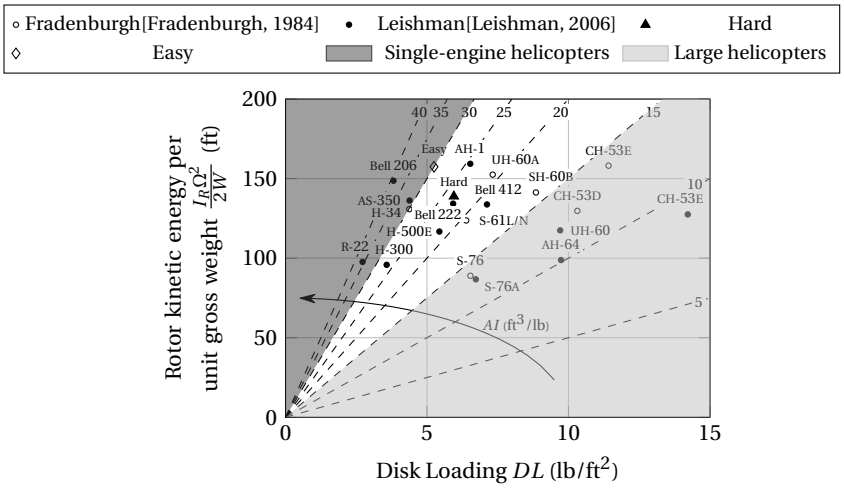

Figure 5.2: Autorotative indices at standard sea level conditions for several helicopters (revised from Fradenburgh [1984] and Leishman [2006]).

From the wide range of configurations studied in Section 4.3.2, two were selected for the current experiment. The "hard" dynamics is representative of the Bo-105 helicopter and was taken from Padfield [2007]. The "easy" dynamics represents a variation of the Bo-105 helicopter with reduced weight in order to achieve a higher AI.

Fig. 5.3 shows a comparison of the dynamics modes in steady descent in autorotation for the two helicopter configurations considered here. The rate of descent for the hard configuration is 1630.2 ft/min, whereas for the easy configuration is 1649.8 ft/min. Although the modes of the two configurations do not differ considerably, in particular in terms of the pitch subsidence, it can be noted that the heave/rotorspeed mode of the hard dynamics is less stable than that of the easy dynamics, whereas the opposite holds for the phugoid. While similar in terms of stability characteristics, these two configurations proved to be considerably different in terms of handling qualities during a pre-experiment with a test pilot, both concerning objective metrics of performance at touchdown (Tab. 5.1) and subjective handling quality ratings provided by the pilot. The selection process of these two helicopter dynamics is extensively discussed in Section 5.2.2.

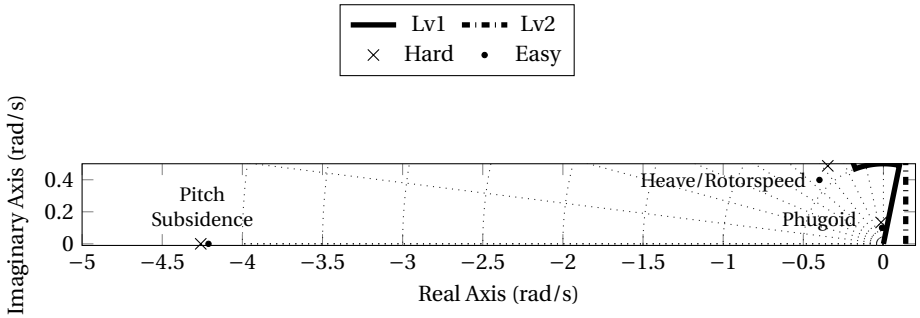

Figure 5.3: Comparison between modes in steady descent in autorotation for the two different helicopter's configurations at standard sea level conditions.

SELECTION OF HELICOPTER CONFIGURATIONS

In Section 4.3.2, the stability characteristics in autorotation of helicopters with a different autorotative flare index (AI) [Fradenburgh, 1984] were compared. Although a high autorotation index is desirable, it was shown that stability in autortation does not always improve when the index increases. Therefore, an additional step was required to isolate only two configurations among those studied in Section 4.3.2, consisting in a pre-experiment with a test pilot.

Thirty-two configurations were studied (Fig. 5.4a). They were the result of the variation from the baseline values (Bo-105 helicopter) of four design parameters (main rotor blade chord c, main rotor radius R, main rotor speed Ω, and helicopter weight W) which affect the value of the AI. This was demonstrated by deriving an approximated expression of the AI in Section 4.2.2. Different types of helicopters have been considered in Fig. 5.2 and all of them have an AI between 5 and 40 ft^3/lb. Therefore, each of the four design parameters affecting the AI was varied individually to obtain eight different values of the AI evenly spaced from 5 to 40 ft^3/lb.

Fig. 5.2 shows that values of the index above 30 ft^3/lb can only be achieved by single-engine helicopters, whereas values below 15 ft^3/lb are typical of large helicopters. Since the baseline helicopter (Bo-105) is a medium weight twin-engine helicopter, those configurations with an AI index below 15 ft^3/lb and above 30 ft^3/lb were excluded. The configurations with an AI of 20 ft^3/lb and 25 ft^3/lb were also excluded because too close to the baseline, meaning that probably the pilot would not be able to notice any difference between these configurations and the baseline. Only the configuration with an AI of 20 ft^3/lb due to a main rotor blade chord (c) variation with respect to the baseline value was retained. Indeed, the main rotor blade chord is the only linear term in the approximated expression of the AI (see Section 4.2.2). Therefore, this parameter is subject to the highest variations with respect to the baseline value and might lead to non-physically feasible configurations for high and low AI. This selection process resulted in nine configurations (Fig. 5.4b and Tab. 5.2) over the thirty-two initially available (Fig. 5.4a).

To determine the easiest and the hardest configurations, a pre-experiment with a helicopter test pilot was conducted. The test pilot performed five autorotative landings with each of the ten pre-selected configurations, the baseline plus the nine listed in Tab. 5.2 and shown in Fig. 5.4b. During each run, pilot's inputs and the helicopter model

response to these inputs were collected. After the completion of each configuration (five runs), the pilot provided Cooper-Harper ratings (HQR) [Cooper et al., 1969] according to performance defined in Tab. 5.1.

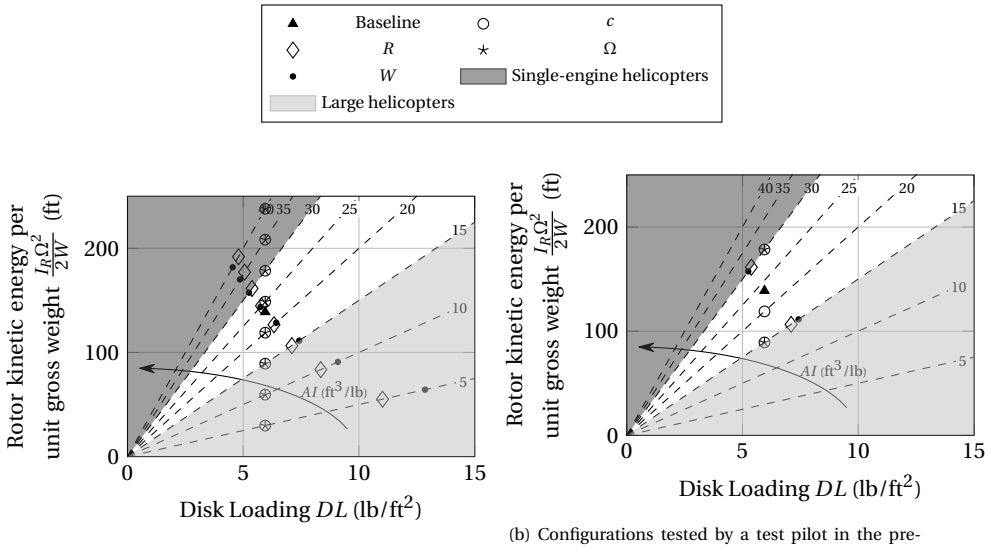

(a) All configurations studied in Section 4.3.2.

(b) Configurations tested by a test pilot in the pre-experiment.

Figure 5.4: Autorotative indices at standard sea level conditions for the helicopter's configurations studied in Section 4.3.2.

Table 5.2: Configuration test matrix.

Design parameter	Autorotative flare index AI (ft^3/lb)	Blade chord c (m)	Main rotor radius R (m)	Main rotor speed Ω (rad/s)	Helicopter weight W (kg$_f$)
Blade chord	15	0.1735	4.91	44.4	2200
	20	0.2313	|	|	|
	30	0.3470	|	|	|
Main rotor radius	15	0.2700	4.49	44.4	2200
	30	|	5.16	|	|
Main rotor speed	15	0.2700	4.91	35.6	2200
	30	|	|	50.3	|
Helicopter weight	15	0.2700	4.91	44.4	2744
	30	|	|	|	1941

The results of the pre-experiment are shown in Fig. 5.5 for each of the four metrics considered in the performance standards of Tab. 5.1. Every box plot represents the variability in performance over the five autorotative landings performed with a specific configuration. Painted stripes are adopted to provide the reader with a visual aid to quickly assess pilot's performance in every configuration. From Fig. 5.5c and 5.5d, it can be

noticed that the pilot can easily attain desired performance for the pitch angle and the pitch rate at touchdown in every run with every configuration. The rate of descent at touchdown always falls within adequate performance (Fig. 5.5b), whereas the horizontal speed at touchdown falls outside performance standards in few runs with some configurations (Fig. 5.5a). Since the performance standards in terms of pitch angle and pitch rate were easily attained, the assessment of the different configurations was based only on the horizontal speed and on the rate of descent (Fig. 5.5a and 5.5b).

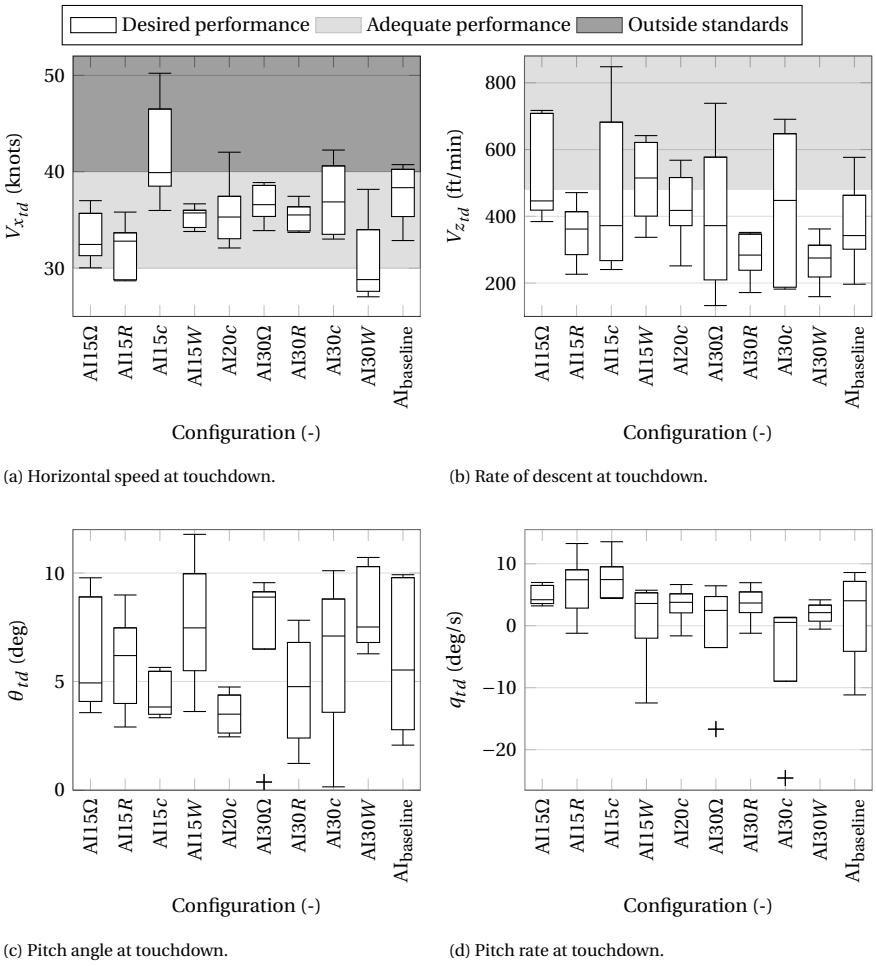

(a) Horizontal speed at touchdown.

(b) Rate of descent at touchdown.

(c) Pitch angle at touchdown.

(d) Pitch rate at touchdown.

Figure 5.5: Distribution of the performance at touchdown for each of the ten configurations.

The configuration AI15*c* shows the highest variability and is characterized by the worst performance for both metrics. The opposite holds for the configuration AI30*W*. These results are in strong agreement with the subjective ratings provided by the pilot listed in Tab. 5.3. AI30*W* was chosen as the easiest configuration. AI15*c*, however, was not selected as the hardest configuration, because it involves a 36% variation of the

main rotor blade chord with respect to the baseline value, hence it was considered not physically feasible. Looking at both the objective metrics (Fig. 5.5a and 5.5b) and the subjective ratings (Tab. 5.3), the baseline configuration takes the second place as worst configuration and so can be safely regarded as the hardest configuration. Therefore, the AI30W configuration, taken as the easiest configuration for the pilots, represents a lighter in weight version of the baseline helicopter that is instead taken as the hardest configuration.

Table 5.3: Cooper-Harper ratings (HQR) for the ten configurations flown by the test pilot.

Configuration	**Autorotation Index**	**Parameter**	**Handling Qualities Rating**	**Selected**	**Comments/Deficiencies on Performance and Control Compensation**
$AI_{baseline}$	23.3413	Baseline	5	Yes (Hard)	The rotor decay is realistic, but rather on the rapid side
AI15c	15	Chord (c)	6	No	Rotor rpm drops quicker than baseline (really aggressive response). Rpm more sensitive in this configuration
AI20c	20	Chord (c)	4	No	Noticed improved pitch stability, hence it is easier to control than baseline
AI30c	30	Chord (c)	4	No	The sink rate drops less faster with respect to previous configurations during flare. Therefore, the flare is initiated at a higher altitude. Too large pitch angle during flare. When pitching-up, the pilot loose sight and has to reposition the point which they is looking in order to assess the rate of descent. The pilot had to adapt their entry in the flare
AI15Ω	15	RPM (Ω)	5	No	Slight nose-down tendency that has to do with the collective position. When changes are made to speed or pitch attitude it takes longer to get it stable again. This configuration appears to be unstable
AI30Ω	30	RPM (Ω)	4	No	More natural position of the collective. The rotor rpm is not very sensitive to pitch attitude
AI15R	15	Radius (R)	3	No	This rating might be affected by learning effects
AI30R	30	Radius (R)	4	No	Pitch response is more pronounced. The pilot had to adapt their control strategy. More difficult to control with regard to pitch response. More agile, therefore more control inputs are required during the flare in order to get the attitude correctly
AI15W	15	Weight (W)	5	No	No pronounced difference with respect to previous configuration. Cross-coupling effect might be slightly bigger. When the pilot lowers the collective they has the feeling that they needs to apply more aft cyclic
AI30W	30	Weight (W)	3	Yes (Easy)	There is likely more energy in the rotor. Therefore, it is much easier to control because the rotor rpm changes much slower. RPM control during entry is much easier

5.2.3. EXPERIMENT STRUCTURE

The experiment is structured as in Tab. 5.4 and consists of four phases:

1. Familiarization: this phase was intended to help the participants get acquainted with the simulation environment (helicopter model, cockpit ergonomy, control inceptors, etc.). For this reason, the simulator motion system was disabled and each participant performed the task with either the hard or the easy helicopter dynamics. These runs were not used in the analysis.
2. Training: each participant performed the task with the same helicopter dynamics used during the Familiarization phase. Starting from this session, the simulator motion system was enabled.
3. Transfer: each participant performed the task with the other helicopter configuration.
4. Back-transfer: each participant performed the task with the initial hard/easy helicopter configuration.

In total, the whole experiment session for each participant lasted approximately 3 hours.

Table 5.4: Experiment phases.

Phase	**HEH group**	**EHE group**	**Duration (number of autorotative landings)**	**Motion**
Familiarization	Hard helicopter dynamics	Easy helicopter dynamics	3	Off
Training	Hard helicopter dynamics	Easy helicopter dynamics	15	On
Transfer	Easy helicopter dynamics	Hard helicopter dynamics	15	On
Back-Transfer	Hard helicopter dynamics	Easy helicopter dynamics	14*	On

* The log file of the 15^{th} run of the back-transfer phase of some participants was corrupted. Due to the loss of these data, the 14^{th} run was considered as the last run of the back-transfer phase.

5.2.4. DEPENDENT MEASURES

To investigate the effect of the helicopter dynamics (independent variable) on autorotation performance and training, the dependent measures related to the MTE definition presented in Tab. 5.1 were considered. Since those measures assess only the performance at touchdown, other metrics were also taken into account to compare the control strategies adopted by the participants of the two experiment groups, namely:

1. Number of landings at least within adequate performance (Tab. 5.1).
2. Number of landings within desired performance (Tab. 5.1).

3. Reaction time: time required by the pilot to lower the collective after engine failure (Fig. 5.1).

4. Recovery time: time required by the pilot to enter a steady descent in autorotation (Fig. 5.1).

5. Flare initiation altitude: altitude at which the pilot initiates the flare by pulling back the cyclic stick (Fig. 5.1).

6. Rotation altitude: altitude at which the pilot levels the skids with the ground by pushing forward the cyclic stick (Fig. 5.1).

7. Cushion altitude: altitude at which the pilot raise the collective to cushion the touchdown (Fig. 5.1).

Metrics 3 to 7 were extracted from the experiment time histories using a newly developed methodology called Control Event Detection (CED), which is presented in Section 5.2.9.

5.2.5. HYPOTHESES

For this experiment only one main hypothesis was tested. Based on previous experimental evidence [Nusseck et al., 2008] and on current in-flight training procedures, it is envisioned that pilots who start the training with the most challenging configuration (hard dynamics), are more likely to develop robust and flexible autorotation skills that can be easily adapted to different helicopter configurations and dynamics. Therefore, it is expected that flying skills are positively transferred from the hard to the easy dynamics, but not conversely. When positive transfer happens, we expect to see lower rates of descent after transition to a different dynamics, as a lower descent rate is a key indicator for a controlled and smooth touchdown [Coyle, 2013]. Among all the dependent measures, the rate of descent is thus expected to cover a key role to corroborate our hypothesis.

5.2.6. PARTICIPANTS

A total of fourteen experienced helicopter pilots with a different background (license type), with a mix of civil and military experience and with a different in-flight and simulator experience took part in the experiment; all of them were male. The participants had an average age of 41.71 years (σ = ±9.50 years) and an average helicopter experience of 2,669 flight hours (σ = ±2,336 flight hours), ranging from a minimum of 120 to a maximum of 6,100 flight hours. Participants were divided in two groups in such a way that they had, on average, a comparable number of flight hours and a similar distribution, as shown in Tab. 5.5. Beside the number of flight hours, also pilots background was considered during the separation of the pilots in the two groups.

Participants signed an informed consent prior to the experiment. The experiment has been approved by the Human Research Ethics Committee of Delft University of Technology under the approval letter number 940.

Table 5.5: Participants.

Participant ID	HEH group		EHE group	
	Age	Flight Hours	Age	Flight Hours
1	40	3000	44	5000
2	43	6100	36	750
3	32	120	33	400
4	40	1500	57	194
5	28	1900	46	3800
6	35	2000	61	5000
7	38	7000	51	600
avg	36.6	3089	46.9	2249
std	5.2	2527	10.4	2242

5.2.7. APPARATUS

The experiment was conducted in the SIMONA Research Simulator (SRS) (Fig. 5.6), which is a moving-base simulator at the Faculty of Aerospace Engineering of TU Delft [Stroosma et al., 2003]. The SRS is equipped with a 6 degrees-of-freedom hydraulic motion system, which was used in the experiment to provide motion cues.

In terms of visual equipment, the SRS is fitted with a $180^\circ \times 40^\circ$ 3-projector Digital Light Processing (DLP®) collimated display. A representative out-of-the-window scenery was presented on this display (Fig. 5.7a). Furthermore, an instrument panel (Fig. 5.7b), consisting of a tachometer, airspeed indicator, artificial horizon, altimeter, yaw string, compass and vertical speed indicator, and a trim display (Fig. 5.8) were projected on two monitors inside the cockpit. Pilots use the trim display only before the start of each run in order to find the trim position of all the flight controls. This enables them to keep the initial equilibrium condition (straight level flight at 60 kn) and avoid a transient response to reestablish it.

The right seat of the cockpit was equipped with a realistic helicopter control inceptor with programmable control loading system, whose parameters were set as reported in Tab. 5.6 after consultation with test pilots [Miletovic et al., 2018]. Since the helicopter model used in the experiment only consists of the longitudinal dynamics, solely the longitudinal cyclic stick and the collective lever were to be controlled by the participants. Therefore, the lateral cyclic stick and the rudder pedals were not used. Lateral cyclic settings are also presented in Tab. 5.6 because the cyclic stick was not constrained to move only longitudinally. Pilots could also move the cyclic stick laterally, but this would not have produced any effect on the flight dynamics model response.

Rotor sound was played during the simulation to increase immersion. The sound was modulated based on the value of the rotor RPM[1], so that the participant could use sound cues as a source of information to control the rotor RPM, rather than by looking at the instrument panel. Moreover, a low-RPM acoustic warning was activated every time the rotorspeed dropped below 85%. The low-RPM warning was used as a backup cue for the rotor sound, so that the failure could be recognized without necessarily looking at the instruments. Engine sound was not included.

[1] A rotor sound recording is played in loop. Its pitch is controlled by the main rotor speed output of the model, whereas its volume is kept constant.

Figure 5.6: The SIMONA Research Simulator at Delft University of Technology.

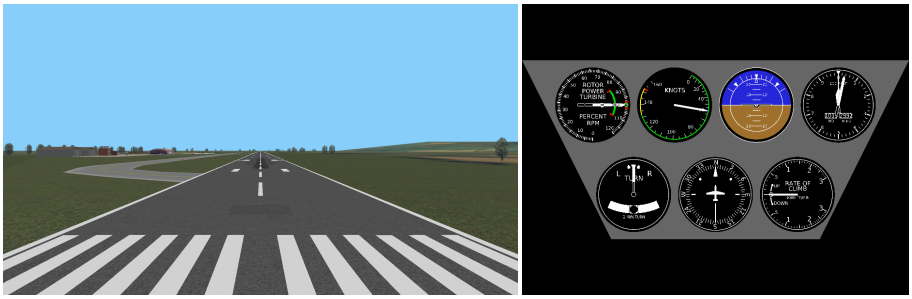

(a) Out-of-the-window scenery.

(b) Instrument panel.

Figure 5.7: Out-of-the-window scenery and instrument panel used for the current experiment.

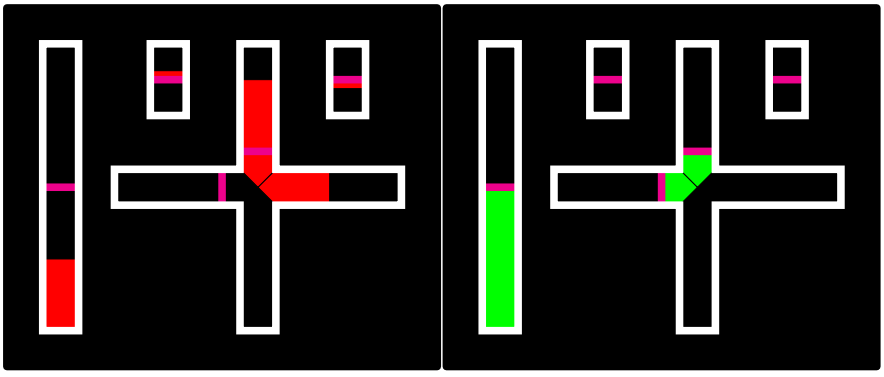

(a) Out of trim.

(b) In trim.

Figure 5.8: Trim display.

Table 5.6: Control loading settings.

Parameter	Longitudinal Cyclic	Lateral Cyclic	Collective
Periodic			
Forward friction level (N)	2.0	2.0	6.0
Positive forward stop (deg)	15.0	15.0	16.0
Negative forward stop (deg)	−15.0	−15.0	−16.0
Non periodic			
Linkage stiffness (N/deg)	50.0	50.0	50.0
Linkage damping (N s/deg)	0.01	0.01	0.01
Positive aft travel limit (deg)	14.8	14.8	15.8
Negative aft travel limit (deg)	−14.8	−14.8	−15.8
Aft friction (N)	2.0	2.0	6.0
Aft inverse damping (deg/N/s)	10.0	10.0	10.0
Second feel spring slope (N/deg)	3.0	3.0	0.0
Breakout level (N)	0.0	0.0	0.0

5.2.8. MOTION FILTER TUNING

The Classical Washout Algorithm (CWA) is used to map the vehicle motion on the simulator workspace [Reid et al., 1985]. In the experiment, only three degrees of freedom (longitudinal dynamics) are active. Therefore, the CWA reduces to a set of three high-pass filters in the pitch, surge and heave axes, respectively. These filters were selected to be of second order for the pitch and surge axes, and of third order for the heave axis. Although surge and heave axes are both translational degrees of freedom, a different order of the filter was selected for these two axes. Indeed, a second order high-pass filter along the surge axis allows to achieve sufficient washout through the use of tilt coordination. This was first observed by Reid et al. [1986] and reiterated by Grant et al. [1997]. Therefore, the combination of the tilt coordination and the body to inertial transformation effectively adds one order of washout. Each second order filter has three adjustable parameters, namely, the scaling gain K, the damping ratio ζ, and the natural break-frequency ω_n. The third order filter features an additional parameter, which is the third order break-frequency ω_b.

The scaling gain K and the damping ratio ζ were fixed for all simulator degrees of freedom at a value of 0.5 and 0.7071, respectively. The third order break-frequency ω_b of the heave axis filter was fixed at a value of 0.2 rad/s. These values were chosen in such a way that the respective degree of freedom does not require a large amount of the motion space, but provides at the same time cues of sufficient fidelity to the pilot to perform the training task. Indeed, a homogeneous scaling gain of 0.5 is the maximum value that can be attained for this maneuver. A two-pole filter with a damping ratio of 0.7071 is a second-order Butterworth filter, which assures a maximally flat magnitude response (sharpest roll-off possible without inducing peaking at the pole frequency) and, at the same time, a relatively smooth step response in the time domain (limited overshoot). Furthermore, the natural break-frequencies of the pitch and surge axes were constrained to be equal. These assumptions reduce the number of tuning parameters to two: the natural break-frequencies of the pitch and heave axes.

The optimal motion settings for the natural frequencies were determined using a two-dimensional grid search, based on the analysis proposed by Gouverneur et al. [2003].

The final motion filter settings for the 3 degrees-of-freedom are presented in Tab. 5.7 and are based on ten data sets from a pilot-in-the-loop pre-experiment. These data sets are representative of very aggressive pilot control behavior and were used to perform a conservative motion tuning, so that the simulator would stay within its physical limits for most of the pilots..

Table 5.7: Motion cueing settings.

DOF	K (-)	ω_n (rad/s)	ζ (-)	ω_b (rad/s)	Order (-)
Heave	0.5	3.5	0.7071	0.2	3
Surge	0.5	1.5	0.7071	0.0	2
Pitch	0.5	1.5	0.7071	0.0	2

Fig. 5.9 shows the critical combinations of heave and surge frequencies for each of the ten data-sets collected during the pre-experiment, indicating the limit bounds below which either a motion system actuator length limit (±0.575 m), speed limit (±1 m/s) or both were exceeded. The selected setting is located above all the limit bounds.

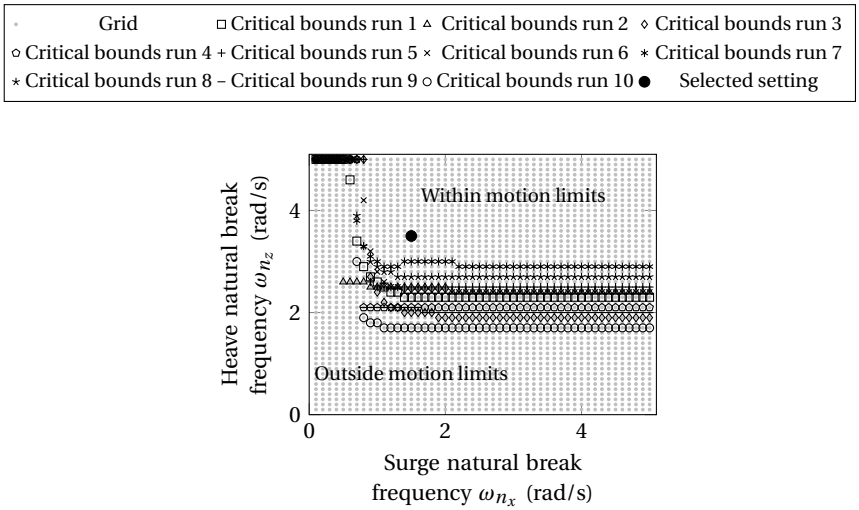

Figure 5.9: Two-dimensional grid search, based on the analysis proposed by Gouverneur et al. [2003] of ten different runs. The black dot indicates the motion filter setting used in the experiment.

5.2.9. DATA PROCESSING AND ANALYSIS

CONTROL EVENT DETECTION METHODOLOGY

The transition between two phases of a maneuver is characterized by a change in the pilot's control strategy. In order to determine when this change actually happens, a pilot's control inputs need to be filtered to remove the high frequency deflections related to the small inputs that are applied by the pilot to correct for small perturbations and deviations from the desired flight condition. According to the authors' knowledge, the

Moving Average Filter (MAF) is the only available technique to find the exact transition time between two consecutive phases of a maneuver. This technique has been used to determine the flare initiation time during landings with fixed-wing aircraft [Arents et al., 2011] and is grounded on the fact that the aircraft phugoid eigenmotion is excited when the pilot initiates the flare by gradually pulling back the control column to increase the elevator deflection. Since this technique is tailored for fixed-wing aircraft, it often fails when applied to rotorcraft. Therefore, a more general method, called Control Event Detection (CED) Methodology, has been developed and proposed here for the first time. This method is applied in this chapter to identify different phases of the autorotation maneuver (Fig. 5.1), but is envisioned to be applicable to other maneuvers and/or to different vehicles/system dynamics as well. For our current analysis, the outcomes of the CED methodology were verified using visual inspection of our data: information deriving from time histories of both control inputs and helicopter states was combined to assess the correctness of the points identified by the CED methodology (e.g., for the flare initiation altitude we focus our attention on the last 150/200 ft altitude of the time history and we look at the longitudinal cyclic stick input, the rotor angular speed, the rate of descent, and the forward speed).

This method only requires that the input is positive. This can be easily achieved by defining the current value of the input as a percentage of the available stroke. The procedure is composed of the following steps:

1. Computation of the time derivative of the control input (Fig. 5.10b).
2. Identification of the sign of the time derivative of the control input (Fig. 5.10c).
3. Intervals in which the sign of the time derivative of the control input is zero and that are bounded both from the left and the right by positive (negative) intervals, are turned into positive (negative) intervals (Fig. 5.10d). This step is required only for noisy control inputs.
4. Multiplication of the control input by the sign of its time derivative (Fig. 5.10e). In this way, the control input is divided into intervals, where it either assumes strictly monotone values or is zero.
5. For each strictly monotone interval, the Root Mean Squared Error (RMSE) of the control input with respect to the initial value of that interval is calculated. In this way, it is possible to quantify the control activity during each interval, by considering the deviation of the control with respect to the initial position.
6. Multiplication of the RMSE of each interval by the sign of the time derivative of the control input (Fig. 5.10e).

The different steps of the method are shown graphically in Fig. 5.10, where the time history after the failure (t_f is the time when the failure happens) of the cyclic stick is analyzed for one experiment run.

Visual inspection can be used to identify the instants of interest, that are characterized by higher RMSE with respect to neighboring regions. In case a large number of time series has to be processed, visual inspection can be used for a sample of them to train a

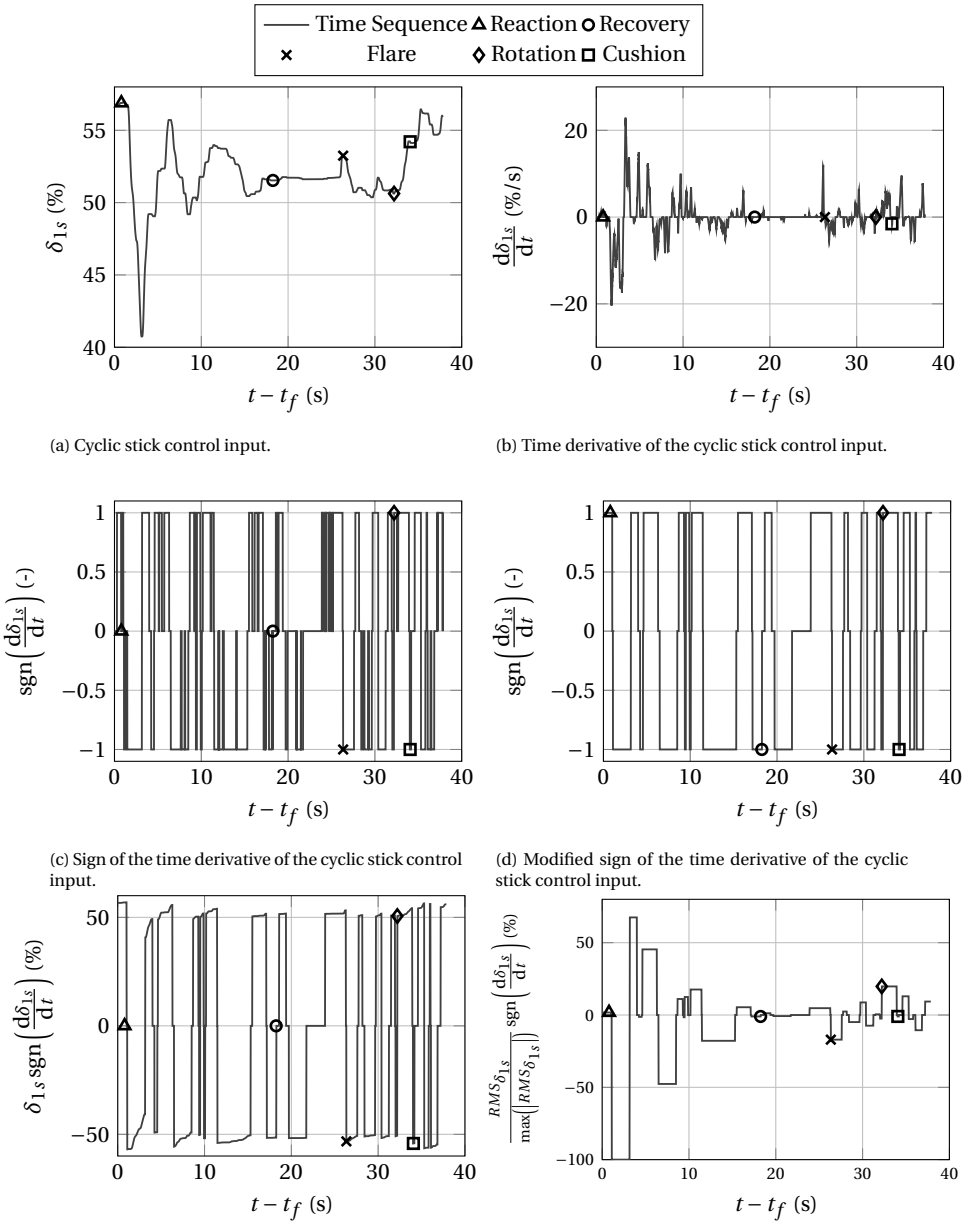

(a) Cyclic stick control input.

(b) Time derivative of the cyclic stick control input.

(c) Sign of the time derivative of the cyclic stick control input.

(d) Modified sign of the time derivative of the cyclic stick control input.

(e) Product between the cyclic stick control input and the sign of its time derivative.

(f) Product between the sign of the time derivative of the cyclic stick input and the normalized RMS.

Figure 5.10: Graphical summary of the Control Event Detection Methodology applied to the cyclic stick input (t_f is the time when the failure happens).

sequence-to-sequence deep neural network. The trained network can be subsequently applied to recognize the instants of interest for the remainder time series. As an alternative to deep learning, the instants of interest can be identified by isolating specific regions and defining threshold for the RMSE.

The CED method was applied to all the experiment runs in order to extract information about pilots' control strategy and activity from the time histories. For example, the reaction time and the cushion altitude are identified by applying the CED Methodology to the collective lever input. The flare initiation altitude and the rotation altitude are identified by analyzing with the same method the cyclic stick input. The identification of the recovery time is based on the analysis of both the collective lever and cyclic stick inputs.

STATISTICAL ANALYSIS

Prior to performing the statistical tests, all the dependent measures defined in Section 5.2.4, except the number of landings at least within adequate performance and that within desired performance, were averaged over the last 10 runs of each phase for every participant. Mixed repeated measures ANOVA (Analysis of Variance) tests [Field, 2013] were conducted on all the dependent variables, considering the experiment phases as main within-subjects factor, characterized by three levels: training, transfer and back-transfer, and the groups as main between-subjects factor, characterized by two levels: HEH and EHE. Before conducting the statistical tests, the fulfillment of the ANOVA assumptions, i.e., normality and sphericity, was verified. Regarding the normality assumption, some skewness in the data was accepted, provided that it was nothing too alarming. Indeed, the ANOVA is a robust technique and should still provide reliable results also in presence of minor violations. For variables in which sphericity was violated according to Mauchly's test [Field, 2013], we adopted either the Greenhouse-Geisser correction, when the Greenhouse-Geisser estimate of sphericity ε is below 0.75 ($\varepsilon < 0.75$), or the Huynd-Feldt correction, when the Greenhouse-Geisser estimate of sphericity ε is above 0.75 ($\varepsilon > 0.75$) [Field, 2013].

In the event of a statistically significant interaction effect between the two main factors (within- and between-subjects factors), main effects may provide misleading information [Field, 2013]. Therefore, the so-called *simple* main effects are investigated. Dependent-samples t-tests between the phases of the experiment for each group are used to investigate the simple within-subjects effect and independent-samples t-tests between the groups in each phase are adopted to examine the simple between-subjects effect. If the interaction effect between the two main factors is not statistically significant, the two main effects are analyzed and if either of them is statistically significant, the respective simple main effect is investigated accordingly.

5.3. RESULTS

Results are presented in the following figures as box-whiskers plots. On each box, the horizontal line represents the median over different data points. The box is delimited by the first and third quartiles, therefore it includes data points between the 25^{th} and the 75^{th} percentile. The difference between first and third quartiles defines the interquartile range. The two edges of the whiskers indicate the lowest and the highest data point

within 1.5 of the interquartile range. All the data points not included in the whiskers are considered as outliers and represented by cross markers.

Statistically significant results of the t-tests are shown as follows. A curly brace with an asterisk on top is used to indicate a statistically significant difference between the two groups in a specific phase of the experiment. A curved arrow with an asterisk on the left indicates a statistically significant transfer of training for a specific group.

5.3.1. PERFORMANCE SCORES

Tab. 5.8 summarizes the results of a repeated measures ANOVA test for the different dependent measures considered in this study.

Table 5.8: Repeated Measures ANOVA results for all the dependent variables.

Dependent Variable	Between-subjects Factor (Group)			Within-subjects					
				Factor (Phase)			Interaction (Phase*Group)		
	df	F	Sig.	df	F	Sig.	df	F	Sig.
N_{ad}	1	1.155	0.304	2	3.043	0.066	2	0.406	0.671
N_{des}	1	0.043	0.838	2	3.796	0.037*	2	2.502	0.103
$\overline{\theta}_{td}$	1	0.394	0.542	2	1.270	0.299	2	0.098	0.907
$\overline{V}_{x_{td}}$	1	0.001	0.971	2	2.040	0.152	2	1.103	0.348
$\overline{V}_{z_{td}}$	1	0.397	0.541	2	4.789	0.018*	2	1.472	0.249
$\overline{q}_{td}$	1	6.237	0.028*	2	0.461	0.636	2	0.863	0.434
$\overline{\Delta t}_{reac}$	1	3.198	0.099	2	0.249	0.782	2	1.926	0.168
$\overline{\Delta t}_{rec}$	1	9.753	0.009*	2	1.818	0.184	2	0.089	0.915
$\overline{h}_{fl}$	1	0.165	0.692	2	0.502	0.611	2	0.501	0.612
$\overline{h}_{rot}$	1	1.466	0.249	2	0.188	0.830	2	0.052	0.949
$\overline{h}_{cush}$	1	5.158	0.042*	2	0.673	0.520	2	1.123	0.342
$\overline{\Omega}_{td}$	1	2.841	0.118	2	1.702	0.204	2	1.244	0.306

* Statistically significant ($p \leq 0.05$) difference between compared samples.

Fig. 5.11 shows the number of landings at least within adequate performance and those within desired performance for each group in each phase. Fig. 5.11a illustrates that participants of both groups were able to attain at least adequate performance, i.e., a survivable landing, in most of the experiment runs. However, the EHE group shows higher within group variability than the HEH group. This is particularly true for the training and the back-transfer phases, where the EHE group controls the easy dynamics.

Participants of both groups struggled to attain desired performance (i.e., a successful landing), as shown in Fig. 5.11b. Nonetheless, the success rate for the participants of the HEH group increases during the transfer phase and decreases again during the back-transfer phase to values comparable to those of the training phase. Therefore, participants of the HEH group are able to more easily attain desirable performance with the easy configuration.

In contrast, there is no substantial difference in the number of successful landings between the training and the transfer phase for the participants of the EHE group, whereas there is an increase in the success rate during the back-transfer phase. Fig. 5.11b suggests that for the HEH group there is positive transfer of training from the hard configu-

ration to the easy configuration and no transfer of training from the easy configuration to the hard configuration. Although not statistically significant, a similar trend is observed also for the EHE group.

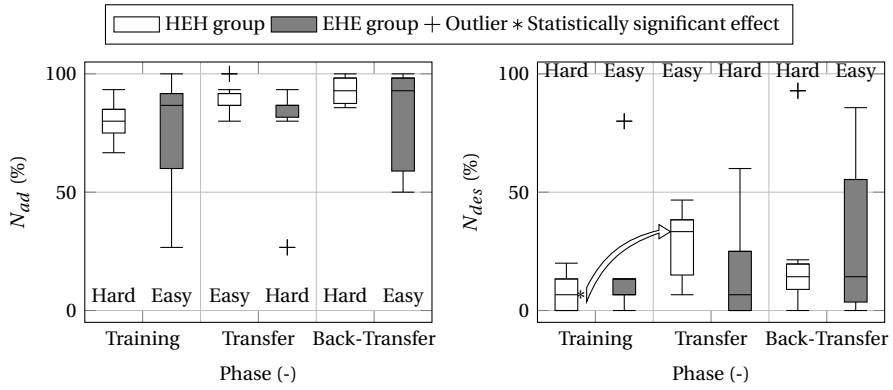

(a) Landings at least within adequate performance.

(b) Landings within desired performance.

Figure 5.11: Distribution of the number of landings at least within adequate performance and those within desired performance for each group in each phase.

Tab. 5.8 highlights a statistically significant difference in terms of number of successful landings between the experiment phases (within-subjects effect: $F(2,24) = 3.796$, $p = 0.037$). The presence of an overall significant effect in the complete data set of the number of successful landings was further investigated by performing t-tests on individual sets of samples. Tab. 5.9 illustrates the results of these tests. A significant difference in terms of number of successful landings only occurs between the training and the transfer phase for the HEH group (from the hard to the easy helicopter dynamics: $t(6) = -3.813$, $p = 0.009$). This partially confirms what has already been observed from Fig. 5.11b.

Table 5.9: Dependent-samples t-test between the experiment phases. Bonferroni correction [Field, 2013] was not applied.

Metric	Group	From	To	t-test			From	To	t-test		
				t	df	Sig. (2-tailed)			t	df	Sig. (2-tailed)
N_{succ}	HEH	Training	Transfer	−3.813	6	0.009*	Transfer	Back-Transfer			0.236[a]
	EHE					0.786[a]					0.080[a]
$\overline{V}_{z_{td}}$	HEH	Training	Transfer	2.429	6	0.050*	Transfer	Back-	0.309	6	0.767
	EHE					0.000[a]**		Transfer	3.562	6	0.012*

* Statistically significant ($p \leq 0.05$) difference between compared samples.
** Statistically highly significant ($p \leq 0.001$) difference between compared samples.
[a] At least one sample not normally distributed. Related-samples Wilcoxon signed-rank test was applied instead of paired-samples t-test.

The effectiveness of the training was further investigated by averaging the performance metrics defined in Section 5.2.1 (horizontal speed, rate of descent, pitch angle, and pitch rate at touchdown) over the over the last 10 runs completed by each participant in each phase. These metrics are shown in Fig. 5.12 as box-whiskers plots to compare

the performance of the two groups in the Training, Transfer and Back-Transfer phases.

Fig. 5.12a and 5.12c show the distribution of the average horizontal speed $\overline{V}_{x_{td}}$ and of the average pitch angle $\overline{\theta}_{td}$ at touchdown, respectively. Although the EHE group has a larger within group variability, the performances of the two groups for these two metrics are comparable in each experiment phase and are flat throughout the experiment. This is confirmed by the repeated measures ANOVA tests performed on the average horizontal speed and on the average pitch angle at touchdown, that do not show any statistically significant effects (Tab. 5.8).

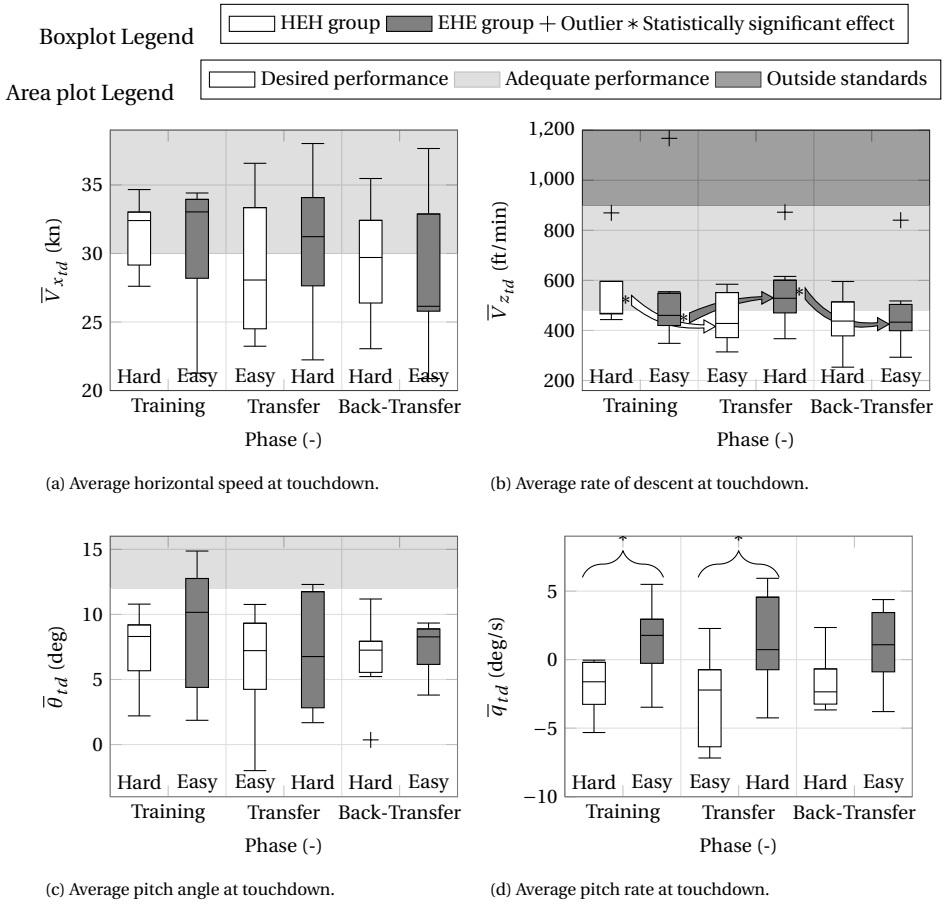

(a) Average horizontal speed at touchdown.

(b) Average rate of descent at touchdown.

(c) Average pitch angle at touchdown.

(d) Average pitch rate at touchdown.

Figure 5.12: Distribution of the average performance at touchdown for each group in each phase.

A completely different trend can be observed for the average rate of descent at touchdown $\overline{V}_{z_{td}}$, as shown in Fig. 5.12b. The HEH group exhibits an improvement from the hard (training phase) to the easy dynamics (transfer phase), whereas performance is unaffected going from the easy (transfer phase) to the hard dynamics (back-transfer phase). A similar situation is found for the EHE group, whose performance degrades from the easy (training phase) to the hard dynamics (transfer phase) and improves from the hard

(transfer phase) to the easy dynamics (back-transfer phase). These behaviors denote a correlation between the average rate of descent at touchdown and the number of successful landings, which is confirmed by the repeated measures ANOVA test performed on the average rate of descent at touchdown, shown in Tab. 5.8 (statistically significant within-subjects effect: $F(2,24) = 4.789$, $p = 0.018$).

The presence of an overall significant effect in the complete data set of the average rate of descent was further investigated by performing t-tests on individual sets of samples. Tab. 5.9 summarizes the results of these testshighlighting the presence of a significant difference for the average rate of descent $\overline{V}_{z_{td}}$ between the training and the transfer phase for the HEH group (from the hard to the easy helicopter dynamics: $Z = -2.028$, $p = 0.028$) and from the transfer to the back-transfer phase for the EHE group (from the hard to the easy helicopter dynamics: $Z = -2.197$, $p = 0.043$).

Table 5.10: Independent-samples t-test between the two groups.

Metric	**Phase**	**t-test**		
		t	df	Sig. (2-tailed)
$\overline{q}_{td}$	Training	−2.465	12	0.030*
	Transfer	−2.245	12	0.045*
	Back-Transfer	−1.806	12	0.096
$\overline{\Delta t}_{rec}$	Training	−2.771	12	0.017*
	Transfer	−1.784	12	0.100
	Back-Transfer	−3.108	12	0.009*
$\overline{h}_{cush}$	Training	−2.075	7.813	0.072
	Transfer	−2.311	12	0.039*
	Back-Transfer	−1.777	8.118	0.113

* Statistically significant ($p \leq 0.05$) difference between compared samples.
[a] At least one sample not normally distributed. Independent-samples Mann-Whitney U test was applied instead of independent-samples t-test.

The surprising result concerns the average pitch rate $\overline{q}_{td}$, which is considerably different between the two groups during the training and the transfer phases, as shown in Fig. 5.12d. This is confirmed by a statistically significant between-subjects effect in the repeated measures ANOVA test of Tab. 5.8 ($F(1,12) = 6.237$, $p = 0.028$). The presence of an overall significant effect in the complete data set of the average pitch rate was further investigated by performing t-tests on individual sets of samples. Tab. 5.10 illustrates the results of these tests and highlights a statistically significant difference between the two groups during the training ($t(12) = -2.465$, $p = 0.030$) and the transfer ($t(12) = -2.245$, $p = 0.045$) phases.

It appears that the two groups adopt a completely different control strategy during the first two phases of the experiment: whereas the HEH group tends to touch down with a negative pitch rate (nose-down), the EHE group shows a positive one (nose-up). The former behavior is usually adopted in reality in order to level the skids with the ground to avoid tail strike and have a better visibility before cushioning the touchdown [Coyle, 2013]. The EHE group aligned with the HEH group during the back-transfer phase. In order to gain more insight into this unexpected result, a detailed analysis of the control techniques adopted by the pilots of the two groups is conducted next.

5.3.2. CONTROL STRATEGY METRICS

As for the performance metrics, the control strategy metrics (reaction time, recovery time, flare intiation altitude, rotation altitude, cushion altitude, and rotor RPM at touchdown) were also averaged over the last 10 runs completed by each participant in each phase. These averaged metrics are shown in Fig. 5.13 as boxwhiskers plots to compare the control strategy of the two groups in the Training, Transfer and Back-Transfer phases. From Fig. 5.13, it appears that the spread of results for the EHE is generally larger than the HEH group, regardless of training, transfer or back transfer phase. The source of the larger spread for the EHE group compared to the HEH group is probably related to the fact that the EHE group indeed seem to use more variable strategies for attaining desired performance (e.g., anticipate the flare, cushion the touchdown before leveling the skids).

Both the average reaction time $\overline{\Delta t}_{reac}$ and the average recovery time $\overline{\Delta t}_{rec}$ are considerably different between the two groups during the training and the back-transfer phases, as shown in Fig. 5.13a and 5.13b, respectively. However, only for the recovery time this is confirmed by a statistically significant between-subjects effect in the repeated measures ANOVA test of Tab. 5.8 ($\overline{\Delta t}_{rec}$: $F(1,12) = 9.753$, $p = 0.009$).

Almost every participant of both groups is able to keep the average reaction time below 1 s, which is usually the value considered as pilot time delay following power failure during the certification of a civil helicopter [Prouty, 2002]. Although the failure was random and unannounced, participants were expecting it to happen, keeping a high level of alertness. This might be the reason for such a good result in terms of reaction time. However, the participants of the HEH group react faster than those of the EHE group during the training and the back-transfer phases. This is explained by the fact that, during these phases, the HEH group was dealing with the hard dynamics, which inherently require a faster reaction than the easy dynamics, that give more margin for error or grants more spare capacity to the pilot. As expected, a faster reaction also leads to a faster recovery, as shown in Fig. 5.13b.

The presence of an overall significant effect in the complete data set of the average recovery time was further investigated by performing t-tests on individual sets of samples. Tab. 5.10 illustrates the results of these tests and highlights a statistically significant difference between the two groups during the training ($t(12) = -2.771$, $p = 0.017$ for the average recovery time) and the back-transfer ($t(12) = -3.108$, $p = 0.009$ for the average recovery time) phases.

Fig. 5.13c shows the distribution of the average flare initiation altitude $\overline{h}_{fl}$, which is comparable for the two groups in each experiment phase and is approximately constant at around 120 ft throughout the experiment. This is confirmed by the repeated measures ANOVA test performed on the average flare initiation altitude, which does not show any statistically significant effects (Tab. 5.8).

Some participants of the EHE group start to level the helicopter with the ground much earlier than the participants of the HEH group during the training and the transfer phases (Fig. 5.13d). This causes the rotor RPM to drop below 100% before pulling up the collective lever and leads to lower values of the rotor speed at touchdown (Fig. 5.13f). Lower RPM may result in a less effective cushion [Coyle, 2013]. However, these differences between the groups in the average rotation altitude $\overline{h}_{rot}$ and in the average rotor speed at touchdown $\overline{\Omega}_{td}$ are not significant and do not change significantly throughout

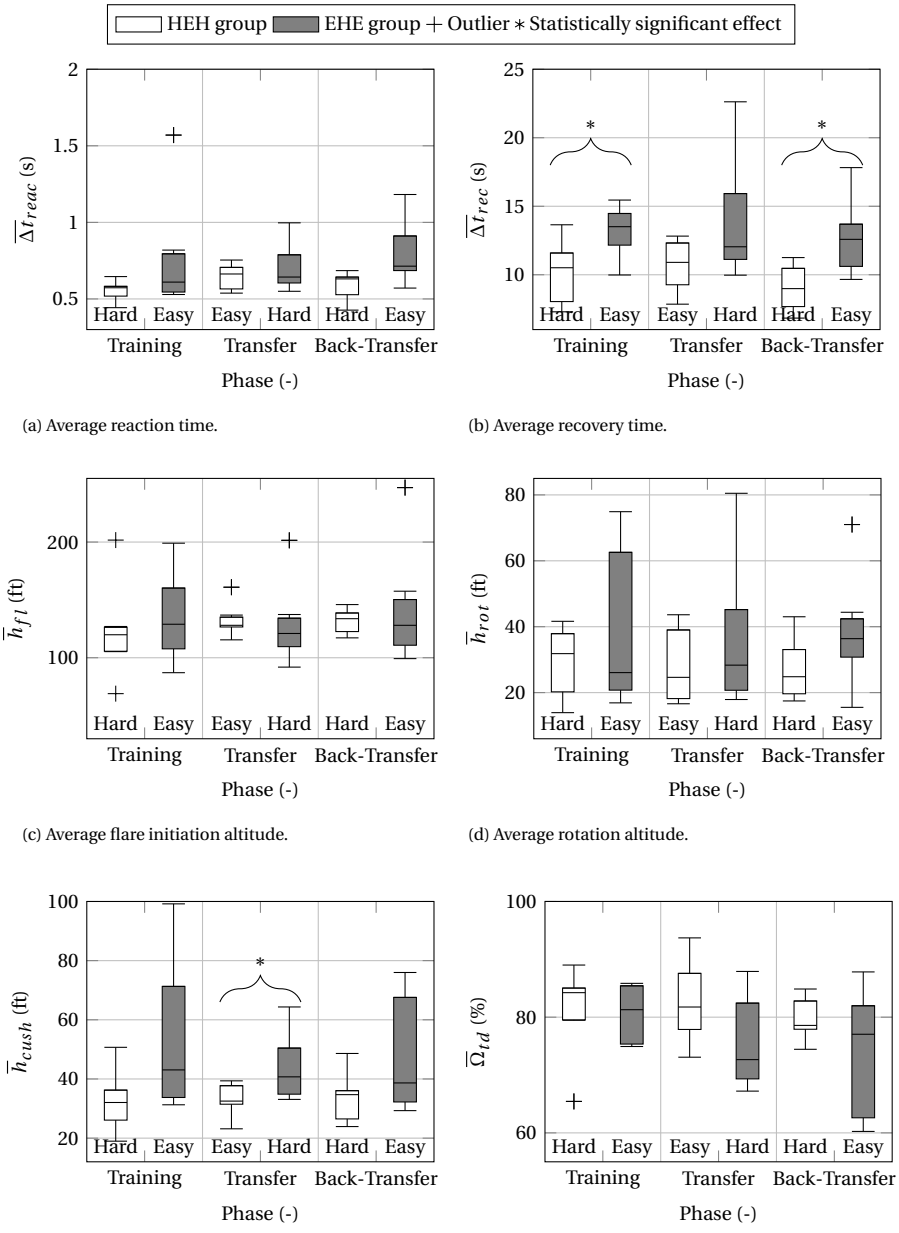

(a) Average reaction time.

(b) Average recovery time.

(c) Average flare initiation altitude.

(d) Average rotation altitude.

(e) Average cushion altitude.

(f) Average rotor RPM at touchdown.

Figure 5.13: Distribution of the average control strategy adopted by each group in each phase.

the experiment, as summarized in Tab. 5.8.

For the average cushion altitude $\overline{h}_{cush}$ (Fig. 5.13e), a statistically significant between-subjects effect is found ($F(1,12) = 5.158$, $p = 0.042$), as shown in Tab. 5.8. Indeed, in

every experiment phase, the participants of the EHE group tend to start the cushion approximately 7 ft earlier than those of the HEH group. As can be verified from Tab. 5.10, only during the training phase a statistically significant difference between the two groups is found ($t(12) = -2.311$, $p = 0.039$).

Overall, the differences in the control strategy of the two groups, as shown in Fig. 5.13, can be used to motivate the difference in the average pitch rate at touchdown during the training and the transfer phases (Fig. 5.12d). Indeed, many participants of the EHE group touch down with a positive pitch rate in most of the runs of those two phases. This is mainly due to the fact that they pull up the collective to cushion the touchdown too early, resulting in a bounce, i.e., the helicopter gains altitude before touchdown. As a consequence, a considerable amount of rotor energy is dissipated and the loss of collective effectiveness is counteracted by starting a second flare.

5.4. DISCUSSION

The quasi-Transfer-of-Training experiment presented in this chapter was designed to investigate how helicopter dynamics affect pilots' acquisition of skills during autorotation training in a flight simulator. Two sets of helicopter dynamics, characterized by a different autorotative index (hard, lower index, and easy, higher index) [Fradenburgh, 1984], and two groups of participants, both chosen among experienced helicopter pilots, were considered. In order to assess whether familiarity with one set of helicopter dynamics affects the learning of new helicopter dynamics, each group started the training with either the hard or the easy dynamics, was then transferred to the other, and, finally, transferred back to the initial dynamics.

Although designed for a different training task, the outcome of this experiment confirms previous experimental evidence which showed positive transfer of skills from agile (hard case, where high control compensation is required to the pilot) to inert (easy case, where low intervention is required to the pilot) dynamics, but not the opposite [Nusseck et al., 2008]. Indeed, in our experiment, both groups of participants exhibit a decrease in the rate of descent at touchdown from the hard to the easy dynamics, but not after a transition from the easy to the hard dynamics. This result corroborates our hypothesis, because a lower rate of descent is an indicator of more controlled and smoother touchdowns. The previous statement is also supported by an increase in the number of landings within desired performance during the transfer from the hard to the easy helicopter dynamics of around 27% for the HEH group (significant effect) and 8% for the EHE group, which however was not statistically significant.

This is in agreement with current flight education, which usually starts with unaugmented helicopters at the beginning. Once proficiency is reached, later training stages involve augmented helicopters [Coyle, 2008].

Pilots' comments yielded a number of interesting recommendations to improve the setup used in this experiment and, more in general, current simulator training, and help to interpret some of the obtained results. For example, participants of both groups were able to achieve adequate performance at touchdown in most of the landings with both sets of dynamics. However, they struggled to attain desired performance for both the horizontal speed and the rate of descent at touchdown. This is most likely due to poor or lack of visual cues. Indeed, the SIMONA Research Simulator was conceived for fixed-

wing simulation and is not equipped with chin bubbles. As a consequence, pilots completely lose sight of the ground during the flare. Therefore, pilots either opt for a less effective flare, ending-up with a higher horizontal speed, or risk either to strike the tail on the ground or not to coordinate the cushion timely, resulting in a higher rate of descent at touchdown.

Besides chin bubbles, another issue related to lack of visual cues is depth perception, which is the human visual ability to perceive the world in three dimensions and sense the distance of an object. Depth perception arises from a variety of depth cues. Not all the depth cues are equally important to every flying task. The depth cues of linear perspective, texture and parallax gradients, apparent/familiar size and streaming are highly useful during landing tasks. In particular, texture gradients and apparent/familiar size are the two elements that can be improved in the current out-of-the-window scenery. Texture gradients cue is the ability to perceive fine details on nearby objects. Such details are not visible on faraway objects. For instance, many pilots commented that, in reality, they start the flare when they see "*the grass becoming grass*", that is when they realize that the grass is no longer a green expanse and they are able to discern the blades of grass.

Apparent/familiar size cue is the ability to determine the absolute depth of an object by combining the fact that the further the object is from the observer, the smaller it appears with previous knowledge of the object's size. Therefore, the use of a finer texture and adding more familiar objects to the scenery may improve depth perception and increase pilots acceptance of the simulation environment.

The hard helicopter dynamics foster the development of more robust and flexible flying skills, because pilots are required to react faster to perceptual changes. Indeed, participants of the HEH group adopted, from the start of the experiment, a control strategy similar to the one adopted in real helicopters, as opposed to the participants of the EHE group, who tend to underestimate the altitude during the first two phases of the experiment, thus preempting the cushion. This sometimes results in a bounce (the helicopter gains altitude before touchdown), causing the rotor speed to drop down and the consequent loss of collective effectiveness that is counteracted by starting a second flare. This is the reason why the participants of the EHE group touch down with a positive pitch rate during the training and the transfer phases. However, they align their control strategy with that of the participants of the HEH group during the back-transfer phase (from the hard to the easy dynamics).

Faster reactions to perceptual changes, i.e., any physical stimulus or a novel interpretation of the stimulus that can be used as an advantage to accomplish a certain task, can translate into a safety enhancement, because pilots trained in high resource demanding conditions are more likely to be able to handle emergencies like engine failures in the real world, where the actual situation may easily divert from the training scenario. Results are promising and represent a solid foundation to extend this study. A new experiment with a more complex flight dynamics model, which incorporates also the helicopter lateral-directional dynamics, will be conducted to obtain more evidence for the findings presented in this chapter, which are based on a flight dynamics model with longitudinal dynamics only.

Furthermore, given the success of the Control Event Detection (CED) methodology

(Sec. 5.2.9) in identifying the different phases of the autorotation maneuver, future work will be conducted to assess its application in other types of experiments and control tasks, such as shipboard helicopter operations.

5.5. CONCLUSIONS

A quasi-Transfer-of-Training experiment with fourteen experienced helicopter pilots was performed in TU Delft's SIMONA Research Simulator (SRS) to compare the effects of helicopter dynamics characterized by a high autototative flare index (hard dynamics) and low index (easy) on autorotation training in a flight simulator. Participants were divided in two groups and trained to perform a straight-in autorotation maneuver controlling a four degrees of freedom non-linear helicopter model with 3-DOF symmetrical dynamics plus rotorspeed. Each group tested the two sets of dynamics in a different training order: hard-easy-hard (HEH group) and easy-hard-easy (EHE group). Results show a positive transfer of skills from the hard helicopter dynamics to the easy dynamics for both groups, with the average rate of descent at touchdown that decreases from 558 ft/min to 447 ft/min ($\Delta\overline{V}_{z_{td}}$ = 111 ft/min) for the HEH group and from 559 ft/min to 480 ft/min ($\Delta\overline{V}_{z_{td}}$ = 79 ft/min) for the EHE group. This corroborates earlier findings that the acquisition of robust flying skills is fostered by initiating training in the most challenging setting.

In addition, participants of the EHE group adopted a sub-optimal control technique during the final part of the maneuver. This is suggested by the different sign of the pitch rate at touchdown for the two groups during the first two phases of the experiment: the HEH group tends to touch down with a negative pitch rate (nose-down), whereas the EHE group shows a positive one (nose-up). The former behavior is usually adopted in reality in order to level the skids with the ground to avoid tail strike and have a better visibility before cushioning the touchdown. Dealing with the difficult dynamics helped the participants of the EHE group to align their control strategy with that of the participants of the HEH group.

Although more experiments are needed to confirm our findings, results suggest that simulator training for autorotation can best start with training in the most resource demanding condition. Difficult dynamics require rapid responses to perceptual changes, forcing pilots to develop more robust and adaptable flying skills. This can enhance helicopter safety as pilots will be better prepared to face unexpected events that may occur during actual flight.

6

AUTOROTATION TRANSFER OF TRAINING: EFFECTS OF HELICOPTER DYNAMICS (6-DOF)

Although designed for a different training task, the outcome of the experiment presented in Chapter 5 confirms previous experimental evidence, which showed positive transfer of skills from high pilot control compensation dynamics to low control compensation dynamics, but not the opposite [Nusseck et al., 2008]. However, the use of a 3-degrees-of-freedom longitudinal helicopter model, although acceptable for a longitudinal maneuver such as the straight-in autorotation, does not provide some of the cues (e.g., initial yaw after failure) that are used by pilots to coordinate the inputs from the different flight controls in a timely manner. Therefore, there is the need to generalize these results with a higher-fidelity helicopter model.

This chapter corroborates the experimental findings presented in Chapter 5, using a 6-degrees-of-freedom helicopter model. The chapter is structured as follows. First, the design of a quasi-transfer-of-training experiment performed on the SIMONA Research Simulator (SRS) aimed at evaluating whether the helicopter dynamics affect the transfer of trained autorotation flying skills is presented in Section 6.2. The results from this experiment are documented and discussed in Sections 6.3 and 6.4, respectively. The chapter is concluded in Section 6.5.

The contents of this chapter have been published in: Scaramuzzino, P. F. et al. (to be submitted). Autorotation Transfer of Training: Effects of Helicopter Dynamics. *Journal of the American Helicopter Society*.

6.1. INTRODUCTION

This chapter investigates whether the acquisition of flying skills for autorotation, and their transfer, are affected by the helicopter dynamics. We hypothesized that dynamics that require more pilot control compensation may lead to the development of a more robust control behavior, one that can be easily adapted to a helicopter with different dynamics, yielding substantial benefits in terms of engine failure handling capabilities. The results of a quasi-Transfer-of-Training (qToT) experiment with ten experienced helicopter pilots, divided in two groups, performed in TU Delft's SIMONA Research Simulator (SRS) are presented to corroborate this hypothesis. The helicopter final states, i.e., attitudes and linear and rotational rates, have been used to compare the performance at touchdown. Additionally, the method developed in this thesis and presented in Section 5.2.9, referred to as Control Event Detection (CED), is used to perform an in-depth analysis of pilot control actions involved in a successful autorotative landing.

6.2. METHODS

6.2.1. TASK

In rotorcraft handling quality research, experimental tasks are usually defined according to the specifications of the mission-oriented design standard, ADS-33E [US Army AMCOM, 2000]. Although conceived for military rotorcraft, ADS-33E are widely used to assess handling qualities characteristics of commercial rotorcraft as well, as there is no counterpart in the civil domain. However, the use of ADS-33E Mission Task Elements (MTEs) is not always relevant, especially in the design of training tasks. Furthermore, ADS-33E does not have a specific Autorotation Maneuver MTE. Since there are no specific handling quality metrics for autorotation, pilot-in-the-loop autorotation maneuvers are usually evaluated based on subjective pilot feedback and comments and on objective measurements of landing survivability metrics [Sunberg et al., 2015].

For this experiment, a MTE was defined for the straight-in autorotation maneuver; the proposed test course is shown in Fig. 6.1. The simulation starts with the helicopter trimmed in straight level flight at 60 knots air speed, at an altitude of 1,000 ft. The symmetry plane of the helicopter is aligned with the center line of a runway, whose starting point is located 3,281 ft (1,000 m) ahead the helicopter initial position. The pilot has to keep constant speed and altitude until the power failure is triggered from the control room. As soon as the pilot recognizes the unannounced failure, he has to recover starting a steady descent in autorotation, maintaining 60 knots air speed and keeping the rotor RPM in the green arc of the tachometer. When close enough to the ground the pilot has to flare, to reduce both the rate of descent and the forward speed and finally level the skids with the ground, to avoid tail strike, and pull-up the collective to cushion the touchdown. The contact accelerations at touchdown were not modeled. Therefore, the simulation stopped automatically once the center of gravity of the helicopter reached two meters above the ground.

Performance standards for the straight-in autorotation maneuver are adapted from Sunberg et al. [2014, 2015] and are listed in Tab. 6.1. The values of the horizontal speed and of the rate of descent at touchdown refer to the AH-1G helicopter [Sunberg et al., 2015], which has a similar skid landing gear as the baseline helicopter (Bo-105) consid-

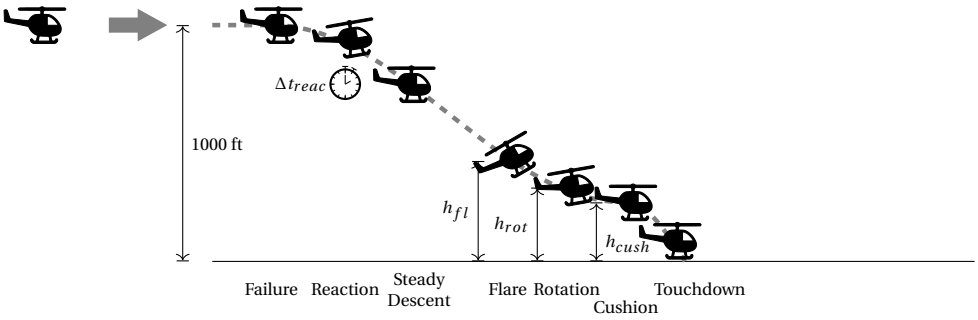

(a) Side view.

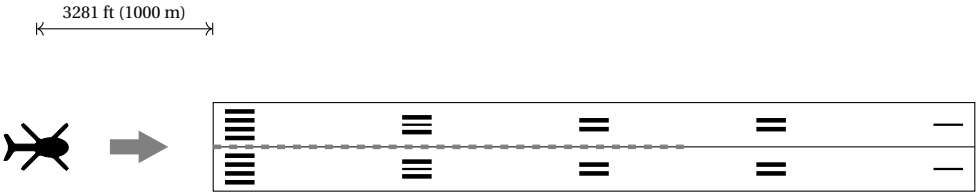

(b) Top view.

Figure 6.1: Suggested course for straight-in autorotation maneuver.

ered in this chapter. Therefore, these were not changed. Although characterized by a similar landing system, the AH-1G and the Bo-105 are different helicopters, with different performance and intended role. Indeed, the AH-1G is a two-blades rotor, single-engine attack helicopter, whereas the Bo-105 is a light, twin-engine, multi-purpose helicopter with a four-blades hingeless rotor. The maximum values of the pitch angle at touchdown, which are responsible of preventing tail strike, were slightly increased due to the different helicopter geometry. Indeed, due to its longer and lower tail boom, the AH-1G helicopter cannot afford to touch down with the same fuselage pitch as the Bo-105.

Desired performance translates into a successful landing, i.e., the helicopter's final state at ground contact is such that the aircraft and crew survivability are not threatened. Adequate performance translates into marginal landing conditions, that would likely result in damage to the aircraft (e.g., an 18 degrees pitch nose up will inevitably lead a tail strike), but be survivable to the occupants and the equipment. The values presented in Tab. 6.1 are defined according to landing survivability metrics that are based on specifications for military helicopters' structural design [Department of the Air Force and Navy Bureau of Aeronautics, 1954; Department of the Army, 1974] and on the accident analysis conducted by Crist et al. [1981].

The threshold values for desired and adequate performance must not only be adapted to the helicopter geometry and type of landing gear, but also according to the ground surface (e.g., paved, concrete, grass, etc.) on which the helicopter touches down. The values listed in Tab. 6.1 can be considered reasonable for landing on a paved or concrete surface. The landing gear on skid-equipped helicopters is designed to spread laterally under

load, dissipating the residual amount of kinetic energy deriving from a non sufficiently effective flare and cushion. This is of course possible only on relatively hard surfaces. Touchdowns to soft surfaces, such as grass, are extremely dangerous, as the skid tubes dig a small depression in the surface and are therefore prevented from moving sideways. This means that the landing gear does not operate in its design conditions and some of the loads that it should withstand are transferred to other parts of the structure. These may bent and eventually fail.

Another problem of touchdowns to soft surfaces is that the friction on a soft surface is greater than a paved hard surface. This is due to the larger contact area between the skids and the surface. The greater friction combined with the high center of gravity of a helicopter may easily lead to a nose over. In these conditions it is extremely important to reduce (in absolute value) the minimum pitch attitude to mitigate tip over occurrences. Furthermore, grass can always hide uneven ground.

The combination of requirements on lateral speed and horizontal speed translates into a requirement also on the sideslip/track angle, that together with the requirement on yaw rate should be responsible for preventing roll-over issues due to the difference between where the airframe nose is pointing and the direction it is travelling. Also in this case it is extremely important to adapt the desired and adequate performance threshold values according to the touchdown surface.

Table 6.1: Performance – Straight-in Autorotation Maneuver (adapted from Sunberg et al. [2015]).

Metric	**Performance**			
	Desired		**Adequate**	
	Minimum	Maximum	Minimum	Maximum
Roll angle at touchdown ϕ_{td} (deg)	−5	5	−10	10
Pitch angle at touchdown θ_{td} (deg)	−5	12	−5	18
Forward speed at touchdown $V_{x_{td}}$ (kn)	0	30	0	40
Lateral speed at touchdown v_{td} (ft/s)	−6	6	−12	12
Rate of descent at touchdown $V_{z_{td}}$ (ft/min)	0	480	0	900
Roll rate at touchdown p_{td} (deg/s)	−8	8	−15	15
Pitch rate at touchdown q_{td} (deg/s)	−10	10	−20	20
Yaw rate at touchdown r_{td} (deg/s)	−8	8	−15	15

6.2.2. HELICOPTER DYNAMICS

Participants performed the straight-in autorotation task by controlling a seven degrees-of-freedom (6-DOF rigid-body dynamics plus rotorspeed DOF), non-linear and generic helicopter model with quasi-steady flapping dynamics [Talbot et al., 1982]. This generic model can be used in combination with different parameters sets to approximate the dynamic response of any conventional helicopter configuration.

From the wide range of configurations studied in Section 4.3.2, two were selected for the study presented in Chapter 5, in which a four degrees-of-freedom (3-DOF longitudinal dynamics plus rotorspeed DOF) helicopter model was used. The “hard” dynamics are representative of the Bo-105 helicopter and the flight model parameters were taken from Padfield [2007]. The “easy” dynamics represent a variation of the Bo-105 helicopter

with reduced weight in order to achieve a higher autorotative flare index (AI) [Fradenburgh, 1984]. The same configurations were considered in the current experiment to corroborate the results from Chapter 5 which were obtained with a 3-DOF helicopter model. The selection process was conducted only on the 3-DoF model and the same settings were adopted for the 6-DoF model to make the two studies as comparable as possible. Although not conclusive, a similar outcome in the two experiments enables to draw preliminary considerations about the potential benefits of a part-task training program during initial autorotation training. The differences in terms of visual and motion stimuli between the current and the previous study (Chapter 5) due to the different helicopter model are illustrated in Fig. 6.2.

While similar in terms of stability characteristics, these two configurations proved to be considerably different in terms of handling qualities during a pre-experiment with a test pilot, both concerning objective metrics of performance at touchdown (Tab. 6.1) and subjective handling quality ratings provided by the pilot (Section 5.2.2).

6.2.3. EXPERIMENT STRUCTURE

The experiment is structured as indicated in Tab. 6.2 and consists of four phases:

1. Familiarization: this phase was intended to help the participants get acquainted with the simulation environment (helicopter model, cockpit ergonomy, control inceptors, etc.). For this reason, the simulator motion system was disabled and each participant performed the task with either the hard or the easy helicopter dynamics. These runs were not used in the analysis.

2. Training: each participant performed the task with the same helicopter dynamics used during the Familiarization phase. Starting from this session, the simulator motion system was enabled.

3. Transfer: each participant performed the task with the other helicopter configuration.

4. Back-transfer: each participant performed the task with the initial hard/easy helicopter configuration.

In total, the complete experiment session for each participant lasted approximately 3 hours.

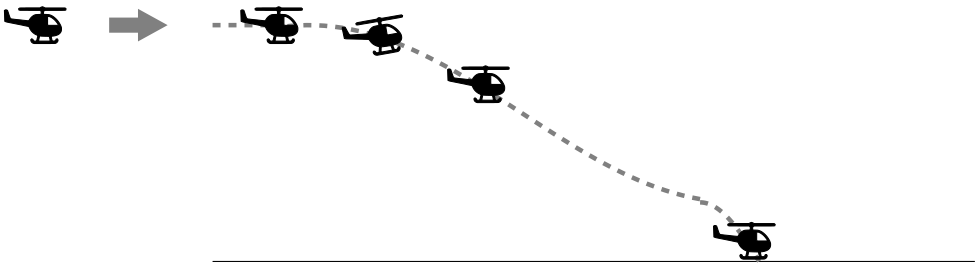

(a) Side view.

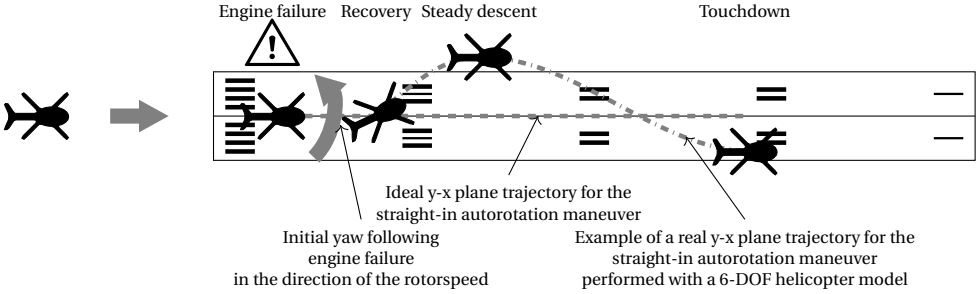

(b) Top view - Current study (6-DOF rigid-body + RPM).

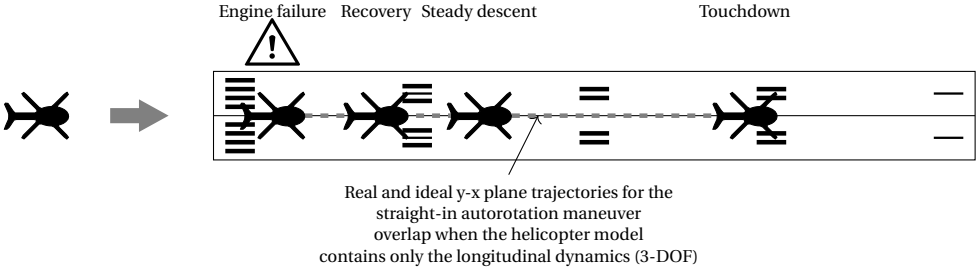

(c) Top view - 3-DOF longitudinal + RPM study (Chapter 5).

Figure 6.2: Comparison in terms of helicopter model between the current study and the previous one, presented in Chapter 5.

Table 6.2: Experiment phases.

Phase	HEH group	EHE group	Duration (number of autorotative landings)	Motion
Familiarization	Hard helicopter dynamics	Easy helicopter dynamics	3	Off
Training	Hard helicopter dynamics	Easy helicopter dynamics	15	On
Transfer	Easy helicopter dynamics	Hard helicopter dynamics	15	On
Back-Transfer	Hard helicopter dynamics	Easy helicopter dynamics	15	On

6.2.4. DEPENDENT MEASURES

To investigate the effect of the helicopter dynamics (independent variable) on autorotation performance and training, the dependent measures related to the MTE definition presented in Tab. 6.1 were considered. Since those measures assess only the performance at touchdown, other metrics were also taken into account to compare the control strategies adopted by the participants of the two experiment groups, namely:

1. Number of landings at least within adequate performance (Tab. 6.1).
2. Number of landings within desired performance (Tab. 6.1).
3. Reaction time: time required by the pilot to lower the collective after engine failure (Fig. 6.1).
4. Flare initiation altitude: altitude at which the pilot initiates the flare by pulling back the cyclic stick (Fig. 6.1).
5. Rotation altitude: altitude at which the pilot levels the skids with the ground by pushing forward the cyclic stick (Fig. 6.1).
6. Cushion altitude: altitude at which the pilot raise the collective to cushion the touchdown (Fig. 6.1).

Metrics 3 to 6 were extracted from the experiment time histories using the methodology developed in Section 5.2.9, named Control Event Detection (CED).

6.2.5. HYPOTHESES

For this experiment only one main hypothesis was tested. Based on previous experimental evidence [Nusseck et al., 2008], including the outcome of the experiment presented in Chapter 5, and on current in-flight training procedures, it is envisioned that pilots who start the training with the most challenging configuration (hard dynamics), are more likely to develop robust and flexible autorotation skills that can be easily adapted to different helicopter configurations and dynamics. Therefore, it is expected that flying skills

are positively transferred from the hard to the easy dynamics, but not conversely. When positive transfer happens, we expect to see lower rates of descent after transition to a different dynamics, as a lower descent rate is a key indicator for a controlled and smooth touchdown [Coyle, 2013]. Among all the dependent measures, the rate of descent is thus expected to cover a key role to corroborate our hypothesis.

The similarities with the study presented in Chapter 5, conducted with a four degrees-of-freedom (3-DOF longitudinal dynamics plus rotorspeed DOF) helicopter model, can be used to formulate a set of secondary hypotheses. Since the final part of the autorotation is mainly a longitudinal maneuver, we expect similar trends in terms of pilots' control strategy, whereas we envision lower reaction times after failure in the current experiment, because the most important cue that is used by pilots to recognize an engine failure, i.e., the initial yaw in the direction of the rotor angular speed, could not be modeled in the previous experiment.

6.2.6. PARTICIPANTS

A total of ten experienced helicopter pilots with different backgrounds (license type) and a mix of civil and military experience took part in the experiment; all of them were male. The participants had an average age of 45.5 years ($\sigma = \pm 11.8$ years) and an average helicopter experience of 1,335 flight hours ($\sigma = \pm 1,778$ flight hours), ranging from a minimum of 100 to a maximum of 5,600 flight hours. Participants were divided in two groups in such a way that they had, on average, a comparable number of flight hours and a similar distribution, as shown in Tab. 6.3 and Fig. 6.3. Beside the number of flight hours, also pilots background was considered during the separation of the pilots in the two groups.

Table 6.3: Participants.

Participant ID	**HEH group**		**EHE group**	
	Age	Flight Hours	Age	Flight Hours
1	19	100	58	190
2	46	5600	34	400
3	53	140	44	3000
4	55	320	56	1200
5	45	2000	45	400
avg	43.6	1632	47.4	1038
std	14.4	2355	9.8	1163

Participants signed an informed consent prior to the experiment. The experiment has been approved by the Human Research Ethics Committee of Delft University of Technology under the approval letter number 1423.

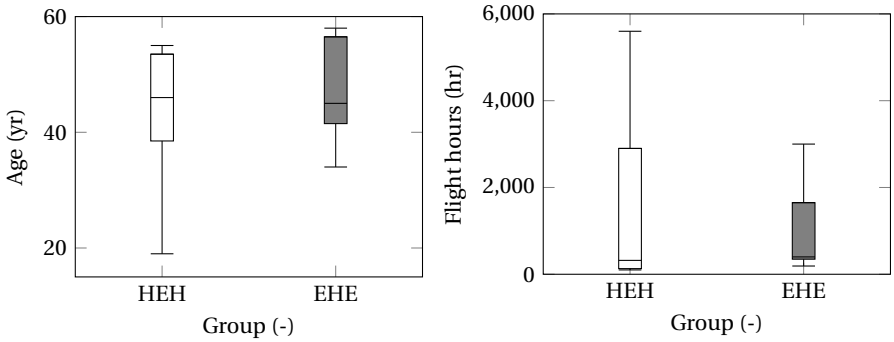

(a) Age distribution among the two groups.

(b) Flight hours distribution among the two groups.

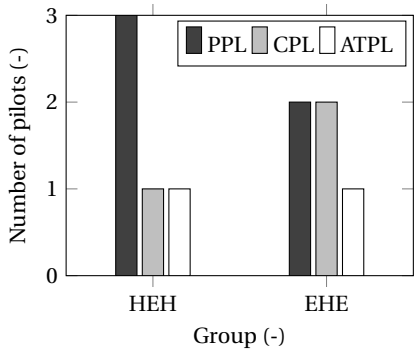

(c) License type distribution among the two groups.

Figure 6.3: Comparison in terms of age, flight hours and license type between the two groups.

6.2.7. APPARATUS

The experiment was conducted in the SIMONA Research Simulator (SRS) (Fig. 6.4), which is a moving-base simulator at the Faculty of Aerospace Engineering of TU Delft [Stroosma et al., 2003]. The SRS is equipped with a 6 degrees-of-freedom hydraulic motion system, which was used in the experiment to provide motion cues.

In terms of visual equipment, the SRS is fitted with a $180° \times 40°$ 3-projector Digital Light Processing (DLP®) collimated display. A representative out-of-the-window scenery was presented on this display (Fig. 6.5a). Furthermore, an instrument panel (Fig. 6.5b), consisting of a tachometer, airspeed indicator, artificial horizon, altimeter, yaw string, compass and vertical speed indicator, and a trim display (Fig. 6.6) were projected on two monitors inside the cockpit. Pilots use the trim display only before the start of each run in order to find the trim position of all the flight controls. This enables them to keep the initial equilibrium condition (straight level flight at 60 kn) and avoid a transient response to reestablish it.

The right seat of the cockpit was equipped with a realistic helicopter control inceptor with programmable control loading system, whose parameters were set as reported in Tab. 6.4 after consultation with test pilots [Miletovic et al., 2018].

Figure 6.4: The SIMONA Research Simulator at Delft University of Technology.

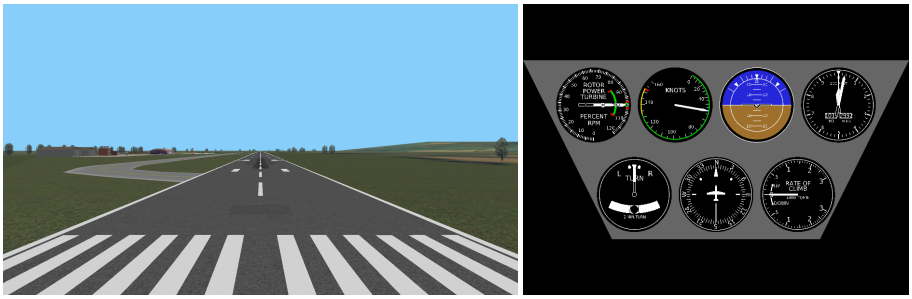

(a) Out-of-the-window scenery.

(b) Instrument panel.

Figure 6.5: Out-of-the-window scenery and instrument panel used for the current experiment.

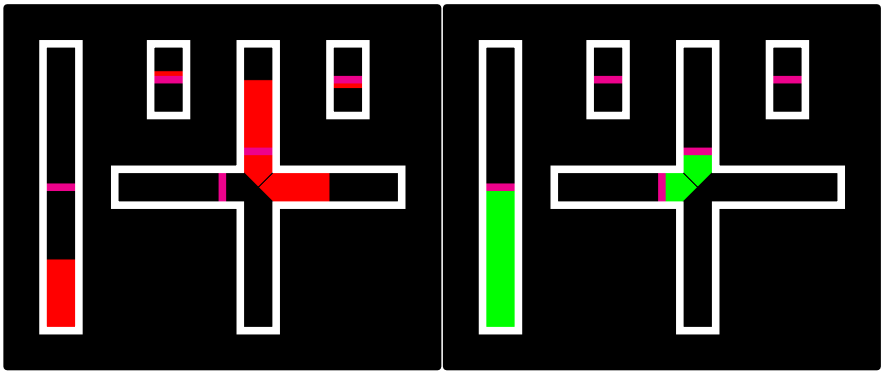

(a) Out of trim.

(b) In trim.

Figure 6.6: Trim display.

Table 6.4: Control loading settings.

Parameter	Longitudinal Cyclic	Lateral Cyclic	Collective
Periodic			
Forward friction level (N)	2.0	2.0	6.0
Positive forward stop (deg)	15.0	15.0	16.0
Negative forward stop (deg)	−15.0	−15.0	−16.0
Non periodic			
Linkage stiffness (N/deg)	50.0	50.0	50.0
Linkage damping (N s/deg)	0.01	0.01	0.01
Positive aft travel limit (deg)	14.8	14.8	15.8
Negative aft travel limit (deg)	−14.8	−14.8	−15.8
Aft friction (N)	2.0	2.0	6.0
Aft inverse damping (deg/N/s)	10.0	10.0	10.0
Second feel spring slope (N/deg)	3.0	3.0	0.0
Breakout level (N)	0.0	0.0	0.0

Rotor sound was played during the simulation to increase immersion. The sound was modulated based on the value of the rotor RPM[1], so that the participant could use sound cues as a source of information to control the rotor RPM, rather than by looking at the instrument panel. Moreover, a low-RPM acoustic warning was activated every time the rotorspeed dropped below 85%. The low-RPM warning was used as a backup cue for the rotor sound, so that the failure could be recognized without necessarily looking at the instruments. Engine sound was not included.

6.2.8. MOTION FILTER TUNING

The Classical Washout Algorithm (CWA) is used to map the vehicle motion on the simulator workspace [Reid et al., 1985]. The three high-pass filters related to the longitudinal dynamics (the pitch, surge and heave axes) were set according to the tuning conducted in Section 5.2.8 on a four degrees-of-freedom (3-DOF longitudinal dynamics plus rotorspeed DOF) helicopter model. So these filters were selected to be of second order for the pitch and surge axes, and of third order for the heave axis. Although surge and heave axes are both translational degrees of freedom, a different order of the filter was selected for these two axes. Indeed, a second order high-pass filter along the surge axis allows to achieve sufficient washout through the use of tilt coordination. This was first observed by Reid et al. [1986] and reiterated by Grant et al. [1997]. Therefore, the combination of the tilt coordination and the body to inertial transformation effectively adds one order of washout.

The high-pass filter parameters related to a rotational DOF in the lateral-directional dynamics (the roll and yaw axes) were set equal to those along the pitch axis. The high-pass filter parameters related to the sway axis were set equal to those along the surge axis. The complete motion filter settings for the 6 degrees-of-freedom are presented in Tab. 6.5.

[1] A rotor sound recording is played in loop. Its pitch is controlled by the main rotor speed output of the model, whereas its volume is kept constant.

Table 6.5: Motion cueing settings.

DOF	K (-)	ω_n (rad/s)	ζ (-)	ω_b (rad/s)	Order (-)
Longitudinal Dynamics					
Heave	0.5	3.5	0.7071	0.2	3
Surge	0.5	1.5	0.7071	0.0	2
Pitch	0.5	1.5	0.7071	0.0	2
Lateral-Directional Dynamics					
Yaw	0.5	1.5	0.7071	0.0	2
Sway	0.5	1.5	0.7071	0.0	2
Roll	0.5	1.5	0.7071	0.0	2

6.2.9. DATA PROCESSING AND ANALYSIS

Prior to performing the statistical tests, all the dependent measures defined in Section 6.2.4, except the number of landings at least within adequate performance and within desired performance, were averaged over the last 10 runs of each phase for every participant. Mixed repeated measures ANOVA (Analysis of Variance) tests [Field, 2013] were conducted on all the dependent variables, considering the experiment phases as main within-subjects factor, characterized by three levels: training, transfer and back-transfer, and the groups as main between-subjects factor, characterized by two levels: HEH and EHE. Before conducting the statistical tests, the fulfillment of the ANOVA assumptions, i.e., normality and sphericity, was verified. Regarding the normality assumption, some skewness in the data was accepted, as long as it is reasonably small. Indeed, the ANOVA is a robust technique and should still provide reliable results also in presence of minor violations. For variables in which sphericity was violated according to Mauchly's test, we adopted either the Greenhouse-Geisser correction, when the Greenhouse-Geisser estimate of sphericity ε is below 0.75 ($\varepsilon < 0.75$), or the Huynd-Feldt correction, when the Greenhouse-Geisser estimate of sphericity ε is above 0.75 ($\varepsilon > 0.75$).

In the event of a statistically significant interaction effect between the two main factors (within- and between-subjects factors), main effects may provide misleading information [Field, 2013]. Therefore, the so-called *simple* main effects are investigated. Dependent-samples t-tests between the phases of the experiment for each group are used to investigate the simple within-subjects effect and independent-samples t-tests between the groups in each phase are adopted to examine the simple between-subjects effect. If the interaction effect between the two main factors is not statistically significant, the two main effects are analyzed and if either of them is statistically significant, the respective simple main effect is investigated accordingly.

This process is shown in the flowchart of Fig. 6.7.

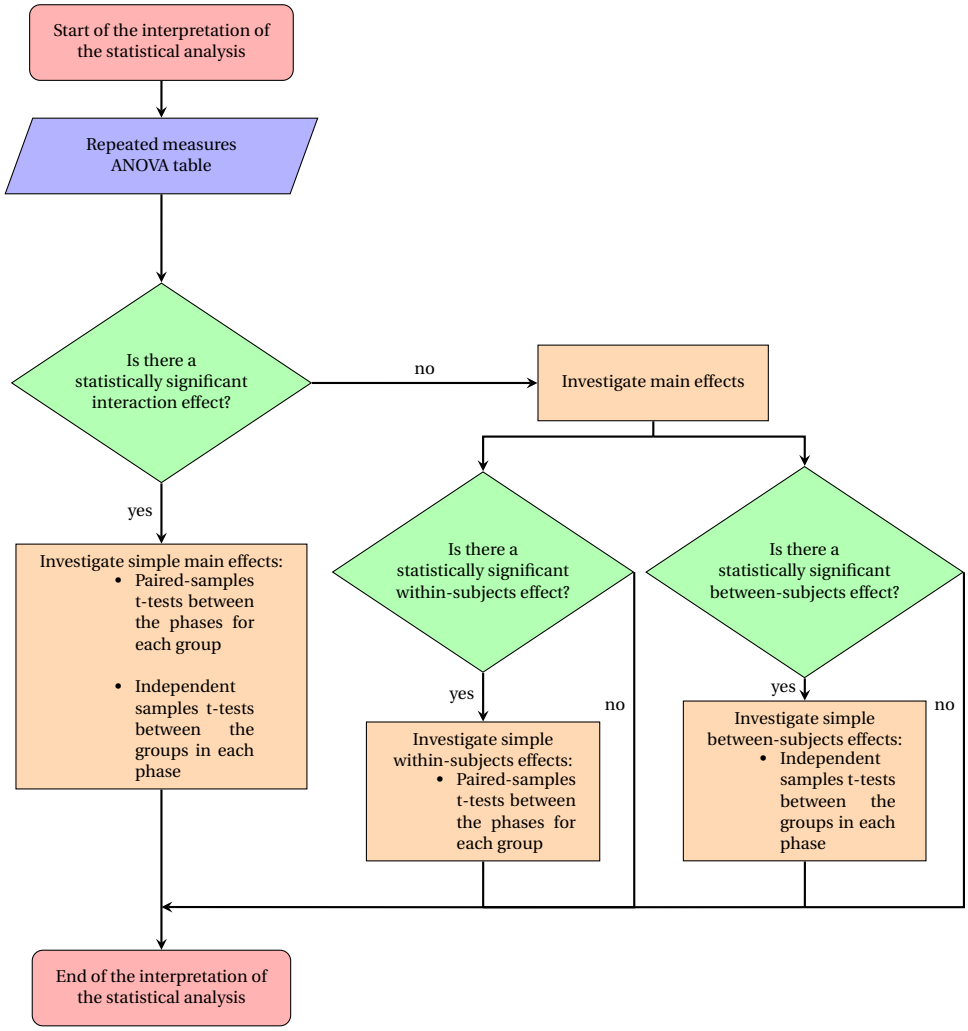

Figure 6.7: Flowchart explaining the interpretation of the statistical analysis.

6.3. RESULTS

Results are presented in the following using box-whiskers plots. On each box, the horizontal line represents the median over different data points. The box is delimited by the first and third quartiles, therefore it includes data points between the 25$^{\text{th}}$ and the 75$^{\text{th}}$ percentile. The difference between first and third quartiles defines the interquartile range. The two edges of the whiskers indicate the lowest and the highest data point within 1.5 of the interquartile range. All the data points not included in the whiskers are considered as outliers and represented by cross markers.

Statistically significant results of the t-tests are shown as follows. A curly brace with an asterisk on top is used to indicate a statistically significant difference between the two groups in a specific phase of the experiment. A curved arrow with an asterisk on the left indicates a statistically significant transfer-of-training effect for a specific group.

6.3.1. PERFORMANCE SCORES

Tab. 6.6 summarizes the results of the repeated measures ANOVA tests for the different dependent measures considered in this study. This test was not performed on the number of landings within desired performance because this metric does not meet the assumption of normal distribution of the data required by the ANOVA test.

Table 6.6: Repeated Measures ANOVA results for all the dependent variables.

Dependent Variable	**Between-subjects Factor (Group)**			**Within-subjects**					
				Factor (Phase)			**Interaction (Phase*Group)**		
	df	F	Sig.	df	F	Sig.	df	F	Sig.
N_{ad}	1	0.570	0.472	2	2.439	0.119	2	4.195	0.034*
$\overline{\theta}_{td}$	1	2.156	0.180	2	0.548	0.589	2	0.862	0.441
$\overline{V}_{x_{td}}$	1	7.750	0.024*	2	0.716	0.504	2	2.302	0.132
$\overline{V}_{z_{td}}$	1	1.072	0.331	2	1.490	0.255	2	5.487	0.015*
$\overline{q}_{td}$	1	4.345	0.071	2	0.459	0.640	2	0.804	0.465
$\overline{\phi}_{td}$	1	2.492	0.153	2	0.367	0.698	2	0.624	0.548
$\overline{v}_{td}$	1	0.144	0.714	2	0.597	0.562	2	1.593	0.234
$\overline{p}_{td}$	1	0.107	0.752	2	0.820	0.458	2	3.615	0.051
$\overline{r}_{td}$	1	2.459	0.155	2	0.398	0.678	2	0.644	0.538
$\overline{\Delta t}_{reac}$	1	0.032	0.863	1.290[hf]	2.546	0.137	1.290[hf]	0.262	0.679
$\overline{h}_{fl}$	1	2.136	0.182	2	0.479	0.628	2	2.087	0.157
$\overline{h}_{rot}$	1	0.170	0.691	2	7.179	0.006*	2	5.855	0.012*
$\overline{h}_{cush}$	1	1.999	0.195	2	0.077	0.926	2	3.947	0.040*
$\overline{\Omega}_{td}$	1	2.543	0.149	2	0.592	0.565	2	2.354	0.127

* Statistically significant ($p < 0.05$) difference between compared samples.
[hf] Huynd-Feldt correction applied.

Fig. 6.8 shows the number of landings at least within adequate performance N_{ad} and those within desired performance N_{des} for each group in each phase. Fig. 6.8a illustrates that participants of both groups were able to attain at least adequate performance, i.e., a survivable landing, in most of the experiment runs. However, the HEH group shows higher within group variability than the EHE group. This is particularly true for the train-

ing and the back-transfer phases, where the EHE group controls the easy dynamics.

The number of survivable landings for the participants of the HEH group increases during the transfer phase and slightly decreases during the transition from the transfer to the back-transfer phase. The opposite is observed for the participants of the EHE group: the number of survivable landings decreases during the transfer phase and increases again during the back-transfer phase to values comparable to those of the training phase. Fig. 6.8a suggests that for the HEH group there is a positive transfer of training from the hard configuration to the easy configuration and no transfer of training from the easy configuration to the hard configuration. Although not statistically significant, a similar trend is observed also for the EHE group.

Participants of both groups struggled to attain desired performance (i.e., a successful landing), as shown in Fig. 6.8b. Nonetheless, the number of successful landings conveys the same information as the number of survivable landings, i.e., a positive transfer of training is observed for both groups from the hard configuration to the easy configuration, but not the opposite.

Tab. 6.6 highlights a statistically significant interaction effect in terms of number of survivable landings N_{ad} (interaction effect: $F(2,16) = 4.195$, $p = 0.034$), which was further investigated by performing t-tests on individual sets of samples. Tab. 6.7 and 6.8 illustrate the results of these tests. A significant difference in terms of survivable landings only occurs between the training and the transfer phase for the HEH group (from the hard to the easy helicopter dynamics: $t(4) = -3.157$, $p = 0.034$). This partially confirms what has already been observed from Fig. 6.8a.

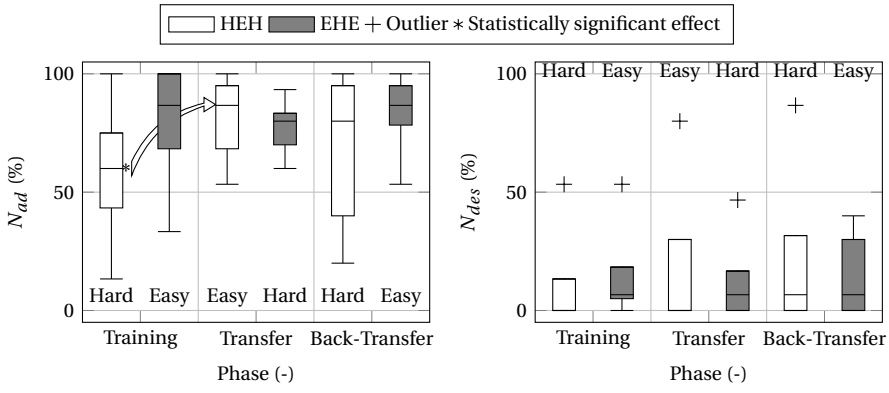

(a) Landings at least within adequate performance.

(b) Landings within desired performance.

Figure 6.8: Distribution of the number of landings at least within adequate performance and that within desired performance for each group in each phase.

The effectiveness of the training was further investigated by averaging the performance metrics defined in Section 6.2.1 (longitudinal metrics: horizontal speed, rate of descent, pitch angle, and pitch rate at touchdown; lateral metrics: roll angle, lateral speed, roll rate, and yaw rate at touchdown) over the last 10 runs completed by each participant in each phase. The longitudinal and the lateral-directional metrics are shown in Fig. 6.9 and 6.10, respectively, as box-whiskers plots to compare the performance of the two groups in the Training, Transfer and Back-Transfer phases.

Table 6.7: Dependent-samples t-test between the experiment phases. Bonferroni correction [Field, 2013] was not applied.

Metric	Group	From	To	t-test			From	To	t-test		
				t	df	Sig. (2-tailed)			t	df	Sig. (2-tailed)
N_{ad}	HEH	Training	Transfer	−3.157	4	0.034*	Transfer	Back-Transfer	1.907	4	0.129
	EHE			0.343	4	0.749			−1.826	4	0.142
$\overline{V}_{z_{td}}$	HEH	Training	Transfer	3.998	4	0.016*	Transfer	Back-Transfer	−1.666	4	0.171
	EHE			−1.715	4	0.162			2.063	4	0.108
$\overline{p}_{td}$	HEH	Training	Transfer			0.500[a]	Transfer	Back-Transfer	0.445	4	0.679
	EHE			0.333	4	0.756			−2.797	4	0.049*
$\overline{h}_{rot}$	HEH	Training	Transfer	1.299	4	0.264	Transfer	Back-Transfer	−0.715	4	0.514
	EHE			0.546	4	0.614			−3.414	4	0.027*
$\overline{h}_{cush}$	HEH	Training	Transfer	1.659	4	0.172	Transfer	Back-Transfer	−1.894	4	0.131
	EHE			−9.614	4	0.001**			0.885	4	0.426

* Statistically significant ($p \leq 0.05$) difference between compared samples.
** Statistically highly significant ($p \leq 0.001$) difference between compared samples.
[a] At least one sample not normally distributed. Related-samples Wilcoxon signed-rank test was applied instead of paired-samples t-test.

Table 6.8: Independent-samples t-test between the two groups.

Metric	Phase	t-test		
		t	df	Sig. (2-tailed)
N_{ad}	Training	−1.150	8	0.283
	Transfer	0.405	8	0.696
	Back-Transfer	−0.934	8	0.378
$V_{x_{td}}$	Training			0.056[a]
	Transfer	−4.406	8	0.002*
	Back-Transfer	−0.946	8	0.372
$V_{z_{td}}$	Training	1.672	8	0.133
	Transfer	0.331	8	0.749
	Back-Transfer	1.056	8	0.322
q_{td}	Training	−4.420	8	0.002*
	Transfer			0.095[a]
	Back-Transfer	−0.554	8	0.595
p_{td}	Training			0.690[a]
	Transfer	0.093	8	0.928
	Back-Transfer	−1.380	8	0.205
$\overline{h}_{rot}$	Training	0.971	8	0.360
	Transfer	0.760	8	0.469
	Back-Transfer	−0.367	8	0.723
$\overline{h}_{cush}$	Training	−0.549	5.147	0.606
	Transfer	−2.552	8	0.034*
	Back-Transfer	−0.943	8	0.373

* Statistically significant ($p \leq 0.05$) difference between compared samples.
[a] At least one sample not normally distributed. Independent-samples Mann-Whitney U test was applied instead of independent-samples t-test.

Fig. 6.9a and 6.9c show the distribution of the average horizontal speed $\overline{V}_{x_{td}}$ and of the average pitch angle $\overline{\theta}_{td}$ at touchdown, respectively. The strong correlation between

these two metrics is a key indicator of the flare effectiveness adopted by the two groups. The participants of the HEH group touched down with a higher pitch angle than those of the EHE group, meaning that they opt for a more effective flare, which translates into a lower horizontal speed at touchdown. Despite this clear difference between the two groups for both metrics, the repeated measures ANOVA tests of Tab. 6.6 highlight a statistically significant between-subjects effect only for the average horizontal speed at touchdown ($F(1,8) = 7.750,\ p = 0.024$), that was further investigated by performing t-tests on individual sets of samples. Tab. 6.8 summarizes the results of these tests, highlighting the presence of a significant difference for the average horizontal speed at touchdown $\overline{V}_{x_{td}}$ between the two groups only during the transfer phase ($t(8) = -4.406,\ p = 0.002$). Although not significant, the difference between the two groups is consistent also during the training phase, as can confirmed by a Mann-Whitney U Test ($U = 3,\ p = 0.056$)..

A completely different trend can be observed for the average rate of descent at touchdown $\overline{V}_{z_{td}}$, as shown in Fig. 6.9b. The HEH group exhibits an improvement from the hard (training phase) to the easy dynamics (transfer phase), whereas performance is unaffected going from the easy (transfer phase) to the hard dynamics (back-transfer phase). Although less evident, a similar variation is found for the EHE group, whose performance degrades from the easy (training phase) to the hard dynamics (transfer phase) and improves from the hard (transfer phase) to the easy dynamics (back-transfer phase). These results suggest a correlation between the average rate of descent at touchdown and the number of survivable landings, as they are both characterized by a similar improvement trend from the hard to the easy configuration, but not the opposite. This improvement trend is confirmed by the repeated measures ANOVA test performed on the average rate of descent at touchdown, shown in Tab. 6.6 (statistically significant interaction effect: $F(2,16) = 5.487,\ p = 0.015$) and was further investigated by performing t-tests on individual sets of samples. Tab. 6.7 and 6.8 summarize the results of these tests, highlighting the presence of a significant difference for the average rate of descent $\overline{V}_{z_{td}}$ between the training and the transfer phase for the HEH group (from the hard to the easy helicopter dynamics: $t(4) = 3.998,\ p = 0.016$).

The surprising result concerns the average pitch rate at touchdown $\overline{q}_{td}$, which is strikingly different between the two groups during the training and the transfer phases, as shown in Fig. 6.9d. Although not significant, the difference between the two groups is confirmed by a low between-subjects p-value in the repeated measures ANOVA test of Tab. 6.6 ($F(1,8) = 4.345,\ p = 0.071$).

The presence of an overall significant effect in the complete data set of the average pitch rate was further investigated by performing t-tests on individual sets of samples. Tab. 6.8 illustrates the results of these tests and highlights a statistically significant difference between the two groups only during the training phase ($t(8) = -4.420,\ p = 0.002$). Although not significant, the difference between the two groups is strong also during the transfer phase, as can be claimed from the Mann-Whitney U Test ($U = 4,\ p = 0.095$).

It appears that the two groups adopt a completely different control strategy during the first two phases of the experiment: whereas the HEH group tends to touch down with a negative pitch rate (nose-down), the EHE group shows a positive $\overline{q}_{td}$ (nose-up). The former behavior is usually adopted in reality in order to level the skids with the ground to avoid tail strike and have a better visibility before cushioning the touchdown [Coyle,

2013]. The EHE group aligned with the HEH group during the back-transfer phase. In order to gain more insight into this unexpected result, a detailed analysis of the control techniques adopted by the pilots of the two groups is conducted in Sec. 6.3.3.

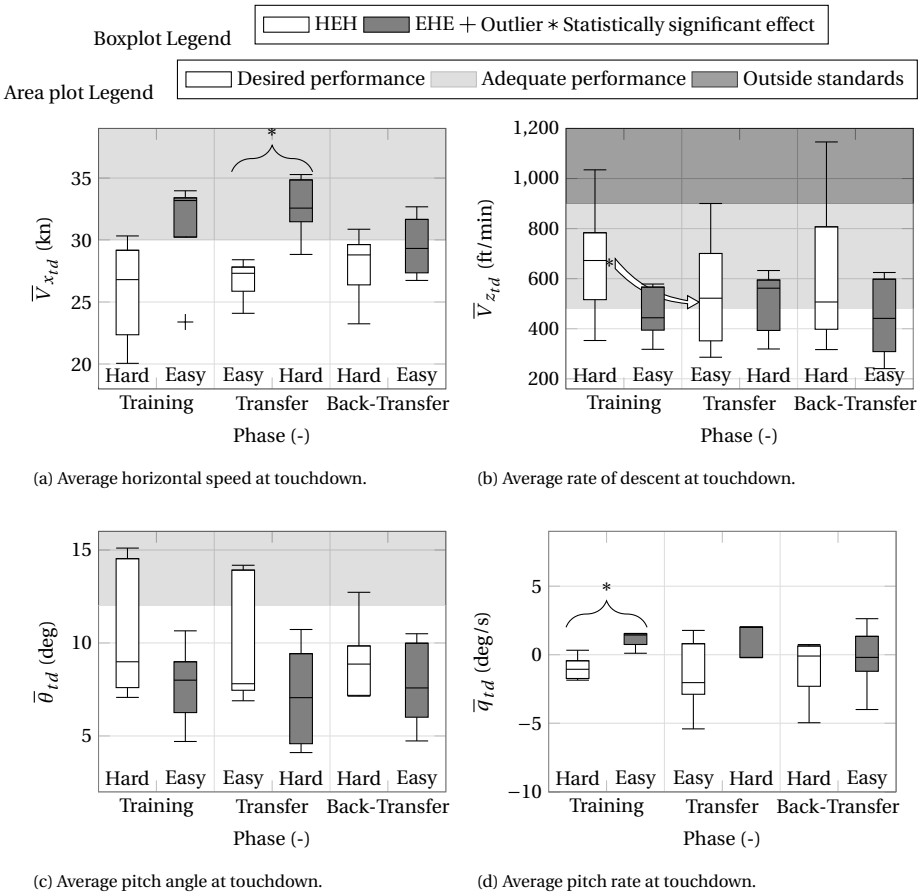

(a) Average horizontal speed at touchdown.

(b) Average rate of descent at touchdown.

(c) Average pitch angle at touchdown.

(d) Average pitch rate at touchdown.

Figure 6.9: Distribution of the average longitudinal performance metrics at touchdown for each group in each phase.

Fig. 6.10a to 6.10d show the distribution of the average roll angle $\overline{\phi}_{td}$, lateral speed $\overline{v}_{td}$, roll $\overline{p}_{td}$ and yaw $\overline{r}_{td}$ rates at touchdown, respectively. Although the HEH group has in general a larger within group variability, the performance in these four metrics is comparable for both groups in each experiment phase and shows little variation throughout the experiment. This is confirmed by the repeated measures ANOVA tests of Tab. 6.6, that do not show any statistically significant effects. Although not significant, the roll rate is characterized by an interaction p-value close to significance ($F(2,16) = 3.615$, $p = 0.051$).

The presence of an overall significant effect in the complete data set of the average roll rate was further investigated by performing t-tests on individual sets of samples. Tab. 6.7 and 6.8 illustrate the results of these tests. The only statistically significant difference

that was identified concerns the transition from the transfer to the back-transfer phase of the EHE group ($t(4) = -2.797$, $p = 0.049$).

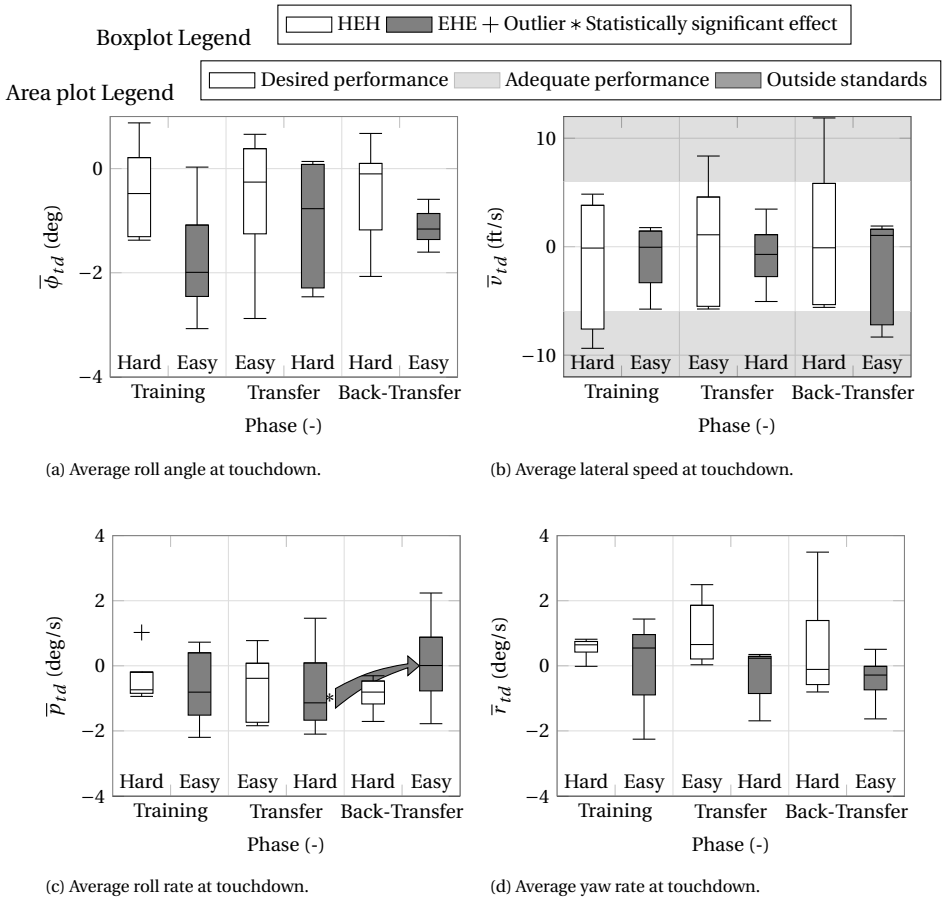

(a) Average roll angle at touchdown.

(b) Average lateral speed at touchdown.

(c) Average roll rate at touchdown.

(d) Average yaw rate at touchdown.

Figure 6.10: Distribution of the average lateral-directional performance metrics at touchdown for each group in each phase.

6.3.2. TOUCHDOWN PRECISION

The relatively high average lateral speed at touchdown (Fig. 6.10b) is an indicator of the efforts made by the pilots to align with the center-line of the runway, as they were briefed to do so. Fig. 6.11 illustrates the touchdown zones for the two groups during each experiment phase, visualized with 95% confidence ellipse. It can be noticed that both groups perform well in terms of landing precision, since all the confidence ellipses almost entirely overlap with the runway.

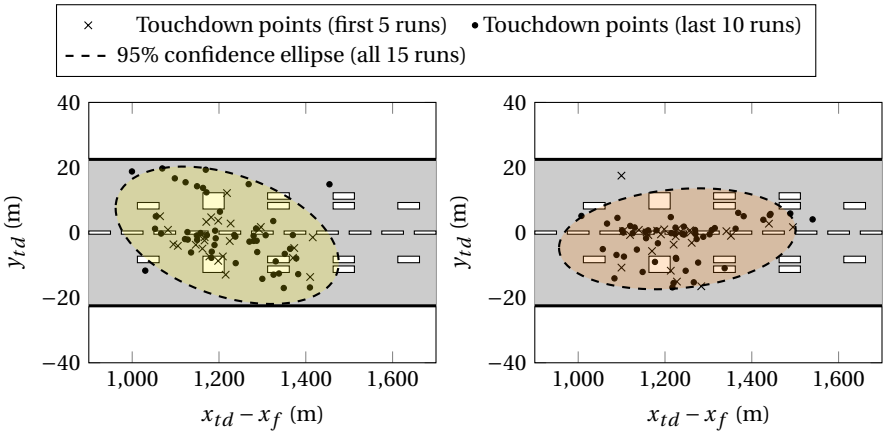

(a) HEH group training phase.

(b) EHE group training phase.

(c) HEH group transfer phase.

(d) EHE group transfer phase.

(e) HEH group back transfer phase.

(f) EHE group back transfer phase.

Figure 6.11: Touchdown zones for the two groups during each phase visualized with a 95% confidence ellipse.

6.3.3. CONTROL STRATEGY METRICS

As for the performance metrics, the control strategy metrics (reaction time, flare intiation altitude, rotation altitude, cushion altitude, and rotor RPM at touchdown) were also

averaged over the last 10 runs completed by each participant in each phase. These averaged metrics are shown in Fig. 6.12 as boxwhiskers plots to compare the control strategy of the two groups in the Training, Transfer and Back-Transfer phases. From Fig. 6.12, it appears that the spread of results for the EHE is generally larger than the HEH group, regardless of training, transfer or back transfer phase. The source of the larger spread for the EHE group compared to the HEH group is likely related to the fact that the EHE group seem to use more variable strategies for attaining desired performance (e.g., anticipate the flare, cushion the touchdown before leveling the skids).

Fig. 6.12a illustrates that every participant of both groups is able to keep the average reaction time below 1 s, which is usually the value considered as the allowable pilot time delay following power failure during the certification of a civil helicopter [Prouty, 2002]. Although the failure was random and unannounced, participants were expecting it to happen, keeping a high level of alertness. This might be the reason for such a good result in terms of reaction time.

Fig. 6.12b shows the distribution of the average flare initiation altitude $\overline{h}_{fl}$, which is comparable for the two groups in each experiment phase and is approximately constant at around 150 ft throughout the experiment. This is confirmed by the repeated measures ANOVA test performed on the average flare initiation altitude, which does not show any statistically significant effects (Tab. 6.6).

Some participants of the HEH group start to level the helicopter with the ground much earlier than the participants of the EHE group during the training and the transfer phases (Fig. 6.12c) to gain a better visibility before cushioning the touchdown. The approach adopted by the participants of the HEH group is successful, because it prevents them from cushioning too early, which is what happens to the participants of the EHE group (Fig. 6.12d). A too early cushion will likely result in a balloon landing, i.e., the helicopter regains altitude before touchdown. As a consequence, a considerable amount of rotor energy is dissipated and the loss of collective effectiveness is counteracted by starting a second flare. This explains why the EHE group exhibits lower RPM values at touchdown (Fig. 6.12e) with respect to the HEH group and positive pitch rates at touchdown (Fig. 6.9d).

For the average rotation altitude $\overline{h}_{rot}$ (Fig. 6.12c) and the average cushion altitude $\overline{h}_{cush}$ (Fig. 6.12d), a statistically significant interaction effect is found ($F(2,16) = 5.855$, $p = 0.012$ and $F(2,16) = 3.947$, $p = 0.040$, respectively), as shown in Tab. 6.6.

The presence of an overall significant effect in the complete data set of the average rotation altitude and of the average cushion altitude was further investigated by performing t-tests on individual sets of samples. Tab. 6.7 and 6.8 illustrate the results of these tests. The only statistically significant difference that was identified for the average rotation altitude concerns the transition of the EHE group from the transfer to the back-transfer phase ($t(4) = -3.414$, $p = 0.027$), indicating that the EHE group aligned its control strategy with that of the HEH group during the last phase of the experiment.

Concerning the average cushion altitude, Tab. 6.7 shows a statistically highly significant difference during the transition of the EHE group from the training to the transfer phase ($t(4) = -9.614$, $p = 0.001$) and Tab. 6.8 indicates a statistically significant difference between the two groups in the transfer phase ($t(8) = -2.552$, $p = 0.034$).

Although the EHE group exhibits lower RPM values at touchdown with respect to the

HEH group, the differences between the groups in the average rotor speed at touchdown $\overline{\Omega}_{td}$ are not significant and do not change significantly throughout the experiment, as summarized in Tab. 6.6.

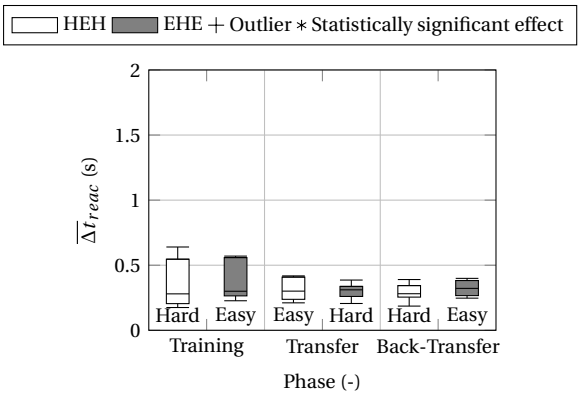

(a) Average reaction time.

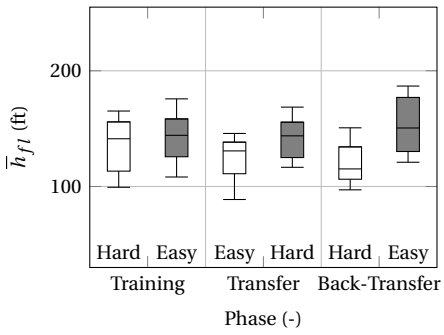

(b) Average flare initiation altitude.

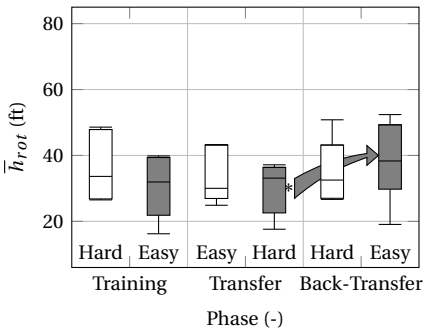

(c) Average rotation altitude.

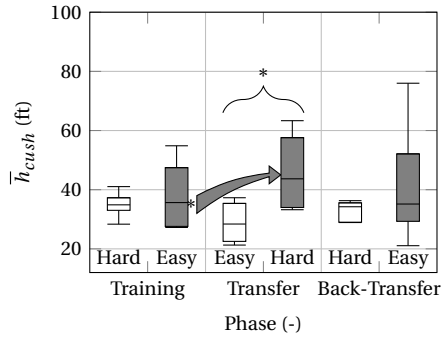

(d) Average cushion altitude.

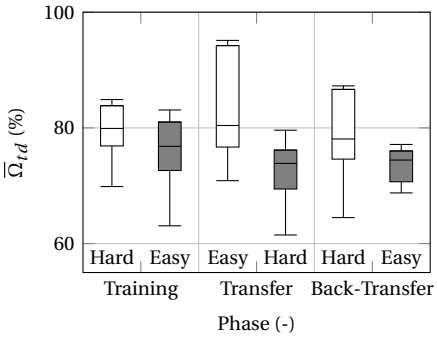

(e) Average rotor RPM at touchdown.

Figure 6.12: Distribution of the average control strategy adopted by each group in each phase.

6.4. DISCUSSION

The quasi-Transfer-of-Training experiment presented in this chapter continues the study introduced in Chapter 5 that was designed to investigate how helicopter dynamics affect pilots' acquisition of skills during autorotation training in a flight simulator. The promising findings from this previous experiment are based on a 3-DOF longitudinal dynamics + RPM flight dynamics model and their relevance was deemed as a solid foundation to further explore this topic with a full 6-DOF rigid-body + RPM flight dynamics model, which incorporates also the helicopter lateral-directional dynamics.

As in the previous experiment (see Chapter 5), two sets of helicopter dynamics, characterized by a different autorotative index (hard, lower index, and easy, higher index) [Fradenburgh, 1984], and two groups of participants, both chosen among experienced helicopter pilots, were considered. In order to assess whether familiarity with one set of helicopter dynamics affects the learning of new helicopter dynamics, each group started the training with either the hard or the easy dynamics, was then transferred to the other, and, finally, transferred back to the initial dynamics.

The outcome of this and the previous (see Chapter 5) experiments confirm previous experimental evidence which showed positive transfer of skills from agile (hard case, where high control compensation is required to the pilot) to inert (easy case, where low intervention is required to the pilot) dynamics, but not the opposite for a different training task [Nusseck et al., 2008]. Indeed, in both our experiments, both groups of participants exhibit a decrease in the rate of descent at touchdown from the hard to the easy dynamics, but not after a transition from the easy to the hard dynamics (Fig. 6.13). This result corroborates our main hypothesis, because a lower rate of descent is an indicator of more controlled and smoother touchdowns. The previous statement is also supported by an increase in the number of landings within adequate performance during the transfer from the hard to the easy helicopter dynamics of around 23% for the HEH group (significant effect) and 7% for the EHE group, which however was not statistically significant.

This is in agreement with current flight education, which usually starts with unaugmented helicopters at the beginning. Once proficiency is reached, later training stages involve augmented helicopters [Coyle, 2008].

The hard helicopter dynamics foster the development of more robust and flexible flying skills, because pilots are required to react faster to perceptual changes. Indeed, participants of the HEH group adopted, from the start of the experiment, a control strategy similar to the one adopted in real helicopters, as opposed to the participants of the EHE group, who tend to underestimate the altitude during the first two phases of the experiment, thus preempting the cushion (Fig. 6.14).

This sometimes results in a balloon landing (the helicopter gains altitude before touchdown), causing the rotor speed to drop down and the consequent loss of collective effectiveness is counteracted by starting a second flare. This is the reason why the participants of the EHE group touch down with a positive pitch rate during the training and the transfer phases (Fig. 6.15). However, they align their control strategy with that of the participants of the HEH group during the back-transfer phase (from the hard to the easy dynamics).

Since the final part of the autorotation is mainly a longitudinal maneuver, the use of

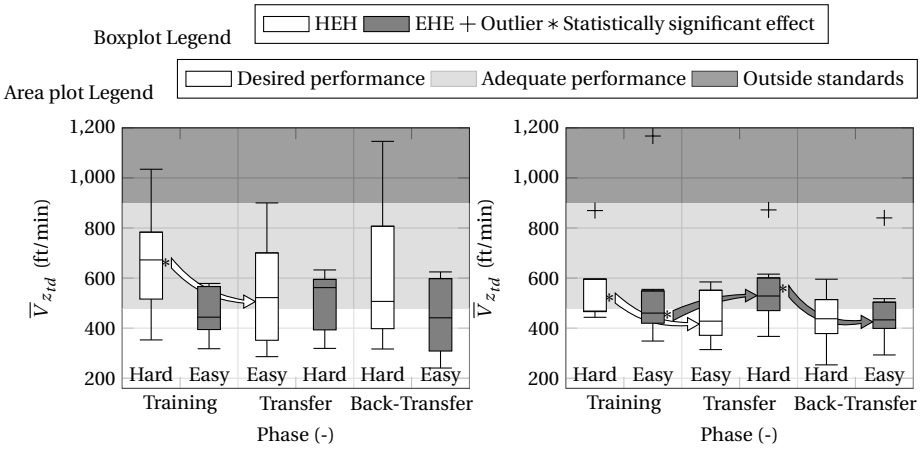

(a) Current study (6-DOF rigid-body + RPM). (b) 3-DOF longitudinal + RPM study (Chapter 5)

Figure 6.13: Comparison of the average rate of descent at touchdown between the current study and the previous one, presented in Chapter 5.

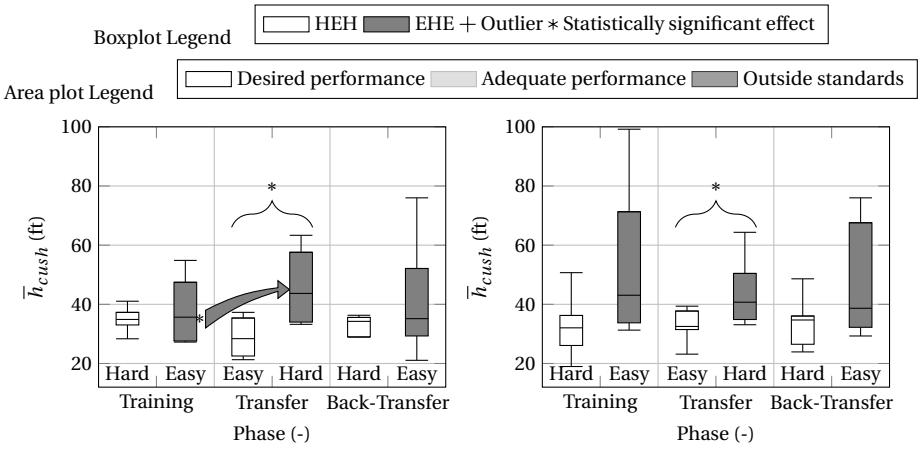

(a) Current study (6-DOF rigid-body + RPM). (b) 3-DOF longitudinal + RPM study (Chapter 5)

Figure 6.14: Comparison of the average cushion altitude between the current study and the previous one, presented in Chapter 5.

a 3-DOF symmetrical helicopter model adopted in our previous study (see Chapter 5) allows for accurate prediction in terms of pilots' performance at touchdown (Fig. 6.13) and control strategy (Fig. 6.14 and 6.15). This is also confirmed by the fact that the participants of both groups succeeded in attaining desired performance at touchdown in the lateral-directional metrics almost in every run of each phase (Fig. 6.10).

However, the 3-DOF symmetrical helicopter model case fails in providing sufficient visual and motion cues to recognize the engine failure, due to its inability to model the initial yaw in the direction of the rotor angular speed which follows a power failure. This is proven by the fact that the average reaction time of the participants of the previous

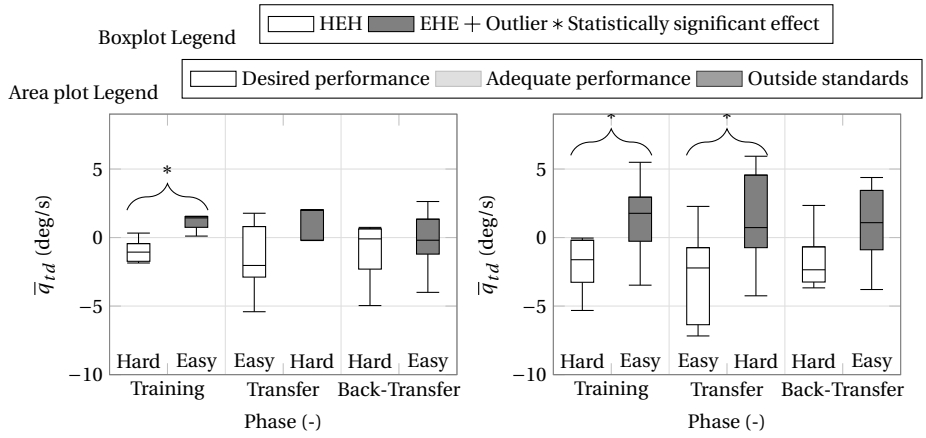

(a) Current study (6-DOF rigid-body + RPM).

(b) 3-DOF longitudinal + RPM (Chapter 5)

Figure 6.15: Comparison of the average pitch rate at touchdown between the current study and the previous one, presented in Chapter 5.

study is approximately twice as high as that of the participants of the current study (Fig. 6.16). Results in terms of control strategy and reaction time are in agreement with our secondary hypotheses.

Although participants managed to keep the reaction time below 1 s in both experiments (which is usually the value considered as pilot time delay following power failure during the certification of a civil helicopter [Prouty, 2002]) and although the failure was random and unannounced, the pilots were still expecting it to happen, keeping a high level of alertness. To circumvent this confounding variable and create more startle and surprise, the failure should be triggered while pilots are asked to perform secondary tasks, such as navigation procedures. Of course this is not always feasible, because it will inevitably increase the time required by every participants to complete the experiment.

The outcomes of this and the previous experiment show that pilots trained in high resource demanding conditions are more likely to be able to handle emergencies like engine failures in the real world, where the actual situation may easily divert from the training scenario, because they develop a more robust control technique. Current simulator training syllabus for autorotation can be updated to include several configurations with different handling characteristics, which can be obtained for example considering different models of the same helicopter family, to give to the trainee the opportunity to familiarize with helicopters with different size and dynamics. This can help inexperienced pilots to better understand that autorotation is not a “by-the-numbers” procedure and that adaptability and judgement of the pilot should always cover a prominent role.

Results are promising and represent a solid foundation to further extend this study. A new experiment will be conducted with student pilots to obtain more evidence for the findings presented in this chapter, which are based on experienced helicopter pilots.

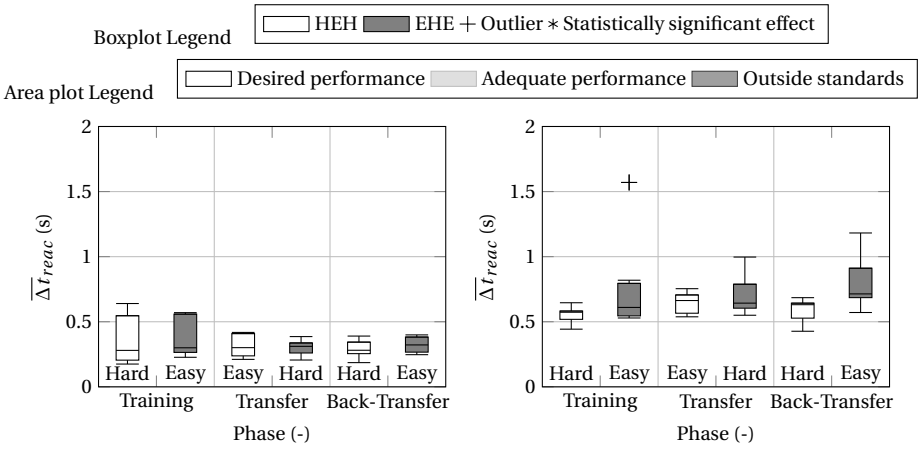

(a) Current study (6-DOF rigid-body + RPM).

(b) 3-DOF longitudinal + RPM study (Chapter 5)

Figure 6.16: Comparison of the average reaction time between the current study and the previous one, presented in Chapter 5.

6.5. CONCLUSIONS

A quasi-Transfer-of-Training experiment with ten experienced helicopter pilots was performed in TU Delft's SIMONA Research Simulator (SRS) to compare the effects of helicopter dynamics characterized by a high autototative flare index (hard dynamics) and low index (easy) on autorotation training in a flight simulator. Participants were divided in two groups and trained to perform a straight-in autorotation maneuver controlling a seven degrees of freedom non-linear helicopter model with 6-DOF rigid-body dynamics plus rotorspeed. Each group tested the two sets of dynamics in a different training order: hard-easy-hard (HEH group) and easy-hard-easy (EHE group). Results show a positive transfer of skills from the hard helicopter dynamics to the easy dynamics for both groups, with the average rate of descent at touchdown that decreases from 666 ft/min to 543 ft/min ($\Delta\overline{V}_{z_{td}}$ = 123 ft/min) for the HEH group and from 502 ft/min to 445 ft/min ($\Delta\overline{V}_{z_{td}}$ = 58 ft/min) for the EHE group. This corroborates earlier findings that the acquisition of robust flying skills is fostered by initiating training in the most challenging setting.

In addition, participants of the EHE group adopted a sub-optimal control technique during the final part of the maneuver. This is suggested by the different sign of the pitch rate at touchdown for the two groups during the first two phases of the experiment: the HEH group tends to touch down with a negative pitch rate (nose-down), whereas the EHE group shows a positive one (nose-up). The former behavior is usually adopted in reality in order to level the skids with the ground to avoid tail strike and have a better visibility before cushioning the touchdown. Dealing with the difficult dynamics helped the participants of the EHE group to align their control strategy with that of the participants of the HEH group.

Although more experiments are needed to confirm our findings, results suggest that simulator training for autorotation can best start with training in the most resource demanding condition. Difficult dynamics require rapid responses to perceptual changes,

forcing pilots to develop more robust and adaptable flying skills. This can enhance helicopter safety as pilots will be better prepared to face unexpected events that may occur during actual flight.

7

CONCLUSIONS & RECOMMENDATIONS

The research presented in this thesis was conducted as part of the European Joint Doctorate NITROS (Network for Innovative Training on Rotorcraft Safety) project and sets out to investigate procedures to prevent or alleviate the occurrence of flight simulator negative *transfer-of-training* for helicopter pilots. Indeed, the improvement of current flight simulator training was identified by safety reports as one of the most *crucial* interventions to reduce helicopter accident rates [European Helicopter Safety Analysis Team, 2010, 2015; U.S. Joint Helicopter Safety Analysis Team, 2011a,b].

The *simulator fidelity model* is the most popular transfer-of-training paradigm, because it is adopted by current regulations on Flight Simulator Training Devices [European Aviation Safety Agency, 2012, 2018; Federal Aviation Administration, 1991, 1992, 1994, 2016]. Such a model is underpinned by the (controversial) assumption that a high-fidelity simulator will yield effective skill transfer and a low-fidelity simulator will yield less – or even negative – transfer and leads to highly sophisticated, complex and expensive devices that may not always be fit, or could be "overfit", for a specific training purpose. Therefore, this thesis had the following goal:

Goal of this thesis

Contribute to an enhanced understanding of the future requirements for helicopter pilot training in flight simulators.

Next, the main conclusions and implications of this thesis work are presented, followed by recommendations for future research.

7.1. CONCLUSIONS

Two critical training tasks for helicopter pilots, i.e., *hover* and *autorotation*, representing two of the most important helicopter capabilities, were chosen in this thesis to provide

indications and guidelines for improved training in flight simulators.

7.1.1. PART I - TRAINING OF BASIC FLYING SKILLS: HOVER

CHAPTER 3 - HOVER TRANSFER OF TRAINING: EFFECTS OF SIMULATOR FIDELITY

In Chapter 3, a quasi-transfer-of-training experiment with 24 *task-naïve learners* (i.e., participants with no prior flight experience neither in actual helicopters nor in simulators) was conducted to explicitly evaluate the extent to which *hover* skills developed on a *Computer Based Trainer (CBT)* are effectively transferred to a more realistic environment. Participants were divided in two groups. The first group (the "*experimental*" group) was trained on a CBT (Training phase) and then transferred to the high-fidelity Max Planck Institute for Biological Cybernetics CyberMotion Simulator (CMS) (Evaluation phase). The second group (the "*control*" group) received the entire training on the CMS. Both groups learned to perform the hover maneuver controlling an identified model of a Robinson R44 civil light helicopter [Geluardi, 2016; Geluardi et al., 2018] through a previously developed part-task training program [Fabbroni et al., 2017a] that is structured as a realistic flight lesson and is intended to bring participants to a satisfactory level of performance. Participants in both groups were able to stabilize the helicopter model, on average, in 60% of the trials during the Evaluation phase. Moreover, no significant difference between CBT and CMS groups was found during the Evaluation phase.

Main finding of Chapter 3

Computer-based Training Devices represent an effective alternative to high-fidelity simulators in the hover training of novice helicopter pilots if supported by a suitable training program, such as a part-task training.

7.1.2. PART II - TRAINING OF ADVANCED FLYING SKILLS: AUTOROTATION

CHAPTER 4 - FLIGHT MECHANICS IN AUTOROTATION (3-DOF & 6-DOF)

Chapter 4 applied linear dynamic system theory to assess helicopter stability characteristics in autorotation and investigate the effects of the rotorspeed degree-of-freedom in autorotation on classical rigid-body modes for two helicopter models characterized by a different level of fidelity (3-degrees-of-freedom (DOF) longitudinal and 6-DOF rigid-body helicopter models).

The analysis carried out on both models shows that the helicopter dynamics change considerably in autorotation as the rotorspeed degree of freedom couples with the classical rigid body modes. Therefore, autorotation requires a different stabilization strategy by the pilot, as also shown through the "paper pilot" analysis [Anderson, 1970; Dillow, 1971] in Appendix E). Indeed, for both models the results show that there are two main differences between the modes in straight level flight and those in steady descent in autorotation for the baseline helicopter (Bo-105) considered in this study:

- The phugoid in autorotation is unstable only at very low or very high speeds.

- The heave subsidence mode couples with the rotorspeed degree of freedom, giving rise to a set of complex conjugate poles.

A good agreement in terms of stability characteristics of the longitudinal modes of motion is found between the two models. Furthermore, the lateral-directional modes of the 6-DOF rigid-body + rotorspeed helicopter model overall do not change significantly in steady-descent in autorotation with respect to straight level flight. As demonstrated in Appendix E, this implies no different pilot control compensation or gains are needed for the lateral-directional control loops in the two flight conditions.

Chapter 4 also investigated whether large variations in the autorotative flare index strongly affect helicopter dynamics in autorotation, because this may impact pilot control strategy and workload. The autorotative flare index is a design parameter and is usually used in any helicopter development programs as a metric for satisfactory autorotative characteristics and, within certain constraints, appears to be a reasonably reliable indicator of the ease of making successful autorotative landings. Four independent design parameters are involved in the calculation of the simplified version of this index: the main rotor blade chord, the main rotor radius, the main rotor RPM and the helicopter weight. Each was varied individually from the baseline value to get eight different values of the autorotation index, spanning from 5 to 40 ft^3/lb. This range was chosen after comparing the index for various existing helicopters.

For each of the four sub-sets of configurations (one subset for each design parameter), the sensitivity of the eigenvalues at 60 kn horizontal speed to changes in the autorotation index shows the same results. When the autorotative flare index increases, the stability of the phugoid mode worsens, because the speed stability derivative M_u decreases. The same holds for the pitch subsidence (the pitch-damping stability derivative M_q increases), whereas the opposite happens for the heave/rotorspeed mode (the rotorspeed stability derivative $M_{\psi_{mr}}$ increases). Thus, higher values of the autorotation index, representative of good autorotative performance in terms of available energy over required energy, do not necessarily mean better stability characteristics.

Main findings of Chapter 4

1. Pilots will need to adapt their control compensation along the longitudinal axes in steady-descent in autorotation with respect to straight level flight, as they will no longer need to keep a constant altitude, but a constant rotorspeed.

2. High values of the autorotative flare index, representative of good autorotative performance in terms of available energy over required energy, may also lead to degraded stability characteristics and hence possibly require more pilot control compensation in autorotation.

CHAPTER 5 - AUTOROTATION TRANSFER OF TRAINING: EFFECTS OF HELICOPTER DYNAMICS (3-DOF)

In Chapter 5, a quasi-Transfer-of-Training experiment with 14 experienced helicopter pilots was performed in TU Delft's SIMONA Research Simulator (SRS) to compare the

effects of helicopter dynamics characterized by a high autototative flare index (hard dynamics) and low index (easy dynamics) on autorotation training in a flight simulator. Participants were divided in two groups and trained to perform a straight-in autorotation maneuver controlling a four degrees of freedom non-linear helicopter model with 3-degrees-of-freedom (DOF) symmetrical dynamics plus rotorspeed, studied in Chapter 4. Each group tested the two sets of dynamics in a different training order: hard-easy-hard (HEH group) and easy-hard-easy (EHE group). The results show a positive transfer of skills from the hard helicopter dynamics to the easy dynamics for both groups, with an average rate of descent at touchdown that decreases from 558 ft/min to 447 ft/min ($\Delta\overline{V}_{z_{td}}$ = 111 ft/min) for the HEH group and from 559 ft/min to 480 ft/min ($\Delta\overline{V}_{z_{td}}$ = 79 ft/min) for the EHE group.

Main finding of Chapter 5

Participants exhibit positive transfer of skills from the hard (lower autorotation index) to the easy dynamics (higher autorotation index), but not after a transition from the easy to the hard dynamics.

CHAPTER 6 - AUTOROTATION TRANSFER OF TRAINING: EFFECTS OF HELICOPTER DYNAMICS (6-DOF)

The quasi-Transfer-of-Training experiment presented in Chapter 6 continues the study described in Chapter 5 that was designed to investigate how helicopter dynamics affect pilots' acquisition of skills during autorotation training in a flight simulator. The promising findings from this previous experiment are further explored with a full 7-degrees-of-freedom (DOF) flight dynamics model, which incorporates also the helicopter lateral-directional dynamics.

As in the previous experiment, two sets of helicopter dynamics, characterized by a different autorotative index (hard, lower index, and easy, higher index) [Fradenburgh, 1984], and two groups of participants, both comprising experienced helicopter pilots, were considered. In order to assess whether familiarity with one set of helicopter dynamics affects the learning of new helicopter dynamics, each group started the training with either the hard or the easy dynamics, was then transferred to the other, and, finally, transferred back to the initial dynamics. As in Chapter 5, the results show a positive transfer of skills from the hard helicopter dynamics to the easy dynamics for both groups, with the average rate of descent at touchdown that decreases from 666 ft/min to 543 ft/min ($\Delta\overline{V}_{z_{td}}$ = 123 ft/min) for the HEH group and from 502 ft/min to 445 ft/min ($\Delta\overline{V}_{z_{td}}$ = 58 ft/min) for the EHE group.

The results indicate that simulator training for autorotation can best start with training in the most resource demanding condition. Difficult dynamics require rapid responses to perceptual changes, forcing pilots to develop more robust and adaptable flying skills. This can enhance helicopter safety as pilots will be better prepared to face also off-nominal conditions that may occur during actual flight.

Main findings of Chapter 6

1. Consistent with the 3-DOF experiment, participants exhibit positive transfer of skills (in terms of rate of descent at touchdown) from the hard (lower autorotation index) to the easy dynamics (higher autorotation index), but not after a transition from the easy to the hard dynamics.

2. The average reaction time of the participants of the experiment with the 3-DOF + rotorspeed DOF helicopter model is approximately twice as high as that of the participants of the experiment with the 6-DOF + rotorspeed DOF model. This indicates that the 3-DOF longitudinal helicopter model case fails in providing sufficient visual and motion cues to recognize the engine failure, due to its inability to model the initial yaw in the direction of the rotor angular speed which follows a power failure.

7.1.3. GENERAL CONCLUSION

In conclusion, this thesis provided insight into helicopter pilots training in flight simulators addressing two critical training tasks, hover (Part I of this thesis) and autorotation (Part II of this thesis), that represent two of a helicopter's most characteristic and relevant capabilities.

Current regulations on flight simulator training devices [European Aviation Safety Agency, 2012, 2018; Federal Aviation Administration, 1991, 1992, 1994, 2016] formulate simulator design criteria in terms of fidelity, assuming that high fidelity will directly result in positive transfer of skills [Klauer, 1997]. However, the experiment on initial hover training presented in Chapter 3 showed that desktop trainers may be a valid alternative to high-fidelity simulators during initial hover training if supported by a suitable training program. The results of Chapter 3 corroborate previous evidence [Alessi, 1988; Lintern, 1995; Noble, 2002], according to which adding more fidelity beyond a certain point results in a diminished degree of transfer of skills. This risk occurs especially for *nonexpert* pilots, because high fidelity also means high complexity, which may require more cognitive skills, thus increasing the trainee's workload: this may, in turn, impede learning [Wickens et al., 2013]. Therefore, the formulation of simulator design criteria should be based also on training effectiveness and not solely on simulator fidelity.

Despite the high-order (coupled fuselage/rotor dynamics) and highly coupled nature of helicopter dynamics compared to fixed-wing aircraft, a 3-DOF longitudinal + rotorspeed helicopter model may provide already a basic understanding of the helicopter flight mechanics in autorotation, as shown in Chapter 4. However, the experiments on autorotation presented in Chapters 5 and 6, which were conducted with a 3-DOF and with a 6-DOF helicopter model, respectively demonstrate the inability of the 3-DOF model to provide sufficient visual and motion cues to identify with a realistic latency the engine failure.

Furthermore, the results of Chapters 5 and 6 showed that positive transfer of skills is observed from helicopter dynamics requiring significant pilot control compensation to those requiring low pilot control compensation, but not the opposite. This challenges

the progressive difficulty approach, according to which emergency situations must be first practiced with easier aircraft [Coyle, 2008]. Such an approach is essential during in-flight training, but can of course be set aside during simulator training, due to the inherently safe nature of flight simulators. These results corroborate earlier findings that the acquisition of robust flying skills is fostered by initiating training in the most challenging setting [Nusseck et al., 2008].

With these new insights, this thesis lays the foundations for an enhanced understanding of the future requirements for helicopter pilots training in flight simulators, which are likely to become even more essential given the current onset of Urban Air Mobility [Antoniou et al., 2020; Mueller et al., 2017; Thipphavong et al., 2018]. Indeed, the transition from helicopters as a niche sector in the aerospace industry to the widespread future use of personal aerial vehicles (PAVs) based on rotorcraft concepts needs to be accompanied by a disruptive change in aviation regulations, encompassing every aspect of safety, including training. Even though these future PAVs will likely be characterized by a high level of automation, human operators will keep playing an important role in the operation of the flight [Gawron, 2019a; Noy et al., 2018; Shladover, 2016], hence raising the need to develop training requirements for PAV pilots.

7.2. RECOMMENDATIONS

In the following, the main recommendations are provided to indicate where the results of this thesis can be applied, or where further research is most needed.

7.2.1. PARADIGM SHIFT IN FSTD REGULATIONS

The literature review conducted in Chapter 2 on aviation training and flight simulation emphasized the shortcomings of current regulations for Flight Simulator Training Devices (FSTDs) [European Aviation Safety Agency, 2012, 2018; Federal Aviation Administration, 1991, 1992, 1994, 2016]. According to these regulations, the ability of a flight simulator to replace or complement in-flight training is attributed to a qualification procedure, and the training effectiveness of devices deriving from this process should be accepted as an axiom, as stated by EASA [2018, (p. 44), 2012, (p. 34)]: *"Fidelity of modern FSTDs is sufficient to permit pilot assessment with the assurance that the observed behaviour will transfer to the aircraft."* However, the results of Chapter 3 suggest that more emphasis should be given on the training program (e.g., the structure and the focus should be adapted based on a trainee's flight experience and on the difficulty of the task), which can still enable effective training even with a simulator that lacks fidelity, especially during ab-initio training.

Future Flight Simulator Training Device requirements should focus on training effectiveness and not only on simulator fidelity. This is not a simple task, because it is indeed easier to formulate simulator design criteria in terms of physical rather than behavioral requirements [National Research Council, 1985]. To achieve this paradigm shift, there is the need to formulate meaningful training outcome specifications involving behavioral and cognitive factors. This requires an in-depth analysis of the psychological requirements of the task to be performed in the simulation situation as well as in the operational environment that is simulated. Each training task will then be characterized by

a set of training outcome specifications (e.g., for autorotation: reaction time, proficiency in maintaining/controlling the airspeed and the rotorspeed, ability to reach the ground with a survivable flight state at touchdown, etc.). So the training outcome specifications are task-dependent and the ability of a simulator to fulfill such requirements will define its validity for the specific training purpose. The degree of validity of a simulator for one purpose always need to be substantiated in relation to a simulator that has already been certified for that specific purpose. Characterization of a simulator as having high or low validity for one purpose or use will not necessarily imply the same degree of validity for another use [National Research Council, 1985].

7.2.2. UPDATE IN SIMULATOR TRAINING SYLLABUS FOR AUTOROTATION

The two experiments on autorotation described in this thesis showed that pilots trained in difficult, high resource demanding conditions develop a more robust control technique that can be easily adjusted to different helicopter handling characteristics. This also results in a better capability to handle emergencies like engine failures in the real world, where the actual situation may easily divert from the training scenario, because they can quickly adapt to unexpected conditions. The current simulator training syllabus for autorotation should be updated to include several configurations with different handling characteristics, which can be obtained for example considering different models of the same helicopter family, to give to the trainee the opportunity to familiarize with helicopters with different sizes, dynamics and "feel". This can help inexperienced pilots to better understand that autorotation is not a "by-the-numbers" procedure and that adaptability and judgement of the pilot should always have a prominent role in the accomplishment of the task.

7.2.3. AUTOROTATION TRANSFER-OF-TRAINING WITH NOVICE PILOTS

Whether due to an actual emergency or during the training for such an event, autorotations often result in an accident in which the pilot fails to perform the maneuver correctly [European Helicopter Safety Analysis Team, 2010, 2015; U.S. Joint Helicopter Safety Analysis Team, 2011a,b]. To minimize risks during practice autorotations and to make training as effective as possible, it is necessary to develop a standardized training program for autorotation. Furthermore, to reduce the burden on the instructor, the student should learn the basics of maintaining/controlling the airspeed and the rotor RPM before practicing autorotation. Mimicking the hover part-task training program used in Chapter 3, this can be achieved through a number of exercises that are preparatory for autorotation [Coyle, 2013], such as:

- *Engine deceleration checks*: to avoid that a practice engine failure becomes a real one, it is essential to check that the throttle and fuel control are going to respond correctly when the engine is put to idle.
- *Rotor RPM decay rates*: the instructor will show how different power/collective settings affect the rate of decay of rotor RPM once the engine is disengaged.
- *Attitude on the ground and in hover*: the instructor will show these two different pitch attitudes by pointing out where the horizon crosses the windshield central

pillar with respect to a convenient rivet or any other reference point on the deck, as these two cues will be used at the end of the flare.

- *Counting down to touchdown*: the student will learn to sense the position of the skids with respect to the ground.
- *Hover engine failures*: the student will learn to:
  - First stop the lateral drift due to the reduction of the tail rotor effectiveness to avoid tip over when touching the ground.
  - Stop the yaw. There is no need to return to the original heading.
  - Cushion the touchdown: try at first from a very low height to help the student judge collective lever application.
- *Running landings with power at slow forward speed*: the instructor will teach the student not to lower the collective until the forward motion has stopped.
- *Hover taxi engine failures*: this task is similar to hover engine failures.
- *Quick stops*: they duplicate most of the flare part of the autorotation quite well and they are an excellent coordination exercise for beginners.
- *Steady descent in autorotation*: the instructor will teach the student the basics of maintaining/controlling the airspeed and the rotor RPM by simulating an engine failure at a higher-than-normal altitude and show the differences in dynamic behavior between helicopter with different handling qualities and sizes.
- *Entry to autorotation*: the student will learn the symptoms of an engine failure and the correct reactions to be able to respond instinctively.
- *Flare*: the student will learn to stop the rate of descent and reduce the airspeed.
- *Power recovery or Touchdown*: A power recovery autorotation terminates in a hover as opposed to landing without power. This is always possible in a training situation, because the engine failure is not real, but simulated by disengaging the rotor shaft from the power shaft by means of a clutch with the engine in an idle state.

Due to time and resource constraints, the effectiveness of this proposed autorotation training program could not be assessed in this thesis. A new experiment with a large group of student pilots should be conducted to obtain more evidence for the findings presented in Chapter 5 and 6, which are based on experienced helicopter pilots, and to further develop the proposed training program towards a new standard.

7.2.4. QUANTITATIVE HANDLING QUALITY ASSESSMENT IN AUTOROTATION

The main limitation of the methodology proposed in Chapter 4 for the analysis of the helicopter dynamics in autorotation consists in the fact that it is applicable only to the steady-descent part of the autorotation maneuver, which is not the most demanding

phase for the pilot [Prouty, 2009]. In Chapter 5, this limitation was overcome by performing a pilot-in-the-loop experiment with a test pilot, who awarded handling quality ratings to the different helicopter configurations studied in Chapter 4. Because it is not always possible to resort to online simulations with test pilots, an offline procedure for the quantitative assessment of handling qualities in autorotation needs to be developed, accounting for all the phases of the maneuver. To this end, a "paper pilot" analysis [Anderson, 1970; Dillow, 1971] as developed in Appendix E can be used by comparing pilot performance for different helicopter configurations when the same gains are used or by comparing pilot gains when the same autorotation performance are achieved flying different configurations. This can be useful for helicopter design, as well as training program development.

7.2.5. TRUE-TRANSFER EXPERIMENTS

The experimental results obtained in this thesis (Chapters 3, 5 and 6) are based on the quasi-transfer paradigm, which relies on the assumption that the more realistic simulator, i.e., the transfer setting, acts as a valid replacement for the real aircraft. Furthermore, a relatively low number of participants took part in these experiments (24, 14, and 10), which affects the statistical reliability of the experimental outcomes.

To confirm the obtained results and overcome these limitations, it is crucial that more experiments adopting a true-transfer paradigm and with large sample sizes are conducted. The financial and human (helicopter pilots) resources required to accomplish this task make this research more suitable for a joint-venture between universities, industrial partners and flight schools. To further explore the results of the two experiments on autorotation (Chapters 3, 5 and 6), a true-transfer experiment could be conducted considering different models of the same helicopter family characterized by different size and dynamics (e.g., AW169, AW139, and AW189).

Following up this recommendation would deliver the final proof of the work presented in this thesis.

REFERENCES

Abbeel, P., Coates, A., Hunter, T., and Ng, A. Y. (2009). Autonomous Autorotation of an RC Helicopter. In *Springer Tracts in Advanced Robotics*, volume 54, pages 385–394. Springer, Berlin, Heidelberg.

Adorian, P., Staynes, W. N., and Bolton, M. (1979). The Evolution of the Flight Simulator. In *Proceedings of the Royal Aeronautical Society Conference, Fifty Years of Flight Simulation*, pages 1–23, London, United Kingdom, April 23-25, 1979. Royal Aeronautical Society.

Advisory Group for Aerospace Research and Development (1980). Fidelity of Simulation for Pilot Training. AGARD-AR-159, North Atlantic Treaty Organization, Neuilly sur Seine, France.

Alessi, S. M. (1988). Fidelity in the Design of Instructional Simulations. *Journal of Computer-Based Instruction*, 15(2):40–47.

Allen, L. (1993). Evolution of flight simulation. In *Proceedings of the Flight Simulation and Technologies Conference*, number AIAA-93-3545-CP, Monterey, California, August 9-11, 1993. American Institute of Aeronautics and Astronautics.

Allerton, D. J. (2009). *Principles of Flight Simulation.* John Wiley & Sons, Ltd.

Allerton, D. J. (2010). The impact of flight simulation in aerospace. *The Aeronautical Journal*, 114(1162):747–756. Paper No. 3581.

Anderson, R. O. (1970). A New Approach to the Specification and Evaluation of Flying Qualities. AFFDL-TR-69-120, Air Force Flight Dynamics Laboratory, Wright-Patterson Air Force Base, Ohio.

Anonymous (1979). R22 Pilot's Handbook and FAA Approved Rotorcraft Flight Manual.

Anonymous (1995). MBB Bo-105 DB/DBS Approved Rotorcraft Flight Manual.

Anonymous (2016). *Unity User Manual.* Unity Technologies.

Antoniou, C., Efthymiou, D., and Chaniotakis, E. (2020). *Demand for Emerging Transportation Systems.* Elsevier.

Aponso, B. L., Lee, D., and Bachelder, E. N. (2007). Evaluation of a Rotorcraft Autorotation Training Display on a Commercial Flight Training Device. *Journal of the American Helicopter Society*, 52(2):123–133.

Apostolo, G. (1984). *The Illustrated Encyclopedia of Helicopters.* Bonanza Books.

Arents, R. R., Groeneweg, J., Borst, C., van Paassen, M., and Mulder, M. (2011). Predictive Landing Guidance in Synthetic Vision Displays. *The Open Aerospace Engineering Journal*, 4(1):11–25.

Ashkenas, I. L. (1986). Collected Flight and Simulation Comparisons and Considerations. In *Proceedings of the AGARD Conference Number 408, Flight Simulation*, pages 26–1–26–34. Advisory Group for Aerospace Research and Development, North Atlantic Treaty Organization.

Ballin, M. G. (1987). Validation of a Real-Time Engineering Simulation of the UH-60A Helicopter. NASA TM-88360, NASA, Ames Research Center, Moffett Field, CA.

Ballin, M. G. (1988). A High Fidelity Real-Time Simulation of a Small Turboshaft Engine. NASA TM-100991, NASA, Ames Research Center, Moffett Field, CA.

Barendswaard, S. (2021). *Modelling Individual Driver Trajectories to Personalise Haptic Shared Steering Control in Curves*. PhD thesis, Delft University of Technology.

Baron, S., Kleinman, D. L., and Levison, W. H. (1970). An Optimal Control Model of Human Response, Part II: Prediction of Human Performance in a Complex Task. *Automatica*, 6(3):371–383.

Bauknecht, A., Raffel, M., and Grebing, B. (2018). Airborne Acquisition of Blade Tip Displacements and Vortices on a Coaxial Helicopter. *Journal of Aircraft*, 55(5):1995–2007.

Beddoes, T. (1985). A Wake Model for High Resolution Airloads. In *Proceedings of the US Army/AHS International conference on Rotorcraft Basic Research*, pages 1–12, North Carolina, February 19-21, 1985.

Boldovici, J. A. (1987). Measuring Transfer in Military Settings. In Cormier, S. M. and Hagman, J. D., editors, *Transfer of Learning: Contemporary Research and Applications*, chapter 9, pages 239–260. Elsevier Science.

Bramwell, A., Done, G. T. S., and Balmford, D. E. H. (2001). *Bramwell's Helicopter Dynamics*. Elsevier Science.

Buckhout, R. (1962). A Bibliography on Aircrew Proficiency Measurement. MRL-TDR-62-49, Aerospace Medical Division, Wright-Patterson AFB, Ohio.

Caro, P. W. (1973). Aircraft Simulators and Pilot Training. *Human Factors*, 15(6):502–509.

Castles, W. and De Leeuw, J. H. (1954). The Normal Component of the Induced Velocity in the Vicinity of a Lifting Rotor and Some Examples of its Application. NACA Report 1184, NACA, Washington D.C.

Chen, R. T., Lebacqz, J. V., Aiken, E. W., and Tischler, M. B. (1988). Helicopter Mathematical Models and Control Law Development for Handling Qualities Research. In *Proceedings of the NASA/Army Rotorcraft Technology Conference, NASA CP-2495*. NASA.

Chen, R. T. N. (1979). A Simplified Rotor System Mathematical Model for Piloted Flight Dynamics Simulation. NASA/TM-78575, NASA.

Chen, R. T. N. (1980). Effects of Primary Rotor Parameters on Flapping Dynamics. NASA/TP-1431, NASA.

Chen, R. T. N. (1987). Flap-Lag Equations of Motion of Rigid, Articulated Rotor Blades with Three Hinge Sequences. NASA/TM-100023, NASA.

Chen, R. T. N. (1990). A Survey of Nonuniform Inflow Models for Rotorcraft Flight Dynamics and Control Applications. NASA/TM-102219, NASA.

Chen, R. T. N. (1992). An Exploratory Investigation of the Flight Dynamics Effects of Rotor RPM Variations and Rotor State Feedback in Hover. NASA/TM-103968, NASA.

Cooper, G. E. and Harper, R. P. (1969). The Use of Pilot Ratings in the Evaluation of Aircraft Handling Qualities. AGARD Report 567, AGARD.

Cormier, S. M. and Hagman, J. D. (1987). *Transfer of Learning: Contemporary Research and Applications*. Elsevier Science.

Coyle, S. (2008). *Cyclic & Collective - More Art and Science of Flying Helicopters*. Eagle Eye Solutions.

Coyle, S. (2013). *The Little Book of Autorotations*. Eagle Eye Solutions, first edition.

Crist, D. and Symes, L. (1981). Helicopter Landing Gear Design and Test Criteria Investigation. USAAVRADCOM-TR-81-D-15, Bell Helicopter Textron.

Damodhar, S. S. and Krishna, S. (2012). Comparison of Participation Factor Method and Selective Eigenvalue Computation for Voltage Stability Analysis. In *Proceedings of the 8th Mediterranean Conference on Power Generation, Transmission, Distribution and Energy Conversion (MEDPOWER 2012)*, pages 1–6, Cagliari, Italy, October 1-3, 2012.

Damveld, H. J. (2009). *A Cybernetic Approach to Assess the Longitudinal Handling Qualities of Aeroelastic Aircraft*. PhD thesis, Delft University of Technology.

Davis, S. J., Rosenstein, H., Stanzione, K. A., and Wisnieveki, J. S. (1979). User's Manual for HESCOMP. The Helicopter Sizing and Performance Computer Program. NADC-78265-60, Boeing Vertol Company, Philadelphia, PA.

De Marco, A., Duke, E., and Berndt, J. (2007). A General Solution to the Aircraft Trim Problem. In *Proceedings of the AIAA Modeling and Simulation Technologies Conference and Exhibit*, number AIAA-2007-6703, Reston, Virigina, August 20-23, 2007. American Institute of Aeronautics and Astronautics.

de Winter, J. C. F., Dodou, D., and Mulder, M. (2012). Training Effectiveness of Whole Body Flight Simulator Motion: A Comprehensive Meta-Analysis. *The International Journal of Aviation Psychology*, 22(2):164–183.

Decker, W., Adam, C., and Gerdes, R. (1986). Pilot Use of Simulator Cues for Autorotation Landings. In *Proceedings of the AHS 42nd Annual Forum*, number 42-2-006, pages 635–656, Washington, D.C., June 2-4, 1986. The American Helicopter Society.

Department of the Air Force and Navy Bureau of Aeronautics (1954). Military Specification - Structural Design Requirements, Helicopters. MIL-S-8698, Department of the Air Force and Navy Bureau of Aeronautics.

Department of the Army (1974). Engineering Design Handbook, Helicopter Engineering, Part I - Preliminary Design. AMCP 706-201, Department of the Army.

Dillow, J. D. (1971). The Paper Pilot - A Digital Computer Program to Predict Pilot Rating for the Hover Task. AFFDL-TR-70-040, Air Force Flight Dynamics Laboratory, Wright-Patterson Air Force Base, Ohio.

Dreier, M. E. (2018). *Introduction to Helicopter and Tiltrotor Flight Simulation, Second Edition*. American Institute of Aeronautics and Astronautics, Inc., Washington, DC.

Durlach, N., Allen, G., Darken, R., Garnett, R. L., Loomis, J., Templeman, J., and von Wiegand, T. E. (2000). Virtual Environments and the Enhancement of Spatial Behavior: Towards a Comprehensive Research Agenda. *Presence: Teleoperators and Virtual Environments*, 9(6):593–615.

EASA (2017). Type Certificate Data Sheet R.011 - BO105. TCDS EASA.R.011, EASA.

Edmond, C. V., Heskamp, D., Sluis, D., Stredney, D., Sessanna, D., Wiet, G., Yagel, R., Weghorst, S., Oppenheimer, P., Miller, J., Levin, M., and Rosenberg, L. (1997). ENT Endoscopic Surgical Training Simulator. *Studies in Health Technology and Informatics*, 39:518–528.

European Aviation Safety Agency (2012). CS-FSTD(H) Helicopter Flight Simulation Training Devices.

European Aviation Safety Agency (2018). CS-FSTD(A) Aircraft Flight Simulation Training Devices.

European Helicopter Safety Analysis Team (2010). EHEST Analysis of 2000-2005 European Helicopter Accidents.

European Helicopter Safety Analysis Team (2015). EHEST Analysis of 2006-2010 European Helicopter Accidents.

European Helicopter Safety Team (2015a). Advantages of Simulators (FSTDs) in Helicopter Flight Training.

European Helicopter Safety Team (2015b). Teaching and Testing in Flight Simulation Training Devices (FSTD).

Eyad H. Abed, M. A. H. and Hashlamoun, W. A. (2009). Modal Participation Factors Revisited: One Definition Replaced by Two. In *ACC'09: Proceedings of the 2009 Conference on American Control Conference*, pages 1140–1145, Hyatt Regency Riverfront, St. Louis, Missouri, June 10-12, 2009. IEE Press.

Fabbroni, D., Bufalo, F., D'Intino, G., Geluardi, S., Gerboni, C. A., Olivari, M., Pollini, L., and Bülthoff, H. H. (2018). Transfer-of-Training: From Fixed- and Motion-base Simulators to a Light-Weight Helicopter. In *Proceedings of the AHS 74th Annual Forum*, number 74-2018-0050, Phoenix, Arizona, May 14-17, 2018. The American Helicopter Society.

Fabbroni, D., Geluardi, S., Gerboni, C. A., Olivari, M., D'Intino, G., Pollini, L., and Bülthoff, H. H. (2017a). Design of a Haptic Helicopter Trainer for Inexperienced Pilots. In *Proceedings of the AHS 73rd Annual Forum*, number 73-2017-0267, pages 2097–2108, Fort Worth, Texas, May 9-11, 2017. The American Helicopter Society.

Fabbroni, D., Geluardi, S., Gerboni, C. A., Olivari, M., Pollini, L., and Bülthoff, H. H. (2017b). Quasi-Transfer-of-Training of Helicopter Trainer from Fixed-Base to Motion-Base Simulator. In *Proceedings of the 43rd European Rotorcraft Forum (ERF 2017)*, pages 696–703. Associazione Italiana di Aeronautica e Astronautica (AIDAA).

Farmer, E., van Rooij, J., Riemersma, J., Jorna, P., and Moraal, J. (1999). *Handbook of Simulator-Based Training*. Routledge.

Federal Aviation Administration (1991). AC 120-40B Airplane Simulator Qualification.

Federal Aviation Administration (1992). AC 120-45A Airplane Flight Training Device Qualification.

Federal Aviation Administration (1994). AC 120-63 Helicopter Simulator Qualification.

Federal Aviation Administration (2011). 14 CFR Part 61 Certification: Pilots, Flight Instructors, and Ground Instructors.

Federal Aviation Administration (2016). 14 CFR Part 60 Flight Simulation Training Device Initial and Continuing Qualification and Use.

Federal Aviation Administration (2018). AC 61-136B FAA Approval of Aviation Training Devices and Their Use for Training and Experience.

Feil, R. and Hajek, M. (2021). Aeromechanics of a Coaxial Ultralight Rotorcraft During Turn, Climb, and Descent Flight. *Journal of Aircraft*, 58(1):43–52.

Femi, T. and Mijaa, S. (2018). Modelling of Hovering Helicopter and its Stability analysis using Participation Factor. *IFAC PapersOnLine*, 51(1):504—511.

Field, A. (2013). *Discovering statistics using IBM SPSS statistics*. Sage.

Fisher, R. (1955). Statistical Methods and Scientific Induction. *Journal of the Royal Statistical Society: Series B (Methodological)*, 17(1):69–78.

Fothergill, S., Loft, S., and Neal, A. (2009). ATC-labAdvanced: An air traffic control simulator with realism and control. *Behavior Research Methods*, 41(1):118–127.

Fradenburgh, E. A. (1984). Technical Notes: A Simple Autorotative Flare Index. *Journal of the American Helicopter Society*, 29(3):73–74.

Gawron, V. (2019a). Automation in Aviation — Accident Analaysis. MTR190013, MITRE, McLean, VA.

Gawron, V. J. (2019b). *Human Performance, Workload, and Situational Awareness Measures Handbook*. CRC Press, Boca Raton, FL, third edition.

Geluardi, S. (2016). *Identification and augmentation of a civil light helicopter: transforming helicopters into Personal Aerial Vehicles*. MPI Series in Biological Cybernetics; 47, University of Pisa and Max Planck Institute for Biological Cybernetics.

Geluardi, S., Nieuwenhuizen, F. M., Venrooij, J., Pollini, L., and Bülthoff, H. H. (2018). Frequency Domain System Identification of a Robinson R44 in Hover. *Journal of the American Helicopter Society*, 63(1):1–18.

Geluardi, S., Venrooij, J., Olivari, M., Bülthoff, H. H., and Pollini, L. (2017). Transforming civil helicopters into personal aerial vehicles: Modeling, control, and validation. *Journal of Guidance, Control, and Dynamics*, 40(10):2481–2495.

Gold, J. I. and Watanabe, T. (2010). Perceptual learning. *Current Biology*, 20(2):R46–R48.

Gouverneur, B., Mulder, J. A., van Paassen, M. M., Stroosma, O., and Field, E. J. (2003). Optimisation of the SIMONA Research Simulator's Motion Filter Settings for Handling Qualities Experiments. In *Proceedings of the AIAA Modeling and Simulation Technologies Conference and Exhibit*, number AIAA-2003-5679, Austin, Texas, August 11-14, 2003.

Grande, N., Tierney, S., Horn, J. F., and Langelaan, J. W. (2016). Safe Autorotation through Wind Shear via Backward Reachable Sets. *Journal of the American Helicopter Society*, 61(2):1–11.

Grant, P. R. and Reid, L. D. (1997). Motion Washout Filter Tuning: Rules and Requirements. *Journal of Aircraft*, 34(2):145–151.

Gray, G. J. (1998). An Investigation of Open-loop and Inverse Simulation as Nonlinear Model Validation Tools for Helicopter Flight Mechanics. *Mathematical and Computer Modelling of Dynamical Systems*, 4(1):32–57.

Hamers, M. and von Grünhagen, W. (1997). Dynamic Engine Model Integrated in Helicopter Simulation. In *Proceedings of the 23rd European Rotorcraft Forum*, number 91, Dresden, Germany, September 16-18, 1997.

Hansen, A. C. (1984). An Analysis of Three Approaches to the Helicopter Preliminary Design Problem. AD-A144 315, Naval Postgraduate School, Monterey, California.

Harris, F. D. (2007). No Accidents-That's the Objective; The 26th Alexander A. Nikolsky Lecture. *Journal of the American Helicopter Society*, 52(1):3–14.

Hays, R. T. (1980). Simulator fidelity: A concept paper. TR 490, U.S. Army Research Institute for the Behavioral and Social Sciences.

Hays, R. T., Jacobs, J. W., Prince, C., and Salas, E. (1992). Flight Simulator Training Effectiveness: A Meta-Analysis. *Military Psychology*, 4(2):63–74.

Hays, R. T. and Singer, M. J. (1989). *Simulation Fidelity in Training System Design: Bridging the Gap Between Reality and Training*. Springer-Verlag.

Heffley, R. K., Jewell, W. F., Lehman, J. M., and Van Winkle, R. A. (1979). A Compilation and Analysis of Helicopter Handling Qualities Data. NASA CR-3144, NASA.

Hess, R. A. (1980). Structural Model of the Adaptive Human Pilot. *Journal of Guidance, Control, and Dynamics*, 3(5):416–423.

Hettinger, L. J. and Haas, M., editors (2003). *Virtual and Adaptive Environments – Applications, Implications, and Human Performance Issues*. Lawrence Erlbaum Associates, Inc.

Heyson, H. H. (1960). Ground Effect for Lifting Rotors in Forward Flight. NACA TN-D-234, NACA, Washington.

Heyson, H. H. and Katzoff, S. (1957). Induced Velocities Near a Lifting Rotor with Non-Uniform Disk Loading. NACA Report 1319, NACA.

Hosman, R. (1999). Are Criteria for Motion Cueing and Time Delays Possible? In *Proceedings of the Modeling and Simulation Technologies Conference and Exhibit*, number AIAA-99-4028, Reston, Virigina, August 9-11, 1999. American Institute of Aeronautics and Astronautics.

Houston, S. S. (1994). Validation of a non-linear individual blade rotorcraft flight dynamics model using a perturbation method. *Aeronautical Journal*, 98(977):260–266.

Houston, S. S. (1996). Longitudinal stability of gyroplanes. *Aeronautical Journal*, 100(991):1–6.

Houston, S. S. (2000). Validation of a Rotorcraft Mathematical Model for Autogyro Simulation. *Journal of Aircraft*, 37(3):403–409.

Houston, S. S. (2002). Analysis of Rotorcraft Flight Dynamics in Autorotation. *Journal of Guidance, Control, and Dynamics*, 25(1):33–39.

Houston, S. S. (2003). Modeling and Analysis of Helicopter Flight Mechanics in Autorotation. *Journal of Aircraft*, 40(4):675–682.

Houston, S. S. and Brown, R. E. (2003). Rotor-Wake Modeling for Simulation of Helicopter Flight Mechanics in Autorotation. *Journal of Aircraft*, 40(5):938–945.

Hui, K. (1999). Advanced Modelling of the Engine Torque Characteristics of a Bell 412HP Helicopter. In *Proceedings of the 24th Atmospheric Flight Mechanics Conference*, number AIAA-99-4110, pages 348–358, Portland, Oregon, August, 9-11, 1999. American Institute of Aeronautics and Astronautics.

International Civil Aviation Organization (2012). Manual of Criteria for the Qualification of Flight Simulators (Doc 9625), Volume II - Helicopters.

International Civil Aviation Organization (2015). Manual of Criteria for the Qualification of Flight Simulators (Doc 9625), Volume I - Aeroplanes.

International Helicopter Safety Team (2012). Accident Analysis Process for a Joint Helicopter Safety Analysis Team (JHSAT).

Jaw, L. and Bryson Jr., A. (1990). Modeling Rotor Dynamics with Rotor Speed Degree of Freedom for Drive Train Torsional Stability Analysis. In *Proceedings of the 16th European Rotorcraft Forum*, Glasgow, United Kingdom, September 18-20, 1990.

Johnson, W. (1975). The Influence of Engine/Transmission/Governor on Tilting Proprotor Aircraft Dynamics. NASA/TM-X-62455, NASA.

Johnson, W. (1988). CAMRAD/JA: A Comprehensive Analytical Model of Rotorcraft Aerodynamics and Dynamics.

Johnson, W. (1994). *Helicopter Theory*. Dover Publications.

Jones, M. (2017). An Objective Method to Determine the Fidelity of Rotorcraft Motion Platforms. In *Proceedings of the AIAA Modeling and Simulation Technologies Conference*, number AIAA-2017-1082, Grapevine, Texas, January 9-13, 2017. American Institute of Aeronautics and Astronautics.

Jump, M. and Padfield, G. (2007). Development of a Nature-Inspired Flare Command Algorithm. In *Proceedings of the AIAA Guidance, Navigation and Control Conference and Exhibit*, number AIAA-2007-6769, Reston, Virigina, August 20-23, 2007. American Institute of Aeronautics and Astronautics.

Jump, M. and Padfield, G. D. (2006). Investigation of the Flare Maneuver Using Optical Tau. *Journal of Guidance, Control, and Dynamics*, 29(5):1189–1200.

Kaempf, G. and Blackwell, N. (1990). Transfer-of-Training Study of Emergency Touchdown Maneuvers in the AH-1 Flight and Weapons Simulator. Research Report 1561, U.S. Army Research Institute for the Behavioral and Social Sciences, Alexandria, VA.

Kaiser, M., Schroeder, J., Sweet, B., and Dearing, M. (2001). Effects of visual texture, grids, and platform motion on unpowered helicopter landings. In *Proceedings of the AIAA Modeling and Simulation Technologies Conference and Exhibit*, number AIAA-2001-4251, Montreal, Canada, August 6-9, 2001. American Institute of Aeronautics and Astronautics.

Kaplita, T. T. (1984). UH-60A Black Hawk Engineering Simulation Model Validation and Proposed Modifications. NASA CR-177360, NASA, Moffett Field, CA.

Klauer, K. M. (1997). Examining the Concept of Total Fidelity Simulation. *Gateway*, 8(2):13–15.

Klein, V. and Morelli, E. A. (2006). *Aircraft System Identification: Theory and Practice*. American Institute of Aeronautics and Astronautics, Reston ,VA.

Kleinman, D. L., Baron, S., and Levison, W. H. (1970). An Optimal Control Model of Human Response, Part I: Theory and Validation. *Automatica*, 6(3):357–369.

Kuczynski, W. A., Cooper, D. E., Twomey, W. J., and Howlett, J. J. (1980). The Influence of Engine/Fuel Control Design on Helicopter Dynamics and Handling Qualities. *Journal of the American Helicopter Society*, 25(2):26–34.

Landman, H. (2019). *Managing Startle and Surprise in the Cockpit*. PhD thesis, Delft University of Technology.

Lane, N. E. (1986). Issues in Performance Measurement for Military Aviation with Applications to Air Combat Maneuvering. NTSC TR-86-008, Naval Training Systems Center, Orlando, FL.

Leishman, J. G. (2006). *Principles of Helicopter Aerodynamics*. Cambridge University Press.

Lin, Y., Wang, X., Wu, F., Chen, X., Wang, C., and Shen, G. (2014). Development and validation of a surgical training simulator with haptic feedback for learning bone-sawing skill. *Journal of Biomedical Informatics*, 48:122–129.

Lintern, G. (1995). Perceptual Learning in the Acquisition of Flight Skills. ARI Research Note 95-47, U.S.Army Research Institute for the Behavioral and Social Sciences, Alexandria, VA.

Liu, D., Macchiarella, N. D., and Vincenzi, D. A. (2008). Simulation Fidelity. In Vincenzi, D. A., Wise, J. A., Mouloua, M., and Hancock, P. A., editors, *Human Factors in Simulation and Training*, chapter 4. CRC Press.

Liu, K., Mittal, M., Prasad, J., and Scholz, C. J. (1995a). A Study of Coupled Engine/Rotor Dynamic Behavior. In *Proceedings of the AHS 51st Annual Forum*, number 51-2-036, pages 1335–1346, Fort Worth, Texas, May 9-11, 1995. American Helicopter Society.

Liu, K., Prasad, J., and Mittal, M. (1995b). Coupling Engine/Rotor Dynamic Behavior for Integrated Flight/Propulsion Study. In *Proceedings of the Flight Simulation Technologies Conference*, pages 96–101, Baltimore, Maryland, August 7-10, 1995. American Institute of Aeronautics and Astronautics.

Lofaro, R. J. and Smith, K. M. (2008). Civil Aviation: Flight Simulators and Training. In Vincenzi, D. A., Wise, J. A., Mouloua, M., and Hancock, P. A., editors, *Human Factors in Simulation and Training*, chapter 14, pages 257–286. CRC Press.

Lu, L., Padfield, G. D., White, M., and Perfect, P. (2011). Fidelity Enhancement of a Rotorcraft Simulation Model Through System Identification. *The Aeronautical Journal*, 115(1170):453–470.

Malaek, S. M. B., Izadi, H., and Pakmehr, M. (2004). *Autolanding Controller Design Using Adaptive Control*, pages 188–199. World Scientific Publishing.

McCauley, M. E. (2006). Do Army Helicopter Training Simulators Need Motion Bases? 1176, U.S. Army Research Institute for the Behavioral and Social Sciences, Fort Rucker, AL.

McRuer, D. T. and Jex, H. R. (1967). A Review of Quasi-Linear Pilot Models. *IEEE Transactions on Human Factors in Electronics*, HFE-8(3):231–249.

Memon, W. A., Owen, I., and White, M. D. (2019). Motion fidelity requirements for helicopter-ship operations in maritime rotorcraft flight simulators. *Journal of Aircraft*, 56(6):2189–2209.

Miletović, I. (2020). *Motion Cueing Fidelity in Rotorcraft Flight Simulation: A New Perspective using Modal Analysis*. PhD thesis, Delft University of Technology.

Miletovic, I., Pavel, M. D., Stroosma, O., Pool, D. M., Van Paassen, M. M., Wentink, M., and Mulder, M. (2018). Eigenmode distortion as a novel criterion for motion cueing fidelity in rotorcraft flight simulation. In *Proceedings of the 44th European Rotorcraft Forum 2018, ERF 2018*, number 45, pages 1091–1102, Delft, Netherlands, September 18-20, 2018. Netherlands Association of Aeronautical Engineers (NVvL).

Miller, R. B. (1954). Psychological Considerations In The Design Of Training Equipment. WADC TR 54-563, Wright Air Development Center.

Mixon, T. R. and Moroney, W. F. (1982). Annotated Bibliography of Objective Pilot Performance Measures. NAVTRAEQUIPCEN IH 330, Naval Training Equipment Center, Orlando, FL.

Moroney, W. F. and Lilienthal, M. G. (2008). Human Factors in Simulation and Training An Overview. In Vincenzi, D. A., Wise, J. A., Mouloua, M., and Hancock, P. A., editors, *Human Factors in Simulation and Training*, chapter 1, pages 3–38. CRC Press.

Mueller, E. R., Kopardekar, P. H., and Goodrich, K. H. (2017). Enabling Airspace Integration for High-Density On-Demand Mobility Operations. In *Proceedings of the 17th AIAA Aviation Technology, Integration, and Operations Conference*, number AIAA-2017-3086, Denver, Colorado, June 5-9, 2017. American Institute of Aeronautics and Astronautics.

Mulder, M., Zaal, P., Pool, D. M., Damveld, H. J., and van Paassen, M. (2013). A Cybernetic Approach to Assess Simulator Fidelity: Looking back and looking forward. In *Proceedings of the AIAA Modeling and Simulation Technologies (MST) Conference*, number AIAA-2013-5225, Boston, Massacchussets, August 19-22, 2013. American Institute of Aeronautics and Astronautics.

Muscarello, V., Cocco, L., Favale, M., Masarati, P., and Quaranta, G. (2017). Novel approach to interaction between engine-drive train system and deformable rotorcraft airframes. In *Proceedings of the AHS 73rd Annual Forum*, number 73-2017-0212, Fort Worth, Texas, May 9-11, 2017. The American Helicopter Society.

Muscarello, V., Colombo, F., Quaranta, G., and Masarati, P. (2019). Aeroelastic Rotorcraft–Pilot Couplings in Tiltrotor Aircraft. *Journal of Guidance, Control, and Dynamics*, 42(3):524–537.

National Research Council (1985). *Human Factors Aspects of Simulation*. National Academies Press, Washington, D.C.

Neyman, J. and Pearson, E. S. (1933). IX. On the problem of the most efficient tests of statistical hypotheses. *Philosophical Transactions of the Royal Society of London. Series A, Containing Papers of a Mathematical or Physical Character*, 231(694-706):289–337.

Nieuwenhuizen, F. M. and Bülthoff, H. H. (2013). The MPI CyberMotion Simulator: A Novel Research Platform to Investigate Human Control Behavior. *Journal of Computing Science and Engineering*, 7(2):122–131.

Nikolsky, A. A. (1952). The Longitudinal Stability and Control of Single Rotor Helicopters in Autorotative Forward Flight. Princeton University Aero. Eng. Lab. Report No. 215, Princeton University.

Nikolsky, A. A. and Seckel, E. (1949a). An Analysis of the Transition of a Helicopter from Hovering to Steady Autorotative Vertical Descent. NACA TN-1907, NACA.

Nikolsky, A. A. and Seckel, E. (1949b). An Analytical Study of the Steady Vertical Descent in Autorotation of Single-Rotor Helicopters. NACA TN-1906, NACA.

Noble, C. (2002). The Relationship between Fidelity and Learning in Aviation Training and Assessment. *Journal of Air Transportation*, 7(3):33–54.

Noy, I. Y., Shinar, D., and Horrey, W. J. (2018). Automated driving: Safety blind spots. *Safety Science*, 102:68–78.

Nusseck, H.-G., Teufel, H. J., Nieuwenhuizen, F. M., and Bülthoff, H. H. (2008). Learning System Dynamics: Transfer of Training in a Helicopter Hover Simulator. In *Proceedings of the AIAA Modeling and Simulation Technologies Conference and Exhibit*, number AIAA-2008-7107, Honolulu, Hawaii, August 18-21, 2008.

Ortiz, G. A. (1994). Effectiveness of PC-Based Flight Simulation. *The International Journal of Aviation Psychology*, 4(3):285–291.

Padfield, G. D. (2007). *Helicopter Flight Dynamics: The Theory and Application of Flying Qualities and Simulation Modelling*. Blackwell Publishing Ltd, Oxford, UK, second edition.

Page, R. L. (2000). Brief History of Flight Simulation. In *SimTecT 2000*, pages 1–11, Sydney, Australia, February 28 - March 02, 2000.

Park, J., Jung, W., Ha, J., and Shin, Y. (2004). Analysis of operators' performance under emergencies using a training simulator of the nuclear power plant. *Reliability Engineering & System Safety*, 83(2):179–186.

Pavel, M. D. (2001). *On the Necessary Degrees of Freedom for Helicopter and Wind Turbine Low-Frequency Mode Modeling*. PhD thesis, Delft University of Technology.

Pavel, M. D. (2008). Prediction of the Necessary Degrees of Freedom for Helicotper Real-Time Simulation Models. *Journal of Aircraft*, 45(4):1256–1266.

Pavel, M. D., Tischler, M. B., White, M., Stroosma, O., Jones, M., Miller, D., Myrand-Lapierre, V., Nadeau-Beaulieu, M., and Taghizad, A. (2021). Simulation fidelity assessment for rotorcraft - Methods and metrics: Sketches from the work of NATO AVT-296. In *Proceedings of the 77th Annual Vertical Flight Society Forum and Technology Display, FORUM 2021: The Future of Vertical Flight*, number F-0077-2021-16826, Virtual, May 10-14, 2021. The Vertical Flight Society.

Pavel, M. D., White, M., Padfield, G. D., Roth, G., Hamers, M., and Taghizad, A. (2013). Validation of Mathematical Models for Helicopter Flight Simulators Past, Present and Future Challenges. *The Aeronautical Journal*, 117(1190):343–388.

Perfect, P., Timson, E., White, M. D., Padfield, G. D., Erdos, R., and Gubbels, A. W. (2014). A rating scale for the subjective assessment of simulation fidelity. *The Aeronautical Journal*, 118(1206):953–974.

Pool, D. M. (2012). *Objective Evaluation of Flight Simulator Motion Cueing Fidelity Through a Cybernetic Approach*. PhD thesis, Delft University of Technology.

Pool, D. M., Harder, G. A., and van Paassen, M. M. (2016). Effects of Simulator Motion Feedback on Training of Skill-Based Control Behavior. *Journal of Guidance, Control, and Dynamics*, 39(4):889–902.

Powers, T. R., McCluskey, M. R., Haggard, D. F., Boycan, G. G., and Steinheiser, F., J. (1975). Determination of the Contribution of Live Firing to Weapons Proficiency. FRCDC- 75-1, Human Resources Research Organization, Alexandria, VA.

Proctor, M. D., Bauer, M., and Lucario, T. (2007). Helicopter Flight Training Through Serious Aviation Gaming. *The Journal of Defense Modeling and Simulation*, 4(3):277–294.

Proctor, M. D., Panko, M., and Donovan, S. J. (2004). Considerations for Training Team Situation Awareness and Task Performance Through PC-Gamer Simulated Multiship Helicopter Operations. *The International Journal of Aviation Psychology*, 14(2):191–205.

Prouty, R. W. (2002). *Helicopter Performance, Stability, and Control*. Krieger Publishing Company, INC., Malabar, Florida.

Prouty, R. W. (2009). *Helicopter Aerodynamics Volume II*. Eagle Eye Solusions, first edition.

Rand, O. and Khromov, V. (2004). Helicopter Sizing by Statistics. *Journal of the American Helicopter Society*, 49(3):300–317.

Rasmussen, J. (1983). Skills, rules, and knowledge; signals, signs, and symbols, and other distinctions in human performance models. *IEEE Transactions on Systems, Man, and Cybernetics*, smc-13(3):257–266.

Rehmann, A. J., Mitman, R. D., and Reynolds, M. C. (1995). A Handbook of Flight Simulation Fidelity Requirements for Human Factors Research. DOT/FAA/CT-TN95/46, U.S. Department of Transportation, Federal Aviation Administration Technical Center, Atlantic City International Airport, NJ 08405.

Reid, L. D. and Nahon, M. A. (1985). Flight Simulation Motion-Base Drive Algorithms. Part 1: Developing and Testing the Equations. UTIAS 296, University of Toronto, Institute for Aerospace Studies.

Reid, L. D. and Nahon, M. A. (1986). Flight Simulation Motion-Base Drive Algorithms. Part 2: Selecting the System Parameters. UTIAS 307, University of Toronto, Institute for Aerospace Studies.

Remple, R. K. and Tischler, M. B. (2006). *Aircraft and Rotorcraft System Identification*. American Institute of Aeronautics and Astronautics, Reston ,VA.

Rogers, S. P. and Asbury, C. N. (2000). A Flight Training Simulator for Instructing the Helicopter Autorotation Maneuver. NASA/FR-1372, NASA.

Roscoe, S. N. (1980). *Aviation Psychology*. The Iowa State University Press.

Roza, Z. C. (2005). *Simulation Fidelity Theory and Practice - A Unified Approach to Defining, Specifying and Measuring the Realism of Simulations*. PhD thesis, Delft University of Technology.

Rudman, D. T., Wiet, G. J., Yagel, R., Stredney, D., Sessanna, D., Heskamp, D., and Edmond, C. V. (1998). Functional endoscopic sinus surgery training simulator. *The Laryngoscope*, 108(11):1643–1647.

Scaramuzzino, P. F., D'Intino, G., Geluardi, S., Pavel, M. D., Pool, D. M., Stroosma, O., Mulder, M., and Bülthoff, H. H. (2018). Effectiveness of a Computer-Based Helicopter Trainer for Initial Hover Training. In *Proceedings of the 44th European Rotorcraft Forum (ERF 2018)*, number 79, pages 1142–1156, Delft, Netherlands, September 18-20, 2018. Netherlands Association of Aeronautical Engineers (NVvL).

Schoen, A. H., Rosenstein, H., Stanzione, K., and Wisniewski, J. S. (1980). User's Manual for VASCOMP II. The V/STOL Aircraft Sizing and Performance Computer Program. AD-A088833, Boeing Vertol Company, Philadelphia, Pennsylvania.

Schroeder, J. and Grant, P. (2010). Pilot Behavioral Observations in Motion Flight Simulation. In *Proceedings of the AIAA Modeling and Simulation Technologies Conference*, number AIAA-2010-8353, Reston, Virigina, August 2-5, 2010. American Institute of Aeronautics and Astronautics.

Schroeder, J., Hosman, R., Lehman, C., Pelchat, Y., and Hamman, B. (2001). Summary of the panel discussion on motion cueing requirements. In *Proceedings of the AIAA Modeling and Simulation Technologies Conference and Exhibit*, number AIAA-2001-4253, Reston, Virigina, August 6-9, 2001. American Institute of Aeronautics and Astronautics.

Seter, D. and Rosen, A. (2014). Theoretical and Experimental Study of Axial Autorotation of Simple Rotary Decelerators. *Journal of Aircraft*, 51(1):236–248.

Shladover, S. E. (2016). The Truth about "Self-Driving" Cars. *Scientific American*, 314(6).

Stewart II, J. E., Barker, W. C., Weiler, D. S., Bonham, J. W., and Johnson, D. M. (2001). Assessing the Effectiveness of a Low-Cost Simulator for Instrument Training for the TH-67 Helicopter. 1780, U.S. Army Research Institute for the Behavioral and Social Sciences, Fort Rucker, AL.

Stroosma, O., van Paassen, R., and Mulder, M. (2003). Using the SIMONA Research Simulator for Human-Machine Interaction research. In *Proceedings of the AIAA Modeling and Simulation Technologies Conference and Exhibit*, number AIAA-2003-5525, Austin, Texas, August 11-14, 2003.

Sunberg, Z. N., Miller, N. R., and Rogers, J. D. (2014). A Real Time Expert Control System for Helicopter Autorotation. In *Proceedings of the AHS 70th Annual Forum*, number 70-2014-0201, pages 1–18, Montreal, Canada, May 20-22, 2014. The American Helicopter Society.

Sunberg, Z. N., Miller, N. R., and Rogers, J. D. (2015). A Real-Time Expert Control System For Helicopter Autorotation. *Journal of the American Helicopter Society*, 60(2):1–15.

Sweller, J. (1994). Cognitive load theory, learning difficulty, and instructional design. *Learning and Instruction*, 4(4):295–312.

Sweller, J., Van Merrienboer, J. J., and Paas, F. G. (1998). Cognitive Architecture and Instructional Design. *Educational Psychology Review*, 10(3):251–296.

Talbot, P. D., Bowles, J. V., and Lee, H. C. (1986). Helicopter rotor and engine sizing for preliminary performance estimation. In *Proceedings of the 22nd Joint Propulsion Conference*, Huntsville, Alabama, June 16-18, 1986. American Institute of Aeronautics and Astronautics.

Talbot, P. D., Tinling, B. E., Decker, W. A., and Chen, R. T. N. (1982). A Mathematical Model of a Single Main Rotor Helicopter for Piloted Simulation. NASA/TM-84281, NASA.

Taylor, H. L., Lintern, G., Hulin, C. L., Talleur, D. A., Emanuel Jr., T. W., and Phillips, S. I. (1999). Transfer of Training Effectiveness of a Personal Computer Aviation Training Device. *The International Journal of Aviation Psychology*, 9(4):319–335.

Taylor, H. L., Lintern, G., and Koonce, J. M. (1993). Quasi-Transfer as a Predictor of Transfer from Simulator to Airplane. *The Journal of General Psychology*, 120(3):257–276.

Thipphavong, D. P., Apaza, R., Barmore, B., Battiste, V., Burian, B., Dao, Q., Feary, M., Go, S., Goodrich, K. H., Homola, J., Idris, H. R., Kopardekar, P. H., Lachter, J. B., Neogi, N. A., Ng, H. K., Oseguera-Lohr, R. M., Patterson, M. D., and Verma, S. A. (2018). Urban Air Mobility Airspace Integration Concepts and Considerations. In *Proceedings of the 2018 Aviation Technology, Integration, and Operations Conference*, number AIAA-2018-3676, Atlanta, Georgia, June 25-29, 2018. American Institute of Aeronautics and Astronautics.

Thompson, T. N., Carroll, M. B., and Deaton, J. E. (2008). Justification for Use of Simulation. In Vincenzi, D. A., Wise, J. A., Mouloua, M., and Hancock, P. A., editors, *Human Factors in Simulation and Training*, chapter 2, pages 39–48. CRC Press.

Thorndike, E. L. (1903). *Educational Psychology*. Lemke and Buechner, New York, NY.

Timson, E., Perfect, P., White, M., Padfield, G., Erdos, R., and Gubbels, W. (2011). Pilot sensitivity to flight model dynamics in rotorcraft simulation. In *Proceedings of the 37th European Rotorcraft Forum (ERF 2011)*, number 172, pages 752–765, Vergiate and Gallarate, Italy, September 13-15, 2011.

Tischler, M. B. and Tobias, E. L. (2016). A Model Stitching Architecture for Continuous Full Flight-Envelope Simulation of Fixed-Wing Aircraft and Rotorcraft from Discrete Point Linear Models. SR-RDMR-AF-16-01, U.S. Army Aviation Development Directorate (AMRDEC), Moffett Field, CA.

US Army AMCOM (2000). Aeronautical Design Standard-33E-PRF, Performance Specification, Handling Qualities Requirements for Military Rotorcraft.

U.S. Joint Helicopter Safety Analysis Team (2011a). The Compendium Report: The U.S. JHSAT Baseline of Helicopter Accident Analysis - Volume I.

U.S. Joint Helicopter Safety Analysis Team (2011b). The Compendium Report: The U.S. JHSAT Baseline of Helicopter Accident Analysis - Volume II.

Vaden, E. A. and Hall, S. (2005). The Effect of Simulator Platform Motion on Pilot Training Transfer: A Meta-Analysis. *The International Journal of Aviation Psychology*, 15(4):375–393.

van der Wall, B. G. (2017). SABRE Shape Adaptive Blades for Rotorcraft Efficiency. Deliverable D1.1: Selection of the Baseline Rotor.

Vincenzi, D. A., Wise, J. A., Mouloua, M., and Hancock, P. A. (2009). *Human Factors in Simulation and Training*. CRC Press.

Weiss, F. and Kessler, C. (2020). Drivetrain Influence on the Lead–Lag Modes of Hingeless Helicopter Rotors. *CEAS Aeronautical Journal*, 11(1):67–79.

White, G., Logan, A. H., and Graves, R. (1982). An Evaluation of Helicopter Autorotation Assist Concepts. In *Proceedings of the AHS 38th Annual Forum*, number 38-0-019, Anaheim, California, May 4-7, 1982. The American Helicopter Society.

White, M. D., Cameron, N., Padfield, G. D., Lu, L., and Advani, S. (2019). The need for increased fidelity in flight training devices to address the 'rotorcraft loss of control in-flight' problem. In *Proceedings of the VFS 75th Annual Forum*, number 75-2019-0323, Philadelphia, Pennsylvania, May 13-16, 2019. The Vertical Flight Society.

Wickens, C. D., Hutchins, S., Carolan, T., and Cumming, J. (2013). Effectiveness of Part-Task Training and Increasing-Difficulty Training Strategies. *Human Factors: The Journal of the Human Factors and Ergonomics Society*, 55(2):461–470.

Wong, T. H. (1993). A Simplified Gas Turbine Engine Model With Heat Storage/Tip Clearance Effects. In *Proceedings of the International Gas Turbine and Aeroengine Congress and Exposition*, volume 3C. American Society of Mechanical Engineers.

Wong, T. H. (1995). Designing and Simulating the Engine Speed Governor for Helicopter Applications. In *Proceedings of the ASME Turbo Expo*, volume 2, Houston, Texas, June 5-8, 1995.

Wood, T. L. (1976). High Energy Rotor System. In *Proceedings of the AHS 32nd Annual Forum*, number 32-1976-0010, Washington, D.C., May 10-12, 1976. The American Helicopter Society.

Yilmaz, D. (2018). *Identification of Manual Control Behaviour to Assess Rotorcraft Handling Qualities*. PhD thesis, Delft University of Technology.

Zaal, P. M. T., Schroeder, J. A., and Chung, W. W. (2015). Transfer of Training on the Vertical Motion Simulator. *Journal of Aircraft*, 52(6):1971–1984.

Zhao Lin, Sun Feng, and Liu Ying (1998). The design of a submarine voyage training simulator. In *Proceedings of the SMC'98 Conference. 1998 IEEE International Conference on Systems, Man, and Cybernetics (Cat. No.98CH36218)*, volume 4, pages 3720–3724, San Diego, California, October 14, 1998. IEEE.

Zheng, Q., Xu, Z., Zhang, H., and Zhu, Z. (2018). A turboshaft engine NMPC scheme for helicopter autorotation recovery maneuver. *Aerospace Science and Technology*, 76:421–432.

APPENDICES

A

FLIGHT MECHANICS MODEL

A.1. EQUATIONS OF MOTION

The aircraft equations of motion are usually derived from Newton-Euler dynamics equation, which hold true in an inertial reference frame (Appendix F):

$$\begin{aligned} \vec{F} &= \frac{{}^{I}\mathrm{d}\vec{Q}}{\mathrm{d}t} \\ \vec{M}_P &= \frac{{}^{I}\mathrm{d}\vec{H}}{\mathrm{d}t} \end{aligned} \tag{A.1}$$

where $\vec{Q} = m\vec{V}$ is the linear momentum and $\vec{H} = \mathbf{J}_P\vec{\omega}$ is the angular momentum. However, it is convenient to write the aircraft equations of motion in a reference frame that is body-fixed (Appendix F), with the origin moving along with the aircraft.

Let P be the origin of this reference frame and Q be a generic point of the aircraft. The velocity of the point Q can be expressed as:

$$\vec{V}_{Q/I} = \vec{V}_{P/I} + \vec{V}_{Q/P} + \vec{\omega}_{B/I} \times (Q - P) \tag{A.2}$$

Under the assumption of rigid-body, the distance between Q and P, both belonging to the aircraft, remains constant ($(Q-P) = \text{const}$), thus meaning that $\vec{V}_Q - \vec{V}_P = \vec{V}_{Q/P} = \vec{0}$. Replacing this condition in Eq. (A.2), we obtain:

$$\vec{V}_{Q/I} = \vec{V}_{P/I} + \vec{\omega}_{B/I} \times (Q - P) \tag{A.3}$$

The acceleration of the point Q can be obtained from the derivation of Eq. (A.3) as:

$$\vec{a}_{Q/I} = \frac{{}^{I}\mathrm{d}\vec{V}_{Q/I}}{\mathrm{d}t} = \frac{{}^{I}\mathrm{d}\vec{V}_{P/I}}{\mathrm{d}t} + \frac{{}^{I}\mathrm{d}\vec{\omega}_{B/I}}{\mathrm{d}t} \times (Q - P) + \vec{\omega}_{B/I} \times \frac{{}^{I}\mathrm{d}(Q - P)}{\mathrm{d}t} \tag{A.4}$$

Using Poisson's theorem, also know as Transport Theorem in analytical dynamics, which provides a formula for the total differentiation of a vector in a rotating reference frame, Eq. (A.4) becomes:

$$\vec{a}_{Q/I} = \frac{{}^{B}\mathrm{d}\vec{V}_{P/I}}{\mathrm{d}t} + \vec{\omega}_{B/I} \times \vec{V}_{P/I} + \left(\frac{{}^{B}\mathrm{d}\vec{\omega}_{B/I}}{\mathrm{d}t} + \cancelto{0}{\vec{\omega}_{B/I} \times \vec{\omega}_{B/I}} \right) \times (Q-P) + \quad \text{(parallel vectors)}$$

$$+ \vec{\omega}_{B/I} \times \left[\cancelto{0}{\frac{{}^{B}\mathrm{d}(Q-P)}{\mathrm{d}t}} + \vec{\omega}_{B/I} \times (Q-P) \right] = \quad \text{(rigid-body)}$$

$$= \frac{{}^{B}\mathrm{d}\vec{V}_{P/I}}{\mathrm{d}t} + \vec{\omega}_{B/I} \times \vec{V}_{P/I} + \frac{{}^{B}\mathrm{d}\vec{\omega}_{B/I}}{\mathrm{d}t} \times (Q-P) + \vec{\omega}_{B/I} \times [\vec{\omega}_{B/I} \times (Q-P)] \tag{A.5}$$

The inertia force acting on the generic point Q of the aircraft is given by:

$$\mathrm{d}\vec{F} = \mathrm{d}m\ \vec{a}_{Q/I} \tag{A.6}$$

To obtain the total force of inertia acting on the aircraft, Eq. (A.6) need to be integrated on the whole body:

$$\vec{F} = \int_B \mathrm{d}\vec{F} = \int_B \mathrm{d}m\ \vec{a}_{Q/I} =$$

$$= \int_B \mathrm{d}m\ \frac{{}^{B}\mathrm{d}\vec{V}_{P/I}}{\mathrm{d}t} + \int_B \mathrm{d}m\ \vec{\omega}_{B/I} \times \vec{V}_{P/I} - \int_B \mathrm{d}m\ (Q-P) \times \frac{{}^{B}\mathrm{d}\vec{\omega}_{B/I}}{\mathrm{d}t} +$$

$$+ \int_B \mathrm{d}m\ [(Q-P) \times \vec{\omega}_{B/I}] \times \vec{\omega}_{B/I} \tag{A.7}$$

For the last two terms of Eq. (A.7) the anticommutative property of the cross product was applied. Defining the mass and the tensor of static moments as:

$$m = \int_B \mathrm{d}m$$

$$\mathbf{S}_P = \int_B \mathrm{d}m\ (Q-P)_\times \tag{A.8}$$

Eq. (A.7) becomes:

$$\vec{F} = m\ \frac{{}^{B}\mathrm{d}\vec{V}_{P/I}}{\mathrm{d}t} + \vec{\omega}_{B/I} \times m\ \vec{V}_{P/I} - \mathbf{S}_P\ \frac{{}^{B}\mathrm{d}\vec{\omega}_{B/I}}{\mathrm{d}t} + (\mathbf{S}_P\ \vec{\omega}_{B/I}) \times \vec{\omega}_{B/I} \tag{A.9}$$

$\mathbf{S}_P$ is an skew-symmetric tensor, i.e., $\mathbf{S}_P = -\mathbf{S}_P^T$, so the minus sign of the third term becomes a plus if $\mathbf{S}_P$ is transposed:

$$\vec{F} = m\,\frac{{}^{B}\mathrm{d}\vec{V}_{P/I}}{\mathrm{d}t} + \vec{\omega}_{B/I} \times m\,\vec{V}_{P/I} + \mathbf{S}_P^T\,\frac{{}^{B}\mathrm{d}\vec{\omega}_{B/I}}{\mathrm{d}t} - \left(\mathbf{S}_P^T\,\vec{\omega}_{B/I}\right) \times \vec{\omega}_{B/I} \tag{A.10}$$

Applying again the anticommutative property of the cross product to the fourth term, Eq. (A.10).

$$\vec{F} = m\,\frac{{}^{B}\mathrm{d}\vec{V}_{P/I}}{\mathrm{d}t} + \vec{\omega}_{B/I} \times m\,\vec{V}_{P/I} + \mathbf{S}_P^T\,\frac{{}^{B}\mathrm{d}\vec{\omega}_{B/I}}{\mathrm{d}t} + \vec{\omega}_{B/I} \times \left(\mathbf{S}_P^T\,\vec{\omega}_{B/I}\right) \tag{A.11}$$

The moment with respect to the point P due to the inertia force acting on the generic point Q of the aircraft is given by:

$$\mathrm{d}\vec{M}_P = (Q-P) \times \mathrm{d}\vec{F} = \mathrm{d}m\;(Q-P) \times \vec{a}_{Q/I} \tag{A.12}$$

To obtain the total moment due to the force of inertia acting on the aircraft with respect to the point P, Eq. (A.12) need to be integrated on the whole body:

$$\begin{aligned}
\vec{M}_P = \int_B \mathrm{d}\vec{M}_P = \int_B \mathrm{d}m\;(Q-P) \times \vec{a}_{Q/I} = \\
= \int_B \mathrm{d}m\;(Q-P) \times \frac{{}^{B}\mathrm{d}\vec{V}_{P/I}}{\mathrm{d}t} + \int_B \mathrm{d}m\;(Q-P) \times \vec{\omega}_{B/I} \times \vec{V}_{P/I} + \\
- \int_B \mathrm{d}m\;(Q-P) \times (Q-P) \times \frac{{}^{B}\mathrm{d}\vec{\omega}_{B/I}}{\mathrm{d}t} + \\
- \int_B \mathrm{d}m\;\vec{\omega}_{B/I} \times (Q-P) \times [(Q-P) \times \vec{\omega}_{B/I}]
\end{aligned} \tag{A.13}$$

Applying Jacobi relation, which states that $\vec{a} \times \left(\vec{b} \times \vec{c}\right) + \vec{b} \times (\vec{c} \times \vec{a}) + \vec{c} \times \left(\vec{a} \times \vec{b}\right) = \vec{0}$, to the second term:

$$\begin{aligned}
\int_B \mathrm{d}m\;(Q-P) \times \left(\vec{\omega}_{B/I} \times \vec{V}_{P/I}\right) = -\int_B \mathrm{d}m\;\vec{\omega}_{B/I} \times \left(\vec{V}_{P/I} \times (Q-P)\right) + \\
- \int_B \mathrm{d}m\;\vec{V}_{P/I} \times ((Q-P) \times \vec{\omega}_{B/I}) = \\
= \int_B \mathrm{d}m\;\vec{\omega}_{B/I} \times \left((Q-P) \times \vec{V}_{P/I}\right) + \\
- \int_B \mathrm{d}m\;\vec{V}_{P/I} \times ((Q-P) \times \vec{\omega}_{B/I}) = \\
= \vec{\omega}_{B/I} \times \mathbf{S}_P\,\vec{V}_{P/I} - \vec{V}_{P/I} \times \mathbf{S}_P\,\vec{\omega}_{B/I}
\end{aligned} \tag{A.14}$$

Defining the tensor of inertia moments as:

$$\mathbf{J}_P = -\int_B \mathrm{d}m\;(Q-P)_\times\,(Q-P)_\times \tag{A.15}$$

applying the definition of $\mathbf{S}_P$ and replacing Eq. (A.14), Eq. (A.13) becomes:

$$\vec{M}_P = \mathbf{S}_P \frac{^B\mathrm{d}\vec{V}_{P/I}}{\mathrm{d}t} + \vec{\omega}_{B/I} \times \mathbf{S}_P\, \vec{V}_{P/I} + \vec{V}_{P/I} \times \mathbf{S}_P^T\, \vec{\omega}_{B/I} + \mathbf{J}_P \frac{^B\mathrm{d}\vec{\omega}_{B/I}}{\mathrm{d}t} + \vec{\omega}_{B/I} \times \mathbf{J}_P\, \vec{\omega}_{B/I} \quad \text{(A.16)}$$

Rearranging the terms and combining like terms:

$$\vec{M}_P = \mathbf{S}_P \frac{^B\mathrm{d}\vec{V}_{P/I}}{\mathrm{d}t} + \mathbf{J}_P \frac{^B\mathrm{d}\vec{\omega}_{B/I}}{\mathrm{d}t} + \vec{\omega}_{B/I} \times \left(\mathbf{S}_P\, \vec{V}_{P/I} + \mathbf{J}_P\, \vec{\omega}_{B/I}\right) + \vec{V}_{P/I} \times \mathbf{S}_P^T\, \vec{\omega}_{B/I} \quad \text{(A.17)}$$

For notation coherence the null term $\vec{V}_{P/I} \times m\, \vec{V}_{P/I}$ is added to Eq. (A.17):

$$\vec{M}_P = \mathbf{S}_P \frac{^B\mathrm{d}\vec{V}_{P/I}}{\mathrm{d}t} + \mathbf{J}_P \frac{^B\mathrm{d}\vec{\omega}_{B/I}}{\mathrm{d}t} + \vec{\omega}_{B/I} \times \left(\mathbf{S}_P\, \vec{V}_{P/I} + \mathbf{J}_P\, \vec{\omega}_{B/I}\right) + \vec{V}_{P/I} \times \left(\mathbf{S}_P^T\, \vec{\omega}_{B/I} + m\, \vec{V}_{P/I}\right) \quad \text{(A.18)}$$

Simplifying the notation, by adopting dot notation for time derivatives in the body reference frame, Eq. (A.11) and (A.18) become:

$$\begin{aligned} m\, \dot{\vec{V}}_{P/I} + \mathbf{S}_P^T\, \dot{\vec{\omega}}_{B/I} + \vec{\omega}_{B/I} \times \left(m\, \vec{V}_{P/I} + \mathbf{S}_P^T\, \vec{\omega}_{B/I}\right) &= \vec{F} \\ \mathbf{S}_P \dot{\vec{V}}_{P/I} + \mathbf{J}_P\, \dot{\vec{\omega}}_{B/I} + \vec{V}_{P/I} \times \left(m\, \vec{V}_{P/I} + \mathbf{S}_P^T\, \vec{\omega}_{B/I}\right) + \vec{\omega}_{B/I} \times \left(\mathbf{S}_P\, \vec{V}_{P/I} + \mathbf{J}_P\, \vec{\omega}_{B/I}\right) &= \vec{M}_P \end{aligned} \quad \text{(A.19)}$$

The origin of the body reference frame P is typically located at the aircraft center of gravity G, meaning that $\mathbf{S}_P = \mathbf{S}_G = 0$. Eq. (A.19) become:

$$\begin{aligned} m\, \dot{\vec{V}}_{G/I} + \vec{\omega}_{B/I} \times m\, \vec{V}_{G/I} &= \vec{F} \\ \mathbf{J}_G\, \dot{\vec{\omega}}_{B/I} + \vec{\omega}_{B/I} \times \mathbf{J}_G\, \vec{\omega}_{B/I} &= \vec{M}_G \end{aligned} \quad \text{(A.20)}$$

To express Eq. (A.20) in scalar form, the components of the velocity vector and the angular velocity vector, and those of the forces and moments in the body reference frame are introduced:

$$\vec{V}_{G/I} = \begin{Bmatrix} u \\ v \\ w \end{Bmatrix} \quad \text{(A.21)}$$

$$\vec{\omega}_{B/I} = \begin{Bmatrix} p \\ q \\ r \end{Bmatrix} \quad \text{(A.22)}$$

$$\vec{F} = \begin{Bmatrix} F_x \\ F_y \\ F_z \end{Bmatrix} \tag{A.23}$$

$$\vec{M}_G = \begin{Bmatrix} L \\ M \\ N \end{Bmatrix} \tag{A.24}$$

and a further simplification is adopted, i.e., the aircraft is symmetric with respect to the plane z-x ($I_{xy} = I_{yx} = 0$, $I_{yz} = I_{zy} = 0$, $I_{xz} = I_{zx}$):

$$\mathbf{J}_G = \begin{bmatrix} I_{xx} & -I_{xy} & -I_{xz} \\ -I_{yx} & I_{yy} & -I_{yz} \\ -I_{zx} & -I_{zy} & I_{zz} \end{bmatrix} = \begin{bmatrix} I_{xx} & 0 & -I_{xz} \\ 0 & I_{yy} & 0 \\ -I_{xz} & 0 & I_{zz} \end{bmatrix} \tag{A.25}$$

In scalar form, Eq. (A.20) becomes:

$$\begin{aligned} m\left(\dot{u} + qw - rv\right) &= F_x \\ m\left(\dot{v} + ru - pw\right) &= F_y \\ m\left(\dot{w} + pv - qu\right) &= F_z \\ I_{xx}\dot{p} - I_{xz}\dot{r} + q\left(I_{zz}r - I_{xz}p\right) - rqI_{yy} &= L \\ I_{yy}\dot{q} + r\left(I_{xx}p - I_{xz}r\right) - p\left(I_{zz}r - I_{xz}p\right) &= M \\ I_{zz}\dot{r} - I_{xz}\dot{p} + q\left(-I_{xx}p + I_{xz}r\right) + pqI_{yy} &= N \end{aligned} \tag{A.26}$$

Separating the gravity components from the external (aerodynamic) force components, Eq. (A.26) becomes:

$$\begin{aligned} m\left(\dot{u} + qw - rv\right) + mg\sin\theta &= X \\ m\left(\dot{v} + ru - pw\right) - mg\cos\theta\sin\phi &= Y \\ m\left(\dot{w} + pv - qu\right) - mg\cos\theta\cos\phi &= Z \\ I_{xx}\dot{p} - I_{xz}\dot{r} + q\left(I_{zz}r - I_{xz}p\right) - rqI_{yy} &= L \\ I_{yy}\dot{q} + r\left(I_{xx}p - I_{xz}r\right) - p\left(I_{zz}r - I_{xz}p\right) &= M \\ I_{zz}\dot{r} - I_{xz}\dot{p} + q\left(-I_{xx}p + I_{xz}r\right) + pqI_{yy} &= N \end{aligned} \tag{A.27}$$

The system of Eq. (A.27) represents the classical 6-DOF (degrees of freedom) rigid-body equations. To simulate autorotation, however, it is necessary to increase the order of the model, to include the main-rotor speed DOF. Assuming that the transmission is rigid, it is sufficient to add a single equation representing a torque balance and update the yaw dynamics equation to account for the coupling with the airframe:

$$(I_{zz} + I_R)\dot{r} - I_R\ddot{\psi}_m r - I_{xz}\dot{p} + q\left(-I_x p + I_{xz} r\right) + pqI_y = N \tag{A.28}$$

$$I_R\left(\ddot{\psi}_{mr} - \dot{r}\right) = \cancelto{0 \text{ in autorotation}}{Q_{eng}} - Q_{mr} - g_{tr}Q_{tr} \tag{A.29}$$

where I_R is the polar inertia of the rotor (it does not keep into account only the inertia of the blades, but also the inertia of the transmission), $g_{tr} = \frac{\Omega_{tr}}{\Omega_{mr}}$. This equation is derived in Appendix D relaxing the constraint of rigid transmission, thus becoming a system of equations, known as engine-drivetrain dynamics.

The external forces and moments can be written as the sum of the contributions from the different aircraft components, i.e., main rotor, tail rotor, fuselage, horizontal tailplane, and vertical fin. As an example:

$$X = X_{mr} + X_{tr} + X_{fus} + X_{tp} + X_{fn} \tag{A.30}$$

where the subscripts stand for: main rotor, mr; tail rotor, tr; fuselage, fus; horizontal tailplane, tp; and vertical fin, fn. Next section summarizes how these different components are calculated in the model developed in this thesis.

A.2. CONTRIBUTION OF THE DIFFERENT HELICOPTER COMPONENTS TO EXTERNAL FORCES AND MOMENTS

A.2.1. ROTORS

The analytical expressions of forces and moments generated by the two rotors are taken from a report by Chen [1979, 1980], then implemented for piloted simulation by Talbot et al. [1982], which are derived according to the following simplifications and assumptions:

- The rotor blade was assumed to be rigid with linear twist.
- Uniform inflow was considered.
- Both flapping and inflow angles were assumed to be small.
- Simple strip theory was used.
- The reversed-flow region was ignored, and compressibility and stall effects were not considered.
- The tail rotor was modeled as a teetering rotor without cyclic pitch.

As an additional assumption, steady-state tip-path plane dynamics was considered for the model developed in this thesis. Furthermore, for the real-time simulation, quasi-steady dynamic inflow was used [Pavel, 2001].

TIP-PATH PLANE DYNAMICS

For small flapping angles, the flapping dynamics equation of each rotor blade is a second order, linear differential equation with non-constant coefficients. To approximate the flapping motion of the whole rotor, tip-path plane dynamics is often used in helicopter theory, which consists in the following transformation:

$$\beta_i = a_0 - \sum_{n=1}^{k} \left(a_n \cos\left(n\psi_i\right) + b_n \sin\left(n\psi_i\right)\right), \text{ with } i = 1 : N_b \tag{A.31}$$

By applying the transformation of Eq. (A.31) with $k = 1$ to the flapping dynamic equation of each rotor blade, the following system of equation is obtained:

$$\ddot{\vec{a}}_{tpp} + D_{tpp}\dot{\vec{a}}_{tpp} + K_{tpp}\vec{a}_{tpp} = \vec{f}_{tpp} + \vec{f}_{tpp_{precone}} \tag{A.32}$$

where:

$$\vec{a}_{tpp} = \left\{ \begin{array}{ccc} a_0 & a_1 & b_1 \end{array} \right\}^T \tag{A.33}$$

and D_{tpp}, K_{tpp} and $\vec{f}_{tpp}$ are taken from Chen [1980], whereas $\vec{f}_{tpp_{precone}}$ is an additional term that was derived to keep into account the effects of the precone, modelled as a pretension in the flapping moment due to the spring rotor stiffness ($M_{R_i} = -K_\beta\left(\beta_i - a_{0_p}\right)$):

$$\vec{f}_{tpp} = \left\{ \begin{array}{ccc} \frac{K_\beta}{I_\beta} a_{0_p} & 0 & 0 \end{array} \right\}^T \tag{A.34}$$

For a two-bladed teetering rotor, configuration typically adopted for tail-rotors, the tip-path plane representation loses its physical meaning. However, if the approximation of Eq. (A.31) for the blade flapping is employed, then a_0 is to be treated as a preset constant. The coefficients $a_1(t)$ and $b_1(t)$ can then be solved by setting $\dot{a}_0 = 0$ and $\ddot{a}_0 = 0$.

This means that the model has 12-DOF in total for a non-teetering main-rotor (6-DOF rigid-body dynamics, 1-DOF main-rotor rpm, 3-DOF main-rotor tip-path plane dynamics, 2-DOF main-rotor tip-path plane dynamics) and 11-DOF for a teetering main rotor (6-DOF rigid-body dynamics, 1-DOF main-rotor rpm, 2-DOF main-rotor tip-path plane dynamics, 2-DOF main-rotor tip-path plane dynamics). However, in the model used in this thesis, steady-state tip-path plane dynamics was considered:

$$\begin{aligned} \dot{a}_0 &= 0 \\ \dot{a}_1 &= 0 \\ \dot{b}_1 &= 0 \end{aligned} \tag{A.35}$$

$$\begin{aligned} \ddot{a}_0 &= 0 \\ \ddot{a}_1 &= 0 \\ \ddot{b}_1 &= 0 \end{aligned} \tag{A.36}$$

reducing the number of DOF to 7 for a non-teetering main-rotor (6 in case of teetering main-rotor), because the following linear system can be solved at every time-step:

$$K_{tpp}\vec{a}_{tpp} = \vec{f}_{tpp} \tag{A.37}$$

$$\vec{a}_{tpp} = K_{tpp}^{-1}\vec{f}_{tpp} \tag{A.38}$$

A.2.2. FUSELAGE

Fuselage force and moment coefficients (forces and moments divided by dynamic pressure $q_{fus} = \frac{1}{2}\rho_{air}V_{fus}^2$) are obtained from look-up tables as a function of the fuselage incidence (from -180 deg to 180 deg) and sideslip (from -90 deg to 90 deg). These tables derive from wind-tunnel tests of the Bo-105 fuselage and are represented in Fig. A.1.

To obtain the fuselage moments at the helicopter center of gravity, it is necessary to transport the fuselage forces from the fuselage aerodynamic pressure to the helicopter center of gravity:

$$\begin{aligned} \vec{F}_{fus_G} &= \vec{F}_{fus_{AC}} \\ \vec{M}_{fus_G} &= \vec{M}_{fus_{AC}} + \left(AC_{fus} - G\right) \times \vec{F}_{fus_{AC}} \end{aligned} \tag{A.39}$$

A.2.3. HORIZONTAL TAILPLANE

Horizontal tailplane force and moment coefficients (forces and moments divided by dynamic pressure $q_{tp} = \frac{1}{2}\rho_{air}V_{tp}^2$) are obtained from look-up tables as a function of the tailplane incidence (from -90 deg to 90 deg) and sideslip (from -90 deg to 90 deg). These tables derive from wind-tunnel tests of the NACA 0010/0020 profile and are represented in Fig. A.2.

To obtain the tailplane moments at the helicopter center of gravity, it is necessary to transport the tailplane forces from the tailplane aerodynamic pressure to the helicopter center of gravity:

$$\begin{aligned} \vec{F}_{tp_G} &= \vec{F}_{tp_{AC}} \\ \vec{M}_{tp_G} &= \vec{M}_{tp_{AC}} + \left(AC_{tp} - G\right) \times \vec{F}_{tp_{AC}} \end{aligned} \tag{A.40}$$

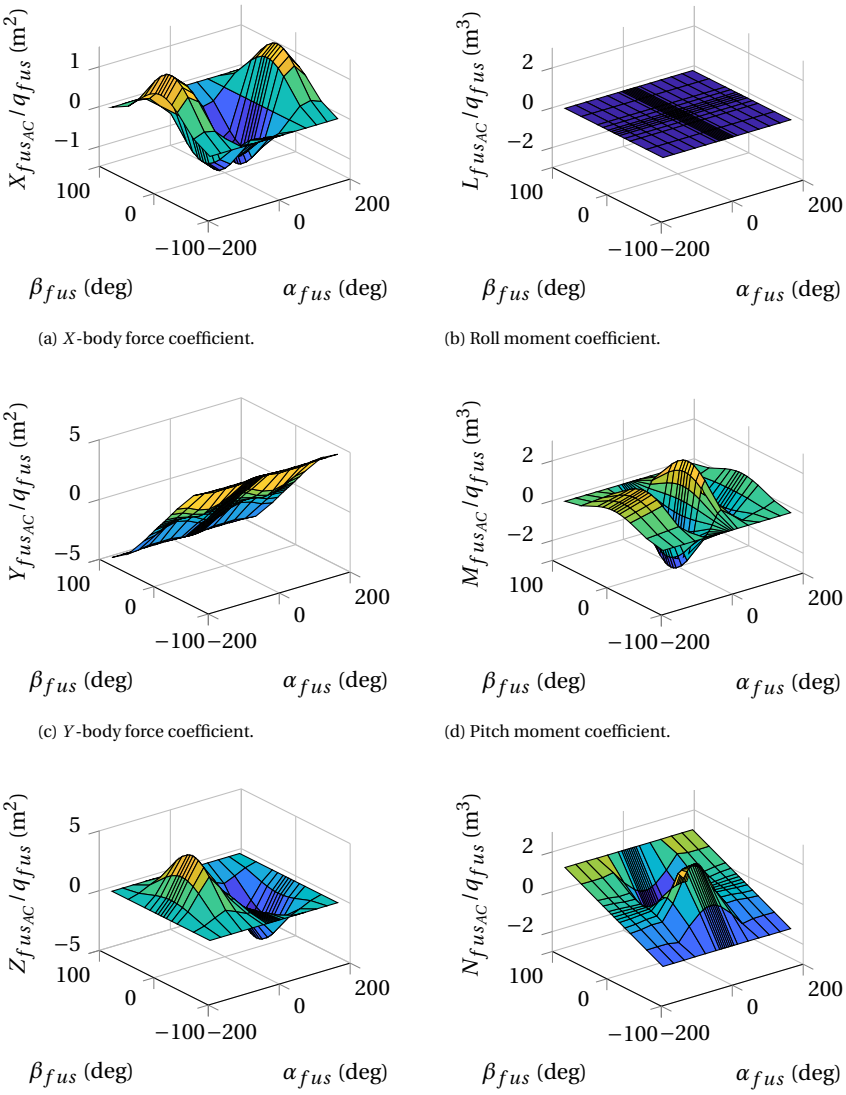

(a) X-body force coefficient.

(b) Roll moment coefficient.

(c) Y-body force coefficient.

(d) Pitch moment coefficient.

(e) Z-body force coefficient.

(f) Yaw moment coefficient.

Figure A.1: Fuselage force and moment coefficients.

A.2.4. VERTICAL FIN

Vertical fin force and moment coefficients (forces and moments divided by dynamic pressure $q_{fn} = \frac{1}{2}\rho_{air}V_{fn}^2$) are obtained from look-up tables as a function of the fin incidence (from -90 deg to 60 deg) and sideslip (from -35 deg to 90 deg). These tables derive from wind-tunnel tests of the NACA 65(3)-618 profile and are represented in Fig. A.3.

To obtain the fin moments at the helicopter center of gravity, it is necessary to trans-

port the fin forces from the fin aerodynamic pressure to the helicopter center of gravity:

$$\begin{aligned}\vec{F}_{fn_G} &= \vec{F}_{fn_{AC}} \\ \vec{M}_{fn_G} &= \vec{M}_{fn_{AC}} + \left(AC_{fn} - G\right) \times \vec{F}_{fn_{AC}}\end{aligned} \tag{A.41}$$

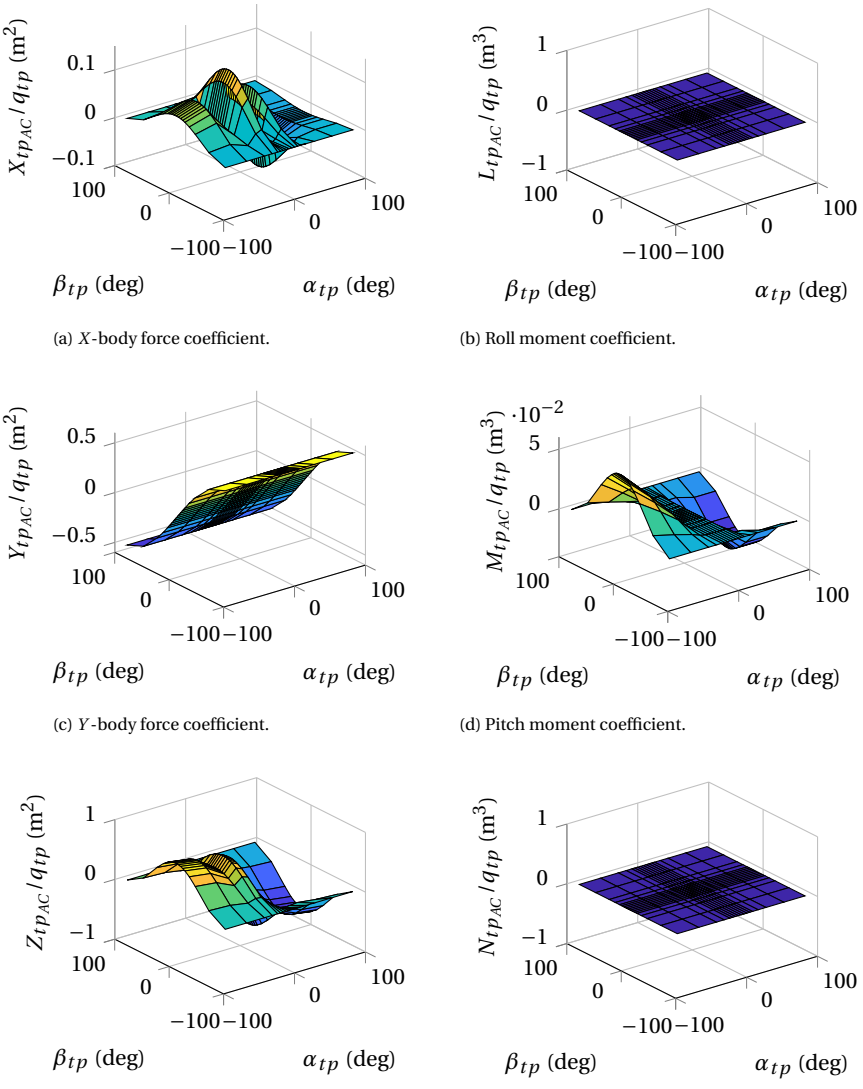

(a) X-body force coefficient.

(b) Roll moment coefficient.

(c) Y-body force coefficient.

(d) Pitch moment coefficient.

(e) Z-body force coefficient.

(f) Yaw moment coefficient.

Figure A.2: Horizontal tailplane force and moment coefficients.

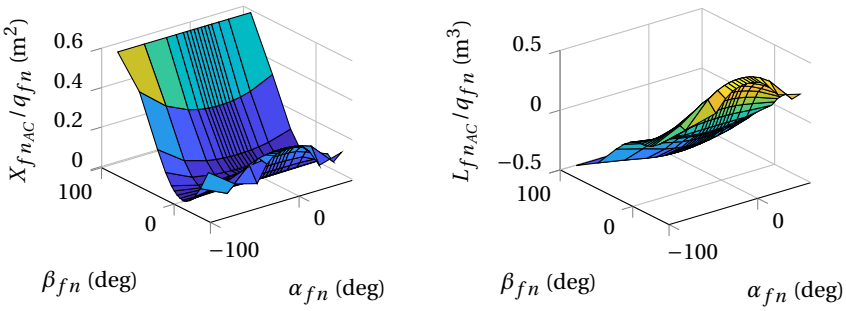

(a) X-body force coefficient.

(b) Roll moment coefficient.

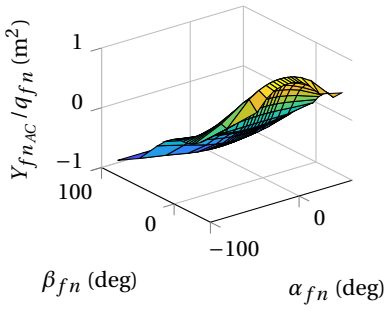

(c) Y-body force coefficient.

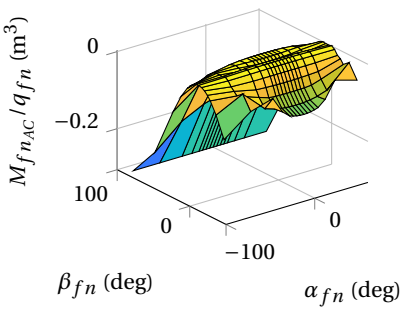

(d) Pitch moment coefficient.

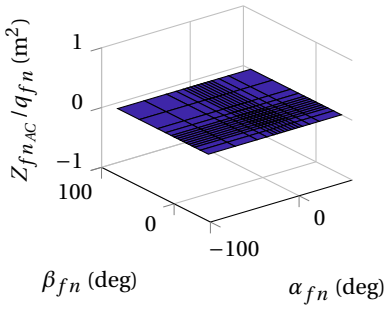

(e) Z-body force coefficient.

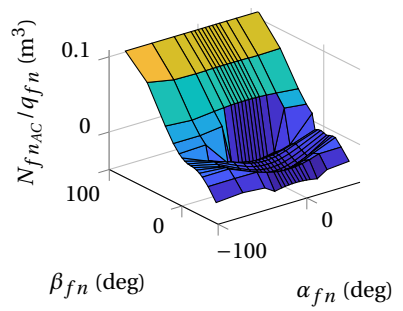

(f) Yaw moment coefficient.

Figure A.3: Vertical fin force and moment coefficients.

A.3. WAKE MODEL

To calculate the downwash at the different helicopter components (i.e., aerodynamic centers of the fuselage, horizontal tailplane and vertical fin, and tail-rotor hub), a wake model was implemented. Essentially, two different approaches to model rotor wakes exist: prescribed and free-wake models. Prescribed wake models are computationally more efficient than free-wake models, but also less accurate.

The wake model implemented in the flight mechanics model developed in this thesis is a prescribed wake model, known as Beddoes wake [Beddoes, 1985]. According to this

wake model, each blade produces a tip vortex. Two different wake geometries can be adopted in this model: the undistorted, which assumes uniform inflow, and the distorted wake, which accounts for the departure from uniform inflow induced by the skewness of the wake. The geometry of the distorted wake considering linear inflow along the disc is shown in Fig. A.4 for a four-bladed rotor with $\frac{C_T}{\sigma} = 0.07$ and $\mu = 0.04$.

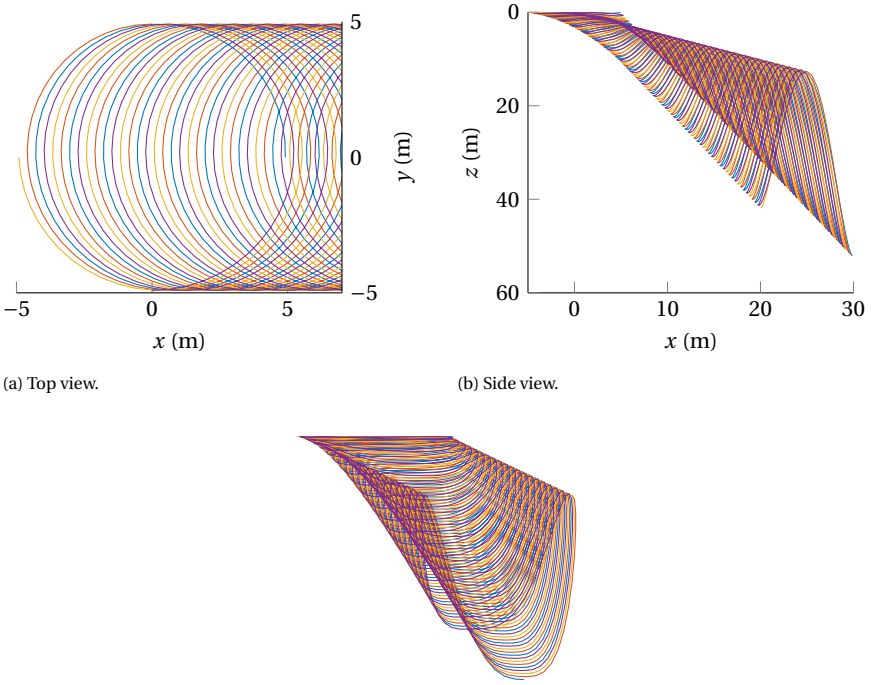

(a) Top view.

(b) Side view.

(c) 3-D view (rear view from above the disc plane).

Figure A.4: Beddoes distorted wake geometry with linear inflow along the disc for a four-bladed rotor with $\frac{C_T}{\sigma} = 0.07$ and $\mu = 0.04$.

The velocity induced by each tip vortex element of length $d\vec{l}$ in a generic point $P(x, y, z)$ is calculated using Biot-Savart law:

$$\vec{V}(x, y, z) = \frac{\Gamma}{4\pi} \int_{-\infty}^{\infty} \frac{d\vec{l} \times \vec{r}}{|\vec{r}|^3} \tag{A.42}$$

where $\vec{r}$ is the distance between the point P and the tip vortex element and the circulation is calculated as:

$$\Gamma = \frac{2C_T}{\sigma} cR\Omega_{mr} \tag{A.43}$$

For numerical evaluation of Eq. (A.42), each tip vortex is discretized in N_v elements:

$$\vec{V}(P) = \frac{\Gamma}{4\pi} \sum_{i=1}^{N_v} \frac{\mathrm{d}\vec{l}_i \times (P - V_i)}{|(P - V_i)|^3} \tag{A.44}$$

The total induced velocity is then obtained by summing the contribution of each blade's tip vortex.

The results from the implemented wake model were compared with those available in the charts of the induced velocity near a lifting rotor produced by Castles et al. [1954] and Heyson et al. [1957]. These charts show the contour of the induced velocity normalized by the induced velocity at the center of the rotor disk in the longitudinal plane of symmetry (z-x plane) for several wake skew angles ($\chi = \arctan_2 \frac{\mu}{-\lambda}$). The results from the implemented wake model are in good agreement with those presented by Castles et al. [1954] and Heyson et al. [1957] for all the wake skew angles. As an example, Fig. A.5 shows the contours of the induced velocity ratio from the Beddoes wake model and those from Castles et al. [1954] and Heyson et al. [1957] for a wake skew angle of 63 deg.

As an alternative to wake models, empirical methods can also be used to estimate the downwash at the points of interest.

A.3.1. GROUND EFFECT

A lifting rotor incurs a favorable interference when operating very close to the ground [Heyson, 1960]. In this condition, the rotor downwash field is strongly influenced by the ground surface. To incorporate this effect, known as ground effect, in the model, a variation of the induced velocity at the center of the rotor was considered as proposed by Heyson [1960] (Fig. A.6):

$$\frac{w_{i_{IGE}}}{w_{i_{OGE}}} = 1 + \frac{\Delta w_i}{w_{i_{OGE}}} \tag{A.45}$$

Fig. A.6 shows that ground effect decreases rapidly with increases in either height above the ground or forward speed (increasing wake skew angle).

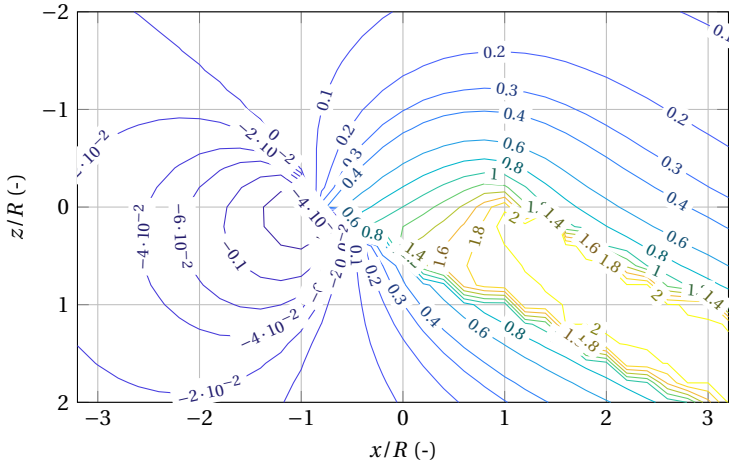

(a) $\chi = 63$ deg (Beddoes wake model developed in this thesis).

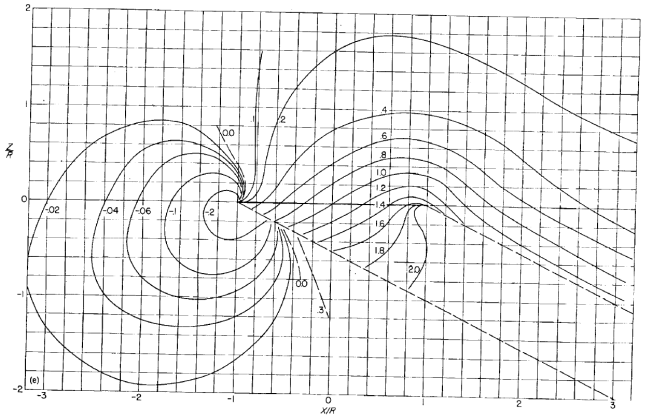

(b) $\chi = 63$ deg [Castles et al., 1954].

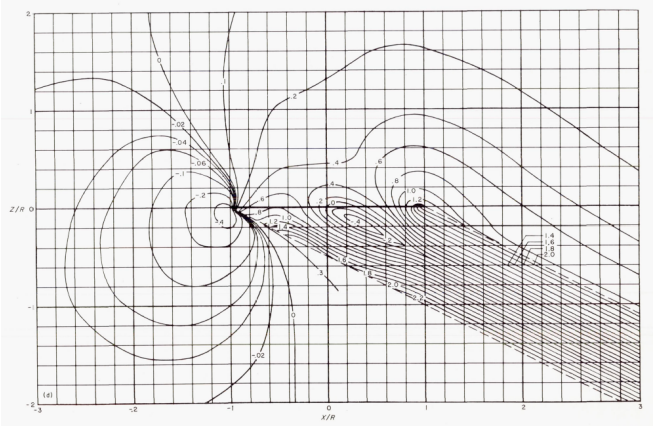

(c) $\chi = 63$ deg [Heyson et al., 1957].

Figure A.5: Contour of the induced velocity ratio in the longitudinal plane of symmetry.

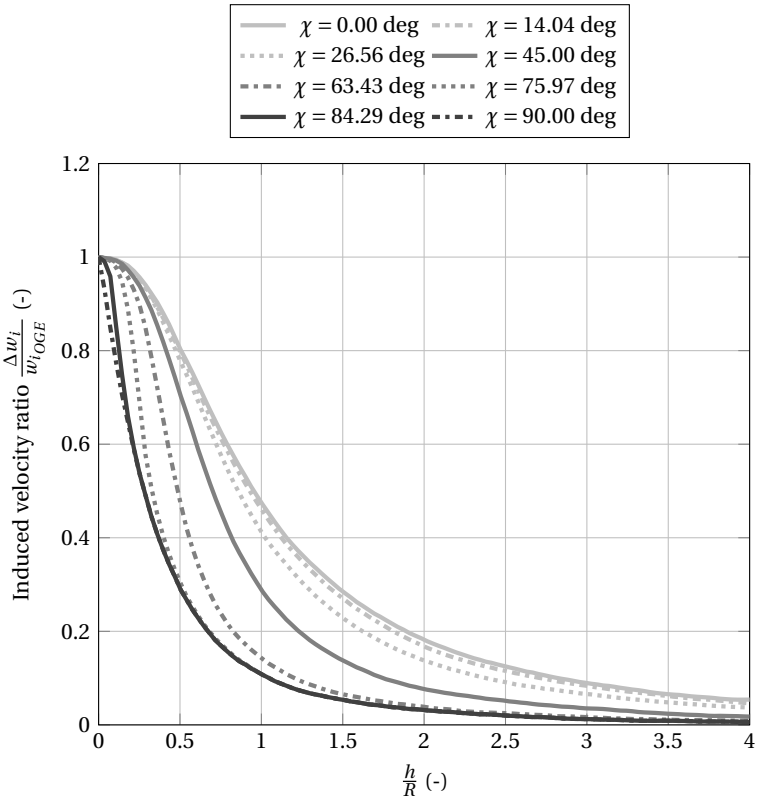

Figure A.6: variation of the induced velocity at the center of the rotor as a function of the altitude above the ground and the wake skew angle [Heyson, 1960].

B

TRIM PROCEDURE

B.1. DEFINITION OF THE TRIM PROBLEM

The classical rigid-body equations of motion are:

$$\begin{aligned}
m\left(\dot{u}+qw-rv\right)+mg\sin\theta &= X\left(u,v,w,p,q,r,\theta_0,A_1,B_1,\theta_{0_{tr}}\right)\\
m\left(\dot{v}+ru-pw\right)-mg\cos\theta\sin\phi &= Y\left(u,v,w,p,q,r,\theta_0,A_1,B_1,\theta_{0_{tr}}\right)\\
m\left(\dot{w}+pv-qu\right)-mg\cos\theta\cos\phi &= Z\left(u,v,w,p,q,r,\theta_0,A_1,B_1,\theta_{0_{tr}}\right)\\
I_{xx}\dot{p}-I_{xz}\dot{r}+q\left(I_{zz}r-I_{xz}p\right)-rqI_{yy} &= L\left(u,v,w,p,q,r,\theta_0,A_1,B_1,\theta_{0_{tr}}\right)\\
I_{yy}\dot{q}+r\left(I_{xx}p-I_{xz}r\right)-p\left(I_{zz}r-I_{xz}p\right) &= M\left(u,v,w,p,q,r,\theta_0,A_1,B_1,\theta_{0_{tr}}\right)\\
I_{zz}\dot{r}-I_{xz}\dot{p}+q\left(-I_{xx}p+I_{xz}r\right)+pqI_{yy} &= N\left(u,v,w,p,q,r,\theta_0,A_1,B_1,\theta_{0_{tr}}\right)
\end{aligned} \tag{B.1}$$

In addition to the dynamics equations of Eq. (B.1), kinematics equations can be derived to express the relationship between:

- the body angular rates and Euler angles and rates:

$$\begin{aligned}
p &= \dot{\phi}-\dot{\psi}\sin\left(\theta\right)\\
q &= \dot{\theta}\cos\left(\phi\right)+\dot{\psi}\sin\left(\phi\right)\cos\left(\theta\right)\\
r &= -\dot{\theta}\sin\left(\phi\right)+\dot{\psi}\cos\left(\phi\right)\cos\left(\theta\right)
\end{aligned} \tag{B.2}$$

- the flight path angle and the vertical and horizontal speed:

$$\gamma = \arctan\left(\frac{V_z}{\sqrt{V_x^2+V_y^2}}\right) \tag{B.3}$$

- the flight speed and the vertical and horizontal speed:

$$V_f = \sqrt{\left(\sqrt{V_x^2 + V_y^2}\right)^2 + V_z^2} = \frac{\sqrt{V_x^2 + V_y^2}}{\sin\gamma} \tag{B.4}$$

- the speed along y-body axis:

$$v = V_f \sin\left(\beta\right) \tag{B.5}$$

- the speed along x-body axis:

$$u = V_f \cos\left(\beta\right)\cos\left(\alpha\right) \tag{B.6}$$

- the speed along z-body axis:

$$w = V_f \cos\left(\beta\right)\sin\left(\alpha\right) = u\tan\alpha \tag{B.7}$$

- the flight path angle:

$$\sin\left(\gamma\right) = \cos\left(\alpha\right)\cos\left(\beta\right)\sin\left(\theta\right) - \sin\left(\beta\right)\sin\left(\phi\right)\cos\left(\theta\right) - \sin\left(\alpha\right)\cos\left(\beta\right)\cos\left(\phi\right)\cos\left(\theta\right) \tag{B.8}$$

In an equilibrium condition, the following relations apply for the dynamics (Eq. (B.1)):

$$\begin{aligned} \dot{u} &= 0 \\ \dot{v} &= 0 \\ \dot{w} &= 0 \\ \dot{p} &= 0 \\ \dot{q} &= 0 \\ \dot{r} &= 0 \end{aligned} \tag{B.9}$$

and for the kinematics (Eq. (B.2)):

$$\begin{aligned} \dot{\phi} &= 0 \\ \dot{\theta} &= 0 \end{aligned} \tag{B.10}$$

Replacing Eq. (B.9) in Eq. (B.1) and using capital letters with subscript e to indicate the linear and angular rates and the attitudes, we obtain:

$$\begin{aligned}
m\left(Q_e W_e - R_e V_e\right) &= -mg\sin\Theta_e + X_e\left(U_e, V_e, W_w, P_e, Q_e, R_e, \theta_{0_e}, A_{1_e}, B_{1_e}, \theta_{0_{tre}}\right)\\
m\left(R_e U_e - P_e W_e\right) &= mg\cos\Theta_e \sin\Phi_e + Y_e\left(U_e, V_e, W_w, P_e, Q_e, R_e, \theta_{0_e}, A_{1_e}, B_{1_e}, \theta_{0_{tre}}\right)\\
m\left(P_e V_e - Q_e U_e\right) &= mg\cos\Theta_e \cos\Phi_e + Z_e\left(U_e, V_e, W_w, P_e, Q_e, R_e, \theta_{0_e}, A_{1_e}, B_{1_e}, \theta_{0_{tre}}\right)\\
Q_e\left(I_{zz}R_e - I_{xz}P_e\right) - R_e Q_e I_{yy} &= L_e\left(U_e, V_e, W_w, P_e, Q_e, R_e, \theta_{0_e}, A_{1_e}, B_{1_e}, \theta_{0_{tre}}\right)\\
R_e\left(I_{xx}P_e - I_{xz}R_e\right) - P_e\left(I_{zz}R_e - I_{xz}P_e\right) &= M_e\left(U_e, V_e, W_w, P_e, Q_e, R_e, \theta_{0_e}, A_{1_e}, B_{1_e}, \theta_{0_{tre}}\right)\\
Q_e\left(-I_{xx}P_e + I_{xz}R_e\right) + P_e Q_e I_{yy} &= N_e\left(U_e, V_e, W_w, P_e, Q_e, R_e, \theta_{0_e}, A_{1_e}, B_{1_e}, \theta_{0_{tre}}\right)
\end{aligned} \tag{B.11}$$

Similarly, replacing Eq. (B.10) in Eq. (B.2), we obtain:

$$\begin{aligned}
P_e &= -\dot{\Psi}_e \sin\left(\Theta_e\right)\\
Q_e &= \dot{\Psi}_e \sin\left(\Phi_e\right)\cos\left(\Theta_e\right)\\
R_e &= \dot{\Psi}_e \cos\left(\Phi_e\right)\cos\left(\Theta_e\right)
\end{aligned} \tag{B.12}$$

Eq. (B.3) to (B.8) can be rewritten in terms of equilibrium quantities:

- the flight path angle:

$$\gamma_e = \arctan\left(\frac{V_{z_e}}{\sqrt{V_{x_e}^2 + V_{y_e}^2}}\right) \tag{B.13}$$

- the flight speed:

$$V_{f_e} = \sqrt{\left(\sqrt{V_{x_e}^2 + V_{y_e}^2}\right)^2 + V_{z_e}^2} = \frac{\sqrt{V_{x_e}^2 + V_{y_e}^2}}{\sin\gamma_e} \tag{B.14}$$

- the speed along y-body axis:

$$V_e = V_{f_e}\sin\left(\beta_e\right) \tag{B.15}$$

- the speed along x-body axis:

$$U_e = V_{f_e}\cos\left(\beta_e\right)\cos\left(\alpha_e\right) \tag{B.16}$$

- the speed along z-body axis:

$$W_e = V_{f_e} \cos\left(\beta_e\right) \sin\left(\alpha_e\right) = U_e \tan \alpha_e \tag{B.17}$$

- the flight path angle:

$$\begin{aligned} \sin\left(\gamma_e\right) = &\cos\left(\alpha_e\right) \cos\left(\beta_e\right) \sin\left(\Theta_e\right) - \sin\left(\beta_e\right) \sin\left(\Phi_e\right) \cos\left(\Theta_e\right) + \\ &- \sin\left(\alpha_e\right) \cos\left(\beta_e\right) \cos\left(\Phi_e\right) \cos\left(\Theta_e\right) \end{aligned} \tag{B.18}$$

In total we have 15 equations and 19 unknowns:

$$\begin{aligned} \{ \; \theta_{0_e} \quad A_{1_e} \quad B_{1_e} \quad \theta_{0_{tr_e}} \quad \Phi_e \quad \Theta_e \quad \dot{\Psi}_e \quad P_e \quad Q_e \quad R_e \quad U_e \quad V_e \quad W_e \quad \alpha_e \quad \beta_e \\ \gamma_e \quad \sqrt{V_{x_e}^2 + V_{y_e}^2} \quad V_{z_e} \quad V_{f_e} \; \} \end{aligned} \tag{B.19}$$

This means that we need to set 4 quantities:

$$\left\{ \; \dot{\Psi}_e \quad \sqrt{V_{x_e}^2 + V_{y_e}^2} \quad V_{z_e} \quad \beta_e \; \right\} \tag{B.20}$$

This leads to 15 unknowns in 15 equations:

$$\{ \; \theta_{0_e} \quad A_{1_e} \quad B_{1_e} \quad \theta_{0_{tr_e}} \quad \Phi_e \quad \Theta_e \quad P_e \quad Q_e \quad R_e \quad U_e \quad V_e \quad W_e \quad \alpha_e \quad \gamma_e \quad V_{f_e} \; \} \tag{B.21}$$

However from the set quantities (B.20), we can evaluate in closed form some of the unknowns, such as P_e, Q_e, and R_e from Eq. (B.12), γ_e from Eq. (B.13), V_{f_e} from Eq. (B.14), and V_e from Eq. (B.15), while α_e can be expressed as a function of U_e and W_e (Eq. (B.17)). This leads to 8 unknowns in 8 equations (Eq. (B.11), (B.16), (B.18)):

$$\{ \; \theta_{0_e} \quad A_{1_e} \quad B_{1_e} \quad \theta_{0_{tr_e}} \quad \Phi_e \quad \Theta_e \quad U_e \quad W_e \; \} \tag{B.22}$$

B.1.1. TRIM IN AUTOROTATION

For helicopters, autorotation represents an emergency maneuver that has to be performed in case of total power loss ($Q_{eng} = 0$). Therefore, the common assumption of constant rotor angular velocity is no longer justified in case of autorotative flight. As soon as the pilot recognizes that an engine failure has occurred, he needs to preserve as much as possible rotorspeed at the expenses of the helicopter's potential energy (altitude). Ideally, the pilot should enter a steady descent in autorotation, i.e. a condition in which the helicopter is descending at a constant rate of descent, whose value is such

that the required torque (main-rotor + tail rotor torques) is zero [Prouty, 2002]. A new equation need to be added to the system of Eq. (B.1):

$$I_R\left(\ddot{\psi}_{mr}-\dot{r}\right)=\cancelto{0 \text{ in autorotation}}{Q_{eng}}-Q_{mr}\left(u,v,w,p,q,r,\dot{\psi}_m r,\theta_0,A_1,B_1,\theta_{0_{tr}}\right)+ \\ -g_{tr}Q_{tr}\left(u,v,w,p,q,r,\dot{\psi}_m r,\theta_0,A_1,B_1,\theta_{0_{tr}}\right) \tag{B.23}$$

In an equilibrium condition, the following condition needs to be added to the system of Eq. (B.9):

$$\ddot{\psi}_{mr}=0 \tag{B.24}$$

Replacing Eq. (B.24) in Eq. (B.23), we obtain:

$$Q_{mr}\left(U_e,V_e,W_w,P_e,Q_e,R_e,\Omega_m r,\theta_{0_e},A_{1_e},B_{1_e},\theta_{0_{tr_e}}\right)+ \\ +g_{tr}Q_{tr}\left(U_e,V_e,W_w,P_e,Q_e,R_e,\Omega_m r,\theta_{0_e},A_{1_e},B_{1_e},\theta_{0_{tr_e}}\right)=0 \tag{B.25}$$

In total we have 16 equations and 19 unknowns (Eq. (B.19)). This means that we need to set only 3 quantities in autorotation:

$$\left\{\begin{array}{ccc}\dot{\Psi}_e & \sqrt{V_{x_e}^2+V_{y_e}^2} & \beta_e\end{array}\right\} \tag{B.26}$$

This leads to 16 unknowns in 16 equations in autorotation:

$$\left\{\begin{array}{cccccccccccccccc}\theta_{0_e} & A_{1_e} & B_{1_e} & \theta_{0_{tr_e}} & \Phi_e & \Theta_e & P_e & Q_e & R_e & U_e & V_e & W_e & \alpha_e & \gamma_e & V_{z_e} & V_{f_e}\end{array}\right\} \tag{B.27}$$

However from the set quantities (B.20), we can evaluate in closed form some of the unknowns, such as P_e, Q_e, and R_e from Eq. (B.12), whereas we can express γ_e from Eq. (B.13), V_{f_e} from Eq. (B.14), and V_e from Eq. (B.15) as a function of V_{z_e} and α_e as a function of U_e and W_e (Eq. (B.17)). This leads to 9 unknowns in 9 equations:

$$\left\{\begin{array}{ccccccccc}\theta_{0_e} & A_{1_e} & B_{1_e} & \theta_{0_{tr_e}} & \Phi_e & \Theta_e & U_e & W_e & V_{z_e}\end{array}\right\} \tag{B.28}$$

B.2. FORMULATION OF THE TRIM PROBLEM AS AN OPTIMIZATION PROCEDURE

Several methods are available to trim the aircraft model or dynamic subsystems, such as sequential-correction, fly-to-trim, and NewtonRaphson or Jacobian method [Dreier, 2018].

Another widely accepted numerical method to find a generic steady-state flight condition is based on the minimization of a cost function [De Marco et al., 2007; Houston,

1994]. The cost function is, by definition, always non-negative and evaluates to zero when the aircraft is in a steady-state flight. A minimization algorithm finds the values of control inputs and of some state variables that make the cost function zero.

Typically the cost function is derived from the dynamic equations of motion. A good choice is the quadratic function:

$$J = \dot{u}^2 + \dot{v}^2 + \dot{w}^2 + \dot{p}^2 + \dot{q}^2 + \dot{r}^2 + \dots \tag{B.29}$$

or more generally:

$$J = \vec{\dot{x}}^T W \vec{\dot{x}} \tag{B.30}$$

with W a symmetric, positive-definite, square matrix of weights yielding a non-negative J. The role of W in the sum of Eq. (B.30) is mainly that of making the single addends of the same order of magnitude, accounting for differences in units of measure and providing control of the minimization.

In normal operating condition, the derivative of the state vector $\vec{\dot{x}}$ is:

$$\vec{\dot{x}} = \begin{bmatrix} \dot{u} & \dot{v} & \dot{w} & \dot{p} & \dot{q} & \dot{r} \end{bmatrix}^T \tag{B.31}$$

An example of weight matrix W is given by:

$$W = \frac{1}{\Omega_{mr}^4} \begin{bmatrix} \frac{1}{R^2} & 0 & 0 & 0 & 0 & 0 \\ 0 & \frac{1}{R^2} & 0 & 0 & 0 & 0 \\ 0 & 0 & \frac{1}{R^2} & 0 & 0 & 0 \\ 0 & 0 & 0 & 1 & 0 & 0 \\ 0 & 0 & 0 & 0 & 1 & 0 \\ 0 & 0 & 0 & 0 & 0 & 1 \end{bmatrix} \tag{B.32}$$

Similarly, in autorotation, the derivative of the state vector $\vec{\dot{x}}$ is augmented by the rotor speed derivative:

$$\vec{\dot{x}} = \begin{bmatrix} \dot{u} & \dot{v} & \dot{w} & \dot{p} & \dot{q} & \dot{r} & \ddot{\psi}_{mr} \end{bmatrix}^T \tag{B.33}$$

An example of weight matrix W is given by:

$$W = \frac{1}{\Omega_{mr}^4} \begin{bmatrix} \frac{1}{R^2} & 0 & 0 & 0 & 0 & 0 & 0 \\ 0 & \frac{1}{R^2} & 0 & 0 & 0 & 0 & 0 \\ 0 & 0 & \frac{1}{R^2} & 0 & 0 & 0 & 0 \\ 0 & 0 & 0 & 1 & 0 & 0 & 0 \\ 0 & 0 & 0 & 0 & 1 & 0 & 0 \\ 0 & 0 & 0 & 0 & 0 & 1 & 0 \\ 0 & 0 & 0 & 0 & 0 & 0 & 1 \end{bmatrix} \tag{B.34}$$

The minimization of the cost function J is subject to the equality constraints of Eq. (B.16) and (B.18). The procedure starts by guessing a suitable initial value for the unknown parameters (Eq. (B.22) in normal operating conditions, and Eq. (B.28) in autorotation). The initial guess for these parameters is obtained by solving a simplified trim procedure [Bramwell et al., 2001], that allows to evaluate all of them in closed form.

At every iteration, body forces and moments (right-hand member of Eq. (B.1) and Eq. (B.23)), that are function of the unknown parameters, are evaluated.

The equations of motion (Eq. (B.1)) can finally be used to calculate the time derivatives of the states and supplied to the optimization algorithm in order to evaluate the cost function (Eq. (B.30)) for the current set of trim parameters.

Among the methods that try to minimize a multi-variate scalar function, a direct search method was preferred in lieu of a gradient-based one, because the former technique does not require explicit expressions of the derivatives.

B.3. TRIM RESULTS

In this section, trim results are shown for the helicopter flight mechanics model developed in Appendix A for two different flight conditions, i.e., straight level flight and steady-descent in autorotation.

The Bo-105 helicopter configuration data have been considered to verify the developed model and the trim procedure, because flight test data are available in literature [Padfield, 2007], at least for straight level flight.

B.3.1. STRAIGHT LEVEL FLIGHT

According to Eq. (B.20), we need to set a value for the turn rate $\dot{\Psi}_e$, horizontal speed $\sqrt{V_{x_e}^2 + V_{y_e}^2}$, vertical speed V_{z_e} and fuselage sideslip angle β_e. In level flight, the following conditions apply:

$$\begin{aligned} \dot{\Psi}_e &= 0 & \sqrt{V_{x_e}^2 + V_{y_e}^2} &= V_{hor} \\ V_{z_e} &= 0 & \beta_e &= 0 \end{aligned} \tag{B.35}$$

with V_{hor} ranging from hover to maximum speed.

The results of the trim procedure in straight level flight are shown in Fig. B.1 for the trim parameters belonging to the longitudinal plane and in Fig. B.2 for those belonging to the lateral-directional plane as a function of the horizontal speed. Even with the use of a 3-DOFs longitudinal model, the results match flight test data quite accurately and do not differ noticeably from other helicopter models of the same helicopter [Heffley et al., 1979; Padfield, 2007]. The use of a uniform inflow model, however, causes an underestimation of the lateral flapping angle [Bramwell et al., 2001, p. 113], especially at low speeds, and a consequent underestimation (in absolute value) of the lateral cyclic pitch (Fig. B.2b). The use of a simple first harmonic nonuniform inflow model which generates an induced velocity field that increases linearly from the leading edge to the trailing edge of the rotor disc, as in the Helisim model [Padfield, 2007], leads to a better prediction of flight test data, but does not solve the problem entirely [Chen, 1990, p. 64-6].

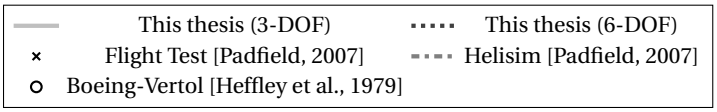

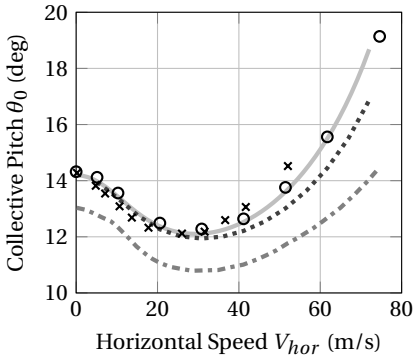

(a) Collective pitch angle.

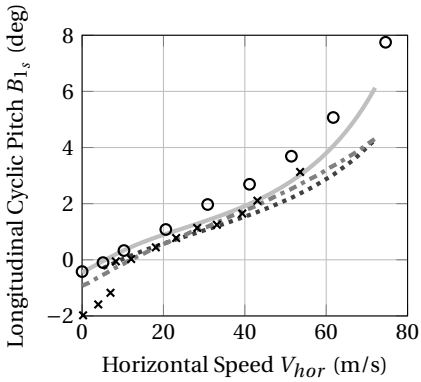

(b) Longitudinal cyclic pitch angle.

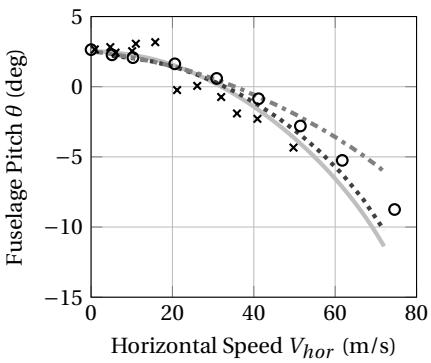

(c) Fuselage pitch angle.

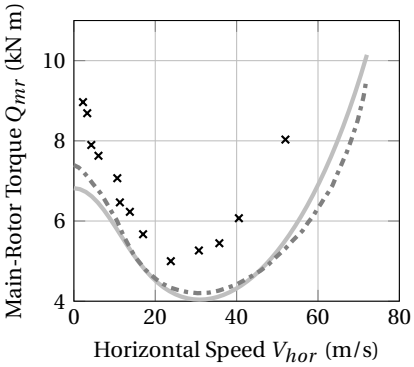

(d) Main-rotor torque.

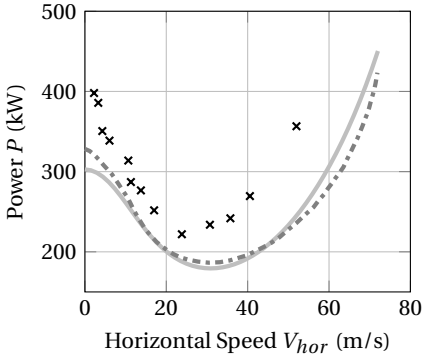

(e) Power.

Figure B.1: Trim results in straight level flight at sea-level (MTOW, $\dot{\psi}_{mr}$ = 100%) as a function of horizontal speed for the trim parameters belonging to the longitudinal plane.

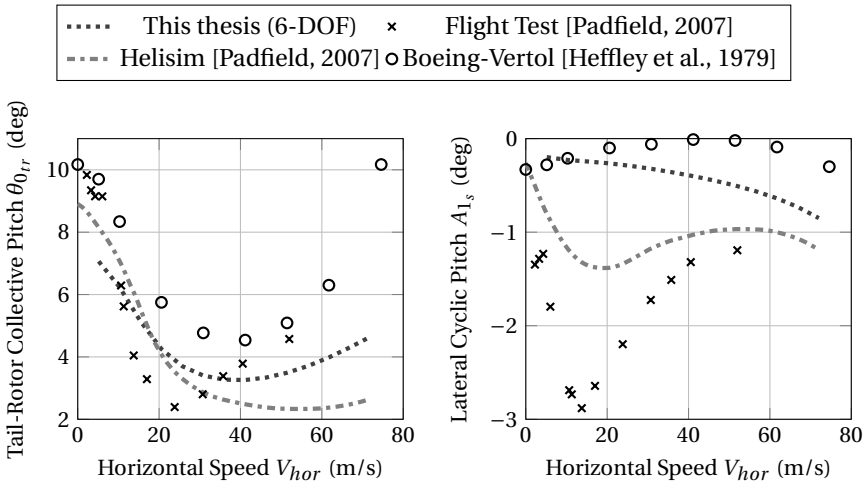

(a) Tail-rotor collective pitch angle.

(b) Lateral cyclic pitch angle.

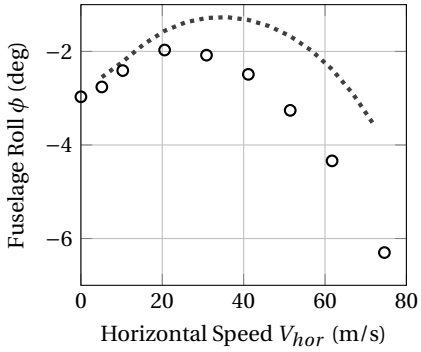

(c) Fuselage roll angle.

Figure B.2: Trim results in straight level flight at sea-level (MTOW, $\dot{\psi}_{mr}$ = 100%) as a function of horizontal speed for the trim parameters belonging to the lateral-directional plane.

B.3.2. STEADY-DESCENT IN AUTOROTATION

According to Eq. (B.26), we need to set a value for the turn rate $\dot{\Psi}_e$, horizontal speed $\sqrt{V_{x_e}^2 + V_{y_e}^2}$ and fuselage sideslip angle β_e. In steady-descent in autorotation, the following conditions apply:

$$\begin{aligned} \dot{\Psi}_e &= 0 \\ \sqrt{V_{x_e}^2 + V_{y_e}^2} &= V_{hor} \\ \beta_e &= 0 \end{aligned} \tag{B.36}$$

with V_{hor} ranging from hover to maximum speed.

The results of the trim procedure in steady descent in autorotation are shown in Fig. B.3 as a function of horizontal speed for the Bo-105 configuration data. Very steep approaches at low horizontal speed would be complicated by the possibility of power settling in the vortex ring state. Therefore, very low horizontal speeds have not been taken into account to avoid the classical boundaries of the vortex ring region (from hover to a rate of descent equal to twice the hover-induced velocity [Prouty, 2002]).

The speed for minimum rate of descent is at the bottom of the curve of Fig. B.3a, whereas the speed for minimum angle of descent (or maximum glide distance) is at a higher speed where a straight line from the origin is tangent to the curve. For the Bo-105 configuration data the speed for minimum rate of descent is equal to 60 kn on a flight path of $-15°$ and that for minimum descent angle is equal to 89 kn on a flight path of $-12°$. The suggested autorotative speed usually falls between these two values. This is confirmed by the flight manual of the Bo-105 helicopter [Anonymous, 1995], which states that the recommended airspeed in autorotation is 75 KIAS, the airspeed for minimum rate of descent is 60 KIAS at 100% rpm and that for maximum range is 100 KIAS at 85% rpm.

Due to the lack of available flight test data in steady-descent in autorotation, the trim of the developed model was compared with that of a high-fidelity model (including elastic modes of the rotor and the fuselage) developed in CAMRAD/JA. The agreement is good for most of the trim parameters, except the collective, but only at high speeds (Fig. B.3b), and the longitudinal cyclic (Fig. B.3c).

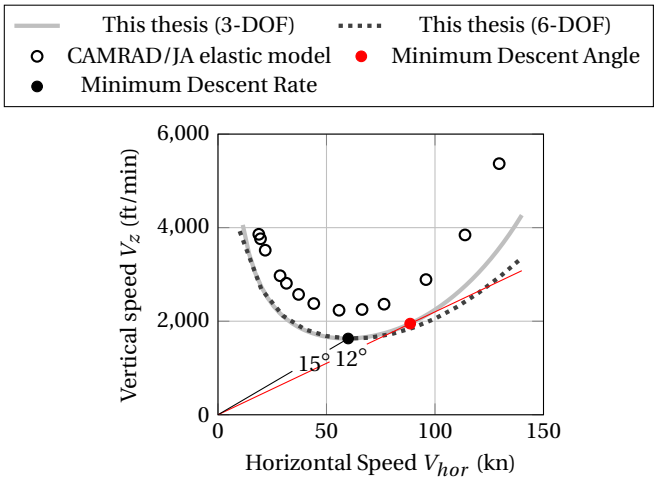

(a) Rate of descent.

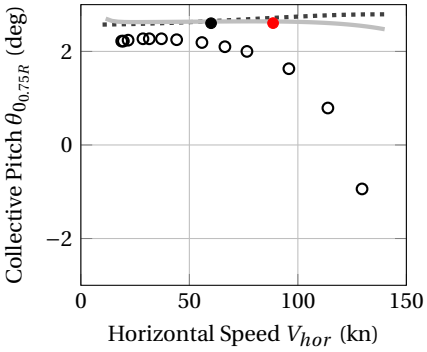

(b) Collective pitch angle.

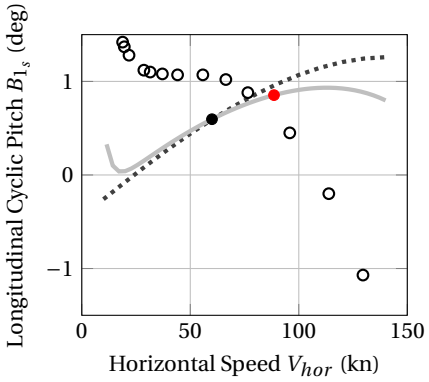

(c) Longitudinal cyclic pitch angle.

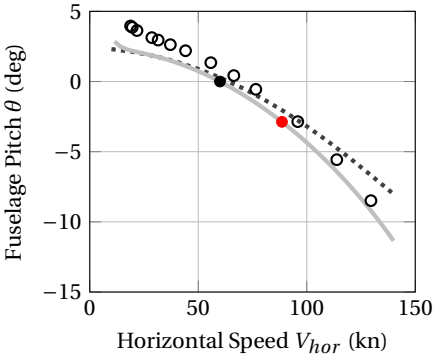

(d) Fuselage pitch angle.

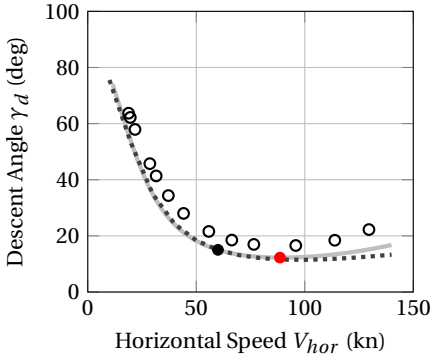

(e) Descent angle.

Figure B.3: Trim results in steady descent in autorotation at sea-level (MTOW, $\dot{\psi}_{mr}$ = 100%) as a function of horizontal speed for the trim parameters belonging to the longitudinal plane.

B

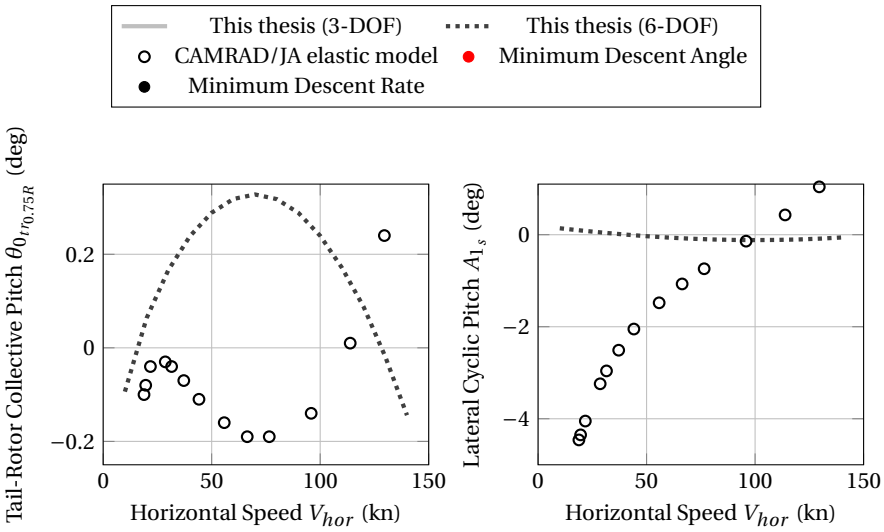

(a) Tail-rotor collective pitch angle.

(b) Lateral cyclic pitch angle.

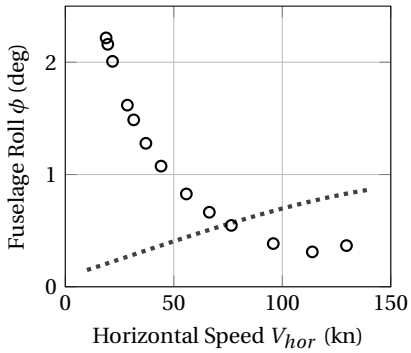

(c) Fuselage roll angle.

Figure B.4: Trim results in steady-descent in autorotation at sea-level (MTOW, $\dot{\psi}_{mr}$ = 100%) as a function of horizontal speed for the trim parameters belonging to the lateral-directional plane.

C

LINEARIZATION OF THE EQUATIONS OF MOTION

C.1. LINEARIZATION IN NORMAL OPERATING CONDITIONS (6-DOF MODEL)

Non-linear equations of motion in vector form (Eq. (A.20)) were derived in Appendix A and are reported here with a simplified notation:

$$\begin{aligned} m\,\dot{\vec{V}} + \vec{\omega} \times m\,\vec{V} &= \vec{F} \\ \mathbf{J}\,\dot{\vec{\omega}} + \vec{\omega} \times \mathbf{J}\,\vec{\omega} &= \vec{M} \end{aligned} \tag{C.1}$$

Let $\vec{V}_e$, $\vec{\omega}_e$, $\vec{F}_e$ and $\vec{M}_e$ be and equilibrium condition satisfying Eq. (C.1):

$$\begin{aligned} m\,\dot{\vec{V}}_e + \vec{\omega}_e \times m\,\vec{V}_e &= \vec{F}_e \\ \mathbf{J}\,\dot{\vec{\omega}}_e + \vec{\omega}_e \times \mathbf{J}\,\vec{\omega}_e &= \vec{M}_e \end{aligned} \tag{C.2}$$

If a small perturbation from the equilibrium condition is considered ($\vec{V} = \vec{V}_e + \Delta\vec{V}$, $\vec{\omega} = \vec{\omega}_e + \Delta\vec{\omega}$, $\vec{F} = \vec{F}_e + \Delta\vec{F}$ and $\vec{M} = \vec{M}_e + \Delta\vec{M}$), Eq. (C.1) becomes:

$$\begin{aligned} &\cancel{m\,\dot{\vec{V}}_e} + m\,\Delta\dot{\vec{V}} + \cancel{\vec{\omega}_e \times m\,\vec{V}_e} + \vec{\omega}_e \times m\,\Delta\vec{V} + \Delta\vec{\omega} \times m\,\vec{V}_e + \Delta\vec{\omega} \times m\,\Delta\vec{V} = \cancel{\vec{F}_e} + \Delta\vec{F} \\ &\cancel{\mathbf{J}\,\dot{\vec{\omega}}_e} + \mathbf{J}\,\Delta\dot{\vec{\omega}} + \cancel{\vec{\omega}_e \times \mathbf{J}\,\vec{\omega}_e} + \vec{\omega}_e \times \mathbf{J}\,\Delta\vec{\omega} + \Delta\vec{\omega} \times \mathbf{J}\,\vec{\omega}_e + \Delta\vec{\omega} \times \mathbf{J}\,\Delta\vec{\omega} = \cancel{\vec{M}_e} + \Delta\vec{M} \end{aligned} \tag{C.3}$$

where the terms satisfying Eq. (C.2) were cancelled, leading to:

$$\begin{aligned} m\,\Delta\dot{\vec{V}} + \vec{\omega}_e \times m\,\Delta\vec{V} + \Delta\vec{\omega} \times m\,\vec{V}_e + \cancel{\Delta\vec{\omega} \times m\,\Delta\vec{V}}^{\approx 0 \text{ second order}} &= \Delta\vec{F} \\ \mathbf{J}\,\Delta\dot{\vec{\omega}} + \vec{\omega}_e \times \mathbf{J}\,\Delta\vec{\omega} + \Delta\vec{\omega} \times \mathbf{J}\,\vec{\omega}_e + \cancel{\Delta\vec{\omega} \times \mathbf{J}\,\Delta\vec{\omega}}^{\approx 0 \text{ second order}} &= \Delta\vec{M} \end{aligned} \tag{C.4}$$

Neglecting second order terms in Eq. (C.4), we obtain the linearized equations of motion:

$$\begin{aligned} \Delta\dot{\vec{V}} + \vec{\omega}_e \times \Delta\vec{V} + \Delta\vec{\omega} \times \vec{V}_e &= \frac{\Delta\vec{F}}{m} \\ \mathbf{J}\,\Delta\dot{\vec{\omega}} + \vec{\omega}_e \times \mathbf{J}\,\Delta\vec{\omega} + \Delta\vec{\omega} \times \mathbf{J}\,\vec{\omega}_e &= \Delta\vec{M} \end{aligned} \tag{C.5}$$

Both in straight level flight and in autorotation, the following equilibrium conditions apply:

$$\vec{V}_e = \begin{Bmatrix} U_e \\ V_e \\ W_e \end{Bmatrix} = \begin{Bmatrix} U_e \\ 0 \\ W_e \end{Bmatrix} \tag{C.6}$$

$$\vec{\omega}_e = \begin{Bmatrix} P_e \\ Q_e \\ R_e \end{Bmatrix} = \begin{Bmatrix} 0 \\ 0 \\ 0 \end{Bmatrix} = \vec{0} \tag{C.7}$$

Replacing Eq. (C.7) in Eq. (C.5), we obtain:

$$\begin{aligned} \Delta\dot{\vec{V}} + \cancelto{0}{\vec{\omega}_e} \times \Delta\vec{V} + \Delta\vec{\omega} \times \vec{V}_e &= \frac{\Delta\vec{F}}{m} \\ \mathbf{J}\,\Delta\dot{\vec{\omega}} + \cancelto{0}{\vec{\omega}_e} \times \mathbf{J}\,\Delta\vec{\omega} + \Delta\vec{\omega} \times \mathbf{J}\,\cancelto{0}{\vec{\omega}_e} &= \Delta\vec{M} \end{aligned} \tag{C.8}$$

$$\begin{aligned} \Delta\dot{\vec{V}} + \Delta\vec{\omega} \times \vec{V}_e &= \frac{\Delta\vec{F}}{m} \\ \Delta\dot{\vec{\omega}} &= \mathbf{J}^{-1}\,\Delta\vec{M} \end{aligned} \tag{C.9}$$

Remembering the definition of the inertia tensor Eq. (A.25):

$$\mathbf{J} = \begin{bmatrix} I_{xx} & 0 & -I_{xz} \\ 0 & I_{yy} & 0 \\ -I_{xz} & 0 & I_{zz} \end{bmatrix} \tag{C.10}$$

Eq. (C.9) can be expressed in scalar form as:

$$
\begin{aligned}
\Delta\dot{u} &= -W_e\Delta q + V_e\Delta r + \frac{\Delta F_x}{m} \\
\Delta\dot{v} &= W_e\Delta p - U_e\Delta r + \frac{\Delta F_y}{m} \\
\Delta\dot{w} &= -V_e\Delta p + U_e\Delta q + \frac{\Delta F_z}{m} \\
\Delta\dot{p} &= \frac{1}{I_{xx}I_{zz} - I_{xz}^2}\left(I_{zz}\Delta L + I_{xz}\Delta N\right) \\
\Delta\dot{q} &= \frac{\Delta M}{I_{yy}} \\
\Delta\dot{r} &= \frac{1}{I_{xx}I_{zz} - I_{xz}^2}\left(I_{xz}\Delta L + I_{xx}\Delta N\right)
\end{aligned}
\tag{C.11}
$$

Separating the gravity components from the external (aerodynamic) force components:

$$
\vec{F}_{grav} = mg\begin{Bmatrix} -\sin\theta \\ \cos\theta\sin\phi \\ \cos\theta\cos\phi \end{Bmatrix}
\tag{C.12}
$$

and linearizing them:

$$
\Delta\vec{F}_{grav} = mg\begin{Bmatrix} -\cos\Theta_e\Delta\theta \\ -\sin\Theta_e\sin\Phi_e\Delta\theta + \cos\Theta_e\cos\Phi_e\Delta\phi \\ -\sin\Theta_e\cos\Phi_e\Delta\theta - \cos\Theta_e\sin\Phi_e\Delta\phi \end{Bmatrix}
\tag{C.13}
$$

Eq. (C.11) becomes:

$$
\begin{aligned}
\Delta\dot{u} &= -W_e\Delta q + V_e\Delta r - g\cos\Theta_e\Delta\theta + \frac{\Delta X}{m} \\
\Delta\dot{v} &= W_e\Delta p - U_e\Delta r - g\sin\Theta_e\sin\Phi_e\Delta\theta + g\cos\Theta_e\cos\Phi_e\Delta\phi + \frac{\Delta Y}{m} \\
\Delta\dot{w} &= -V_e\Delta p + U_e\Delta q - g\sin\Theta_e\cos\Phi_e\Delta\theta - g\cos\Theta_e\sin\Phi_e\Delta\phi + \frac{\Delta Z}{m} \\
\Delta\dot{p} &= \frac{1}{I_{xx}I_{zz} - I_{xz}^2}\left(I_{zz}\Delta L + I_{xz}\Delta N\right) \\
\Delta\dot{q} &= \frac{\Delta M}{I_{yy}} \\
\Delta\dot{r} &= \frac{1}{I_{xx}I_{zz} - I_{xz}^2}\left(I_{xz}\Delta L + I_{xx}\Delta N\right)
\end{aligned}
\tag{C.14}
$$

Assuming that the external (aerodynamics) forces and moments are a function of the linear and the angular rates and of the flight controls:

$$X = X\left(u, v, w, p, q, r, \theta_0, A_1, B_1, \theta_{0_{tr}}\right) \tag{C.15}$$

we can linearize the external forces and moments, by using Taylor series:

$$\begin{aligned}\Delta X = &\frac{\partial X}{\partial u}\Delta u + \frac{\partial X}{\partial v}\Delta v + \frac{\partial X}{\partial w}\Delta w + \frac{\partial X}{\partial p}\Delta p + \frac{\partial X}{\partial q}\Delta q + \frac{\partial X}{\partial r}\Delta r + \\ &+ \frac{\partial X}{\partial \theta_0}\Delta\theta_0 + \frac{\partial X}{\partial A_1}\Delta A_1 + \frac{\partial X}{\partial B_1}\Delta B_1 + \frac{\partial X}{\partial \theta_{0_{tr}}}\Delta\theta_{0_{tr}}\end{aligned} \tag{C.16}$$

Also the kinematics equations need to be linearized:

$$\begin{aligned}p &= \dot{\phi} - \dot{\psi}\sin(\theta) \\ q &= \dot{\theta}\cos(\phi) + \dot{\psi}\sin(\phi)\cos(\theta) \\ r &= -\dot{\theta}\sin(\phi) + \dot{\psi}\cos(\phi)\cos(\theta)\end{aligned} \tag{C.17}$$

$$\begin{aligned}\Delta p &= \Delta\dot{\phi} - \Delta\dot{\psi}\sin(\Theta_e) - \dot{\Psi}_e\cos(\Theta_e)\Delta\theta \\ \Delta q &= \Delta\dot{\theta}\cos(\Phi_e) - \dot{\Theta}_e\sin(\Phi_e)\Delta\phi + \Delta\dot{\psi}\sin(\Phi_e)\cos(\Theta_e) + \\ &\quad + \dot{\psi}_e\left[\cos(\Phi_e)\cos(\Theta_e)\Delta\phi - \sin(\Phi_e)\sin(\Theta_e)\Delta\theta\right] \\ \Delta r &= -\Delta\dot{\theta}\sin(\Phi_e) - \dot{\Theta}_e\cos(\Phi_e)\Delta\phi + \Delta\dot{\psi}\cos(\Phi_e)\cos(\Theta_e) + \\ &\quad - \dot{\psi}_e\left[\sin(\Phi_e)\cos(\Theta_e)\Delta\phi + \cos(\Phi_e)\sin(\Theta_e)\Delta\theta\right]\end{aligned} \tag{C.18}$$

In straight level flight and in steady-descent in autorotation $\dot{\Psi}_e = 0$ and $\dot{\Theta}_e = 0$, therefore Eq. (C.18) becomes:

$$\begin{aligned}\Delta p &= \Delta\dot{\phi} - \Delta\dot{\psi}\sin(\Theta_e) \\ \Delta q &= \Delta\dot{\theta}\cos(\Phi_e) + \Delta\dot{\psi}\sin(\Phi_e)\cos(\Theta_e) \\ \Delta r &= -\Delta\dot{\theta}\sin(\Phi_e) + \Delta\dot{\psi}\cos(\Phi_e)\cos(\Theta_e)\end{aligned} \tag{C.19}$$

Eq. (C.19) in vector form becomes:

$$\Delta\vec{\omega} = \begin{Bmatrix}\Delta p \\ \Delta q \\ \Delta r\end{Bmatrix} = \begin{bmatrix}1 & 0 & -\sin\Theta_e \\ 0 & \cos\Phi_e & \sin\Phi_e\cos\Theta_e \\ 0 & -\sin\Phi_e & \cos\Phi_e\cos\Theta_e\end{bmatrix}\begin{Bmatrix}\Delta\dot{\phi} \\ \Delta\dot{\theta} \\ \Delta\dot{\psi}\end{Bmatrix} = \mathbf{S}_{321}^{B}\Delta\dot{\vec{e}}_{321} \tag{C.20}$$

$$\Delta\dot{\vec{e}}_{321} = \mathbf{S}_{321}^{B^{-1}}\Delta\vec{\omega} = \begin{bmatrix}1 & \tan\Theta_e\sin\Phi_e & \tan\Theta_e\cos\Phi_e \\ 0 & \cos\Phi_e & -\sin\Phi_e \\ 0 & \frac{\sin\Phi_e}{\cos\Theta_e} & \frac{\cos\Phi_e}{\cos\Theta_e}\end{bmatrix}\begin{Bmatrix}\Delta p \\ \Delta q \\ \Delta r\end{Bmatrix} \tag{C.21}$$

Combining Eq. (C.14), Eq. (C.16) and (C.21), we obtain a state space system:

$$\Delta\dot{\vec{x}} = \mathbf{A}\,\Delta\vec{x} + \mathbf{B}\,\Delta\vec{u} \tag{C.22}$$

$$\Delta\vec{x} = \begin{Bmatrix} \Delta u \\ \Delta w \\ \Delta q \\ \Delta\theta \\ \Delta v \\ \Delta p \\ \Delta\phi \\ \Delta r \end{Bmatrix} \tag{C.23}$$

$$\Delta\vec{u} = \begin{Bmatrix} \Delta\theta_0 \\ \Delta A_1 \\ \Delta B_1 \\ \Delta\theta_{0_{tr}} \end{Bmatrix} \tag{C.24}$$

Defining:

$$I_c^2 = I_{xx} I_{zz} - I_{xz}^2 \tag{C.25}$$

C

$$\mathbf{A} = \begin{bmatrix} \frac{X_u}{m} & \frac{X_w}{m} & \frac{X_q}{m} - W_e & -g\cos\Theta_e & \frac{X_v}{m} & \frac{X_p}{m} & 0 & \frac{X_r}{m} \\ \frac{Z_u}{m} & \frac{Z_w}{m} & \frac{Z_q}{m} + U_e & -g\cos\Phi_e\sin\Theta_e & \frac{Z_v}{m} & \frac{Z_p}{m} - V_e & -g\sin\Phi_e\cos\Theta_e & \frac{Z_r}{m} \\ \frac{M_u}{I_{yy}} & \frac{M_w}{I_{yy}} & \frac{M_q}{I_{yy}} & 0 & \frac{M_v}{I_{yy}} & \frac{M_p}{I_{yy}} & 0 & \frac{M_r}{I_{yy}} \\ 0 & 0 & \cos\Phi_e & 0 & 0 & 0 & 0 & -\sin\Phi_e \\ \frac{Y_u}{m} & \frac{Y_w}{m} & \frac{Y_q}{m} & -g\sin\Phi_e\sin\Theta_e & \frac{Y_v}{m} & \frac{Y_p}{m} + W_e & g\cos\Phi_e\cos\Theta_e & \frac{Y_r}{m} - U_e \\ \frac{I_{zz}L_u + I_{xz}N_u}{I_c^2} & \frac{I_{zz}L_w + I_{xz}N_w}{I_c^2} & \frac{I_{zz}L_q + I_{xz}N_q}{I_c^2} & 0 & \frac{I_{zz}L_v + I_{xz}N_v}{I_c^2} & \frac{I_{zz}L_p + I_{xz}N_p}{I_c^2} & 0 & \frac{I_{zz}L_r + I_{xz}N_r}{I_c^2} \\ 0 & 0 & \sin\Phi_e\tan\Theta_e & 0 & 0 & 1 & 0 & \cos\Phi_e\tan\Theta_e \\ \frac{I_{xz}L_u + I_{xx}N_u}{I_c^2} & \frac{I_{xz}L_w + I_{xx}N_w}{I_c^2} & \frac{I_{xz}L_q + I_{xx}N_q}{I_c^2} & 0 & \frac{I_{xz}L_v + I_{xx}N_v}{I_c^2} & \frac{I_{xz}L_p + I_{xx}N_p}{I_c^2} & 0 & \frac{I_{xz}L_r + I_{xx}N_r}{I_c^2} \end{bmatrix} \tag{C.26}$$

$$\mathbf{B} = \begin{bmatrix} \frac{X_{\theta_0}}{m} & \frac{X_{B_1}}{m} & \frac{X_{A_1}}{m} & \frac{X_{\theta_{0_{tr}}}}{m} \\ \frac{Z_{\theta_0}}{m} & \frac{Z_{B_1}}{m} & \frac{Z_{A_1}}{m} & \frac{Z_{\theta_{0_{tr}}}}{m} \\ \frac{M_{\theta_0}}{I_{yy}} & \frac{M_{B_1}}{I_{yy}} & \frac{M_{A_1}}{I_{yy}} & \frac{M_{\theta_{0_{tr}}}}{I_{yy}} \\ 0 & 0 & 0 & 0 \\ \frac{Y_{\theta_0}}{m} & \frac{Y_{B_1}}{m} & \frac{Y_{A_1}}{m} & \frac{Y_{\theta_{0_{tr}}}}{m} \\ \frac{I_{zz}L_{\theta_0} + I_{xz}N_{\theta_0}}{I_c^2} & \frac{I_{zz}L_{B_1} + I_{xz}N_{B_1}}{I_c^2} & \frac{I_{zz}L_{A_1} + I_{xz}N_{A_1}}{I_c^2} & \frac{I_{zz}L_{\theta_{0_{tr}}} + I_{xz}N_{\theta_{0_{tr}}}}{I_c^2} \\ 0 & 0 & 0 & 0 \\ \frac{I_{xz}L_{\theta_0} + I_{xx}N_{\theta_0}}{I_c^2} & \frac{I_{xz}L_{B_1} + I_{xx}N_{B_1}}{I_c^2} & \frac{I_{xz}L_{A_1} + I_{xx}N_{A_1}}{I_c^2} & \frac{I_{xz}L_{\theta_{0_{tr}}} + I_{xx}N_{\theta_{0_{tr}}}}{I_c^2} \end{bmatrix} \tag{C.27}$$

C.1.1. 3-DOF LONGITUDINAL MODEL

Neglecting the DOF and the flight controls related to the lateral-directional dynamics:

$$\begin{array}{lll} v=0 & p=0 & r=0 \\ \phi=0 & A_1=0 & \theta_{0_{tr}}=0 \\ L=0 & N=Q_{req}=Q_{mr} & \end{array} \tag{C.28}$$

the state matrix and the control matrix become:

$$\mathbf{A}=\begin{bmatrix} \frac{X_u}{m} & \frac{X_w}{m} & \frac{X_q}{m}-W_e & -g\cos\Theta_e \\ \frac{Z_u}{m} & \frac{Z_w}{m} & \frac{Z_q}{m}+U_e & -g\sin\Theta_e \\ \frac{M_u}{I_{yy}} & \frac{M_w}{I_{yy}} & \frac{M_q}{I_{yy}} & 0 \\ 0 & 0 & 1 & 0 \end{bmatrix} \tag{C.29}$$

$$\mathbf{B}=\begin{bmatrix} \frac{X_{\theta_0}}{m} & \frac{X_{B_1}}{m} \\ \frac{Z_{\theta_0}}{m} & \frac{Z_{B_1}}{m} \\ \frac{M_{\theta_0}}{I_{yy}} & \frac{M_{B_1}}{I_{yy}} \\ 0 & 0 \end{bmatrix} \tag{C.30}$$

C.2. LINEARIZATION IN AUTOROTATION (7-DOF MODEL)

Eq. (C.9) can also be used to accommodate the torque equation, which is needed to simulate autorotation, by defining the inertia tensor as:

$$\mathbf{J}=\begin{bmatrix} I_{xx} & 0 & -I_{xz} & 0 \\ 0 & I_{yy} & 0 & 0 \\ -I_{xz} & 0 & I_{zz}+I_R & -I_R \\ 0 & 0 & -I_R & I_R \end{bmatrix} \tag{C.31}$$

In this case, Eq. (C.9) in scalar form becomes:

$$
\begin{aligned}
\Delta\dot{u} &= -W_e\Delta q + V_e\Delta r - g\cos\Theta_e\Delta\theta + \frac{\Delta X}{m}\\
\Delta\dot{v} &= W_e\Delta p - U_e\Delta r - g\sin\Theta_e\sin\Phi_e\Delta\theta + g\cos\Theta_e\cos\Phi_e\Delta\phi + \frac{\Delta Y}{m}\\
\Delta\dot{w} &= -V_e\Delta p + U_e\Delta q - g\sin\Theta_e\cos\Phi_e\Delta\theta - g\cos\Theta_e\sin\Phi_e\Delta\phi + \frac{\Delta Z}{m}\\
\Delta\dot{p} &= \frac{1}{I_{xx}I_{zz} - I_{xz}^2}\left[I_{zz}\Delta L + I_{xz}\left(\Delta N - \Delta Q_{mr} - g_{tr}\Delta Q_{tr}\right)\right]\\
\Delta\dot{q} &= \frac{\Delta M}{I_{yy}}\\
\Delta\dot{r} &= \frac{1}{I_{xx}I_{zz} - I_{xz}^2}\left[I_{xz}\Delta L + I_{xx}\left(\Delta N - \Delta Q_{mr} - g_{tr}\Delta Q_{tr}\right)\right]\\
\Delta\ddot{\psi}_{mr} &= \frac{1}{I_{xx}I_{zz} - I_{xz}^2}\left[I_{xz}\Delta L + I_{xx}\Delta N + \left(I_{xx} + \frac{I_{xx}I_{zz} - I_{xz}^2}{I_R}\right)\left(-\Delta Q_{mr} - g_{tr}\Delta Q_{tr}\right)\right]
\end{aligned}
\tag{C.32}
$$

$$
\begin{aligned}
\Delta\dot{u} &= -W_e\Delta q + V_e\Delta r - g\cos\Theta_e\Delta\theta + \frac{\Delta X}{m}\\
\Delta\dot{v} &= W_e\Delta p - U_e\Delta r - g\sin\Theta_e\sin\Phi_e\Delta\theta + g\cos\Theta_e\cos\Phi_e\Delta\phi + \frac{\Delta Y}{m}\\
\Delta\dot{w} &= -V_e\Delta p + U_e\Delta q - g\sin\Theta_e\cos\Phi_e\Delta\theta - g\cos\Theta_e\sin\Phi_e\Delta\phi + \frac{\Delta Z}{m}\\
\Delta\dot{p} &= \frac{1}{I_{xx}I_{zz} - I_{xz}^2}\left[I_{zz}\Delta L + I_{xz}\left(\Delta N - \Delta Q_{mr} - g_{tr}\Delta Q_{tr}\right)\right]\\
\Delta\dot{q} &= \frac{\Delta M}{I_{yy}}\\
\Delta\dot{r} &= \frac{1}{I_{xx}I_{zz} - I_{xz}^2}\left[I_{xz}\Delta L + I_{xx}\left(\Delta N - \Delta Q_{mr} - g_{tr}\Delta Q_{tr}\right)\right]\\
\Delta\ddot{\psi}_{mr} &= \Delta\dot{r} + \frac{1}{I_R}\left(-\Delta Q_{mr} - g_{tr}\Delta Q_{tr}\right)
\end{aligned}
\tag{C.33}
$$

Assuming that the external (aerodynamics) forces and moments are a function of the linear and the angular rates and of the flight controls:

$$
X = X\left(u, v, w, p, q, r, \dot{\psi}_m r, \theta_0, A_1, B_1, \theta_{0_{tr}}\right) \tag{C.34}
$$

we can linearize the external forces and moments, by using Taylor series:

$$
\begin{aligned}
\Delta X = {} & \frac{\partial X}{\partial u}\Delta u + \frac{\partial X}{\partial v}\Delta v + \frac{\partial X}{\partial w}\Delta w + \frac{\partial X}{\partial p}\Delta p + \frac{\partial X}{\partial q}\Delta q + \frac{\partial X}{\partial r}\Delta r + \frac{\partial X}{\partial \dot{\psi}_{mr}}\Delta\dot{\psi}_{mr} +\\
& + \frac{\partial X}{\partial \theta_0}\Delta\theta_0 + \frac{\partial X}{\partial A_1}\Delta A_1 + \frac{\partial X}{\partial B_1}\Delta B_1 + \frac{\partial X}{\partial \theta_{0_{tr}}}\Delta\theta_{0_{tr}}
\end{aligned}
\tag{C.35}
$$

Combining Eq. (C.32), Eq. (C.35) and (C.21), we obtain a state space system with:

$$\Delta\vec{x} = \left\{ \begin{array}{c} \Delta u \\ \Delta w \\ \Delta q \\ \Delta\theta \\ \Delta v \\ \Delta p \\ \Delta\phi \\ \Delta r \\ \Delta\dot{\psi}_{mr} \end{array} \right\} \tag{C.36}$$

Defining:

$$Q_{req} = \Delta Q_{mr} + g_{tr}\Delta Q_{tr} \tag{C.37}$$

$$\mathbf{A} = \begin{bmatrix} \frac{X_u}{m} & \frac{X_w}{m} & \frac{X_q}{m} - W_e & -g\cos\Theta_e & \frac{X_v}{m} & \frac{X_p}{m} & 0 & \frac{X_r}{m} & \frac{X_{\dot{\psi}_{mr}}}{m} \\ \frac{Z_u}{m} & \frac{Z_w}{m} & \frac{Z_q}{m} + U_e & -g\cos\Phi_e\sin\Theta_e & \frac{Z_v}{m} & \frac{Z_p}{m} - V_e & -g\sin\Phi_e\cos\Theta_e & \frac{Z_r}{m} & \frac{Z_{\dot{\psi}_{mr}}}{m} \\ \frac{M_u}{I_{yy}} & \frac{M_w}{I_{yy}} & \frac{M_q}{I_{yy}} & 0 & \frac{M_v}{I_{yy}} & \frac{M_p}{I_{yy}} & 0 & \frac{M_r}{I_{yy}} & \frac{M_{\dot{\psi}_{mr}}}{I_{yy}} \\ 0 & 0 & \cos\Phi_e & 0 & 0 & 0 & 0 & -\sin\Phi_e & 0 \\ \frac{Y_u}{m} & \frac{Y_w}{m} & \frac{Y_q}{m} & -g\sin\Phi_e\sin\Theta_e & \frac{Y_v}{m} & \frac{Y_p}{m} + W_e & g\cos\Phi_e\cos\Theta_e & \frac{Y_r}{m} - U_e & \frac{Y_{\dot{\psi}_{mr}}}{m} \\ \frac{I_{zz}L_u + I_{xz}\left(N_u - Qreq_u\right)}{I_c^2} & \frac{I_{zz}L_w + I_{xz}\left(N_w - Qreq_w\right)}{I_c^2} & \frac{I_{zz}L_q + I_{xz}\left(N_q - Qreq_q\right)}{I_c^2} & 0 & \frac{I_{zz}L_v + I_{xz}\left(N_v - Qreq_v\right)}{I_c^2} & \frac{I_{zz}L_p + I_{xz}\left(N_p - Qreq_p\right)}{I_c^2} & 0 & \frac{I_{zz}L_r + I_{xz}\left(N_r - Qreq_r\right)}{I_c^2} & \frac{I_{zz}L_{\dot{\psi}_{mr}} + I_{xz}\left(N_{\dot{\psi}_{mr}} - Qreq_{\dot{\psi}_{mr}}\right)}{I_c^2} \\ 0 & 0 & \sin\Phi_e\tan\Theta_e & 0 & 0 & 1 & 0 & \cos\Phi_e\tan\Theta_e & 0 \\ \frac{I_{xz}L_u + I_{xx}\left(N_u - Qreq_u\right)}{I_c^2} & \frac{I_{xz}L_w + I_{xx}\left(N_w - Qreq_w\right)}{I_c^2} & \frac{I_{xz}L_q + I_{xx}\left(N_q - Qreq_q\right)}{I_c^2} & 0 & \frac{I_{xz}L_v + I_{xx}\left(N_v - Qreq_v\right)}{I_c^2} & \frac{I_{xz}L_p + I_{xx}\left(N_p - Qreq_p\right)}{I_c^2} & 0 & \frac{I_{xz}L_r + I_{xx}\left(N_r - Qreq_r\right)}{I_c^2} & \frac{I_{xz}L_{\dot{\psi}_{mr}} + I_{xx}\left(N_{\dot{\psi}_{mr}} - Qreq_{\dot{\psi}_{mr}}\right)}{I_c^2} \\ \frac{I_{xz}L_u + I_{xx}\left(N_u - Qreq_u\right)}{I_c^2} - \frac{Qreq_u}{I_R} & \frac{I_{xz}L_w + I_{xx}\left(N_w - Qreq_w\right)}{I_c^2} - \frac{Qreq_w}{I_R} & \frac{I_{xz}L_q + I_{xx}\left(N_q - Qreq_q\right)}{I_c^2} - \frac{Qreq_q}{I_R} & 0 & \frac{I_{xz}L_v + I_{xx}\left(N_v - Qreq_v\right)}{I_c^2} - \frac{Qreq_v}{I_R} & \frac{I_{xz}L_p + I_{xx}\left(N_p - Qreq_p\right)}{I_c^2} - \frac{Qreq_p}{I_R} & 0 & \frac{I_{xz}L_r + I_{xx}\left(N_r - Qreq_r\right)}{I_c^2} - \frac{Qreq_r}{I_R} & \frac{I_{xz}L_{\dot{\psi}_{mr}} + I_{xx}\left(N_{\dot{\psi}_{mr}} - Qreq_{\dot{\psi}_{mr}}\right)}{I_c^2} - \frac{Qreq_{\dot{\psi}_{mr}}}{I_R} \end{bmatrix} \tag{C.38}$$

$$\mathbf{B} = \begin{bmatrix} \frac{X_{\theta_0}}{m} & \frac{X_{B_1}}{m} & \frac{X_{A_1}}{m} & \frac{X_{\theta_{0_{tr}}}}{m} \\ \frac{Z_{\theta_0}}{m} & \frac{Z_{B_1}}{m} & \frac{Z_{A_1}}{m} & \frac{Z_{\theta_{0_{tr}}}}{m} \\ \frac{M_{\theta_0}}{I_{yy}} & \frac{M_{B_1}}{I_{yy}} & \frac{M_{A_1}}{I_{yy}} & \frac{M_{\theta_{0_{tr}}}}{I_{yy}} \\ 0 & 0 & 0 & 0 \\ \frac{Y_{\theta_0}}{m} & \frac{Y_{B_1}}{m} & \frac{Y_{A_1}}{m} & \frac{Y_{\theta_{0_{tr}}}}{m} \\ \frac{I_{zz}L_{\theta_0} + I_{xz}\left(N_{\theta_0} - Qreq_{\theta_0}\right)}{I_c^2} & \frac{I_{zz}L_{B_1} + I_{xz}\left(N_{B_1} - Qreq_{B_1}\right)}{I_c^2} & \frac{I_{zz}L_{A_1} + I_{xz}\left(N_{A_1} - Qreq_{A_1}\right)}{I_c^2} & \frac{I_{zz}L_{\theta_{0_{tr}}} + I_{xz}\left(N_{\theta_{0_{tr}}} - Qreq_{\theta_{0_{tr}}}\right)}{I_c^2} \\ 0 & 0 & 0 & 0 \\ \frac{I_{xz}L_{\theta_0} + I_{xz}\left(N_{\theta_0} - Qreq_{\theta_0}\right)}{I_c^2} & \frac{I_{xz}L_{B_1} + I_{xz}\left(N_{B_1} - Qreq_{B_1}\right)}{I_c^2} & \frac{I_{xz}L_{A_1} + I_{xz}\left(N_{A_1} - Qreq_{A_1}\right)}{I_c^2} & \frac{I_{xz}L_{\theta_{0_{tr}}} + I_{xz}\left(N_{\theta_{0_{tr}}} - Qreq_{\theta_{0_{tr}}}\right)}{I_c^2} \\ \frac{I_{xz}L_{\theta_0} + I_{xx}\left(N_{\theta_0} - Qreq_{\theta_0}\right)}{I_c^2} - \frac{Qreq_{\theta_0}}{I_R} & \frac{I_{xz}L_{B_1} + I_{xx}\left(N_{B_1} - Qreq_{B_1}\right)}{I_c^2} - \frac{Qreq_{B_1}}{I_R} & \frac{I_{xz}L_{A_1} + I_{xx}\left(N_{A_1} - Qreq_{A_1}\right)}{I_c^2} - \frac{Qreq_{A_1}}{I_R} & \frac{I_{xz}L_{\theta_{0_{tr}}} + I_{xx}\left(N_{\theta_{0_{tr}}} - Qreq_{\theta_{0_{tr}}}\right)}{I_c^2} - \frac{Qreq_{\theta_{0_{tr}}}}{I_R} \end{bmatrix} \tag{C.39}$$

C.2.1. 3-DOF LONGITUDINAL MODEL + MAIN-ROTOR SPEED DOF

Neglecting the DOF and the flight controls related to the lateral-directional dynamics:

$$\begin{aligned} v &= 0 \\ p &= 0 \\ r &= 0 \\ \phi &= 0 \\ A_1 &= 0 \\ \theta_{0_{tr}} &= 0 \\ N &= Q_{req} = Q_{mr} \\ L &= 0 \end{aligned} \tag{C.40}$$

the state matrix and the control matrix become:

$$\mathbf{A} = \begin{bmatrix} \frac{X_u}{m} & \frac{X_w}{m} & \frac{X_q}{m} - W_e & -g\cos\Theta_e & \frac{X_{\psi_{mr}}}{m} \\ \frac{Z_u}{m} & \frac{Z_w}{m} & \frac{Z_q}{m} + U_e & -g\sin\Theta_e & \frac{Z_{\psi_{mr}}}{m} \\ \frac{M_u}{I_{yy}} & \frac{M_w}{I_{yy}} & \frac{M_q}{I_{yy}} & 0 & \frac{M_{\psi_{mr}}}{m} \\ 0 & 0 & 1 & 0 & 0 \\ -\frac{Q_{mr_u}}{I_R} & -\frac{Q_{mr_w}}{I_R} & -\frac{Q_{mr_q}}{I_R} & 0 & -\frac{Q_{mr_{\psi_{mr}}}}{I_R} \end{bmatrix} \tag{C.41}$$

$$\mathbf{B} = \begin{bmatrix} \frac{X_{\theta_0}}{m} & \frac{X_{B_1}}{m} \\ \frac{Z_{\theta_0}}{m} & \frac{Z_{B_1}}{m} \\ \frac{M_{\theta_0}}{I_{yy}} & \frac{M_{B_1}}{I_{yy}} \\ 0 & 0 \\ -\frac{Q_{mr\theta_0}}{I_R} & -\frac{Q_{mr_{B_1}}}{I_R} \end{bmatrix} \tag{C.42}$$

C.2.2. NATURAL MODES OF MOTION

It is common practice in studying the stability and control of both fixed- and rotary-wing aircraft to linearize the equations of motion around an equilibrium point and evaluate the natural modes of motion of the equivalent linear system. Indeed, linearization allows for interpreting the helicopter motion as a linear combination of natural modes, each having its own unique frequency, damping and distribution of the response states. Thus, the stability of the motion caused by small disturbances from a trim condition is strictly related to the stability of the individual modes.

The result of the linearization procedure is typically a state-space model of the form of Eq. (C.43).

$$\begin{cases} \delta\dot{\vec{x}}(t) = \mathbf{A}\,\delta\vec{x}(t) + \mathbf{B}\,\delta\vec{u}(t) \\ \delta\vec{x}(t_0) = \delta\vec{x}_0 \end{cases} \tag{C.43}$$

According to Lagrange's formula for linear time-invariant systems (Eq. (C.44)), the motion of the state $\delta\vec{x}$ is made of two different contributions: the natural response $\delta\vec{x}_{ZIR}$ (also known as Zero Input Response (ZIR)) and the forced response (also known as Zero State Response (ZSR)) $\delta\vec{x}_{ZSR}$.

$$\begin{aligned}\delta\vec{x}(t) &= \delta\vec{x}_{ZIR}(t) + \delta\vec{x}_{ZSR}(t) = \\ &= \overbrace{\exp\left[\mathbf{A}(t-t_0)\right]\,\delta\vec{x}_0}^{\text{Zero-Input Response}} + \\ &+ \underbrace{\int_{t_0}^{t} \exp\left[\mathbf{A}(t-\tau)\right]\mathbf{B}\,\delta\vec{u}(\tau)}_{\text{Zero-State Response}}\end{aligned} \tag{C.44}$$

The natural response is strictly related to the stability of the system. The eigenvectors $\vec{w}_i$ of the matrix $\mathbf{A}$, if arranged into columns to form a square matrix $\mathbf{W}$, satisfy Eq. (C.45).

$$\mathbf{W}\,\mathrm{Diag}(\lambda_i) = \mathbf{A}\,\mathbf{W} \tag{C.45}$$

where $\mathrm{Diag}(\lambda_i)$ is a diagonal matrix whose elements are the eigenvalues of $\mathbf{A}$. Thus, $\mathbf{A}$ can be expressed as in Eq. (C.46).

$$\mathbf{A} = \mathbf{W}\,\mathrm{Diag}(\lambda_i)\mathbf{W}^{-1} \tag{C.46}$$

where the columns of $\mathbf{W}$ are referred to as right eigenvectors ($\vec{w}_i$) and the rows of $\mathbf{W^{-1}}$ as left eigenvectors ($\vec{v}_i^H$):

$$\mathbf{W} = \begin{bmatrix}\vec{w}_1 & \vec{w}_2 & \cdots & \vec{w}_i & \cdots & \vec{w}_n\end{bmatrix} \tag{C.47}$$

$$\mathbf{W}^{-1} = \begin{bmatrix}\vec{v}_1^H \\ \vec{v}_2^H \\ \vdots \\ \vec{v}_i^H \\ \vdots \\ \vec{v}_n^H\end{bmatrix} \tag{C.48}$$

Substituting Eq. (C.46) in Eq. (C.44), the natural response can be obtained from Eq. (C.49).

$$\delta\vec{x}_{ZIR}(t) = \mathbf{W}\,\mathrm{Diag}\left[e^{\lambda_i(t-t_0)}\right]\mathbf{W}^{-1}\,\delta\vec{x}_0 \tag{C.49}$$

In order to isolate the contribution of each mode to the natural response, index notation is used, leading to Eq. (C.50).

$$\delta\vec{x}_{ZIR}(t) = \sum_{i=1}^{n} \vec{v}_i^{\mathrm{H}} \delta\vec{x}_0 e^{\lambda_i (t-t_0)} \vec{w}_i \tag{C.50}$$

where $\vec{v}_i^{\mathrm{H}}$ represents the i-th row of $\mathbf{W}^{-1}$ and H indicates the conjugate transpose (also known as Hermitian transpose). The contribution of each mode to the k-th state can be written as:

$$\delta x_{ZIR_k}(t) = \sum_{i=1}^{n} \left(\vec{v}_i^{\mathrm{H}} \delta\vec{x}_0\right) e^{\lambda_i (t-t_0)} w_{ik} \tag{C.51}$$

Assuming that the perturbation of the initial condition is a versor along the k-th state:

$$\delta\vec{x}_0 = \hat{\vec{e}}_k \tag{C.52}$$

the contribution of each mode to the k-th state (Eq. (C.51)) can be rewritten as:

$$\delta x_{ZIR_k}(t) = \sum_{i=1}^{n} v_{ik}^{\mathrm{H}} e^{\lambda_i (t-t_0)} w_{ik} = \sum_{i=1}^{n} \underbrace{v_{ki} w_{ki}}_{p_{ki}} e^{\lambda_i (t-t_0)} = \sum_{i=1}^{n} p_{ki} e^{\lambda_i (t-t_0)} \tag{C.53}$$

where p_{ki} is known as Mode Participation Factor (MPF) of the i-th mode on the k-th state. Using Eq. (C.45), the eigenvalue matrix can be written as:

$$\mathrm{Diag}(\lambda_i) = \mathbf{W}^{-1}\mathbf{A}\mathbf{W} \tag{C.54}$$

Expressing Eq. (C.54) in index notation:

$$\lambda_{ii} = \sum_{k=1}^{n} \sum_{\substack{j=1 \\ j\neq k}}^{n} v_{ik}^{H} a_{kj} w_{ji} + \sum_{k=1}^{n} v_{ik}^{H} a_{kk} w_{ki} \tag{C.55}$$

and deriving it with respect to the diagonal elements of the state matrix, the MPF can also be interpreted as the sensitivity of the i-th eigenvalue to variations of the k-th diagonal element of the state matrix:

$$\frac{\partial \lambda_{ii}}{\partial a_{kk}} = v_{ik}^{H} w_{ki} = v_{ki} w_{ki} = p_{ki} \tag{C.56}$$

Unlike eigenvectors, Mode Participation Factors are dimensionless. However, if the state matrix has complex-conjugate sets of eigenvalues, the MPF related to these eigenvalues is complex as well. Several variations of the basic definition of MPF can be found

in literature [Damodhar et al., 2012; Eyad H. Abed et al., 2009] to avoid this issue. One of this definitions has already been applied to conduct helicopter stability analysis [Femi et al., 2018]:

$$p_{ki} = |v_{ki}||w_{ki}| \tag{C.57}$$

which can be normalized by the maximum contribution of the i-th mode, enabling the possibility to compare also coupled and uncoupled eigenmodes:

$$p_{ki} = \frac{|v_{ki}||w_{ki}|}{\sum_{k=1}^{n} |v_{ki}||w_{ki}|} \tag{C.58}$$

According to Eq. (C.50), the natural response of the system is given by the linear combination of the individual contributions of each mode of motion. The distribution of the response states due to each mode is specified by the corresponding eigenvector, while the information about the time evolution is contained in the respective eigenvalue. The linear approximation that allows this interpretation is extremely powerful in enhancing physical understanding of vehicle's complex motions.

C.3. RESULTS

The result of the linearization procedure is a state-space model (Eq. (C.22)), whose matrices are expressed in Eq. (C.26) (Eq. (C.29) for the 3-DOF longitudinal dynamics) and (C.27) (Eq. (C.30) for the 3-DOF longitudinal dynamics) for normal operating conditions, and in Eq. (C.38) (Eq. (C.41) for the 3-DOF longitudinal dynamics + main-rotor speed DOF) and (C.39) (Eq. (C.42) for the 3-DOF longitudinal dynamics + main-rotor speed DOF) for autorotation. The terms in the state matrix **A** are referred to as *stability derivatives*, because they are strictly related to the stability of the system, i.e. to its eigenvalues. Whilst the terms in the control matrix **B** are referred to as *control derivatives*.

According to [Padfield, 2007], three different methods can be used for derivative calculation:

- Analytical differentiation of the force and moment expressions.
- Numerical differentiation.
- System identification.

Both numerical and analytical differentiation was adopted in this thesis. Analytical expressions of the derivatives allow to trace back to physical parameters (e.g., helicopter configuration data) that actually affect the dynamic behavior of the helicopter. This method can be adopted because the rotor model developed in this thesis (Appendix A) is analytical.

The analytical expression of the derivatives in Eq. (C.26) (Eq. (C.29) for the 3-DOF longitudinal dynamics) and (C.27) (Eq. (C.30) for the 3-DOF longitudinal dynamics) is

widely available in literature, e.g. [Bramwell et al., 2001]. However, in autorotation, the inclusion of the rotor speed degree of freedom in the conventional model structure (Eq. (A.28) non-linear, Eq. (C.33) linearized) give rise to new derivative terms that are not available analytically in literature. These extra terms appear in the last column of the state matrix Eq. (C.38) (Eq. (C.41) for the 3-DOF longitudinal dynamics + main-rotor speed DOF). The derivative terms in the last row of the state matrix Eq. (C.38) (Eq. (C.41) for the 3-DOF longitudinal dynamics + main-rotor speed DOF) and of the control matrix (C.39) (Eq. (C.42) for the 3-DOF longitudinal dynamics + main-rotor speed DOF) are computed during the calculation of the derivatives of the yaw moment N.

Due to the fact that the complexity of the analytical derivatives quickly increases when the effect of many design parameters is included and many degrees of freedom are modelled, we decided to adopt analytical differentiation only for the 3-DOF longitudinal dynamics model + main rotor speed DOF, and to neglect flapping hinge offset ($\epsilon = 0$) and pitch-flap coupling ($\delta_3 = 0$) from the analytical expression of forces and moments. A summary of the rotor derivatives is reported in Tab. C.1. The derivatives of the other helicopter components is not reported here, because it is dependent from the adopted models.

The Bo-105 configuration data have been considered to verify the developed model and the linearization procedure. The stability and control derivatives in straight level flight for the longitudinal dynamics are shown in Fig. C.1 and C.5, respectively, as a function of the horizontal speed. Also the results of the 3-DOF longitudinal model match quite accurately the derivative data generated by Boeing-Vertol Y-92 trim and stability analysis computer program for a 6-DOFs model [Heffley et al., 1979].

Heffley et al. [1979] do not provide any data for the main-rotor torque derivatives. Therefore, Q_u, Q_w, Q_q, Q_{θ_0} and Q_{B_1} have been compared with the corresponding derivatives of the yaw moment N (Fig. C.1g, C.1h, C.1o, C.5g and C.5h, respectively).

There are little substantive data at present about derivatives with respect to the rotorspeed, thus no basis for comparison was available for $X_{\dot{\psi}_{mr}}$, $Z_{\dot{\psi}_{mr}}$, $M_{\dot{\psi}_{mr}}$ and $Q_{\dot{\psi}_{mr}}$ (Fig. C.1j, C.1l, C.1n and C.1p, respectively).

Due to the lack of available data in steady-descent in autorotation, the stability derivatives of the developed model were compared with those of a high-fidelity model (including elastic modes of the rotor and the fuselage) developed in CAMRAD/JA.

Table C.1: Analytical derivatives summary for the 3-DOF longitudinal dynamics model + main-rotor speed DOF.

Name	Expression	Derivatives					
		Stability				Control	
		μ or u	$\bar{w}$ or w	$\bar{q}$ or q	$\dot{\psi}_{mr}$	θ_0	$B1$
Horizontal speed at the hub	$u_h=(u-qh_R)\cos i_s+(w+qx_R)\sin i_s$	$u_{hu}=\cos i_s\simeq 1$	$u_{hw}=\sin i_s\simeq 0$	$u_{hq}=-h_R\cos i_s+x_R\sin i_s\simeq -h_R$	$u_{h\dot{\psi}_{mr}}=0$	$u_{h\theta_0}=0$	$u_{hB_1}=0$
Vertical speed at the hub	$w_h=(w+qx_R)\cos i_s-(u-qh_R)\sin i_s$	$w_{hu}=\sin i_s\simeq 0$	$w_{hw}=\cos i_s\simeq 1$	$w_{hq}=x_R\cos i_s+h_R\sin i_s\simeq x_R\simeq 0$	$w_{h\dot{\psi}_{mr}}=0$	$w_{h\theta_0}=0$	$w_{hB_1}=0$
Advance ratio	$\mu=\frac{u_h}{\dot{\psi}_{mr}R}$	$\mu_u=\frac{1}{\dot{\psi}_{mr}R}$	$\mu_w=0$	$\mu_q=-\frac{h_R}{\dot{\psi}_{mr}R}$	$\mu_{\dot{\psi}_{mr}}=-\frac{\mu}{\dot{\psi}_{mr}}$	$\mu_{\theta_0}=0$	$\mu_{B_1}=0$
Normalized vertical speed	$\bar{w}=\mu_z=\frac{w_h}{\dot{\psi}_{mr}R}=\frac{u_h}{\dot{\psi}_{mr}R}\tan\alpha_h=\mu\tan\alpha_h$	$\mu_{z\mu}=\tan\alpha_h\simeq\alpha_h$	$\mu_{zw}=\frac{1}{\dot{\psi}_{mr}R}$	$\mu_{zq}=0$	$\mu_{z\dot{\psi}_{mr}}=-\frac{\mu_z}{\dot{\psi}_{mr}}$	$\mu_{z\theta_0}=0$	$\mu_{zB_1}=-\mu$
Inflow ratio	$\lambda_i=\frac{w_i}{\dot{\psi}_{mr}R}$				$\lambda_{i\dot{\psi}_{mr}}=\frac{w_{i\dot{\psi}_{mr}}}{\dot{\psi}_{mr}R}-\frac{\lambda_i}{\dot{\psi}_{mr}}$		
Inflow ratio - Glauert	$\lambda_i=\frac{C_T}{2\sqrt{\mu^2+(\mu_z-\lambda_i)^2}}$ $w_i=\frac{T}{2\rho A\sqrt{u_h^2+(w_h-w_i)^2}}$	$\lambda_{i\mu}=\frac{\lambda_i}{C_T}C_{T\mu}-4\frac{\lambda_i^3}{C_T^2}\left[\mu+\lambda\left(\alpha_h-\lambda_{i\mu}\right)\right]$	$\lambda_{i\bar{w}}=\frac{\lambda_i}{C_T}C_{T\bar{w}}-4\frac{\lambda_i^3}{C_T^2}\lambda(1-\lambda_{i\bar{w}})$	$\lambda_{i\bar{q}}=0$	$w_{i\dot{\psi}_{mr}}=\frac{w_i T T_{\dot{\psi}_{mr}}}{T^2-4\rho^2A^2w_i^3(w_h-w_i)}$	$\lambda_{i\theta_0}=\frac{\lambda_i}{C_T}C_{T\theta_0}+4\frac{\lambda_i^3}{C_T^2}\lambda\lambda_{i\theta_0}$	$\lambda_{iB_1}=\frac{\lambda_i}{C_T}C_{TB_1}+-4\frac{\lambda_i^3}{C_T^2}\lambda\left(-\mu-\lambda_{iB_1}\right)$
Inflow ratio	$\lambda=\mu_z-\lambda_i$	$\lambda_\mu=\mu_{z\mu}-\lambda_{i\mu}$	$\lambda_{\bar{w}}=\mu_{z\bar{w}}-\lambda_{i\bar{w}}$	$\lambda_{\bar{q}}=\mu_{z\bar{q}}-\lambda_{i\bar{q}}$	$\lambda_{\dot{\psi}_{mr}}=\mu_{z\dot{\psi}_{mr}}-\lambda_{i\dot{\psi}_{mr}}$	$\lambda_{\theta_0}=\mu_{z\theta_0}-\lambda_{i\theta_0}$	$\lambda_{B_1}=\mu_{zB_1}-\lambda_{iB_1}$
Main-rotor thrust	$T=\rho A(\dot{\psi}_{mr}R)^2C_T$	$T_u=\rho A(\dot{\psi}_{mr}R)^2\mu_uC_{T\mu}$	$T_{\bar{w}}=\rho A(\dot{\psi}_{mr}R)^2\bar{w}_wC_{T\bar{w}}$	$T_{\bar{q}}=\rho A(\dot{\psi}_{mr}R)^2\bar{q}_qC_{T\bar{q}}$	$T_{\dot{\psi}_{mr}}=2\rho A\dot{\psi}_{mr}R^2C_T+\rho A(\dot{\psi}_{mr}R)^2C_{T\dot{\psi}_{mr}}$	$T_{\theta_0}=\rho A(\dot{\psi}_{mr}R)^2C_{T\theta_0}$	$T_{B_1}=\rho A(\dot{\psi}_{mr}R)^2C_{TB_1}$
Main-rotor thrust coefficient	$C_T=\frac{\sigma C_{L\alpha}}{2}\left[\frac{\mu_z}{2}-\frac{\lambda_i}{2}+\frac{\theta_0}{3}\left(1+\frac{3}{2}\mu^2\right)+\frac{\theta_{tw}}{4}\left(1+\mu^2\right)-\frac{\mu}{2}B_1\right]$	$C_{T\mu}=\frac{\sigma C_{L\alpha}}{2}\left(\frac{\lambda_\mu}{2}+\theta_0\mu+\frac{\theta_{tw}}{2}\mu-\frac{1}{2}B_1\right)$	$C_{T\bar{w}}=\frac{\sigma C_{L\alpha}}{2}\frac{\lambda_{\bar{w}}}{2}$	$C_{T\bar{q}}=\frac{\sigma C_{L\alpha}}{2}\frac{\lambda_{\bar{q}}}{2}$	$C_{T_{\dot{\psi}_{mr}}}=\frac{\sigma C_{L\alpha}}{2}\left(\frac{\lambda_{\dot{\psi}_{mr}}}{2}+\theta_0\mu\mu_{\dot{\psi}_{mr}}+\frac{\theta_{tw}}{2}\mu\mu_{\dot{\psi}_{mr}}-\frac{\mu_{\dot{\psi}_{mr}}}{2}B_1\right)$	$C_{T_{\theta_0}}=\frac{\sigma C_{L\alpha}}{2}\left[\frac{\lambda_{\theta_0}}{2}+\frac{1}{3}\left(1+\frac{3}{2}\mu^2\right)\right]$	$C_{T_{B_1}}=\frac{\sigma C_{L\alpha}}{2}\left(\frac{\lambda_{B_1}}{2}-\frac{\mu}{2}\right)$
Normalized pitch rate	$\bar{q}=\frac{q}{\dot{\psi}_{mr}}$	$\bar{q}_\mu=0$	$\bar{q}_{\mu_z}=0$	$\bar{q}_q=\frac{1}{\dot{\psi}_{mr}}$	$\bar{q}_{\dot{\psi}_{mr}}=-\frac{\bar{q}}{\dot{\psi}_{mr}}$	$\bar{q}_{\theta_0}=0$	$\bar{q}_{B_1}=0$

Table C.1: Analytical derivatives summary for the 3-DOF longitudinal dynamics model + main-rotor speed DOF. *(Continues.)*

Name	Expression	Derivatives					
		Stability				Control	
		μ or u	$\bar{w}$ or w	$\bar{q}$ or q	$\dot{\psi}_{mr}$	θ_0	$B1$
Coning angle	$a_0 = \frac{\gamma}{8}\left(\mu^2+1\right)\theta_0 + \frac{\gamma}{2}\left(\frac{1}{5}+\frac{1}{6}\mu^2\right)\theta_{tw} + -\frac{\gamma}{6}\mu B_1 + \frac{\gamma}{6}\lambda$	$a_{0\mu} = \frac{\gamma}{4}\mu\theta_0 + \frac{\gamma}{6}\mu\theta_{tw} - \frac{\gamma}{6}B_1 + \frac{\gamma}{6}\lambda\mu$	$a_{0\bar{w}} = \frac{\gamma}{6}\lambda_{\bar{w}}$	$a_{0\bar{q}} = \frac{\gamma}{6}\lambda_{\bar{q}}$	$a_{0\dot{\psi}_{mr}} = \frac{\gamma}{4}\mu\mu_{\dot{\psi}_{mr}}\theta_0 + \frac{\gamma}{6}\mu\mu_{\dot{\psi}_{mr}}\theta_{tw} + -\frac{\gamma}{6}\mu_{\dot{\psi}_{mr}}B_1 + \frac{\gamma}{6}\lambda_{\dot{\psi}_{mr}}$	$a_{0\theta_0} = \frac{\gamma}{8}\left(\mu^2+1\right) + \frac{\gamma}{6}\lambda_{\theta_0}$	$a_{0B_1} = -\frac{\gamma}{6}\mu + \frac{\gamma}{6}\lambda_{B_1}$
Longitudinal flapping angle	$a_1 = \frac{\frac{8}{3}\mu\theta_0 + 2\mu\theta_{tw}}{1-\frac{\mu^2}{2}} \frac{-\left(1+\frac{3}{2}\mu^2\right)B_1 - \frac{16}{\gamma}\bar{q} + 2\mu\lambda}{1-\frac{\mu^2}{2}}$	$a_{1\mu} = \frac{\left(\frac{8}{3}\theta_0 + 2\theta_{tw} + 2\lambda\right)\left(1+\frac{\mu^2}{2}\right)}{\left(1-\frac{\mu^2}{2}\right)^2} + \frac{2\mu\lambda_\mu\left(1-\frac{\mu^2}{2}\right) - 4\mu B_1 - \frac{16}{\gamma}\mu\bar{q}}{\left(1-\frac{\mu^2}{2}\right)^2}$	$a_{1\bar{w}} = \frac{2\mu\lambda_{\bar{w}}}{1-\frac{\mu^2}{2}}$	$a_{1\bar{q}} = \frac{-\frac{16}{\gamma}}{1-\frac{\mu^2}{2}}$	$a_{1\dot{\psi}_{mr}} = \frac{\frac{8}{3}\mu_{\dot{\psi}_{mr}}\theta_0 + 2\mu_{\dot{\psi}_{mr}}\theta_{tw} - 3\mu\mu_{\dot{\psi}_{mr}}B_1}{1-\frac{\mu^2}{2}} + \frac{-\frac{16}{\gamma}\bar{q}_{\dot{\psi}_{mr}} + 2\mu_{\dot{\psi}_{mr}}\lambda + 2\mu\lambda_{\dot{\psi}_{mr}}}{1-\frac{\mu^2}{2}} + \frac{\left(\frac{8}{3}\mu\theta_0 + 2\mu\theta_{tw}\right)\mu\mu_{\dot{\psi}_{mr}}}{\left(1-\frac{\mu^2}{2}\right)^2} + \frac{\left(-\left(1+\frac{3}{2}\mu^2\right)B_1 - \frac{16}{\gamma}\bar{q} + 2\mu\lambda\right)\mu\mu_{\dot{\psi}_{mr}}}{\left(1-\frac{\mu^2}{2}\right)^2}$	$a_{1\theta_0} = \frac{\frac{8}{3}\mu + 2\mu\lambda_{\theta_0}}{1-\frac{\mu^2}{2}}$	$a_{1B_1} = \frac{-\left(1+\frac{3}{2}\mu^2\right)}{1-\frac{\mu^2}{2}} + \frac{2\mu\lambda_{B_1}}{1-\frac{\mu^2}{2}}$
Lateral flapping angle	$b_1 = \frac{\frac{4}{3}\mu a_0 - \bar{q}}{1+\frac{\mu^2}{2}}$	$b_{1\mu} = \frac{\left(\frac{4}{3}a_0 + \frac{4}{3}\mu a_{0\mu}\right)\left(1+\frac{\mu^2}{2}\right)}{\left(1+\frac{\mu^2}{2}\right)^2} - \frac{\left(\frac{4}{3}\mu a_0 - \bar{q}\right)\mu}{\left(1+\frac{\mu^2}{2}\right)^2}$	$b_{1\bar{w}} = \frac{\frac{4}{3}\mu a_{0\bar{w}}}{1+\frac{\mu^2}{2}}$	$b_{1\bar{q}} = \frac{\frac{4}{3}\mu a_{0\bar{q}} - 1}{1+\frac{\mu^2}{2}}$	$b_{1\dot{\psi}_{mr}} = \frac{\frac{4}{3}\mu_{\dot{\psi}_{mr}}a_0 + \frac{4}{3}\mu a_{0\dot{\psi}_{mr}} - \bar{q}_{\dot{\psi}_{mr}}}{1+\frac{\mu^2}{2}} - \frac{\frac{4}{3}\mu a_0 - \frac{q}{\dot{\psi}_{mr}}}{\left(1+\frac{\mu^2}{2}\right)^2}\mu\mu_{\dot{\psi}_{mr}}$	$b_{1\theta_0} = \frac{\frac{4}{3}\mu a_{0\theta_0}}{1+\frac{\mu^2}{2}}$	$b_{1B_1} = \frac{\frac{4}{3}\mu a_{0B_1}}{1+\frac{\mu^2}{2}}$
Hub moment	$M_h = \frac{1}{2}N_b K_\beta a_1$	$M_{hu} = \frac{1}{2}N_b K_\beta \mu_u a_{1\mu}$	$M_{hw} = \frac{1}{2}N_b K_\beta \bar{w}_w a_{1\bar{w}}$	$M_{hq} = \frac{1}{2}N_b K_\beta \bar{q}_q a_{1\bar{q}}$	$M_{h\dot{\psi}_{mr}} = \frac{1}{2}N_b K_\beta a_{1\dot{\psi}_{mr}} + \frac{1}{2}N_b K_\beta \psi_{mr} a_1$	$M_{h\theta_0} = \frac{1}{2}N_b K_\beta a_{1\theta_0}$	$M_{hB_1} = \frac{1}{2}N_b K_\beta a_{1B_1}$
Blade profile drag coefficient	$\delta = \delta_0 + \delta_2 C_T^2$	$\delta_\mu = \delta_2 \cdot 2C_T C_{T\mu}$	$\delta_{\bar{w}} = \delta_2 \cdot 2C_T C_{T\bar{w}}$	$\delta_{\bar{q}} = \delta_2 \cdot 2C_T C_{T\bar{q}}$	$\delta_{\dot{\psi}_{mr}} = \delta_2 \cdot 2C_T C_{T\dot{\psi}_{mr}}$	$\delta_{\theta_0} = \delta_2 \cdot 2C_T C_{T\theta_0}$	$\delta_{B_1} = \delta_2 \cdot 2C_T C_{TB_1}$

Table C.1: Analytical derivatives summary for the 3-DOF longitudinal dynamics model + main-rotor speed DOF. *(Continues.)*

Name	Expression	Derivatives					
		Stability				Control	
		μ or u	$\bar{w}$ or w	$\bar{q}$ or q	$\dot{\psi}_{mr}$	θ_0	$B1$
Main-rotor torque	$Q = \rho A(\dot{\psi}_{mr}R)^2 R C_Q$	$Q_u = \rho A(\dot{\psi}_{mr}R)^2 R \mu_u C_{Q\mu}$	$Q_w = \rho A(\dot{\psi}_{mr}R)^2 R \bar{w}_w C_{Q\bar{w}}$	$Q_q = \rho A(\dot{\psi}_{mr}R)^2 R \bar{q}_q C_{Q\bar{q}}$	$Q_{\dot{\psi}_{mr}} = \rho A \dot{\psi}_{mr} R^3 C_Q + \rho A(\dot{\psi}_{mr}R)^2 R C_{Q\dot{\psi}_{mr}}$	$Q_{\theta_0} = \rho A(\dot{\psi}_{mr}R)^2 R C_{Q\theta_0}$	$Q_{B_1} = \rho A(\dot{\psi}_{mr}R)^2 R C_{QB_1}$
Main-rotor torque coefficient	$C_Q = \frac{\sigma C_{L\alpha}}{2}\left\{\frac{\delta}{4C_{L\alpha}}\left(1+\mu^2\right) - \theta_0\frac{\lambda}{3} + B_1\left[-\frac{1}{8}a_1\mu + \frac{\lambda}{4} + \frac{\mu\lambda}{4} + \frac{a_1}{8}\mu + \frac{a_1\mu}{16}\mu^2\right] + \theta_{tw}\frac{\lambda\mu}{4} - \frac{1}{2}\left[\lambda^2 + \lambda\mu a_1 + \lambda\mu a_1\mu + \mu^2\left(\frac{1}{2}a_0^2 + \frac{3}{8}a_1^2 + \frac{1}{8}b_1^2\right)\right] + \frac{\mu}{3}a_0 b_1 - \left[-\frac{\mu}{3}a_0 + \frac{1}{4}b_1\right]\bar{q} + -\frac{1}{8}\bar{q}^2 - \frac{1}{8}\left(b_1^2 + a_1^2\right)\right\}$	$\frac{2C_{Q\mu}}{\sigma C_{L\alpha}} = \frac{\delta_\mu}{4C_{L\alpha}}\left(1+\mu^2\right) + \frac{\delta}{2C_{L\alpha}}\mu - \theta_0\frac{\lambda_\mu}{3} + B_1\left[-\frac{1}{8}a_{1\mu} + \frac{\lambda}{4} + \frac{\mu\lambda_\mu}{4} + \frac{a_1}{8}\mu + \frac{a_{1\mu}}{16}\mu^2\right] + \theta_{tw}\frac{\lambda_\mu}{4} - \frac{1}{2}\left[2\lambda\lambda_\mu + \lambda a_{1\mu} + \lambda_\mu\mu a_1 + \lambda\mu a_{1\mu} + 2\mu\left(\frac{1}{2}a_0^2 + \frac{3}{8}a_1^2 + \frac{1}{8}b_1^2\right) + \mu^2\left(a_0 a_{0\mu} + \frac{3}{4}a_1 a_{1\mu} + \frac{1}{4}b_1 b_{1\mu}\right)\right] + \frac{1}{3}a_0 b_1 + \frac{\mu}{3}a_{0\mu} b_1 + \frac{\mu}{3}a_0 b_{1\mu} + -\left[-\frac{1}{3}a_0 - \frac{\mu}{3}a_{0\mu} + \frac{1}{4}b_{1\mu}\right]\bar{q} + -\frac{1}{4}\left(b_1 b_{1\mu} + a_1 a_{1\mu}\right)$	$\frac{2C_{Q\bar{w}}}{\sigma C_{L\alpha}} = \frac{\delta_{\bar{w}}}{4C_{L\alpha}}\left(1+\mu^2\right) - \theta_0\frac{\lambda_{\bar{w}}}{3} + B_1\left[-\frac{1}{8}a_{1\bar{w}} + \frac{\mu\lambda_{\bar{w}}}{4} + \frac{a_{1\bar{w}}}{16}\mu^2\right] - \theta_{tw}\frac{\lambda_{\bar{w}}}{4} - \frac{1}{2}\left[2\lambda\lambda_{\bar{w}} + \lambda_{\bar{w}}\mu a_1 + \lambda\mu a_{1\bar{w}} + \mu^2\left(a_0 a_{0\bar{w}} + \frac{3}{4}a_1 a_{1\bar{w}} + \frac{1}{4}b_1 b_{1\bar{w}}\right)\right] + \frac{\mu}{3}a_{0\bar{w}} b_1 + \frac{\mu}{3}a_0 b_{1\bar{w}} + -\left[-\frac{\mu}{3}a_{0\bar{w}} + \frac{1}{4}b_{1\bar{w}}\right]\bar{q} + -\frac{1}{4}\left(b_1 b_{1\bar{w}} + a_1 a_{1\bar{w}}\right)$	$\frac{2C_{Q\bar{q}}}{\sigma C_{L\alpha}} = \frac{\delta_{\bar{q}}}{4a_0}\left(1+\mu^2\right) - \theta_0\frac{\lambda_{\bar{q}}}{3} + B_1\left[-\frac{1}{8}a_{1\bar{q}} + \frac{\mu\lambda_{\bar{q}}}{4} + \frac{a_{1\bar{q}}}{16}\mu^2\right] - \theta_{tw}\frac{\lambda_{\bar{q}}}{4} - \frac{1}{2}\left[2\lambda\lambda_{\bar{q}} + \lambda_{\bar{q}}\mu a_1 + \lambda\mu a_{1\bar{q}} + \mu^2\left(a_0 a_{0\bar{q}} + \frac{3}{4}a_1 a_{1\bar{q}} + \frac{1}{4}b_1 b_{1\bar{q}}\right)\right] + \frac{\mu}{3}a_{0\bar{q}} b_1 + \frac{\mu}{3}a_0 b_{1\bar{q}} + -\left[-\frac{\mu}{3}a_{0\bar{q}} + \frac{1}{4}b_{1\bar{q}}\right]\bar{q} + \frac{\mu}{3}a_0 - \frac{1}{4}b_1 - \frac{1}{4}\bar{q} + -\frac{1}{4}\left(b_1 b_{1\bar{q}} + a_1 a_{1\bar{q}}\right)$	$\frac{2C_{Q\dot{\psi}_{mr}}}{\sigma C_{L\alpha}} = \frac{\delta_{\dot{\psi}_{mr}}}{4C_{L\alpha}}\left(1+\mu^2\right)\frac{\delta}{4C_{L\alpha}}\mu\mu_{\dot{\psi}_{mr}} - \theta_0\frac{\lambda_{\dot{\psi}_{mr}}}{3} - \theta_{tw}\frac{\lambda_{\dot{\psi}_{mr}}}{4} + B_1\left[-\frac{1}{8}a_1\dot{\psi}_{mr} + \mu_{\dot{\psi}_{mr}}\frac{\lambda}{4} + \frac{\mu\lambda_{\dot{\psi}_{mr}}}{4} + \frac{a_1\dot{\psi}_{mr}}{16}\mu^2 + \frac{a_1}{8}\mu\mu_{\dot{\psi}_{mr}}\right] + -\frac{1}{2}\left[2\lambda\lambda_{\dot{\psi}_{mr}} + \lambda_{\dot{\psi}_{mr}}\mu a_1 + \lambda\mu_{\dot{\psi}_{mr}}a_1 + \lambda\mu a_1\dot{\psi}_{mr} + 2\mu\mu_{\dot{\psi}_{mr}}\left(\frac{1}{2}a_0^2 + \frac{3}{8}a_1^2 + \frac{1}{8}b_1^2\right) + \mu^2\left(a_0 a_{0\dot{\psi}_{mr}} + \frac{3}{4}a_1 a_{1\dot{\psi}_{mr}} + \frac{1}{4}b_1 b_{1\dot{\psi}_{mr}}\right)\right] + \frac{1}{3}\mu_{\dot{\psi}_{mr}}a_0 b_1 + \frac{\mu}{3}a_{0\dot{\psi}_{mr}} b_1 + \frac{\mu}{3}a_0 b_1\dot{\psi}_{mr} + -\left[-\frac{1}{3}\mu_{\dot{\psi}_{mr}}a_0 - \frac{\mu}{3}a_{0\dot{\psi}_{mr}} + \frac{1}{4}b_{1\dot{\psi}_{mr}}\right]\bar{q} + -\left[-\frac{\mu}{3}a_0 + \frac{1}{4}b_1\right]\bar{q}\dot{\psi}_{mr} - \frac{1}{4}\bar{q}\bar{q}\dot{\psi}_{mr} + -\frac{1}{4}\left(b_1 b_1\dot{\psi}_{mr} + a_1 a_1\dot{\psi}_{mr}\right)$	$\frac{2C_{Q\theta_0}}{\sigma C_{L\alpha}} = \frac{\delta_{\theta_0}}{4C_{L\alpha}}\left(1+\mu^2\right) - \frac{\lambda}{3} + -\theta_0\frac{\lambda_{\theta_0}}{3} - \theta_{tw}\frac{\lambda_{\theta_0}}{4} + B_1\left[-\frac{1}{8}a_1\theta_0 + \frac{\mu\lambda_{\theta_0}}{4} + \frac{a_1\theta_0}{16}\mu^2\right] + -\frac{1}{2}\left[2\lambda\lambda_{\theta_0} + \lambda_{\theta_0}\mu a_1 + \lambda\mu a_1\theta_0 + \mu^2\left(a_0 a_{0\theta_0} + \frac{3}{4}a_1 a_{1\theta_0} + \frac{1}{4}b_1 b_{1\theta_0}\right)\right] + \frac{\mu}{3}a_{0\theta_0} b_1 + \frac{\mu}{3}a_0 b_{1\theta_0} + -\left[-\frac{\mu}{3}a_{0\theta_0} + \frac{1}{4}b_{1\theta_0}\right]\bar{q} + -\frac{1}{4}\left(b_1 b_{1\theta_0} + a_1 a_{1\theta_0}\right)$	$\frac{2C_{QB_1}}{\sigma C_{L\alpha}} = \frac{\delta_{B_1}}{4C_{L\alpha}}\left(1+\mu^2\right) + -\theta_0\frac{\lambda_{B_1}}{3} - \theta_{tw}\frac{\lambda_{B_1}}{4} + + \left[-\frac{1}{8}a_1 + \frac{\mu\lambda}{4} + \frac{a_1}{16}\mu^2\right] + B_1\left[-\frac{1}{8}a_1 B_1 + \frac{\mu\lambda_{B_1}}{4} + \frac{a_1 B_1}{16}\mu^2\right] + -\frac{1}{2}\left[2\lambda\lambda_{B_1} + \lambda_{B_1}\mu a_1 + \lambda\mu a_1 B_1 + \mu^2\left(a_0 a_{0B_1} + \frac{3}{4}a_1 a_{1B_1} + \frac{1}{4}b_1 b_{1B_1}\right)\right] + \frac{\mu}{3}a_{0B_1} b_1 + \frac{\mu}{3}a_0 b_{1B_1} + -\left[-\frac{\mu}{3}a_{0B_1} + \frac{1}{4}b_{1B_1}\right]\bar{q} + -\frac{1}{8}\left(2b_1 b_{1B_1} + 2a_1 a_{1B_1}\right)$
Main-rotor horizontal force	$H = \rho A(\dot{\psi}_{mr}R)^2 C_H$	$H_u = \rho A(\dot{\psi}_{mr}R)^2 \mu_u C_{H\mu}$	$H_{\bar{w}} = \rho A(\dot{\psi}_{mr}R)^2 \bar{w}_w C_{H\bar{w}}$	$H_{\bar{q}} = \rho A(\dot{\psi}_{mr}R)^2 \bar{q}_q C_{H\bar{q}}$	$H_{\dot{\psi}_{mr}} = 2\rho A\dot{\psi}_{mr}R^2 C_H + \rho A(\dot{\psi}_{mr}R)^2 C_{H\dot{\psi}_{mr}}$	$H_{\theta_0} = \rho A(\dot{\psi}_{mr}R)^2 C_{H\theta_0}$	$H_{B_1} = \rho A(\dot{\psi}_{mr}R)^2 C_{HB_1}$

Table C.1: Analytical derivatives summary for the 3-DOF longitudinal dynamics model + main-rotor speed DOF.

Name	Expression	Derivatives					
		Stability				Control	
		μ or u	$\bar{w}$ or w	$\bar{q}$ or q	$\dot{\psi}_{mr}$	θ_0	$B1$
Main-rotor horizontal force coefficient	$C_H = \frac{\sigma C_{L\alpha}}{2}\left\{\frac{\delta\mu}{2C_{L\alpha}} - \frac{1}{4}\theta_0\left(2\lambda\mu - \frac{4}{3}a_1\right) + \right.$ $- \frac{1}{4}\theta_{tw}(\lambda\mu - a_1) +$ $+ \frac{1}{4}B_1\left(-\frac{1}{4}\mu a_1 - \frac{3}{4}\mu a_1 + \lambda\right) +$ $+ \frac{1}{4}\left(3\lambda a_1 - \frac{2}{3}a_0 b_1 - \frac{2}{3}a_0\bar{q}\right) +$ $\left. + \frac{\mu}{4}\left(a_0^2 + a_1^2 - \frac{1}{4}b_1\bar{q}\right)\right\}$	$\frac{2C_{H\mu}}{\sigma C_{L\alpha}} =$ $\frac{\delta\mu\mu}{2C_{L\alpha}} + \frac{\delta}{2C_{L\alpha}} +$ $- \frac{1}{4}\theta_0\left(2\lambda\mu\mu + 2\lambda - \frac{4}{3}a_1\mu\right) +$ $- \frac{1}{4}\theta_{tw}\left(\lambda\mu\mu + \lambda - a_1\mu\right) +$ $+ \frac{1}{4}B_1\left(-a_1 - \mu a_1\mu + \lambda\mu\right) +$ $+ \frac{1}{4}\left(3\lambda\mu a_1 + 3\lambda a_1\mu - \frac{2}{3}a_0\mu b_1 + \right.$ $\left. - \frac{2}{3}a_0 b_1\mu - \frac{2}{3}a_{0\mu}\bar{q}\right) +$ $+ \frac{\mu}{4}\left(2a_0 a_{0\mu} + 2a_1 a_1\mu - \frac{1}{4}b_{1\mu}\bar{q}\right)$	$\frac{2C_{H\bar{w}}}{\sigma C_{L\alpha}} = \frac{\delta_{\bar{w}}\mu}{2a_0} -$ $\frac{1}{4}\theta_0\left(2\lambda_{\bar{w}}\mu - \frac{4}{3}a_{1\bar{w}}\right) +$ $- \frac{1}{4}\theta_{tw}\left(\lambda_{\bar{w}}\mu - a_{1\bar{w}}\right) +$ $+ \frac{1}{4}B_1\left(-\mu a_{1\bar{w}} + \lambda_{\bar{w}}\right) +$ $+ \frac{1}{4}\left(3\lambda_{\bar{w}} a_1 + 3\lambda a_{1\bar{w}} - \frac{2}{3}a_{0\bar{w}} b_1 + \right.$ $\left. - \frac{2}{3}a_0 b_{1\bar{w}} - \frac{2}{3}a_{0\bar{w}}\bar{q}\right) +$ $+ \frac{\mu}{4}\left(2a_0 a_{0\bar{w}} + 2a_1 a_{1\bar{w}} - \frac{1}{4}b_{1\bar{w}}\bar{q}\right)$	$\frac{2C_{H\bar{q}}}{\sigma C_{L\alpha}} = \frac{\delta_{\bar{q}}\mu}{2C_{L\alpha}} -$ $\frac{1}{4}\theta_0\left(2\lambda_{\bar{q}}\mu - \frac{4}{3}a_{1\bar{q}}\right) +$ $- \frac{1}{4}\theta_{tw}\left(\lambda_{\bar{q}}\mu - a_{1\bar{q}}\right) +$ $+ \frac{1}{4}B_1\left(-\mu a_{1\bar{q}} + \lambda_{\bar{q}}\right) +$ $+ \frac{1}{4}\left(3\lambda_{\bar{q}} a_1 + 3\lambda a_{1\bar{q}} - \frac{2}{3}a_{0\bar{q}} b_1 + \right.$ $\left. - \frac{2}{3}a_0 b_{1\bar{q}} - \frac{2}{3}a_{0\bar{q}}\bar{q} - \frac{2}{3}a_0\right) +$ $+ \frac{\mu}{4}\left(2a_0 a_{0\bar{q}} + 2a_1 a_{1\bar{q}} - \frac{1}{4}b_{1\bar{q}}\bar{q} - \frac{1}{4}b_1\right)$	$\frac{2C_{H\dot{\psi}_{mr}}}{\sigma C_{L\alpha}} = \frac{\delta_{\dot{\psi}_{mr}}\mu}{2C_{L\alpha}} +$ $\frac{\delta}{2C_{L\alpha}}\mu_{\dot{\psi}_{mr}} +$ $- \frac{1}{4}\theta_0\left(2\lambda_{\dot{\psi}_{mr}}\mu + 2\lambda\mu_{\dot{\psi}_{mr}} - \frac{4}{3}a_{1\dot{\psi}_{mr}}\right) +$ $- \frac{1}{4}\theta_{tw}\left(\lambda_{\dot{\psi}_{mr}}\mu + \lambda\mu_{\dot{\psi}_{mr}} - a_{1\dot{\psi}_{mr}}\right) +$ $+ \frac{1}{4}B_1\left(-\mu_{\dot{\psi}_{mr}} a_1 - \mu a_{1\dot{\psi}_{mr}} + \lambda_{\dot{\psi}_{mr}}\right) +$ $+ \frac{1}{4}\left(3\lambda_{\dot{\psi}_{mr}} a_1 + 3\lambda a_{1\dot{\psi}_{mr}} - \frac{2}{3}a_{0\dot{\psi}_{mr}} b_1 + \right.$ $- \frac{2}{3}a_0 b_{1\dot{\psi}_{mr}} - \frac{2}{3}a_{0\dot{\psi}_{mr}}\bar{q}$ $\left. - \frac{2}{3}a_0\bar{q}_{\dot{\psi}_{mr}}\right) +$ $+ \frac{\mu}{4}\left(2a_0 a_{0\dot{\psi}_{mr}} + 2a_1 a_{1\dot{\psi}_{mr}} - \frac{1}{4}b_{1\dot{\psi}_{mr}}\bar{q}\right.$ $\left. - \frac{1}{4}b_1\bar{q}_{\dot{\psi}_{mr}}\right) +$ $+ \frac{\mu_{\dot{\psi}_{mr}}}{4}\left(a_0^2 + a_1^2 - \frac{1}{4}b_1\bar{q}\right)$	$\frac{2C_{H\theta_0}}{\sigma C_{L\alpha}} = \frac{\delta_{\theta_0}\mu}{2C_{L\alpha}} -$ $\frac{1}{4}\left(2\lambda\mu - \frac{4}{3}a_1\right) +$ $- \frac{1}{4}\theta_0\left(2\lambda_{\theta_0}\mu - \frac{4}{3}a_{1\theta_0}\right) +$ $- \frac{1}{4}\theta_{tw}\left(\lambda_{\theta_0}\mu - a_{1\theta_0}\right) +$ $+ \frac{1}{4}B_1\left(\lambda_{\theta_0} - \mu a_{1\theta_0} + \lambda_{\theta_0}\right) +$ $+ \frac{1}{4}\left(3\lambda\theta_0 a_1 + 3\lambda a_{1\theta_0} - \frac{2}{3}a_{0\theta_0} b_1 \right.$ $- \frac{2}{3}a_0 b_{1\theta_0}$ $\left. - \frac{2}{3}a_{0\theta_0}\bar{q}\right) +$ $+ \frac{\mu}{4}\left(2a_0 a_{0\theta_0} + 2a_1 a_{1\theta_0} - \frac{1}{4}b_{1\theta_0}\bar{q}\right)$	$\frac{2C_{HB_1}}{\sigma C_{L\alpha}} = \frac{\delta_{B_1}\mu}{2C_{L\alpha}} +$ $- \frac{1}{4}\theta_0\left(2\lambda_{B_1}\mu - \frac{4}{3}a_{1B_1}\right) +$ $- \frac{1}{4}\theta_{tw}\left(\lambda_{B_1}\mu - a_{1B_1}\right) +$ $+ \frac{1}{4}\left(-\mu a_1 + \lambda\right) +$ $+ \frac{1}{4}B_1\left(-\mu a_{1B_1} + \lambda_{B_1}\right) +$ $+ \frac{1}{4}\left(3\lambda_{B_1} a_1 + 3\lambda a_{1B_1} - \frac{2}{3}a_{0B_1} b_1 + \right.$ $\left. - \frac{2}{3}a_0 b_{1B_1} - \frac{2}{3}a_{0B_1}\bar{q}\right) +$ $+ \frac{\mu}{4}\left(2a_0 a_{0B_1} + 2a_1 a_{1B_1} - \frac{1}{4}b_{1B_1}\bar{q}\right)$

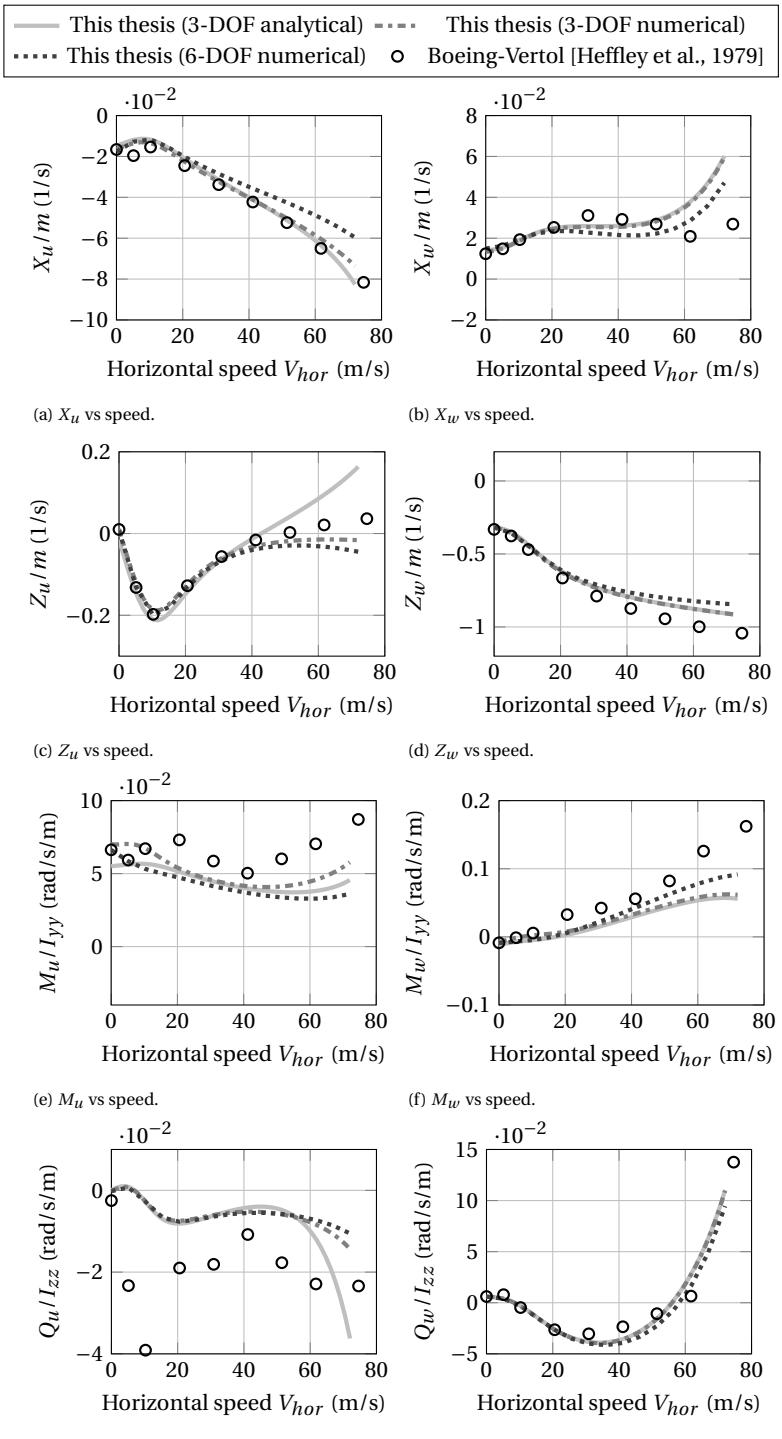

(a) X_u vs speed.

(b) X_w vs speed.

(c) Z_u vs speed.

(d) Z_w vs speed.

(e) M_u vs speed.

(f) M_w vs speed.

(g) Q_u vs speed.

(h) Q_w vs speed.

Figure C.1: Stability derivatives in straight level flight at sea-level (MTOW, ψ_{mr} = 100%) as a function of horizontal speed for the longitudinal dynamics. *(Continues.)*

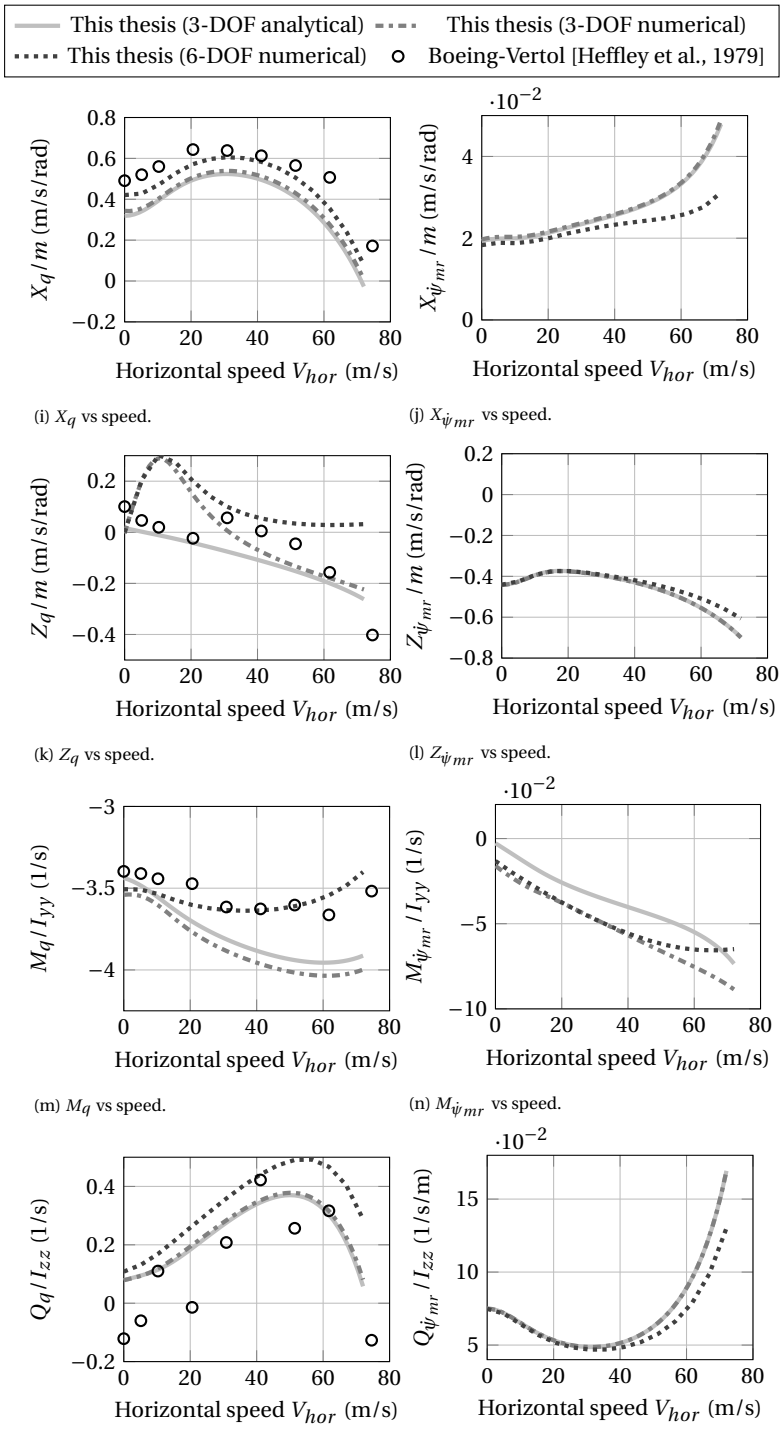

(i) X_q vs speed.

(j) $X_{\dot{\psi}_{mr}}$ vs speed.

(k) Z_q vs speed.

(l) $Z_{\dot{\psi}_{mr}}$ vs speed.

(m) M_q vs speed.

(n) $M_{\dot{\psi}_{mr}}$ vs speed.

(o) Q_q vs speed.

(p) $Q_{\dot{\psi}_{mr}}$ vs speed.

Figure C.1: Stability derivatives in straight level flight at sea-level (MTOW, $\dot{\psi}_{mr}$ = 100%) as a function of horizontal speed for the longitudinal dynamics. *(Concluded.)*

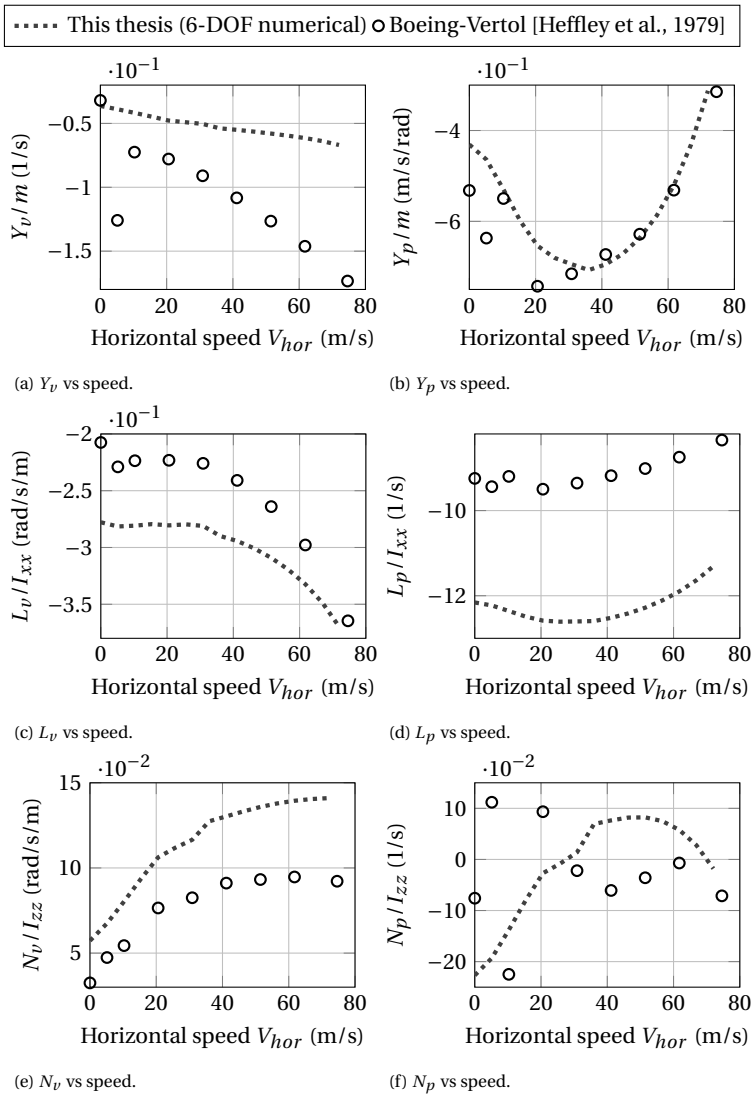

(a) Y_v vs speed.

(b) Y_p vs speed.

(c) L_v vs speed.

(d) L_p vs speed.

(e) N_v vs speed.

(f) N_p vs speed.

Figure C.2: Stability derivatives in straight level flight at sea-level (MTOW, $\dot{\psi}_{mr}$ = 100%) as a function of horizontal speed for the lateral-directional dynamics. *(Continues.)*

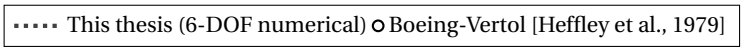

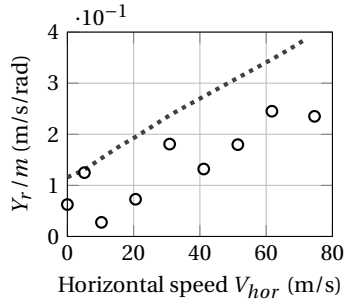

(g) Y_r vs speed.

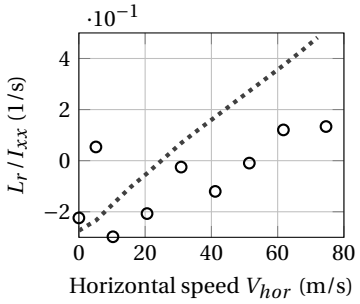

(h) L_r vs speed.

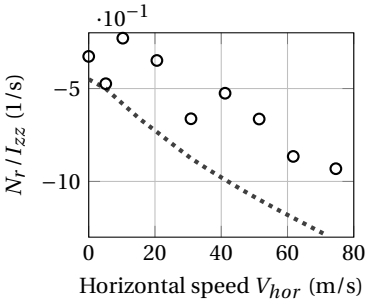

(i) N_r vs speed.

Figure C.2: Stability derivatives in straight level flight at sea-level (MTOW, $\dot{\psi}_{mr}$ = 100%) as a function of horizontal speed for the lateral-directional dynamics. *(Concluded.)*

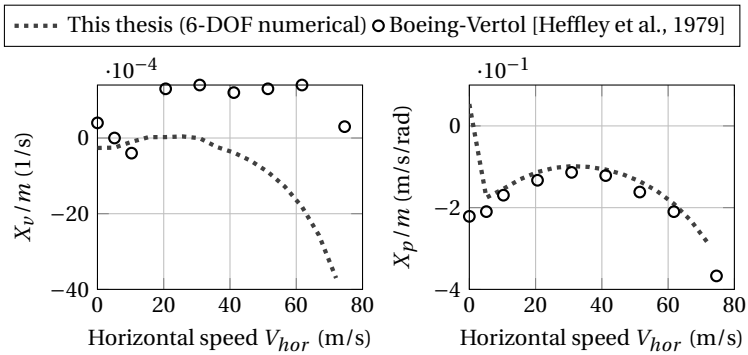

(a) X_v vs speed.

(b) X_p vs speed.

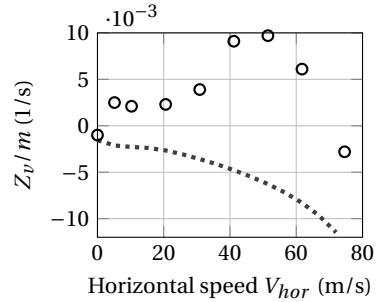

(c) Z_v vs speed.

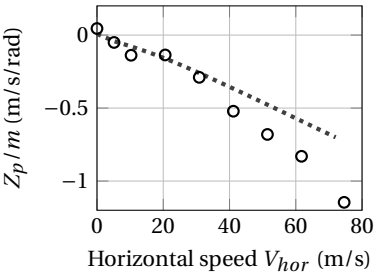

(d) Z_p vs speed.

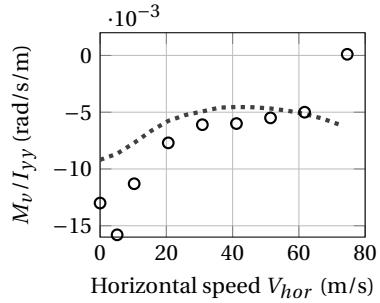

(e) M_v vs speed.

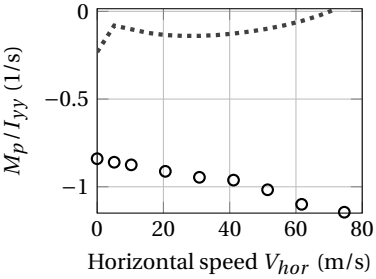

(f) M_p vs speed.

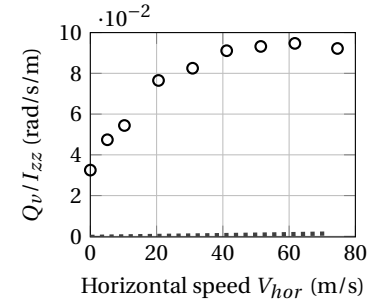

(g) Q_v vs speed.

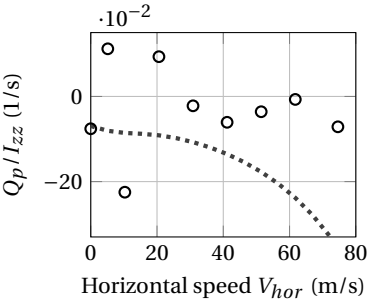

(h) Q_p vs speed.

Figure C.3: Stability derivatives in straight level flight at sea-level (MTOW, $\dot{\psi}_{mr}$ = 100%) as a function of horizontal speed for the longitudinal to lateral-directional couplings. *(Continues.)*

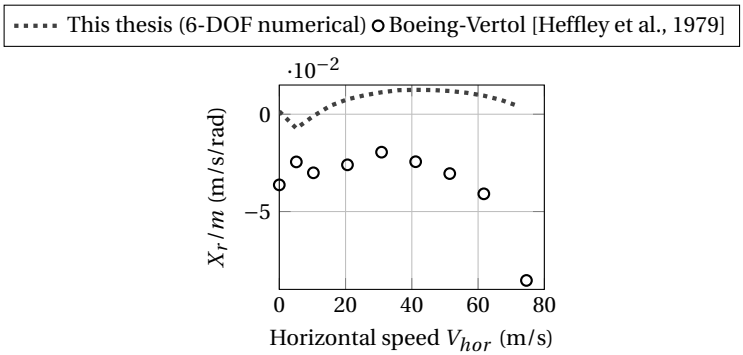

(i) X_r vs speed.

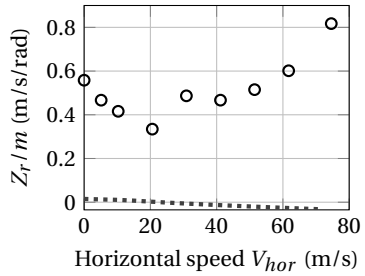

(j) Z_r vs speed.

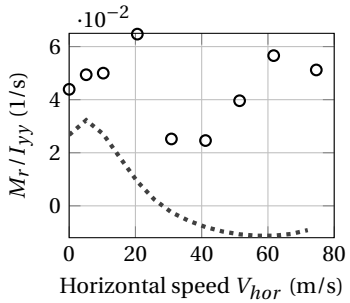

(k) M_r vs speed.

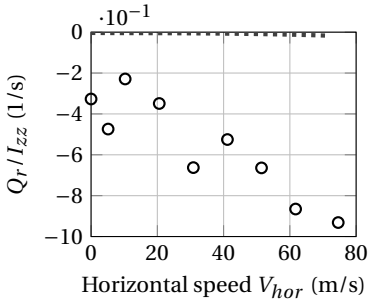

(l) Q_r vs speed.

Figure C.3: Stability derivatives in straight level flight at sea-level (MTOW, $\dot{\psi}_{mr}$ = 100%) as a function of horizontal speed for the longitudinal to lateral-directional couplings. *(Concluded.)*

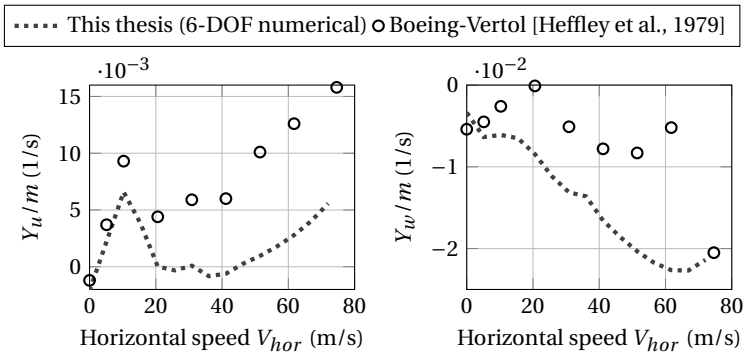

(a) Y_u vs speed.

(b) Y_w vs speed.

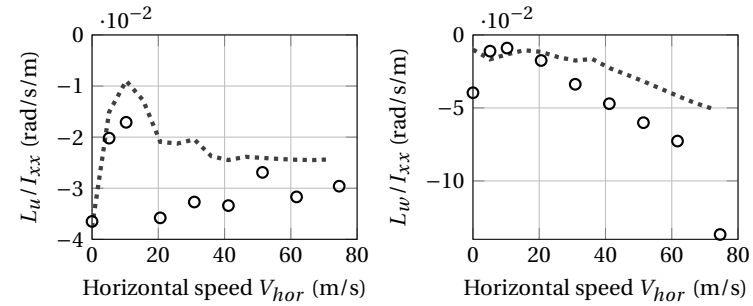

(c) L_u vs speed.

(d) L_w vs speed.

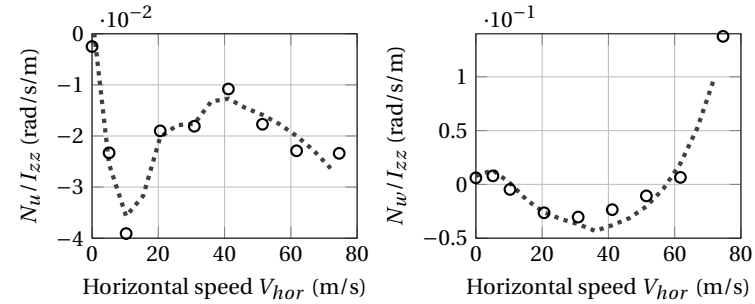

(e) N_u vs speed.

(f) N_w vs speed.

Figure C.4: Stability derivatives in straight level flight at sea-level (MTOW, $\dot{\psi}_{mr} = 100\%$) as a function of horizontal speed for the lateral-directional to longitudinal couplings. *(Continues.)*

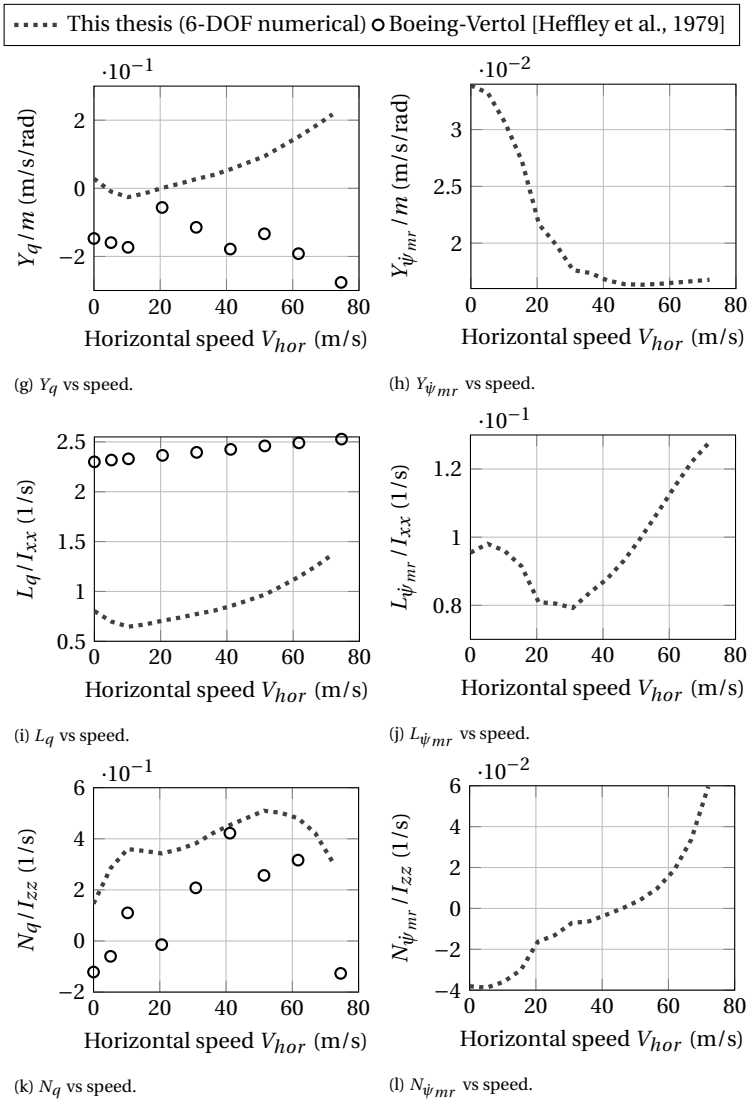

(g) Y_q vs speed.

(h) $Y_{\dot{\psi}_{mr}}$ vs speed.

(i) L_q vs speed.

(j) $L_{\dot{\psi}_{mr}}$ vs speed.

(k) N_q vs speed.

(l) $N_{\dot{\psi}_{mr}}$ vs speed.

Figure C.4: Stability derivatives in straight level flight at sea-level (MTOW, $\dot{\psi}_{mr}$ = 100%) as a function of horizontal speed for the lateral-directional to longitudinal couplings. *(Concluded.)*

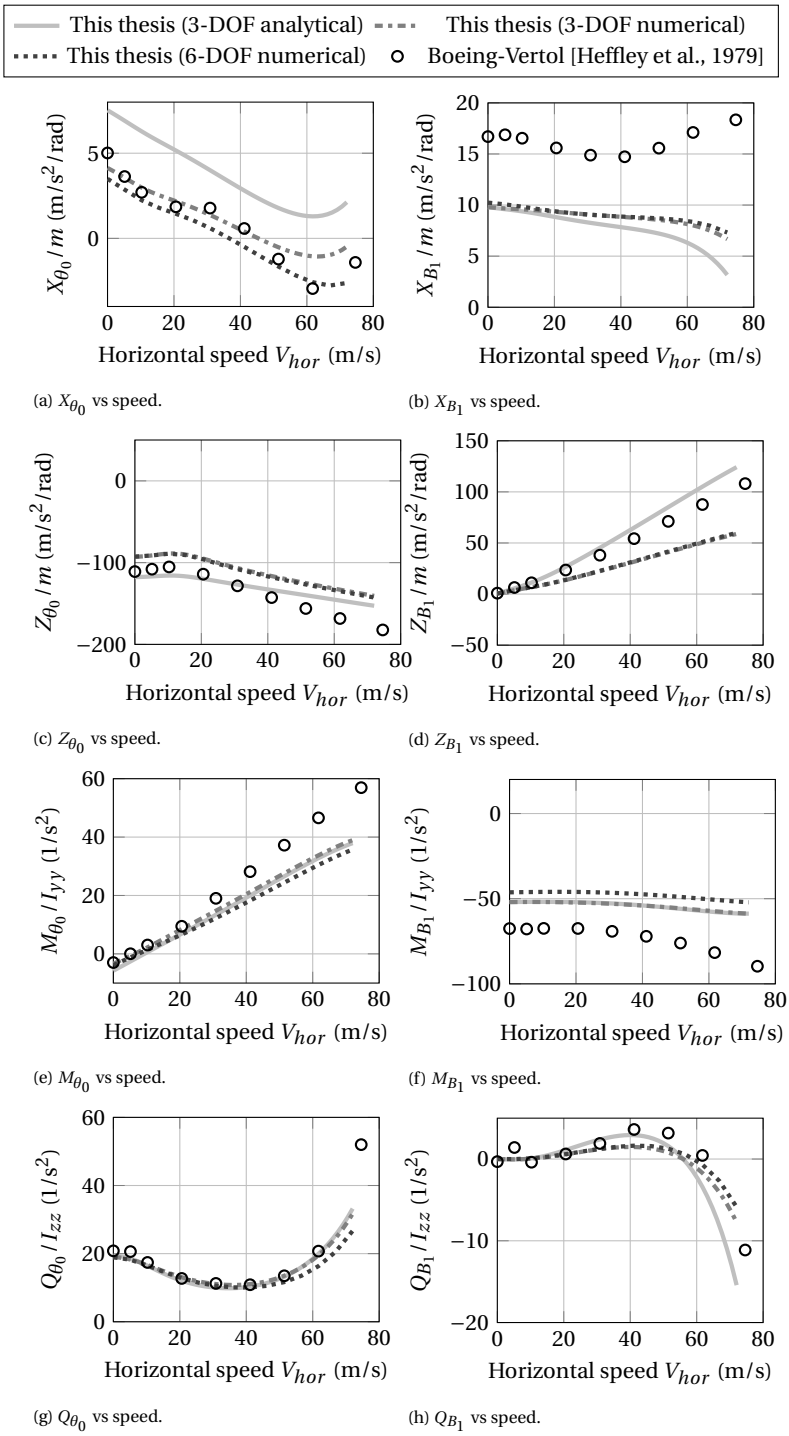

(a) X_{θ_0} vs speed.

(b) X_{B_1} vs speed.

(c) Z_{θ_0} vs speed.

(d) Z_{B_1} vs speed.

(e) M_{θ_0} vs speed.

(f) M_{B_1} vs speed.

(g) Q_{θ_0} vs speed.

(h) Q_{B_1} vs speed.

Figure C.5: Control derivatives in straight level flight at sea-level (MTOW, $\dot{\psi}_{mr}$ = 100%) as a function of horizontal speed for the longitudinal dynamics.

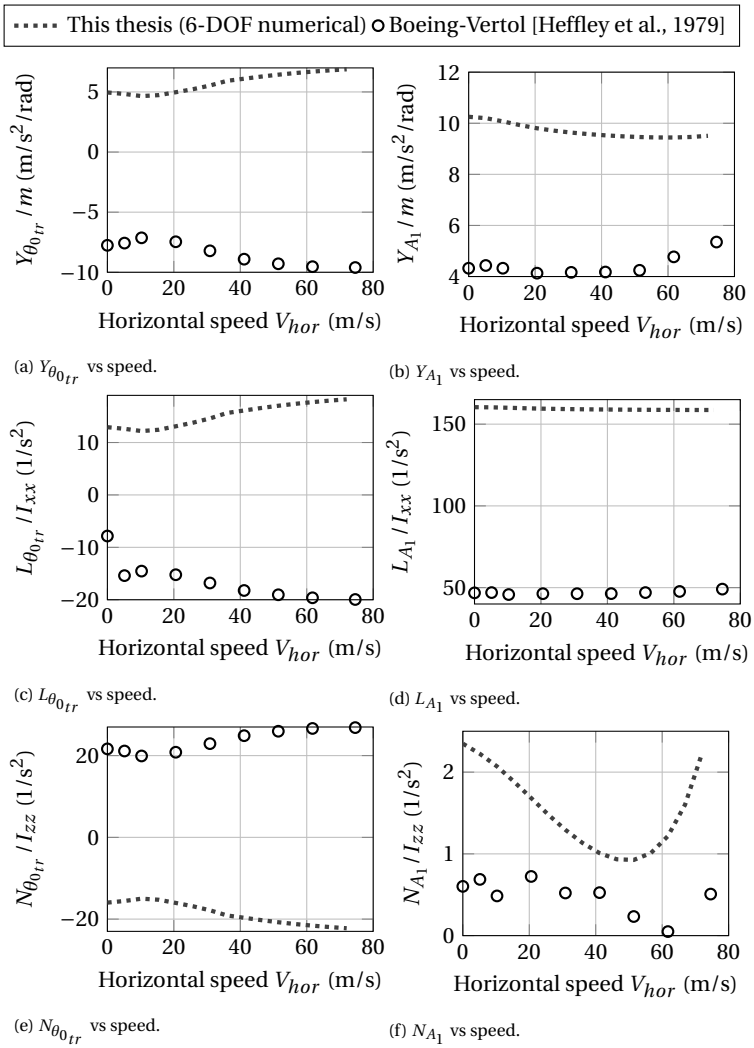

(a) $Y_{\theta_{0_{tr}}}$ vs speed.

(b) Y_{A_1} vs speed.

(c) $L_{\theta_{0_{tr}}}$ vs speed.

(d) L_{A_1} vs speed.

(e) $N_{\theta_{0_{tr}}}$ vs speed.

(f) N_{A_1} vs speed.

Figure C.6: Control derivatives in straight level flight at sea-level (MTOW, $\dot{\psi}_{mr}$ = 100%) as a function of horizontal speed for the lateral-directional dynamics.

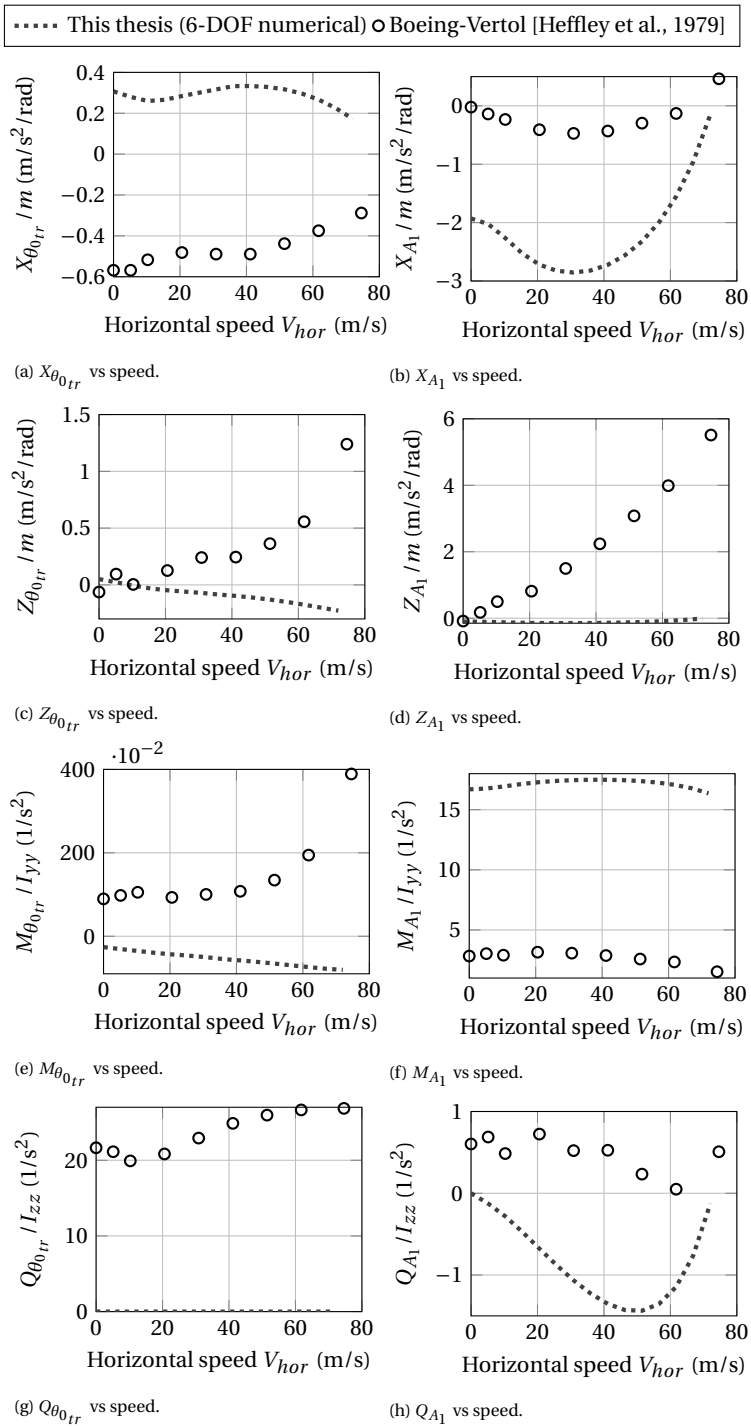

(a) $X_{\theta_{0_{tr}}}$ vs speed.

(b) X_{A_1} vs speed.

(c) $Z_{\theta_{0_{tr}}}$ vs speed.

(d) Z_{A_1} vs speed.

(e) $M_{\theta_{0_{tr}}}$ vs speed.

(f) M_{A_1} vs speed.

(g) $Q_{\theta_{0_{tr}}}$ vs speed.

(h) Q_{A_1} vs speed.

Figure C.7: Control derivatives in straight level flight at sea-level (MTOW, $\dot{\psi}_{mr}$ = 100%) as a function of horizontal speed for the longitudinal to lateral-directional controls.

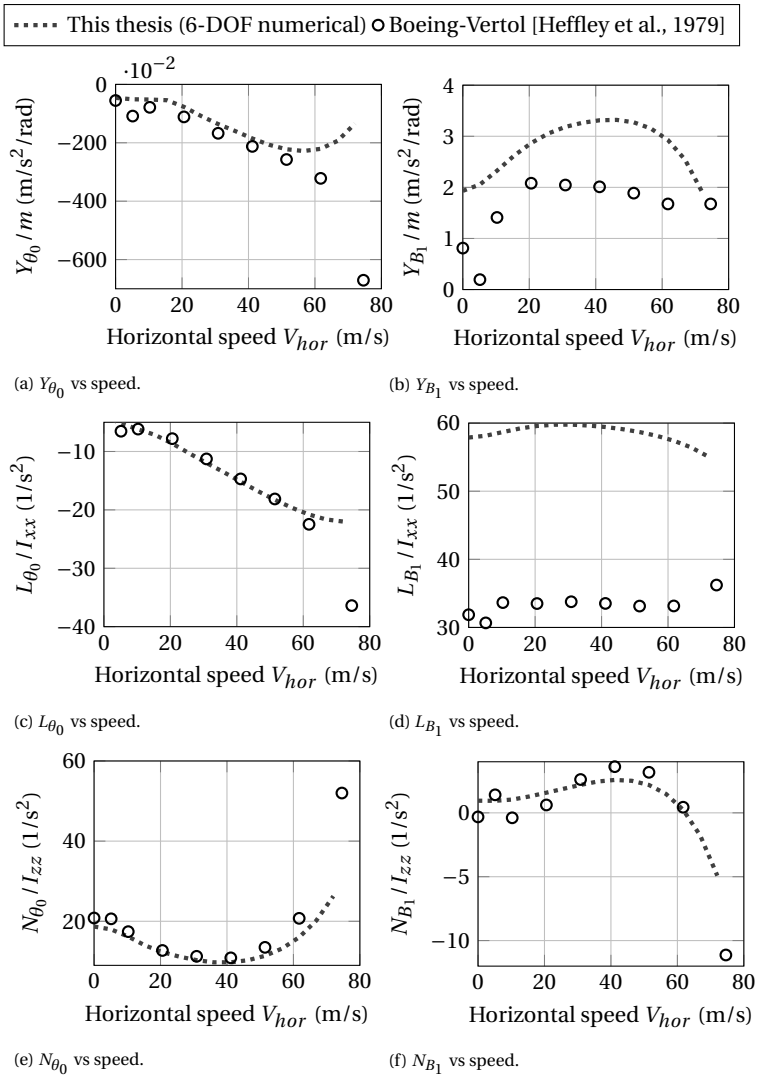

(a) Y_{θ_0} vs speed.

(b) Y_{B_1} vs speed.

(c) L_{θ_0} vs speed.

(d) L_{B_1} vs speed.

(e) N_{θ_0} vs speed.

(f) N_{B_1} vs speed.

Figure C.8: Control derivatives in straight level flight at sea-level (MTOW, $\dot{\psi}_{mr}$ = 100%) as a function of horizontal speed for the lateral-directional to longitudinal controls.

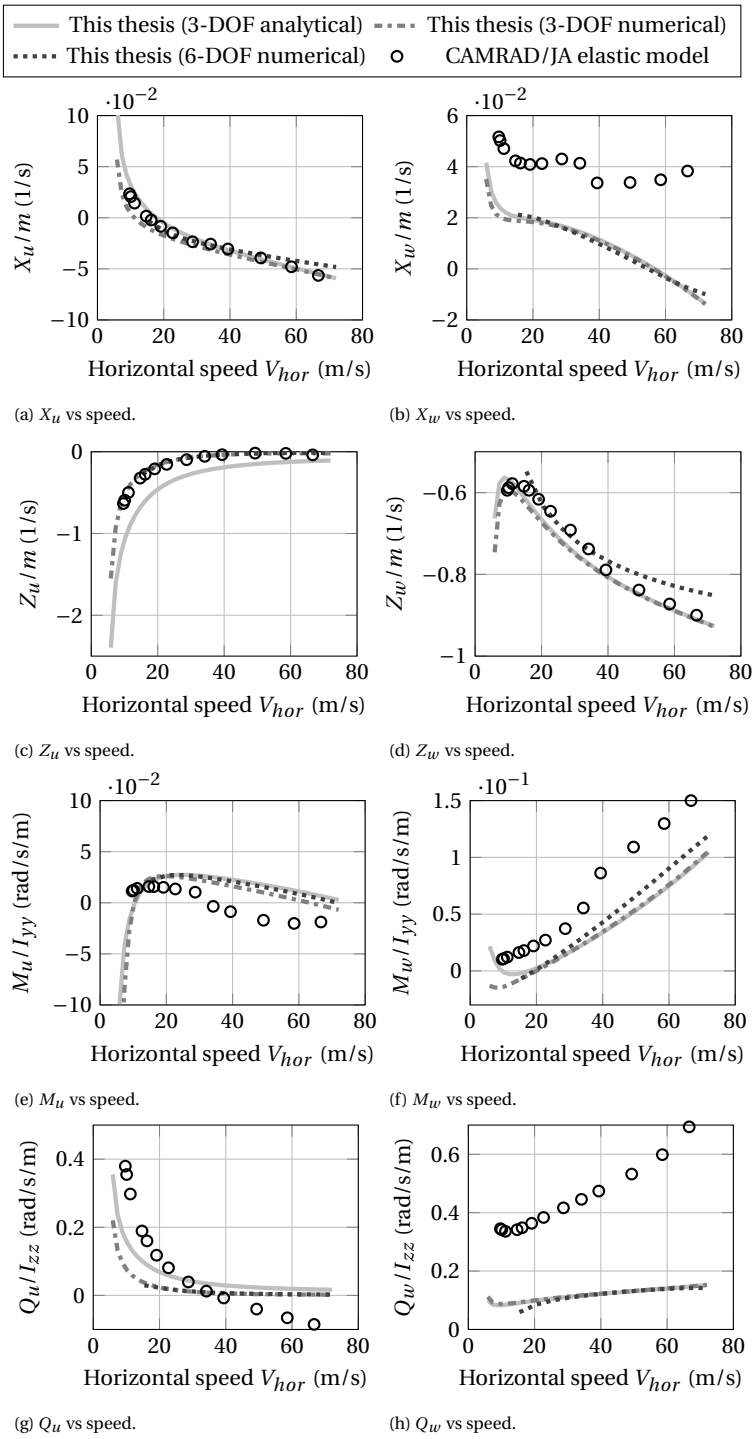

(a) X_u vs speed.

(b) X_w vs speed.

(c) Z_u vs speed.

(d) Z_w vs speed.

(e) M_u vs speed.

(f) M_w vs speed.

(g) Q_u vs speed.

(h) Q_w vs speed.

Figure C.9: Stability derivatives in steady-descent in autorotation at sea-level(MTOW, $\dot{\psi}_{mr} = 100\%$) as a function of horizontal speed for the longitudinal dynamics. *(Continues.)*

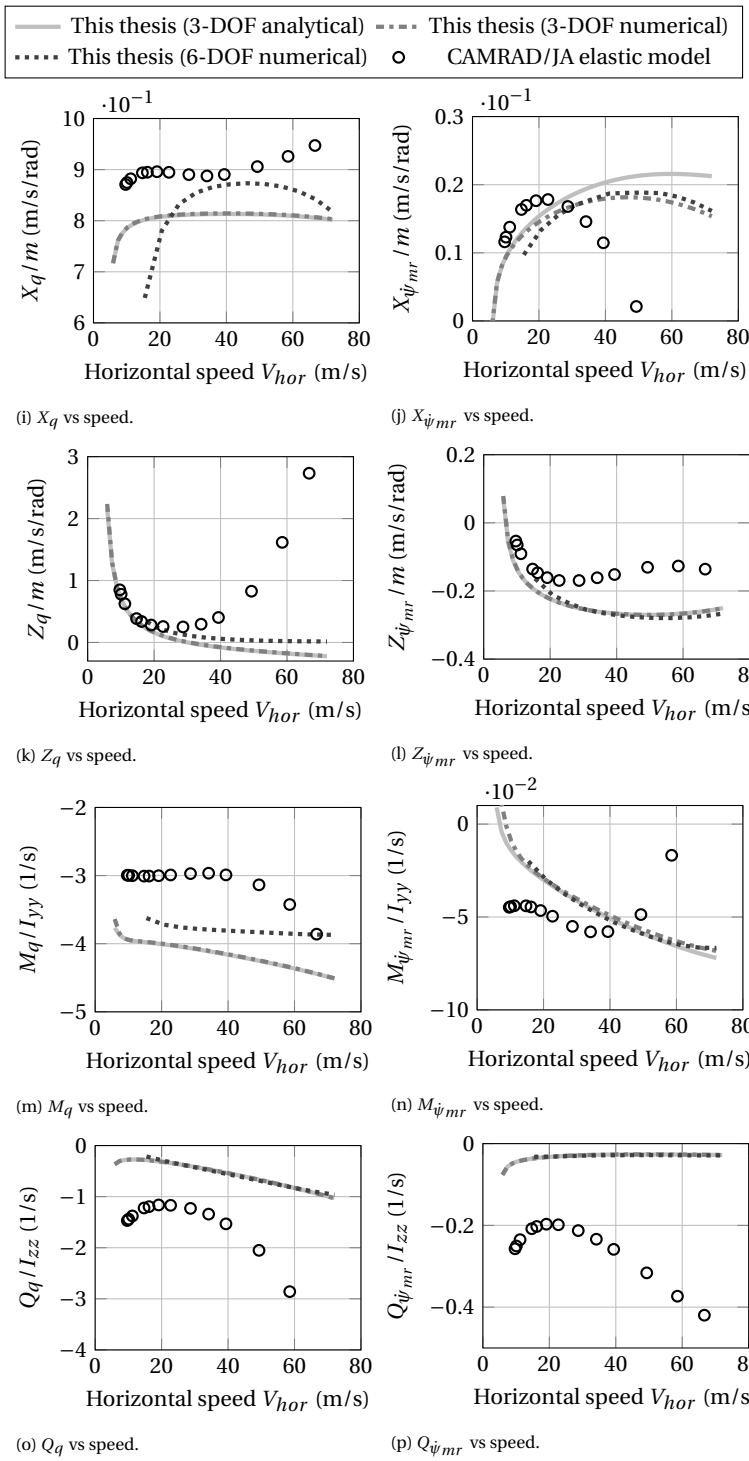

(i) X_q vs speed.

(j) $X_{\dot{\psi}_{mr}}$ vs speed.

(k) Z_q vs speed.

(l) $Z_{\dot{\psi}_{mr}}$ vs speed.

(m) M_q vs speed.

(n) $M_{\dot{\psi}_{mr}}$ vs speed.

(o) Q_q vs speed.

(p) $Q_{\dot{\psi}_{mr}}$ vs speed.

Figure C.9: Stability derivatives in steady-descent in autorotation at sea-level (MTOW, $\dot{\psi}_{mr}$ = 100%) as a function of horizontal speed for the longitudinal dynamics. *(Concluded.)*

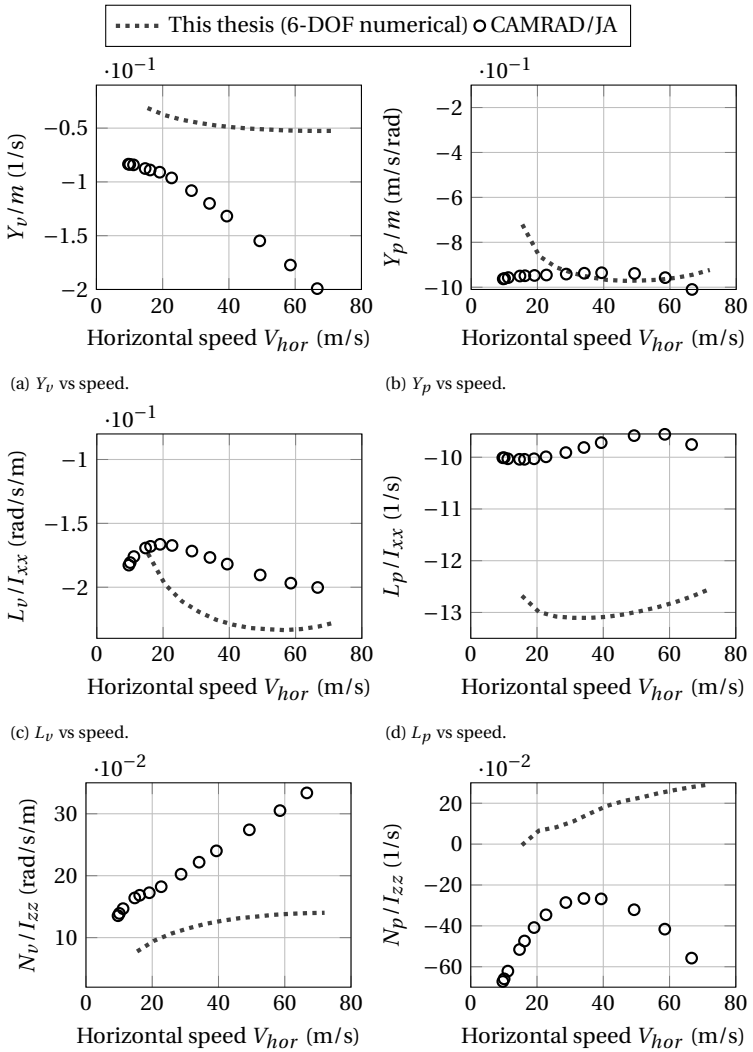

(a) Y_v vs speed.

(b) Y_p vs speed.

(c) L_v vs speed.

(d) L_p vs speed.

(e) N_v vs speed.

(f) N_p vs speed.

Figure C.10: Stability derivatives in steady-descent in autorotation at sea-level (MTOW, $\dot{\psi}_{mr} = 100\%$) as a function of horizontal speed for the lateral-directional dynamics. *(Continues.)*

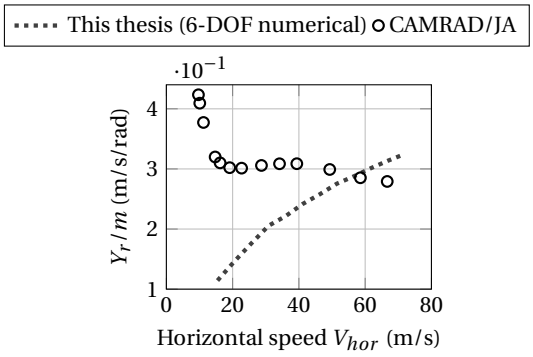

(g) Y_r vs speed.

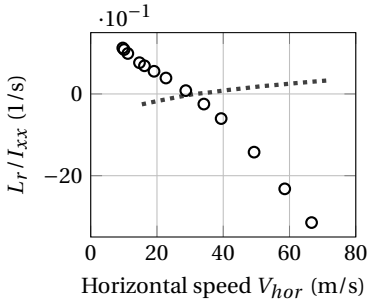

(h) L_r vs speed.

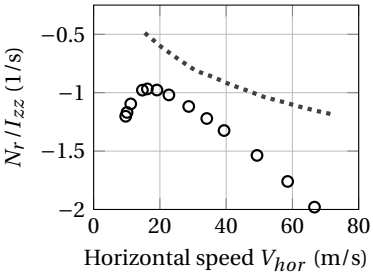

(i) N_r vs speed.

Figure C.10: Stability derivatives in steady-descent in autorotation at sea-level (MTOW, $\dot{\psi}_{mr} = 100\%$) as a function of horizontal speed for the lateral-directional dynamics. *(Concluded.)*

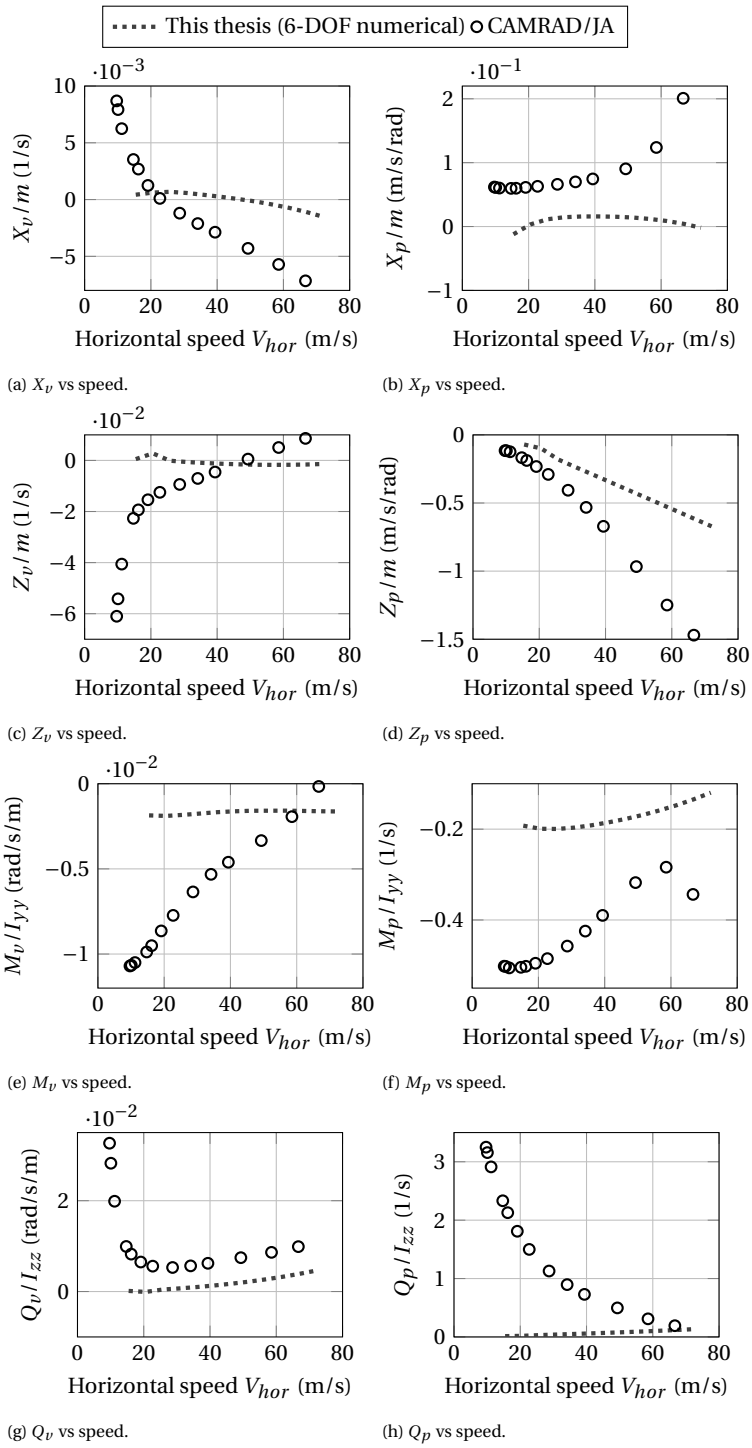

(a) X_v vs speed.

(b) X_p vs speed.

(c) Z_v vs speed.

(d) Z_p vs speed.

(e) M_v vs speed.

(f) M_p vs speed.

(g) Q_v vs speed.

(h) Q_p vs speed.

Figure C.11: Stability derivatives in steady-descent in autorotation at sea-level (MTOW, $\dot{\psi}_{mr} = 100\%$) as a function of horizontal speed for the longitudinal to lateral-directional couplings. *(Continues.)*

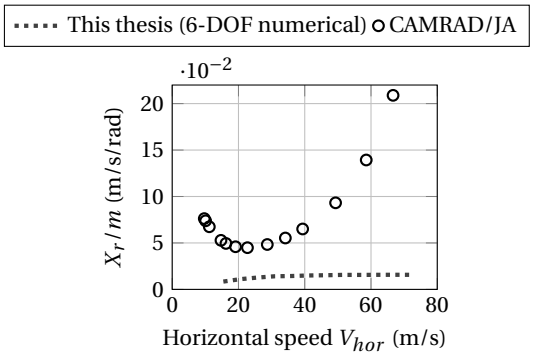

(i) X_r vs speed.

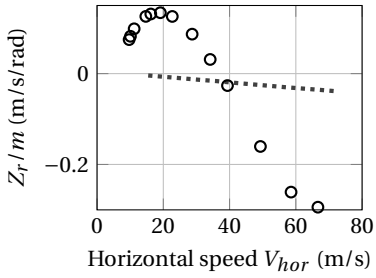

(j) Z_r vs speed.

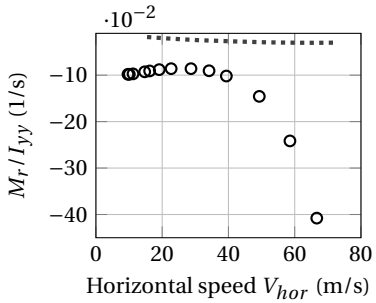

(k) M_r vs speed.

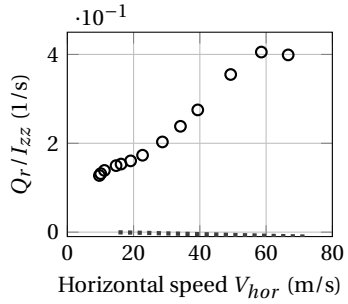

(l) Q_r vs speed.

Figure C.11: Stability derivatives in steady-descent in autorotation at sea-level (MTOW, ψ_{mr} = 100%) as a function of horizontal speed for the longitudinal to lateral-directional couplings. *(Concluded.)*

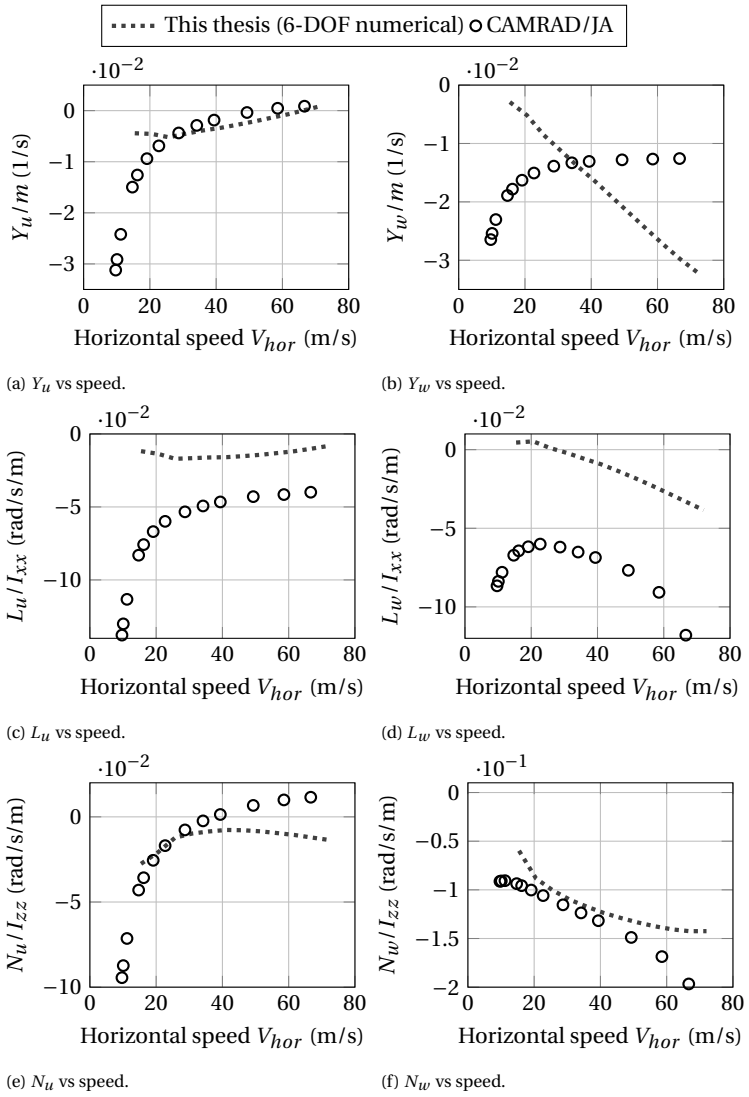

(a) Y_u vs speed.

(b) Y_w vs speed.

(c) L_u vs speed.

(d) L_w vs speed.

(e) N_u vs speed.

(f) N_w vs speed.

Figure C.12: Stability derivatives in steady-descent in autorotation at sea-level (MTOW, $\dot{\psi}_{mr} = 100\%$) as a function of horizontal speed for the lateral-directional to longitudinal couplings. *(Continues.)*

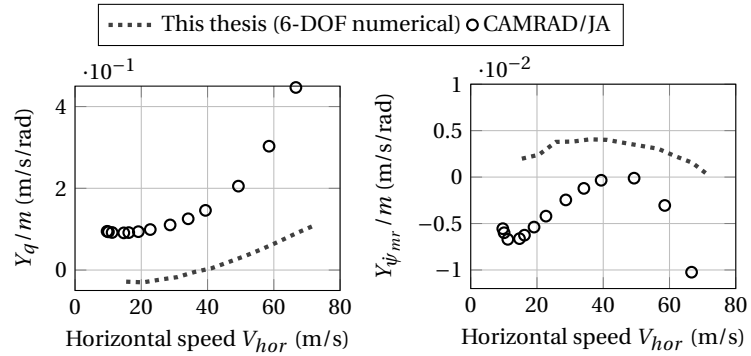

(g) Y_q vs speed.

(h) $Y_{\dot{\psi}_{mr}}$ vs speed.

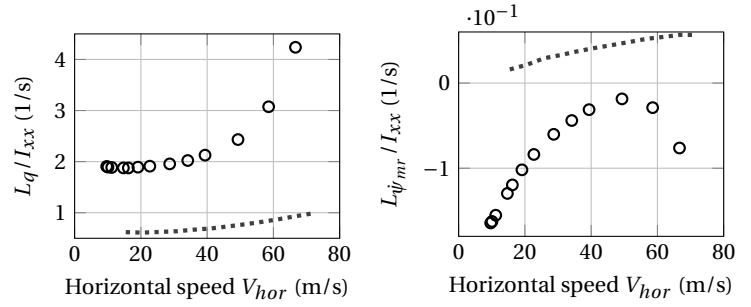

(i) L_q vs speed.

(j) $L_{\dot{\psi}_{mr}}$ vs speed.

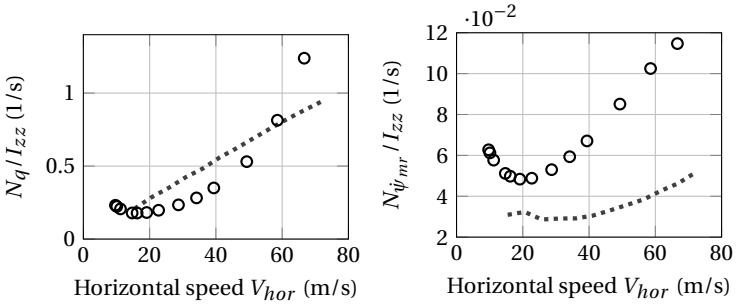

(k) N_q vs speed.

(l) $N_{\dot{\psi}_{mr}}$ vs speed.

Figure C.12: Stability derivatives in steady-descent in autorotation at sea-level (MTOW, $\dot{\psi}_{mr} = 100\%$) as a function of horizontal speed for the lateral-directional to longitudinal couplings. *(Concluded.)*

D

ENGINE DRIVETRAIN DYNAMICS

D.1. DRIVETRAIN ARCHITECTURE

This section describes the architecture of the drivetrain of a twin-engine conventional helicopter, taking as example the Bo-105 helicopter, whose power train is shown in Fig. D.1. The power train transmits engine power to both rotors and the transmission-mounted accessories. In general, the drivetrain of a twin-engine conventional helicopter comprises two engine drive shafts, a main transmission with accessory drives, tail rotor drive shafts, an intermediate gearbox, and a tail rotor gearbox.

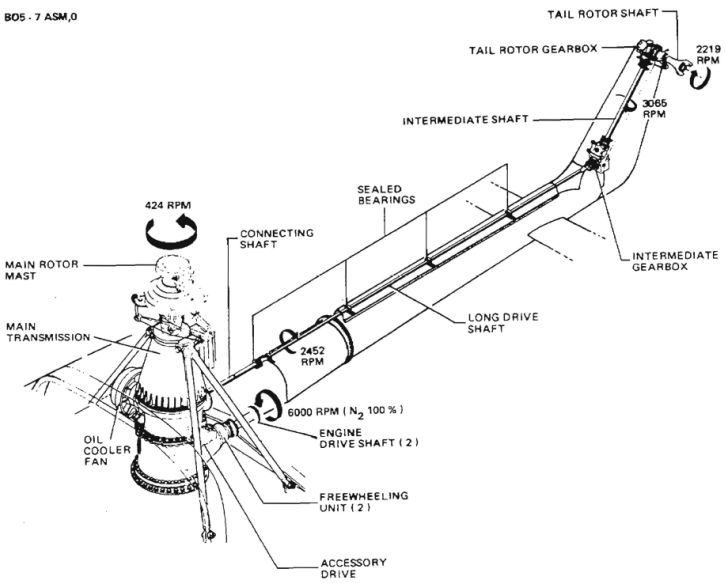

Figure D.1: Bo-105 helicopter power train [Anonymous, 1995]

Fig. D.2 illustrates a schematic of the drivetrain architecture of a twin-engine conventional helicopter with all the main components involved and their connection. In the next sections, these components are analyzed in more detail.

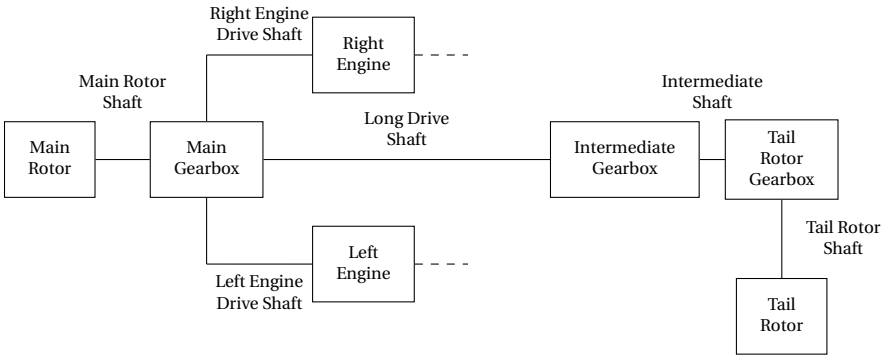

Figure D.2: Schematic of a twin-engine conventional helicopter power train.

D.1.1. MAIN TRANSMISSION

The main transmission combines the two engine drive shaft inputs and provides drive to the main rotor, tail rotor, accessories, and oil cooler fan. Two freewheeling units at the main transmission inputs permit either engine to be disengaged from the transmission during single-engine operation (One Engine Inoperative (OEI) condition) or both engines during autorotation (All Engines Inoperative (AEI) condition).

Power from the engines is transmitted through various stages of reduction gearing to obtain the necessary speed for the main rotor (Fig. D.4) and tail rotor (Fig. D.5 and D.6). Fig.D.4, D.5 and D.6 are extremely simplified schematics of a twin-engine conventional helicopter power train, since only one stage of reduction is represented for every transmission, whereas in reality the reduction of the engines' angular speed is achieved through several stages. For example, the main transmission usually consists of a collector gear (which is the one ideally represented in Fig. D.4 and D.5 as directly connected to the main rotor shaft) and one or more epicyclic modules (Fig. D.3). The three basic components of an epicyclic gear are:

1. The sun gear, which is the central gear.

2. The planet carrier, which holds one or more peripheral planet gears, all of the same size, meshed with the sun gear.

3. The ring gear or annulus, which is an outer ring with inward-facing teeth that mesh with the planet gear or gears.

The collector gear is connected to the solar gear of the epicyclic module, which transmits the motion to the main rotor mast through the planet carrier.

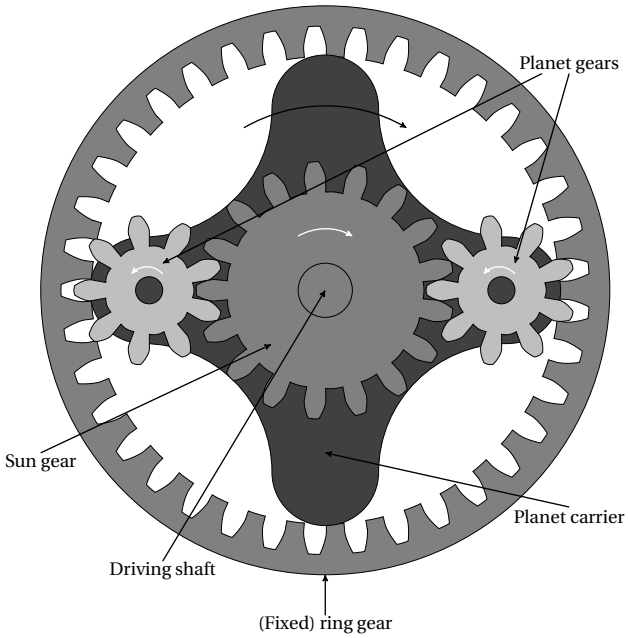

Figure D.3: Bottom view of an epicyclic module with two planets.

In the Bo-105 helicopter, the main gearbox is mounted forward of the engines above the cargo compartment (see Fig. D.1). Two hydraulic pumps and a rotor rpm (N_{R_0}) tach-generator are driven by the accessory gearbox mounted on the transmission left side. Mounted on the transmission right side is an oil cooler blower fan and reduction gearbox assembly.

D.1.2. TAIL ROTOR DRIVE SHAFTS

The tail rotor drive shafts of the Bo-105 helicopter consist of three tubular shaft sections comprising:

- a connecting shaft with flexible couplings,
- a long shaft supported by sealed bearings and fitted with a flexible coupling at the intermediate gearbox end,
- an intermediate shaft with flexible couplings installed at the vertical fin between the intermediate and tail rotor gearboxes.

The connecting shaft is routed through a tunnel in the engine compartment dividing firewall. The long drive shaft and the intermediate shaft are covered by fairings which may be opened for maintenance and inspection.

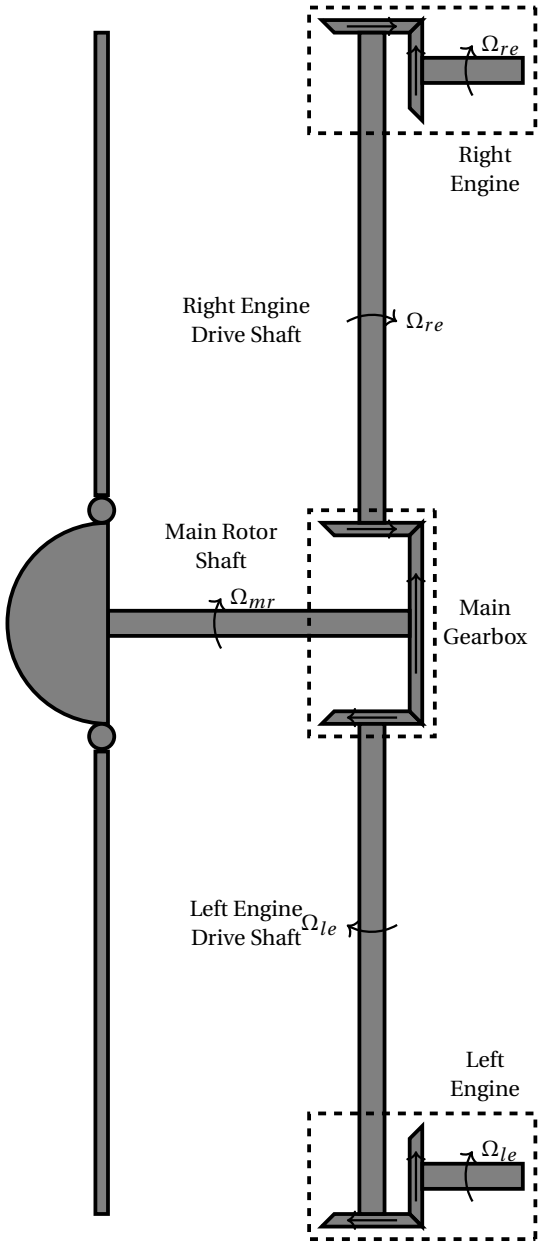

Figure D.4: Main gearbox - Transmission from the engine drive shafts to the main rotor shaft.

D.1.3. INTERMEDIATE GEARBOX

The intermediate gearbox of the Bo-105 helicopter is mounted at the base of the vertical fin, increases the main transmission output rpm and changes the angle of drive of 50 degrees. The gearbox housing provides for mounting of a tail rotor yaw control bell

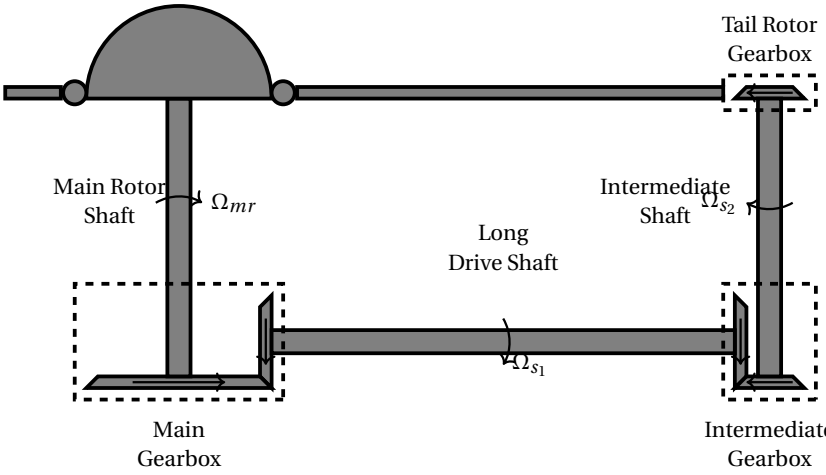

Figure D.5: Main gearbox and intermediate gearbox - Transmission from the main rotor shaft to the intermediate shaft.

crank.

D.1.4. TAIL ROTOR GEARBOX

The tail rotor gearbox of the Bo-105 helicopter is mounted on top of the vertical fin, reduces the output rpm and changes the angle of drive of 90 degrees. The tail rotor shaft passes through and is supported by the gearbox output bevel gear. The gearbox housing provides for mounting of a tail rotor yaw control bell crank.

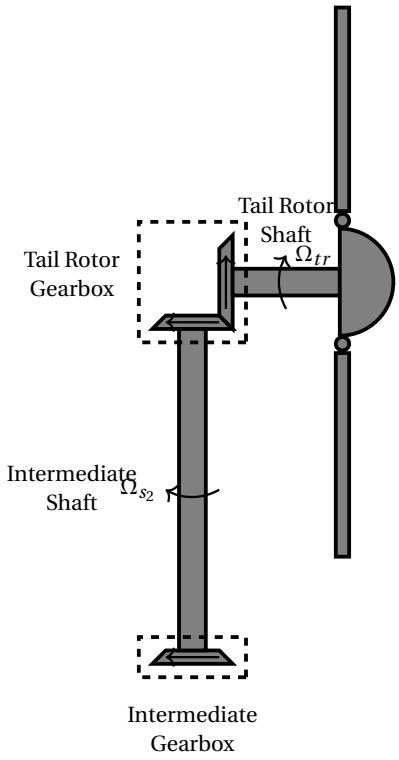

Figure D.6: Tail rotor gearbox - Transmission from the intermediate shaft to the tail rotor shaft.

D.2. DRIVETRAIN DYNAMICS

The drivetrain model derived in this section represents the torsional dynamics only. More realistic drivetrain models would require an extremely detailed level of 3D modeling (e.g., contact between neighboring gear wheels), which would make them unsuitable for real-time flight simulation applications. Furthermore, this level of complexity is not necessary for certification purposes. Fig. D.7 illustrates a three dimensional representation of the extremely simplified architectures reported in Fig. D.4, D.5 and D.6. To derive the drivetrain torsional model, further simplifications are necessary:

1. Lumped inertia: each gear mesh will be modelled as a rigid disk, whose moment of inertia takes into account the inertia of the gear mesh and a portion of the inertia of the shaft connected to it. This contribution is determined according to the position of the center of flexibility of the shaft.

2. Lumped torsional stiffness: each shaft will be represented as a torsional spring, whose stiffness takes into account the torsional flexibility of the shaft (within the main torsional load path) and that of the gear meshes to which its ends are connected.

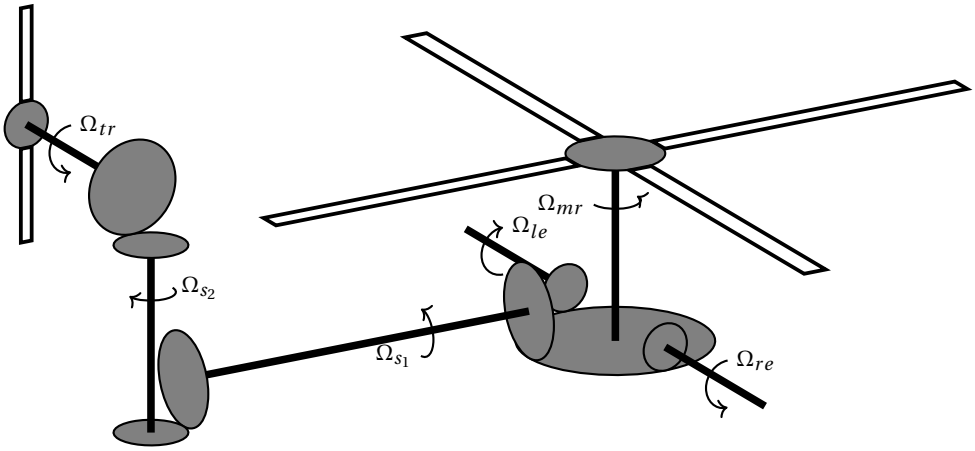

Figure D.7: Simplified three dimensional representation of the drive train of a twin-engine conventional helicopter.

D.2.1. LUMPED MODEL

Add how to calculate inertia of shaft and how to split it at its ends and how to calculate stiffness of shafts and gear meshes

KINEMATICS

According to the assumptions of lumped inertia and torsional stiffness, the drivetrain of a twin-engine conventional helicopter can be represented as shown in Fig. D.8 and D.9. To describe the kinematics of the drivetrain, the rotation of each disk can be chosen as a coordinate. This leads to a total of 12 coordinates (ψ_{mr}, ψ_{tr}, ψ_{mgb_1}, ψ_{mgb_2}, ψ_{mgb_3}, ψ_{mgb_4}, ψ_{igb_1}, ψ_{igb_2}, ψ_{tgb_1}, ψ_{tgb_2}, ψ_{re}, ψ_{le}).

However, these 12 coordinates are not all independent from each other, because there are 5 constraints of pure rolling at the contact point between neighboring gear meshes:

$$\dot{\psi}_{mgb_1} R_{mgb_1} = \dot{\psi}_{mgb_2} R_{mgb_2} \Longrightarrow \dot{\psi}_{mgb_2} = \frac{R_{mgb_1}}{R_{mgb_2}} \dot{\psi}_{mgb_1} \text{ at MGB}_{1-2} \tag{D.1}$$

$$\dot{\psi}_{mgb_1} R_{mgb_1} = \dot{\psi}_{mgb_3} R_{mgb_3} \Longrightarrow \dot{\psi}_{mgb_3} = \frac{R_{mgb_1}}{R_{mgb_3}} \dot{\psi}_{mgb_1} \text{ at MGB}_{1-3} \tag{D.2}$$

$$\dot{\psi}_{mgb_1} R_{mgb_1} = \dot{\psi}_{mgb_4} R_{mgb_4} \Longrightarrow \dot{\psi}_{mgb_4} = \frac{R_{mgb_1}}{R_{mgb_4}} \dot{\psi}_{mgb_1} \text{ at MGB}_{1-4} \tag{D.3}$$

$$\dot{\psi}_{igb_1} R_{igb_1} = \dot{\psi}_{igb_2} R_{igb_2} \Longrightarrow \dot{\psi}_{igb_2} = \frac{R_{igb_1}}{R_{igb_2}} \dot{\psi}_{igb_1} \text{ at IGB}_{1-2} \tag{D.4}$$

$$\dot{\psi}_{tgb_1} R_{tgb_1} = \dot{\psi}_{tgb_2} R_{tgb_2} \Longrightarrow \dot{\psi}_{tgb_2} = \frac{R_{tgb_1}}{R_{tgb_2}} \dot{\psi}_{tgb_1} \text{ at TGB}_{1-2} \tag{D.5}$$

The torsional drivetrain dynamics can be therefore described by 7 degrees of freedom (ψ_{mr}, ψ_{tr}, ψ_{mgb_1}, ψ_{igb_1}, ψ_{tgb_1}, ψ_{re}, ψ_{le}).

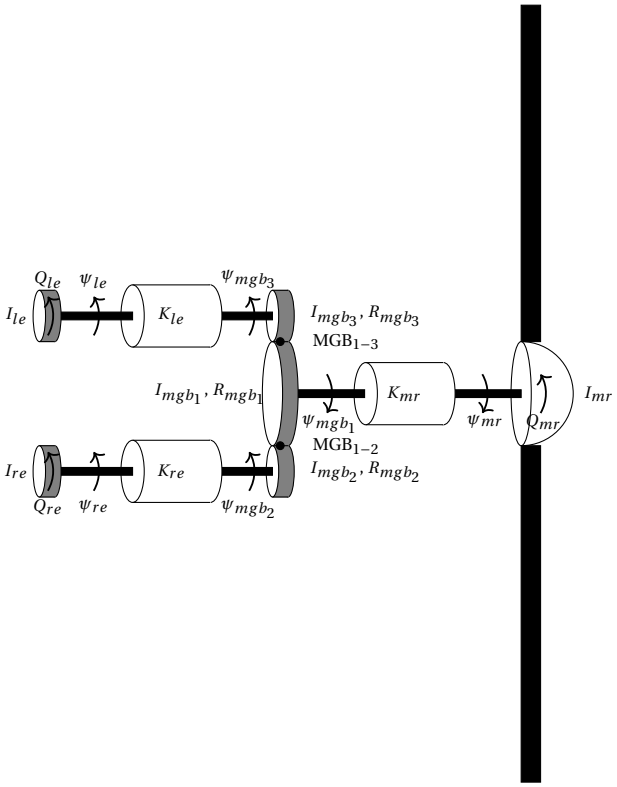

Figure D.8: Main gearbox lumped model - Transmission from the engine drive shafts to the main rotor shaft.

Furthermore, the following conditions apply at the steady state condition:

$$\lim_{t\to\infty} \dot{\psi}_{mgb_1} = \Omega_{mr} = \Omega_{mgb_1} = 424 \text{ rpm} \tag{D.6}$$

$$\lim_{t\to\infty} \dot{\psi}_{mgb_2} = \Omega_{re} = 6000 \text{ rpm} \tag{D.7}$$

$$\lim_{t\to\infty} \dot{\psi}_{mgb_3} = \Omega_{le} = 6000 \text{ rpm} \tag{D.8}$$

$$\lim_{t\to\infty} \dot{\psi}_{mgb_4} = \Omega_{s_1} = 2452 \text{ rpm} \tag{D.9}$$

$$\lim_{t\to\infty} \dot{\psi}_{igb_1} = \Omega_{s_1} \tag{D.10}$$

$$\lim_{t\to\infty} \dot{\psi}_{igb_2} = \Omega_{s_2} = 3065 \text{ rpm} \tag{D.11}$$

$$\lim_{t\to\infty} \dot{\psi}_{tgb_1} = \Omega_{s_2} \tag{D.12}$$

$$\lim_{t\to\infty} \dot{\psi}_{tgb_2} = \Omega_{tr} = 2219 \text{ rpm} \tag{D.13}$$

$$\lim_{t\to\infty} \dot{\psi}_{tr} = \Omega_{tr} \tag{D.14}$$

For the sake of a more compact notation, it is convenient to define the reciprocal of the gear ratios:

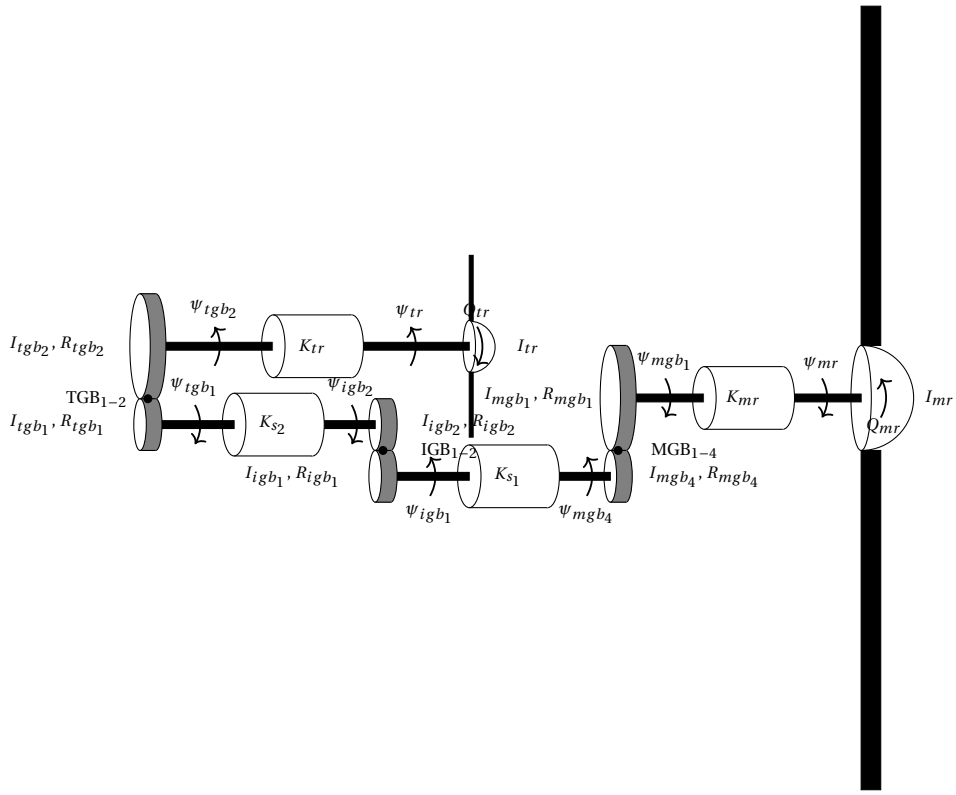

Figure D.9: Main gearbox lumped model - Transmission from the engine drive shafts to the main rotor shaft.

$$r_{mgb_{1-2}} = \frac{\dot{\psi}_{mgb_2}}{\dot{\psi}_{mgb_1}} = \frac{R_{mgb_1}}{R_{mgb_2}} = \frac{\Omega_{re}}{\Omega_{mr}} = 14.15 \tag{D.15}$$

$$r_{mgb_{1-3}} = \frac{\dot{\psi}_{mgb_3}}{\dot{\psi}_{mgb_1}} = \frac{R_{mgb_1}}{R_{mgb_3}} = \frac{\Omega_{le}}{\Omega_{mr}} = 14.15 \tag{D.16}$$

$$r_{mgb_{1-4}} = \frac{\dot{\psi}_{mgb_4}}{\dot{\psi}_{mgb_1}} = \frac{R_{mgb_1}}{R_{mgb_4}} = \frac{\Omega_{s_1}}{\Omega_{mr}} = 5.78 \tag{D.17}$$

$$r_{igb_{1-2}} = \frac{\dot{\psi}_{igb_2}}{\dot{\psi}_{igb_1}} = \frac{R_{igb_1}}{R_{igb_2}} = \frac{\Omega_{s_2}}{\Omega_{s_1}} = 1.25 \tag{D.18}$$

$$r_{tgb_{1-2}} = \frac{\dot{\psi}_{tgb_2}}{\dot{\psi}_{tgb_1}} = \frac{R_{tgb_1}}{R_{tgb_2}} = \frac{\Omega_{tr}}{\Omega_{s_2}} = 0.72 \tag{D.19}$$

Replacing equations from (D.15) to (D.19) in equations from (D.1) to (D.5) leads to:

$$\dot{\psi}_{mgb_2} = r_{mgb_{1-2}} \dot{\psi}_{mgb_1} \tag{D.20}$$
$$\dot{\psi}_{mgb_3} = r_{mgb_{1-3}} \dot{\psi}_{mgb_1} \tag{D.21}$$
$$\dot{\psi}_{mgb_4} = r_{mgb_{1-4}} \dot{\psi}_{mgb_1} \tag{D.22}$$
$$\dot{\psi}_{igb_2} = r_{igb_{1-2}} \dot{\psi}_{igb_1} \tag{D.23}$$
$$\dot{\psi}_{tgb_2} = r_{tgb_{1-2}} \dot{\psi}_{tgb_1} \tag{D.24}$$

D.2.2. DRIVETRAIN DYNAMICS IN LAGRANGIAN COORDINATES

The torsional drivetrain dynamics will be derived through the application of the Principle of Virtual Work, which can be formulated as:

$$\delta W_{inertia} + \delta W_{internal} + \delta W_{external} = 0 \tag{D.25}$$

$$\begin{aligned}
\delta W_{external} &= \delta\psi_{mr}(-Q_{mr}) + \delta\psi_{tr}(-Q_{tr}) + \delta\psi_{re}(Q_{re}) + \delta\psi_{le}(Q_{le}) \\
&= \underbrace{\begin{bmatrix} \delta\psi_{mr} & \delta\psi_{tr} & \delta\psi_{mgb_1} & \delta\psi_{igb_1} & \delta\psi_{tgb_1} & \delta\psi_{re} & \delta\psi_{le} \end{bmatrix}}_{\delta\vec{\psi}^T} \underbrace{\begin{Bmatrix} -Q_{mr} \\ -Q_{tr} \\ 0 \\ 0 \\ 0 \\ Q_{re} \\ Q_{le} \end{Bmatrix}}_{\vec{Q}} \\
&= \delta\vec{\psi}^T \vec{Q}
\end{aligned} \tag{D.26}$$

$$\begin{aligned}
\delta W_{inertia} = {} & \delta\psi_{mr}\left(-I_{mr}\ddot{\psi}_{mr}\right) + \\
& + \delta\psi_{tr}\left(-I_{tr}\ddot{\psi}_{tr}\right) + \\
& + \delta\psi_{mgb_1}\left(-I_{mgb_1}\ddot{\psi}_{mgb_1}\right) + \delta\psi_{mgb_2}\left(-I_{mgb_2}\ddot{\psi}_{mgb_2}\right) + \\
& + \delta\psi_{mgb_3}\left(-I_{mgb_3}\ddot{\psi}_{mgb_3}\right) + \delta\psi_{mgb_4}\left(-I_{mgb_4}\ddot{\psi}_{mgb_4}\right) + \\
& + \delta\psi_{igb_1}\left(-I_{igb_1}\ddot{\psi}_{igb_1}\right) + \delta\psi_{igb_2}\left(-I_{igb_2}\ddot{\psi}_{igb_2}\right) + \\
& + \delta\psi_{tgb_1}\left(-I_{tgb_1}\ddot{\psi}_{tgb_1}\right) + \delta\psi_{tgb_2}\left(-I_{tgb_2}\ddot{\psi}_{tgb_2}\right) + \\
& + \delta\psi_{re}\left(-I_{re}\ddot{\psi}_{re}\right) + \delta\psi_{le}\left(-I_{le}\ddot{\psi}_{le}\right)
\end{aligned} \tag{D.27}$$

Replacing Eq. from (D.20) to (D.24) in Eq. (D.27):

$$\begin{aligned}\delta W_{inertia} = {} & \delta\psi_{mr}\left(-I_{mr}\ddot{\psi}_{mr}\right) + \\ & + \delta\psi_{tr}\left(-I_{tr}\ddot{\psi}_{tr}\right) + \\ & + \delta\psi_{mgb_1}\left(-I_{mgb_1}\ddot{\psi}_{mgb_1}\right) + \delta\psi_{mgb_1} r_{mgb_{1-2}}\left(-I_{mgb_2} r_{mgb_{1-2}}\ddot{\psi}_{mgb_1}\right) + \\ & + \delta\psi_{mgb_1} r_{mgb_{1-3}}\left(-I_{mgb_3} r_{mgb_{1-3}}\ddot{\psi}_{mgb_1}\right) + \\ & + \delta\psi_{mgb_1} r_{mgb_{1-4}}\left(-I_{mgb_4} r_{mgb_{1-4}}\ddot{\psi}_{mgb_1}\right) + \\ & + \delta\psi_{igb_1}\left(-I_{igb_1}\ddot{\psi}_{igb_1}\right) + \delta\psi_{igb_1} r_{igb_{1-2}}\left(-I_{igb_2} r_{mgb_{1-2}}\ddot{\psi}_{igb_1}\right) + \\ & + \delta\psi_{tgb_1}\left(-I_{tgb_1}\ddot{\psi}_{tgb_1}\right) + \delta\psi_{tgb_1} r_{tgb_{1-2}}\left(-I_{tgb_2} r_{tgb_{1-2}}\ddot{\psi}_{tgb_1}\right) + \\ & + \delta\psi_{re}\left(-I_{re}\ddot{\psi}_{re}\right) + \delta\psi_{le}\left(-I_{le}\ddot{\psi}_{le}\right) \end{aligned} \tag{D.28}$$

Combining like terms:

$$\begin{aligned}\delta W_{inertia} = {} & \delta\psi_{mr}\left(-I_{mr}\ddot{\psi}_{mr}\right) + \\ & + \delta\psi_{tr}\left(-I_{tr}\ddot{\psi}_{tr}\right) + \\ & + \delta\psi_{mgb_1}\left(-I_{mgb_1} - I_{mgb_2} r_{mgb_{1-2}}^2 - I_{mgb_3} r_{mgb_{1-3}}^2 - I_{mgb_4} r_{mgb_{1-4}}^2\right)\ddot{\psi}_{mgb_1} + \\ & + \delta\psi_{igb_1}\left(-I_{igb_1} - I_{igb_2} r_{igb_{1-2}}^2\right)\ddot{\psi}_{igb_1} + \\ & + \delta\psi_{tgb_1}\left(-I_{tgb_1} - I_{tgb_2} r_{tgb_{1-2}}^2\right)\ddot{\psi}_{tgb_1} + \\ & + \delta\psi_{re}\left(-I_{re}\ddot{\psi}_{re}\right) + \delta\psi_{le}\left(-I_{le}\ddot{\psi}_{le}\right) \end{aligned} \tag{D.29}$$

D

$$\delta W_{inertia} = -\underbrace{\begin{Bmatrix} \delta\psi_{mr} \\ \delta\psi_{tr} \\ \delta\psi_{mgb_1} \\ \delta\psi_{igb_1} \\ \delta\psi_{tgb_1} \\ \delta\psi_{re} \\ \delta\psi_{le} \end{Bmatrix}^T}_{\delta\vec{\psi}^T} \underbrace{\begin{bmatrix} I_{mr} & & & & & & & \\ & I_{tr} & & & & & & \\ & & I_{mgb_1} + \sum_{i=2}^{n_{mgb}} r_{mgb_{1-i}}^2 I_{mgb_i} & & & & & \\ & & & I_{igb_1} + \sum_{i=2}^{n_{igb}} r_{igb_{1-i}}^2 I_{igb_i} & & & & \\ & & & & I_{tgb_1} + \sum_{i=2}^{n_{tgb}} r_{tgb_{1-i}}^2 I_{tgb_i} & & & \\ & & & & & I_{re} & & \\ & & & & & & I_{le} \end{bmatrix}}_{\mathbf{M}} \underbrace{\begin{Bmatrix} \ddot{\psi}_{mr} \\ \ddot{\psi}_{tr} \\ \ddot{\psi}_{mgb_1} \\ \ddot{\psi}_{igb_1} \\ \ddot{\psi}_{tgb_1} \\ \ddot{\psi}_{re} \\ \ddot{\psi}_{le} \end{Bmatrix}}_{\ddot{\vec{\psi}}}$$

$$= -\delta\vec{\psi}^T \mathbf{M} \ddot{\vec{\psi}} \tag{D.30}$$

$$\vec{\psi} = \begin{Bmatrix} \psi_{mr} \\ \psi_{tr} \\ \psi_{mgb_1} \\ \psi_{igb_1} \\ \psi_{tgb_1} \\ \psi_{re} \\ \psi_{le} \end{Bmatrix} \tag{D.31}$$

$$\mathbf{M} = \begin{bmatrix} I_{mr} & & & & & & & \\ & I_{tr} & & & & & & \\ & & I_{mgb_1} + \sum_{i=2}^{n_{mgb}} r_{mgb_{1-i}}^2 I_{mgb_i} & & & & & \\ & & & I_{igb_1} + \sum_{i=2}^{n_{igb}} r_{igb_{1-i}}^2 I_{igb_i} & & & & \\ & & & & I_{tgb_1} + \sum_{i=2}^{n_{tgb}} r_{tgb_{1-i}}^2 I_{tgb_i} & & & \\ & & & & & I_{re} & & \\ & & & & & & I_{le} \end{bmatrix} \tag{D.32}$$

$$
\begin{aligned}
\delta W_{internal} = & -\delta\left(\psi_{mgb_1} - \psi_{mr}\right) K_{mr}\left(\psi_{mgb_1} - \psi_{mr}\right) + \\
& -\delta\left(\psi_{tgb_2} - \psi_{tr}\right) K_{tr}\left(\psi_{tgb_2} - \psi_{tr}\right) + \\
& -\delta\left(\psi_{mgb_4} - \psi_{igb_1}\right) K_{s_1}\left(\psi_{mgb_4} - \psi_{igb_1}\right) + \\
& -\delta\left(\psi_{igb_2} - \psi_{tgb_1}\right) K_{s_2}\left(\psi_{igb_2} - \psi_{tgb_1}\right) + \\
& -\delta\left(\psi_{mgb_2} - \psi_{re}\right) K_{re}\left(\psi_{mgb_2} - \psi_{re}\right) + \\
& -\delta\left(\psi_{mgb_3} - \psi_{le}\right) K_{le}\left(\psi_{mgb_3} - \psi_{le}\right) + \\
& = -\delta\psi_{mgb_1} K_{mr}\left(\psi_{mgb_1} - \psi_{mr}\right) + \delta\psi_{mr} K_{mr}\left(\psi_{mgb_1} - \psi_{mr}\right) + \\
& -\delta\psi_{tgb_2} K_{tr}\left(\psi_{tgb_2} - \psi_{tr}\right) + \delta\psi_{tr} K_{tr}\left(\psi_{tgb_2} - \psi_{tr}\right) + \\
& -\delta\psi_{mgb_4} K_{s_1}\left(\psi_{mgb_4} - \psi_{igb_1}\right) + \delta\psi_{igb_1} K_{s_1}\left(\psi_{mgb_4} - \psi_{igb_1}\right) + \\
& -\delta\psi_{igb_2} K_{s_2}\left(\psi_{igb_2} - \psi_{tgb_1}\right) + \delta\psi_{tgb_1} K_{s_2}\left(\psi_{igb_2} - \psi_{tgb_1}\right) + \\
& -\delta\psi_{mgb_2} K_{re}\left(\psi_{mgb_2} - \psi_{re}\right) + \delta\psi_{re} K_{re}\left(\psi_{mgb_2} - \psi_{re}\right) + \\
& -\delta\psi_{mgb_3} K_{le}\left(\psi_{mgb_3} - \psi_{le}\right) + \delta\psi_{le} K_{le}\left(\psi_{mgb_3} - \psi_{le}\right)
\end{aligned} \tag{D.33}
$$

Replacing Eq. from (D.20) to (D.24) in Eq. (D.33):

$$
\begin{aligned}
\delta W_{internal} = & \delta\psi_{mr} K_{mr}\left(\psi_{mgb_1} - \psi_{mr}\right) + \\
& + \delta\psi_{tr} K_{tr}\left(r_{tgb_{1-2}}\psi_{tgb_1} - \psi_{tr}\right) + \\
& - \delta\psi_{mgb_1} K_{mr}\left(\psi_{mgb_1} - \psi_{mr}\right) + \\
& - \delta\psi_{mgb_1} r_{mgb_{1-4}} K_{s_1}\left(r_{mgb_{1-4}}\psi_{mgb_1} - \psi_{igb_1}\right) + \\
& - \delta\psi_{mgb_1} r_{mgb_{1-2}} K_{re}\left(r_{mgb_{1-2}}\psi_{mgb_1} - \psi_{re}\right) + \\
& - \delta\psi_{mgb_1} r_{mgb_{1-3}} K_{le}\left(r_{mgb_{1-3}}\psi_{mgb_1} - \psi_{le}\right) + \\
& + \delta\psi_{igb_1} K_{s_1}\left(r_{mgb_{1-4}}\psi_{mgb_1} - \psi_{igb_1}\right) + \\
& - \delta\psi_{igb_1} r_{igb_{1-2}} K_{s_2}\left(r_{igb_{1-2}}\psi_{igb_1} - \psi_{tgb_1}\right) + \\
& + \delta\psi_{tgb_1} K_{s_2}\left(r_{igb_{1-2}}\psi_{igb_1} - \psi_{tgb_1}\right) + \\
& - \delta\psi_{tgb_1} r_{tgb_{1-2}} K_{tr}\left(r_{tgb_{1-2}}\psi_{tgb_1} - \psi_{tr}\right) + \\
& + \delta\psi_{re} K_{re}\left(r_{mgb_{1-2}}\psi_{mgb_1} - \psi_{re}\right) + \\
& + \delta\psi_{le} K_{le}\left(r_{mgb_{1-3}}\psi_{mgb_1} - \psi_{le}\right)
\end{aligned} \tag{D.34}
$$

Combining like terms:

$$
\begin{aligned}
\delta W_{internal} = {} & \delta\psi_{mr} K_{mr}\left(\psi_{mgb_1} - \psi_{mr}\right) + \\
& + \delta\psi_{tr} K_{tr}\left(r_{tgb_{1-2}}\psi_{tgb_1} - \psi_{tr}\right) + \\
& - \delta\psi_{mgb_1}\left[K_{mr}\left(\psi_{mgb_1} - \psi_{mr}\right) + \right. \\
& \qquad + r_{mgb_{1-4}} K_{s_1}\left(r_{mgb_{1-4}}\psi_{mgb_1} - \psi_{igb_1}\right) + \\
& \qquad + r_{mgb_{1-2}} K_{re}\left(r_{mgb_{1-2}}\psi_{mgb_1} - \psi_{re}\right) + \\
& \qquad \left. + r_{mgb_{1-3}} K_{le}\left(r_{mgb_{1-3}}\psi_{mgb_1} - \psi_{le}\right)\right] + \\
& + \delta\psi_{igb_1}\left[K_{s_1}\left(r_{mgb_{1-4}}\psi_{mgb_1} - \psi_{igb_1}\right) + \right. \\
& \qquad \left. - r_{igb_{1-2}} K_{s_2}\left(r_{igb_{1-2}}\psi_{igb_1} - \psi_{tgb_1}\right)\right] + \\
& + \delta\psi_{tgb_1}\left[K_{s_2}\left(r_{igb_{1-2}}\psi_{igb_1} - \psi_{tgb_1}\right) + \right. \\
& \qquad \left. - r_{tgb_{1-2}} K_{tr}\left(r_{tgb_{1-2}}\psi_{tgb_1} - \psi_{tr}\right)\right] + \\
& + \delta\psi_{re} K_{re}\left(r_{mgb_{1-2}}\psi_{mgb_1} - \psi_{re}\right) + \\
& + \delta\psi_{le} K_{le}\left(r_{mgb_{1-3}}\psi_{mgb_1} - \psi_{le}\right) = \\
& = -\delta\psi_{mr}\left(K_{mr}\psi_{mr} - K_{mr}\psi_{mgb_1}\right) + \\
& - \delta\psi_{tr}\left(K_{tr}\psi_{tr} - r_{tgb_{1-2}} K_{tr}\psi_{tgb_1}\right) + \\
& - \delta\psi_{mgb_1}\left[\left(K_{mr} + r^2_{mgb_{1-2}} K_{re} + r^2_{mgb_{1-3}} K_{le} + r^2_{mgb_{1-4}} K_{s_1}\right)\psi_{mgb_1} + \right. \\
& \qquad - K_{mr}\psi_{mr} + \\
& \qquad - r_{mgb_{1-4}} K_{s_1}\psi_{igb_1} + \\
& \qquad - r_{mgb_{1-2}} K_{re}\psi_{re} + \\
& \qquad \left. - r_{mgb_{1-3}} K_{le}\psi_{le}\right] + \\
& - \delta\psi_{igb_1}\left[\left(K_{s_1} + r^2_{igb_{1-2}} K_{s_2}\right)\psi_{igb_1} - r_{mgb_{1-4}} K_{s_1}\psi_{mgb_1} + \right. \\
& \qquad \left. - r_{igb_{1-2}} K_{s_2}\psi_{tgb_1}\right] + \\
& - \delta\psi_{tgb_1}\left[\left(K_{s_2} + r^2_{tgb_{1-2}} K_{tr}\right)\psi_{tgb_1} - r_{igb_{1-2}} K_{s_2}\psi_{igb_1} + \right. \\
& \qquad \left. - r_{tgb_{1-2}} K_{tr}\psi_{tr}\right] + \\
& + \delta\psi_{re} K_{re}\left(r_{mgb_{1-2}}\psi_{mgb_1} - \psi_{re}\right) + \\
& + \delta\psi_{le} K_{le}\left(r_{mgb_{1-3}}\psi_{mgb_1} - \psi_{le}\right)
\end{aligned}
\tag{D.35}
$$

$$\delta W_{internal} = -\underbrace{\begin{Bmatrix} \delta\psi_{mr} \\ \delta\psi_{tr} \\ \delta\psi_{mgb_1} \\ \delta\psi_{igb_1} \\ \delta\psi_{tgb_1} \\ \delta\psi_{re} \\ \delta\psi_{le} \end{Bmatrix}^T}_{\delta\vec{\psi}^T} \underbrace{\begin{bmatrix} K_{mr} & 0 & -K_{mr} & 0 & 0 & 0 & 0 \\ 0 & K_{tr} & 0 & 0 & -r_{tgb_{1-2}}K_{tr} & 0 & 0 \\ -K_{mr} & 0 & K_{mr} + r^2_{mgb_{1-2}}K_{re} + r^2_{mgb_{1-3}}K_{le} + r^2_{mgb_{1-4}}K_{s_1} & -r_{mgb_{1-4}}K_{s_1} & 0 & -r_{mgb_{1-2}}K_{re} & -r_{mgb_{1-3}}K_{le} \\ 0 & 0 & -r_{mgb_{1-4}}K_{s_1} & K_{s_1} + r^2_{igb_{1-2}}K_{s_2} & -r_{igb_{1-2}}K_{s_2} & 0 & 0 \\ 0 & -r_{tgb_{1-2}}K_{tr} & 0 & -r_{igb_{1-2}}K_{s_2} & K_{s_2} + r^2_{tgb_{1-2}}K_{tr} & 0 & 0 \\ 0 & 0 & -r_{mgb_{1-2}}K_{re} & 0 & 0 & K_{re} & 0 \\ 0 & 0 & -r_{mgb_{1-3}}K_{le} & 0 & 0 & 0 & K_{le} \end{bmatrix}}_{\mathbf{K}} \underbrace{\begin{Bmatrix} \psi_{mr} \\ \psi_{tr} \\ \psi_{mgb_1} \\ \psi_{igb_1} \\ \psi_{tgb_1} \\ \psi_{re} \\ \psi_{le} \end{Bmatrix}}_{\vec{\psi}}$$

$$= -\delta\vec{\psi}^T \mathbf{K} \vec{\psi} \tag{D.36}$$

$$\mathbf{K} = \begin{bmatrix} K_{mr} & 0 & -K_{mr} & 0 & 0 & 0 & 0 \\ 0 & K_{tr} & 0 & 0 & -r_{tgb_{1-2}}K_{tr} & 0 & 0 \\ -K_{mr} & 0 & K_{mr} + r^2_{mgb_{1-2}}K_{re} + r^2_{mgb_{1-3}}K_{le} + r^2_{mgb_{1-4}}K_{s_1} & -r_{mgb_{1-4}}K_{s_1} & 0 & -r_{mgb_{1-2}}K_{re} & -r_{mgb_{1-3}}K_{le} \\ 0 & 0 & -r_{mgb_{1-4}}K_{s_1} & K_{s_1} + r^2_{igb_{1-2}}K_{s_2} & -r_{igb_{1-2}}K_{s_2} & 0 & 0 \\ 0 & -r_{tgb_{1-2}}K_{tr} & 0 & -r_{igb_{1-2}}K_{s_2} & K_{s_2} + r^2_{tgb_{1-2}}K_{tr} & 0 & 0 \\ 0 & 0 & -r_{mgb_{1-2}}K_{re} & 0 & 0 & K_{re} & 0 \\ 0 & 0 & -r_{mgb_{1-3}}K_{le} & 0 & 0 & 0 & K_{le} \end{bmatrix} \tag{D.37}$$

Replacing Eq. (D.26), (D.30), and (D.36) in Eq. (D.25):

$$\delta\vec{\psi}^T\mathbf{M}\ddot{\vec{\psi}} + \delta\vec{\psi}^T\mathbf{K}\vec{\psi} - \delta\vec{\psi}^T\vec{Q} = 0 \tag{D.38}$$

$$\delta\vec{\psi}^T\left(\mathbf{M}\ddot{\vec{\psi}} + \mathbf{K}\vec{\psi} - \vec{Q}\right) = 0 \tag{D.39}$$

This means that for a non-zero virtual displacement, the following equation holds:

$$\mathbf{M}\ddot{\vec{\psi}} + \mathbf{K}\vec{\psi} = \vec{Q} \tag{D.40}$$

Including structural damping, Eq. (D.40) becomes:

$$\mathbf{M}\ddot{\vec{\psi}} + \mathbf{C_s}\dot{\vec{\psi}} + \mathbf{K}\vec{\psi} = \vec{Q} \tag{D.41}$$

Explain how to include structural damping.

FREE-TURBINE TURBOSHAFT

For free-turbine engines, in which the power turbine is not mechanically linked to the gas turbine (also known as gas generator), there is the need to increase the order of the model of Eq. (D.41) by 2, because also the gas generator speed ($\dot{\psi}_{gg}$) of each engine becomes a degree of freedom.

$$\vec{Q} = \begin{Bmatrix} -Q_{mr} \\ -Q_{tr} \\ 0 \\ 0 \\ 0 \\ Q_{re} \\ Q_{le} \\ Q_{gg_{re}} \\ Q_{gg_{le}} \end{Bmatrix} \tag{D.42}$$

$$\vec{\psi} = \begin{Bmatrix} \psi_{mr} \\ \psi_{tr} \\ \psi_{mgb_1} \\ \psi_{igb_1} \\ \psi_{tgb_1} \\ \psi_{re} \\ \psi_{le} \\ \psi_{gg_{re}} \\ \psi_{gg_{le}} \end{Bmatrix} \tag{D.43}$$

$$\mathbf{M} = \begin{bmatrix} I_{mr} & & & & & & & & & \\ & I_{tr} & & & & & & & & \\ & & I_{mgb_1} + \sum_{i=2}^{n_{mgb}} r_{mgb_{1-i}}^2 I_{mgb_i} & & & & & & & \\ & & & I_{igb_1} + \sum_{i=2}^{n_{igb}} r_{igb_{1-i}}^2 I_{igb_i} & & & & & & \\ & & & & I_{tgb_1} + \sum_{i=2}^{n_{tgb}} r_{tgb_{1-i}}^2 I_{tgb_i} & & & & & \\ & & & & & I_{re} & & & & \\ & & & & & & I_{le} & & & \\ & & & & & & & I_{gg_{re}} & & \\ & & & & & & & & I_{gg_{le}} & \end{bmatrix} \tag{D.44}$$

$$\mathbf{K} = \begin{bmatrix} K_{mr} & 0 & -K_{mr} & 0 & 0 & 0 & 0 & 0 & 0 \\ 0 & K_{tr} & 0 & 0 & -r_{tgb_{1-2}} K_{tr} & 0 & 0 & 0 & 0 \\ -K_{mr} & 0 & K_{mr} + r_{mgb_{1-2}}^2 K_{re} + r_{mgb_{1-3}}^2 K_{le} + r_{mgb_{1-4}}^2 K_{s_1} & -r_{mgb_{1-4}} K_{s_1} & 0 & -r_{mgb_{1-2}} K_{re} & -r_{mgb_{1-3}} K_{le} & 0 & 0 \\ 0 & 0 & -r_{mgb_{1-4}} K_{s_1} & K_{s_1} + r_{igb_{1-2}}^2 K_{s_2} & -r_{igb_{1-2}} K_{s_2} & 0 & 0 & 0 & 0 \\ 0 & -r_{tgb_{1-2}} K_{tr} & 0 & -r_{igb_{1-2}} K_{s_2} & K_{s_2} + r_{tgb_{1-2}}^2 K_{tr} & 0 & 0 & 0 & 0 \\ 0 & 0 & -r_{mgb_{1-2}} K_{re} & 0 & 0 & K_{re} & 0 & 0 & 0 \\ 0 & 0 & -r_{mgb_{1-3}} K_{le} & 0 & 0 & 0 & K_{le} & 0 & 0 \\ 0 & 0 & 0 & 0 & 0 & 0 & 0 & 0 & 0 \\ 0 & 0 & 0 & 0 & 0 & 0 & 0 & 0 & 0 \end{bmatrix} \tag{D.45}$$

RIGID TRANSMISSION

If the hypothesis of rigid transmission is adopted, we can neglect the stiffness matrix in Eq. (D.39):

$$\delta\vec{\psi}^T\left(\mathbf{M}\ddot{\vec{\psi}}-\vec{Q}\right)=0 \tag{D.46}$$

and only one coordinate is independent. Choosing ψ_{mr} as free coordinate, we can express $\vec{\psi}$ as:

$$\vec{\psi}=\begin{Bmatrix}\psi_{mr}\\ \psi_{tr}\\ \psi_{mgb_1}\\ \psi_{igb_1}\\ \psi_{tgb_1}\\ \psi_{re}\\ \psi_{le}\end{Bmatrix}=\begin{Bmatrix}1\\ r_{tgb_{1-2}}r_{igb_{1-2}}r_{mgb_{1-4}}\\ 1\\ r_{mgb_{1-4}}\\ r_{igb_{1-2}}r_{mgb_{1-4}}\\ r_{mgb_{1-2}}\\ r_{mgb_{1-3}}\end{Bmatrix}\psi_{mr}=\begin{Bmatrix}1\\ \frac{\Omega_{tr}}{\Omega_{mr}}\\ 1\\ \frac{\Omega_{s_1}}{\Omega_{mr}}\\ \frac{\Omega_{s_2}}{\Omega_{mr}}\\ \frac{\Omega_{re}}{\Omega_{mr}}\\ \frac{\Omega_{le}}{\Omega_{mr}}\end{Bmatrix}\psi_{mr}=\begin{Bmatrix}1\\ g_{tr}\\ 1\\ g_{s_1}\\ g_{s_2}\\ g_{re}\\ g_{le}\end{Bmatrix}\psi_{mr}=\vec{g}\psi_{mr} \tag{D.47}$$

$$\mathbf{M}=\begin{bmatrix}I_{mr} & & & & & & \\ & I_{tr} & & & & & \\ & & I_{mgb_1}+g_{re}^2I_{mgb_2}+g_{le}^2I_{mgb_3}+g_{s_1}^2I_{mgb_4} & & & & \\ & & & I_{igb_1}+r_{igb_{1-2}}^2I_{igb_2} & & & \\ & & & & I_{tgb_1}+r_{tgb_{1-2}}^2I_{tgb_2} & & \\ & & & & & I_{re} & \\ & & & & & & I_{le}\end{bmatrix} \tag{D.48}$$

Replacing Eq. (D.47) in Eq. (D.46), we obtain:

$$\delta\psi_{mr}\vec{g}^T\left(\mathbf{M}\vec{g}\ddot{\psi}_{mr}-\vec{Q}\right)=0 \tag{D.49}$$

$$\delta\psi_{mr}\left(\vec{g}^T\mathbf{M}\vec{g}\ddot{\psi}_{mr}-\vec{g}^T\vec{Q}\right)=0 \tag{D.50}$$

$$\delta\psi_{mr}\left\{\overbrace{\left[I_{mr}+I_{mgb_1}+g_{tr}^2\left(I_{tr}+I_{tgb_2}\right)+g_{re}^2\left(I_{re}+I_{mgb_2}\right)+g_{le}^2\left(I_{le}+I_{mgb_3}\right)+g_{s_1}^2\left(I_{mgb_4}+I_{igb_1}\right)+g_{s_2}^2\left(I_{igb_2}+I_{tgb_1}\right)\right]}^{I_R}\ddot{\psi}_{mr}+\right.$$
$$\left.-\left(\underbrace{g_{re}Q_{re}+g_{le}Q_{le}}_{Qeng}-Q_{mr}-g_{tr}Q_{tr}\right)\right\}=0 \tag{D.51}$$

This means that for a non-zero virtual displacement, the following equation holds:

$$I_R\left(\ddot{\psi}_{mr}-\dot{r}\right)=\cancelto{0\text{ in autorotation}}{Q_{eng}}-Q_{mr}-g_{tr}Q_{tr} \tag{D.52}$$

D.2.3. FROM LAGRANGIAN TO REDUCED COORDINATES

It is often convenient to reformulate the engine-drivetrain model using reduced coordinates, because they enable to further simplify the architecture of the drivetrain, as they intrinsically account for all the kinematic relations (Eq. from (D.20) to (D.24)). Reduced coordinates are defined as:

$$\psi_i = \frac{\Omega_i}{\Omega_{ref}} \hat{\psi}_i \tag{D.53}$$

Main rotor speed is usually used as reference angular speed: $\Omega_{ref} = \Omega_{mr}$. Therefore, Eq. (D.53) can be expressed in matrix form as:

$$\vec{\psi} = \mathbf{T}\vec{\hat{\psi}} \tag{D.54}$$

where:

$$\begin{aligned}\mathbf{T} &= \frac{1}{\Omega_{mr}} \begin{bmatrix} \Omega_{mr} & & & & & & & \\ & \Omega_{tr} & & & & & & \\ & & \Omega_{mgb_1} & & & & & \\ & & & \Omega_{igb_1} & & & & \\ & & & & \Omega_{tgb_1} & & & \\ & & & & & \Omega_{re} & & \\ & & & & & & \Omega_{le} \end{bmatrix} \\ &= \frac{1}{\Omega_{mr}} \begin{bmatrix} \Omega_{mr} & & & & & & \\ & \Omega_{tr} & & & & & \\ & & \Omega_{mr} & & & & \\ & & & \Omega_{s_1} & & & \\ & & & & \Omega_{s_2} & & \\ & & & & & \Omega_{re} & \\ & & & & & & \Omega_{le} \end{bmatrix}\end{aligned} \tag{D.55}$$

Applying the transformation (Eq. (D.54)) to Eq. (D.39):

$$\underbrace{\mathbf{T}^T\mathbf{M}\mathbf{T}}_{\hat{\mathbf{M}}}\vec{\hat{\psi}} + \underbrace{\mathbf{T}^T\mathbf{C}\mathbf{T}}_{\hat{\mathbf{C}}_\mathbf{s}}\vec{\hat{\psi}} + \underbrace{\mathbf{T}^T\mathbf{K}\mathbf{T}}_{\hat{\mathbf{K}}}\vec{\hat{\psi}} = \underbrace{\mathbf{T}^T\vec{Q}}_{\vec{\hat{Q}}} \tag{D.56}$$

$$\hat{\mathbf{M}}\vec{\hat{\psi}} + \hat{\mathbf{C}}_\mathbf{s}\vec{\hat{\psi}} + \hat{\mathbf{K}}\vec{\hat{\psi}} = \vec{\hat{Q}} \tag{D.57}$$

$$\hat{\mathbf{M}} = \begin{bmatrix} \hat{I}_{mr} & & & & & & \\ & \hat{I}_{tr} & & & & & \\ & & \hat{I}_{mgb} & & & & \\ & & & \hat{I}_{igb} & & & \\ & & & & \hat{I}_{tgb} & & \\ & & & & & \hat{I}_{re} & \\ & & & & & & \hat{I}_{le} \end{bmatrix} \tag{D.58}$$

$$\hat{\mathbf{K}} = \begin{bmatrix} \hat{K}_{mr} & 0 & -\hat{K}_{mr} & 0 & 0 & 0 & 0 \\ 0 & \hat{K}_{tr} & 0 & 0 & -\hat{K}_{tr} & 0 & 0 \\ -\hat{K}_{mr} & 0 & \hat{K}_{mr} + \hat{K}_{re} + \hat{K}_{le} + \hat{K}_{s_1} & -\hat{K}_{s_1} & 0 & -\hat{K}_{re} & -\hat{K}_{le} \\ 0 & 0 & -\hat{K}_{s_1} & \hat{K}_{s_1} + \hat{K}_{s_2} & -\hat{K}_{s_2} & 0 & 0 \\ 0 & -\hat{K}_{tr} & 0 & -\hat{K}_{s_2} & \hat{K}_{s_2} + \hat{K}_{tr} & 0 & 0 \\ 0 & 0 & -\hat{K}_{re} & 0 & 0 & \hat{K}_{re} & 0 \\ 0 & 0 & -\hat{K}_{le} & 0 & 0 & 0 & \hat{K}_{le} \end{bmatrix} \tag{D.59}$$

The reduced inertia of the main rotor shaft is equal to its standard inertia:

$$\hat{I}_{mr} = I_{mr} \left(\frac{\Omega_{mr}}{\Omega_{mr}} \right)^2 = I_{mr} \tag{D.60}$$

The reduced inertia of the tail rotor shaft is defined as:

$$\hat{I}_{tr} = I_{tr} \left(\frac{\Omega_{tr}}{\Omega_{mr}} \right)^2 \tag{D.61}$$

The reduced inertia of the engines is defined as:

$$\hat{I}_{re} = \hat{I}_{le} = \hat{I}_e = I_e \left(\frac{\Omega_e}{\Omega_{mr}} \right)^2 = I_e r_{mgb1-2}^2 = I_e r_{mgb1-3}^2 \tag{D.62}$$

The reduced inertia of a generic gearbox with n_{gb} gear wheels is defined as:

$$\hat{I}_{gb} = \sum_{i=1}^{n_{gb}} I_{gb_i} \left(\frac{\Omega_i}{\Omega_{mr}} \right)^2 \tag{D.63}$$

The reduced stiffness of a generic shaft is defined as:

$$\hat{K}_s = K_s \left(\frac{\Omega_s}{\Omega_{mr}} \right)^2 \tag{D.64}$$

The reduced torque applied to the main rotor shaft shaft is defined as:

$$\hat{Q}_{mr} = Q_{mr} \left(\frac{\Omega_{mr}}{\Omega_{mr}} \right) = Q_{mr} \tag{D.65}$$

The reduced torque applied to the tail rotor shaft shaft is defined as:

$$\hat{Q}_{tr} = Q_{tr} \left(\frac{\Omega_{tr}}{\Omega_{mr}} \right) \tag{D.66}$$

The reduced torque of the engines is defined as:

$$\hat{Q}_{re} = Q_{re} \left(\frac{\Omega_e}{\Omega_{mr}} \right) = Q_{re} r_{mgb1-2} = Q_{re} r_{mgb1-3} \tag{D.67}$$

$$\hat{Q}_{le} = Q_{le} \left(\frac{\Omega_e}{\Omega_{mr}} \right) = Q_{le} r_{mgb1-2} = Q_{le} r_{mgb1-3} \tag{D.68}$$

At this point a first check is required, consisting of two steps:

- The stiffness matrix must be singular ($\det(\hat{\mathbf{K}}) = 0$), i.e., there is a rigid mode.
- The drive train natural frequencies must be different than the $kN_b\Omega_{mr}$, where $k = 1,2,\ldots$ and N_b is the number of blades of the main rotor.

D.2.4. CRITICAL SPEED

The drivetrain model derived in this section represents the torsional dynamics only. However, even though drivetrain bending dynamics can be neglected for preliminary certification purposes, there are some design aspects concerning bending that should be considered. Indeed, bending produces an offset of the center of gravity of a shaft with respect to its rotation axis, thus acting as a periodic forcing function on the shaft with a frequency equal to the angular speed of the shaft, as shown in Fig. D.10. Therefore, it is paramount to check that the angular speed of a shaft differs from its bending frequencies.

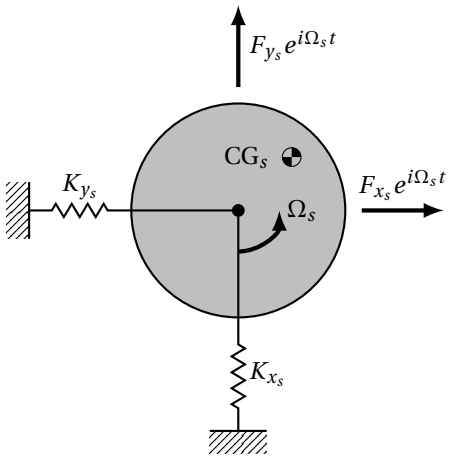

Figure D.10: Representation of the effects of the center of gravity offset due to bending on a rotating shaft.

D.2.5. ENGINE DYNAMICS

The engine torque can be expressed as the sum of two contributions:

$$Q_e = -Q_{e/\dot{\psi}_e}\dot{\psi}_e + Q_{e/\delta_t}\delta_t \tag{D.69}$$

where $Q_{e/\dot{\psi}_e}$ is called engine damping and is part of the stability derivatives and δ_t is the throttle, meaning that Q_{e/δ_t} is part of the control derivatives and is provided by the manufacturer.

According to Johnson [1975], the engine damping can be approximated as:

$$Q_{e/\dot{\psi}_e} = \frac{\partial Q_e}{\partial \dot{\psi}_e} \approx \frac{Q_e^{trim}}{\Omega_e} \tag{D.70}$$

In a trim condition, the engine power needs to balance the required power:

$$P_e^{trim} = P_{req}^{trim} \tag{D.71}$$

$$P_e^{trim} = Q_e^{trim}\Omega_e \tag{D.72}$$

$$P_{req}^{trim} = Q_{mr}^{trim}\Omega_{mr} + Q_{tr}^{trim}\Omega_{tr} \tag{D.73}$$

Therefore, Eq. (D.70) becomes:

$$Q_{e/\dot{\psi}_e} \approx \frac{P_e^{trim}}{\Omega_e^2} \tag{D.74}$$

Eq. (D.74) considers ideal engines, therefore it is more appropriate to reformulate it considering the engine efficiency $\eta < 1$:

$$Q_{e/\dot{\psi}_e} \approx \left(1-\eta\right)\frac{P_e^{trim}}{\Omega_e^2} \tag{D.75}$$

Replacing Eq. (D.69) in the torque vector from Eq. (D.26), the torque can be expressed as the sum of three components, i.e., the rotors torque, the engine damping torque and the control torque:

$$\begin{aligned}
\vec{Q} &= \begin{Bmatrix} -Q_{mr} \\ -Q_{tr} \\ 0 \\ 0 \\ 0 \\ Q_{re} \\ Q_{le} \end{Bmatrix} = \begin{Bmatrix} -Q_{mr} \\ -Q_{tr} \\ 0 \\ 0 \\ 0 \\ -Q_{e/\dot{\psi}_e}\dot{\psi}_{re} + Q_{e/\delta_t}\delta_t \\ -Q_{e/\dot{\psi}_e}\dot{\psi}_{le} + Q_{e/\delta_t}\delta_t \end{Bmatrix} = \\
&= \begin{Bmatrix} -Q_{mr} \\ -Q_{tr} \\ 0 \\ 0 \\ 0 \\ 0 \\ 0 \end{Bmatrix} - \begin{Bmatrix} 0 \\ 0 \\ 0 \\ 0 \\ 0 \\ Q_{e/\dot{\psi}_e}\dot{\psi}_{re} \\ Q_{e/\dot{\psi}_e}\dot{\psi}_{le} \end{Bmatrix} + \begin{Bmatrix} 0 \\ 0 \\ 0 \\ 0 \\ 0 \\ Q_{e/\delta_t} \\ Q_{e/\delta_t} \end{Bmatrix}\delta_t = \\
&= \underbrace{\begin{Bmatrix} -Q_{mr} \\ -Q_{tr} \\ 0 \\ 0 \\ 0 \\ 0 \\ 0 \end{Bmatrix}}_{\vec{Q}_r} - \underbrace{\begin{bmatrix} 0 & 0 & 0 & 0 & 0 & 0 & 0 \\ 0 & 0 & 0 & 0 & 0 & 0 & 0 \\ 0 & 0 & 0 & 0 & 0 & 0 & 0 \\ 0 & 0 & 0 & 0 & 0 & 0 & 0 \\ 0 & 0 & 0 & 0 & 0 & 0 & 0 \\ 0 & 0 & 0 & 0 & 0 & Q_{e/\dot{\psi}_e} & 0 \\ 0 & 0 & 0 & 0 & 0 & 0 & Q_{e/\dot{\psi}_e} \end{bmatrix}}_{\mathbf{C_e}} \underbrace{\begin{Bmatrix} \dot{\psi}_{mr} \\ \dot{\psi}_{tr} \\ \dot{\psi}_{mgb_1} \\ \dot{\psi}_{igb_1} \\ \dot{\psi}_{tgb_1} \\ \dot{\psi}_{re} \\ \dot{\psi}_{le} \end{Bmatrix}}_{\vec{\dot{\psi}}} + \underbrace{\begin{Bmatrix} 0 \\ 0 \\ 0 \\ 0 \\ 0 \\ Q_{e/\delta_t} \\ Q_{e/\delta_t} \end{Bmatrix}}_{\vec{Q}_{e/\delta_t}}\delta_t = \\
&= \vec{Q}_r - \mathbf{C_e}\vec{\dot{\psi}} + \vec{Q}_{e/\delta_t}\delta_t
\end{aligned} \tag{D.76}$$

Replacing Eq. (D.76) in Eq. (D.41):

$$\mathbf{M}\ddot{\vec{\psi}} + (\mathbf{C_s} + \mathbf{C_e})\dot{\vec{\psi}} + \mathbf{K}\vec{\psi} = \vec{Q}_r + \vec{Q}_{e/\delta_t}\delta_t \tag{D.77}$$

which in reduced coordinates becomes:

$$\hat{\mathbf{M}}\ddot{\vec{\psi}} + \left(\hat{\mathbf{C}}_\mathbf{s} + \hat{\mathbf{C}}_\mathbf{e}\right)\dot{\vec{\psi}} + \hat{\mathbf{K}}\vec{\psi} = \vec{\hat{Q}}_r + \vec{\hat{Q}}_{e/\delta_t}\delta_t \tag{D.78}$$

FREE-TURBINE TURBOSHAFT

The engine torque can be expressed as the sum of three contributions:

$$Q_e = -Q_{e/\dot{\psi}_e}\dot{\psi}_e - Q_{e/\dot{\psi}_{gg}}\dot{\psi}_{gg} + Q_{e/\delta_t}\delta_t \tag{D.79}$$

The gas generator torque can be expressed as the sum of two contributions:

$$Q_{gg} = -Q_{gg/\dot{\psi}_{gg}}\dot{\psi}_{gg} + Q_{gg/\delta_t}\delta_t \tag{D.80}$$

Replacing Eq. (D.79) and (D.80) in the torque vector from Eq. (D.42), the torque can be expressed as the sum of three components, i.e., the rotors torque, the engine damping torque and the control torque:

$$\vec{Q} = \begin{Bmatrix} -Q_{mr} \\ -Q_{tr} \\ 0 \\ 0 \\ 0 \\ Q_{re} \\ Q_{le} \\ Q_{gg_{re}} \\ Q_{gg_{le}} \end{Bmatrix} = \begin{Bmatrix} -Q_{mr} \\ -Q_{tr} \\ 0 \\ 0 \\ 0 \\ -Q_{e/\psi_e}\dot{\psi}_{re} - Q_{e/\psi_{gg}}\dot{\psi}_{re_{gg}} + Q_{e/\delta_t}\delta_t \\ -Q_{e/\psi_e}\dot{\psi}_{le} - Q_{e/\psi_{gg}}\dot{\psi}_{gg_{le}} + Q_{e/\delta_t}\delta_t \\ -Q_{gg/\psi_{gg}}\dot{\psi}_{re_{gg}} + Q_{gg/\delta_t}\delta_t \\ -Q_{gg/\psi_{gg}}\dot{\psi}_{gg_{le}} + Q_{gg/\delta_t}\delta_t \end{Bmatrix} =$$

$$= \begin{Bmatrix} -Q_{mr} \\ -Q_{tr} \\ 0 \\ 0 \\ 0 \\ 0 \\ 0 \\ 0 \\ 0 \end{Bmatrix} - \begin{Bmatrix} 0 \\ 0 \\ 0 \\ 0 \\ 0 \\ Q_{e/\psi_e}\dot{\psi}_{re} + Q_{e/\dot{\psi}_{gg}}\dot{\psi}_{gg_{re}} \\ Q_{e/\psi_e}\dot{\psi}_{le} + Q_{e/\dot{\psi}_{gg}}\dot{\psi}_{gg_{le}} \\ Q_{gg/\dot{\psi}_{gg}}\dot{\psi}_{gg_{re}} \\ Q_{gg/\dot{\psi}_{gg}}\dot{\psi}_{gg_{le}} \end{Bmatrix} + \begin{Bmatrix} 0 \\ 0 \\ 0 \\ 0 \\ 0 \\ Q_{e/\delta_t} \\ Q_{e/\delta_t} \\ Q_{gg/\delta_t} \\ Q_{gg/\delta_t} \end{Bmatrix} \delta_t =$$

$$= \underbrace{\begin{Bmatrix} -Q_{mr} \\ -Q_{tr} \\ 0 \\ 0 \\ 0 \\ 0 \\ 0 \\ 0 \\ 0 \end{Bmatrix}}_{\vec{Q}_r} - \underbrace{\begin{bmatrix} 0 & 0 & 0 & 0 & 0 & 0 & 0 & 0 & 0 \\ 0 & 0 & 0 & 0 & 0 & 0 & 0 & 0 & 0 \\ 0 & 0 & 0 & 0 & 0 & 0 & 0 & 0 & 0 \\ 0 & 0 & 0 & 0 & 0 & 0 & 0 & 0 & 0 \\ 0 & 0 & 0 & 0 & 0 & 0 & 0 & 0 & 0 \\ 0 & 0 & 0 & 0 & 0 & Q_{e/\dot{\psi}_e} & 0 & Q_{e/\dot{\psi}_{gg}} & 0 \\ 0 & 0 & 0 & 0 & 0 & 0 & Q_{e/\dot{\psi}_e} & 0 & Q_{e/\dot{\psi}_{gg}} \\ 0 & 0 & 0 & 0 & 0 & 0 & 0 & Q_{gg/\dot{\psi}_{gg}} & 0 \\ 0 & 0 & 0 & 0 & 0 & 0 & 0 & 0 & Q_{gg/\dot{\psi}_{gg}} \end{bmatrix}}_{\mathbf{C_e}} \underbrace{\begin{Bmatrix} \dot{\psi}_{mr} \\ \dot{\psi}_{tr} \\ \dot{\psi}_{mgb_1} \\ \dot{\psi}_{igb_1} \\ \dot{\psi}_{tgb_1} \\ \dot{\psi}_{re} \\ \dot{\psi}_{le} \\ \dot{\psi}_{gg_{re}} \\ \dot{\psi}_{gg_{le}} \end{Bmatrix}}_{\dot{\vec{\psi}}} + \underbrace{\begin{Bmatrix} 0 \\ 0 \\ 0 \\ 0 \\ 0 \\ Q_{e/\delta_t} \\ Q_{e/\delta_t} \\ Q_{gg/\delta_t} \\ Q_{gg/\delta_t} \end{Bmatrix}}_{\vec{Q}_{e/\delta_t}} \delta_t =$$

$$= \vec{Q}_r - \mathbf{C_e}\dot{\vec{\psi}} + \vec{Q}_{e/\delta_t}\delta_t \tag{D.81}$$

D.3. COUPLED ENGINE-DRIVETRAIN AND LEAD-LAG DYNAMICS

Augmenting Eq. (D.78) with Eq. (G.22) (refer to Appendix G for its derivation):

$$\underbrace{\begin{bmatrix} N_b I_\xi & -N_b\left(I_\xi + S_\xi e_\xi\right) & 0 & 0 & 0 & 0 & 0 & 0 \\ -N_b\left(I_\xi + S_\xi e_\xi\right) & & & & & & & \\ 0 & & & & & & & \\ 0 & & & & & & & \\ 0 & & & \hat{\mathbf{M}} & & & & \\ 0 & & & & & & & \\ 0 & & & & & & & \\ 0 & & & & & & & \end{bmatrix}}_{\hat{\mathbf{M}}_{\mathbf{ll}}} \begin{Bmatrix} \ddot{\xi}_0 \\ \ddot{\psi}_{mr} \\ \ddot{\psi}_{tr} \\ \ddot{\psi}_{mgb_1} \\ \ddot{\psi}_{igb_1} \\ \ddot{\psi}_{tgb_1} \\ \ddot{\psi}_{re} \\ \ddot{\psi}_{le} \end{Bmatrix} +$$

$$+ \underbrace{\begin{bmatrix} N_b C_\xi & \vec{0}^T \\ \vec{0} & \hat{\mathbf{C}}_\mathbf{s} + \hat{\mathbf{C}}_\mathbf{e} \end{bmatrix}}_{\hat{\mathbf{C}}_{\mathbf{ll}}} \begin{Bmatrix} \dot{\xi}_0 \\ \dot{\vec{\psi}} \end{Bmatrix} + \underbrace{\begin{bmatrix} N_b K_\xi & \vec{0}^T \\ \vec{0} & \hat{\mathbf{K}} \end{bmatrix}}_{\hat{\mathbf{K}}_{\mathbf{ll}}} \underbrace{\begin{Bmatrix} \xi_0 \\ \vec{\psi} \end{Bmatrix}}_{\vec{\psi}_{ll}} = \underbrace{\begin{Bmatrix} N_b Q_\xi^{aero} \\ \vec{Q}_r \end{Bmatrix}}_{\vec{Q}_{r_{ll}}} + \underbrace{\begin{Bmatrix} 0 \\ \vec{Q}_{e/\delta_t} \end{Bmatrix}}_{\vec{Q}_{e_{ll}/\delta_t}} \delta_t \tag{D.82}$$

$$\hat{\mathbf{M}}_{\mathbf{ll}} \ddot{\vec{\psi}}_{ll} + \hat{\mathbf{C}}_{\mathbf{ll}} \dot{\vec{\psi}}_{ll} + \hat{\mathbf{K}}_{\mathbf{ll}} \vec{\psi}_{ll} = \vec{Q}_{r_{ll}} + \vec{Q}_{e_{ll}/\delta_t} \delta_t \tag{D.83}$$

The coupled engine-drive train and lead-lag natural frequencies must be different than the $kN_b\Omega_{mr}$, where $k = 1, 2, \ldots$.

D.4. GOVERNOR DESIGN

The governor's function consists in keeping a constant rotorspeed (rotor rpm) during flight. The governor measures and regulates the speed of the engine (engine rpm) using a feedback controller on the error in rpm (difference between the measured rpm and the reference value, which is 100%), as shown in Fig. D.11.

The feedback on the error in rpm is slow (frequency of the order of 1 Hz) and hence cannot anticipate power demands in a timely manner. To overcome this issue, a synergistic approach between feedback on the error in rpm and feedforward on the collective input variation with respect to the trim value is usually adopted, as shown in Fig. D.12.

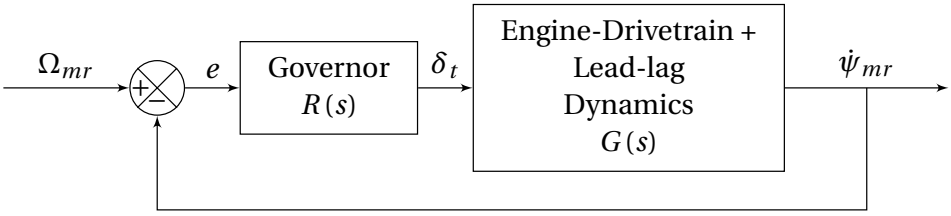

Figure D.11: Block diagram for the controller of the governor only with feedback.

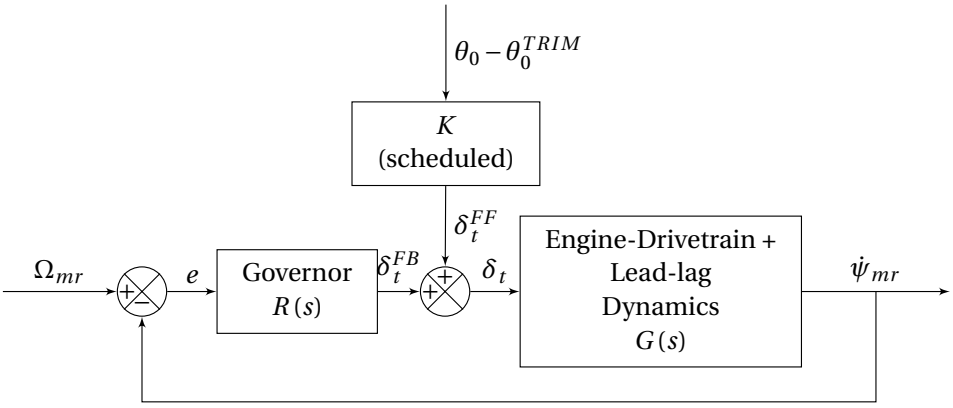

Figure D.12: Block diagram for the controller of the governor with feedback and feedforward.

Eq. (D.83) can be formulated as a single-input single-output state space system:

$$\underbrace{\begin{bmatrix}\mathbf{I} & \mathbf{0}\\ \mathbf{0} & \hat{\mathbf{M}}_{\mathbf{ll}}\end{bmatrix}}_{\hat{\mathbf{M}}_{\mathbf{ss}}}\begin{Bmatrix}\ddot{\vec{\psi}}_{ll}\\ \ddot{\vec{\psi}}_{ll}\end{Bmatrix}+\underbrace{\begin{bmatrix}\mathbf{0} & -\mathbf{I}\\ \hat{\mathbf{K}}_{\mathbf{ll}} & \hat{\mathbf{C}}_{\mathbf{ll}}\end{bmatrix}}_{\hat{\mathbf{K}}_{\mathbf{ss}}}\underbrace{\begin{Bmatrix}\vec{\psi}_{ll}\\ \dot{\vec{\psi}}_{ll}\end{Bmatrix}}_{\vec{x}}=\underbrace{\begin{Bmatrix}\vec{0}\\ \vec{Q}_{r_{ll}}\end{Bmatrix}}_{\vec{Q}_{r_{ss}}}+\underbrace{\begin{Bmatrix}0\\ \vec{Q}_{e_{ll}/\delta_t}\end{Bmatrix}}_{\vec{Q}_{e_{ss}/\delta_t}}\delta_t \tag{D.84}$$

$$\hat{\mathbf{M}}_{\mathbf{ss}}\ddot{\vec{x}}+\hat{\mathbf{K}}_{\mathbf{ss}}\vec{x}=\vec{Q}_{r_{ss}}+\vec{Q}_{e_{ss}/\delta_t}\delta_t \tag{D.85}$$

$$\dot{\vec{x}}=\underbrace{-\hat{\mathbf{M}}_{\mathbf{ss}}^{-1}\hat{\mathbf{K}}_{\mathbf{ss}}}_{\mathbf{A}}\vec{x}+\hat{\mathbf{M}}_{\mathbf{ss}}^{-1}\vec{Q}_{r_{ss}}+\underbrace{\hat{\mathbf{M}}_{\mathbf{ss}}^{-1}\vec{Q}_{e_{ss}/\delta_t}}_{\mathbf{B}}\underbrace{\delta_t}_{u} \tag{D.86}$$

$$\dot{\vec{x}}=\mathbf{A}\vec{x}+\mathbf{B}u \tag{D.87}$$

$$y=\mathbf{C}\vec{x}=\begin{bmatrix}0&0&0&0&0&0&0&0&0&1&0&0&0&0&0&0\end{bmatrix}\vec{x}=\dot{\psi}_{mr} \tag{D.88}$$

The transfer function of the engine-drivetrain plus lead-lag dynamics can be expressed as:

$$s\vec{x}=\mathbf{A}\vec{x}+\mathbf{B}u \tag{D.89}$$

$$y=\mathbf{C}\vec{x} \tag{D.90}$$

$$(s\mathbf{I}-\mathbf{A})\,\vec{x}=\mathbf{B}u \tag{D.91}$$

$$y=\mathbf{C}\vec{x} \tag{D.92}$$

$$\dot{\vec{x}} = (s\mathbf{I} - \mathbf{A})^{-1}\mathbf{B}u \tag{D.93}$$

$$y = \underbrace{\mathbf{C}(s\mathbf{I} - \mathbf{A})^{-1}\mathbf{B}}_{G(s)} u = G(s)\,u \tag{D.94}$$

The rotor speed governor typically consists of a proportional-plus-integral controller:

$$R(s) = k_p + \frac{k_I}{s} \tag{D.95}$$

The open loop transfer function is given by:

$$L(s) = R(s)\,G(s) \tag{D.96}$$

The closed loop transfer function is given by:

$$H(s) = \frac{L(s)}{1 + L(s)} \tag{D.97}$$

The first requirement on the closed loop transfer function is the asymptotic stability. To achieve this goal, the Bode criterion can be applied if $L(s)$ meets the following assumptions:

1. All the poles of $L(s)$ have negative real part.
2. The Bode plot of the magnitude of $L(s)$ intersects the axis of 0 dB only once (see Fig. D.13).

Under these assumptions, the closed loop transfer function is asymptotically stable if and only if the loop gain μ_L and the phase margin ϕ_m are both positive.

To calculate the phase margin ϕ_m, the following step need to be followed:

1. Calculate the critical frequency ω_c, i.e., the frequency at which the Bode plot of the magnitude of $L(s)$ intersects the axis of 0 dB ($\left|L\left(j\omega_c\right)\right| = 1$).
2. Calculate the critical phase ϕ_c, i.e., the phase at critical frequency ($\phi_c = \angle L\left(j\omega_c\right)$).
3. Calculate the phase margin ϕ_m as $\phi_m = 180° - \left|\phi_c\right|$.

Typical design goal for a robust controller require a gain margin of 6 dB at the torsional frequency and a phase margin of 45 deg [Kuczynski et al., 1980] or more (e.g., 60 deg). In general, when these margins are achieved by analysis, the actual flight characteristics of the helicopter are also satisfactory.

The governor usually has a bandwidth which is much lower than 1 Hz ($\omega_c \approx 0.3 \div 0.4$ Hz), as shown in Fig. D.13.

The coupled engine/drive train/helicopter rotor has a lightly damped torsional mode, the natural frequency of which is typically much less than the rotational frequency of the main rotor. This mode is commonly called the first torsional mode. Because of its relatively low frequency, it can interact with the fuel control system and at, a high loop gain, can cause system instability or limit cycles (see Fig. D.14). A notch filter is usually used in the fuel control system to attenuate this and higher frequencies torsional modes [Chen, 1992; Wong, 1995], whose transfer function of Eq. (D.98) is represented using Bode diagrams in Fig. D.15.

The torsional frequencies peaks at high frequencies shown in Fig. D.14 are related to the modes of deformation of the shafts. These peaks would not be visible with a rigid transmission model.

$$NF(s) = \frac{s^2 + \omega_{nf}^2}{s^2 + \omega_{bw} s + \omega_{nf}^2} \tag{D.98}$$

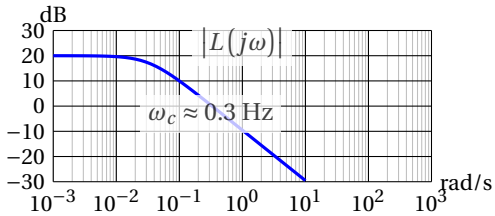

Figure D.13: Bode plot of the open loop transfer function.

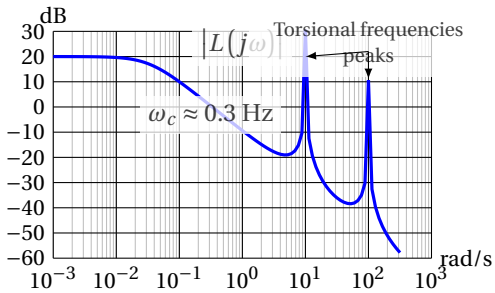

Figure D.14: Bode plot of the open loop transfer function with torsional frequencies peaks.

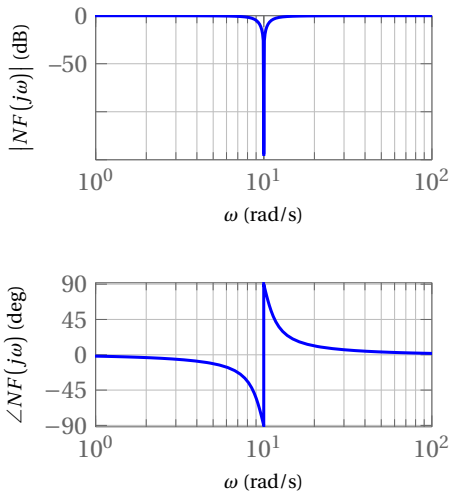

Figure D.15: Bode plot of the notch filter transfer function.

D.5. COUPLING WITH THE AIRFRAME YAW DYNAMICS

Yaw and heave degrees of freedom are the rigid-body dynamics that are affected the most by the engine-drivetrain plus lead-lag dynamics [Hui, 1999]. In this section, the engine-drivetrain plus lead-lag dynamics will be coupled with the aircraft yaw dynamics. However, this analytical approach does not follow the correct load path. Indeed, the engine-drivetrain torques are not applied to the hub, but to the gear boxes, which are directly connected to the airframe [Muscarello et al., 2017].

The moment with respect to the hub of the inertia forces can be calculated as:

$$\begin{aligned} \mathrm{d}\vec{M}^{O_h}_{Inertia_{bl}} &= -(P-O_h)\times\vec{a}_P\mathrm{d}m \\ &= -\left\{\begin{array}{c} e_\xi\sin\xi \\ r_P+e_\xi\cos\xi \\ 0 \end{array}\right\}^l \times \left\{\begin{array}{c} a_{P_x} \\ a_{P_y} \\ a_{P_z} \end{array}\right\}^l \mathrm{d}m \\ &= -\left\{\begin{array}{c} \left(r_P+e_\xi\cos\xi\right)a^l_{P_z} \\ -e_\xi\sin\xi\, a^l_{P_z} \\ e_\xi\sin\xi\, a^l_{P_y}-\left(r_P+e_\xi\cos\xi\right)a^l_{P_x} \end{array}\right\}\mathrm{d}m \end{aligned} \tag{D.99}$$

$$\mathrm{d}M^{O_h}_{Inertia_{z_{bl}}} = \left[-e_\xi\cancelto{0}{\sin\xi}\, a^l_{P_y}+\left(r_P+e_\xi\cancelto{1}{\cos\xi}\right)a^l_{P_x}\right]\mathrm{d}m \approx \left(r_P+e_\xi\right)a^l_{P_x}\mathrm{d}m \tag{D.100}$$

Replacing the expression for $a^l_{P_x}$ from Eq. (H.26) (refer to Appendix H for its derivation) in Eq. (D.100):

$$\begin{aligned}
\mathrm{d}M^{O_h}_{Inertia_{z_{bl}}} &= \left(r_P + e_\xi\right)\left[e_\xi\left(\ddot{\psi}_{mr} - \dot{r}_h\right) + r_P\left(\ddot{\psi}_{mr} - \ddot{\xi} - \dot{r}_h\right)\right]\mathrm{d}m = \\
&= \left[r_P^2\left(\ddot{\psi}_{mr} - \ddot{\xi} - \dot{r}_h\right) + r_P e_\xi\left(2\ddot{\psi}_{mr} - \ddot{\xi} - 2\dot{r}_h\right) + e_\xi^2\left(\ddot{\psi}_{mr} - \dot{r}_h\right)\right]\mathrm{d}m = \\
&= \left[\left(r_P^2 + 2r_P e_\xi + e_\xi^2\right)\left(\ddot{\psi}_{mr} - \dot{r}_h\right) - \left(r_P^2 + r_P e_\xi\right)\ddot{\xi}\right]\mathrm{d}m
\end{aligned} \tag{D.101}$$

Integrating Eq. (D.101):

$$\begin{aligned}
M^{O_h}_{Inertia_{z_{bl}}} &= \int_0^{R-e_\xi}\left[\left(r_P^2 + 2r_P e_\xi + e_\xi^2\right)\left(\ddot{\psi}_{mr} - \dot{r}_h\right) - \left(r_P^2 + r_P e_\xi\right)\ddot{\xi}\right]\mathrm{d}m = \\
&= \left(\int_0^{R-e_\xi} r_P^2\mathrm{d}m + 2e_\xi\int_0^{R-e_\xi} r_P\mathrm{d}m + e_\xi^2\int_0^{R-e_\xi}\mathrm{d}m\right)\left(\ddot{\psi}_{mr} - \dot{r}_h\right) + \\
&- \left(\int_0^{R-e_\xi} r_P^2\mathrm{d}m + e_\xi\int_0^{R-e_\xi} r_P\mathrm{d}m\right)\ddot{\xi} = \\
&= \left(I_\xi + 2e_\xi S_\xi + e_\xi^2 m_{bl}\right)\left(\ddot{\psi}_{mr} - \dot{r}_h\right) - \left(I_\xi + e_\xi S_\xi\right)\ddot{\xi} = \\
&= I_{bl}\left(\ddot{\psi}_{mr} - \dot{r}_h\right) - \left(I_\xi + e_\xi S_\xi\right)\ddot{\xi}
\end{aligned} \tag{D.102}$$

Summing over the number of blades:

$$\begin{aligned}
M^{O_h}_{Inertia_z} &= \sum_{bl=1}^{N_{bl}} M^{O_h}_{Inertia_{z_{bl}}} = \\
&= N_{bl} I_{bl}\left(\ddot{\psi}_{mr} - \dot{r}_h\right) - N_{bl}\left(I_\xi + e_\xi S_\xi\right)\ddot{\xi} = \\
&= I_{mr}\left(\ddot{\psi}_{mr} - \dot{r}_h\right) - N_{bl}\left(I_\xi + e_\xi S_\xi\right)\ddot{\xi}
\end{aligned} \tag{D.103}$$

The moment with respect to the hub of the aerodynamic forces can be calculated as:

$$\begin{aligned}
\mathrm{d}\vec{M}^{O_h}_{Aero_{bl}} &= (P - O_h) \times \vec{f}_P \mathrm{d}r_P \\
&= \left\{\begin{matrix} e_\xi \sin\xi \\ r_P + e_\xi\cos\xi \\ 0 \end{matrix}\right\}^l \times \left\{\begin{matrix} f_{P_x} \\ f_{P_y} \\ f_{P_z} \end{matrix}\right\}^l \mathrm{d}r_P \\
&= \left\{\begin{matrix} \left(r_P + e_\xi\cos\xi\right) f^l_{P_z} \\ -e_\xi \sin\xi\, f^l_{P_z} \\ e_\xi \sin\xi\, f^l_{P_y} - \left(r_P + e_\xi\cos\xi\right) f^l_{P_x} \end{matrix}\right\}\mathrm{d}r_P
\end{aligned} \tag{D.104}$$

$$\mathrm{d}M^{O_h}_{Aero_{z_{bl}}} = \left[\cancelto{0}{e_\xi \sin\xi} f^l_{P_y} - \left(r_P + \cancelto{1}{e_\xi\cos\xi}\right) f^l_{P_x}\right]\mathrm{d}r_P \approx -\left(r_P + e_\xi\right) f^l_{P_x}\mathrm{d}r_P \tag{D.105}$$

$$M^{O_h}_{Aero_{z_{bl}}} = \int_0^{R-e_\xi}\mathrm{d}M^{O_h}_{Aero_{z_{bl}}} \tag{D.106}$$

$$Q_{mr} = M^{O_h}_{Aero_z} = \sum_{bl=1}^{N_{bl}} M^{O_h}_{Aero_{z_{bl}}} \tag{D.107}$$

The total moment of the main rotor with respect to the hub is given by the sum of Eq. (D.107) and (D.103):

$$N_h = Q_{mr} + I_{mr}\left(\ddot{\psi}_{mr} - \dot{r}_h\right) - N_{bl}\left(I_\xi + e_\xi S_\xi\right)\ddot{\xi} \tag{D.108}$$

The equation of motion for the yaw dynamics can be written as:

$$I_{zz}\dot{r} - \left(I_{xx} - I_{yy}\right)pq - I_{xz}\left(\dot{p} - rq\right) = N \tag{D.109}$$

The yaw moment N is given by the contribution of the different helicopter components (e.g., main rotor, horizontal tail plane, vertical stabilizer, fuselage, tail rotor):

$$N = N_h + N_{fus} + N_{tp} + N_{vs} + N_{tr} \tag{D.110}$$

Replacing Eq. (D.110) in Eq. (D.109), we obtain:

$$I_{zz}\dot{r} - \left(I_{xx} - I_{yy}\right)pq - I_{xz}\left(\dot{p} - rq\right) = N_h + N_{fus} + N_{tp} + N_{vs} + N_{tr} \tag{D.111}$$

Replacing Eq. (D.108) in Eq. (D.111), we obtain:

$$\begin{aligned}\left(I_{zz} + I_{mr}\right)\dot{r} - I_{mr}\ddot{\psi}_{mr} + N_{bl}\left(I_\xi + e_\xi S_\xi\right)\ddot{\xi} - \left(I_{xx} - I_{yy}\right)pq - I_{xz}\left(\dot{p} - rq\right) = \\ = Q_{mr} + N_{fus} + N_{tp} + N_{vs} + N_{tr}\end{aligned} \tag{D.112}$$

Augmenting Eq. (D.83) with Eq. (D.112):

$$\begin{bmatrix} I_{zz}+I_{mr} & 0 & -I_{mr} & 0 & 0 & 0 & 0 & 0 & 0 \\ 0 & & & & & & & & \\ -I_{mr} & & & & & & & & \\ 0 & & & & & & & & \\ 0 & & & & & & & & \\ 0 & & & & \hat{\mathbf{M}}_{\mathbf{ll}} & & & & \\ 0 & & & & & & & & \\ 0 & & & & & & & & \\ 0 & & & & & & & & \end{bmatrix} \begin{Bmatrix} \dot{r} \\ \ddot{\xi}_0 \\ \ddot{\psi}_{mr} \\ \ddot{\vec{\psi}}_{tr} \\ \ddot{\vec{\psi}}_{mgb_1} \\ \ddot{\vec{\psi}}_{igb_1} \\ \ddot{\vec{\psi}}_{tgb_1} \\ \ddot{\vec{\psi}}_{re} \\ \ddot{\vec{\psi}}_{le} \end{Bmatrix} +$$

$$+ \begin{bmatrix} 0 & \vec{0}^T \\ \vec{0} & \hat{\mathbf{C}}_{\mathbf{ll}} \end{bmatrix} \begin{Bmatrix} r \\ \dot{\vec{\psi}}_{ll} \end{Bmatrix} \begin{bmatrix} 0 & \vec{0}^T \\ \vec{0} & \hat{\mathbf{K}}_{\mathbf{ll}} \end{bmatrix} \begin{Bmatrix} \int r \\ \vec{\psi}_{ll} \end{Bmatrix} = \begin{Bmatrix} Q_{mr} + \sum_i N_i \\ \vec{Q}_{r_{ll}} \end{Bmatrix} + \begin{Bmatrix} 0 \\ \vec{Q}_{e_{ll}/\delta_t} \end{Bmatrix} \delta_t \tag{D.113}$$

E

PILOT MODEL

The development of fully autonomous vehicles is still far from becoming reality, because safe and reliable automation cannot be guaranteed under all operational circumstances. Even though the level of automation is increasing, the human operator keeps playing an important role in the execution of the required task. Based on the situation, the human operator exerts different levels of control authority on the controlled system, ranging from supervisory to manual control. Therefore, understanding how humans interact with machines is still crucial in the design of manual control systems of considerable complexity and for providing deeper understanding of human performance and learning behavior in such systems.

Different studies have been carried out in order to develop mathematical models of human control behavior. All of them share the idea of treating the human operator as an intelligent, adaptive and versatile control system. Indeed, humans are characterized by the two essential elements that can be found in a control system: sensors (sensory nervous system) to "measure" the current state of the controlled system, and actuators (musculoskeletal system) to correct the current state in order to match the target.

The application of classical control theory to model human control behavior dates back to 1960s and is referred to as *Cybernetics*. With their *Crossover Model*, McRuer et al. [1967] have been two of the pioneers of this branch of science. This model is based on two parameters (the phase margin and the crossover frequency) and, according to it, humans unconsciously adapt their control strategy to the dynamics of the system they are controlling, such that the open-loop transfer function of the combination of pilot and controlled system can be described by a single integrator. The crossover model is very simple and accurate, showing a good correlation with the results of human-in-the-loop experiments, but it is only valid around the crossover frequency and for compensatory tracking tasks.

Kleinman and Baron [Baron et al., 1970; Kleinman et al., 1970] developed a quantitative model for the response characteristics of the human operator, assuming that a well-trained and well-motivated human operator behaves in an "optimal" manner, subject to their inherent psycho-physical limitations and to the requirements of the control

task. This model is known as *Optimal Control Model (OCM)*. Unlike the crossover model, the OCM can be used for a wide range of frequencies and can be applied to study complex tasks. However, the physical interpretation of the OCM parameters is non-trivial. For this reason, they cannot be estimated directly from experimental data.

Hess [1980] attempted to provide a more realistic representation of the human's signal processing structure than that which is exhibited by the crossover model and by the OCM. His *Structural Pilot Model (SPM)* implements two novel features that distinguish it from the two models previously described. First, the proprioceptive information from the control stick or manipulator constitutes one of the major feedback paths in the model, extending its validity beyond the region of crossover. Second, the error rate information is continuously derived and independently but intermittently controlled to keep into account the effect of inaccuracies such as time variations in the pilot's internal model of the controlled-element dynamics. Such model is envisioned to be able to provide a more unified theoretical framework within which to interpret a variety of empirical pilot/vehicle response phenomena, like the ability of the pilot to adapt to different vehicle dynamics and to displays of varying quality. However, the SPM is only valid for compensatory tracking tasks, like the crossover model.

The use of models of human control behavior should not be restricted only to analytical/quantitative handling qualities assessment (ADS-33E [US Army AMCOM, 2000]) of newly developed vehicles Damveld [2009]; Yilmaz [2018], but has strong implications also on pilot training, especially with regards to the formulation of design criteria for flight simulator training devices, which are usually based merely on technology-push considerations, rather than task behavioral requirements. For future work in this direction, a "paper pilot" [Anderson, 1970; Dillow, 1971] based on PID (Proportional-Integral-Derivative) controllers has been developed to perform the straight-in autorotation maneuver with the helicopter model developed in this thesis (Appendix A).

E.1. PAPER PILOT BASED ON PID CONTROLLERS

To design the paper pilot, it is first necessary to understand which loops need to be closed by the pilot in the different phases of the maneuver. To this end, the tasks performed by the pilot in each phase of the maneuver have been analyzed and summarized in Tab. E.1.

The same design can be adopted for the longitudinal cyclic pitch, lateral cyclic pitch, and tail-rotor collective controllers both for straight level flight and steady-descent in autorotation (Fig. E.1, E.2, and E.3). The collective controller instead is an altitude-hold in straight level flight (Fig. E.4) a rotor RPM-hold in steady-descent in autorotation (Fig. E.5).

E.1.1. FINAL PHASES OF THE STRAIGHT-IN AUTOROTATION MANEUVER: CYCLIC FLARE TO TOUCHDOWN

The final phases of the straight-in autorotation maneuver, i.e., cyclic flare, rotation, and collective flare, are unsteady conditions. This means that the target followed by the controller must not be steady, because there is no continuous source of energy to reach that target and maintain it. The only way to design a working controller is by prescribing a

Table E.1: Autorotation phases.

Phase	**Pilot task**	**Target values**
Level flight	Hold: • altitude • horizontal speed • lateral speed • heading	Level flight trim parameters at initial speed
Failure, recognition, entry in autorotation		
Steady descent	Hold: • rotor RPM • horizontal speed • lateral speed • heading	Steady descent trim parameters at suggested autorotative speed
Cyclic flare	Reduce: • descent rate • horizontal speed Hold: • lateral speed • heading Increase: • rotor RPM	• Trim parameters at hover • Collective as in steady descent
Rotation and collective flare	• Level the helicopter with the ground • Reduce descent rate Hold: • lateral speed • heading	Trim parameters at hover
Touchdown		

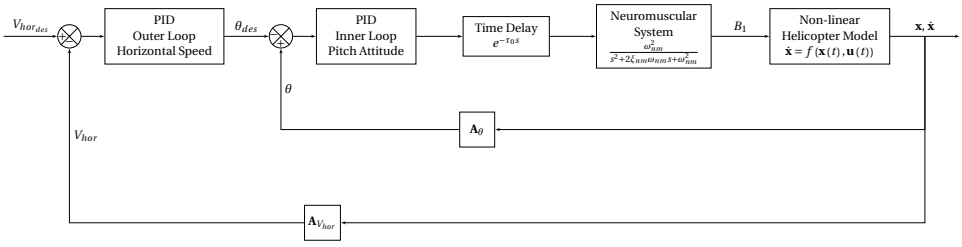

Figure E.1: Block diagram for the PID controller of the longitudinal cyclic pitch during straight level flight and steady-descent in autorotation.

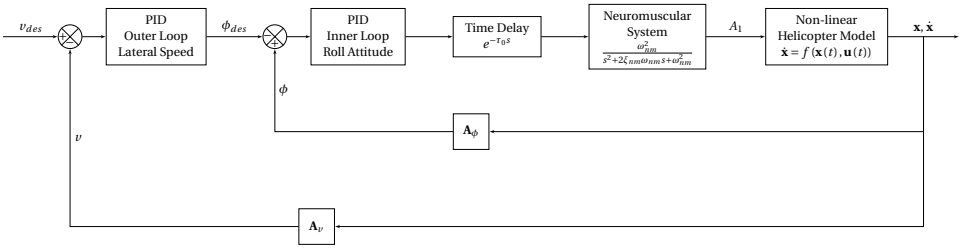

Figure E.2: Block diagram for the PID controller of the lateral cyclic pitch during straight level flight and steady-descent in autorotation.

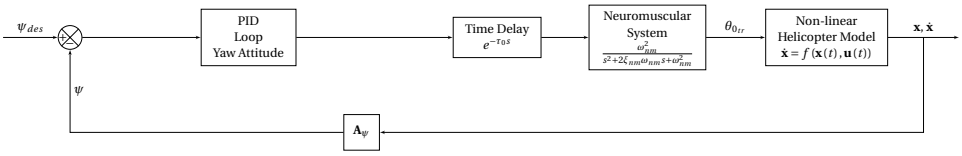

Figure E.3: Block diagram for the PID controller of the tail-rotor collective pitch during straight level flight and steady-descent in autorotation (heading-hold).

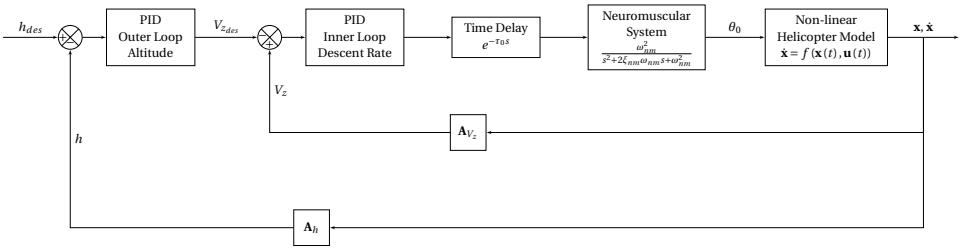

Figure E.4: Block diagram for the PID controller of the collective pitch during straight level flight (altitude-hold).

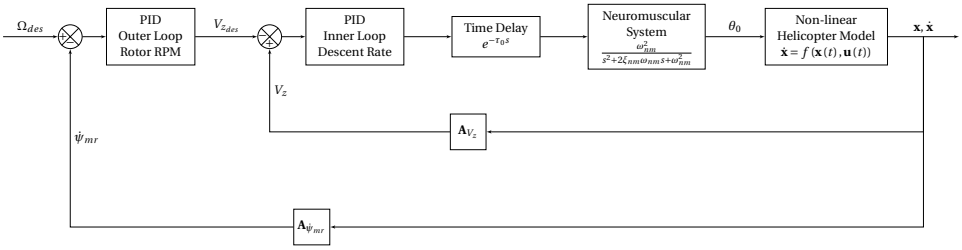

Figure E.5: Block diagram for the PID controller of the collective pitch during steady-descent in autorotation (rpm-hold).

reference trajectory to be followed.

There are several methods that can be used to estimate the flare trajectory:

- Use piloted simulation data (e.g., best pilot's autorotative landing, or even an idealized version automatically estimated from the pilot's many suboptimal autorotative landings [Abbeel et al., 2009]).
- Use estimated time to ground impact (tau) theory [Sunberg et al., 2014, 2015].
- Prescribe what looks like a feasible trajectory. For example, the exponential flare path is one of the flare techniques usually adopted in fixed-wing aircraft [Jump et al., 2007, 2006]. An exponential flare trajectory, although non-optimal, can also be tested for helicopter autorotation. A possible analytical formulation was proposed by Malaek et al. [2004]:

$$h_{ref}(x) = \frac{h_{fl}}{\dot{h}_{fl} - \dot{h}_{td}} \left[\dot{h}_{fl}\, e^{-\frac{\left(x - x_{fl}\right)}{\tau}} - \dot{h}_{td} \right] \tag{E.1}$$

  where the parameter τ can be estimated by imposing that:

$$h_{ref}(x_{td}) = h_{td} \tag{E.2}$$

- Reverse engineering process: known the initial condition and the desired condition at touch down, estimate a feasible and safe trajectory by setting-up an optimization procedure [Grande et al., 2016].

The reference flare trajectory supplied to the controller was estimated according to the method proposed by Grande et al. [2016], who adopt a helicopter point-mass model [Aponso et al., 2007]. The equations of motion, expressed as a function of the time, are reformulated as a function of the altitude and then discretized, because we do not know a priori how long the flare is going to last, but we do know the final altitude. Known the desired final condition (touch-down with a helicopter final state that is safe) and the initial condition (helicopter's state in steady-descent in autorotation), we only need the input sequence, i.e., the inputs at each altitude step, to integrate the equations of motion. The inputs at each altitude step need to provide a feasible and safe trajectory. Feasible means that the constraints on the helicopter state during the flare (e.g., the rotor speed must remain between 85% and 110% for the Bo-105 helicopter) are satisfied, whereas safe means that the helicopter final state at touchdown is, at least, survivable. To determine an input sequence leading to a feasible and safe trajectory, Grande et al. [2016] set up an optimization procedure. The inputs at each altitude step are the design variables, whose optimal sequence minimizes a cost function subject to several equality and inequality constraints.

The constraints on the final state at touchdown were set according to the desired performance listed in Tab. 5.1. Other constraints were set, for example, on the pitch attitude (during the flare it should not exceed 25 degrees for the Bo-105 helicopter) and the rotor speed (during the flare it must remain between 85% and 110% for the Bo-105 helicopter).

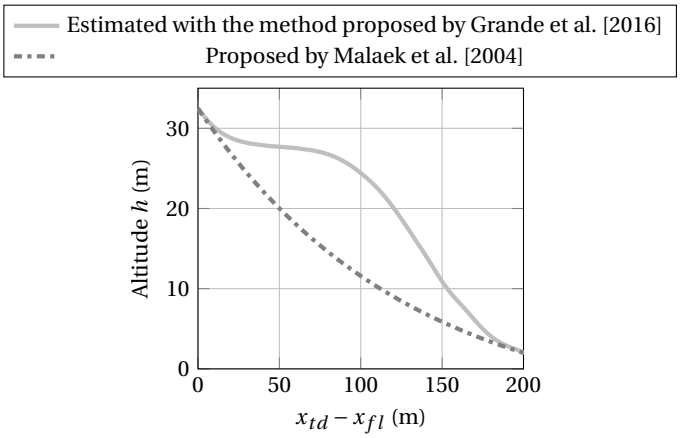

Figure E.6: Comparison between the flare trajectory estimated with the method proposed by Grande et al. [2016] and that proposed by Malaek et al. [2004], typical of fixed-wing aircraft.

E

E.1.2. RESULTS

Fig. E.7 and E.8 shows the results of the straight-in autorotation maneuver performed by the pilot model with the helicopter non-linear model developed in this thesis (Appendix A). The engine failure is triggered at 10 seconds. To incorporate a reasonable intervention time of a human pilot, the switch from the straight level flight controller (Fig. E.4) to the steady-descent in autorotation controller (Fig. E.5) happens 0.5 second after the failure. The switch from the steady-descent in autorotation controller (Fig. E.5) to the flare/rotation/cushion controller happens when the helicopter reaches 100 ft above the ground level as suggested in the Bo-105 helicopter flight manual. The rate of descent at touchdown (Fig. E.8c) is 259 ft/min well below the threshold for desired performance (480 ft/min from Tab. 5.1). The horizontal speed at touchdown (Fig. E.7b) is around 30 knots, matching the threshold for desired performance (Tab. 5.1). The pitch attitude at touchdown (Fig. E.7c) is approximately 14 degrees, slightly above the threshold for desired performance (12 degrees from Tab. 5.1).

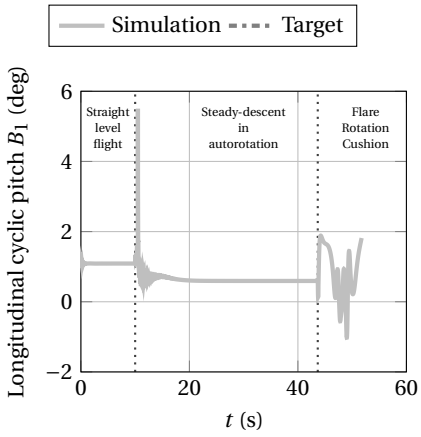

(a) Longitudinal cyclic pitch input.

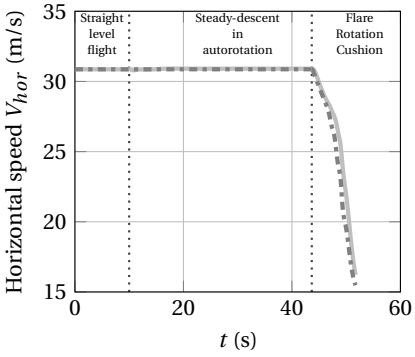

(b) Horizontal speed.

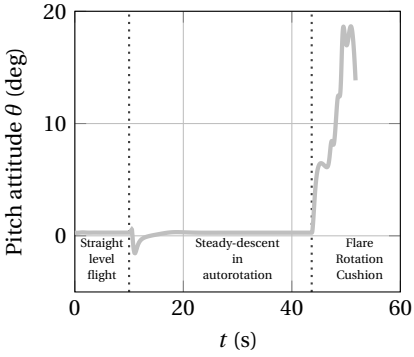

(c) Pitch attitude.

Figure E.7: Simulation results for the longitudinal cyclcic controller of the pilot model performing the straight-in autorotation maneuver.

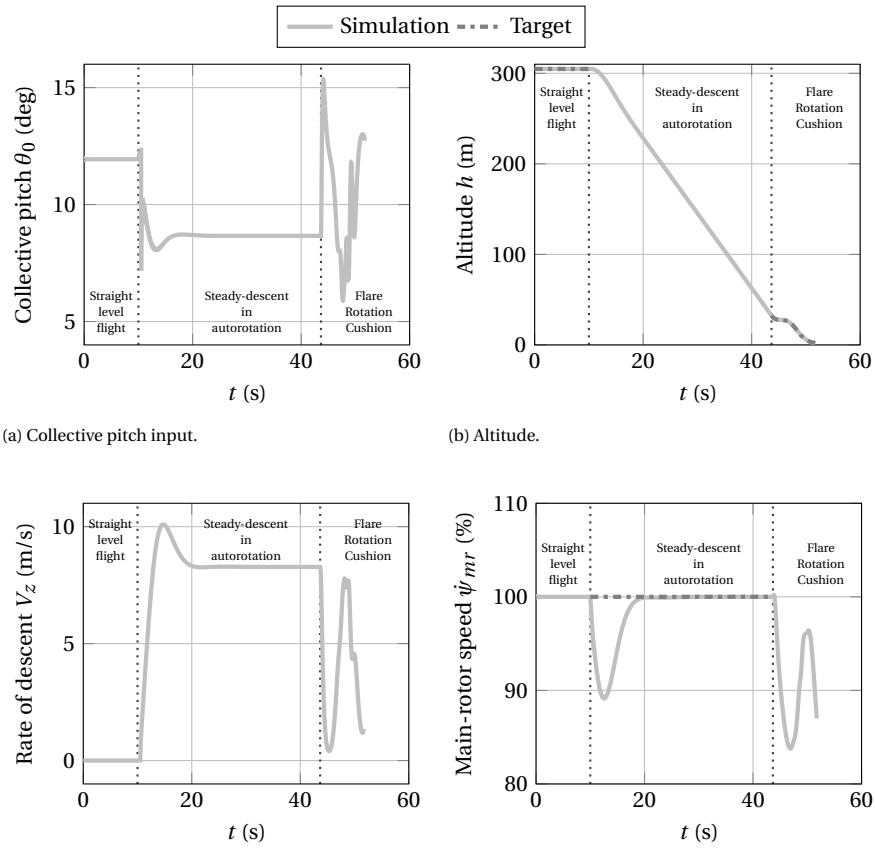

(a) Collective pitch input.

(b) Altitude.

(c) Rate of descent.

(d) Main-rotor speed.

Figure E.8: Simulation results for the collective controller of the pilot model performing the straight-in autorotation maneuver.

F

REFERENCE FRAMES

This chapter presents a general description of the reference frames used in this thesis.

1. Local Tangent Plane Coordinates (LTP) or Local Vertical, Local Horizontal Coordinates (LVLH) are a geographical coordinate system based on the local vertical direction and the Earth's axis of rotation. It consists of three coordinates: one represents the position along the northern axis, one along the local eastern axis, and one represents the vertical position. Two right-handed variants exist: east, north, up (ENU) coordinates and north, east, down (NED) coordinates.

2. Body frame

3. Hub-body frame

F.1. INERTIAL REFERENCE FRAME

It can be demonstrated that the NED reference frame can be approximated to an inertial reference frame for atmospheric flight mechanics purposes. The origin of this reference frame is defined at the aircraft center of gravity, as shown in Fig. F.1. The z-axis (identified by the versor $\vec{g}_3$) points towards the center of the Earth (local vertical) and the (x-y) plane is tangent to the Earth's surface (local horizontal), with the x-axis (identified by the versor $\vec{g}_1$) pointing towards north. The y-axis (identified by the versor $\vec{g}_2$) is defined by the right-hand rule as $\vec{g}_2 = \vec{i}_3 \times \vec{i}_1$, thus pointing towards east.

F.2. BODY REFERENCE FRAME

The body reference frame is integral with the aircraft and its origin is defined at the aircraft center of gravity, as shown in Fig. F.2. The (x-z) plane is parallel to (usually coincident with) the aircraft symmetry plane, with the x-axis (identified by the versor $\vec{b}_1$) parallel to the fuselage reference line and pointing towards the aircraft nose and the z-axis

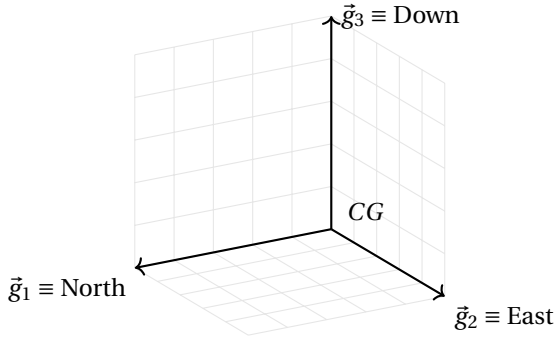

Figure F.1: Inertial reference frame.

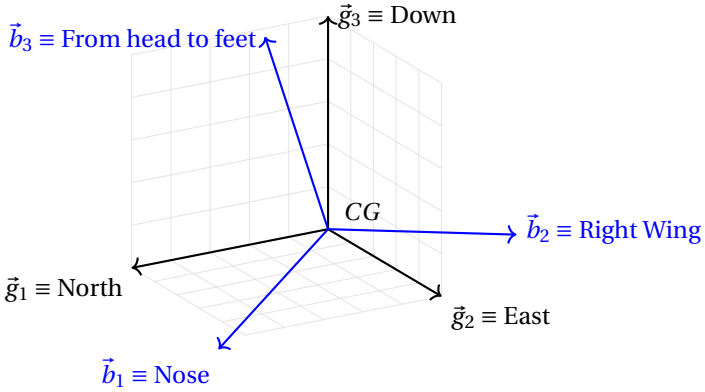

Figure F.2: Body reference frame.

(identified by the versor $\vec{b}_3$) pointing from pilot's head to pilot's feet. The y-axis (identified by the versor $\vec{b}_2$) is defined by the right-hand rule as $\vec{b}_2 = \vec{b}_3 \times \vec{b}_1$, thus pointing towards the aircraft right wing.

Euler angles are a non-vectorial parametrization to represent rotations: three angles that describe a sequence of three planar rotations. The only requirement is that two consecutive rotations must not be accomplished around the same axis. Therefore, there are 12 possible sequences that can be adopted. The sequence 321 is the most commonly used in flight mechanics and enables to switch from the inertial to the body reference frame:

- a rotation of an angle ψ around the z-axis of the inertial reference frame (identified by the versor $\vec{g}_3$) leads to a first intermediate reference frame $CG\left(\vec{j}_1, \vec{j}_2, \vec{j}_3\right)$, as shown in Fig. F.3a. ψ is known as azimuth, yaw or heading angle.

- a rotation of an angle θ around the y-axis of the first intermediate reference frame (identified by the versor $\vec{j}_2$) leads to a second intermediate reference frame $CG\left(\vec{k}_1, \vec{k}_2, \vec{k}_3\right)$, as shown in Fig. F.3b. θ is known as elevation or pitch angle.

- a rotation of an angle ϕ around the x-axis of the intermediate reference frame (identified by the versor $\vec{k}_1$) leads to the body reference frame $CG\left(\vec{b}_1, \vec{b}_2, \vec{b}_3\right)$, as shown in Fig. F.3c. ϕ is known as proper rotation, roll or bank angle.

These three angles are usually called Cardan or Tait-Bryan angles, a sub-category of Euler angles. There are situations in which two of the three axes around which two consecutive rotations are accomplished are orthogonal (e.g., if $\psi = 0$ and $\theta = 90$ deg, yaw and pitch axes are orthogonal and roll rotations are also yaw rotations. This means that roll and yaw axes are parallel). Euler angles parametrization fails to catch this condition. Such phenomenon is called "gimbal lock". For this reason, a different parametrization that prevents this phenomenon is usually adopted in modern flight dynamics code: the so-called quaternions.

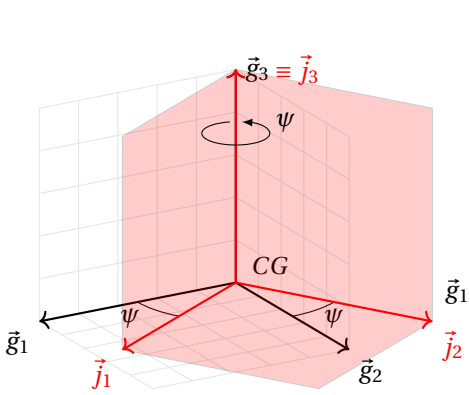

(a) First intermediate reference frame.

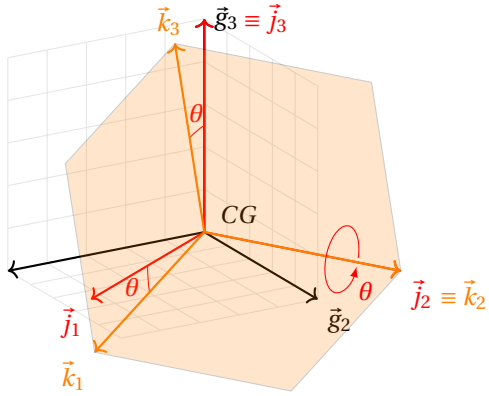

(b) Second intermediate reference frame.

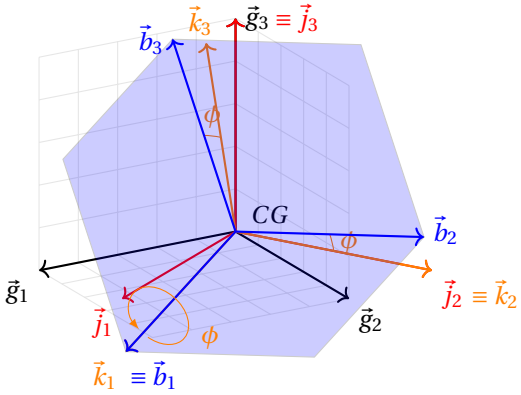

(c) Body reference frame.

Figure F.3: Cardan or Tait-Bryan angles.

F.3. HUB-BODY REFERENCE FRAME

Fig.F.4 illustrates the orientation of the body reference frame with respect to the fuselage, whereas Fig. F.5 shows the orientation of the hub reference frame with respect to the body axes. The hub is usually tilted forward of a few degrees (around $-\vec{b}_2$) to obtain a slightly negative fuselage pitch angle in hover, thus guaranteeing a better visibility to pilots in this condition.

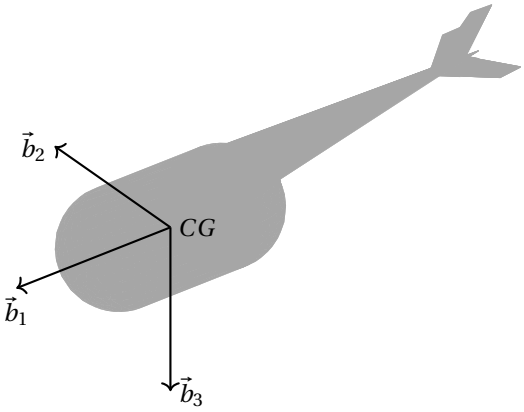

Figure F.4: Helicopter body reference frame.

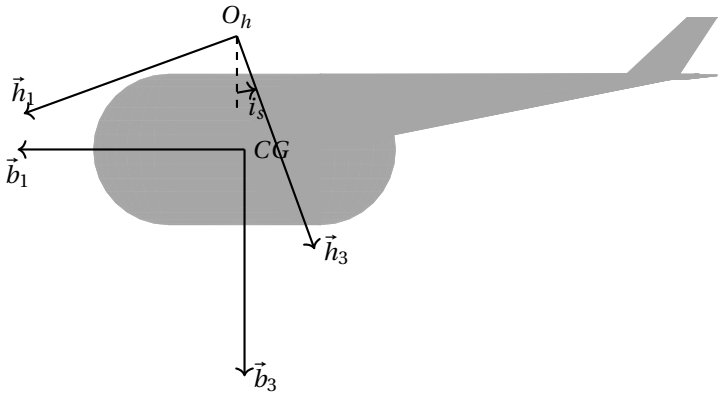

Figure F.5: Helicopter hub-body reference frame.

G

LEAD-LAG DYNAMICS

In this chapter, the lead-lag dynamics is derived using Newton's second law of motion. The notation used in this chapter is defined according to Fig. G.1.

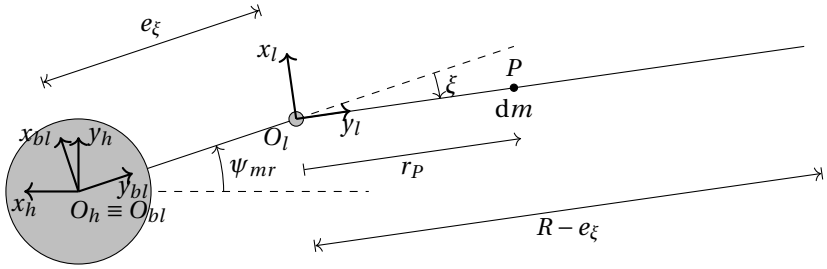

Figure G.1: Lead-lag dynamics.

The following assumptions are made:

- Body angular rates are negligible compared to the rotor angular speed: $\frac{p}{\Omega}$, $\frac{q}{\Omega}$, and $\frac{r}{\Omega} << 1$
- Body angular accelerations
- Body linear accelerations

The lead-lag dynamics is usually derived assuming constant rotor angular speed ($\ddot{\psi}_{mr} = 0$). However, this constraint needs to be relaxed in order to couple the engine-drivetrain dynamics with the lead-lag dynamics.

The following reference frames (Appendix F) will be used:

- $O_h\left(x_h, y_h, z_h\right)$: Hub reference frame

- $O_{bl}\left(x_{bl}, y_{bl}, z_{bl}\right)$: Rotor reference frame (rotating around the shaft axis)
- $O_l\left(x_l, y_l, z_l\right)$: Lead-lag reference frame

The position of a generic point P along the blade can be expressed as:

$$(P-O_h)^h = (O_l-O_h)^h + (P-O_l)^h \tag{G.1}$$

$$(O_l-O_h)^h = e_\xi \begin{bmatrix} -\cos\psi_{mr} & \sin\psi_{mr} & 0 \end{bmatrix}^T \tag{G.2}$$

$$(P-O_l)^h = r_P \begin{bmatrix} -\cos\left(\xi-\psi_{mr}\right) & -\sin\left(\xi-\psi_{mr}\right) & 0 \end{bmatrix}^T \tag{G.3}$$

The velocity of the point O_l can be expressed using the rigid-body relation:

$$\vec{v}^h_{O_l} = \vec{v}^h_{O_h} + \vec{\Omega}^h_{bl/h} \times (O_l-O_h)^h \tag{G.4}$$

where $\vec{v}^h_{O_h} = 0$, $\vec{\Omega}^h_{bl/h} = \begin{bmatrix} 0 & 0 & -\dot{\psi}_{mr} \end{bmatrix}^T$, and $(O_l-O_h)^h$ is taken from Eq. (G.2), leading to:

$$\vec{v}^h_{O_l} = e_\xi \dot{\psi}_{mr} \begin{bmatrix} \sin\psi_{mr} & \cos\psi_{mr} & 0 \end{bmatrix}^T \tag{G.5}$$

The acceleration of the point O_l can be obtained deriving Eq. (G.5):

$$\vec{a}^h_{O_l} = e_\xi \left(\ddot{\psi}_{mr} \begin{Bmatrix} \sin\psi_{mr} \\ \cos\psi_{mr} \\ 0 \end{Bmatrix} + \dot{\psi}^2_{mr} \begin{Bmatrix} \cos\psi_{mr} \\ -\sin\psi_{mr} \\ 0 \end{Bmatrix} \right) \tag{G.6}$$

The velocity of the point P can be expressed using the rigid-body relation:

$$\vec{v}^h_P = \vec{v}^h_{O_l} + \vec{\Omega}^h_{l/h} \times (P-O_l)^h \tag{G.7}$$

where $\vec{v}^h_{O_l}$ is taken from Eq. (G.5), $\vec{\Omega}_{l/h} = \begin{bmatrix} 0 & 0 & \dot{\xi}-\dot{\psi}_{mr} \end{bmatrix}^T$, and $(P-O_l)^h$ is taken from Eq. (G.3), leading to:

$$\vec{v}^h_P = \vec{v}^h_{O_l} + r_P\left(\dot{\xi}-\dot{\psi}_{mr}\right) \begin{bmatrix} \sin\left(\xi-\psi_{mr}\right) & -\cos\left(\xi-\psi_{mr}\right) & 0 \end{bmatrix}^T \tag{G.8}$$

The acceleration of the point P can be obtained deriving Eq. (G.8):

$$\vec{a}_P^h = \vec{a}_{O_l}^h + r_P \left(\left(\ddot{\xi} - \ddot{\psi}_{mr}\right) \begin{Bmatrix} \sin\left(\xi - \psi_{mr}\right) \\ -\cos\left(\xi - \psi_{mr}\right) \\ 0 \end{Bmatrix} + \left(\dot{\xi} - \dot{\psi}_{mr}\right)^2 \begin{Bmatrix} \cos\left(\xi - \psi_{mr}\right) \\ \sin\left(\xi - \psi_{mr}\right) \\ 0 \end{Bmatrix} \right) \tag{G.9}$$

Eq. (G.3) and (G.9) can be used to calculate the moment due to element of inertia force with respect to the lead-lag hinge:

$$\mathrm{d}\vec{M}_{inertia}^{O_l} = -\left(P - O_l\right)^h \times \vec{a}_P^h \, \mathrm{d}m = -\left(P - O_l\right)^h \times \vec{a}_{O_l}^h \, \mathrm{d}m - r_P^2 \left(\ddot{\xi} - \ddot{\psi}_{mr}\right) \begin{Bmatrix} 0 \\ 0 \\ 1 \end{Bmatrix} \mathrm{d}m \tag{G.10}$$

The minus is used to take into account the fact that inertia forces are opposite to accelerations.

where $\left(P - O_l\right)^h \times \vec{a}_{O_l}^h \, \mathrm{d}m$ can be obtained from Eq. (G.3) and (G.6):

$$\left(P - O_l\right)^h \times \vec{a}_{O_l}^h \, \mathrm{d}m = e_\xi r_P \left(-\ddot{\psi}_{mr} \cos\xi + \dot{\psi}_{mr}^2 \sin\xi\right) \begin{Bmatrix} 0 \\ 0 \\ 1 \end{Bmatrix} \mathrm{d}m \tag{G.11}$$

Replacing Eq. (G.11) in Eq. (G.10) and integrating on the volume of the blade (or along the radius, if we assume uniform density on the blade section: $\mathrm{d}m = \rho_b(r)\,\mathrm{d}r$, where $\rho_b(r)$ is the blade linear mass-density):

$$\vec{M}_{inertia}^{O_l} = -e_\xi \left(-\ddot{\psi}_{mr} \cos\xi + \dot{\psi}_{mr}^2 \sin\xi\right) \begin{Bmatrix} 0 \\ 0 \\ 1 \end{Bmatrix} \underbrace{\int_0^{R-e_\xi} r_P \, \mathrm{d}m}_{S_\xi} +$$

$$- \left(\ddot{\xi} - \ddot{\psi}_{mr}\right) \begin{Bmatrix} 0 \\ 0 \\ 1 \end{Bmatrix} \underbrace{\int_0^{R-e_\xi} r_P^2 \, \mathrm{d}m}_{I_\xi} \tag{G.12}$$

Considering only the component along z:

$$\begin{aligned} M_{z_{inertia}}^{O_l} &= -e_\xi \left(-\ddot{\psi}_{mr} \cos\xi + \dot{\psi}_{mr}^2 \sin\xi\right) S_\xi - \left(\ddot{\xi} - \ddot{\psi}_{mr}\right) I_\xi \\ &= \left(I_\xi + S_\xi e_\xi \cos\xi\right) \ddot{\psi}_{mr} - I_\xi \ddot{\xi} - S_\xi e_\xi \dot{\psi}_{mr}^2 \sin\xi \end{aligned} \tag{G.13}$$

The contribution of the inertia forces to the lead-lag dynamics is non-linear. Under the assumption of small lead-lag angles ($\xi << 1$ deg: $\cos\xi \approx 1$ and $\sin\xi \approx \xi$), Eq. (G.13) becomes:

$$M_{z_{inertia}}^{O_l} = \left(I_\xi + S_\xi e_\xi\right) \ddot{\psi}_{mr} - I_\xi \ddot{\xi} - S_\xi e_\xi \dot{\psi}_{mr}^2 \xi \tag{G.14}$$

Linearizing Eq. G.14 and imposing that $\dot{\psi}_{mr}|_{trim} = \Omega_{mr}$ and $\xi|_{trim} \approx 0$:

$$\begin{aligned} M^{O_l}_{z_{inertia}} &= \left(I_\xi + S_\xi e_\xi\right)\ddot{\psi}_{mr} - I_\xi\ddot{\xi} - 2S_\xi e_\xi \dot{\psi}_{mr}|_{trim}\xi|_{trim}\left(\dot{\psi}_{mr} - \dot{\psi}_{mr}|_{trim}\right) + \\ &\quad - S_\xi e_\xi \dot{\psi}_{mr}|^2_{trim}\left(\xi - \xi|_{trim}\right) \\ &= \left(I_\xi + S_\xi e_\xi\right)\ddot{\psi}_{mr} - I_\xi\ddot{\xi} - S_\xi e_\xi \Omega^2_{mr}\xi \end{aligned} \tag{G.15}$$

Another contribution to the lead-lag dynamics is provided by the spring-damper installed on the lead-lag hing to prevent ground resonance:

$$M^{O_l}_{z_{spring-damper}} = -K_\xi\xi - C_\xi\dot{\xi} \tag{G.16}$$

$$M^{O_l}_{z_{aero}} = Q^{aero}_\xi \tag{G.17}$$

Summing Eq. (G.15), (G.16), and (G.17) and imposing that the sum is equal to zero:

$$-\left(I_\xi + S_\xi e_\xi\right)\ddot{\psi}_{mr} + I_\xi\ddot{\xi} + C_\xi\dot{\xi} + \left(S_\xi e_\xi\Omega^2_{mr} + K_\xi\right)\xi = Q^{aero}_\xi \tag{G.18}$$

The lead-lag frequency is defined as:

$$\omega^2_\xi = \frac{S_\xi e_\xi \Omega^2_{mr} + K_\xi}{I_\xi} \tag{G.19}$$

and the non-dimensional one as:

$$\nu^2_\xi = \frac{\omega^2_\xi}{\Omega^2_{mr}} = \frac{S_\xi e_\xi}{I_\xi} + \frac{K_\xi}{I_\xi\Omega^2_{mr}} \tag{G.20}$$

Replacing Eq. (G.20) in Eq. (G.18):

$$-\left(I_\xi + S_\xi e_\xi\right)\ddot{\psi}_{mr} + I_\xi\ddot{\xi} + C_\xi\dot{\xi} + I_\xi\nu^2_\xi\Omega^2_{mr}\xi = Q^{aero}_\xi \tag{G.21}$$

G.1. MULTI-BLADE COORDINATES

The collective lead-lag dynamics can be therefore written as:

$$-N_b\left(I_\xi + S_\xi e_\xi\right)\ddot{\psi}_{mr} + N_b I_\xi\ddot{\xi}_0 + N_b C_\xi\dot{\xi}_0 + N_b I_\xi\nu^2_\xi\Omega^2_{mr}\xi_0 = N_b Q^{aero}_\xi \tag{G.22}$$

H

KINEMATICS OF A BLADE ELEMENT

In this chapter, the kinematics of a blade element is derived. The notation used in this chapter is defined according to Fig. G.1.

The following assumptions are made:

- The flapping motion of the blade is neglected.

The following reference frames will be used (Appendix F):

- $O_g\left(x_g, y_g, z_g\right)$: Inertial reference frame (e.g., NED)
- $O_b\left(x_b, y_b, z_b\right)$: Body reference frame
- $O_h\left(x_h, y_h, z_h\right)$: Hub reference frame
- $O_{bl}\left(x_{bl}, y_{bl}, z_{bl}\right)$: Rotor reference frame (rotating around the shaft axis)
- $O_l\left(x_l, y_l, z_l\right)$: Lead-lag reference frame

The position of a generic point P along the blade can be expressed as:

$$\left(P - O_g\right)^g = \left(O_b - O_g\right)^g + \left(O_h - O_b\right)^b + \left(O_{bl} - O_h\right)^h + \left(O_l - O_{bl}\right)^{bl} + \left(P - O_l\right)^l \tag{H.1}$$

$$\begin{aligned}\vec{V}^g_P - \cancelto{0}{\vec{V}^g_{O_g}} = \vec{V}^g_{O_b} - \cancelto{0}{\vec{V}^g_{O_g}} + \\ + \cancelto{0}{\vec{V}^b_{O_h}} - \cancelto{0}{\vec{V}^b_{O_b}} + \vec{\Omega}^b_{b/g} \times (O_h - O_b)^b + \\ + \cancelto{0}{\vec{V}^h_{O_{bl}}} - \cancelto{0}{\vec{V}^h_{O_h}} + \vec{\Omega}^h_{h/g} \times \cancelto{0}{(O_{bl} - O_h)^h} + \\ + \cancelto{0}{\vec{V}^{bl}_{O_l}} - \cancelto{0}{\vec{V}^{bl}_{O_{bl}}} + \vec{\Omega}^{bl}_{bl/g} \times (O_l - O_{bl})^{bl} + \\ + \cancelto{0}{\vec{V}^l_P} - \cancelto{0}{\vec{V}^l_{O_l}} + \vec{\Omega}^l_{l/g} \times (P - O_l)^l\end{aligned} \tag{H.2}$$

$$\vec{V}^g_P = \vec{V}^g_{O_b} + \vec{\Omega}^b_{b/g} \times (O_h - O_b)^b + \vec{\Omega}^{bl}_{bl/g} \times (O_l - O_{bl})^{bl} + \vec{\Omega}^l_{l/g} \times (P - O_l)^l \tag{H.3}$$

where $\vec{\Omega}^b_{b/g} = \begin{bmatrix} p & q & r \end{bmatrix}^T$, and $(O_h - O_b)^b = \begin{bmatrix} x_{cg} & y_{cg} & -h_R \end{bmatrix}^T$.

$$\vec{V}^g_{O_b} = \begin{Bmatrix} \dot{x} \\ \dot{y} \\ \dot{z} \end{Bmatrix}^g = \vec{V}^b_{O_b} + \vec{\Omega}^b_{b/g} \times \cancelto{0}{(O_b - O_g)} = \vec{V}^b_{O_b} = \begin{Bmatrix} u \\ v \\ w \end{Bmatrix}^b \tag{H.4}$$

$$\vec{V}^b_{O_b} + \vec{\Omega}^b_{b/g} \times (O_h - O_b)^b = \begin{Bmatrix} u - q h_R - r y_{cg} \\ v + p h_R + r x_{cg} \\ w + p y_{cg} - q x_{cg} \end{Bmatrix} \tag{H.5}$$

$$\vec{\Omega}^{bl}_{bl/g} = \vec{\Omega}^{bl}_{bl/h} + \cancelto{0}{\vec{\Omega}^{bl}_{h/b}} + \vec{\Omega}^{bl}_{b/g} \tag{H.6}$$

$$\vec{\Omega}^{bl}_{bl/h} = \begin{bmatrix} 0 & 0 & -\dot{\psi}_{mr} \end{bmatrix}^T \tag{H.7}$$

$$\begin{aligned}\vec{\Omega}^{bl}_{b/g} &= R_{b2bl} \vec{\Omega}^b_{b/g} = R_{h2bl} R_{b2h} \vec{\Omega}^b_{b/g} = \\ &= \begin{bmatrix} \sin\psi_{mr} & \cos\psi_{mr} & 0 \\ -\cos\psi_{mr} & \sin\psi_{mr} & 0 \\ 0 & 0 & 1 \end{bmatrix} \begin{bmatrix} \cos\gamma_s & 0 & \sin\gamma_s \\ 0 & 1 & 0 \\ -\sin\gamma_s & 0 & \cos\gamma_s \end{bmatrix} \begin{Bmatrix} p \\ q \\ r \end{Bmatrix} = \\ &= \begin{bmatrix} \sin\psi_{mr} & \cos\psi_{mr} & 0 \\ -\cos\psi_{mr} & \sin\psi_{mr} & 0 \\ 0 & 0 & 1 \end{bmatrix} \begin{Bmatrix} p_h \\ q_h \\ r_h \end{Bmatrix} = \begin{Bmatrix} \sin\psi_{mr} p_h + \cos\psi_{mr} q_h \\ -\left(\cos\psi_{mr} p_h - \sin\psi_{mr} q_h\right) \\ r_h \end{Bmatrix} = \begin{Bmatrix} \omega_y \\ -\omega_x \\ r_h \end{Bmatrix}\end{aligned} \tag{H.8}$$

$$(O_l - O_{bl})^{bl} = e_\xi \begin{bmatrix} 0 & 1 & 0 \end{bmatrix}^T \tag{H.9}$$

$$\vec{\Omega}^{bl}_{bl/g} \times (O_l - O_{bl})^{bl} = e_\xi \begin{bmatrix} \dot{\psi}_{mr} - r_h & 0 & \omega_y \end{bmatrix}^T \tag{H.10}$$

$$\vec{\Omega}^{l}_{l/g} = \vec{\Omega}^{l}_{l/bl} + \vec{\Omega}^{l}_{bl/h} + \cancelto{0}{\vec{\Omega}^{l}_{h/b}} + \vec{\Omega}^{l}_{b/g} \tag{H.11}$$

$$\vec{\Omega}^{l}_{l/bl} = \begin{bmatrix} 0 & 0 & \dot{\xi} \end{bmatrix}^T \tag{H.12}$$

$$\vec{\Omega}^{l}_{bl/h} = R_{bl2l}\vec{\Omega}^{bl}_{bl/h} = \begin{bmatrix} \cos\xi & \sin\xi & 0 \\ -\sin\xi & \cos\xi & 0 \\ 0 & 0 & 1 \end{bmatrix} \begin{Bmatrix} 0 \\ 0 \\ -\dot{\psi}_{mr} \end{Bmatrix} = \begin{Bmatrix} 0 \\ 0 \\ -\dot{\psi}_{mr} \end{Bmatrix} \tag{H.13}$$

$$\vec{\Omega}^{l}_{b/g} = R_{bl2l}\vec{\Omega}^{bl}_{b/g} = \begin{bmatrix} \cos\xi & \sin\xi & 0 \\ -\sin\xi & \cos\xi & 0 \\ 0 & 0 & 1 \end{bmatrix} \begin{Bmatrix} \omega_y \\ -\omega_x \\ r_h \end{Bmatrix} = \begin{Bmatrix} \omega_y\cos\xi - \omega_x\sin\xi \\ -\omega_y\sin\xi - \omega_x\cos\xi \\ r_h \end{Bmatrix} = \begin{Bmatrix} \Omega_y \\ -\Omega_x \\ r_h \end{Bmatrix} \tag{H.14}$$

$$(P - O_l)^l = r_P \begin{bmatrix} 0 & 1 & 0 \end{bmatrix}^T \tag{H.15}$$

$$\vec{\Omega}^{l}_{l/g} \times (P - O_l)^l = r_P \begin{Bmatrix} \dot{\psi}_{mr} - \dot{\xi} - r_h \\ 0 \\ \Omega_y \end{Bmatrix} \tag{H.16}$$

Replacing Eq. (H.5), (H.10) and (H.16), Eq. (H.3) becomes:

$$\begin{aligned}
\vec{V}^g_P &= \begin{Bmatrix} u - qh_R - ry_{cg} \\ v + ph_R + rx_{cg} \\ w + py_{cg} - qx_{cg} \end{Bmatrix}^b + e_\xi \begin{Bmatrix} \dot{\psi}_{mr} - r_h \\ 0 \\ \omega_y \end{Bmatrix}^{bl} + r_P \begin{Bmatrix} \dot{\psi}_{mr} - \dot{\xi} - r_h \\ 0 \\ \Omega_y \end{Bmatrix}^l = \\
&= R_{bl2l}R_{h2bl}R_{b2h} \begin{Bmatrix} u - qh_R - ry_{cg} \\ v + ph_R + rx_{cg} \\ w + py_{cg} - qx_{cg} \end{Bmatrix}^b + e_\xi R_{bl2l} \begin{Bmatrix} \dot{\psi}_{mr} - r_h \\ 0 \\ \omega_y \end{Bmatrix}^{bl} + \\
&+ r_P \begin{Bmatrix} \dot{\psi}_{mr} - \dot{\xi} - r_h \\ 0 \\ \Omega_y \end{Bmatrix}^l = \\
&= R_{bl2l}R_{h2bl} \begin{Bmatrix} u_h \\ v_h \\ w_h \end{Bmatrix}^h + e_\xi \begin{Bmatrix} (\dot{\psi}_{mr} - r_h)\cos\xi \\ -(\dot{\psi}_{mr} - r_h)\sin\xi \\ \omega_y \end{Bmatrix}^l + r_P \begin{Bmatrix} \dot{\psi}_{mr} - \dot{\xi} - r_h \\ 0 \\ \Omega_y \end{Bmatrix}^l
\end{aligned} \tag{H.17}$$

$$\vec{V}_P^g = R_{bl2l}\begin{Bmatrix} u_h\sin\psi_{mr} + v_h\cos\psi_{mr} \\ -u_h\cos\psi_{mr} + v_h\sin\psi_{mr} \\ w_h \end{Bmatrix}^{bl} + e_\xi\begin{Bmatrix} \left(\dot{\psi}_{mr} - r_h\right)\cos\xi \\ -\left(\dot{\psi}_{mr} - r_h\right)\sin\xi \\ \omega_y \end{Bmatrix}^{l} +$$
$$+ r_P\begin{Bmatrix} \dot{\psi}_{mr} - \dot{\xi} - r_h \\ 0 \\ \Omega_y \end{Bmatrix}^{l} =$$
$$= \begin{Bmatrix} \left(u_h\sin\psi_{mr} + v_h\cos\psi_{mr}\right)\cos\xi + \left(-u_h\cos\psi_{mr} + v_h\sin\psi_{mr}\right)\sin\xi \\ -\left(u_h\sin\psi_{mr} + v_h\cos\psi_{mr}\right)\sin\xi + \left(-u_h\cos\psi_{mr} + v_h\sin\psi_{mr}\right)\cos\xi \\ w_h \end{Bmatrix}^{l} +$$
$$+ e_\xi\begin{Bmatrix} \left(\dot{\psi}_{mr} - r_h\right)\cos\xi \\ -\left(\dot{\psi}_{mr} - r_h\right)\sin\xi \\ \omega_y \end{Bmatrix}^{l} + r_P\begin{Bmatrix} \dot{\psi}_{mr} - \dot{\xi} - r_h \\ 0 \\ \Omega_y \end{Bmatrix}^{l} \tag{H.18}$$

Deriving Eq. (H.3), we obtain the acceleration:

$$\vec{a}_P^g = \vec{a}_{O_b}^g + \dot{\vec{\Omega}}_{b/g}^b \times (O_h - O_b)^b +$$
$$+ \vec{\Omega}_{b/g}^b \times \cancelto{0}{\vec{V}_{O_h}^b} + \vec{\Omega}_{b/g}^b \times \vec{\Omega}_{b/g}^b \times (O_h - O_b)^b +$$
$$+ \dot{\vec{\Omega}}_{bl/g}^{bl} \times (O_l - O_{bl})^{bl} + \vec{\Omega}_{bl/g}^{bl} \times \cancelto{0}{V_{O_l}^{bl}} + \vec{\Omega}_{bl/g}^{bl} \times \vec{\Omega}_{bl/g}^{bl} \times (O_l - O_{bl})^{bl} +$$
$$+ \dot{\vec{\Omega}}_{l/g}^{l} \times (P - O_l)^l + \vec{\Omega}_{l/g}^{l} \times \cancelto{0}{V_P^l} + \vec{\Omega}_{l/g}^{l} \times \vec{\Omega}_{l/g}^{l} \times (P - O_l)^l \tag{H.19}$$

H

$$\vec{a}_P^g = \vec{a}_{O_b}^b + \vec{\Omega}_{b/g}^b \times \vec{V}_{O_b}^b + \dot{\vec{\Omega}}_{b/g}^b \times (O_h - O_b)^b + \vec{\Omega}_{b/g}^b \times \vec{\Omega}_{b/g}^b \times (O_h - O_b)^b +$$
$$+ \dot{\vec{\Omega}}_{bl/g}^{bl} \times (O_l - O_{bl})^{bl} + \vec{\Omega}_{bl/g}^{bl} \times \vec{\Omega}_{bl/g}^{bl} \times (O_l - O_{bl})^{bl} +$$
$$+ \dot{\vec{\Omega}}_{l/g}^{l} \times (P - O_l)^l + \vec{\Omega}_{l/g}^{l} \times \vec{\Omega}_{l/g}^{l} \times (P - O_l)^l \tag{H.20}$$

$$\vec{a}_{O_b}^b + \vec{\Omega}_{b/g}^b \times \vec{V}_{O_b}^b + \dot{\vec{\Omega}}_{b/g}^b \times (O_h - O_b)^b + \vec{\Omega}_{b/g}^b \times \vec{\Omega}_{b/g}^b \times (O_h - O_b)^b =$$
$$= \begin{Bmatrix} \dot{u} \\ \dot{v} \\ \dot{w} \end{Bmatrix} + \begin{Bmatrix} qw - rv \\ -pw + ru \\ pv - qu \end{Bmatrix} + \begin{Bmatrix} -\dot{q}h_R - \dot{r}y_{cg} \\ \dot{p}h_R + \dot{r}x_{cg} \\ \dot{p}y_{cg} - \dot{q}x_{cg} \end{Bmatrix} + \begin{Bmatrix} q\left(py_{cg} - qx_{cg}\right) - r\left(ph_R + rx_{cg}\right) \\ -p\left(py_{cg} - qx_{cg}\right) + r\left(-qh_R - ry_{cg}\right) \\ p\left(ph_R + rx_{cg}\right) - q\left(-qh_R - ry_{cg}\right) \end{Bmatrix} =$$
$$= \begin{Bmatrix} \dot{u} + qw - rv - \dot{q}h_R - \dot{r}y_{cg} + q\left(py_{cg} - qx_{cg}\right) - r\left(ph_R + rx_{cg}\right) \\ \dot{v} - pw + ru + \dot{p}h_R + \dot{r}x_{cg} - p\left(py_{cg} - qx_{cg}\right) + r\left(-qh_R - ry_{cg}\right) \\ \dot{w} + pv - qu + \dot{p}y_{cg} - \dot{q}x_{cg} + p\left(ph_R + rx_{cg}\right) - q\left(-qh_R - ry_{cg}\right) \end{Bmatrix} \tag{H.21}$$

$$\dot{\vec{\Omega}}^{bl}_{bl/g} \times (O_l - O_{bl})^{bl} + \vec{\Omega}^{bl}_{bl/g} \times \vec{\Omega}^{bl}_{bl/g} \times (O_l - O_{bl})^{bl} =$$
$$= e_\xi \begin{Bmatrix} \ddot{\psi}_{mr} - \dot{r}_h \\ 0 \\ \dot{\omega}_y \end{Bmatrix} + e_\xi \begin{Bmatrix} -\omega_x\omega_y \\ -\omega_y^2 - \left(\dot{\psi}_{mr} - r_h\right)^2 \\ \omega_x\left(\dot{\psi}_{mr} - r_h\right) \end{Bmatrix} =$$
$$= e_\xi \begin{Bmatrix} \ddot{\psi}_{mr} - \dot{r}_h - \omega_x\omega_y \\ -\omega_y^2 - \left(\dot{\psi}_{mr} - r_h\right)^2 \\ \dot{\omega}_y + \omega_x\left(\dot{\psi}_{mr} - r_h\right) \end{Bmatrix} =$$
$$= e_\xi \begin{Bmatrix} \ddot{\psi}_{mr} - \dot{r}_h - \omega_x\omega_y \\ -\omega_y^2 - \left(\dot{\psi}_{mr} - r_h\right)^2 \\ \omega_x\dot{\psi}_{mr} + \dot{p}_h \sin\psi_{mr} + \dot{q}_h \cos\psi_{mr} + \omega_x\left(\dot{\psi}_{mr} - r_h\right) \end{Bmatrix} =$$
$$= e_\xi \begin{Bmatrix} \ddot{\psi}_{mr} - \dot{r}_h - \omega_x\omega_y \\ -\omega_y^2 - \left(\dot{\psi}_{mr} - r_h\right)^2 \\ \dot{p}_h \sin\psi_{mr} + \dot{q}_h \cos\psi_{mr} + \omega_x\left(2\dot{\psi}_{mr} - r_h\right) \end{Bmatrix} \tag{H.22}$$

$$\dot{\vec{\Omega}}^{l}_{l/g} \times (P - O_l)^{l} + \vec{\Omega}^{l}_{l/g} \times \vec{\Omega}^{l}_{l/g} \times (P - O_l)^{l} =$$
$$= r_P \begin{Bmatrix} \ddot{\psi}_{mr} - \ddot{\xi} - \dot{r}_h \\ 0 \\ \dot{\Omega}_y \end{Bmatrix} + r_P \begin{Bmatrix} -\Omega_x\Omega_y \\ -\Omega_y^2 - \left(\dot{\psi}_{mr} - \dot{\xi} - r_h\right)^2 \\ \Omega_x\left(\dot{\psi}_{mr} - \dot{\xi} - r_h\right) \end{Bmatrix} =$$
$$= r_P \begin{Bmatrix} \ddot{\psi}_{mr} - \ddot{\xi} - \dot{r}_h - \Omega_x\Omega_y \\ -\Omega_y^2 - \left(\dot{\psi}_{mr} - \dot{\xi} - r_h\right)^2 \\ \dot{\Omega}_y + \Omega_x\left(\dot{\psi}_{mr} - \dot{\xi} - r_h\right) \end{Bmatrix} =$$
$$= r_P \begin{Bmatrix} \ddot{\psi}_{mr} - \ddot{\xi} - \dot{r}_h - \Omega_x\Omega_y \\ -\Omega_y^2 - \left(\dot{\psi}_{mr} - \dot{\xi} - r_h\right)^2 \\ -\dot{\xi}\Omega_x + \dot{\psi}_{mr}\Omega_x + \cos\xi\left(\dot{p}_h \sin\psi_{mr} + \dot{q}_h \cos\psi_{mr}\right) - \sin\xi\left(\dot{p}_h \cos\psi_{mr} - \dot{q}_h \sin\psi_{mr}\right) + \Omega_x\left(\dot{\psi}_{mr} - \dot{\xi} - r_h\right) \end{Bmatrix} =$$
$$= r_P \begin{Bmatrix} \ddot{\psi}_{mr} - \ddot{\xi} - \dot{r}_h - \Omega_x\Omega_y \\ -\Omega_y^2 - \left(\dot{\psi}_{mr} - \dot{\xi} - r_h\right)^2 \\ \cos\xi\left(\dot{p}_h \sin\psi_{mr} + \dot{q}_h \cos\psi_{mr}\right) - \sin\xi\left(\dot{p}_h \cos\psi_{mr} - \dot{q}_h \sin\psi_{mr}\right) + \Omega_x\left(2\dot{\psi}_{mr} - 2\dot{\xi} - r_h\right) \end{Bmatrix} \tag{H.23}$$

Replacing Eq. (H.21), (H.22) and (H.23), Eq. (H.20) becomes:

$$\vec{a}^{g}_{P} = \begin{Bmatrix} \dot{u} + qw - rv - \dot{q}h_R - \dot{r}y_{cg} + q\left(py_{cg} - qx_{cg}\right) - r\left(ph_R + rx_{cg}\right) \\ \dot{v} - pw + ru + \dot{p}h_R + \dot{r}x_{cg} - p\left(py_{cg} - qx_{cg}\right) + r\left(-qh_R - ry_{cg}\right) \\ \dot{w} + pv - qu + \dot{p}y_{cg} - \dot{q}x_{cg} + p\left(ph_R + rx_{cg}\right) - q\left(-qh_R - ry_{cg}\right) \end{Bmatrix}^{b} +$$
$$+ e_\xi \begin{Bmatrix} \ddot{\psi}_{mr} - \dot{r}_h - \omega_x\omega_y \\ -\omega_y^2 - \left(\dot{\psi}_{mr} - r_h\right)^2 \\ \dot{p}_h \sin\psi_{mr} + \dot{q}_h \cos\psi_{mr} + \omega_x\left(2\dot{\psi}_{mr} - r_h\right) \end{Bmatrix}^{bl} +$$
$$+ r_P \begin{Bmatrix} \ddot{\psi}_{mr} - \ddot{\xi} - \dot{r}_h - \Omega_x\Omega_y \\ -\Omega_y^2 - \left(\dot{\psi}_{mr} - \dot{\xi} - r_h\right)^2 \\ \cos\xi\left(\dot{p}_h \sin\psi_{mr} + \dot{q}_h \cos\psi_{mr}\right) - \sin\xi\left(\dot{p}_h \cos\psi_{mr} - \dot{q}_h \sin\psi_{mr}\right) + \Omega_x\left(2\dot{\psi}_{mr} - 2\dot{\xi} - r_h\right) \end{Bmatrix}^{l} =$$
$$= R_{bl2l}R_{h2bl}R_{b2h} \begin{Bmatrix} \dot{u} + qw - rv - \dot{q}h_R - \dot{r}y_{cg} + q\left(py_{cg} - qx_{cg}\right) - r\left(ph_R + rx_{cg}\right) \\ \dot{v} - pw + ru + \dot{p}h_R + \dot{r}x_{cg} - p\left(py_{cg} - qx_{cg}\right) + r\left(-qh_R - ry_{cg}\right) \\ \dot{w} + pv - qu + \dot{p}y_{cg} - \dot{q}x_{cg} + p\left(ph_R + rx_{cg}\right) - q\left(-qh_R - ry_{cg}\right) \end{Bmatrix}^{b} +$$
$$+ e_\xi R_{bl2l} \begin{Bmatrix} \ddot{\psi}_{mr} - \dot{r}_h - \omega_x\omega_y \\ -\omega_y^2 - \left(\dot{\psi}_{mr} - r_h\right)^2 \\ \dot{p}_h \sin\psi_{mr} + \dot{q}_h \cos\psi_{mr} + \omega_x\left(2\dot{\psi}_{mr} - r_h\right) \end{Bmatrix}^{bl} +$$
$$+ r_P \begin{Bmatrix} \ddot{\psi}_{mr} - \ddot{\xi} - \dot{r}_h - \Omega_x\Omega_y \\ -\Omega_y^2 - \left(\dot{\psi}_{mr} - \dot{\xi} - r_h\right)^2 \\ \cos\xi\left(\dot{p}_h \sin\psi_{mr} + \dot{q}_h \cos\psi_{mr}\right) - \sin\xi\left(\dot{p}_h \cos\psi_{mr} - \dot{q}_h \sin\psi_{mr}\right) + \Omega_x\left(2\dot{\psi}_{mr} - 2\dot{\xi} - r_h\right) \end{Bmatrix}^{l} \tag{H.24}$$

$$
\begin{aligned}
\vec{a}_P^{\,g} = {} & R_{bl2l} R_{h2bl} \begin{Bmatrix} \dot{u}_h \\ \dot{v}_h \\ \dot{w}_h \end{Bmatrix}^h + \\
& + e_\xi \begin{Bmatrix} \left(\ddot{\psi}_{mr} - \dot{r}_h - \omega_x \omega_y\right) \cos\xi + \left[-\omega_y^2 - \left(\dot{\psi}_{mr} - r_h\right)^2\right] \sin\xi \\ -\left(\ddot{\psi}_{mr} \dot{r}_h - \omega_x \omega_y\right) \sin\xi + \left[-\omega_y^2 - \left(\dot{\psi}_{mr} - r_h\right)^2\right] \cos\xi \\ \dot{p}_h \sin\psi_{mr} + \dot{q}_h \cos\psi_{mr} + \omega_x \left(2\dot{\psi}_{mr} - r_h\right) \end{Bmatrix}^l + \\
& + r_P \begin{Bmatrix} \ddot{\psi}_{mr} - \ddot{\xi} - \dot{r}_h - \Omega_x \Omega_y \\ -\Omega_y^2 - \left(\dot{\psi}_{mr} - \dot{\xi} - r_h\right)^2 \\ \cos\xi \left(\dot{p}_h \sin\psi_{mr} + \dot{q}_h \cos\psi_{mr}\right) - \sin\xi \left(\dot{p}_h \cos\psi_{mr} - \dot{q}_h \sin\psi_{mr}\right) + \Omega_x \left(2\dot{\psi}_{mr} - 2\dot{\xi} - r_h\right) \end{Bmatrix}^l
\end{aligned}
\tag{H.25}
$$

If we neglect the linear accelerations of the hub, as well as the non-linear terms, Eq. (H.25) becomes:

$$
\begin{aligned}
\vec{a}_P^{\,g} = {} & e_\xi \begin{Bmatrix} \ddot{\psi}_{mr} - \dot{r}_h \\ -\left(\dot{\psi}_{mr} - r_h\right)^2 \\ \dot{p}_h \sin\psi_{mr} + \dot{q}_h \cos\psi_{mr} + \omega_x \left(2\dot{\psi}_{mr} - r_h\right) \end{Bmatrix}^l + \\
& + r_P \begin{Bmatrix} \ddot{\psi}_{mr} - \ddot{\xi} - \dot{r}_h \\ -\left(\dot{\psi}_{mr} - \dot{\xi} - r_h\right)^2 \\ \dot{p}_h \sin\psi_{mr} + \dot{q}_h \cos\psi_{mr} + \Omega_x \left(2\dot{\psi}_{mr} - 2\dot{\xi} - r_h\right) \end{Bmatrix}^l
\end{aligned}
\tag{H.26}
$$

ACKNOWLEDGEMENTS

After 5 years, my PhD journey has finally come to an end. Such an enriching and educational experience deserves a moment of retrospection, recalling the challenging, but rewarding route followed to reach the destination of this amazing journey. In the collection of lifetime souvenirs dwelling in my memory, filled with the places I visited, the obstacles I overcome, and the dreams and expectations that came true, a special place is held by the people I met. Many of them contributed in several ways to the realization of this thesis and deserve my gratitude.

First and foremost, I would like to thank my promotors, Prof. Dr. Giuseppe Quaranta and Prof. Dr. Marilena Pavel, for giving me the opportunity to pursue this PhD. This journey has initiated with their efforts in the conception of the NITROS program to raise awareness about the topic of rotorcraft safety in aerospace engineering education. Thank you Giuseppe for pushing me to apply to the NITROS scholarships and for the precious advice that you have been providing since the beginning of my MSc thesis. I would also like to express my appreciation to you for covering the role of project coordinator with such a great care towards all the PhD students involved in NITROS.

Thank you Marilena for sharing with me your broad knowledge about the rotorcraft discipline and for providing your invaluable ideas and feedback throughout my PhD. You have supported my relocation to PoliMI during the last two years of my PhD demonstrating empathy toward my personal situation and continuous trust in me and in my work. I feel extremely lucky that you are involved in my professional and personal growth.

A special debt of gratitude goes to my copromotor and daily supervisor Dr. Ir. Daan Pool. Thank you Daan for your enthusiasm and kind words that are always able to push away all my moments of discouragement. You are always the first to review my manuscripts and provide constructive recommendations. When you welcomed me at the Control and Simulation Section in October 2017, pilot-in the-loop experiments were a completely unexplored field for me. You introduced me to this topic and a few months later I put into practice everything I learned. I really admire your talent in teaching and supervising students.

The completion of my PhD could not have been accomplished without the support and guidance of Prof. Dr. Ir. Max Mulder and Ir. Olaf Stroosma. Thank you Max for always finding the time to read my manuscripts and give valuable feedback, despite your busy schedule, and for always having the right words to keep me motivated. Thank you Olaf for your essential support during my simulator experiments and for the extremely enlightening discussions on eigenmodes and mode participation factors. When the fate seemed to be against me and Daniel during our last experiments, you have been the last man standing against the countless troubles we encountered and still succeeded in letting us complete our activity.

I would also like to express my gratitude to Prof. Dr. Heinrich Bülthoff for supporting my internship at the Max Planck Institute for Biological Cybernetics in Tübingen and the

CAPA group for welcoming me and making me feel part of the family since day 1 of my internship. So thank you Stefano, Giulia, Carlo, Mario, Frank, and Urs for making this internship experience enjoyable and memorable.

I would like to thank also everybody that made my PhD a pleasant experience. Thank you to my NITROS fellows: Daniel, Ezgi, Noor, Ying, Myles, Neda, Sara, Sergio, Simone, and Federico. Thank you to all the other C&S colleagues and staff: Malik, Lorenzo, Jelmer, Ivan, Mario, Dirk, Kasper, Wei Fu, Sarah, Annemarie, Yingfu, Sihao, Bo, Jaime, Jan, Ye, Julien, Nilay, Tom, Sven, Diana, Federico, Sunyi, Jacco, Jost, Erik-Jan, Bob, Xander, Guido, Hans, Coen, Anahita, Clark, René, Bart, Christophe, Alwine, Andries, Harold, and Bertine.

I found in Daniel and Malik two of my closest friends. Thank you Daniel for sharing with me the whole PhD journey and, in particular, two of the most stressful periods during our PhD. Conducting those two experiments without our mutual support would have challenged my (already precarious) mental health. Thank you Malik for your smile and your kind advice that always helped me overcome all the moments of discouragement during my PhD.

I am of course extremely grateful to all the pilots who volunteered in my experiments and still beg the pardon of those who got motion sickness during one of my simulator sessions.

I would like to express my gratitude to my high school teacher of Math and Physics, Pierangela Lentini, for instilling in me a genuine curiosity towards everything related to these subjects by means of her passion and enthusiasm.

I cannot forget my PoliMI friends Andrea, Simone, Carmelo, Valeria, Gaia, Pietro, Lorenzo, Jacopo, and Gabriele. I am always delighted to share knowledge and experience with you.

Also my "old" summer friends cannot remain unmentioned. Thank you Paolo, Nicola, Carmelo, Daniele, Natalia, Andrea, Maxence, Mélyna, Pietro, Carmelino, and Francesca for all the unforgettable moments at our usual hangout, "il muretto". Last summer did not taste the same without being in your company.

I am also extremely grateful to my two best men and friends of a lifetime, Davide and Lorenzo, and to Francesco for always being next to me through the ups and downs of life since the first time we met in September 2005. Some friendships are so strong. Neither time, nor distance, nor circumstances diminish them.

It is unfortunate that not all my dear ones can share with me this new achievement. All of them contributed to make me the person I am now, and although some of them are no longer with me, they will always be in my heart. My thought goes especially to my grandpa Giuseppe, who recently passed away. He has been a source of inspiration for his dedication to his work and his family.

Words cannot express my gratitude to my mom and dad for their inexhaustible support, continuous encouragement and faith in my ambitions. I owe all my accomplishments to them for teaching me perseverance and hard work. If I could be a half as good parent as they are to me then that would be my best achievement.

Among the dearest persons in my life, there is my brother Giuseppe. Although I am the older brother and, hopefully, I have been an example for him, I would like to thank him for all the times he has been an example for me and for everything he unconsciously

teaches me. My greatest admiration goes to my grandma Bruna for her strength and dignity despite the pain and sorrow that she often encountered in her life.

Last but not least, my deepest gratitude goes to my relentless wife, Giulia, who supported me in the decision to start a PhD abroad even though it meant to stay apart for more than two years. You are my person and believe in me more than anybody else. Thank you for your unconditional love and patience in these seven years. I will always be grateful for the baby you are carrying in your womb.

As an African adage says: “If you want to go fast, go alone. If you want to go far, go together”. I would not have gone this far without all of you.
Thank you,

Milano, October 2022

Paolo

CURRICULUM VITÆ

Paolo Francesco SCARAMUZZINO

18-10-1991 Born in Melito di Porto Salvo (RC), Italy.

EDUCATION

2017-2022 PhD. Aerospace Engineering (Double Degree)
Delft University of Technology and Politecnico di Milano
Thesis: Flight Simulator Transfer of Training Effectiveness in Helicopter Maneuvering Flight
Promotors: Dr. M.D. Pavel, Prof. dr. G. Quaranta
Copromotor: Dr. D.M. Pool

2013-2016 MSc. Aerospace Engineering (Double Degree)
Politecnico di Milano and Politecnico di Torino
Thesis: Multidisciplinary High-Fidelity Optimization of a Transport Aircraft through Mesh Morphing
Supervisor: Prof. dr. G. Quaranta

2010-2013 BSc. Aerospace Engineering
Politecnico di Milano

RECENT WORK EXPERIENCE

2022-ongoing Flight Mechanics Engineer
Leonardo Helicopter Division
Activities: Rotorcraft sizing and performance evaluation, flight data analysis, rotorcraft model development and validation, handling quality analysis

2018 Research Intern
Max Planck Institute for Biological Cybernetics
Activities: Worked on the assessment of the effectiveness of a computer-based simulator for initial hover training

2016-2017 Structural Engineer
iChrome
Activities: Manage and support FEM numerical analysis

LIST OF PUBLICATIONS

7. **Scaramuzzino, P. F.**, Pool, D. M., Pavel, M. D., Strosma, O., Mulder, M., and Quaranta, G. (to be submitted). Investigation of the Effects of the Rotorspeed Degree of Freedom on Helicopter Flight Dynamics in Autorotation. *Journal of Guidance, Control, and Dynamics*.

6. **Scaramuzzino, P. F.**, Pool, D. M., Pavel, M. D., Strosma, O., Mulder, M., and Quaranta, G. (to be submitted). Autorotation Transfer of Training: Effects of Helicopter Dynamics. *Journal of the American Helicopter Society*.

5. **Scaramuzzino, P. F.**, Pavel, M. D., Pool, D. M., Strosma, O., Mulder, M., and Quaranta, G. (2022). Effects of Helicopter Dynamics on Autorotation Transfer of Training. *Journal of Aircraft*, 59(1):73-88. https://doi.org/10.2514/1.C036217.

4. **Scaramuzzino, P. F.**, Pavel, M. D., Pool, D. M., Strosma, O., Mulder, M., and Quaranta, G. (2021). Rotorcraft Safety: A Simulator-based Training Perspective. In *47th European Rotorcraft Forum (ERF 2019)*, number 58, Virtual, September 7-10, 2021. RAeS.

3. **Scaramuzzino, P. F.**, Pavel, M. D., Pool, D. M., Strosma, O., Mulder, M., and Quaranta, G. (2019). Investigation of the Effects of Autorotative Flare Index Variation on Helicopter Flight Dynamics in Autorotation. In *45th European Rotorcraft Forum (ERF 2019)*, number 89, pages 893–906, Warsaw, Poland, September 17-19, 2019. PSAA.

2. **Scaramuzzino, P. F.**, D'Intino, G., Geluardi, S., Pavel, M.D., Pool, D.M., Strosma, O., Mulder, M., and Bülthoff, H. H. (2018). Effectiveness of a Computer-Based Helicopter Trainer for Initial Hover Training. In *44th European Rotorcraft Forum (ERF 2018)*, number 79, pages 1142–1156, Delft, Netherlands, September 18-20, 2018. NVvL.

1. Morelli, M., Ghiasvand, S., Nabi, H. N., Taymourtash, N., Masarati, P., Quaranta, G., Barakos, G., Fasiello, S., Huercas, S., White, M., Akel, E., Yu, Y., Friesen, D., **Scaramuzzino, P. F.**, and Pavel, M. D. (2018). Assessment of the Feasibility of an Extended Range Helicopter Operational Standard for Offshore Flights. In *44th European Rotorcraft Forum (ERF 2018)*, number 171, pages 1083–1089, Delft, Netherlands, September 18-20, 2018. NVvL.